Fakultät für Mathematik, Informatik und Naturwissenschaften | RWTH AACHEN UNIVERSITY

Ultrasound-induced Polymer Mechanochemistry Enabling Molecule Release

Von der Fakultät für Mathematik, Informatik und Naturwissenschaften der RWTH Aachen University zur Erlangung des akademischen Grades eines Doktors der Naturwissenschaften genehmigte Dissertation

vorgelegt von

Jilin Fan, M.Sc.

Aus

Anhui, China

Berichter: Universitätsprofessor Dr. rer. Nat. Andreas Herrmann

Universitätsprofessorin Dr.-Ing. Laura De Laporte

Tag der mündlichen Prüfung: 18.06.2025

Eidesstattliche Erklärung

Declaration of Authorship

I, *Jilin Fan*

declare that this thesis and the work presented in it are my own and has been generated by me as the result of my own original research.

Hiermit erkläre ich an Eides statt / I do solemnely swear that:

1. This work was done wholly or mainly while in candidature for the doctoral degree at this faculty and university;

2. Where any part of this thesis has previously been submitted for a degree or any other qualification at this university or any other institution, this has been clearly stated;

3. Where I have consulted the published work of others or myself, this is always clearly attributed;

4. Where I have quoted from the work of others or myself, the source is always given. This thesis is entirely my own work, with the exception of such quotations;

5. I have acknowledged all major sources of assistance;

6. Where the thesis is based on work done by myself jointly with others, I have made clear exactly what was done by others and what I have contributed myself;

7. None of this work has been published before submission. or Parts of this work have been published before as:

   [1]. **Jilin Fan**, Mingjun Xuan, Pengkun Zhao, Mark Loznik, Junlin Chen, Fabian Kiessling, Lifei Zheng*, Andreas Herrmann*. Ultrasound responsive microcapsules for antibacterial nanodrug delivery. *Nano Res.* 2023, *16*, 2738-2748.
   [2]. **Jilin Fan**, Kuan Zhang, Mingjun Xuan*, Xiang Gao, Rostislav Vinokur, Robert Göstl, Lifei Zheng*, Andreas Herrmann*. High-Intensity Focused Ultrasound-Induced Disulfide Mechanophore Activation in Polymeric Nanostructures for Molecule Release. *CCS Chem.* 2024, *6*, 1895-1907.
   [3]. **Jilin Fan**, Mingjun Xuan*, Kuan Zhang, Rostislav Vinokur, Lifei Zheng, Robert Göstl, Andreas Herrmann*. Accelerated Mechanophore Activation and Drug Release in Network Core-structured Star Polymers Using High-Intensity Focused Ultrasound. *Small Science*. 2024, *4*, 2400082.

date

signature

INSPIRING QUOTES

Contentment is the only real wealth.

---Alfred Bernhard Nobel (1833.10 - 1896.12)

An experiment is a question which science poses to Nature, and a measurement is the recording of Nature's answer.

---Max Karl Ernst Ludwig Planck (1858. 4 - 1947.10)

You never fail until you stop trying.

---Albert Einstein (1879.3 - 1955.4)

ACKNOWLEDGMENTS

I arrived in Aachen in October 2018, my first time abroad. At that time, everything around me was strange. I still remember the curious emotion. I was on a bus alone, surrounded by strangers. I am nervous when I go shopping in the supermarket. By now, I have spent five and a half years in Aachen. There is no doubt that Aachen is my second hometown. I love Aachen, an ancient, multicultural and friendly city. Here, I would sincerely thank the people who helped and supported me in the long and unforgettable PhD study journey.

First of all, I want to thank my supervisor **Prof. Andreas Herrmann**. You gave me the opportunity to study in Germany. This study journey made me understand another country, another culture besides China. To some extent, you changed the trajectory of my life. I am grateful for working in your group. In addition, you and your life experience encouraged me a lot. Your indomitable spirit encourages me to fight in life and work. From you, I see the meaning of hard work. I believe this will benefit me in my future life. Moreover, thanks for your help on my research work; you guided me into the field of polymer mechanochemistry. In the microbubble project, your suggestions pushed me to finish the synthesis of the compounds. Your insistence on 'frequency selective mechanophore activation' has infected me; I hope we could get good data in the next step. At last, I wish you and your family all the best in the future life.

I would like to thank my second supervisor, **Prof. Dr.-Ing. Laura De Laporte**, for giving suggestions to my projects and taking the time to review my PhD thesis.

I would also like to thank **Prof. Robert Göstl** for helping me improve the writing of my manuscripts. Your constructive and professional suggestions impressed me a lot. I believe there will be more results in our future cooperation. I wish you a big success in your future work.

Next, I would like to thank **Prof. Lifei Zheng** for helping me start my research work at the end of 2018. You guided my work on the right track. You are a smart and friendly daily supervisor. You helped me revise the manuscript and gave me many helpful suggestions. I wish you all the best in your future life.

I would like to express my sincere gratitude to **Prof. Mingjun Xuan** for your help during my PhD study. When I have questions, you always take the time to communicate with me. You are the person who has given me the most suggestions. You made me feel that every problem we encountered in our experiment would be solved. Thanks for your encouragement when my experiments were not going well. You taught me how to operate the microfluidic system. I can't complete the microbubble project without your help. You like a friend or big brother, guided me forward. I hope you are doing well in Wenzhou.

Thanks to all my colleagues. **Prof. Shuaidong Huo**, you showed me how to prepare the vancomycin-modified gold nanoparticles. Thanks for your help. I wish you a big success in your future work. **Dr. Ming Luo**, your optimistic attitude impressed me deeply. I hope you doing well in Shenzhen. **Dr. Pengkun Zhao**, you helped me perform the IC_{50} assay in the microcapsule project. You taught me to do the experiments in the S2 Bio lab. I wish you all the best in your future life. **Dr. Yu Zhou**, you are a hard-working person. Usually, we are the last two people to leave the lab at night. You helped me prepare ferritin for the magnetic induction heating project. I am deeply impressed by your professional knowledge and proficient operating skills. I hope you doing well in Finland. **Dr. Miancheng Zou**, you are a smart man. You helped me a lot in the microgel project. Moreover, I

have a lot of fun playing games with you. I hope you and your wife have a wonderful life in Shanghai. **Dr. Xintong Yang**, you have travelled to many places in Europe. You told us many interesting things you encountered. You know a lot about European history and culture. We went to Turkey and Greece together, two very happy journeys. **Dr. Hongyan Li**, we worked together on the TEM measurements. Thank you for helping me with my work. **Dr. Zhiyuan Shi**, thanks for your help. When I first arrived in Aachen, you picked me up at the train station. Your work in polymer mechanochemistry benefits me a lot. I hope you are doing well at Tianjin University. **Weiyan**, we almost joined Herrmann's group at the same time. We travelled together to Greece and Turkey; you told me a lot about ancient Greek history. Wish you all the best in the future. **Qi**, you arrived at Aachen two months later than me. Your mahjong brings us a lot of fun. Good luck with your graduation defence. **Xiang**, we drank a lot when we first met. You have an optimistic attitude. You helped me measure samples and collect the data for ESI-MS. I hope you are doing well in Zhengzhou. **Kuan**, thanks for helping me draw the figures. You work hard and efficiently. I hope your projects going well. **Dr. Chaolei Hu**, thank you for teaching me how to operate DLS device. I wish you a big success in your future work. **Dr. Xin Li**, I borrowed many chemicals from you. Thanks for your generosity. I hope you doing well at Tongji University. Thanks to **Zhiyuan Cui**, you synthesized several compounds for me in your two months of internship research. You are a nice guy. Good luck with your graduation internship. Thanks to **Junlin**, we worked together to prepare the microbubbles. You spent precious time on our cooperation projects. I gained a lot from working with you. **Dr. Chuanjiang He**, you were kind enough to teach me how to operate the HIFU system. Thanks for your help. I wish you all the best. **Dr. Xiaolong Zeng**, we graduated from the same University in Guangzhou. Thank you for sharing your experience in Germany. I wish you and your wife a happy life in Germany. **Xiaofeng**, you shared many interesting stories at the parties. I hope your projects going well. **Zhiling**, you arrived in Aachen for half a year. I hope you have a colorful life in Europe. **Ke**, you are an optimistic and enthusiastic girl. I hope you can maintain your interest in scientific research. **Hongyu**, thanks for sharing your experience in Guangzhou. I hope you are doing well in your work. **Oliver**, thanks for building the microfluidic system. **Matthias**, we worked together on the SFB C9 project. I learned a lot from you. **Metin**, we worked together for around 1 year. I learned new knowledge about diamond-based DNA detection from you. **Ahmed**, thanks for helping me measure the samples and collect the AFM data. **Rostislav**, thanks for building the HIFU system. Your comments on the manuscript benefit me a lot. **Mark**, you helped me order hundreds of chemicals. You are a qualified lab manager. No one can achieve success without your help and dedication. I wish you all the best.

Moreover, I would like to thank **Dustin**, **Deniz**, **Aman**, **Tina**, **Fahimeh**, **Bruke**, **Cuba**, **Milara**, **Philippe**, **Wolfgang**, **Melina**, **Johannes**, **Marcus**, **Thomas**, **Diptendu**, **Deepanshu**, **Fabian**, **Christiane**, **Siyang**, **Xinpei**, **Gurudas**, **Arjuna**, and all the members in our group for supporting me in the past years. The wonderful memories with all of you in Aachen will be my precious treasure.

Thanks to **Ding**, **Hao**, **Xiyang**, **Zhanqi**, **yuting**, **Jie**, **Ting**, **Zibin** and **Yujiang** for the unforgettable experience you give me. I enjoyed a colorful life with you all. Thanks to all the friends in Aachen.

I would also thank **Yan Xu** and **Chen Li**, my friends in China, you guys helped me a lot when I went abroad. I wish you all the best in your future life. Thanks to all my friends in China.

I wish to thank my family for supporting me in studying abroad. Thanks to my parents, I cannot achieve this without your love and support. Dad, you are my life mentor. Mom, you are my guardian angel. Thanks to my brother and sister for taking care of our parents.

Finally, I want to thank **Xiaoya**, my beloved girlfriend and my other half, for your companionship, understanding and support, which enabled me to complete my studies. When I was lonely, you were there. When I was lost, you were there. When I was depressed, you were there. You told me that there is no conflict between loving whom I want to love and doing what I want to do. I am very grateful to have you in my life. I love you so much.

Thanks to all the people who gave me kind, support and encouragement.

SUMMARY

In polymer mechanochemistry, ultrasound (US) has become a highly effective and commonly used tool to induce mechanochemical transformations in solutions. In addition, the non-invasive nature and precise spatiotemporal control render ultrasound-induced mechanochemistry attractive for biomedical applications. In recent years, the rapid developments in US-induced activation of prodrugs (Sonophamacology) have opened a new era of polymer mechanochemistry. However, the ultrasonication experiments in polymer mechanochemistry studies were commonly conducted by high intensity 20 kHz ultrasound. Low-frequency (20 kHz) ultrasound can generate strong cavitation, and operated at high acoustic pressures that are toxic to cells and tissues.

During my PhD study, I explored biocompatible ultrasound-responsive polymer systems for molecule release. The polymer architecture is an important parameter that influences the bond scission and degradation rates of polymers. Based on the exploration of different polymer architectures, I developed four biocompatible ultrasound-responsive polymer systems, namely polymeric microcapsules, network core-structured star polymers (NCSPs), polymeric microgels and polymeric microbubbles.

In **Chapter 1** of this thesis, mechanical stimuli-induced polymer mechanochemistry is reviewed. Then, the background of ultrasound is introduced and ultrasound-induced bond scission in polymers are described. Next, I summarized the recent decade's achievements in ultrasound-induced polymer mechanochemistry.

In **Chapter 2**, polymeric microcapsules as protection shells or cages to inhibit the activity of drugs. Before sonication, the polymer shell is intact and stops the drug release from microcapsules, hence, the activity of drugs is suppressed. After US sonication, the polymer shell consisting of ionic bonds is destroyed and polymer chain scission occurs. The released drug then exerts its bioactive properties. This strategy for controlling the activity of drugs is a method based on physical isolation of the drugs to the target.

In **Chapters 3**, **4**, and **5**, the molecules or drugs were covalently loaded in the polymer architectures, and ultrasound-induced molecule or drug release are based on mechanophores activation. In **Chapter 3**, I prepared Network Core-Structured Star Polymers (NCSPs) containing multiple disulfide mechanophores by reversible-addition-fragmentation chain-transfer (RAFT) polymerization. 1.5 MHz high-intensity focused ultrasound (HIFU) was applied to verify the mechanochemical responsivity of NCSPs. Over 60% of disulfide mechanophores were activated within 60 minutes of sonication. Importantly, mechanophore-free network core-structured star polymers (FNCSPs) as control sample showed a low degradation rate of polymers, which indicates the significant influence of the mechanophores on mechanochemical bond scission. In addition, as a comparison, HIFU-induced mechanophore activation from linear polymers was not observed. In **Chapter 4**, I presented the preparation of microgels (MGLs) containing disulfide mechanophores, as well as inactive fluorescent probes (umbelliferone, UMB) or a small molecule drug (Camptothecin, CPT). Upon HIFU irradiation, the disulfide mechanophores undergo bond scission, generating free thiols. Then, the thiols activate a carbonate unit within the polymer scaffolds through thiol-disulfide exchange and intramolecular cyclization, resulting in the release of UMB or CPT. In **Chapter 5**, I presented a polymeric microbubbles (PMBs) system. The PMBs consist of an N_2 gas-core and a polymer shell, which was produced in a double emulsion (gas in oil in water) microfluidic chip. The mechanophores were covalently incorperated into the polymer shell. Upon US irradiations, the PMBs burst accompanied by the mechanophore activation. In this chapter, we demonstrated US

remote-controlled versatile mechanochemical transformations in PMBs. The first two strategies are based on disulfide mechanophore activation, the third approach illustrated the US-triggered release of fluorogenic molecules from the masked furfuryl carbonate through retro Diels-Alder reaction. In the fourth approach, we demonstrated fluorophore release via US-induced “Flex-activation”.

In summary, we have developed four biocompatible ultrasound-responsive polymer systems, which were successfully used for molecule or drug release under megahertz HIFU irradiation. We further investigated the cytotoxic effects of the released drug and its potential for therapy by cell proliferation assays. This thesis demonstrates the potential of megahertz HIFU-responsive polymer systems for molecules or drug release based on mechanochemical transformations. Overall, the utilization of HIFU as a stimulus to activate drugs in our polymer systems represents an important step for exploiting polymer mechanochemistry applied in biomedicine.

ZUSAMMENFASSUNG

In der Polymermechanochemie hat sich Ultraschall (US) zu einem äußerst effektiven und häufig verwendeten Werkzeug entwickelt, um mechanochemische Polymerumwandlungen in Lösung herbeizuführen. Darüber hinaus bergen die nichtinvasive Natur und die präzise räumlich-zeitliche Steuerung die durch Ultraschall induzierte Mechanochemie großes Potential für biomedizinische Anwendungen. In den letzten Jahren haben die rasanten Entwicklungen der US induzierten Aktivierung von Prodrugs (Sonopharmakologie) eine neue Ära der Polymermechanochemie eingeleitet. Die Ultraschallexperimente in Studien zur Polymermechanochemie wurden jedoch üblicherweise mit 20-kHz-Ultraschall der eine hohe intensitätaufweist durchgeführt. Niederfrequenter (20 kHz) Ultraschall kann starke Kavitation und die Bildung von flüssigen Mikrojets erzeugen, was für biologische Systeme ungünstig ist.

Während meiner Doktorarbeit habe ich versucht, biokompatible, ultraschallreaktive Polymersysteme für die Molekülfreisetzung oder Sonopharmakologie zu entwickeln. Dabei stellt die Polymerarchitektur einen wichtigen Parameter dar, der die Bindungsspaltung und Abbauraten von Polymeren beeinflusst. Basierend auf der Erforschung der Polymerarchitektur habe ich vier biokompatible, ultraschallreaktive Polymersysteme entwickelt, nämlich Polymermikrokapseln, sternförmige Polymere mit Netzwerkkernstruktur (NCSPs), Polymermikrogele und Polymermikrobläschen.

In **Kapitel 1** dieser Arbeit wurde zunächst die durch mechanische Stimuli induzierte Polymermechanochemie zusammengefaßt. Anschließend wird der Hintergrund von Ultraschall und ultraschallinduzierter Bindungsspaltung in Polymeren vorgestellt. Als Nächstes werden die Erfolge der letzten Dekade in der ultraschallinduzierten Polymermechanochemie beschrieben.

In **Kapitel 2** werden polymere Mikrokapseln als Schutzhüllen oder Käfige hergestellt, um die Wirkung von Medikamenten zu hemmen. Vor der Ultraschallbehandlung ist die Polymerhülle intakt, was die Freisetzung von Medikamenten aus den Mikrokapseln verhindert und deren Wirkung unterdrückt. Nach der Ultraschallbehandlung wirde die Polymerhüll die durch ionische Bindungen stabilisiert wird, zerstört. Die freigesetzten Medikamente entfalten dann ihre medizinischen Eigenschaften. Diese Strategie zur Kontrolle der Aktivität von Medikamenten basiert auf physikalischer Isolierung.

In den **Kapiteln 3**, **4** und **5** werden die Moleküle oder Medikamente kovalent in die Polymer architekturen inkorporiert, und die durch Ultraschall induzierte Freisetzung von Molekülen oder Medikamenten basiert auf der Aktivierung von Mechanophoren. In **Kapitel 3** haben wir Netzwerkkernstrukturierte Sternpolymere (NCSPs) mit mehreren Disulfid-Mechanophoren durch reversible Additions-Fragmentierungs-Kettenübertragungspolymerisation (RAFT) hergestellt. Zur Überprüfung der mechanochemischen Reaktionsfähigkeit der NCSPs wurde hochintensiver fokussierter Ultraschall (HIFU) mit 1.5 MHz angewendet. Über 60% der Disulfid-Mechanophore wurde innerhalb von 60 Minuten Ultraschallbehandlung aktiviert. Wichtig ist, dass Mechanophor-freie Netzwerkkernstrukturierte Sternpolymere (FNCSPs) als Kontrollproben eine niedrige Abbaurate der Polymere zeigten, was auf den signifikanten Einfluss der Mechanophore auf die mechanochemische Bindungsspaltung hindeutet. Darüber hinaus wurde im Vergleich dazu keine HIFU-induzierte Aktivierung von Mechanophoren bei linearen Polymeren beobachtet. In **Kapitel 4** wird die Herstellung von Mikrogelen (MGLs) vorgestellt, die Disulfid-Mechanophore sowie inaktive Fluoreszenzsonden

(Umbelliferon, UMB) oder ein niedermolekulares Arzneimittel (Camptothecin, CPT) enthalten. Bei HIFU-Bestrahlung werden die Disulfid-Mechanophore gespalten, wodurch freie Thiole entstehen. Anschließend aktivieren die Thiole durch Thiol-Disulfid-Austausch und intramolekulare Zyklisierung eine Carbonateinheit innerhalb der Polymergerüste, was zur Freisetzung von UMB oder CPT führt. In **Kapitel 5** wird ein System aus polymeren Mikrobläschen (PMBs) beschrieben. Die PMBs bestehen aus einem N_2-Gaskern und einer Polymerhülle, die in einem Mikrofluidchip mit doppelter Emulsion (Gas in Öl in Wasser) hergestellt wurde. Die Mechanophore wurden kovalent in die Polymerhülle inkorporiert. Bei US-Bestrahlung platzen die PMBs, begleitet von der Aktivierung der Mechanophore. In diesem Kapitel haben wir US-ferngesteuerte, vielseitige mechanochemische Transformationen in PMBs anhand von vier Strategien demonstriert. Die ersten beiden Strategien basieren auf der Aktivierung von Disulfid-Mechanophoren, der dritte Ansatz veranschaulicht die US-ausgelöste Freisetzung fluoreszierender Moleküle aus dem maskierten Furfurylcarbonat durch eine Retro-Diels-Alder Reaktion. Im vierten Ansatz demonstrierten wir die Fluorophorfreisetzung durch US-induzierte „Flex-Aktivierung“.

Zusammenfassend wurden vier biokompatible, ultraschallreaktive Polymersysteme entwickelt, die erfolgreich zur Freisetzung von Molekülen oder Medikamenten unter Megahertz-HIFU-Bestrahlung eingesetzt wurden. Wir untersuchten außerdem die zytotoxischen Effekte des freigesetzten Medikaments und sein therapeutisches Potenzial durch Zellproliferationstests. Diese Arbeit zeigt das Potenzial von Megahertz-HIFU-reaktiven Polymersystemen zur Freisetzung von Molekülen oder Medikamenten auf der Grundlage mechanochemischer Transformationen. Insgesamt stellt die Verwendung von HIFU als Stimulus zur Aktivierung von Medikamenten in unseren Polymersystemen einen wichtigen Schritt zur Nutzung der Polymermechanochemie in der Biomedizin dar.

CONTENTS

1. Introduction

1.1 Mechanical stimuli-induced polymer mechanochemistry

Polymers are widely used in consumer products, packaging, coatings, medical devices, electronics, and engineering composites due to their strength, flexibility, and ease of processing. Understanding how external forces affect polymers' stability and mechanical performance is an interesting and important area of polymer research, and this could help determine their performance in use. Stimulus-responsive polymers, which exhibit specific response to physical or chemical triggers, have attracted growing interest.[1-4] Recently, external stimuli-responsive polymers have been well studied, polymers properties were altered in response to light,[5–7] heat,[5,8] pH,[4,8–10] or redox potential[4,11,12].

The chain-like nature of polymers is ideal for the instantaneous accumulation of mechanical energy along the backbone. This behavior has led to mechano-responsive polymers that harness mechanical energy to drive chemical transformations. The response of polymeric materials to mechanical forces may range from simple conformational changes to bond bending and bond stretching deformations. If enough force is applied, bond breaking occurs and mechanical properties are compromised.

In industrial production, mechanical stimuli-induced polymer mechanochemistry has broad relevance for various applications. Rubber mastic coating, polymer injection moulding, and fiber drawing are all closely related to mechanochemistry.[13-14] In academic research, polymer mechanochemistry induced by mechanical stimulation has been applied in fields such as catalysis,[15–16] synthesis,[17] sensing,[18-19] damage detection,[20-21] surface patterning,[22-23] and drug delivery.[24-27]

1.1.1 History of polymer mechanochemistry

Staudinger and his colleagues first investigated the molecular response of polymers to mechanical stress in 1934. They described the reduction of the molecular weight of polystyrene under the action of a high-speed ball milling or turbid flow.[28–30] Early studies in the field of polymer mechanochemistry are mainly focused on the mechanochemical degradation of polymers.

Following Staudinger's work, Encina and co-workers found that relatively weak O-O bonds (bond dissociation energy ~150 kJ mol^{-1}) incorporated in the polymer backbone were preferentially broken over the more abundant C-C bonds (bond dissociation energy ~376 kJ mol^{-1}).[31-32] This exciting discovery highlight that the location and products of mechanochemical reactions can be precisely programmed by the structural design of polymers. It offers the possibility of achieving a transformation from mechanical energy to chemical energy at the molecular level. Notably, Encina's work also reveals a key distinction between mechanochemical transformations and mechanically induced physical transformations, emphasizing that understanding the atomic fundamentals is essential to unlocking the full potential of polymer mechanochemistry. Then, continued study by researchers, the field of polymer mechanochemistry emerged, along with a renewed focus on more refined perspectives and novel terminology.

In the early 2000s, researchers reported the site-specific bond cleavage in polymers, highlighting the potential to manipulate the polymer mechanochemistry through the strategic placement and design of functional groups. These groups were thought to undergo covalent transformations induced by mechanical forces that go beyond simple homolytic bonds cleavage in polymers. Moore and co-workers first introduced the term "mechanophore"

to describe the force-sensitive molecular unit.[33] Mechanophores have mechanically labile bonds that undergo chemical transformations when incorporated into mechanically stressed polymers.

From the 2000s, Moore, Craig, and other researchers have made many breakthroughs in polymer mechanochemistry. These studies encompass the utilization of mechanical forces to uncover forbidden reaction pathways[34] or prolong the lifespan of diradical intermediates[35]. Boulatov's work exemplifies the significance of molecular restoring force, as opposed to strain energy, in modulating the reaction barriers within stretched macromolecules.[36] This pioneering research significantly contributed to the advancement of mechano-responsive materials and heralds a new epoch in the field of polymer mechanochemistry.

In recent years, advancements in polymer mechanochemistry have primarily concentrated on two key areas: (i) the design and synthesis of mechanophores for diverse applications, including stress sensing, catalysis, and self-healing, and (ii) the investigation of polymer structures that enable the efficient conversion of mechanical force into chemical transformations.

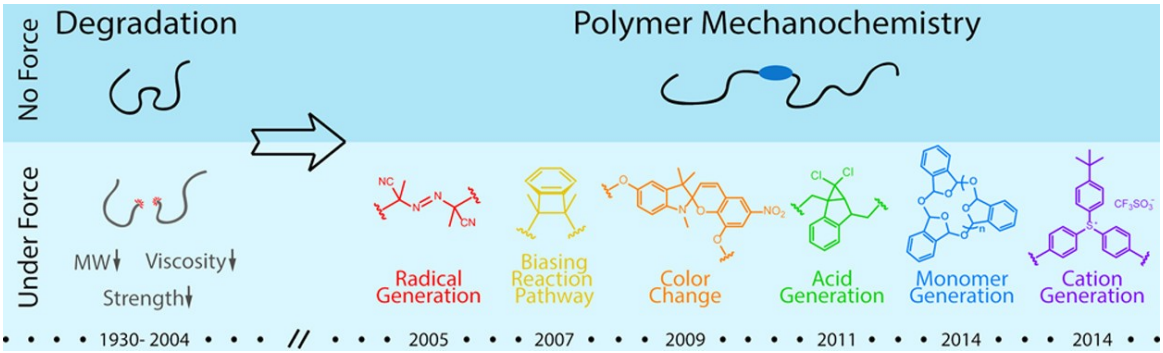

Figure 1. Historical perspective on the development of polymer mechanochemistry. Adapted from ref. 22. Copyright © 2015 American Chemical Society.

1.1.2 Compression and tension-induced polymer mechanochemistry

Over the past decade, the study of mechanical force-triggered chemical transformations in polymeric materials has advanced significantly. By incorporating the mechanophore at specific points along the polymer chain, researchers have explored the use of compression or tension as mechanical stimuli to induce polymer mechanochemistry for applications such as sensing, catalysis, and molecular release.

Among the developments in polymer mechanochemistry, mechanochromophores have been designed as damage sensors in polymeric materials and composites, exhibiting color responses upon the direct formation of chromophores after compression or tension stimuli. This color change in polymers allows for rapid visual assessment of materials under high strain. Notably, the spiropyran mechanophore has been reported as a molecular force sensor, enabling visible detection and mapping of mechanical stresses within bulk polymeric materials.[37-38] Researchers, including Moore, Sottos, and their collaborators, have developed mechanoresponsive synthetic polymeric materials by directly integrating spiropyran mechanophores into the polymer chains of bulk polymers or by using these mechanophores as cross-linkers (**Figure 2**). Representative images of active PMA-1-PMA samples undergoing cyclic loading, as shown in **Figure 2e**, demonstrate the appearance of a red color with increasing plastic deformation. Control structures were prepared to determine whether the observed color change was dependent on the specific linking through the 'spiropyran-junction' or was influenced by other factors such as localized heating or radical generation from polymer chain cleavage during mechanical deformation. The

absence of activation in the control samples strongly indicates that the color change is exclusively due to the application of mechanical force, rather than the influence of temperature changes or photolytic activation.

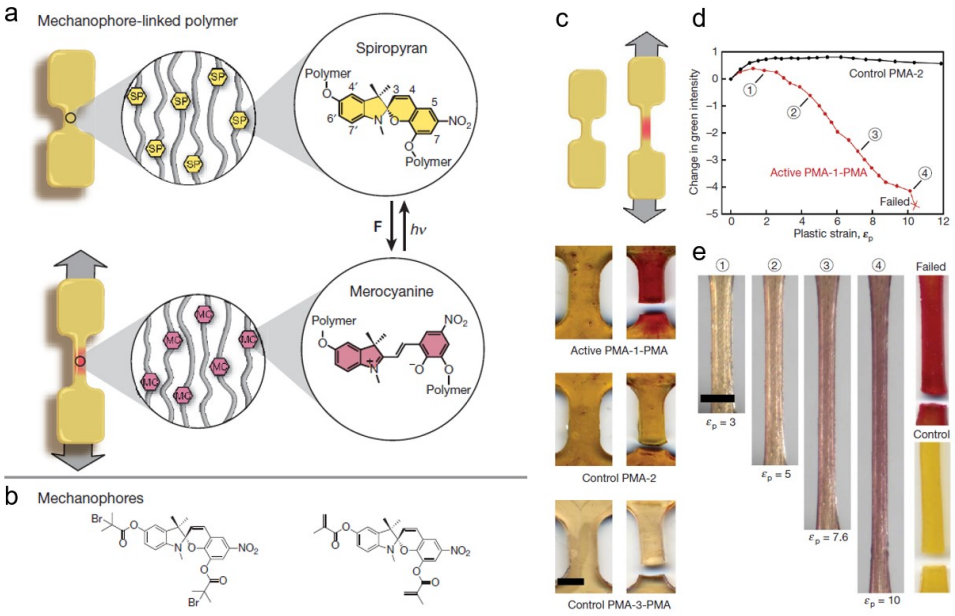

Figure 2. Mechanochromic response of spiropyran-linked PMA elastomer under tensile loading. Adapted from ref. 37. Copyright © 2009 Macmillan Publishers Limited.

Göstl and Sijbesma reported the synthesis of π-extended anthracenes that can be released from their respective maleimide Diels–Alder adducts upon the application of mechanical stress in the solid state (**Figure 3**).[39] This π-extension of anthracenes, and their integration into mechanochemically active Diels-Alder adducts, has proven to be a highly effective approach for enhancing stress-reporting optical probes compared to bare anthracene. The novel π-extended anthracenes exhibit excellent fluorescence quantum yields, low oxygen sensitivity, and red-shifted absorption and emission spectra.

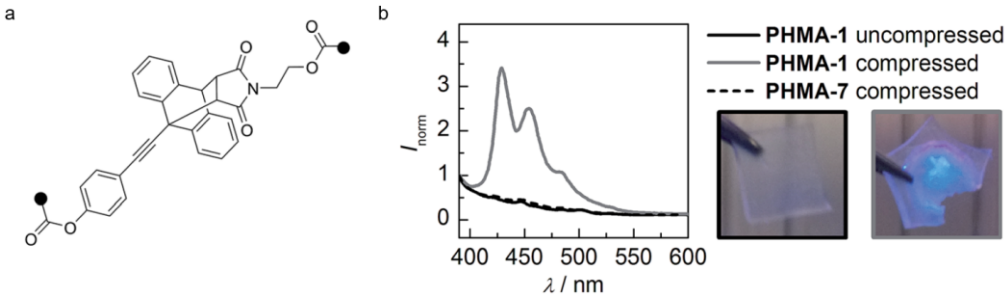

Figure 3. The mechanochemical study of Diels–Alder adduct of π-extended anthracenes. Adapted from ref. 39. Copyright © 2016 The Royal Society of Chemistry.

The Robb research group developed a mechanophore based on a masked donor–acceptor Stenhouse adducts (DASA) precursor, which facilitates a mechanically gated multicolour chromogenic response in polymeric materials.[40] Application of mechanical force, such as compression in solid materials, triggers a retro-Diels–Alder reaction in the polymers, revealing an activated furan species. Subsequent reaction with a secondary amine results in the formation of an intensely colored DASA photoswitch. Importantly, the chromogenic response critically depends on the specific secondary amine used, enabling the generation of a variety of DASAs with diverse photophysical and photochemical properties from a single mechanophore (**Figure 4**).

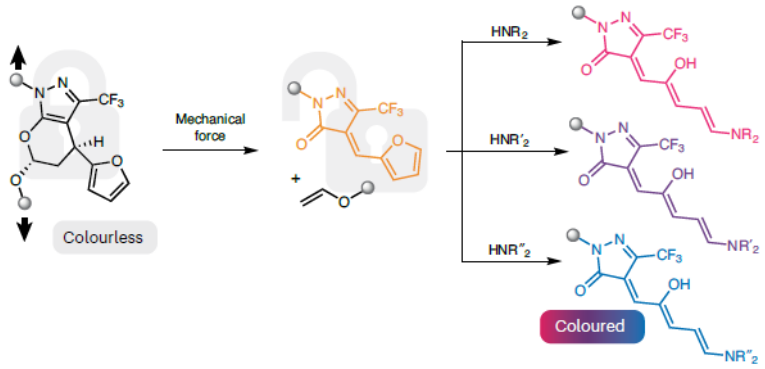

Figure 4. The formation of mechanically gated DASA (multicolor chromism). Adapted from ref. 40. Copyright © 2023 Springer Nature Limited.

They exploit the distinctive reactivity of this system to pioneer the concept of mechanochemical multicolour soft lithography. This approach involves imprinting a complex multicolour composite image into a mechanophore-crosslinked elastomer through a series of localized compression events followed by amine development. This mechanochemical platform offers precise control and flexibility in dye formation using mechanical force, demonstrating significant potential for a wide array of patterning and sensing applications (**Figure 5**).

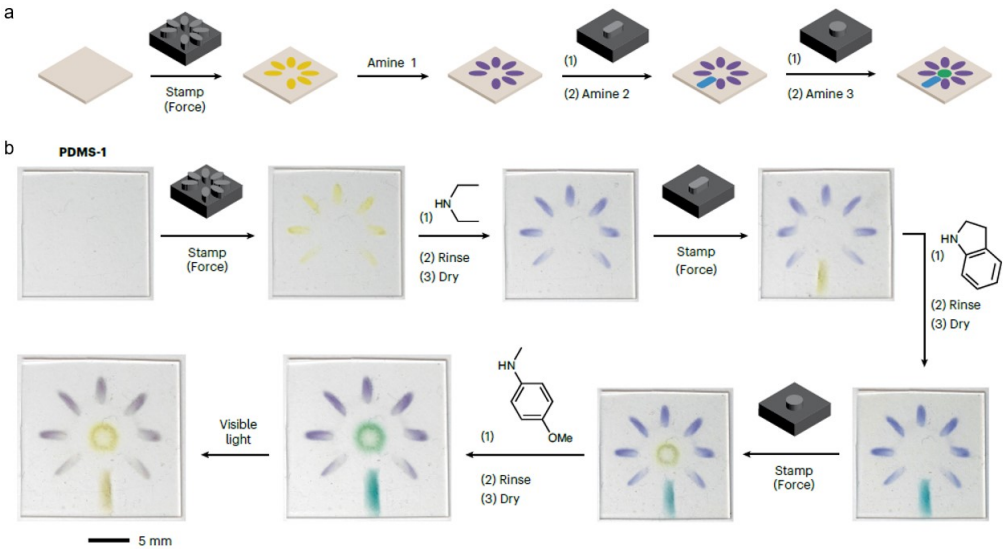

Figure 5. Schematic illustrating the process of mechanochemical multicolor soft lithography, involving iterative localized compression followed by pattern development through DASA formation using a secondary amine. Adapted from ref. 40. Copyright © 2023 Springer Nature Limited.

1.1.3 Ball milling-induced polymer mechanochemistry

Mechanical force induced formation and cleavage of chemical bonds in polymers can be achieved through various experimental methods. Ultrasonication and ball milling of polymeric matrices are two prominent approaches in polymer mechanochemistry. Pulsed ultrasonication in polymer mechanochemistry is noted for its precise control at the microscopic level. In contrast, ball milling protocols exert more pronounced effects at the macroscopic level, such as comminution, amorphization, polymorphic transformations, and even sample melting.[41]

Ball milling techniques exert forces on samples in a stochastic manner, where friction, shearing, and compression dominate over pulling forces. Kobayashi and colleagues investigated the depolymerization of chitin via ball milling, recognizing the impact of both tensile and compressive forces generated by the balls impacting the sample during milling (**Figure 6**).[42]

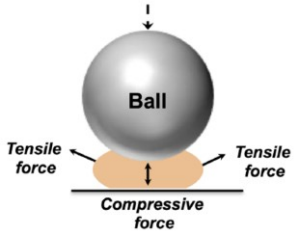

Figure 6. Illustration of the collision between a ball and the solid polymer sample. Adapted from ref. 42. Copyright © 2021 The Owner Societies.

Baytekin et al. demonstrated the application of ball milling to activate mechanophores integrated within polymers. They showed that ball milling of cross-linked polyacrylate polymer 1 could induce the release of singlet oxygen from anthracene–endoperoxide mechanophores (**Figure 7a**).[43] In 2021, Otsuka and colleagues incorporated a bis(9-methylphenyl-9-fluorenyl) peroxide mechanophore into glassy and rubbery polymeric networks such as poly(butyl methacrylate) and poly(hexyl methacrylate).[44] Treatment of polymeric material 2 in a mixer mill (**Figure 7b**) triggered mechanical homolytic fragmentation of the O-O peroxide bond in BMPF units, releasing fluorescent 9-fluorenone (3) via β-scission.

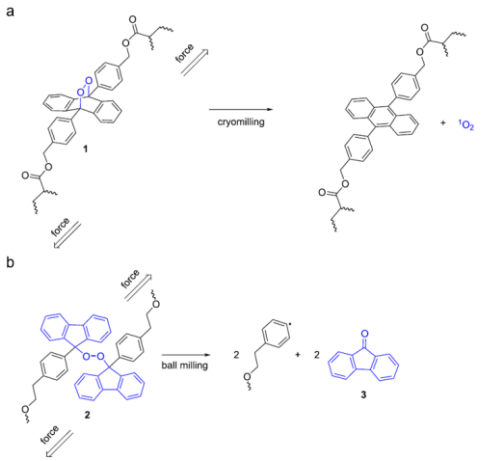

Figure 7. **a**) Activation of the anthracene–endoperoxide mechanophore in polyacrylate polymer 1 through cryo-milling in a mixer mill. Adapted from ref. 43. Copyright © 2020 The Royal Society of Chemistry. **b**) Mechanophore activation in the polymer network matrix by ball milling. Adapted from ref. 44. Copyright © 2021 American Chemical Society.

1.1.4 Blade cutting and puncturing-induced polymer mechanochemistry

In contrast to compression and tension, blade-cutting or needle-puncturing processes offer alternative methods for applying conventional forces. The Göstl group developed poly(N-isopropyl acrylamide) (PNIPAAm) hydrogel networks incorporating Diels–Alder adducts of π-extended anthracenes (**Figure 8**).[45] This mechanofluorophore sensitivity enabled the detection of subtle mechanical stresses. Using confocal laser scanning microscopy (CLSM), they conducted an unprecedented analysis to investigate the micro-scale fracture behavior of PNIPAAm hydrogels following mechanical disruption using a simple and readily implementable needle-puncturing method. CLSM images revealed a distinct circular fluorescence pattern in punctured hydrogel samples (**Figure 8d**), while the absence of fluorescence confirmed no mechanical disruption in pristine (non-activated) specimens (**Figure 8c**).

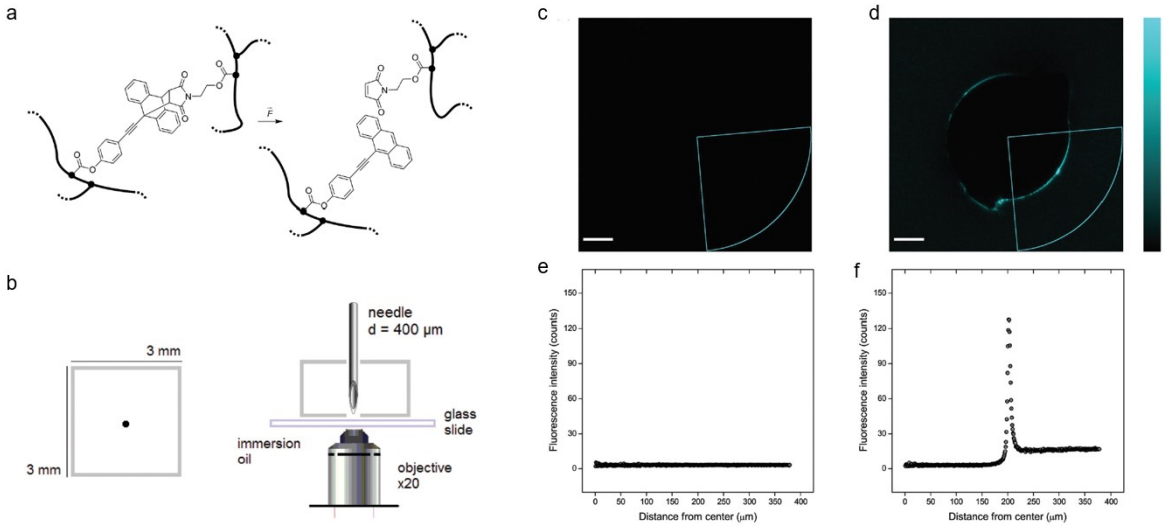

Figure 8. Needle puncturing-induced activation of Diels–Alder adducts from 9-π-extended anthracene and maleimide in a cross-linked polymeric network. Adapted from ref. 45. Copyright © 2020 The Royal Society of Chemistry.

Subsequently, they introduced a novel mechanofluorophore based on Diels–Alder adducts of π-extended anthracenes and maleimide (**Figure 9**).[46] The central aromatic structure of these optical stress probes was easily modified with dihalide building blocks, enabling access to red-shifted absorption and emission spectra, as well as dual fluorescence capabilities. The mechanically induced bond scission process was qualitatively observed in rubber networks using confocal laser scanning microscopy. Micrographs of the elastomer network precisely localized the expected bond scission events (**Figure 9c**), highlighting the immediate advantage of employing dual fluorescent mechanophores.

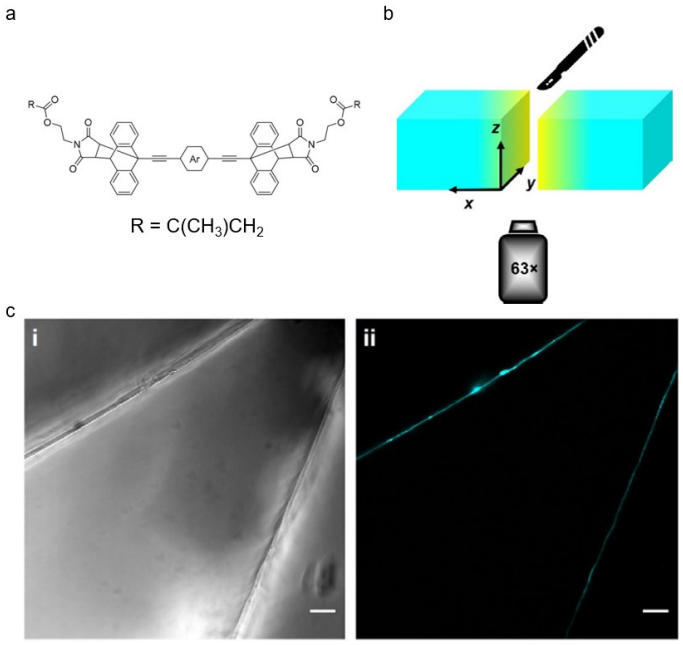

Figure 9. Blade cutting-induced mechanofluorophore activation in elastomer network. Adapted from ref. 46. Copyright © 2021 Wiley-VCH GmbH.

1.1.5 The application of single-molecule force spectroscopy in polymer mechanochemistry

Atomic force microscopy (AFM) enables single-molecule force spectroscopy (SMFS) to investigate mechanochemistry at the molecular level. This technique involves anchoring one end of the target polymer to a silicone substrate and the other end to an AFM tip, as depicted in **Figure 10**. Retracting the tip at a constant velocity generates a force-extension curve that exhibits a characteristic shape for each polymer. Bond rupture typically occurs in the nano-newton range.[47] SMFS offers high resolution down to the pico-newton regime, allowing detailed exploration of how structural and conformational changes in the mechanophore influence the mechanical activation force.

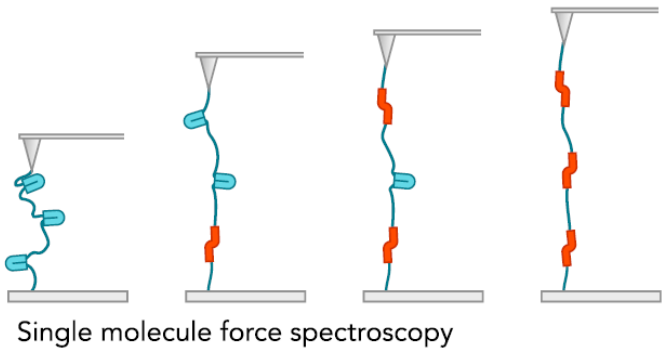

Figure 10. Single-molecule force spectroscopy (SMFS) to investigate mechanochemistry at the molecular level.

AFM provides detailed insights into the underlying principles of mechanochemistry. For instance, Wang et al. recently demonstrated that the force required to activate an *E*-alkene-substituted *gem*-dichlorocyclopropane (*g*DCC) mechanophore was 0.4 nN lower than that needed for the corresponding *Z*-alkene-substituted mechanophore, occurring at approximately 800 pN (**Figure 11**).[48] The extension along the polymer backbone during the transition from the ground state to the transition state is termed the activation length. Through a

combination of experiments and molecular modeling, these activation lengths were determined to be 1.65 and 1.24 Å for the *E*- and *Z*-alkene-mechanophores, respectively, using density functional theory (DFT), and 1.67 ± 0.05 and 1.20 ± 0.05 Å from single-molecule force spectroscopy (SMFS) experiments. The authors propose that relative to the *Z* isomer, the *E* isomer functions akin to a mechanical lever, offering a greater mechanical advantage for a given applied force. This lever arm effect was initially demonstrated with *g*DCC and *gem*-dibromocyclopropane (*g*DBC) mechanophores integrated into poly(butadiene) (PB) and linear poly(norbornene) (PNB), where changes in the polymer backbone were found to exert a more significant influence on the plateau force compared to halogen substitution within the mechanophore.[49]

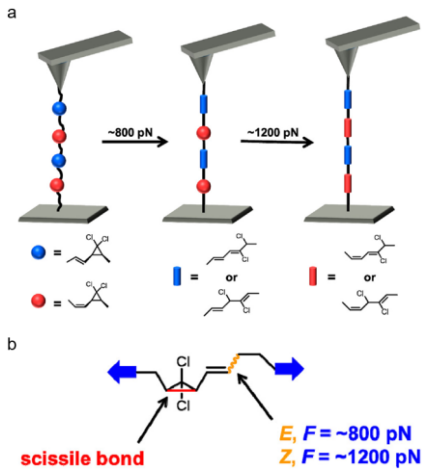

Figure 11. Schematic representation of the SMFS experiment. The *E* (blue) and *Z* (red) α-alkene stereoisomers open in sequential transitions at ~800 and ~1200 pN, respectively. Adapted from ref. 48. Copyright © 2014 American Chemical Society.

Additionally, employing SMFS techniques, Gossweiler et al. discovered that the force necessary to activate two spiropyran (SP) mechanophores was significantly lower than that required for *g*DCC, mentioned above, at approximately 240 pN.[50] The SP mechanophores differed in their regiochemistry, with the anchoring polymer chains attached at different positions within the SP-ring system. Specifically, the isomer linked via the two outermost phenyl rings demonstrated a slightly more difficult opening compared to the isomer connected through one outer phenyl ring and the nitrogen species (**Figure 12**).

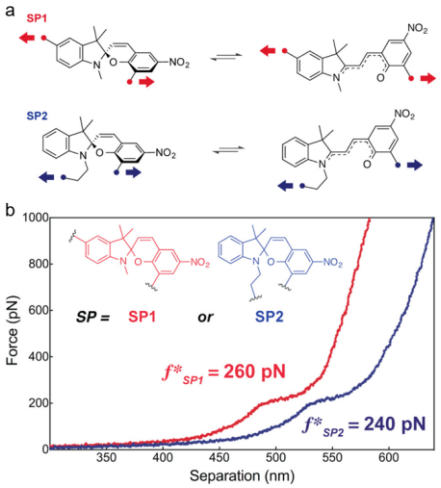

Figure 12. Regiochemical effects on spiropyran (SP) mechanophore activation. Adapted from ref. 50. Copyright © 2015 American Chemical Society.

Mechanochemical cycloreversion of cyclobutane has been observed in ultrasound experiments,[51-52] but the forces required to induce this reaction remain unclear. In atomic force microscopy (AFM) studies, Beyer and colleagues determined the force needed for this mechanochemical process by incorporating cyclobutane into a macrocycle containing a precisely defined ethylene glycol safety line (**Figure 13**).[53] This macrocycle is connected via polyethylene glycol spacers to a glass surface and an AFM cantilever. When the macrocycle is mechanically stretched, cycloreversion occurs, characterized by a specific increase in polymer length. The measured length change aligns closely with values calculated using the external force explicitly included (EFEI) method. By employing two different lengths of the ethylene glycol safety line, the assignment of the mechanochemical cycloreversion becomes unequivocal. This reaction is observed to occur at forces exceeding 1.7 nN.

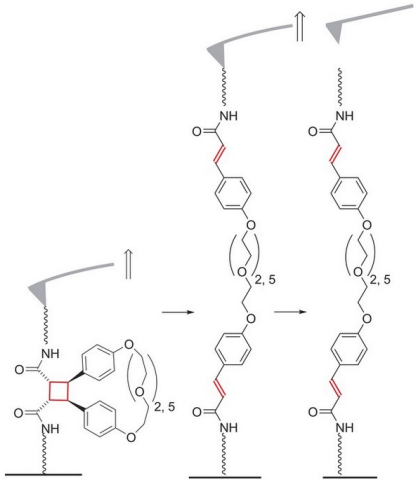

Figure 13. Mechanochemical cycloreversion of cyclobutane observed at the single molecule level. Adapted from ref. 53. Copyright © 2016 Wiley-VCH Verlag GmbH & Co. KGaA, Weinheim.

1.2 Ultrasound-induced polymer mechanochemistry

Most studies on polymer mechanochemistry have been conducted in solution phases. Early investigations utilized turbulent and elongational flow fields to mechanically induce chain scission, although the predominant method today involves the application of ultrasound energy through probe sonication. This technique activates mechanophores by generating solvodynamic shear forces through cavitation. Remarkably, ultrasound has been applied in polymer chemistry even before the formalization of the 'mechanophore' concept. The concept itself was articulated in a seminal paper titled "Ultrasound-Induced Site-Specific Cleavage of Azo-Functionalized Poly(ethylene glycol)," published in 2005 in Macromolecules by Kimberly L. Berkowski, Stephanie L. Potisek, Charles R. Hickenboth, and Jeffrey S. Moore (**Figure 14**).[54]

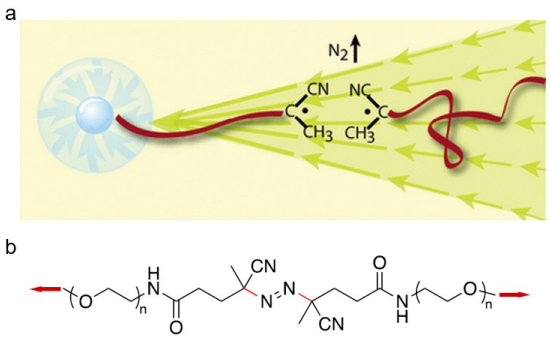

Figure 14. Ultrasound-induced Azo-mechanophore activation in linear polymers. Adapted from ref. 54. Copyright © 2005 American Chemical Society.

1.2.1 Sound and energy

Sound is fundamentally mechanical energy characterized by properties such as frequency, pitch, and intensity when propagating as a compressional wave in air or any fluid medium. Intensity represents the average power transmitted per unit area perpendicular to the wave's direction. The unit traditionally used is the bel (B), although the decibel (dB), one-tenth of a bel, is more commonly employed. For instance, conversational speech emits approximately 60 dB at a distance of 1 meter, while traffic on a busy street can reach 75–80 dB.

Sound propagation involves the transmission of energy through matter, where work is performed and energy expended when a fluid is disturbed at one point. The compression reappears at another point, signifying energy transfer via longitudinal wave propagation. The average rate of energy transfer per unit time per unit area of the wave front is also termed intensity. In practical terms, intensity is expressed as the average flow of power per unit area, measured in watts per square centimeter (W/cm^2).

The term "sonochemistry" refers to the utilization of sound waves to induce chemical and physical effects for various applications (**Figure 15**). Although these effects can be achieved across a broad frequency range, "sonochemical" typically pertains to ultrasound, or sound above the human hearing range (generally above 20 kHz). Natural phenomena, such as animal communication or navigation (ultrasonic) and earthquakes or tidal motions (infrasonic), are sources of these waves. Ultrasonics has garnered public interest due to its applications in medical imaging, metal cleaning, industrial and dental drills, and non-destructive material characterization.

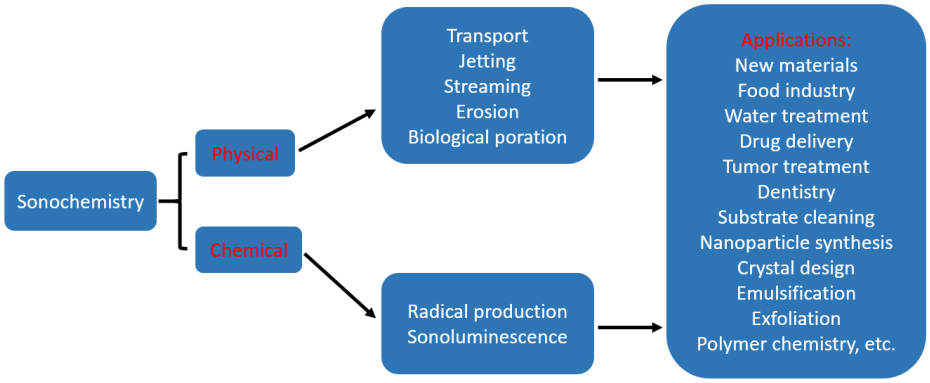

Figure 15. Roadmap of sonochemical research.

The field of ultrasonics is divided into two main categories: low-energy waves and high-energy waves. Low-energy waves have amplitudes low enough to pass through a medium without significant distortion, causing minimal changes except for a slight temperature increase due to intensity variations proportional to wave amplitude. In contrast, high-energy waves induce physical and chemical effects as the medium undergoes changes from significant mechanical stress and/or intense local heating. The interaction of high-energy sinusoidal waves with a medium result in distortion and important nonlinear effects, falling under the complex field of physical acoustics. These effects include shock wave formation, acoustic streaming, cavitation, and acoustic levitation.

1.2.2 Cavitation and polymer chain scission

Sonochemists recognize two types of cavitation: stable and transient. In stable cavitation, bubbles oscillate around their equilibrium positions through repeated cycles of compression and rarefaction. This occurs because the acoustic pressure acts as a force that drives the bubble, causing its radius to vary. Experimental observations

indicate that bubbles undergoing stable cavitation gradually grow, a phenomenon linked to rectified diffusion. During compression, the gas inside the bubble is at a pressure higher than equilibrium, leading to diffusion out of the bubble. Conversely, during rarefaction, the pressure within the bubble drops, allowing gas to diffuse back in. Due to the larger surface area during expansion compared to compression, there is a net increase in gas content in the bubble over each cycle. However, bubbles cannot grow indefinitely. When they reach a critical size during expansion, they collapse violently due to inertial forces of the spherically converging liquid, resulting in transient (or inertial) cavitation.[55] This collapse triggers significant mechanical shocks and potential chemical effects. Additionally, the pulsating bubbles generate microstreaming, a small fluid flow that varies with distance from the bubble, creating high shear stress near the bubble.

Cavitation involves the nucleation, growth, and collapse of bubbles within a solution, driven by pressure waves generated by ultrasound energy. As bubbles collapse, the ends of polymer chains near the void are pulled toward the collapsing bubble more rapidly than those further away. This creates a velocity gradient along the polymer backbone, resulting in elongation and the buildup of force along the chain.[56] Such forces can induce mechanochemical effects, including polymer chain scission or ring opening (**Figure 16**).

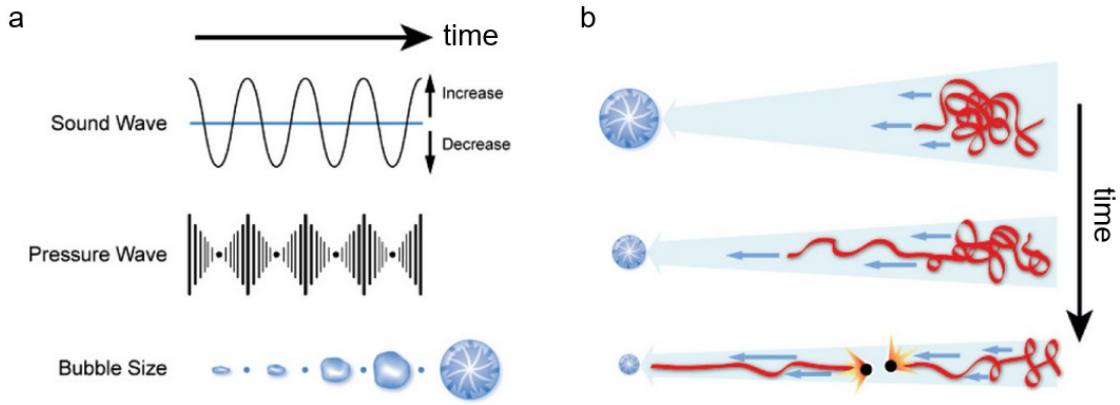

Figure 16. Mechanism for ultrasound-induced polymer chain scission. **a**) Gradual bubble formation induced by the acoustic field; **b**) Polymer extension and chain scission during the collapse process. Adapted from ref. 56. Copyright © 2009 American Chemical Society.

1.2.3 Ultrasound-induced noncovalent bond scission

Ultrasound-induced non-covalent bond scission in polymers primarily focuses on hydrogen bond scission. A notable example involves nucleic acid superstructures-aptamers, which bind their cargo strongly via hydrogen bond interactions.[57] Aptamers are short, single-stranded segments of DNA or RNA capable of binding to specific target molecules. The R23 RNA aptamer, for instance, has been shown to bind aminoglycoside antibiotics, such as neomycin B (NeoB) and paramomycin, thereby inhibiting their activity.[58] In the case of aminoglycosides, the major binding forces are generated from ionic interaction (NeoB contains 5 net charges). Mechanochemical activity is highly dependent on molar mass of the polymers. Therefore, nucleic acid-based polymers (repeating RNA strands) were synthesized using rolling circle transcription that are characterized by very high molar masses (**Figure 17**). After 30 minutes of sonication, the minimum inhibitory concentration (MIC) of these nucleic acid-based polymers was found to be comparable to that of pristine NeoB.[57] This aptamer-antibiotic complex represents the first example of non-covalent bond scission in RNA-based polymers induced by ultrasound.

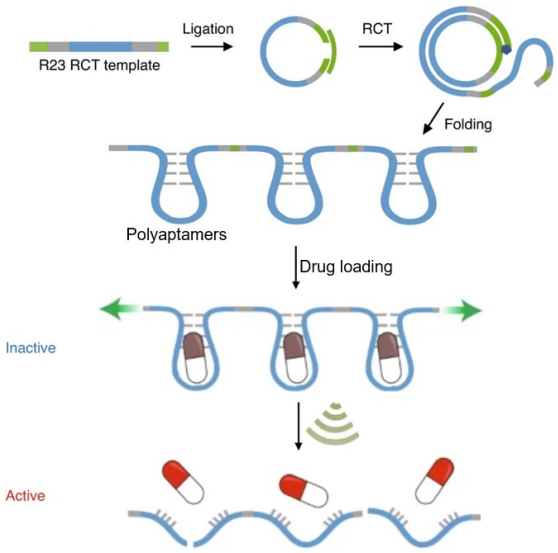

Figure 17. The activation of antibiotic in a nucleic acid-based polymer system. Adapted from ref. 57. Copyright © 2021 Springer Nature Limited.

In 2021, our group identified the hydrogen-bond-based supramolecular dimer of the antibiotic vancomycin (Van) and its complementary peptide target sequence, Cys-Lys-Lys(Ac)-D-Ala-D-Ala (DADA), as a force-responsive motif within a particle-polymer system.[57] Subsequently, the Van-DADA supramolecular dimer was integrated into linear polymers and polymer brushes to investigate the effect of topological structure on mechanochemical activation. Polymer brushes were synthesized using vancomycin-functionalized hyaluronic acid (HA) as the backbone and DADA-terminated POEGMEMA chains as the brushes in a "grafting to" approach (**Figure 18**).[59] MIC tests demonstrated that just 5 minutes of sonication (20 kHz) disassembled the supramolecular brush, thereby activating antimicrobial behavior as effectively as pristine vancomycin. This study illustrates that ultrasound-induced hydrogen bond scission can be achieved in polymer systems.

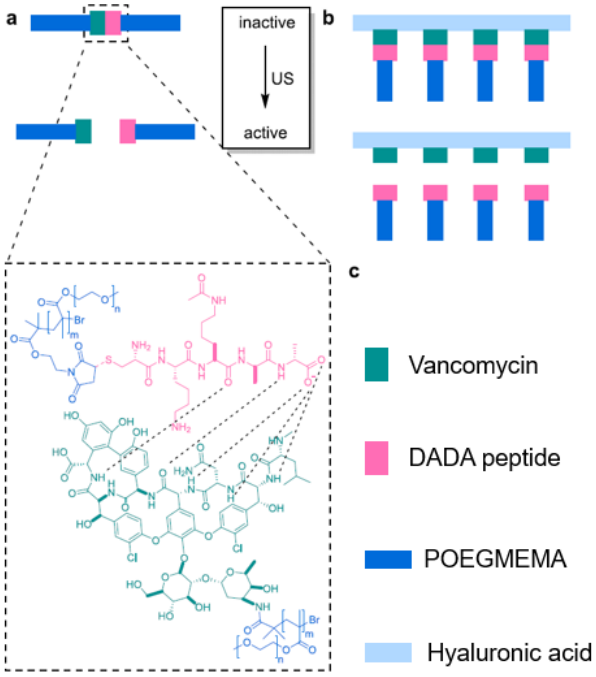

Figure 18. Activation of antibiotic-grafted polymer brushes by ultrasound. Adapted from ref. 59. Copyright © 2021 American Chemical Society.

1.2.4 Ultrasound-induced covalent bond scission

Early work in polymer mechanochemistry was centered on understanding the mechanochemical degradation of polymers. However, recent research has shifted towards mechanophore activation and the design of functional polymer materials. Most mechanophores reported to date feature a weak bond, a strained ring, or an isomerizable bond that selectively undergoes scission or conformational changes when mechanical force is applied (**Figure 19**).

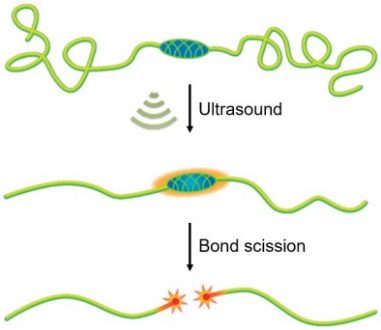

Figure 19. Bond scission in polymers.

C-C bond scission:

During the 1950s, Melville and other researchers investigated ultrasound-induced polymers degradation in solution.[60] They observed that ultrasonic treatment of polymethacrylate solutions, including styrene, initiated polymerization events, suggesting that cavitation induced the generation of free radicals. In addition, homolytic bond breakage was found during the cleavage of polymers (**Figure 20**). Later, Sohma et al. confirmed the homolytic scission of carbon-carbon single bond (C-C) in the polymer backbone under applied mechanical force using electron spin resonance (ESR) spectroscopy.[61]

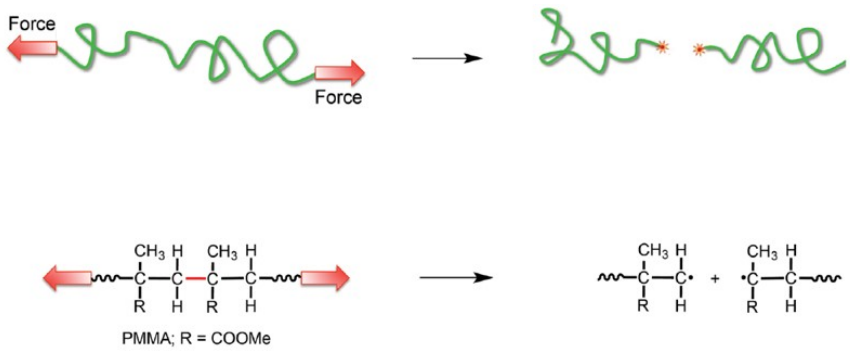

Figure 20. Homolytic scission of C-C covalent bond along the polymer backbone. Adapted from ref. 33. Copyright © 2015 American Chemical Society.

O-O bond scission:

Encina and coworkers provided evidence for the weak-link hypothesis in polymer mechanochemistry by incorporating peroxide linkages randomly along the polymer backbone.[62] Their experiments confirmed that polymers with these peroxide links degraded more rapidly than control polymers when subjected to ultrasound irradiation (**Figure 21**).

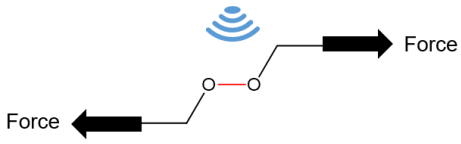

Figure 21. Homolytic cleavage of O-O bond.

N-N bond scission:

The seminal demonstration of mechanochemical selectivity was reported by Berkowski et al. In their study, a single azo linkage was inserted in the center of a PEG chain and subjected to ultrasonication-induced degradation (**Figure 22**).[54] Experimental results showed that this polymer degraded faster than a control polymer, as evidenced by kinetic analysis of molecular weight reduction, akin to the study of peroxide-linked polymers. More notably, the azo polymer exhibited nearly perfect cleavage at the azo group, contrasting with the random cleavage profile of the control polymer.

Figure 22. Ultrasound-induced site-specific reactivity of polymers containing azo mechanophores.

S-S bond scission:

In polymer mechanochemistry, disulfide bond has been investigated due to its low bond energy and thermal stability. Fritze et al. reported that disulfide bond incorporated into linear-structured polymers could be cleavage by ultrasound irradiation.[63-64] Based on ultrasound-induced disulfide bond scission, our group developed a mechanoresponsive prodrug system for releasing anticancer drugs from polymers, utilizing a disulfide-centered polymer platform.[65] This system demonstrated that ultrasound-induced bond scission of disulfide-centered polymers could lead to furan-derivative release (**Figure 23**). The thiol-terminated polymers participated in a Michael addition reaction with the Diels−Alder adducts, initiating furan-drug release through a retro Diels−Alder reaction.

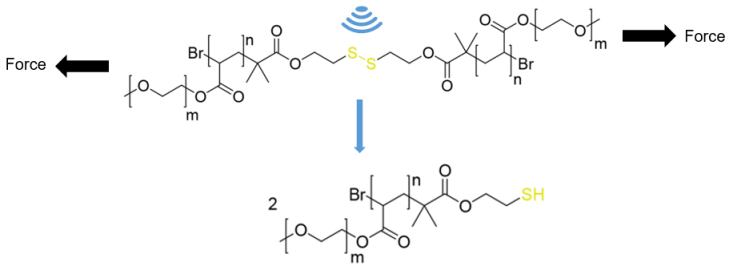

Figure 23. Disulfide bond scission in linear polymers. Adapted from ref. 65. Copyright © 2020 American Chemical Society.

C-S bond scission:

The mechanical scission of chemical bonds in homopolymers predominantly involves homolytic cleavage, generating radical species. Examples of more selective cleavage include introducing strained rings or weak bonds like peroxide, azo, and disulfide linkages into polymer backbones. In contrast, reports of heterolytic bond scission are rare. The Moore group designed a new mechanophore featuring a highly polarized chemical bond intended to promote heterolytic bond scission (**Figure 24**).[66] Triarylsulfonium salts (TAS) are well-known photoacid generators commonly used in photolithography. Various mechanisms for photochemical acid production, involving either heterolysis or homolysis of the C–S bond, have been proposed and debated in the literature.[67-68] Moore's team investigated the mechanochemical scission of TAS through sonication experiments in solution. Surprisingly, upon C-S bond cleavage, the resulting phenyl cations reacted with trifluoromethanesulfonate counterions to produce trifluoromethylphenyl structures.

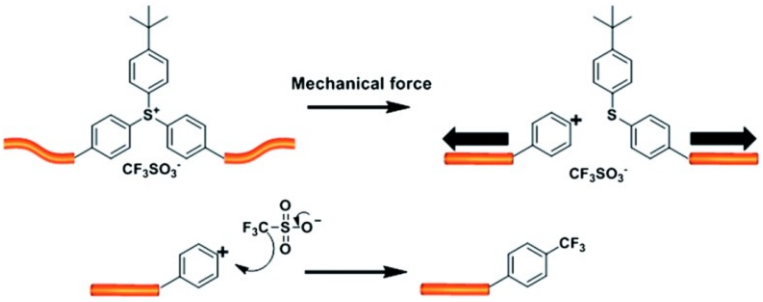

Figure 24. Ultrasound-induced heterolytic scission of the C–S bond in the triarylsulfonium salt (TAS) moiety. Adapted from ref. 66. Copyright © 2014 The Royal Society of Chemistry.

C-O bond scission:

Moore and colleagues demonstrated the use of mechanical force to depolymerize cyclic poly(o-phthalaldehyde) (PPA) into o-phthalaldehyde (OPA) monomers. The obtained OPA can then undergo anionic polymerization initiated by n-BuLi to regenerate PPA (**Figure 25**).[69] The mechanochemical depolymerization mechanism involves heterolytic scission of the C-O bond, producing oxocarbenium and hemiacetalate chain ends. These intermediates subsequently undergo head-to-tail depolymerization to yield OPA monomers.

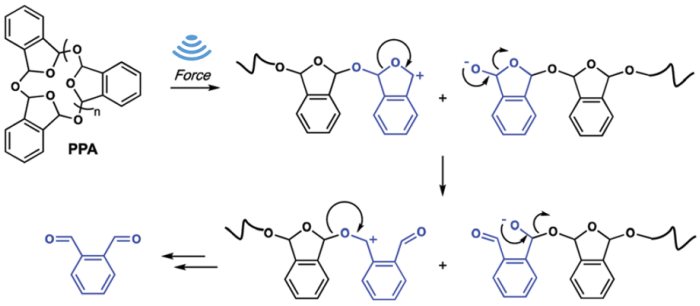

Figure 25. Mechanically triggered depolymerization of cyclic poly(ophthalaldehyde) (PPA).

C-N bond scission:

Chen and colleagues explored the geometric and polar (thermodynamic equilibrium) control of mechano-responsive polymers.[70] They achieved this by strategically incorporating two spirolactam rings into

aminobenzopyranoxanthene, leading to the development of a series of stereo- and regio-isomeric rhodamine-like mechanophores (**Figure 26**). The key innovation in this study lies in combining two reactive sites (rhodamine ring) within a single mechanophore. They achieved the stereo- and regio-selective synthesis of isomeric mechanophores with significant mechanochromic sensitivity. These polymers exhibited varied mechanochromic responses, attributed to distinct geometric adjustments induced by mechanical forces and enhanced polarity.

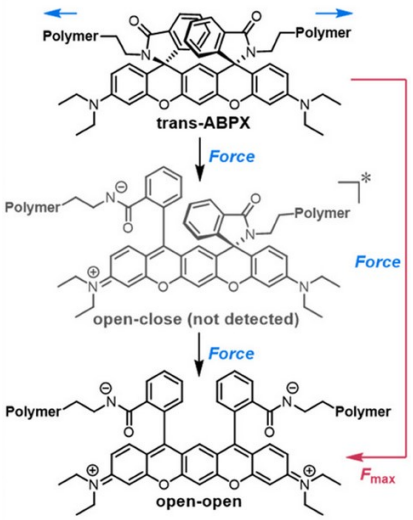

Figure 26. Ultrasound induced ring-opening from bis-mechanophores. Adapted from ref. 70. Copyright © 2014 The Royal Society of Chemistry.

O-S bond scission:

In 2016, the Moore group introduced an oxime sulfonate-based mechanophore capable of acid generation under mechanical force, accompanied by NOx release (**Figure 27**).[71] Under ultrasonication, the oxime sulfonate's S-O bond is preferentially cleaved, yielding sulfonic acid and oxime structures at the chain ends. The generation of sulfonic acid was confirmed by the decrease in pH observed in the sonicated solution. The oxime then decomposes to form the corresponding ketone.

Figure 27. Ultrasound-induced release of NO_x from an oxime sulfonate-based mechanophore, which is induced by 'S-O' bond scission. Adapted from ref. 71. Copyright © 2016 American Chemical Society.

O-N bond scission:

Göstl and colleagues introduced the carbamoyloximes as mechanochemical protecting groups for secondary amines.[72] They demonstrated that carbamoyloximes undergo homolytic bond scission under mechanical force in

polymers, releasing the free amine (**Figure 28**). This reaction process lead to the formation of carbamoyloxyl and aminyl radicals, mirroring its photochemical counterpart.

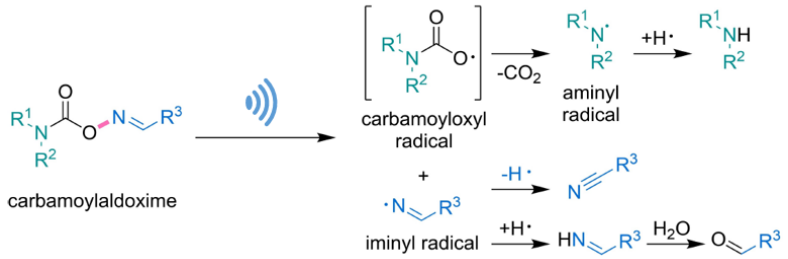

Figure 28. Force-induced scission of carbamoyloximes. Adapted from ref. 72. Copyright © 2022 Wiley-VCH GmbH.

Se-Se bond scission:

Selenium (Se) is increasingly studied for its distinctive redox properties and ability to form dynamic chemical bonds.[73-74] Researchers have employed molecular selenium or incorporated it into polymer structures[75] to explore diverse applications such as catalysis,[76] drug delivery,[77] antioxidant,[78] and anticancer properties.[79] The degradation of diselenide bonds typically occurs through redox processes[77] and light activation.[80] Chen and colleagues have shown that sonication offers an alternative approach to cleave Se-Se bonds, enabling selective metathesis reactions between diselenide-linked polymers and small molecules (**Figure 29**).[81] This pioneering study in the sonochemistry of diselenide-centered polymers enhances our understanding of diselenide chemistry.

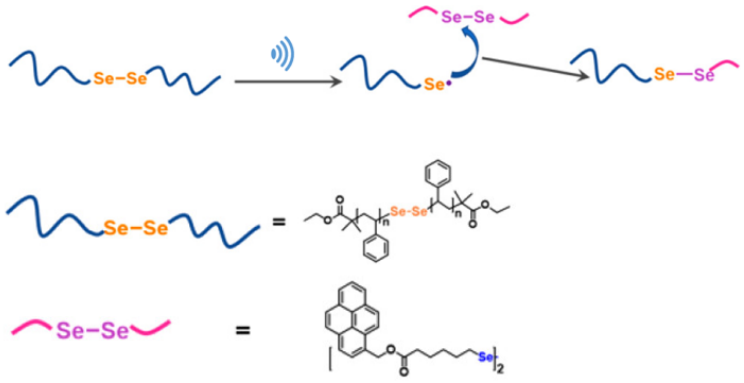

Figure 29. Ultrasound induced diselenide scission in polymers. Adapted from ref. 81. Copyright © 2020 American Chemical Society.

1.2.5 Ultrasound-induced coordinate bond scission

Recent research on metallocenes has demonstrated that the metal ions can be completely dissociated from the parent polymer. In 2018, Di Giannantonio et al. ultrasonically treated a polymer solution with ferrocene units on the main chain. They verified the release of metal ions through complexation with $K_4[Fe(CN)_6]$ and KSCN.[82] During ultrasonic treatment, mechanical force breaks the coordinate bonds to release Fe^{2+}, followed by rapid oxidation in air to form Fe^{3+} (**Figure 30a**). Shortly after, Craig and colleagues conducted similar studies on ferrocene polymers and successfully captured the released Fe^{2+} with phenanthroline, ultimately forming the stable complex, $[Fe(phen)_3]^{2+}$ (**Figure 30b**).[83] They showed that the dissociation process of ferrocene could be

constrained by the distal spatial conformation between two cyclopentadienyl ligands.[84] When the polymer is treated with sonication, the mechanical force can peel the cyclopentadienyl ligand off the metal center, destroying the responsive structure of ansa-bridged ferrocene.

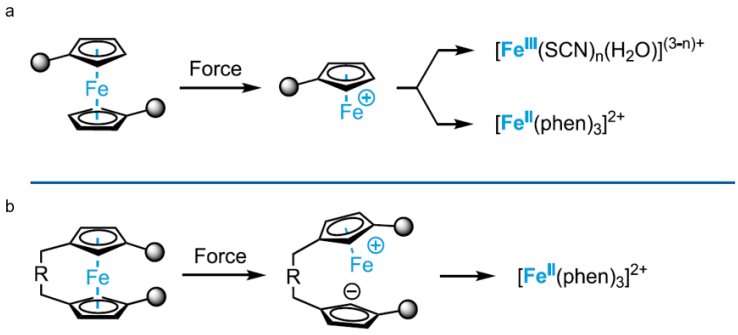

Figure 30. Mechanochemical scission of metal-ligand bond in ferrocene mechanophore.

Mechanochemical reactions commonly involve the force-induced cleavage of 'weak bonds.' When molecular strain builds up along the direction of these 'weak bonds', weak linkages such as dative bonds (with bond dissociation energies (BDE) of about 36 kcal/mol^{-1} for palladium-phosphorus,[85] 61 kcal/mol^{-1} for silver-carbene,[86] and 66 kcal/mol^{-1} for ruthenium-carbene coordinative bonds[86]) show mechanochemical activity (**Figure 31**). Ultrasonic scission of coordination polymers based on palladium(II) dichloride and diphenylphosphine telechelic polytetrahydrofuran selectively occurs at the palladium-phosphorus coordinative bond and is fully reversible.[85] In 2008, Sijbesma et al. demonstrated that polymeric Ag-N-heterocyclic carbene coordination complexes are highly susceptible to scission when sonicated.[86] In the presence of water, this scission is irreversible, and the formation of the imidazolium product is easily measured. Additionally, in 2009, Sijbesma and colleagues investigated the ultrasonic activation of a ruthenium-biscarbene complex with polymer chains, resulting in the catalysis of olefin metathesis reactions.[87] In each instance, the catalytic activity is driven by ligand dissociation, resulting from the transfer of mechanical forces from the polymeric substituents to the coordination bond.

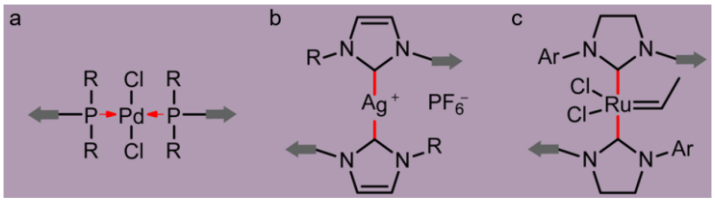

Figure 31. Ultrasound-induced palladium-phosphorus, silver-carbene, and ruthenium-carbene coordinative bonds scission. Adapted from ref. 33. Copyright © 2015 American Chemical Society.

Simultaneously, the mechanochemical activation of various metal-ligand bonds (including metallocenes; complexes of Zn, Cu, Ni, and Rh;[88-89] N-heterocyclic carbene complexes with Ag, Ru, and Cu;[90-93] as well as Pd phosphanes) was successfully achieved. In 2021, Schmidt, Göstl, and co-workers introduced the first example of a supramolecular coordination cage that forms a star-shaped, water-soluble polymer structure responsive to sonication-induced shear forces in solution (**Figure 32**).[94]

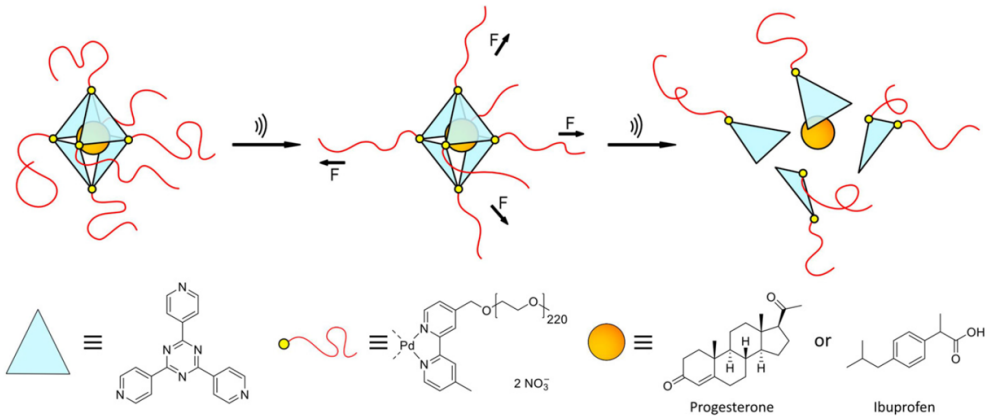

Figure 32. Sonication-induced fragmentation of the cage that based on Pd-N coordinative bonds scission. Adapted from ref. 94. Copyright © 2021 Wiley-VCH GmbH.

1.2.6 Ultrasound-responsive polymer systems

The architecture of polymers is a critical factor influencing the rates of mechanochemical scission under mechanical force. Studies have investigated the kinetics of mechanochemical scission and/or activation efficiency of mechanophores in various polymer architectures including linear, cyclic,[95-96] star-shaped,[97] helical,[98] brush,[99] dendronized polymers,[100] and polymer cross-linked microgels[101] (**Figure 33**).

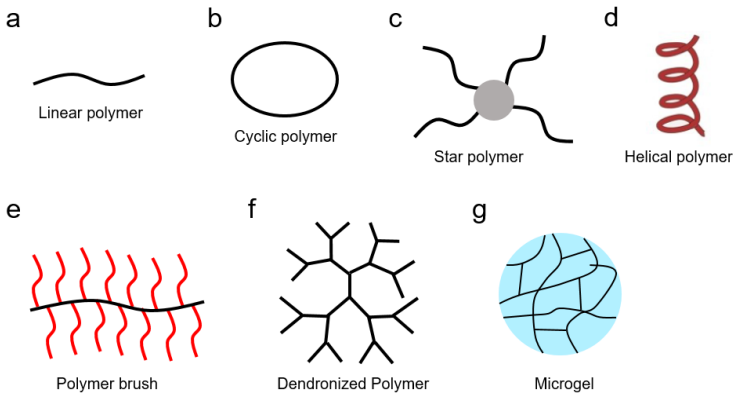

Figure 33. Ultrasound-responsive polymer architectures.

Cyclic polymers possess unique chemical, thermal (e.g., glass-transition temperature (T_g), crystallization temperature, and melt-transition temperature), and physical/rheological properties, influenced by their topological features such as the lack of end groups and constrained conformational flexibility. Craig and colleagues found that cyclic polymers exhibit slower scission rates compared to linear polymers (**Figure 34**).[96] This is because cyclic polymers require two scission events to produce daughter fragments: the first scission yields a linear intermediate with the same molecular weight, followed by a second scission event for fragmentation.

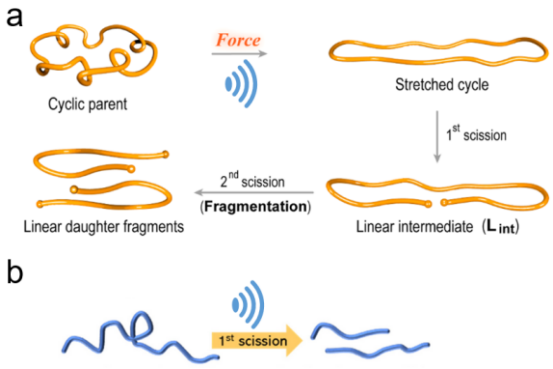

Figure 34. Mechanical scission of cyclic polymer and linear polymer. Adapted from ref. 96. Copyright © 2019 American Chemical Society.

Boydston et al. investigated how the architecture of star-shaped polymers compared to linear polymers affects the rates of ultrasound-induced bond scission.[97] Their study indicated that star polymers exhibit greater shear stability compared to linear polymer counterparts of equivalent total molecular weight. Furthermore, the study supported a mechanistic understanding where the scission of star polymer chains is governed by their spanning molecular weight rather than their total molecular weight (**Figure 35**).

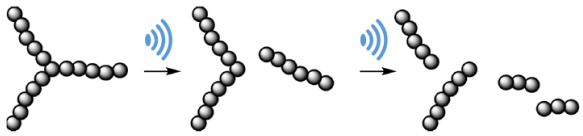

Figure 35. Chain scission sequences in star polymers. Adapted from ref. 97. Copyright © 2014 American Chemical Society.

Mechanical stretching of helices in biopolymers like DNA and proteins has been studied using single-molecule force spectroscopy, revealing smooth helix-coil transitions in force-extension curves.[102-104] Diesendruck and colleagues investigated poly-γ-benzyl-glutamate, a homopolymer with exceptionally high helicity, as an extreme case to explore how helicity influences the rate of backbone polymer mechanochemistry in solution (**Figure 36**).[98] Model polymers of poly(γ-benzyl glutamate) with varying helicities demonstrated that chains with higher helicity exhibit increased mechanochemical rate constants, whether for backbone fragmentation or mechanophore activation. This correlation suggests that the naturally occurring helical secondary structure significantly impacts the mechanochemical response of polymers.

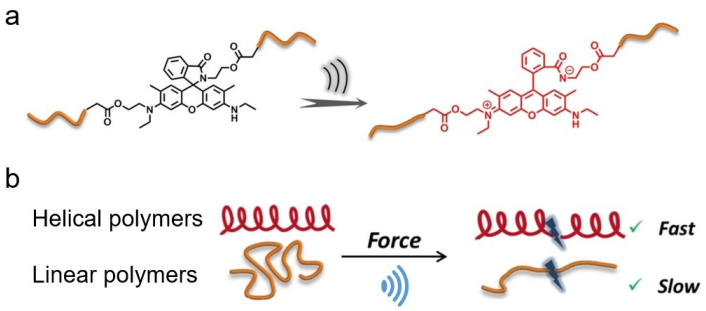

Figure 36. Ultrasound induced bond scission in helical polymers and linear polymers. Adapted from ref. 98. Copyright © 2022 Wiley-VCH GmbH.

1.3 Recent achievements in ultrasound-induced polymer mechanochemistry

Polymer mechanochemistry has arisen to convert the mechanical force acting on macromolecules into useful chemical reactions. Mechanophores, embedded within polymer chains and responsive to force, undergo selective cleavage of poised bonds along reaction pathways when subjected to external force. This field has been instrumental in investigating how mechanical force affects chemical bonds within polymer backbones. Recently, ultrasound-induced polymer mechanochemistry has been applied to catalysis, recycling of synthetic polymers, and activation of prodrugs or proteins.

1.3.1 Ultrasound-induced mechanochemical catalysis and synthesis

In 2004, Sijbesma and colleagues investigated the use of mechanical force to induce ligand dissociation from transition-metal complexes, introducing a novel strategy to study and control the chemistry of coordination complexes. This approach creates vacant coordination sites and offers complete reversibility, paving the way for applications in transition metal catalysis.[87] In 2009, Sijbesma's group reported the mechanical activation of latent metathesis catalysts. They discovered that silver(I) complexes incorporating polymer-functionalized N-heterocyclic carbenes, serving as latent organocatalysts, demonstrate catalytic activity in transesterification reactions under sonication in organic solvents. Moreover, applying mechanical force to a ruthenium biscarbene complex with polymer chains attached induced the catalysis of olefin metathesis reactions.

"Click" chemistry represents a potent method for linking molecules in chemistry and materials science. In 2015, Binder et al. reported the pressure-sensitive activation of a homogeneous CuI "click" catalyst anchored at the center of a polymer chain using mechanical force (**Figure 37**). Upon sonication, the activated "click" catalyst triggers successive "click" reactions.[93]

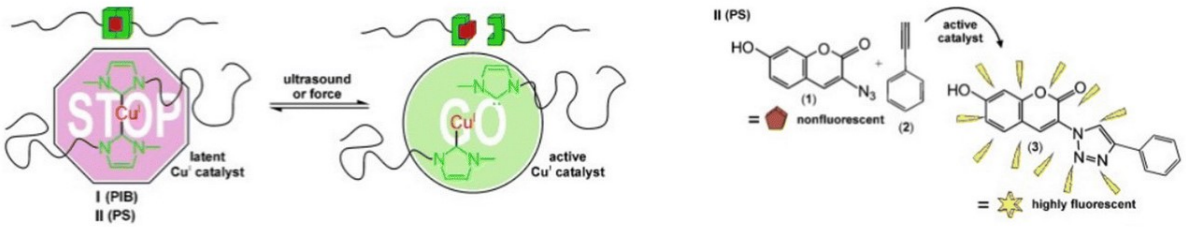

Figure 37. Ultrasound-induced activation of "Click" catalyst. Adapted from ref. 93. Copyright © 2015 Wiley-VCH GmbH.

In 2021, Burns and colleagues employed polymer mechanochemistry to synthesize a fluorinated polyacetylene, a long-desired air-stable polymer that had been challenging to produce using traditional methods (**Figure 38**).[17] Following polymerization, ultrasonication resulting in a gold-colored semiconducting fluoropolymer. This research underscores the utility of polymer mechanochemistry as a powerful synthetic approach for creating materials on a practical scale.

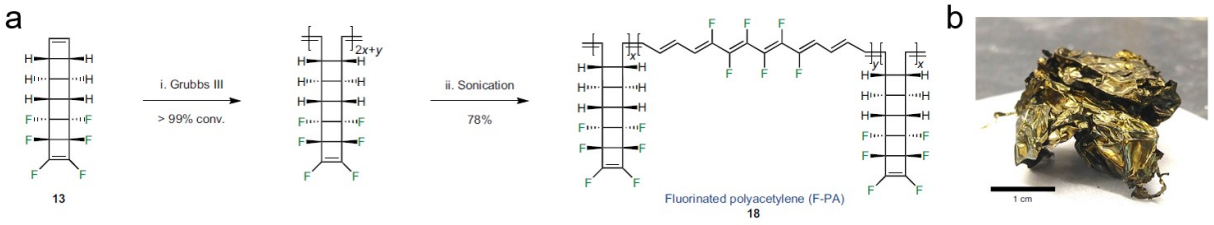

Figure 38. Mechanochemical synthesis of an elusive fluorinated polyacetylene. Adapted from ref. 17. Copyright © 2021 Springer Nature Limited.

1.3.2 Ultrasound-induced mechanochemistry for sustainable polymer degradation

The accumulation of plastic waste, exacerbated by inadequate recycling efforts, has led to severe environmental pollution. Addressing this unsustainable use of resources requires urgent identification of effective polymer recycling methods. Advances in polymer mechanochemistry, particularly the incorporation of force-responsive groups, have demonstrated potential in harnessing destructive mechanical forces for beneficial chemical transformations. Recent studies have highlighted efficient mechanochemical degradation and recycling of synthetic polymers based on these principles.

In 2020, Craig and collaborators developed a mechanophore based on 7,8-dimethanol-functionalized [4.2.0]bicyclooctene (BCOE). This mechanophore undergoes force-induced electrocyclic ring opening of cyclobutene, followed by spontaneous lactonization, resulting in backbone cleavage and release of a bis-lactone product (**Figure 39**).[105] They synthesized a polymer that includes the dimethanol-functionalized BCOE. Ultrasonication of the polymer solution for 60 minutes decreased its molecular weight from 120 kDa to 4.4 kDa.

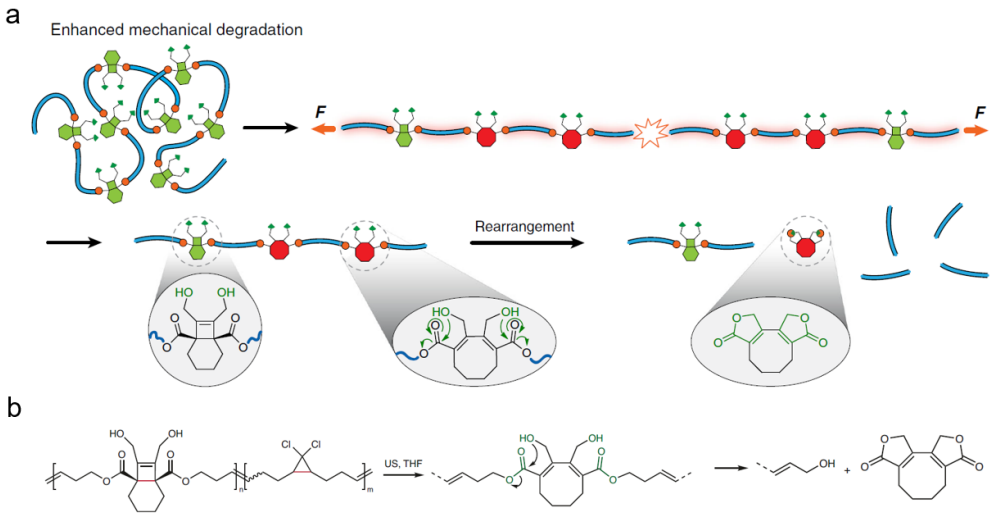

Figure 39. Polymer degradation via mechanochemically unveiled lactonization. Adapted from ref. 105. Copyright © 2020 Springer Nature Limited.

In 2023, inspired by the concept of mechanically gated degradation, Wang and colleagues proposed a novel polymer concept: a high-ceiling temperature (T_c) polymer that can transform into a low-T_c polymer upon demand (**Figure 40**).[106] They designed and synthesized a polyether containing cyclobutane-fused tetrahydrofuran in each repeat unit. Mechanochemical activation of this polymer produces poly(2,5-dihydrofuran), a low-T_c polymer.

Activation was demonstrated through ultrasonication in solution, as well as extrusion, compression, and ball milling in bulk. While extrusion and compression showed limited activation (<1%), ultrasonication and ball milling achieved activation levels of up to 68% and 17%, respectively. The sonicated and ball-milled polymers contained significant proportions of poly(2,5-dihydrofuran). Upon addition to a dichloromethane solution of a 2nd-generation Grubbs catalyst, depolymerization yielding 2,5-dihydrofuran was observed.

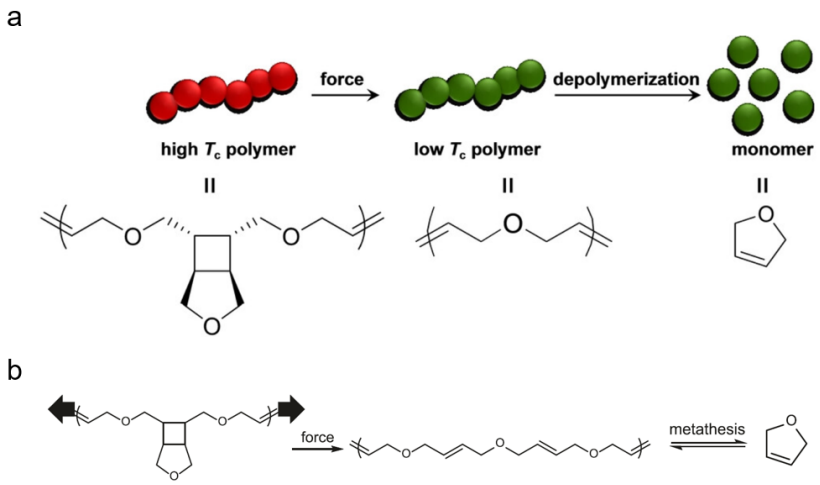

Figure 40. Mechanically converting a poly(cyclobutane-fused tetrahydrofuran) into poly(2,5-dihydrofuran) for depolymerization. Adapted from ref. 106. Copyright © 2023 Springer Nature Limited.

In 2024, Bruns and colleagues introduced cyclobutene-based monomers capable of co-polymerizing with conventional monomers to confer mechanically triggered degradability to resulting polymers.[107] These monomers serve as mechanophores, undergoing a ring-opening reaction triggered by mechanical force. This reaction leads to a structural rearrangement that renders the polymer chains susceptible to hydrolysis under basic conditions. These monomers are versatile for use in both free radical and controlled radical polymerizations, introducing functional groups into polymer backbones. They facilitate the mechanical control of high-molecular-weight materials or cross-linked polymer networks, transforming them into lower-molecular-weight species (**Figure 41**).

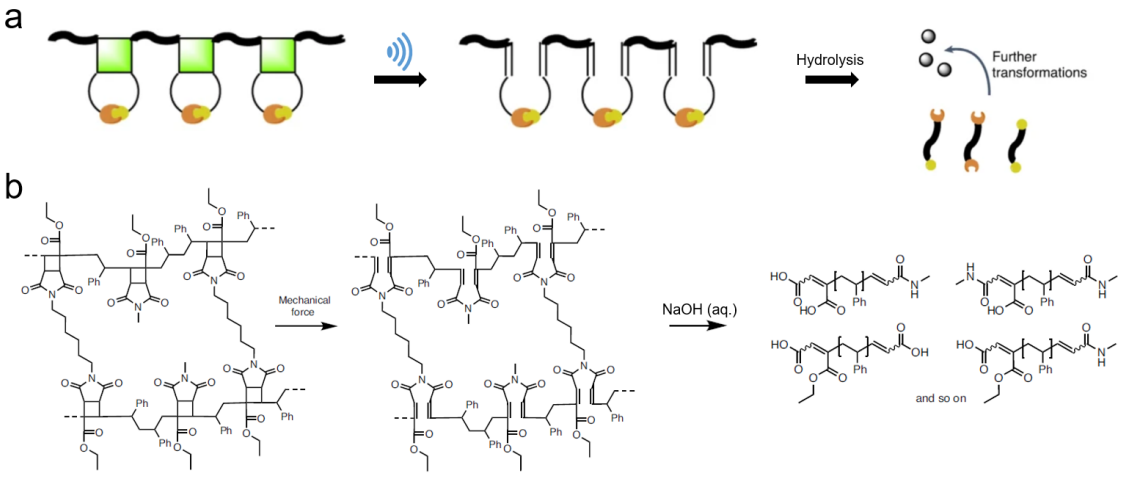

Figure 41. Mechanically triggered on-demand degradation of polymer networks. Adapted from ref. 107. Copyright © 2024 Springer Nature Limited.

1.3.3 Ultrasound-controlled prodrug activation

Ultrasound has become a highly effective and commonly used tool in polymer mechanochemistry due to its noninvasive nature and spatiotemporal control. The emerging field of ultrasound-responsive prodrug systems harnesses the mechanical effects of ultrasonication to control the activation of prodrugs. In polymer mechanochemistry, researchers explored the mechanochemical activation of force-sensitive prodrugs by ultrasound.

In 2020, our group firstly reported a drug release system for furan-containing drugs based on the ultrasound-induced (20 kHz) homolytic scission of disulfide bonds in linear polymers.[65] Sonication was used to break the polymer chain at the central disulfide site yielding active thiols. These thiols then reacted with the prodrug Diels-Alder adducts through a Michael addition, leading to a retro Diels-Alder reaction that released furylated drug derivatives (**Figure 42a**). However, adding a furan group to the drug reduced its effectiveness. Despite being limited to drugs with furan groups, this study demonstrated the potential of ultrasound-induced drug molecule release by mechanochemical transformations.

In 2021, we introduced an enhanced disulfide-centered linear polymer where drugs were attached covalently to the β-position of the disulfide group via a carbonate linker (**Figure 42b**).[27] Under ultrasound (US) exposure, the linear POEGMEA polymer broke apart to release thiols. These thiols then underwent an intramolecular 5-exo-trig cyclization to liberate the drug molecule from the carbonate linker. Similar release patterns were observed with the anti-cancer drug camptothecin. Cell proliferation assays showed increased cytotoxicity with longer sonication times, correlating with enhanced drug release. To advance this intramolecular mechanochemical release system further, we achieved real-time tracking of drug activity by replacing one drug molecule with a fluorescent reporter on the mechanophore (**Figure 42c**).[108] This allowed simultaneous release of the reporter and drug molecule, enabling spatiotemporal imaging of delivery and cell uptake processes.

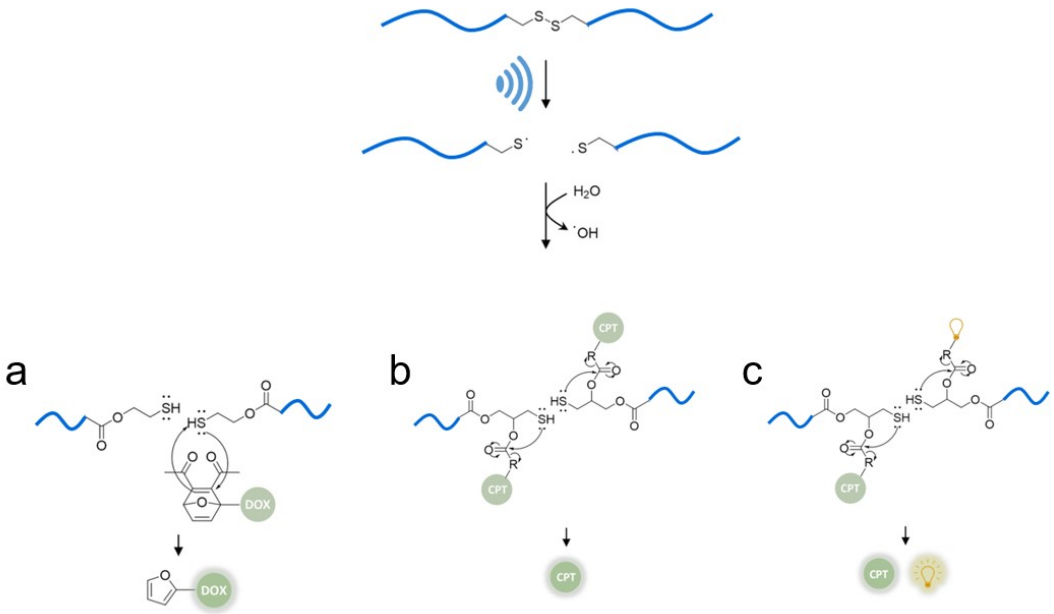

Figure 42. Ultrasound-induced disulfide mechanophore activation and release of drug or reporting molecules.

In 2022, Li and Moore demonstrated the activation of mechanophores in cross-linked polymer networks using high-intensity focused ultrasound (HIFU) at 550 kHz.[24] They introduced the concept of mechanochemical

dynamic therapy (MDT), employing ultrasound to mechanically activate azo mechanophores. This activation generates reactive free radicals, which enhance ROS-induced cytotoxicity in cancer cells (**Figure 43**).

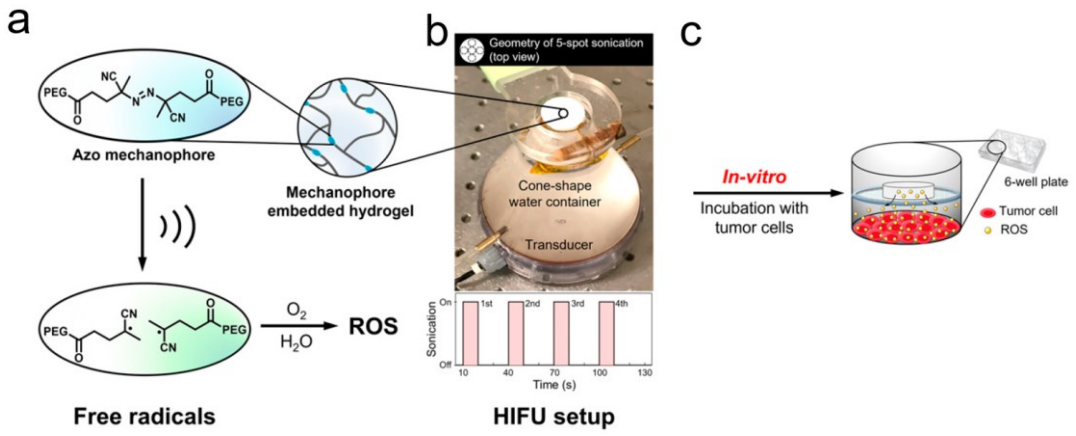

Figure 43. HIFU-induced Azo mechanophore activation and ROS generation. Adapted from ref. 24. Copyright © 2022 Proceedings of the National Academy of Sciences.

In 2023, Robb and Shapiro introduced a new platform that combines the mechanochemical activation of mechanophores with biocompatible focused ultrasound (330 kHz), using gas vesicles (GVs) as acoustic-mechanical transducers (**Figure 44**).[25] In this synergistic approach, GVs acted as seeds for bubble formation and cavitation under biocompatible ultrasound, enhancing the mechanical effects. This setup effectively triggered the mechanochemical activation of mechanophores. As a proof-of-concept, they successfully achieved prodrug activation by focused ultrasound in the presence of GVs. This activation led to the expected cytotoxic effects on Raji cells in vitro.

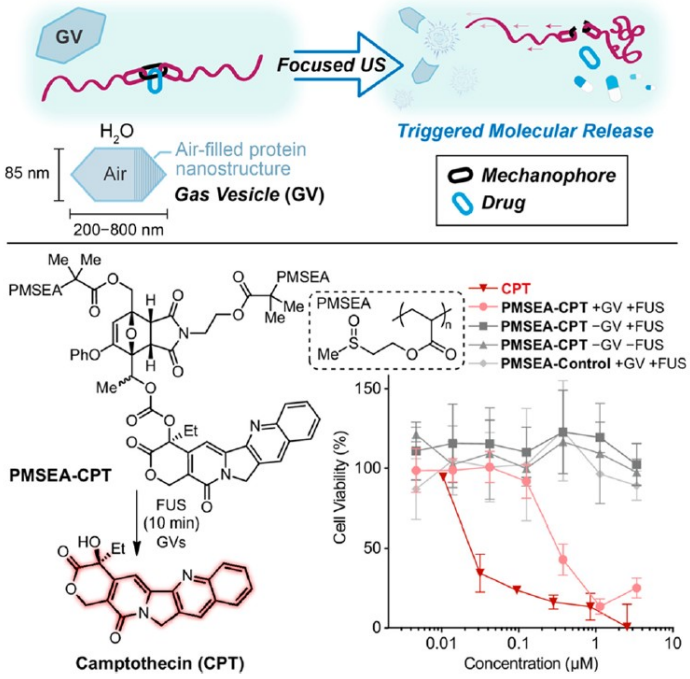

Figure 44. Ultrasound triggered camptothecin release using a biocompatible focused ultrasound. Adapted from ref. 25. Copyright © 2023 Proceedings of the National Academy of Sciences.

In 2024, De Bo and colleagues demonstrated that a rotaxane, an interlocked molecule with a macrocycle trapped on a stoppered axle, could effectively achieve the release of cargo molecules attached to its axle by mechanical force (**Figure 45**).[109] They attached a bulky maleimide cargo unit via a valine-citrulline peptide linker, connected to the drug through a self-immolative *para*-aminobenzyloxycarbonyl spacer. This design, commonly used in antibody-drug conjugates, relies on the overexpression of cathepsin B, a lysosomal cysteine protease in cancer cells, to initiate the release cascade.[110] As a proof-of-concept, they loaded the cargo with doxorubicin, a potent broad-spectrum chemotherapy agent, achieving a release efficiency of 65% in solution under sonication. The rotaxane architecture enables repeated activation of scissile mechanophores without covalent attachment to the actuating polymers. However, drug activation requires high-intensity US, not compatible with cells and tissues.

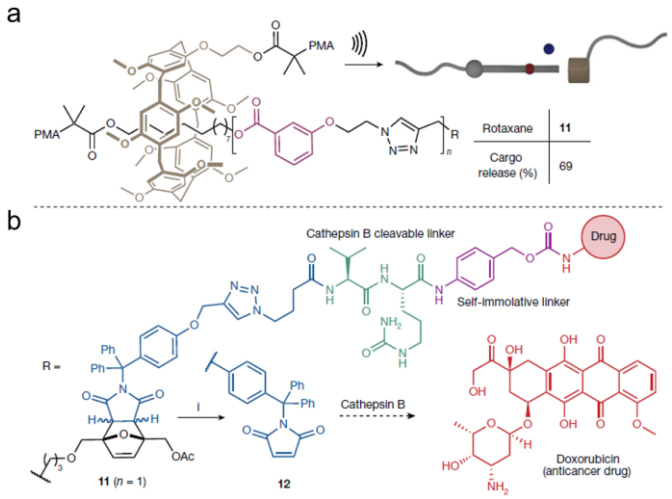

Figure 45. Ultrasound-controlled release of cargo via retro-cycloaddition. Adapted from ref. 109. Copyright © 2024 Springer Nature Limited.

1.3.4 Ultrasound to control the activity of proteins

Ultrasound generates cavitation-induced mechanical forces that stretch and break polymer chains in solution. While this type of polymer mechanochemistry is commonly used in synthetic polymer systems, it is less explored in bio-macromolecules. In 2021, our group pioneered the selective activation and deactivation of proteins using US (**Figure 46**).[111] Zhou et al. using GFP as a model system, demonstrated the response of protein to US (20 kHz) through the incorporation of long, highly charged domains that efficiently transfer force to the protein scaffold. After that, they utilized this principle to activate trypsin's catalytic activity by inducing the release of its inhibitor.

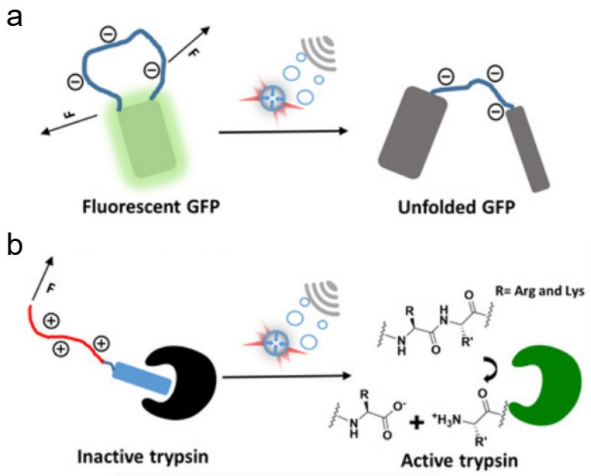

Figure 46. Ultrasound-controlled activation of protein activity. Adapted from ref. 111. Copyright © 2020 Wiley-VCH GmbH.

In the same year, Zhao et al. developed an alternative approach for ultrasound-triggered activation of enzymatic activity. They designed the polyaptamers capable of specifically binding to thrombin to inhibit its catalytic function.[112] The deactivating polyaptamers (pTBA15) were synthesized by rolling circle amplification (RCA) (**Figure 47**).[113-115] Leveraging the strong recognition and protein-loading capabilities of the TBA15 aptamer, thrombin was captured and its activity suppressed through the formation of a well-defined aptamer-protein complex. Upon exposure to irradiations, the polyaptamer complexed with thrombin underwent stretching, leading to the disruption of specific non-covalent interactions between thrombin and the polyaptamer (such as hydrogen bonds and hydrophobic interactions) within the loop structures. Subsequent exposure to low-intensity focused ultrasound (LIFU) at 5 MHz facilitated the release of thrombin from the complex, thereby restoring its enzymatic function to catalyze the conversion of fibrinogen to fibrin. This work shows a great potential of biocompatible (high-frequency and low-intensity) ultrasound for inducing activation of protein activity.

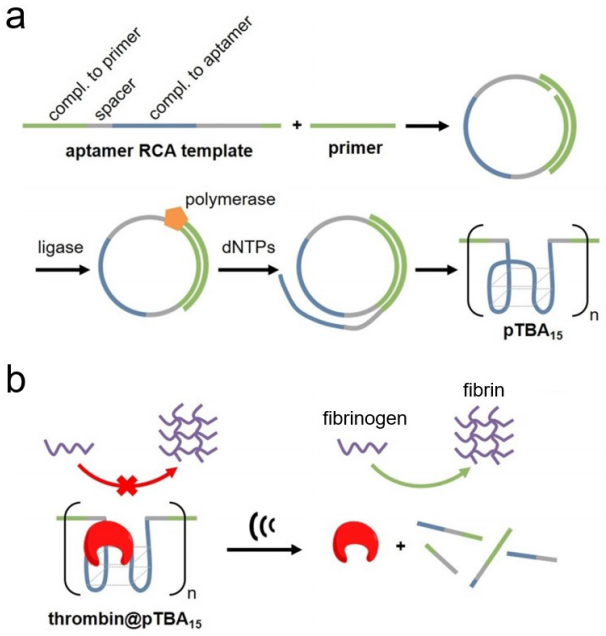

Figure 47. Ultrasound-controlled the activation of thrombin activity. Adapted from ref. 112. Copyright © 2021 Wiley-VCH GmbH.

Recently, Rath et al. showcased the mechanochemical activation of an RNA-cleaving DNAzyme by ultrasound (**Figure 48**).[116] They encoded the reverse complementary sequence of the DNAzyme within the nucleic acid polymer-a RCA product. The DNAzyme is deactivated through hybridization with the complementary strand within the RCA product. Under ultrasonication, the supramolecular interactions between the polynucleic acid and the DNAzyme were mechanically disrupted, which finally resulted in the recovery of DNAzyme activity.

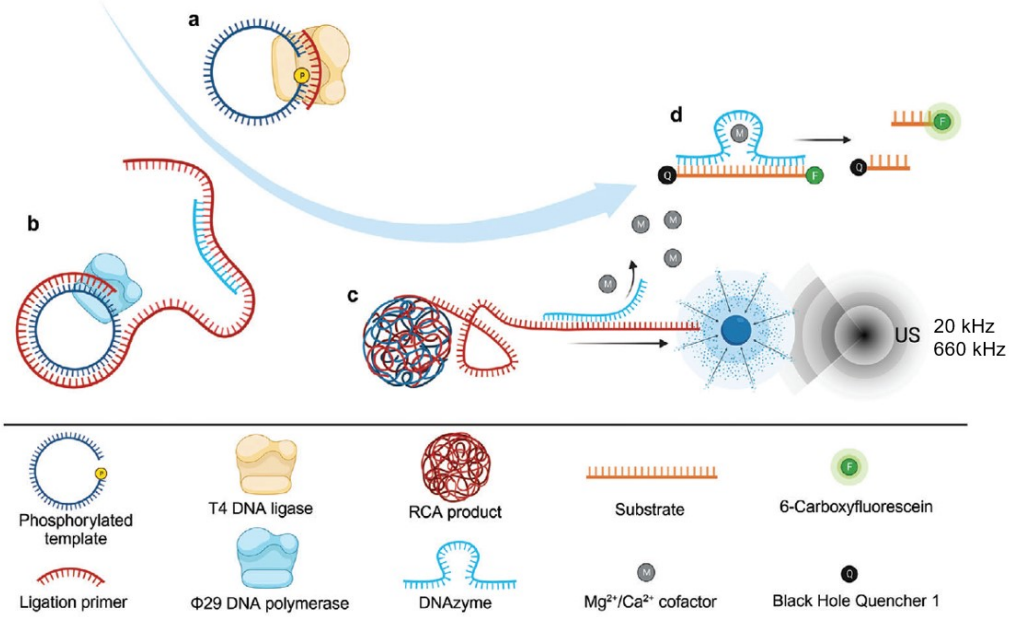

Figure 48. US-induced activation of DNAzyme. Adapted from ref. 116. Copyright © 2024 Wiley-VCH GmbH.

1.4 Motivations and thesis outline

In polymer mechanochemistry, ultrasound exhibits lots of advantages compared to other mechanical stimuli (ball milling, compression or tension). For example, easy operation, a small amount of sample required and precise spatial-temporal control. In addition, exploring the mechanochemical transformation of polymers in solutions renders ultrasonication a highly effective and commonly used method in polymer mechanochemistry.

Ultrasound-induced polymer mechanochemistry has gained significant attention to achieve diverse functions in catalysis, polymer degradation, sensing, and activation of drugs or proteins. Particularly, the selective and controlled release of covalently bound payloads for pharmacology has been a rapidly growing field in polymer mechanochemistry. However, the ultrasonication experiments in polymer mechanochemistry studies were commonly conducted by a low-frequency (20 kHz) pulsed ultrasound with high-intensity (~10 W/cm^2). This type of ultrasound generates heavy cavitation and liquid micro-jets, which destroys mammalian cells or tissues. Moreover, the comparably long sonication times limited the application of polymer mechanochemistry in biological systems. Hence, it is highly desirable to develop biocompatible ultrasound-responsive polymer systems to achieve molecule or drug release for sonopharmacology.

In this thesis, I presented two kinds of strategies to achieve molecule or drug release from polymers by sonication. In **Chapter 2**, we show a polymeric microcapsule system; physical isolation was used to concentrate drugs inside the polymeric microcapsules, in which the drug activity is suppressed. After ultrasonic treatment,

the polymer shell is destroyed by cavitation and the drugs are released, at which point the drug can exhibit activity in the biological system. In **Chapters 3**, **4** and **5**, ultrasound-induced molecule or drug release from polymers by mechanochemical transformations that involve mechanophore activation.

In **Chapter 1**, I introduced the background of ultrasound-induced polymer mechanochemistry. Moreover, recent achievements in ultrasound-induced polymer mechanochemistry are briefly reviewed.

In **Chapter 2**, a novel design of ultrasound-responsive nanodrug delivery system by the combination of nanodrug and microcapsule was presented. Nanodrug was fabricated by covalently attaching the small molecular drug Vancomycin on the surface of gold nanoparticles (Vanco-Au NPs) to overcome the leakage problem in microcapsule-based drug delivery systems. During sonication, cavitation destroys the ionic bonds and polymer chains that belong to polyelectrolytes, finally leading to the decomposition of the polymer shell. We investigated the effect of unfocused high-intensity ultrasound (20 kHz) on these microcapsules and investigated the nanodrug release. Moreover, silica-doped polymeric microcapsules were investigated, not only response to 20 kHz ultrasound but also to high-frequency (MHz) ultrasound. Finally, the effect of US-induced drug release on *S.aureus* was investigated to determine the medical potential of this novel drug release system.

In **Chapter 3**, we prepared network core-structured star polymers (NCSPs) with multiple end chains as another ultrasound responsive polymer architecture. 1.5 MHz high-intensity focused ultrasound (HIFU) irradiation was applied to verify the responsiveness of NCSPs to sonication. The NCSPs showed high sensitivity to megahertz HIFU irradiation. The activation of disulfide in NCSPs showed an acceleration effect compared to linear polymers. The fluorophore and drug release from polymers is based on the activation of disulfide mechanophores. By exposing HeLa cells to the released drug, its cytotoxic effects and potential for cancer treatment were further investigated. This study assesses the potential of HIFU-triggered drug release from polymers for sonophamacology.

In **Chapter 4**, we reported the design and synthesis of ultrasound-responsive polymeric microgels. The fluorescence probe (umbelliferone, UMB) and small molecule drug (camptothecin, CPT) were successively released from microgels via HIFU sonication. This strategy relies on HIFU-induced selective scission of disulfide bonds to generate reducing agent thiol groups, which activate carbonate-contained polymer by thiol-disulfide exchange reaction and intramolecular cyclization, to achieve the release of small molecules.

In **Chapter 5**, we investigate an US-responsive polymeric microbubbles (PMBs) system. In this regard, we probe if new colloidal polymer architectures with high compressibility are suited scaffolds for polymer mechanochemistry. Uniform-sized N_2-filled PMBs were prepared by microfluidic engineering. The US remote-controlled versatile mechanochemical transformations in PMBs were investigated. In this chapter, the commonly used 20 kHz ultrasound and megahertz biocompatible HIFU were applied to study the mechanical response of microbubbles.

1.5 References

1. Gil, E. S., & Hudson, S. M. (2004). Stimuli-reponsive polymers and their bioconjugates. *Progress in Polymer Science*, *29*(12), 1173-1222.

2. Mano, J. F. (2008). Stimuli ‐ responsive polymeric systems for biomedical applications. *Advanced Engineering Materials*, *10*(6), 515-527.

3. Ganta, S., Devalapally, H., Shahiwala, A., & Amiji, M. (2008). A review of stimuli-responsive nanocarriers for drug and gene delivery. *Journal of Controlled Release*, *126*(3), 187-204.

4. Klaikherd, A., Nagamani, C., & Thayumanavan, S. (2009). Multi-stimuli sensitive amphiphilic block copolymer assemblies. *Journal of the American Chemical Society*, *131*(13), 4830-4838.

5. Jochum, F. D., & Theato, P. (2013). Temperature-and light-responsive smart polymer materials. *Chemical Society Reviews*, *42*(17), 7468-7483.

6. Zhao, Y. (2012). Light-responsive block copolymer micelles. *Macromolecules*, *45*(9), 3647-3657.

7. Katz, J. S., & Burdick, J. A. (2010). Light ‐ responsive biomaterials: development and applications. *Macromolecular Bioscience*, *10*(4), 339-348.

8. Schmaljohann, D. (2006). Thermo-and pH-responsive polymers in drug delivery. *Advanced Drug Delivery Reviews*, *58*(15), 1655-1670.

9. Du, J. Z., Du, X. J., Mao, C. Q., & Wang, J. (2011). Tailor-made dual pH-sensitive polymer–doxorubicin nanoparticles for efficient anticancer drug delivery. *Journal of the American Chemical Society*, *133*(44), 17560-17563.

10. Huh, K. M., Kang, H. C., Lee, Y. J., & Bae, Y. H. (2012). pH-sensitive polymers for drug delivery. *Macromolecular Research*, *20*, 224-233.

11. Wen, Y., Zhang, Z., & Li, J. (2014). Highly Efficient Multifunctional Supramolecular Gene Carrier System Self ‐ Assembled from Redox ‐ Sensitive and Zwitterionic Polymer Blocks. *Advanced Functional Materials*, *24*(25), 3874-3884.

12. Cho, H., Bae, J., Garripelli, V. K., Anderson, J. M., Jun, H. W., & Jo, S. (2012). Redox-sensitive polymeric nanoparticles for drug delivery. *Chemical Communications*, *48*(48), 6043-6045.

13. Pike, M., & Watson, W. F. (1952). Mastication of rubber, I. Mechanism of plasticizing by cold mastication. *Journal of Polymer Science*, *9*(3), 229-251.

14. Angier, D. J., Chambers, W. T., & Watson, W. F. (1957). Mastication of rubber. VI. Viscosity and molecular weight relationships for natural rubber after cold mastication. *Journal of Polymer Science*, *25*(109), 129-138.

15. Mohapatra, H., Kleiman, M., & Esser-Kahn, A. P. (2017). Mechanically controlled radical polymerization initiated by ultrasound. *Nature Chemistry*, *9*(2), 135-139.

16. Piermattei, A., Karthikeyan, S., & Sijbesma, R. P. (2009). Activating catalysts with mechanical force. *Nature Chemistry*, *1*(2), 133-137.

17. Boswell, B. R., Mansson, C. M., Cox, J. M., Jin, Z., Romaniuk, J. A., Lindquist, K. P., Cegelski, L., Xia, Y., Lopez, S. A., & Burns, N. Z. (2021). Mechanochemical synthesis of an elusive fluorinated polyacetylene. *Nature Chemistry*, *13*(1), 41-46.

18. Gunckel, R., & Nofen, E. (2018). Stress-Sensing Thermoset Polymer Networks via Grafted Cinnamoyl Mechanophores in Epoxy. *APS March Meeting* 2018. (Abstract id: A52.005).

19. Göstl, R., & Sijbesma, R. P. (2016). π-extended anthracenes as sensitive probes for mechanical stress. *Chemical Science*, *7*(1), 370-375.

20. Zhang, Y., Lund, E., Gossweiler, G. R., Lee, B., Niu, Z., Khripin, C., Munch, E., Couty, M., & Craig, S. L. (2021). Molecular damage detection in an elastomer nanocomposite with a coumarin dimer mechanophore. *Macromolecular Rapid Communications*, *42*(1), 2000359.

21. Clough, J. M., Van Der Gucht, J., & Sijbesma, R. P. (2017). Mechanoluminescent imaging of Osmotic stress-induced damage in a glassy polymer network. *Macromolecules*, *50*(5), 2043-2053.

22. Sulkanen, A. R., Sung, J., Robb, M. J., Moore, J. S., Sottos, N. R., & Liu, G. Y. (2019). Spatially selective and density-controlled activation of interfacial mechanophores. *Journal of the American Chemical Society*, *141*(9), 4080-4085.

23. Overholts, A. C., Granados Razo, W., & Robb, M. J. (2023). Mechanically gated formation of donor–acceptor Stenhouse adducts enabling mechanochemical multicolour soft lithography. *Nature Chemistry*, *15*(3), 332-338.

24. Kim, G., Wu, Q., Chu, J. L., Smith, E. J., Oelze, M. L., Moore, J. S., & Li, K. C. (2022). Ultrasound controlled mechanophore activation in hydrogels for cancer therapy. *Proceedings of the National Academy of Sciences*, *119*(4), e2109791119.

25. Yao, Y., McFadden, M. E., Luo, S. M., Barber, R. W., Kang, E., Bar-Zion, A., Smith, C. A., Jin, Z., Legendre, M., Ling, B., Malounda, D., Torres, A., Hamza, T., Edwards, C. E. R., Shapiro, M. G., & Robb, M. J. (2023). Remote control of mechanochemical reactions under physiological conditions using biocompatible focused ultrasound. *Proceedings of the National Academy of Sciences*, *120*(39), e2309822120.

26. Shi, Z., Song, Q., Göstl, R., & Herrmann, A. (2021). Correction: Mechanochemical activation of disulfide-based multifunctional polymers for theranostic drug release. *Chemical Science*, *12*(11), 4184-4184.

27. Huo, S., Zhao, P., Shi, Z., Zou, M., Yang, X., Warszawik, E., Loznik, M., Göstl, R., & Herrmann, A. (2021). Mechanochemical bond scission for the activation of drugs. *Nature Chemistry*, *13*(2), 131-139.

28. Staudinger, H., & Bondy, H. F. (1930). Isoprene and rubber. XIX. The molecular size of rubber and balata. *Rubber Chemistry and Technology*, *3*(3), 519-521.

29. Staudinger, H., & Leupold, E. O. (1930). Über Isopren und Kautschuk, 18. Mitteil.: Viscositäts-Untersuchungen an Balata. *Berichte der deutschen chemischen Gesellschaft (A and B Series)*, *63*(3), 730-733.

30. Staudinger, H., & Heuer, W. (1934). Über hochpolymere Verbindungen, 93. Mitteil.: Über das Zerreißen der Faden-Moleküle des Poly-styrols. *Berichte der deutschen chemischen Gesellschaft (A and B Series)*, *67*(7), 1159-1164.

31. Encina, M. V., Lissi, E., Sarasua, M., Gargallo, L., & Radic, D. (1980). Ultrasonic degradation of polyvinylpyrrolidone: Effect of peroxide linkages. *Journal of Polymer Science: Polymer Letters Edition*, *18*(12), 757-760.

32. Blanksby, S. J., & Ellison, G. B. (2003). Bond dissociation energies of organic molecules. *Accounts of Chemical Research*, *36*(4), 255-263.

33. Li, J., Nagamani, C., & Moore, J. S. (2015). Polymer mechanochemistry: from destructive to productive. *Accounts of Chemical Research*, *48*(8), 2181-2190.

34. Hickenboth, C. R., Moore, J. S., White, S. R., Sottos, N. R., Baudry, J., & Wilson, S. R. (2007). Biasing reaction pathways with mechanical force. *Nature*, *446*(7134), 423-427.

35. Lenhardt, J. M., Ong, M. T., Choe, R., Evenhuis, C. R., Martinez, T. J., & Craig, S. L. (2010). Trapping a diradical transition state by mechanochemical polymer extension. *Science*, *329*(5995), 1057-1060.

36. Huang, Z., & Boulatov, R. (2011). Chemomechanics: chemical kinetics for multiscale phenomena. *Chemical Society Reviews*, *40*(5), 2359-2384.

37. Davis, D. A., Hamilton, A., Yang, J., Cremar, L. D., Van Gough, D., Potisek, S. L., Ong, M. T., Braun, P. V., Martínez, T. J., White, S. R., Moore, J. S., & Sottos, N. R. (2009). Force-induced activation of covalent bonds in mechanoresponsive polymeric materials. *Nature*, *459*(7243), 68-72.

38. Gossweiler, G. R., Hewage, G. B., Soriano, G., Wang, Q., Welshofer, G. W., Zhao, X., & Craig, S. L. (2014). Mechanochemical activation of covalent bonds in polymers with full and repeatable macroscopic shape recovery. *ACS Macro Letters*, *3*(3), 216-219.

39. Göstl, R., & Sijbesma, R. P. (2016). π-extended anthracenes as sensitive probes for mechanical stress. *Chemical Science*, *7*(1), 370-375.

40. Overholts, A. C., Granados Razo, W., & Robb, M. J. (2023). Mechanically gated formation of donor–acceptor Stenhouse adducts enabling mechanochemical multicolour soft lithography. *Nature Chemistry*, *15*(3), 332-338.

41. James, S. L., Adams, C. J., Bolm, C., Braga, D., Collier, P., Friščić, T., Grepioni, F., Harris, K. D., Hyett, G., Jones, W., Krebs, A., Mack, J., Maini, L., Orpen, A. G., Parkin, I. P., Shearouse, W. C., Steed, J. W., & Waddell, D. C. (2012). Mechanochemistry: opportunities for new and cleaner synthesis. *Chemical Society Reviews*, *41*(1), 413-447.

42. Kobayashi, H., Suzuki, Y., Sagawa, T., Kuroki, K., Hasegawa, J. Y., & Fukuoka, A. (2021). Impact of tensile and compressive forces on the hydrolysis of cellulose and chitin. *Physical Chemistry Chemical Physics*, *23*(30), 15908-15916.

43. Turksoy, A., Yildiz, D., Aydonat, S., Beduk, T., Canyurt, M., Baytekin, B., & Akkaya, E. U. (2020). Mechanochemical generation of singlet oxygen. *RSC Advances*, *10*(16), 9182-9186.

44. Lu, Y., Sugita, H., Mikami, K., Aoki, D., & Otsuka, H. (2021). Mechanochemical reactions of bis (9-methylphenyl-9-fluorenyl) peroxides and their applications in cross-linked polymers. *Journal of the American Chemical Society*, *143*(42), 17744-17750.

45. Stratigaki, M., Baumann, C., van Breemen, L. C., Heuts, J. P., Sijbesma, R. P., & Göstl, R. (2020). Fractography of poly (N-isopropylacrylamide) hydrogel networks crosslinked with mechanofluorophores using confocal laser scanning microscopy. *Polymer Chemistry*, *11*(2), 358-366.

46. Baumann, C., Stratigaki, M., Centeno, S. P., & Göstl, R. (2021). Multicolor mechanofluorophores for the quantitative detection of covalent bond scission in polymers. *Angewandte Chemie International Edition*, *60*(24), 13287-13293.

47. Lenhardt, J. M., Black Ramirez, A. L., Lee, B., Kouznetsova, T. B., & Craig, S. L. (2015). Mechanistic insights into the sonochemical activation of multimechanophore cyclopropanated polybutadiene polymers. *Macromolecules*, *48*(18), 6396-6403.

48. Wang, J., Kouznetsova, T. B., Kean, Z. S., Fan, L., Mar, B. D., Martínez, T. J., & Craig, S. L. (2014). A remote stereochemical lever arm effect in polymer mechanochemistry. *Journal of the American Chemical Society*, *136*(43), 15162-15165.

49. Klukovich, H. M., Kouznetsova, T. B., Kean, Z. S., Lenhardt, J. M., & Craig, S. L. (2013). A backbone lever-arm effect enhances polymer mechanochemistry. *Nature Chemistry*, *5*(2), 110-114.

50. Gossweiler, G. R., Kouznetsova, T. B., & Craig, S. L. (2015). Force-rate characterization of two spiropyran-based molecular force probes. *Journal of the American Chemical Society*, *137*(19), 6148-6151.

51. Kryger, M. J., Munaretto, A. M., & Moore, J. S. (2011). Structure–mechanochemical activity relationships for cyclobutane mechanophores. *Journal of the American Chemical Society*, *133*(46), 18992-18998.

52. Kean, Z. S., Niu, Z., Hewage, G. B., Rheingold, A. L., & Craig, S. L. (2013). Stress-responsive polymers containing cyclobutane core mechanophores: reactivity and mechanistic insights. *Journal of the American Chemical Society*, *135*(36), 13598-13604.

53. Pill, M. F., Holz, K., Preußke, N., Berger, F., Clausen‐Schaumann, H., Lüning, U., & Beyer, M. K. (2016). Mechanochemical cycloreversion of cyclobutane observed at the single molecule level. *Chemistry–A European Journal*, *22*(34), 12034-12039.

54. Berkowski, K. L., Potisek, S. L., Hickenboth, C. R., & Moore, J. S. (2005). Ultrasound-induced site-specific cleavage of azo-functionalized poly (ethylene glycol). *Macromolecules*, *38*(22), 8975-8978.

55. Humphrey, V. F. (2007). Ultrasound and matter—Physical interactions. *Progress in Biophysics and Molecular Biology*, *93*(1-3), 195-211.

56. Caruso, M. M., Davis, D. A., Shen, Q., Odom, S. A., Sottos, N. R., White, S. R., & Moore, J. S. (2009). Mechanically-induced chemical changes in polymeric materials. *Chemical Reviews*, *109*(11), 5755-5798.

57. Huo, S., Zhao, P., Shi, Z., Zou, M., Yang, X., Warszawik, E., Loznik. M., & Herrmann, A. (2021). Mechanochemical bond scission for the activation of drugs. *Nature Chemistry*, *13*(2), 131-139.

58. Bastian, A. A., Marcozzi, A., & Herrmann, A. (2012). Selective transformations of complex molecules are enabled by aptameric protective groups. *Nature Chemistry*, *4*(10), 789-793.

59. Zou, M., Zhao, P., Huo, S., Göstl, R., & Herrmann, A. (2021). Activation of antibiotic-grafted polymer brushes by ultrasound. *ACS Macro Letters*, *11*(1), 15-19.

60. Melville, H. W., & Murray, A. J. R. (1950). The ultrasonic degradation of polymers. *Transactions of the Faraday Society*, *46*, 996-1009.

61. Sohma, J. (1989). Mechanochemistry of polymers. *Progress in Polymer Science*, *14*(4), 451-596.

62. Encina, M. V., Lissi, E., Sarasua, M., Gargallo, L., & Radic, D. (1980). Ultrasonic degradation of polyvinylpyrrolidone: Effect of peroxide linkages. *Journal of Polymer Science: Polymer Letters Edition*, *18*(12), 757-760.

63. Fritze, U. F., Craig, S. L., & von Delius, M. (2018). Disulfide‐centered poly (methyl acrylates): Four different stimuli to cleave a polymer. *Journal of Polymer Science Part A: Polymer Chemistry*, *56*(13), 1404-1411.

64. Fritze, U. F., & von Delius, M. (2016). Dynamic disulfide metathesis induced by ultrasound. *Chemical Communications*, *52*(38), 6363-6366.

65. Shi, Z., Wu, J., Song, Q., Göstl, R., & Herrmann, A. (2020). Toward drug release using polymer mechanochemical disulfide scission. *Journal of the American Chemical Society*, *142*(34), 14725-14732.

66. Shiraki, T., Diesendruck, C. E., & Moore, J. S. (2014). The mechanochemical production of phenyl cations through heterolytic bond scission. *Faraday Discussions*, *170*, 385-394.

67. Shirai, M., & Tsunooka, M. (1996). Photoacid and photobase generators: chemistry and applications to polymeric materials. *Progress in Polymer Science*, *21*(1), 1-45.

68. Hacker, N. P., Hofer, D. C., & Welsh, K. M. (1992). Photochemical and photophysical studies on chemically amplified resists. *Journal of Photopolymer Science and Technology*, *5*(1), 35-46.

69. Diesendruck, C. E., Peterson, G. I., Kulik, H. J., Kaitz, J. A., Mar, B. D., May, P. A., White, S. R., Martínez, T. J., Boydston, A. J., & Moore, J. S. (2014). Mechanically triggered heterolytic unzipping of a low-ceiling-temperature polymer. *Nature Chemistry*, *6*(7), 623-628.

70. Wu, M., Li, Y., Yuan, W., De Bo, G., Cao, Y., & Chen, Y. (2022). Cooperative and geometry-dependent mechanochromic reactivity through aromatic fusion of two rhodamines in polymers. *Journal of the American Chemical Society*, *144*(37), 17120-17128.

71. Nagamani, C., Liu, H., & Moore, J. S. (2016). Mechanogeneration of acid from oxime sulfonates. *Journal of the American Chemical Society*, *138*(8), 2540-2543.

72. Campagna, D., & Göstl, R. (2022). Mechanoresponsive Carbamoyloximes for the Activation of Secondary Amines in Polymers. *Angewandte Chemie International Edition*, *61*(39), e202207557.

73. Reich, H. J., & Hondal, R. J. (2016). Why nature chose selenium. *ACS Chemical Biology*, *11*(4), 821-841.

74. Ji, S., Cao, W., Yu, Y., & Xu, H. (2014). Dynamic diselenide bonds: exchange reaction induced by visible light without catalysis. *Angewandte Chemie International Edition*, *53*(26), 6781-6785.

75. Xia, J., Li, T., Lu, C., & Xu, H. (2018). Selenium-containing polymers: perspectives toward diverse applications in both adaptive and biomedical materials. *Macromolecules*, *51*(19), 7435-7455.

76. Singh, F. V., & Wirth, T. (2019). Selenium reagents as catalysts. *Catalysis Science & Technology*, *9*(5), 1073-1091.

77. Ye, H., Zhou, Y., Liu, X., Chen, Y., Duan, S., Zhu, R., Liu, Y., & Yin, L. (2019). Recent advances on reactive oxygen species-responsive delivery and diagnosis system. *Biomacromolecules*, *20*(7), 2441-2463.

78. Bhowmick, D., & Mugesh, G. (2015). Insights into the catalytic mechanism of synthetic glutathione peroxidase mimetics. *Organic & Biomolecular Chemistry*, *13*(41), 10262-10272.

79. Pan, S., Yang, J., Ji, S., Li, T., Gao, S., Sun, C., & Xu, H. (2020). Cancer therapy by targeting thioredoxin reductase based on selenium-containing dynamic covalent bond. *CCS Chemistry*, *2*(3), 225-235.

80. Sun, C., Wang, L., Xianyu, B., Li, T., Gao, S., & Xu, H. (2019). Selenoxide elimination manipulate the oxidative stress to improve the antitumor efficacy. *Biomaterials*, *225*, 119514.

81. Wu, Q., Yuan, Y., Chen, F., Sun, C., Xu, H., & Chen, Y. (2020). Diselenide-linked polymers under sonication. *ACS Macro Letters*, *9*(11), 1547-1551.

82. Di Giannantonio, M., Ayer, M. A., Verde‐Sesto, E., Lattuada, M., Weder, C., & Fromm, K. M. (2018). Triggered metal ion release and oxidation: ferrocene as a mechanophore in polymers. *Angewandte Chemie International Edition*, *57*(35), 11445-11450.

83. Sha, Y., Zhang, Y., Xu, E., Wang, Z., Zhu, T., Craig, S. L., & Tang, C. (2018). Quantitative and mechanistic mechanochemistry in ferrocene dissociation. *ACS Macro Letters*, *7*(10), 1174-1179.

84. Zhang, Y., Wang, Z., Kouznetsova, T. B., Sha, Y., Xu, E., Shannahan, L., Fermen-Coker, M., Lin, Y., Tang, C., & Craig, S. L. (2021). Distal conformational locks on ferrocene mechanophores guide reaction pathways for increased mechanochemical reactivity. *Nature Chemistry*, *13*(1), 56-62.

85. Paulusse, J. M., & Sijbesma, R. P. (2004). Reversible mechanochemistry of a PdII coordination polymer. *Angewandte Chemie International Edition*, *43*(34), 4460-4462.

86. Karthikeyan, S., Potisek, S. L., Piermattei, A., & Sijbesma, R. P. (2008). Highly efficient mechanochemical scission of silver-carbene coordination polymers. *Journal of the American Chemical Society*, *130*(45), 14968-14969.

87. Piermattei, A., Karthikeyan, S., & Sijbesma, R. P. (2009). Activating catalysts with mechanical force. *Nature Chemistry*, *1*(2), 133-137.

88. Zhang, X., Vidavsky, Y., Aharonovich, S., Yang, S. J., Buche, M. R., Diesendruck, C. E., & Silberstein, M. N. (2020). Bridging experiments and theory: isolating the effects of metal–ligand interactions on viscoelasticity of reversible polymer networks. *Soft Matter*, *16*(37), 8591-8601.

89. Levy, A., Feinstein, R., & Diesendruck, C. E. (2019). Mechanical unfolding and thermal refolding of single-chain nanoparticles using ligand–metal bonds. *Journal of the American Chemical Society*, *141*(18), 7256-7260.

90. Rupp, H., & Binder, W. H. (2021). Multicomponent Stress-Sensing Composites Fabricated by 3D-Printing Methodologies. *Macromolecular Rapid Communications*, *42*(1), 2000450.

91. Funtan, S., Funtan, A., Paschke, R., & Binder, W. H. (2020). Biomimetic Elastin-Like Polypeptides as Materials for the Activation of Mechanophoric Catalysts. *Organic Materials*, *2*(02), 116-128.

92. Michael, P., Sheidaee Mehr, S. K., & Binder, W. H. (2017). Synthesis and characterization of polymer linked copper (I) bis (N‐heterocyclic carbene) mechanocatalysts. *Journal of Polymer Science Part A: Polymer Chemistry*, *55*(23), 3893-3907.

93. Michael, P., & Binder, W. H. (2015). A mechanochemically triggered "click" catalyst. *Angewandte Chemie International Edition*, *54*(47), 13918-13922.

94. Küng, R., Pausch, T., Rasch, D., Göstl, R., & Schmidt, B. M. (2021). Mechanochemical Release of Non-Covalently Bound Guests from a Polymer-Decorated Supramolecular Cage. *Angewandte Chemie International Edition*, *60*(24), 13626-13630.

95. Noh, J., Koo, M. B., Jung, J., Peterson, G. I., Kim, K. T., & Choi, T. L. (2023). Monodisperse Cyclic Polymer Mechanochemistry: Scission Kinetics and the Dynamic Memory Effect with Ultrasonication and Ball-Mill Grinding. *Journal of the American Chemical Society*, *145*(33), 18432-18438.

96. Lin, Y., Zhang, Y., Wang, Z., & Craig, S. L. (2019). Dynamic memory effects in the mechanochemistry of cyclic polymers. *Journal of the American Chemical Society*, *141*(28), 10943-10947.

97. Church, D. C., Peterson, G. I., & Boydston, A. J. (2014). Comparison of mechanochemical chain scission rates for linear versus three-arm star polymers in strong acoustic fields. *ACS Macro Letters*, *3*(7), 648-651.

98. Zhang, H., & Diesendruck, C. E. (2022). Accelerated mechanochemistry in helical polymers. *Angewandte Chemie*, *134*(14), e202115325.

99. Peterson, G. I., Noh, J., Bang, K. T., Ma, H., Kim, K. T., & Choi, T. L. (2020). Mechanochemical degradation of brush polymers: Kinetics of ultrasound-induced backbone and arm scission. *Macromolecules*, *53*(5), 1623-1628.

100. Peterson, G. I., Bang, K. T., & Choi, T. L. (2018). Mechanochemical degradation of denpols: synthesis and ultrasound-induced chain scission of polyphenylene-based dendronized polymers. *Journal of the American Chemical Society*, *140*(27), 8599-8608.

101. Izak-Nau, E., Demco, D. E., Braun, S., Baumann, C., Pich, A., & Göstl, R. (2020). Shear-induced structural and functional transformations of poly (N-vinylcaprolactam) microgels. *ACS Applied Polymer Materials*, *2*(4), 1682-1691.

102. Kageshima, M., Lantz, M. A., Jarvis, S. P., Tokumoto, H., Takeda, S., Ptak, A., Nakamura, C., & Miyake, J. (2001). Insight into conformational changes of a single α-helix peptide molecule through stiffness measurements. *Chemical Physics Letters*, *343*(1-2), 77-82.

103. Sluysmans, D., Willet, N., Thevenot, J., Lecommandoux, S., & Duwez, A. S. (2020). Single-molecule mechanical unfolding experiments reveal a critical length for the formation of α-helices in peptides. *Nanoscale Horizons*, *5*(4), 671-678.

104. Berkemeier, F., Bertz, M., Xiao, S., Pinotsis, N., Wilmanns, M., Gräter, F., & Rief, M. (2011). Fast-folding α-helices as reversible strain absorbers in the muscle protein myomesin. *Proceedings of the National Academy of Sciences*, *108*(34), 14139-14144.

105. Lin, Y., Kouznetsova, T. B., Chang, C. C., & Craig, S. L. (2020). Enhanced polymer mechanical degradation through mechanochemically unveiled lactonization. *Nature Communications*, *11*(1), 4987.

106. Hsu, T. G., Liu, S., Guan, X., Yoon, S., Zhou, J., Chen, W. Y., Gaire, S., Seylar, J., Chen, H., Wang, Z., Rivera, J., Wu, L., Ziegler, C. J., McKenzie, R., & Wang, J. (2023). Mechanochemically accessing a challenging-to-synthesize depolymerizable polymer. *Nature Communications*, *14*(1), 225.

107. Liu, P., Jimaja, S., Immel, S., Thomas, C., Mayer, M., Weder, C., & Bruns, N. (2024). Mechanically triggered on-demand degradation of polymers synthesized by radical polymerizations. *Nature Chemistry*, *16*, 1184-1192.

108. Shi, Z., Song, Q., Göstl, R., & Herrmann, A. (2021). Mechanochemical activation of disulfide-based multifunctional polymers for theranostic drug release. *Chemical Science*, *12*(5), 1668-1674.

109. Chen, L., Nixon, R., & De Bo, G. (2024). Force-controlled release of small molecules with a rotaxane actuator. *Nature*, *628*, 320-325.

110. Dubowchik, G. M., Firestone, R. A., Padilla, L., Willner, D., Hofstead, S. J., Mosure, K., Knipe, J. O., Lasch, S. J., & Trail, P. A. (2002). Cathepsin B-labile dipeptide linkers for lysosomal release of doxorubicin from internalizing immunoconjugates: model studies of enzymatic drug release and antigen-specific in vitro anticancer activity. *Bioconjugate Chemistry*, *13*(4), 855-869.

111. Zhou, Y., Huo, S., Loznik, M., Göstl, R., Boersma, A. J., & Herrmann, A. (2021). Controlling optical and catalytic activity of genetically engineered proteins by ultrasound. *Angewandte Chemie International Edition*, *60*(3), 1493-1497.

112. Zhao, P., Huo, S., Fan, J., Chen, J., Kiessling, F., Boersma, A. J., Göstl, R., & Herrmann, A. (2021). Activation of the catalytic activity of thrombin for fibrin formation by ultrasound. *Angewandte Chemie International Edition*, *60*(26), 14707-14714.

113. Mohsen, M. G., & Kool, E. T. (2016). The discovery of rolling circle amplification and rolling circle transcription. *Accounts of Chemical Research*, *49*(11), 2540-2550.

114. Zhao, W., Ali, M. M., Brook, M. A., & Li, Y. (2008). Rolling circle amplification: applications in nanotechnology and biodetection with functional nucleic acids. *Angewandte Chemie International Edition*, *47*(34), 6330-6337.

115. Ali, M. M., Li, F., Zhang, Z., Zhang, K., Kang, D. K., Ankrum, J. A., Le, X. C., & Zhao, W. (2014). Rolling circle amplification: a versatile tool for chemical biology, materials science and medicine. *Chemical Society Reviews*, *43*(10), 3324-3341.

116. Rath, W. H., Göstl, R., & Herrmann, A. (2024). Mechanochemical Activation of DNAzyme by Ultrasound. *Advanced Science*, 2306236.

2. Ultrasound-triggered antibacterial nanodrug release from polymeric microcapsules

The research contained within this chapter has been published in the journal of Nano Research (**Jilin Fan**, Mingjun Xuan*, Pengkun, Mark Loznik, Junlin Chen, Fabian Kiessling, Lifei Zheng*, and Andreas Herrmann*. Ultrasound responsive microcapsules for antibacterial nanodrug delivery. Nano Res. 2023, 16, 2738-2748). The author (Jilin Fan) of this thesis contributed to experimental design; synthesized and characterized the materials; analyzed the data and co-wrote the manuscript.
In addition, I (Jilin Fan) declare as follows:
1. I designed and performed the experiments (Microcapsules preparation; Nanodrug preparation; Sonication Assay; Response of microcapsules to sonication; Quantification of Vanco-Au NPs release; Minimal inhibitory concentration (MIC) assay; Live/dead staining assay) contained in the publication.
2. I synthesized and characterized the materials (Microcapsules and Nanodrugs) contained in the publication.
3. I collected the data (TEM images; SEM images; IR spectra; Confocal images; Absorption spectra; DLS analysis; MIC test; Photographs of agar Petri dishes; Live/dead staining test) contained in the publication.
4. I analyzed the data and drew all the figures and tables contained in the publication.
5. I wrote the first version of the manuscript and then co-revised the manuscript.
6. Other authors' contribution to this publication; Pengkun and Mark Loznik gave suggestions on MIC assay; Fabian Kiessling and Junlin Chen gave suggestions on LIFU sonication; Mingjun Xuan and Lifei Zheng gave suggestions on experimental design; Andreas Herrmann gave suggestions on experimental design and revised the first version of the manuscript.

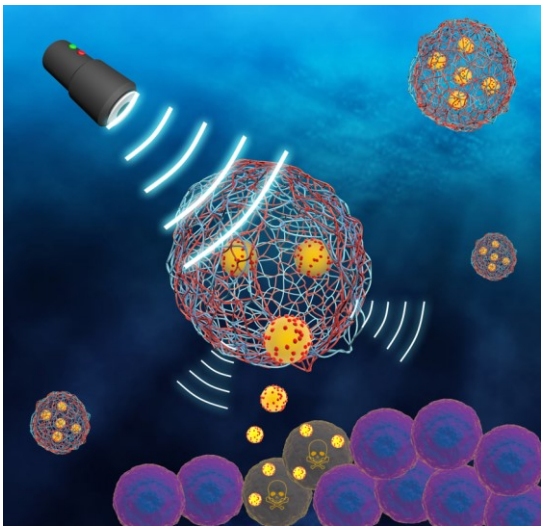

In **Chapter 2**, a novel design of an ultrasound-responsive nanodrug delivery system by the combination of nanodrug and polymeric microcapsule was presented. Nanodrug was fabricated by covalently attaching the small molecular drug Vancomycin on the surface of gold nanoparticles (Vanco-Au NPs) to overcome the leakage problem in microcapsule-based drug delivery systems. During sonication, cavitation destroys the ionic bonds and polymer chains that belong to polyelectrolytes, finally leading to the decomposition of the polymer shell and drug release. Polymeric microcapsules demonstrated excellent sensitivity to the unfocused high-intensity ultrasound (20 kHz). 80% of Vanco-Au NPs were released under five minutes of sonication. Notably, silica-doped polymeric microcapsules were responsive not only to 20 kHz ultrasound but also to high-frequency (MHz) ultrasound. The released Vanco-Au nanodrug showed comparable antibacterial properties as the free nanodrug against *S. aureus*, which has the potential for therapeutic use.

2.1 Abstract

The development of ultrasound-responsive microcapsules has led to advanced spatiotemporally controlled drug delivery systems for macromolecular cargoes like proteins, nucleic acids, and even cells for biomedical applications. However, using microcapsules to deliver small molecular cargoes remains challenging due to potential drug leakage before ultrasound activation, which can cause side effects and reduce the effective drug concentration at the target site. To address these issues, we propose a novel strategy using nanodrugs-nanoparticles coated with small molecule drugs. We demonstrated that encapsulating nanodrugs in microcapsules prevents drug leakage. Additionally, the drug delivery system we developed responds to both unfocused high-intensity ultrasound and clinically relevant high-intensity focused ultrasound. As a proof of concept, we showed that the antibacterial activity of nanodrug-loaded microcapsules could be activated in situ by ultrasound. These findings offer new insights into the development of ultrasound-triggered small molecule drug delivery systems enhanced by metallic nanoparticles.

2.2 Introduction

Microcapsules, which typically have hollow shelled structures, are a significant class of compartmental materials with diverse applications in catalysis, sensing, and drug delivery.[1-13] Their high loading capacity, semi-permeability, biocompatibility, and potential for easy surface functionalization make them efficient carriers of various macromolecular cargoes, including proteins, nucleic acids, and even cells for medical diagnostics and treatments.[14-26] However, loading small molecular cargoes poses a challenge due to drug leakage before reaching the target site, leading to undesired toxicity and reduced drug efficacy.[27-29] To enable on-demand drug delivery, stimuli-responsive microcapsules have been developed. These structures allow controlled drug release triggered by external factors such as temperature, pH, enzymes, light, magnetic fields, and ultrasound.[30-35]

Among these triggers, ultrasound is particularly attractive due to its non-invasiveness, deep tissue penetration, and spatiotemporal control. Most research in this field has focused on using unfocused high-intensity ultrasound, with few systems responding to the clinically relevant low-intensity focused ultrasound (LIFU). To enhance sensitivity to ultrasound, polyelectrolyte microcapsule shells have been combined with inorganic nanoparticles (NPs).[36-40] Despite this, small molecule cargo leakage still occurs, as evidenced by fluorescent probes or doxorubicin molecules easily penetrating the NPs-polymer hybrid microcapsule shells consisting of eight bilayers.[41-42]

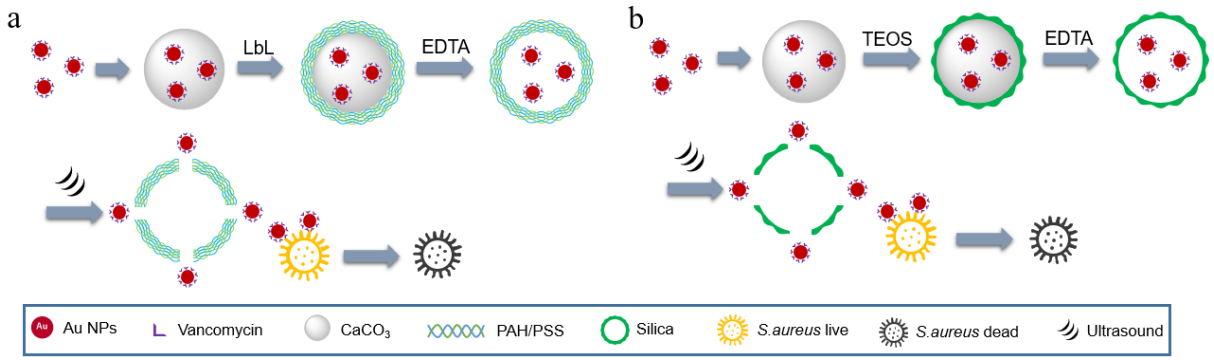

Figure 1. Schematic illustration of the preparation of Vanco-Au@Polyelectrolyte Microcapsules **a**) and Vanco-Au@Silica Microcapsules **b**) and their responsiveness to ultrasound.

To address these challenges, we present a novel ultrasound-responsive nanodrug delivery system combining two components: nanodrugs and polymeric microcapsules (**Figure 1**). The nanodrug was prepared by covalently attaching the small molecule drug vancomycin to the surface of gold nanoparticles (Vanco-Au NPs), effectively preventing leakage in microcapsule-based drug delivery systems. We fabricated two types of microcapsules: PAH/PSS [PAH: poly(allylamine hydrochloride); PSS: poly(sodium-p-styrene sulfonate)] polyelectrolyte microcapsules and silica microcapsules. No significant drug leakage was observed with either type. When subjected to ultrasound, the polyelectrolyte microcapsules with four bilayers showed excellent sensitivity to unfocused high-intensity ultrasound (20 KHz, power intensities >10 W/cm²), releasing 80% of the Vanco-Au NPs after 5 minutes of sonication. Additionally, silica microcapsules responded to both low-frequency and high-frequency ultrasound, making them suitable for therapeutic applications. During sonication, cavitation destroys the ionic bonds and polymer chains that belong to polyelectrolytes, finally leading to the decomposition of the polymer shell and drug release. *In situ* activation of Vanco-Au nanodrugs by ultrasound was performed in the

presence of bacteria. The application of ultrasound destroyed the microcapsule shells, releasing the Vanco-Au nanodrug, which exhibited antibacterial properties comparable to the free nanodrug against *S. aureus*.

2.3 Results and discussion

2.3.1 Synthesis and characterization of Vanco-Au NPs

First, Vanco-Au NPs were synthesized following the method described in the literature (**Figure 2a**).[46] By transmission electron microscopy (TEM, **Figure 2b** and **Figure 2c**) an average diameter of Vanco-Au NPs of 8 nm was measured. Accordingly, a diameter of 12.1 nm was determined by dynamic light scattering (DLS) (**Figure S1a**). The particle size distribution was larger in DLS compared to TEM, which might be attributed to the hydrodynamic shell on the gold nanoparticles. Scanning Electron Microscopy (SEM) with Energy Dispersive X-Ray Analysis (EDX) results showed the characteristic signal of the element chlorine indicating that vancomycin was successfully conjugated on the surface of gold nanoparticles (**Figure 2d**). **Figure 2e** presents the Infrared Radiation (IR) spectra of both Vanco-Au NPs and pristine vancomycin. Within the fingerprint region (900–1200 cm^{-1}), the characteristic C-O stretching peaks at 1152 and 1174 cm^{-1} were absent in the spectrum of Vanco-Au NPs. This result can be explained by the oxidation of glycosides and thier reaction with tetrachloroauric acid during the preparation of Vanco-Au NPs. The absorption spectrum of the Vanco-Au NPs (**Figure S1b**) showed a characteristic Au NP absorption peak at 520 nm. To determine the vancomycin drug molecules loading on each nanoparticle, the supernatant containing excess vancomycin was analyzed based on a standard absorbance calibration curve (**Figure S2**). From this analysis, the amount of vancomycin loaded onto each gold nanoparticle was estimated to be 3250 molecules.

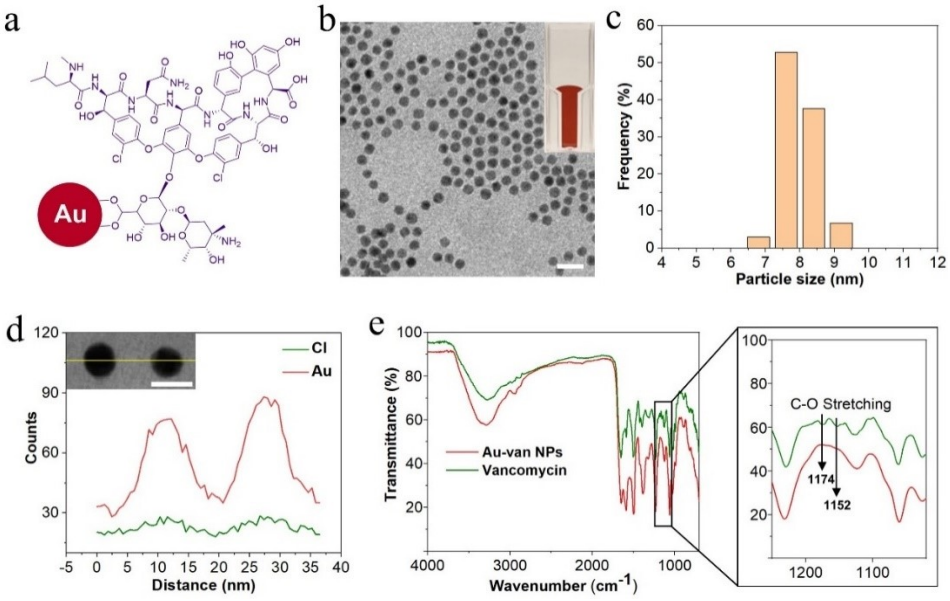

Figure 2. **Synthesis and characterization of Vanco-Au NPs**. **a**) Schematic representation of Vanco-Au NPs. **b**) TEM image of Vanco-Au NPs (Scale bar: 20 nm). **c**) Vanco-Au NPs size distribution from DLS measurements. **d**) EDX elemental mapping of Vanco-Au NPs. Scale bar in inset: 10 nm. **e**) IR spectra of Vanco-Au NPs and the pristine vancomycin.

2.3.2 Fabrication of Vanco-Au@Polyelectrolyte Microcapsules and their responsiveness to Ultrasound

For the Layer-by-Layer (LbL) assembly of polyelectrolyte microcapsules, $CaCO_3$ particles (Figure S3) with an average diameter of approximately 5 μm were synthesized to serve as the core template. To encapsulate Vanco-Au NPs into the microcapsules, $CaCO_3$ particles that contain Vanco-Au NPs (Vanco-Au@$CaCO_3$) were prepared by adding Vanco-Au NPs into the reaction mixture of $CaCl_2$ and Na_2CO_3. Once the particles were obtained, ethylenediaminetetraacetic acid (EDTA) was used to dissolve the $CaCO_3$ particles again to quantify the concentration of Vanco-Au in Vanco-Au@$CaCO_3$ suspension.[44] The absorption intensity at 450 nm was used for the determination of the concentration of Vanco-Au, which was 18 nM in respect to Au NPs (**Figure S4**). This method was later applied to quantify the encapsulated Vanco-Au, enabling the calculation of nanodrug release efficiency following ultrasound exposure. Given the high encapsulation efficiency of $CaCO_3$ particles within microcapsules, the loss of Vanco-Au during this process was considered negligible.

Next, Vanco-Au@$CaCO_3$ or $CaCO_3$ particles were used as the template to assemble polyelectrolyte microcapsules. The oppositely charged polyelectrolytes PAH and PSS were used as the alternating layers. Following the well-established LbL assembly procedure (four and six bilayers were absorbed on the $CaCO_3$ templates, which were removed subsequently by EDTA to obtain Vanco-Au@Polyelectrolyte (**Figure 3b**, **Figure S7**) and empty Polyelectrolyte Microcapsules (**Figure S8**), exhibiting red and off-white color, respectively (**Figure 3c**). The attempt to fabricate microcapsules with two bilayers was not successful (**Figure S9**). In comparison to the empty polyelectrolyte microcapsule, the absorption spectrum of Vanco-Au@Polyelectrolyte showed an absorption maximum at 520 nm, indicating that Vanco-Au NPs were successfully encapsulated into the microcapsules. This was further verified by the well overlapping gold and chlorine signals of elemental mapping with the morphology of microcapsules as shown in **Figure S10**. Moreover, simple statistics were conducted according to the TEM study. Approximately 7500 Vanco-Au NPs per μm^2 were observed on each polyelectrolyte microcapsule, highlighting the remarkable loading capacity of microcapsules (**Figure S11** and **Figure S12**).

We also investigated the stability of the prepared Vanco-Au@Polyelectrolyte microcapsules. For this purpose, the leakage of Vanco-Au NPs from microcapsules was evaluated. The supernatants of the freshly prepared Vanco-Au@Polyelectrolyte microcapsules before and after 24 h shaking (500 rpm) were collected and measured by UV/Vis absorption spectroscopy. For both of four and six bilayers' polyelectrolyte microcapsules, no obvious increase of the absorbance at 450 nm was observed from the spectra (**Figure 3d**). This result suggests that no Vanco-Au NPs leaked out of the microcapsules during shaking. In contrast, encapsulating the small molecule cyanine 3 (Cy3) in microcapsules led to a noticeable change after 24 hours of shaking. The collected supernatant exhibited a pink colour and a marked rise in absorbance at 560 nm, indicating the presence of Cy3. These findings indicated strong leakage of the small molecule Cy3 from microcapsules (**Figure S13**). Thus, the nanodrug strategy represents an efficient way for the encapsulation of small molecular drugs inside polyelectrolyte microcapsule drug delivery carriers.

To evaluate the responsiveness of the fabricated microcapsules to ultrasound, we exposed Vanco-Au@Polyelectrolyte microcapsules to ultrasound irradiation (20 kHz, pulsed: 2.0 s on and 1.0 s off). The samples were placed in an ice bath to maintain low temperature to exclude any sonothermal effects (**Figure S14**). The experimental parameters affecting the fragmentation of microcapsules including amplitude (Amp) referring to the strength of the US wave and irradiation time were systematically investigated. Firstly, optical

microscopy was applied to investigate the morphological changes of the microcapsules after US activation (**Figure 3e**). Almost all polyelectrolyte microcapsules with 4 bilayers disintegrated into fragments within 5 minutes of sonication at 25% amplitude; those with 6 bilayers required an extended irradiation time for complete disruption (**Figure 3f**). This result indicates that microcapsules with thicker layers show higher resistance to US activation than the thinner ones. Increasing the US amplitude to 50% resulted in shorter irradiation times of 3 min and 5 min that were required to fragment microcapsules with four and six bilayers, respectively. With the ultrasound amplitude set to 100%, both types of microcapsules were destroyed within one minute.

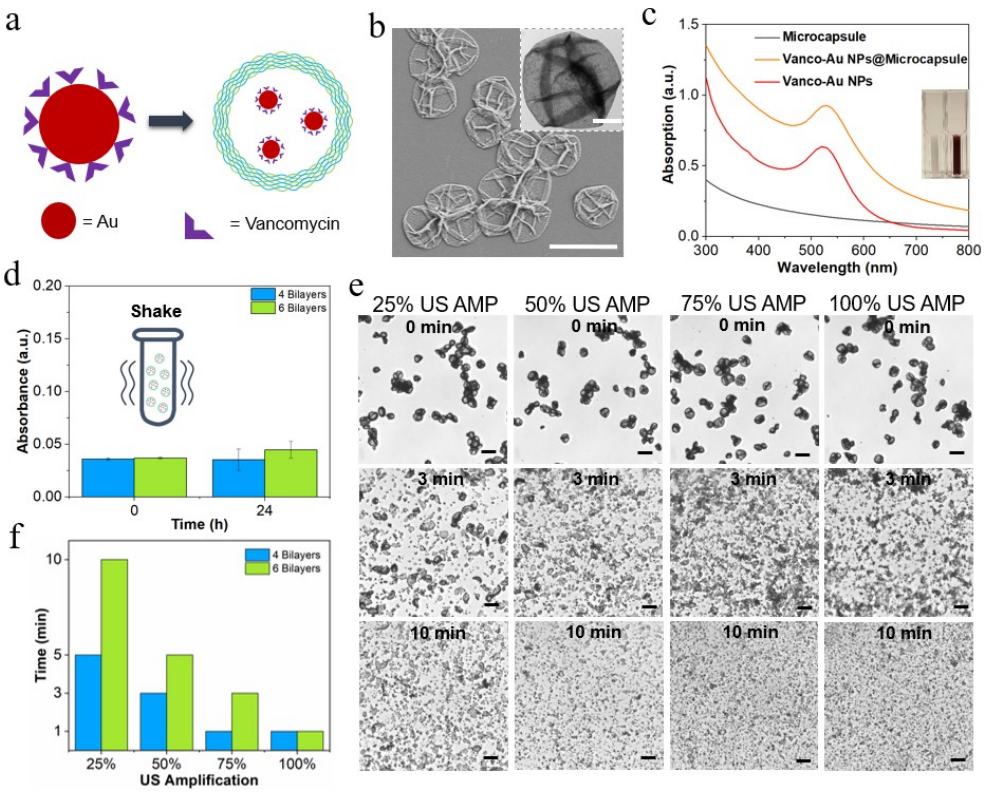

Figure 3. **Production and Ultrasound Response of Vanco-Au@Polyelectrolyte Microcapsules.** **a**) The structural composition of Vanco-Au@Polyelectrolyte Microcapsules. **b**) SEM image of Vanco-Au@Polyelectrolyte Microcapsules, with a TEM image in the inset. Scale bars: 10 µm (main), 2 µm (inset). **c**) UV-Vis spectra illustrating the absorption profiles of empty polyelectrolyte (PAH/PSS) microcapsules, Vanco-Au@Polyelectrolyte Microcapsules, and Vanco-Au NPs. **d**) Absorbance values of supernatants obtained after centrifugation of Vanco-Au@Polyelectrolyte Microcapsule suspensions, recorded before and after 24 h of shaking. Data presented as mean ± s.d., $N = 3$ independent experiments. **e**) Microscopic images of four-bilayer microcapsules following ultrasound exposure. Scale bar: 10 µm. **f**) Duration of sonication for complete disruption of polyelectrolyte microcapsules with four and six bilayers.

Next, the collected fragments were subjected to DLS analysis, revealing a decrease in the sizes of the microcapsules during ultrasound irradiation (**Figure 4a** and **4b**). For example, the fragment sizes of four and six bilayers microcapsules with initial size of 5.5 µm were around 0.8 µm and 1.8 µm after 10 min sonication with 25% amplitude. Under 100% amplitude sonication, the sizes of both microcapsules decreased to 0.8 µm within one minute (**Figure 4c**).

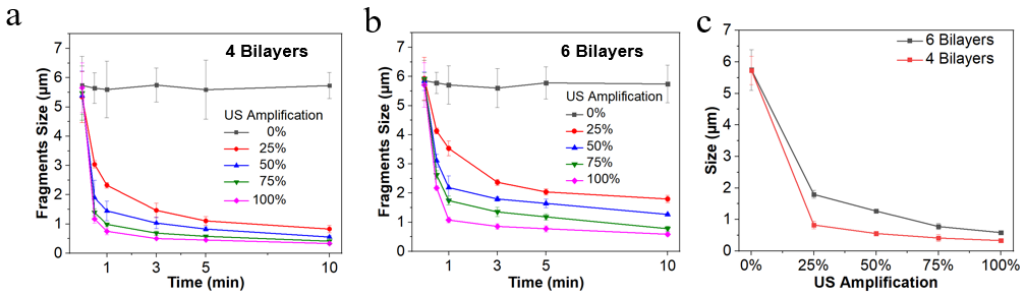

Figure 4. **Ultrasound-Induced Fragmentation of Microcapsules**. **a**) DLS measurement of fragmented four-bilayer microcapsules post-ultrasound exposure. Data represented as mean ± s.d., $N = 3$ independent experiments. **b**) DLS analysis of six-bilayer microcapsule fragments following ultrasound treatment. Mean ± s.d., $N = 3$ independent experiments. **c**) Size distribution comparison of fragments from four- and six-bilayer polyelectrolyte microcapsules after 10 min of sonication at varying ultrasound amplitudes (25%, 50%, 75%, 100%). Mean ± s.d., $N = 3$ independent experiments.

To assess nanodrug release triggered by US activation, UV/Vis absorption spectroscopy was used to analyze the supernatants from sonicated Vanco-Au@Polyelectrolyte and empty microcapsule suspensions (**Figure 5a**). Here, the measurement of empty microcapsules was used as a reference to eliminate the absorbance of the polymer shell fragments. **Figure 5b** shows the absorption spectra of the supernatant from the microcapsules with four bilayers, from which the concentration of the released Vanco-Au NPs was calculated. As shown in **Figure 5c**, under sonication with different US amplitudes, prolonging the irradiation time gradually increased the released amount of the nanodrug. In comparison to the theoretically encapsulated amount of Vanco-Au NPs, it was estimated that more than 80% of the nanodrugs could be released from the four bilayers' microcapsules when the US amplitude was set to be more than 50% (**Figure 5d**). When the US amplitude was 100%, nearly 40% vanco-Au NPs were liberated out of the microcapsules within half a minute. Compared to these results, less amount of vanco-Au NPs was released from the microcapsules with six bilayers (**Figure S16**), probably due to their higher resistance to US as demonstrated before.[36]

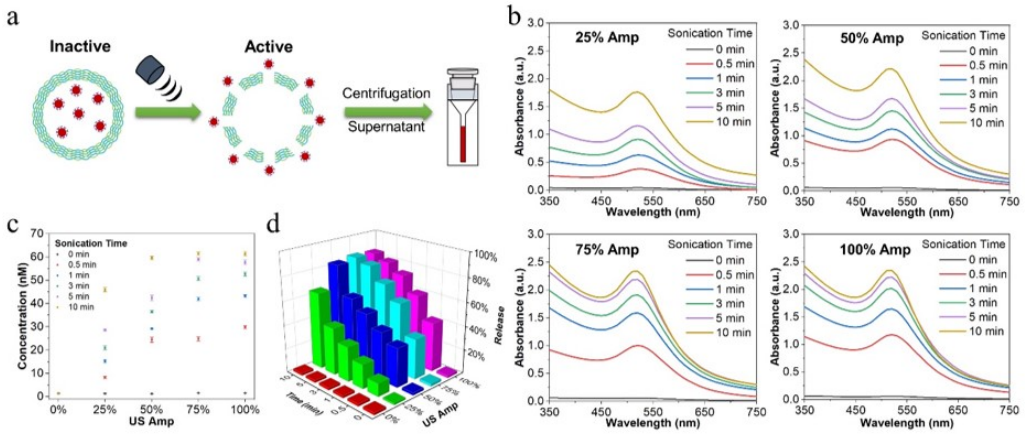

Figure 5. **Quantification of Vanco-Au NPs released from Polyelectrolyte Microcapsules upon US activation. a**) Schematic representation of the quantification process of the released Vanco-Au NPs. **b**) Absorption spectra of the supernatant of vanco-Au NPs @ 4 bilayers PAH/PSS Microcapsules after sonication with 25%, 50%, 75% and 100% Amp. **c**) Calculated concentrations of released Vanco-Au NPs, Mean values ± s.d. from the mean, N = 3 independent experiments. **d**) Release percentage of Vanco-Au NPs from 4 bilayers PAH/PSS microcapsules triggered by sonication.

2.3.3 Fabrication of Vanco-Au@Silica Microcapsules and their responsiveness to ultrasound

Vanco-Au@Silica Microcapsules (**Figure 6a**) were synthesized according to the reported literature.[45] Tetraethyl orthosilicate (TEOS) was used as a monomer to form silicone polymer shells on Vanco-Au@$CaCO_3$ template under basic conditions. After removing $CaCO_3$ with EDTA solution, Vanco-Au@Silica Microcapsules were obtained with a red color, in agreement with the appearance of a characteristic gold NPs absorption maximum of 520 nm in the spectrum (**Figure S17**). The size of the prepared microcapsules was determined by SEM, which exhibited an average size of ~ 5 µm (**Figure 6b**). Moreover, the elemental mapping results showed well overlapping signals of silicon, gold and chlorine (**Figure S18**). Altogether, these results indicate that vanco-Au NPs were successfully encapsulated inside the silica microcapsules. Using a similar procedure as described before, the leakage of Vanco-Au NPs from silica microcapsules was studied. The supernatant spectra of Vanco-Au@Silica Microcapsules before and after 24 hours of shaking did not change in absorbance at 450 nm (**Figure S19**), indicating negligible Vanco-Au NPs leakage from the silica microcapsules.

Next, we tested the responsiveness of Vanco-Au@Silica Microcapsules to unfocused ultrasound (20 kHz). **Figure 6c** shows the microcapsule fragments after 1 minute sonication with 50% amplitude. As shown in **Figures 6d** and **6e**, extending the ultrasound irradiation time from five seconds to one minute gradually increased the release of Vanco-Au NPs. Figure S20 shows the concentrations of released Vanco-Au NPs under different conditions. Within one minute of sonication, approximately 60% of the Vanco-Au NPs were released from the silica microcapsules.

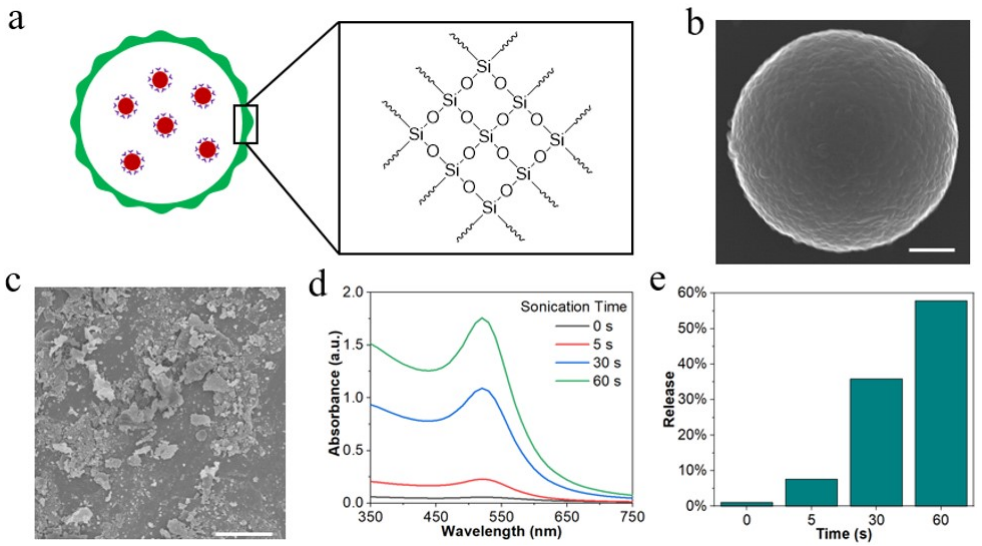

Figure 6. **Fabrication of Vanco-Au@Silica Microcapsules.** **a**) Schematic representation of the Vanco-Au@Silica Microcapsule structure. **b**) SEM image of silica microcapsule. Scale bar: 1 µm. **c**) SEM image of silica microcapsule fragments after 60 s ultrasound (20 KHz) sonication. Scale bar: 2 µm. **d**) Absorption spectra of the supernatant of vanco-Au NPs@Silica Microcapsules suspensions after sonication for 5 s, 30 s, and 60 s. **e**) Release percentage of Vanco-Au NPs from silica microcapsules triggered by sonication.

To prove that the developed nanodrug delivery system can be used with clinically relevant US, Vanco-Au@Silica Microcapsules were subjected to LIFU (5 MHz) (**Figure S21**). **Figure 7b** shows the structures of silica microcapsules after 10 min sonication with LIFU. Besides fragment formation, small holes appeared in the capsule wall. With longer sonication from 0.5 to 10 minutes, the supernatant darkened, suggesting increased Vanco-Au NPs release from silica microcapsules (**Figure 7c**). **Figure 7d** displays the absorption spectra. Accordingly, the release percentages of Vanco-Au NPs under LIFU irradiation were calculated as shown in **Figure 7e**. It was found that around 30% of the nanodrug were liberated from the carrier within the first 3 min and afterwards only a slight increase of release was observed. Three reasons could apply for this finding: first, silica microcapsules were not completely destroyed so that the NPs might be mostly released from the holes in the microcapsules; second, the LIFU sonicator focused on a small spot with the area of less than 4 mm^2, and the sound wave did not act on all microcapsules in the well; third, during the preparation of Vanco-Au@Silica Microcapsules, a certain amount of NPs might be trapped inside the polymer shell. Although the release of nanodrugs triggered by LIFU is currently less efficient compared to unfocused ultrasound, our findings underscore the potential of using clinically compatible ultrasound to activate the nanodrug from the microcapsule carrier.

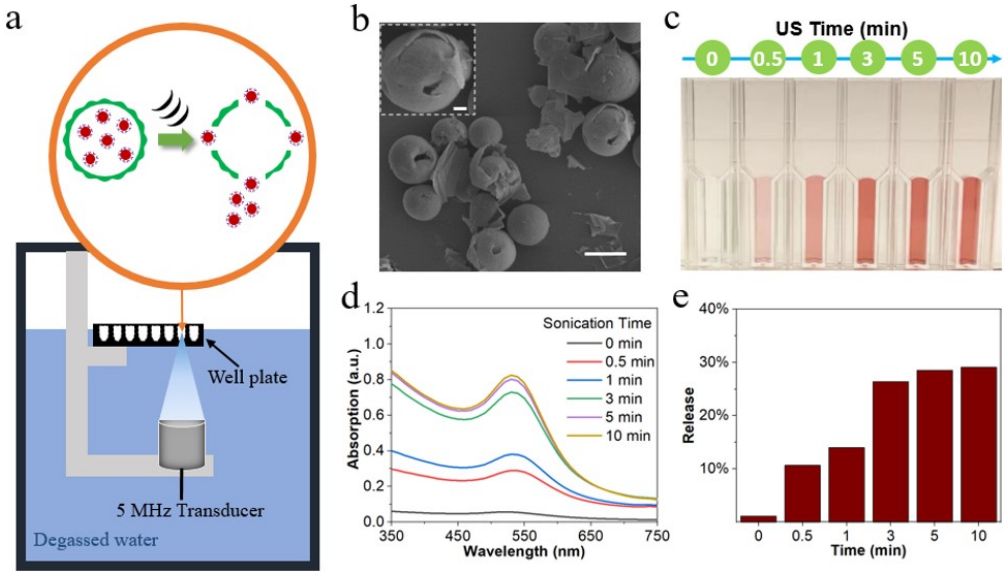

Figure 7. **Ultrasound Responsiveness of Vanco-Au@Silica Microcapsules**. **a**) Schematic representation of the experimental process of LIFU sonication (5 MHz). **b**) SEM images of silica microcapsule after for 10 min. Scale bar: 5 µm. Scale bar in inset: 1 µm. **c**) Images of the supernatant of vanco-Au NPs@Silica Microcapsules collected vanco-Au NPs after sonication using LIFU for 0 min, 0.5 min, 1 min, 3min, 5min and 10 min. **d**) Absorption spectra of the supernatant of vanco-Au NPs@Silica Microcapsules after sonication using LIFU for 0.5 min, 1 min, 3min, 5min and 10 min. **e**) Release percentage of Vanco-Au NPs from silica microcapsules triggered by LIFU.

2.3.4 US triggered antibacterial drug release against *S. aureus*

To prove the potential of the microcapsule system for controlled delivery of drugs, we investigated the antibacterial action of the released nanodrugs from polyelectrolyte microcapsules upon in situ US irradiation (**Figure 8a**). As positive controls, we measured the minimum inhibitory concentrations (MICs) of pristine vancomycin and Vanco-Au nanodrug against S. aureus by the broth dilution method.[46-47] Notably, Vanco-Au showed a MIC value of 4 µgml^{-1} which is only slightly higher than vancomycin. Then, the effect of carriers was examined. For this purpose, MIC tests of PAH/PSS hollow microcapsules and Vanco-Au@Polyelectrolyte Microcapsules before US treatment were performed, showing no obvious antibacterial activity (**Figure 8b**). Then, Vanco-Au@Polyelectrolyte Microcapsules were subjected to US in the presence of *S. aureus*. For this proof-of-concept experiment, US with a frequency of 20 kHz was used for the following reasons. First, the horn-type instrumentation and experiment are straightforward. Moreover, the application of US at 20 kHz had no considerable effect on the viability of S. aureus, indicating that this sonication treatment is compatible with the bacterial culture (**Figure 8c** and **Figure S22**). It was found that the MIC value of Vanco-Au@Polyelectrolyte Microcapsules after 10 min sonication decreased significantly to 8 µg ml^{-1}. Control tests confirmed that ultrasound had no notable impact on the MIC of Vanco-Au or polyelectrolyte microcapsules (**Figure S23**).

To visually assess the antimicrobial activity of the released Vanco-Au NPs, bacterial colonies were counted after culturing S. aureus with PBS (i), pristine vancomycin (ii), Vanco-Au NPs (iii), Vanco-Au@Polyelectrolyte Microcapsules (iv), and US-triggered Vanco-Au@Polyelectrolyte Microcapsules (v) on agar petri dishes (**Figure 8d, 8e**). A marked decrease in bacterial colonies was observed on Petri dishes (v) containing US-treated Vanco-Au@Microcapsules.

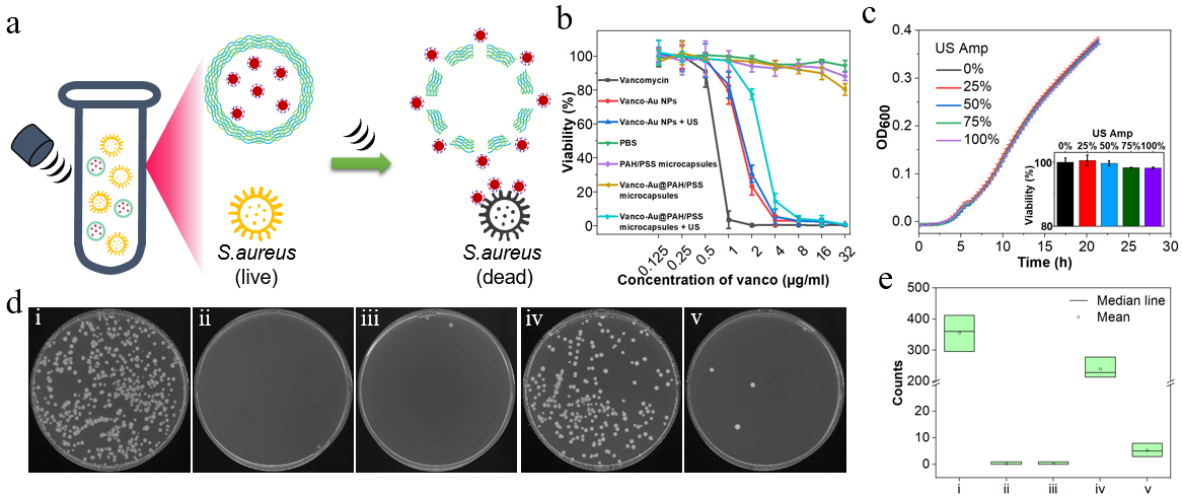

Figure 8. **US-triggered nanodrug release from microcapsules against *S. aureus***. **a**) Schematic representation of in-situ nanodrug activation in the presence of *S. aureus*. **b**) MIC test in the presence of vancomycin, Vanco-Au NPs with or without sonication, PBS, PAH/PSS hollow microcapsules, Vanco-Au@PAH/PSS Microcapsules with or without sonication against *S. aureus*. Mean values ± s.d. from the mean, $N = 3$ independent experiments. **c**) Growth curve of *S. aureus* after 10 min ultrasound treatment. Mean values ± s.d. from the mean, $N = 3$ independent experiments. Insert image: Viability of *S. aureus* after US irradiation with different amplitude. **d**) Photographs of agar Petri dishes that were incubated with *S. aureus* containing PBS (i), vancomycin (ii), Vanco-Au NPs (iii), Vanco-Au@PAH/PSS Microcapsules without sonication (iv), Vanco-Au@PAH/PSS Microcapsules with sonication (v). **e**) Counts of bacterial colonies from agar petri dish shown in Figure 8d.

Additionally, a live/dead staining assay for bacteria was conducted using a DMAO probe (green for live cells) and EthD-III (red for dead cells). Results showed that pure vancomycin and Vanco-Au NPs eradicated nearly all bacteria, whereas Vanco-Au@Polyelectrolyte Microcapsules exhibited antimicrobial activity after irradiation (**Figure 9**).

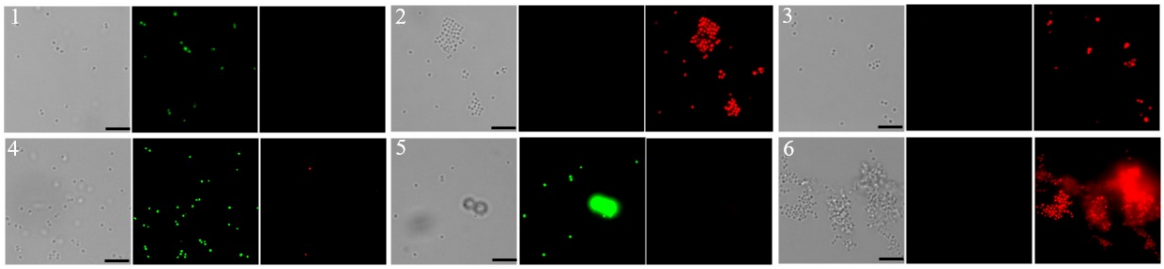

Figure 9. Live/dead staining assay. Live/dead staining assay of *S. aureus* in presence of PBS (1), vancomycin (2), Vanco-Au NPs (3), In the presence of PBS with in situ ultrasound treatment for 10 min (4), and in the presence of vanco-Au@Polyelectrolyte Microcapsules without (5) or with (6) in situ ultrasound treatment for 10 min. Left images represent bright field; Middle images were taken with a FITC filter showing live bacteria; Right images were taken with a Cy3 filter showing dead bacteria. Scale bar: 5 μm.

Previous studies have achieved US-triggered drug release from polyelectrolyte or silica microcapsules by breaking the capsule shells with high-intensity ultrasound (> 5 W/cm^2).[36-42, 48] However, such a high acoustic intensity might induce local temperature elevation and thus cause thermal injury to nearby tissues.[49-51] In this context, we have successfully achieved nanodrug release from silica microcapsules using low intensity focused

ultrasound (LIFU), which not only prevents thermal damage to the surrounding tissues but eliminates strong cavitation effects as compared to the systems employing kHz ultrasound.[52] Although the delivery of antibiotics using microcapsule carriers has been investigated,[53-54] in these systems the release of drugs was dependent on the diffusion of the small molecules drugs through the shell of the microcapsule. On-demand activation of drugs was not realized. In this regard, the nanodrug strategy enabled the controlled release of drugs by LIFU with high spatial precision to further improve ultrasound enabled therapeutic approaches. This capability also opens up opportunities for utilizing our system to deliver other nanodrugs, such as kanamycin- or ampicillin-conjugated Au NPs, silver nanodrugs, and nanoparticles modified with peptidic ligands.[55-60]

2.4 Conclusions

In this work, we introduced a novel ultrasound-responsive drug delivery system using Vanco-Au nanodrugs encapsulated in polyelectrolyte and silica microcapsules with high loading efficiencies. Associating the small molecule drug with a gold carrier effectively prevents undesired non-triggered leakage from the microcapsules. The nanodrug@Microcapsule structures demonstrated high responsiveness to unfocused ultrasound, enabling the in-situ activation of antibiotics against *S. aureus*. Additionally, the release of nanodrugs from silica microcapsules was successfully achieved using clinically compatible low-intensity focused ultrasound (LIFU). This advancement paves the way for future microcapsule-based drug delivery systems that could minimize side effects, reduce antibiotic resistance, and be compatible with established clinical techniques, offering high spatiotemporal precision.

2.5 Experimental section

2.5.1 Materials

All chemical reagents were of analytical grade and used without further purification unless otherwise specified. Vancomycin (United States Pharmacopeia Reference Standard), poly(allylamine hydrochloride) (PAH, average Mw 50,000), calcium carbonate ($CaCl_2$, ⩾99.0%), ethylenediaminetetraacetic acid (EDTA, ⩾99%), nitric acid (HNO_3, 65%), tetraethyl orthosilicate (TEOS), ammonium hydroxide (30 wt %), vancomycin-hydrochloride (Pharmaceutical Secondary Standard) were purchased from Sigma-Aldrich. Poly(styrene sulfonic acid) sodium salt (PSS, Mw 70,000) was purchased from Alfa Aesar. Hydrogen tetrachloroaurate (III) hydrate ($HAuCl_4$, 99.999 %) was purchased from ACROS and sodium carbonate (Na_2CO_3, 99.95%) was acquired from ACROS Organics™. Hydrochloric acid (HCl, 37%) was purchased from VWR. Aqua regia solution (highly corrosive and must be used with extreme caution!) was prepared by mixing HCl and HNO_3 with the volume ratio of 3:1. All glassware used for gold nanoparticle synthesis was cleaned with freshly prepared aqua regia. S. aureus (ATCC 6538) was obtained from ATCC. Hirn-Herz-Glucose-Bouillon and Mueller-Hinto-Bouillon were purchased from Carl Roth (Germany). Viability/Cytotoxicity Assay Kit for Bacteria Live&Dead staining (DMAO and EthD-III) was purchased from BIOTIUM (USA). Ultrapure Milli-Q water (18.2 MΩ·cm) was used for all experiments.

2.5.2 Characterization

Transmission electron microscopy (TEM) images were captured on a LIBRA®120 transmission electron microscope (Carl Zeiss) with an accelerating voltage of 120 kV. Scanning electron microscopy (SEM) images were captured by a scanning electron microscope S-4800 (Hitachi). FTIR spectra were recorded on Nexus 470 (Thermo Nicolet). Sonication was applied by a 20 KHz Sonicator (Q125, Qsonica) with 125 W power. Ultraviolet-visible (UV-vis) absorption spectra were collected using a SpectraMax M3 Spectrophotometer (Molecular Devices). Dynamic light scattering (DLS) was measured on a Zetasizer Ultra ZS instrument (Malvern). Fluorescence images were captured using a Leica DM6000 B fluorescent microscope.

2.5.3 Low-intensity focused ultrasound (LIFU) setup

The LIFU system is comprised of a waveform generator with an integrated oscilloscope function (Model SDS1202X-E, Siglent.eu, Helmond, Netherlands), a second waveform generator (Model 33622A, Keysight Technologies, Böblingen, Germany), a radiofrequency (RF) broadband power amplifier (Model AG1021, T&C Power Conversion, Rochester, NY, USA), and a waterproof 5 MHz focused immersion transducer (Model V308-SU, Olympus Europa SE & Co. KG, Hamburg, Germany). The transducer is placed in a 20 L transparent glass water tank.

2.5.4 Synthesis of vancomycin modified gold nanoparticles (Vanco-Au NPs)

8 nm vancomycin-modified gold nanoparticles were synthesized by a one-pot reaction, which was previously reported.[43] Typically, 2 mL chloroauric acid (10 mM) and 550 µL vancomycin (10 mM) were mixed and kept stirring for 15 min. Then 400 µL NaOH solution (2 M) was added under 1000 rpm stirring at room temperature. The reaction mixture was kept in dark for 24 h. The obtained nanoparticles were rinsed with water 3 times. The suspensions were filtered through a membrane filter (MW cutoff 3 kDa) using centrifugation at 4000 rpm. The

filtrate after each rinsing step was collected and used to determine the amount of vancomycin that was not conjugated on NPs. By subtracting this from the starting amount of vancomycin, the amount of vancomycin immobilized on the gold nanoparticles was obtained. In addition, the concentration of Au NPs was obtained by performing UV-vis spectroscopy measurements according to a previous report.[44] Accordingly, the amount of vancomycin loading on each gold nanoparticle was estimated to be 3250. The resulting Vanco-Au NPs were ready for characterization (optical absorption, TEM, IR, DLS, elemental mapping) and further use. The resulting Vanco-Au NPs were characterized by optical absorption, TEM, IR, DLS, elemental mapping, and for subsequent use.

2.5.5 Characterization of Vanco-Au NPs

UV-vis absorption spectra were collected on the spectrophotometer at room temperature. 10 µl Vanco-Au NPs were added into a 2 ml centrifugation tube. Ultrapure water was then added to dilute the solution, which was transferred to a quartz cuvette (Hellma Analytics) for spectrophotometric measurement. Moreover, concentrated Vanco-Au NPs were mixed with potassium bromide (KBr) powder. This wet sample was allowed to dry for 12 h in an oven at 60 °C. Subsequently, the dried sample was analyzed with an FTIR-Spectrometer (Nexus 470, Thermo Nicolet) and pristine vancomycin was measured as a control.

2.5.6 Preparation of $CaCO_3$ particles

Without Vanco-Au NPs

The $CaCl_2$ solution was prepared by dissolving 183 mg $CaCl_2$ in 5 ml water. The Na_2CO_3 solution was prepared by dissolving 175 mg Na_2CO_3 in 5 ml water. These solutions were added into a 50 ml round-bottomed flask and stirred for 1 min at 1000 rpm. The solution was then transferred into a centrifuge tube and washed with water 5 times (3000 rpm, 10 s). The synthesized $CaCO_3$ particles were collected by centrifugation for further use.

With Vanco-Au NPs

In addition to the above procedure, 400 µl vancomycin modified gold nanoparticles (Vanco-Au NPs) were added into the solution. After stirring for 1 min at 1000 rpm, the solution was transferred into a centrifuge tube and washed with water 5 times (3000 rpm, 10 s). The synthesized Vanco-Au @$CaCO_3$ particles were collected by centrifugation. In order to quantify the amount of Vanco-Au NPs loaded into $CaCO_3$. EDTA (0.2 M) was used to dissolve $CaCO_3$. Afterwards, the concentration of Vanco-Au NPs was measured by absorption spectroscopy. By comparing this value to the initial concentration of Vanco-Au NPs, the encapsulation efficiency of Vanco-Au NPs into $CaCO_3$ was determined to be approximately 74% (Figure S18b).

2.5.7 Preparation of layer-by-layer PAH/PSS polyelectrolyte microcapsules

$CaCO_3$ and Vanco-Au@$CaCO_3$ particles were utilized as the core templates for microcapsule formation. The polyelectrolyte microcapsules were fabricated using the established layer-by-layer assembly method.[4] Briefly, 2 ml freshly synthesized $CaCO_3$ particles were dispersed in 0.5 M NaCl solution, which contained 1 mg/ml PAH. This mixture was allowed to incubate at room temperature for 15 min. The excess polyelectrolyte was removed by centrifugation (3000 rpm, 10 s) and the precipitate was washed with 0.5 M NaCl solution 3 times. Then, the second polymer layer was assembled in the same way by dispersing the particles in 0.5 M NaCl solution, which

contained 1 mg/ml PSS. This process was repeated to obtain the desired bilayer polyelectrolyte coated templates. Then, the templates were removed using 2 ml EDTA (0.2 M) to obtain the Au-vanco NPs@Microcapsules and hollow microcapsules.

2.5.8 Determination of the leakage of nanodrug from polyelectrolyte microcapsules

The leakage of nanodrug from polyelectrolyte microcapsules was determined by comparing the concentration of gold particles released from microcapsules before and after 24 h shaking (500 rpm). Firstly, the freshly prepared Vanco-Au@Polyelectrolyte Microcapsules were centrifuged at 5000 rpm for 1 min. The supernatant was collected and analyzed by optical absorption spectroscopy. Then, the microcapsules were allowed to shake for 24 h on a shaker. Again, after centrifugation (5000 rpm), the supernatant of this solution was collected to measure the optical absorption. For the 4-layer and 6-layer bilayer polyelectrolyte microcapsules, the absorbance values of the supernatant before shaking and after shaking for 24 h were similar, indicating that the leakage of nanodrugs from the microcapsules was minimal.

2.5.9 Determination of Vanco-Au NPs released from polyelectrolyte microcapsules upon sonication

Ultrasound sonication was carried out using a 20 KHz sonicator with a 3 mm-diameter micro-tip probe (A12628PRB20, Qsonica). The sonication was applied in pulsed mode, with 2.0 seconds on and 1.0 second off. The tubes were placed in an ice bath to maintain low temperature inside the tube throughout sonication (Figure S14). The freshly prepared 1 ml Vanco-Au@Polyelectrolyte Microcapsules were added into a 2 ml Eppendorf tube. Then, the sonicator micro-tip was positioned in the microcapsule suspensions. Subsequently, sonication was applied at different power amplification (25%, 50%, 75% and 100%) for different times (0 min, 0.5 min, 1 min, 3 min, 5 min and 10 min). After sonication, the suspensions were centrifuged at 5000 rpm for 1 min. The supernatants were collected and optical absorption was measured.

2.5.10 Preparation of Vanco-Au@Silica Capsule

Vanco-Au@Silica Capsule were prepared referring to a previous report.[45] The $CaCl_2$ solution was prepared by dissolving 183 mg $CaCl_2$ in 5 ml starch aqueous solution. 400 µl Vancomycin modified gold nanoparticles (Vanco-Au NPs) were added into the $CaCl_2$ solution. Na_2CO_3 solution was prepared by dissolving 175 mg Na_2CO_3 in 5 ml water. Then, mix the Na_2CO_3 solution with $CaCl_2$ solution and stir for 1 min at 1000 rpm. The solution was then transferred into a centrifuge tube and washed with water 3 times (3000 rpm, 10 s). 2 ml the synthesized Vanco-Au@$CaCO_3$ particles were washed with water and ethanol. Then the particles were incubated in 1.5 ml TEOS/Ethanol (1:1, v/v) solution for 2 h. After adsorbing TEOS, the particles were centrifuged and transferred to a flask with a solvent mixture (2.5 mL water, 2.5 mL ammonium hydroxide (30 wt %), 5 mL ethanol) for overnight hydrolysis at 1000 rpm. Then the $CaCO_3$ templates were removed with 0.2 M EDTA solution (pH 7.4). At last silica capsules were obtained after washing with water 3 times.

2.5.11 Vanco-Au@Silica Microcapsule subjected to US irradiation

Irradiation with unfocused US was similar as described before. For LIFU radiation, a transparent 96-well plate (SARSTEDT AG & Co. KG, Neubrecht, Germany) was placed 2.5 cm above the transducer. This setup allowed the focus to be adjusted to the sample's location. Sonication was performed at 5 MHz with a duty cycle of 20%, and a peak rarefaction pressure of 2.28 MPa at the focus point. The Mechanical Index (MI) was 1.02. Specifically, 100 µl Vanco-Au@Silica Microcapsules were added into a well of a 96 well plate. The sonication point was set at the center of the well. Then, we set the 5s, 30s, 60s, 3min or 5 min 'on' time in the LIFU driver. After sonication, the solution was centrifuged at 5000 rpm for 1 min, and the supernatant was collected and optical absorption was measured.

2.5.12 Bacterial growth (*S. aureus*) after sonication

S. aureus (ATCC 6538) was allowed to grow in Mueller-Hinto-Bouillon (MHB medium) for 8 h at 37 ºC to reach the late log phase. Then, the bacteria were rinsed with 0.9 % NaCl solution 2 times and collected by centrifugation (3000 rpm, 3 min). The bacteria suspension was then diluted to reach an OD_{600} of around 0.01. 1 mL of bacterial suspension was pipetted into a 2 mL tube and subjected to 20 KHz US sonication at different power levels (0%, 25%, 50%, 75%, and 100%) for 10 minutes (irradiation: 2 s on, 1 s off). The sonication-treated bacteria were allowed to grow for 22 h at 37 ℃. Then the optical density of bacteria was monitored by the spectrophotometer at 600 nm (OD_{600}) every 20 min. Finally, the growth curves were obtained by recording the OD_{600} over time.

2.5.13 Minimal inhibitory concentration (MIC) assay (in situ experiments in presence of bacteria)

The Minimal Inhibitory Concentration (MIC) assay was used to evaluate the antimicrobial activities of various samples, including pure vancomycin, Vanco-Au NPs before and after sonication, hollow PAH/PSS polyelectrolyte microcapsules, and Vanco-Au@Polyelectrolyte Microcapsules before and after sonication. Firstly, *S. aureus* (ATCC 6538) was allowed to grow in MHB medium under gentle shaking for 8 h at 37 ºC. The bacteria were rinsed with 0.9% NaCl solution 2 times and collected by centrifugation (3000 rpm, 3 min) for further use. For each sample, the antimicrobial solution was serially two-fold diluted into multiple wells in a 96-well plate to obtain a concentration gradient ranging from 64 µg/ml to 0.125 µg/ml. To each well, 50 µL of the re-suspended bacteria solution was added to give a final bacterial concentration of 5×10^5 cells/mL. The OD_{600} value was recorded by the spectrometer before and after incubation at 37 °C to examine the viability of bacteria in each well. From these measurements, the lowest concentration of each sample at which no growth occurred was obtained.

2.5.14 Culturing *S. aureus* on agar petri dishes

20 µL *S. aureus* (~10^4 cells/mL) suspensions were mixed with 20 µL of different samples, including PBS buffer (sample i), vancomycin (1000 µg·mL^{-1}, sample ii), Vanco-Au NPs (1000 µg·mL^{-1} based on vancomycin, sample iii), suspension of 1 ml Vanco-Au@Polyelectrolyte Microcapsules (4 bilayers) without sonication (sample iv) or with sonication (50% power amplification for 10 min, sample v), suspension of 1 ml Vanco-Au@Silica Microcapsules after 10 min LIFU sonication, sample vi). Then 160 µL PBS buffer was added to adjust the volume to 200 µL. The mixed samples were allowed to gently shaken (~200 rpm) for 2 h at room temperature. After the incubation, the mixtures were added on agar Petri dishes (diameter: 12 cm), separately. The agar petri dishes were incubated at 37 °C for 24 hours, after which the bacterial colonies were counted.[46-47]

2.5.15 Live/dead staining of S. aureus

11 µL 100 X staining solution was prepared by mixing 1 µL DMAO, 2µL EthD-III and 8 µL 0.9% NaCl. Then, 1 µL of this stock solution was added to 100 µL of the above-mentioned bacteria suspensions. After mixing in the dark at room temperature for 15 minutes, 5 µL of the stained bacterial suspension was imaged using the fluorescence microscopy (Leica DM6000 B). Live bacteria were observed with a FITC filter set (green fluorescence), while dead bacteria were visualized using a Cy3 filter set (red fluorescence).[46-47]

2.6 Supporting figures and tables

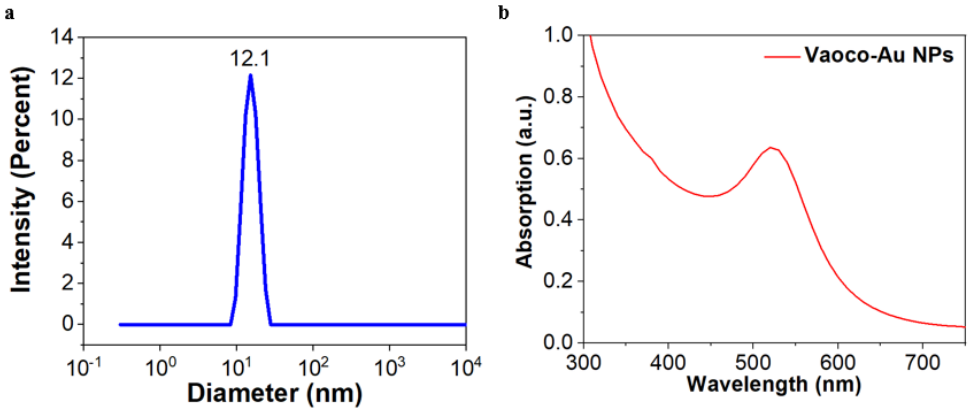

Figure S1. Characterization of Vanco-Au NPs. a) Size of Vanco-Au NPs measured by Dynamic Light Scattering (DLS). b) Absorption spectrum of Vanco-Au NPs.

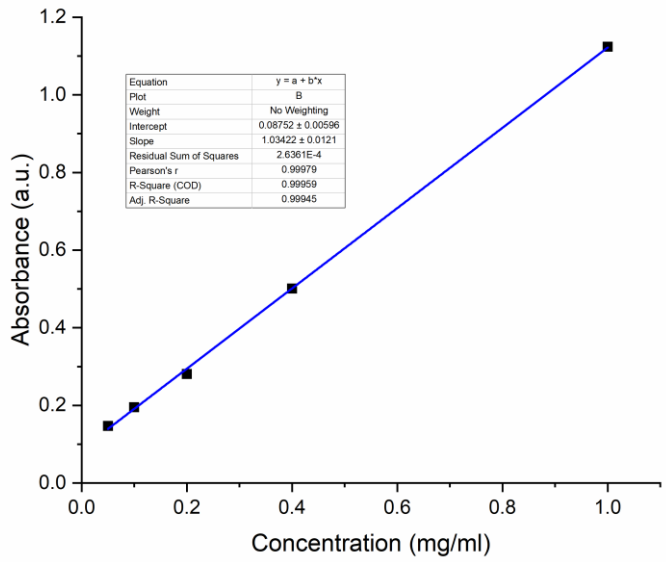

Figure S2. Standard absorption curve of vancomycin. A series of different concentrations (0.05, 0.1, 0.2, 0.4, 1 mg/ml) of vancomycin solutions were prepared to measure the absorbance at 282 nm.

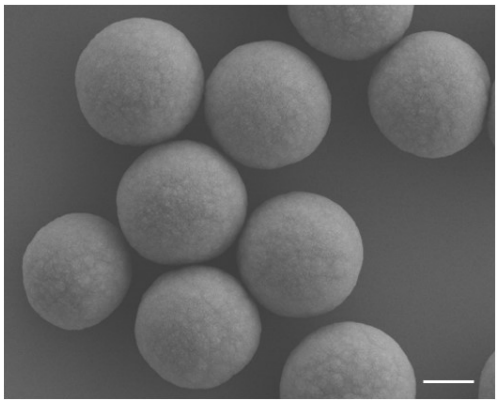

Figure S3. SEM image of $CaCO_3$ particles, scale bar: 2 µm.

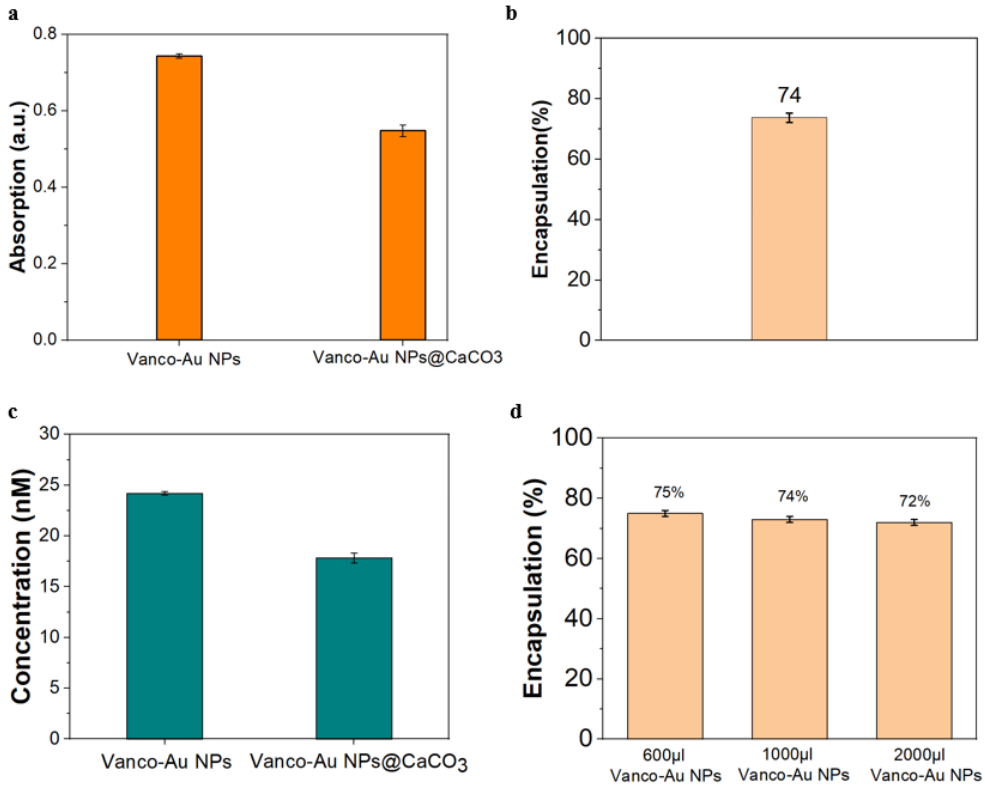

Figure S4. Determination of the percentage of Vanco-Au NPs loading into $CaCO_3$. **a**) Absorbance of Vanco-Au NPs in starting solution and Vanco-Au NPs trapped in $CaCO_3$ particles. Mean values ± s.d. from the mean, *N* = 3 independent experiments. **b**) Percentage of Vanco-Au NPs loading inside the $CaCO_3$ particles, calculated by the absorbance values. **c**) Concentrations of Vanco-Au NPs in starting solution and Vanco-Au NPs trapped in $CaCO_3$ particles. **d**) Percentage of Vanco-Au NPs loading inside the $CaCO_3$ particles when added 600µl, 1000µl or 2000µl Vanco-Au NPs.

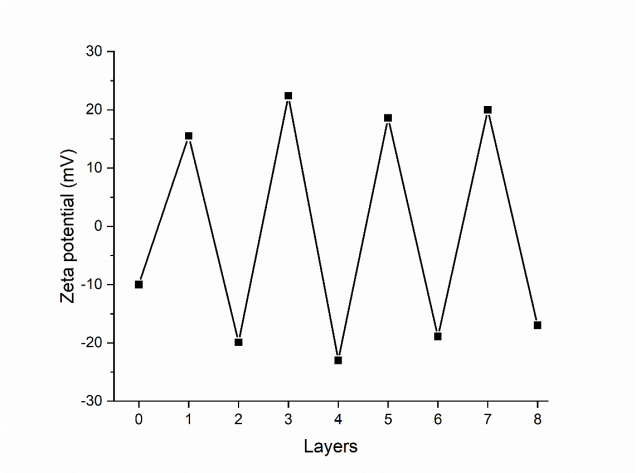

Figure S5. Zeta potential of the alternating layers of the polyelectrolyte microcapsules.

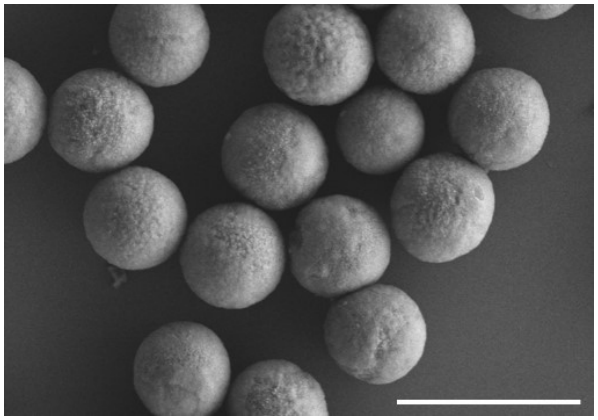

Figure S6. SEM image of the template with 4 bilayers polyelectrolyte, scale bar: 10 µm.

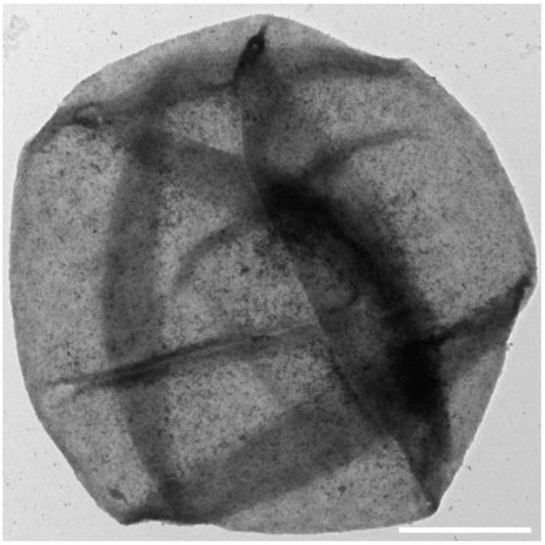

Figure S7. TEM image of 4 bilayers Vanco-Au@Polyelectrolyte microcapsules, scale bar: 2µm.

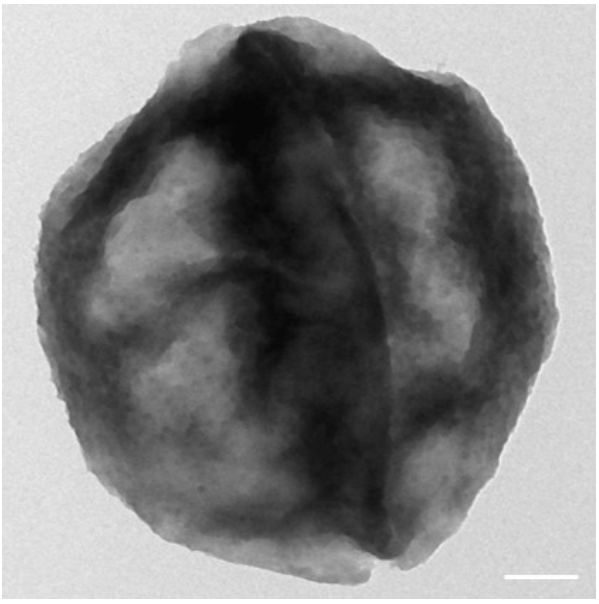

Figure S8. TEM image of 4 bilayers hollow polyelectrolyte microcapsules, scale bar: 1 µm.

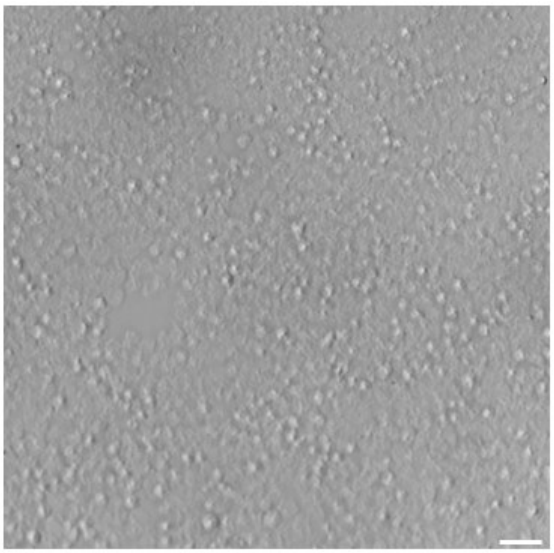

Figure S9. Preparation of 2 bilayers polyelectrolyte microcapsules, scale bar: 10 µm.

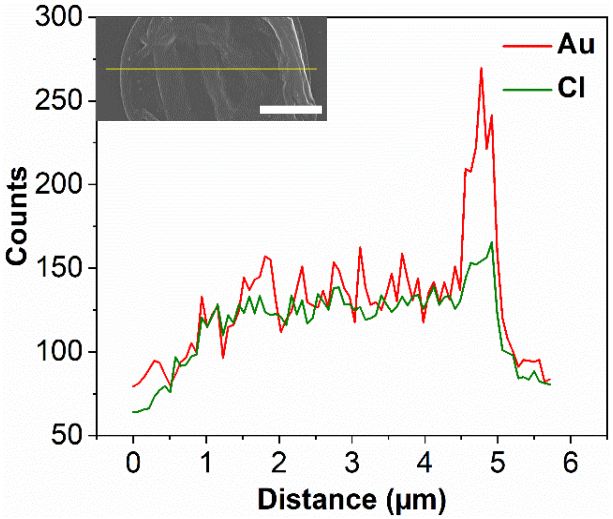

Figure S10. EDX elemental mapping of Vanco-Au@Polyelectrolyte microcapsule (4 bilayers). Scale bar in inset: 2 µm.

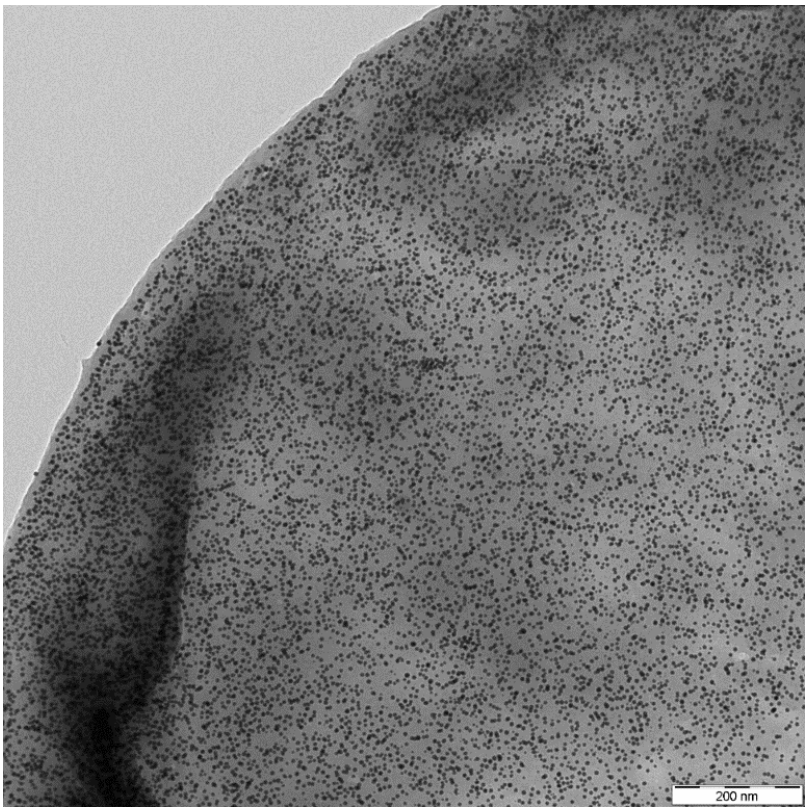

Figure S11. TEM image of Vanco-Au@Polyelectrolyte microcapsules (4 bilayers).

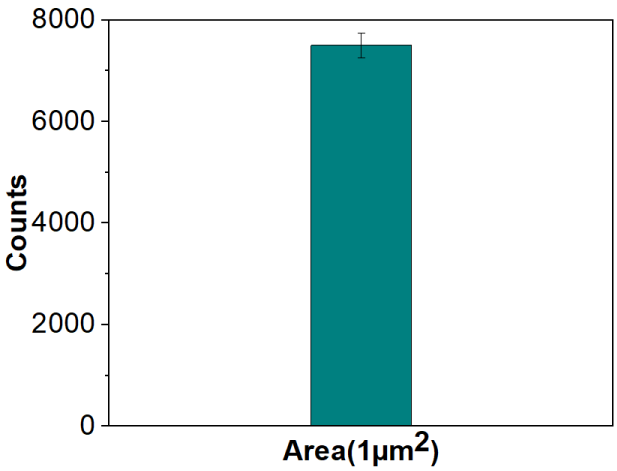

Figure S12. Number of Vanco-Au NPs in 1 μm^2 polyelectrolyte microcapsules (4 bilayers) calculated from TEM image shown in Figure S11.

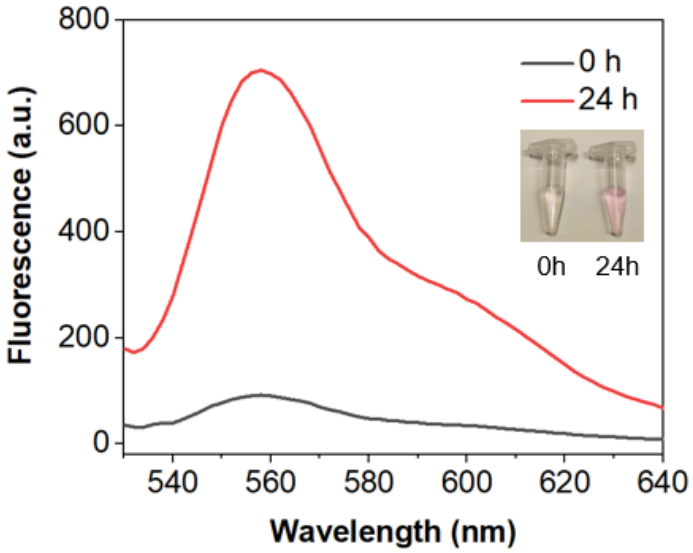

Figure S13. Emission spectra of the supernatants of polyelctrolyte capsules containing Cy3 before (0 h) and after (24 h) shaking.

Figure S14. Unfocused US setup (f = 20 kHz, with ice bath). Temperature record: 0.3 °C (before sonication), 2.1 °C (after 10 min sonication).

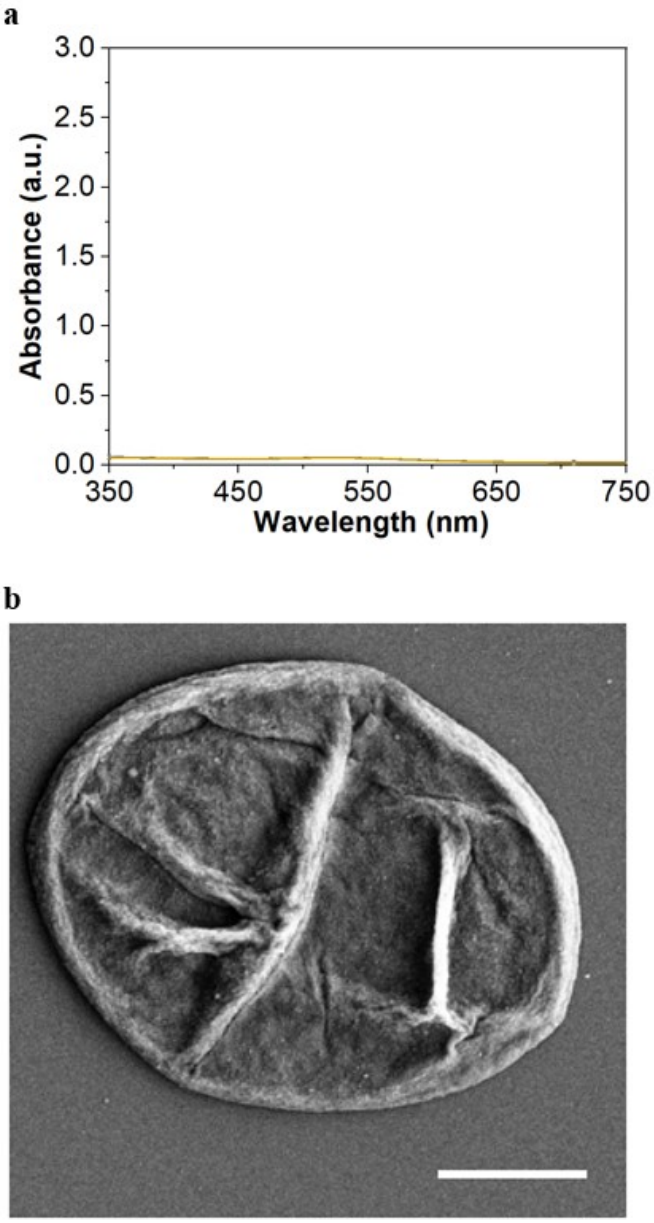

Figure S15. **a**) Absorption spectra of the supernatants of 4 bilayers polyelectrolyte microcapsules with 0% US Amp sonication. **b**) SEM image of vanco-Au@Polyelectrolyte microcapsules dealt by LIFU sonication.

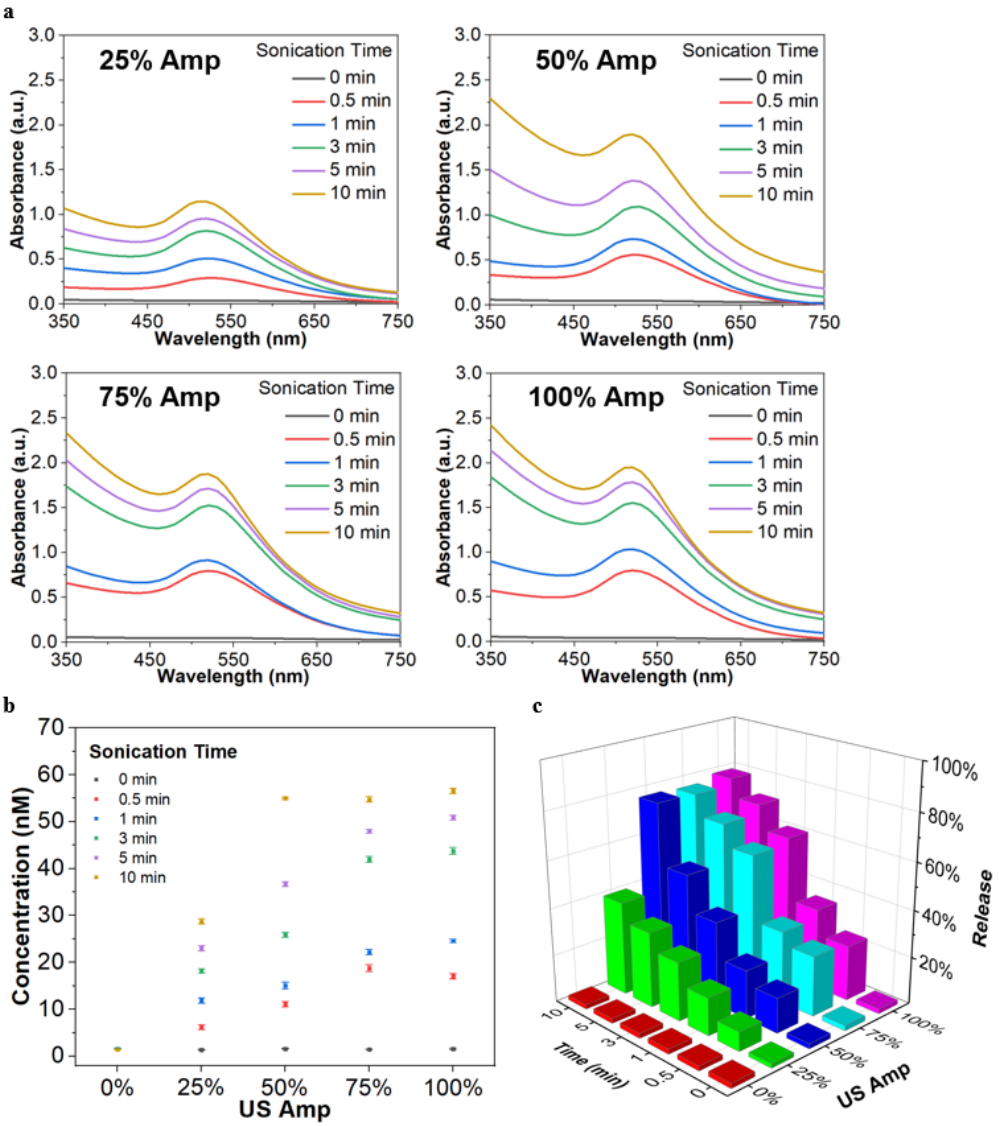

Figure S16. Quantification of Vanco-Au NPs released from 6 bilayers Polyelectrolyte Microcapsules upon US activation. **a**) Absorption spectra of the supernatant of vanco-Au NPs @ 6 bilayers PAH/PSS Microcapsules after sonication with 25%, 50%, 75% and 100% Amp. **b**) Calculated concentrations of released Vanco-Au NPs, Mean values ± s.d. from the mean, $N = 3$ independent experiments. **c**) Release percentage of Vanco-Au NPs from 6 bilayers PAH/PSS microcapsules triggered by sonication.

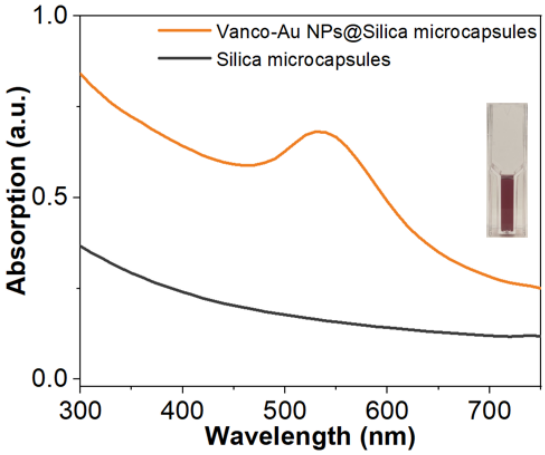

Figure S17. Absorption spectra of Vanco-Au@Silica microcapsules and silica microcapsules.

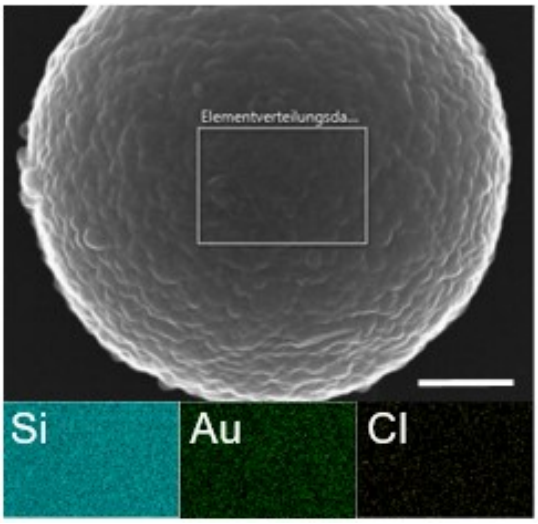

Figure S18. EDX elemental mapping of Vanco-Au@Silica microcapsule, elements: silica, gold and chlorine. Scale bar: 1 μm.

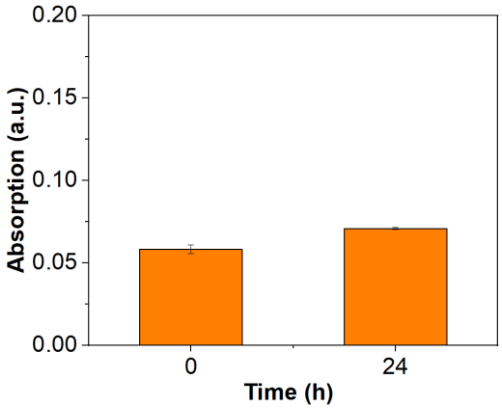

Figure S19. Absorption values of the supernatants of Vanco-Au@Silica microcapsule before and after 24h shaking. Mean values ± s.d. from the mean, $N = 3$ independent experiments.

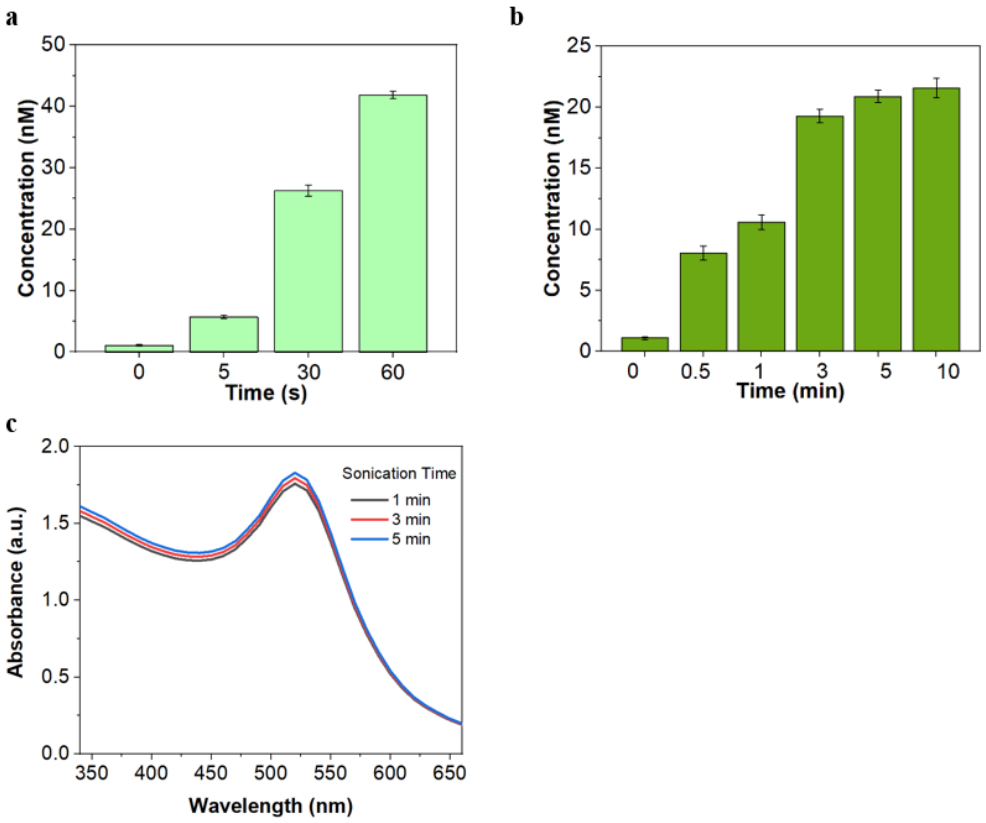

Figure S20. Concentrations of released vanco-Au NPs from silica microcapsules after sonication. **a**) Concentrations of released vanco-Au NPs under 20 KHz US sonication. Mean values ± s.d. from the mean, $N = 3$ independent experiments. **b**) Concentrations of released vanco-Au NPs under LIFU sonication. Mean values ± s.d. from the mean, $N = 3$ independent experiments. **c**) Absorption spectra of the supernatant of vanco-Au NPs@Silica microcapsules suspensions after 1 min, 3 min or 5 min sonication by LIFU.

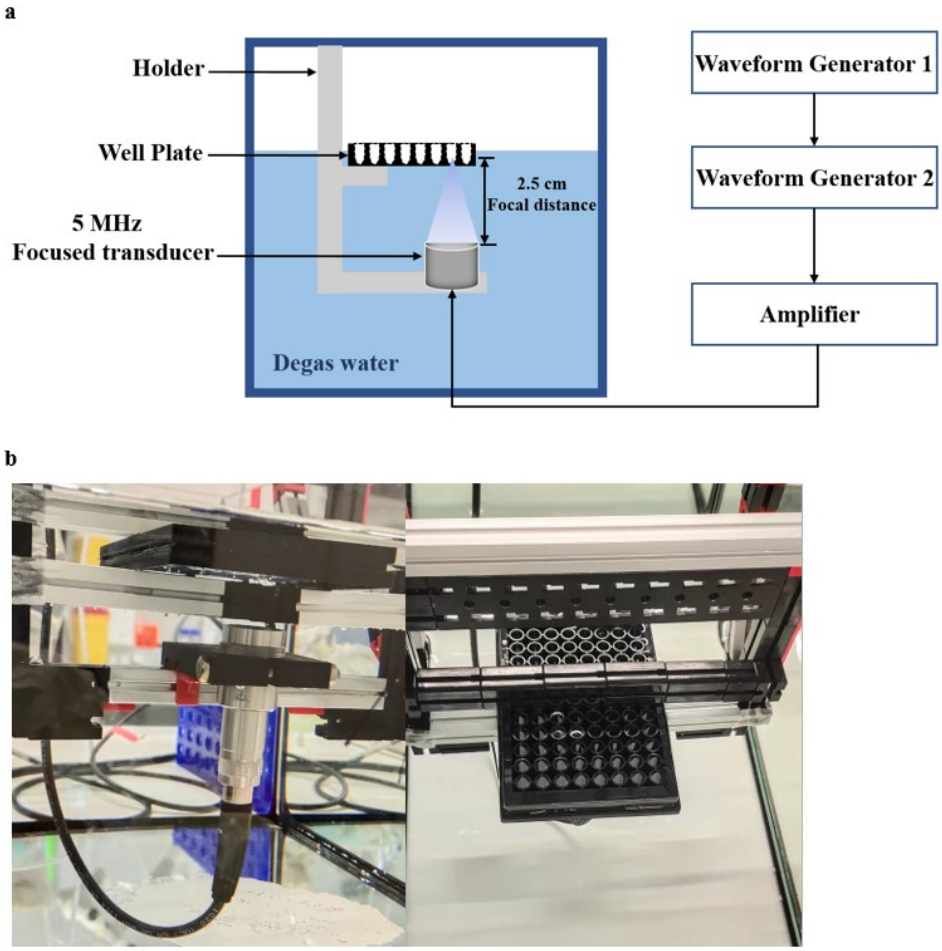

Figure S21. LIFU(5 MHz) setup. a) Schematic illustration. **b**) Real setup (left: side view, right: top view). Temperature of degassed water: 23 °C.

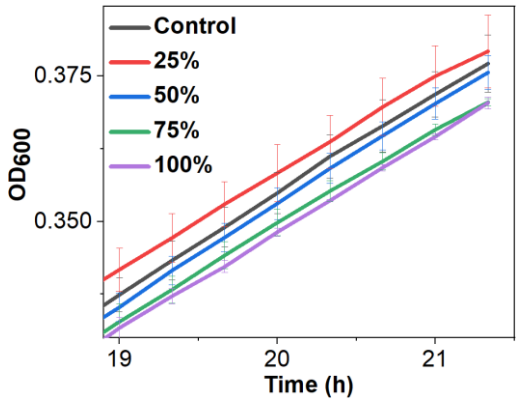

Figure S22. Growth curves (19 - 21 h) of *S. aureus* after 10 min ultrasound treatment. Mean values ± s.d. from the mean, $N = 3$ independent experiments.

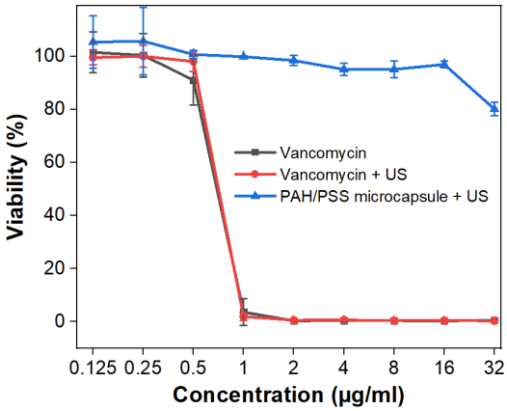

Figure S23. MIC test in the presence of vancomycin, vancomycin + US or PAH/PSS hollow microcapsules with sonication against S. aureus. Mean values ± s.d. from the mean, $N = 3$ independent experiments.

2.7 References

1. Caruso, F., Caruso, R. A., & Mohwald, H. (1998). Nanoengineering of inorganic and hybrid hollow spheres by colloidal templating. *Science*, *282*(5391), 1111-1114.

2. Parak, W. J. (2011). Complex colloidal assembly. *Science*, *334*(6061), 1359-1360.

3. Ochs, M., Carregal-Romero, S., Rejman, J., Braeckmans, K., De Smedt, S. C., & Parak, W. J. (2012). Light-addressable capsules as caged compound matrix for controlled triggering of cytosolic reactions. In *Bio-Nano Interfaces* (pp. 1195-1208). Jenny Stanford Publishing.

4. Yang, Y., Liu, H., Han, M., Sun, B., & Li, J. (2016). Multilayer microcapsules for FRET analysis and two-photon-activated photodynamic therapy. *Angewandte Chemie International Edition*, *55*(43), 13538-13543.

5. He, Q., Cui, Y., & Li, J. (2009). Molecular assembly and application of biomimetic microcapsules. *Chemical Society Reviews*, *38*(8), 2292-2303.

6. Pavlov, A. M., De Geest, B. G., Louage, B., Lybaert, L., De Koker, S., Koudelka, Z., Sapelkin, A., & Sukhorukov, G. B. (2013). Magnetically engineered microcapsules as intracellular anchors for remote control over cellular mobility. *Advanced Materials*, *25*(48), 6945-6950.

7. Ejima, H., Richardson, J. J., Liang, K., Best, J. P., van Koeverden, M. P., Such, G. K., Cui, J., & Caruso, F. (2013). One-step assembly of coordination complexes for versatile film and particle engineering. *Science*, *341*(6142), 154-157.

8. Kolbe, A., del Mercato, L. L., Abbasi, A. Z., Rivera Gil, P., Gorzini, S. J., Huibers, W. H., Poolman, B., Parak, W. J. & Herrmann, A. (2011). De novo design of supercharged, unfolded protein polymers, and their assembly into supramolecular aggregates. *Macromolecular Rapid Communications*, *32*(2), 186-190.

9. Skirtach, A. G., De Geest, B. G., Mamedov, A., Antipov, A. A., Kotov, N. A., & Sukhorukov, G. B. (2007). Ultrasound stimulated release and catalysis using polyelectrolyte multilayer capsules. *Journal of Materials Chemistry*, *17*(11), 1050-1054.

10. Boehnke, N., Correa, S., Hao, L., Wang, W., Straehla, J. P., Bhatia, S. N., & Hammond, P. T. (2020). Theranostic layer-by-layer nanoparticles for simultaneous tumor detection and gene silencing. *Angewandte Chemie*, *132*(7), 2798-2805.

11. Peyratout, C. S., & Dähne, L. (2004). Tailor‐made polyelectrolyte microcapsules: from multilayers to smart containers. *Angewandte Chemie International Edition*, *43*(29), 3762-3783.

12. Muslimov, A. R., Timin, A. S., Petrova, A. V., Epifanovskaya, O. S., Shakirova, A. I., Lepik, K. V., Gorshkov, A., Il'inskaja, E. V., Vasin, A. V., Afanasyev, B. V., Fehse, B., & Sukhorukov, G. B. (2017). Mesenchymal stem cells engineering: microcapsules-assisted gene transfection and magnetic cell separation. *ACS Biomaterials Science & Engineering*, *3*(10), 2314-2324.

13. Park, J. H., Kim, K., Lee, J., Choi, J. Y., Hong, D., Yang, S. H., Caruso, F., Lee, Y., & Choi, I. S. (2014). A cytoprotective and degradable metal‐polyphenol nanoshell for single‐cell encapsulation. *Angewandte Chemie*, *126*(46), 12628-12633.

14. Decher, G. (1997). Fuzzy nanoassemblies: toward layered polymeric multicomposites. *Science*, *277*(5330), 1232-1237.

15. Popov, A. L., Popova, N., Gould, D. J., Shcherbakov, A. B., Sukhorukov, G. B., & Ivanov, V. K. (2018). Ceria nanoparticles-decorated microcapsules as a smart drug delivery/protective system: protection of encapsulated P. pyralis luciferase. *ACS Applied Materials & Interfaces*, *10*(17), 14367-14377.

16. Fakhrullin, R. F., & Lvov, Y. M. (2012). “Face-lifting” and “make-up” for microorganisms: layer-by-layer polyelectrolyte nanocoating. *ACS Nano*, *6*(6), 4557-4564.

17. Liu, X. Q., & Picart, C. (2016). Layer-by-Layer assemblies for cancer treatment and diagnosis. *Advanced Materials*, *28*(6), 1295-1301.

18. Ariga, K., Lvov, Y. M., Kawakami, K., Ji, Q., & Hill, J. P. (2011). Layer-by-layer self-assembled shells for drug delivery. *Advanced Drug Delivery Reviews*, *63*(9), 762-771.

19. Zelikin, A. N., Li, Q., & Caruso, F. (2006). Degradable polyelectrolyte capsules filled with oligonucleotide sequences. *Angewandte Chemie International Edition*, *45*(46), 7743-7745.

20. Richardson, J. J., Maina, J. W., Ejima, H., Hu, M., Guo, J., Choy, M. Y., Gunawan, S. T., Lybaert, L., Hagemeyer, C. E., De Geest, B. G., & Caruso, F. (2015). Versatile loading of diverse cargo into functional polymer capsules. *Advanced Science*, *2*(1-2), 1400007.

21. De Koker, S., De Geest, B. G., Singh, S. K., De Rycke, R., Naessens, T., Van Kooyk, Y., Demeester, Jo., De Smedt, S. C., & Grooten, J. (2009). Polyelectrolyte microcapsules as antigen delivery vehicles to dendritic cells: uptake, processing, and cross‐presentation of encapsulated antigens. *Angewandte Chemie*, *121*(45), 8637-8641.

22. Song, W., Möhwald, H., & Li, J. (2010). Movement of polymer microcarriers using a biomolecular motor. *Biomaterials*, *31*(6), 1287-1292.

23. Du, C., Zhao, J., Fei, J., Cui, Y., & Li, J. (2013). Assembled microcapsules by doxorubicin and polysaccharide as high effective anticancer drug carriers. *Advanced Healthcare Materials*, *2*(9), 1246-1251.

24. Ju, Y., Cui, J., Sun, H., Mullner, M., Dai, Y., Guo, J., Bertleff-Zieschang, Nadja., Suma, T., Richardson, J. J., & Caruso, F. (2016). Engineered metal-phenolic capsules show tunable targeted delivery to cancer cells. *Biomacromolecules*, *17*(6), 2268-2276.

25. Zhao, S., Caruso, F., Dähne, L., Decher, G., De Geest, B. G., Fan, J., & Parak, W. J. (2019). The future of layer-by-layer assembly: a tribute to ACS nano associate editor Helmuth Mohwald. *ACS Nano*, *13*(6), 6151-6169.

26. Zhao, J., Wang, A., Si, T., Hong, J. D., & Li, J. (2019). Gold nanorods based multicompartment mesoporous silica composites as bioagents for highly efficient photothermal therapy. *Journal of Colloid and Interface Science*, *549*, 9-15.

27. Zieringer, M. A., Carroll, N. J., Abbaspourrad, A., Koehler, S. A., & Weitz, D. A. (2015). Microcapsules for enhanced cargo retention and diversity. *Small*, *11*(24), 2903-2909.

28. Wu, Y., Ihme, S., Feuring-Buske, M., Kuan, S. L., Eisele, K., Lamla, M., Wang, Y., Buske, C., & Weil, T. (2013). A Core–Shell Albumin Copolymer Nanotransporter for High Capacity Loading and Two-Step Release of Doxorubicin with Enhanced Anti-Leukemia Activity. *Advanced Healthcare Materials*, *2*(6), 884-894.

29. Hitchcock, J. P., Tasker, A. L., Baxter, E. A., Biggs, S., & Cayre, O. J. (2015). Long-term retention of small, volatile molecular species within metallic microcapsules. *ACS Applied Materials & Interfaces*, *7*(27), 14808-14815.

30. Deshmukh, P. K., Ramani, K. P., Singh, S. S., Tekade, A. R., Chatap, V. K., Patil, G. B., & Bari, S. B. (2013). Stimuli-sensitive layer-by-layer (LbL) self-assembly systems: targeting and biosensory applications. *Journal of Controlled Release*, *166*(3), 294-306.

31. De Koker, S., De Geest, B. G., Cuvelier, C., Ferdinande, L., Deckers, W., Hennink, W. E., De Smedt, S. C., & Mertens, N. (2007). In vivo cellular uptake, degradation, and biocompatibility of polyelectrolyte microcapsules. *Advanced Functional Materials*, *17*(18), 3754-3763.

32. Radt, B., Smith, T. A., & Caruso, F. J. A. M. (2004). Optically addressable nanostructured capsules. *Advanced Materials*, *16*(23-24), 2184-2189.

33. Timin, A. S., Muslimov, A. R., Lepik, K. V., Saprykina, N. N., Sergeev, V. S., Afanasyev, B. V., Vilesov, A. D., & Sukhorukov, G. B. (2016). Triple-responsive inorganic-organic hybrid microcapsules as a biocompatible smart platform for the delivery of small molecules. *Journal of Materials Chemistry B*, *4*(45), 7270-7282.

34. Carregal-Romero, S., Guardia, P., Yu, X., Hartmann, R., Pellegrino, T., & Parak, W. J. (2015). Magnetically triggered release of molecular cargo from iron oxide nanoparticle loaded microcapsules. *Nanoscale*, *7*(2), 570-576.

35. Mura, S., Nicolas, J., & Couvreur, P. (2013). Stimuli-responsive nanocarriers for drug delivery. *Nature Materials*, *12*(11), 991-1003.

36. De Geest, B. G., Skirtach, A. G., Mamedov, A. A., Antipov, A. A., Kotov, N. A., De Smedt, S. C., & Sukhorukov, G. B. (2007). Ultrasound-triggered release from multilayered capsules. *Small*, *3*(5), 804-808.

37. Gao, H., Wen, D., & Sukhorukov, G. B. (2015). Composite silica nanoparticle/polyelectrolyte microcapsules with reduced permeability and enhanced ultrasound sensitivity. *Journal of materials chemistry b*, *3*(9), 1888-1897.

38. Shchukin, D. G., Gorin, D. A., & Möhwald, H. (2006). Ultrasonically induced opening of polyelectrolyte microcontainers. *Langmuir*, *22*(17), 7400-7404.

39. Anandhakumar, S., Mahalakshmi, V., & Raichur, A. M. (2012). Silver nanoparticles modified nanocapsules for ultrasonically activated drug delivery. *Materials Science and Engineering: C*, *32*(8), 2349-2355.

40. Kolesnikova, T. A., Gorin, D. A., Fernandes, P., Kessel, S., Khomutov, G. B., Fery, A., Shchukin, D. G., & Möhwald, H. (2010). Nanocomposite microcontainers with high ultrasound sensitivity. *Advanced Functional Materials*, *20*(7), 1189-1195.

41. Chen, J., Ratnayaka, S., Alford, A., Kozlovskaya, V., Liu, F., Xue, B., Hoyt, K., & Kharlampieva, E. (2017). Theranostic multilayer capsules for ultrasound imaging and guided drug delivery. *ACS Nano*, *11*(3), 3135-3146.

42. Alford, A., Rich, M., Kozlovskaya, V., Chen, J., Sherwood, J., Bolding, M., Warram, J., Bao, Y., & Kharlampieva, E. (2018). Ultrasound-Triggered Delivery of Anticancer Therapeutics from MRI-Visible Multilayer Microcapsules. *Advanced Therapeutics*, *1*(5), 1800051.

43. Lai, H. Z., Chen, W. Y., Wu, C. Y., & Chen, Y. C. (2015). Potent antibacterial nanoparticles for pathogenic bacteria. *ACS Applied Materials & Interfaces*, *7*(3), 2046-2054.

44. Haiss, W., Thanh, N. T., Aveyard, J., & Fernig, D. G. (2007). Determination of size and concentration of gold nanoparticles from UV-Vis spectra. *Analytical Chemistry*, *79*(11), 4215-4221.

45. Wang, A., Yang, Y., Qi, Y., Qi, W., Fei, J., Ma, H., Zhao, J., Cui, W., & Li, J. (2016). Fabrication of mesoporous silica nanoparticle with well-defined multicompartment structure as efficient drug carrier for cancer therapy in vitro and in vivo. *ACS Applied Materials & Interfaces*, *8*(14), 8900-8907.

46. Huo, S., Zhao, P., Shi, Z., Zou, M., Yang, X., Warszawik, E., Loznik, M., Göstl, R., & Herrmann, A. (2021). Mechanochemical bond scission for the activation of drugs. *Nature Chemistry*, *13*(2), 131-139.

47. Wiegand, I., Hilpert, K., & Hancock, R. E. (2008). Agar and broth dilution methods to determine the minimal inhibitory concentration (MIC) of antimicrobial substances. *Nature Protocols*, *3*(2), 163-175.

48. Liang, X., Gao, J., Jiang, L., Luo, J., Jing, L., Li, X., Jin, Y., & Dai, Z. (2015). Nanohybrid liposomal cerasomes with good physiological stability and rapid temperature responsiveness for high intensity focused ultrasound triggered local chemotherapy of cancer. *ACS Nano*, *9*(2), 1280-1293.

49. Song, F., Gao, H., Li, D., Petrov, A. V., Petrov, V. V., Wen, D., & Sukhorukov, G. B. (2021). Low intensity focused ultrasound responsive microcapsules for non-ablative ultrafast intracellular release of small molecules. *Journal of Materials Chemistry B*, *9*(10), 2384-2393.

50. Devarakonda, S. B., Myers, M. R., Lanier, M., Dumoulin, C., & Banerjee, R. K. (2017). Assessment of gold nanoparticle-mediated-enhanced hyperthermia using MR-guided high-intensity focused ultrasound ablation procedure. *Nano Letters*, *17*(4), 2532-2538.

51. Kennedy, J. E. (2005). High-intensity focused ultrasound in the treatment of solid tumours. *Nature Reviews Cancer*, *5*(4), 321-327.

52. Zhu, L., Zhao, H., Zhou, Z., Xia, Y., Wang, Z., Ran, H., Li, P., & Ren, J. (2018). Peptide-functionalized phase-transformation nanoparticles for low intensity focused ultrasound-assisted tumor imaging and therapy. *Nano Letters*, *18*(3), 1831-1841.

53. Said, F. A., Bousserrhine, N., Alphonse, V., Michely, L., & Belbekhouche, S. (2020). Antibiotic loading and development of antibacterial capsules by using porous $CaCO_3$ microparticles as starting material. *International Journal of Pharmaceutics*, *579*, 119175.

54. Gessner, I., Krakor, E., Jurewicz, A., Wulff, V., Kling, L., Christiansen, S., & Mathur, S. (2018). Hollow silica capsules for amphiphilic transport and sustained delivery of antibiotic and anticancer drugs. *RSC Advances*, *8*(44), 24883-24892.

55. Tarrat, N., Benoit, M., Giraud, M., Ponchet, A., & Casanove, M. J. (2015). The gold/ampicillin interface at the atomic scale. *Nanoscale*, *7*(34), 14515-14524.

56. Feng, Y., Chen, W., Jia, Y., Tian, Y., Zhao, Y., Long, F., Rui, Y., & Jiang, X. (2016). N-Heterocyclic molecule-capped gold nanoparticles as effective antibiotics against multi-drug resistant bacteria. *Nanoscale*, *8*(27), 13223-13227.

57. Payne, J. N., Waghwani, H. K., Connor, M. G., Hamilton, W., Tockstein, S., Moolani, H., Chavda, F., Badwaik, V. D., Lawrenz, M., & Dakshinamurthy, R. (2016). Novel synthesis of kanamycin conjugated gold nanoparticles with potent antibacterial activity. *Frontiers in Microbiology*, *7*, 177773.

58. Li, X., Robinson, S. M., Gupta, A., Saha, K., Jiang, Z., Moyano, D. F., Sahar, A., Riley, M. A., & Rotello, V. M. (2014). Functional gold nanoparticles as potent antimicrobial agents against multi-drug-resistant bacteria. *ACS Nano*, *8*(10), 10682-10686.

59. Shaikh, S., Nazam, N., Rizvi, S. M. D., Ahmad, K., Baig, M. H., Lee, E. J., & Choi, I. (2019). Mechanistic insights into the antimicrobial actions of metallic nanoparticles and their implications for multidrug resistance. *International Journal of Molecular Sciences*, *20*(10), 2468.

60. Sanchez, C., El Hajj Diab, D., Connord, V., Clerc, P., Meunier, E., Pipy, B., Payré, B., Tan, R. P., Gougeon, M., Carrey, J., Gigoux, V., & Fourmy, D. (2014). Targeting a G-protein-coupled receptor overexpressed in endocrine tumors by magnetic nanoparticles to induce cell death. *ACS Nano*, *8*(2), 1350-1363.

3. Accelerated mechanophore activation and drug release in network core-structured star polymers

The research contained within this chapter has been published in Small Science (**Jilin Fan**, Mingjun Xuan*, Kuan Zhang, Rostislav Vinokur, Lifei Zheng, Robert Göstl, and Andreas Herrmann*. Accelerated Mechanophore Activation and Drug Release in Network Core-structured Star Polymers Using High-Intensity Focused Ultrasound. Small Science. 2024, 4, 2400082.). The author (Jilin Fan) of this thesis contributed to experimental design; synthesized and characterized the materials; analyzed the data and co-wrote the manuscript. In addition, I (Jilin Fan) declare as follows:

1. I designed and performed the experiments (Polymer synthesis; Small molecules synthesis; Sonication Assay; Response of polymers to sonication; Quantification of mechanophore activation; Quantification of drug release; MTS proliferation assay; Live/dead cell staining assay) contained in the publication.
2. I synthesized and characterized the materials (polymers and small molecules) contained in the publication.
3. I collected the data (TEM images; DLS analysis; NMR data; ESI-MS; GPC data; Fluorescence intensity; MTS proliferation test; Live/dead cell staining test) contained in the publication.
4. I analyzed the data and drew all the figures and tables contained in the publication.
5. I wrote the first version of the manuscript and then co-revised the manuscript.
6. Other authors' contribution to this publication; Kuan Zhang gave suggestions on MTS proliferation assay; Rostislav Vinokur built the HIFU setup; Mingjun Xuan and Lifei Zheng gave suggestions on experimental design; Robert Göstl and Andreas Herrmann revised the first version of the manuscript.

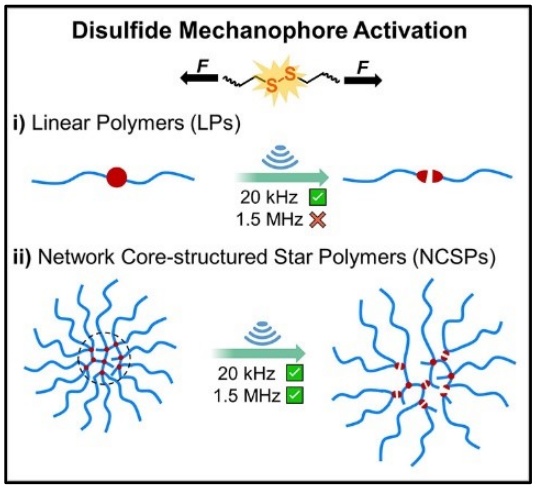

In **Chapter 3**, we prepared network core-structured star polymers (NCSPs) with multiple end chains as another interesting polymer system. 1.5 MHz high-intensity focused ultrasound (HIFU) irradiation was applied to verify the responsiveness of NCSPs to sonication. The NCSPs showed high sensitivity to megahertz HIFU irradiation. The efficiency of mechanophore chain scission in network core-structured star polymers with 1.5 MHz HIFU irradiation is comparable to the efficiency achieved with 20 kHz sonication. Although the spanning molar masses of star and linear polymers are comparable, a 108 times faster mechanochemical bond scission is achieved compared to linear polymers under HIFU irradiation. The activation of disulfide in NCSPs showed an acceleration effect compared to linear polymers.

The fluorophore and drug release from polymers is based on the activation of disulfide mechanophores. By exposing HeLa cells to the released drug, its cytotoxic effects and potential for cancer treatment were further investigated. This work demonstrates the potential of HIFU-triggered drug release from polymers for sonophamacology.

3.1 Abstract

The ultrasound (US)-induced activation of mechanophores embedded in linear polymers (LPs) is the most widely employed technique to realize chemical function by polymer mechanochemistry. However, the typical US frequency used, around 20 kHz, generates strong inertial cavitation that limits its biomedical applications. Here, we explore the use of both 20 kHz US and 1.5 MHz high-intensity focused ultrasound (HIFU) to activate disulfide mechanophores and induce polymer chain scission in network core-structured star polymers (NCSPs). We discovered that the efficiency of activating disulfide mechanophores in NCSPs using 1.5 MHz HIFU irradiation is comparable to that achieved with 20 kHz sonication. This was evaluated using 'turn on' sensor molecules that exploit the Michael addition of mechanochemically generated thiol groups, followed by retro Diels-Alder reaction to release a fluorophore. Furthermore, the anti-cancer drug doxorubicin (Dox), covalently loaded into NCSPs, is efficiently released upon 1.5 MHz HIFU activation. Lastly, an *in vitro* study of drug release from NCSPs confirms the potential of HIFU-activated polymer mechanochemistry for sonopharmacology applications.

3.2 Introduction

Ultrasound (US)-induced polymer mechanochemistry has garnered significant interest for its applications in biological systems, such as drug activation (sonopharmacology),[1-6] protein manipulation,[7-8] and biomaterials engineering.[9-10] US offers advantages over other stimuli like light,[11-12] heat,[13] pH,[14-16] or redox potential due to its widespread clinical use,[17-18] deep tissue penetration, and precise spatiotemporal control. However, current polymer mechanochemical systems typically utilize a frequency of 20 kHz,[19] which induces strong inertial cavitation that can damage tissues and biological systems.[20]

Conversely, high-intensity focused ultrasound (HIFU) driven in the MHz frequency range is an established modality in biomedical applications[21-22] including tumor ablation,[23] pain management,[24] neurosurgery,[25-26] and drug release.[27-28] A metric to quantify the biosafety of such high-frequency US is the mechanical index (MI) where an MI < 1.9 is considered medically safe as approved by the FDA.[29] HIFU is, however, often operated above this safety limit for therapeutic applications that exploit destructive mechanical properties and thermal effects of sonication, such as cancer treatment.[30] Therefore, it is crucial to develop polymer mechanochemical reactions that can be activated at medically safe US intensities while integrating mechanochemical principles with biomedical conditions.

Recently, Li, Moore, and coworkers reported the *in vitro* mechanochemical free radical generation in hydrogels for noninvasive cancer therapy. They activated azo mechanophores by HIFU with spatiotemporal precision to generate free radicals that converted to reactive oxygen species for the inhibition of cancer cell growth. Robb, Shapiro, and coworkers reported a synergistic platform that coupled the selective mechanophore activation in LPs with biocompatible focused ultrasound by leveraging pressure-sensitive gas vesicles as acousto-mechanical transducers.[6] Although using auxiliary agents such as bubbles can increase the sensitivity of traditional polymers to sonication,[31-33] thus opening the way for polymer biomedical applications, another feasible approach is to modify the structure of the polymers itself, which contains mechanoresponsive molecules.[34-36] The acceleration of mechanochemical bond scission has thereby been demonstrated in dendrimers, polymer brushes, and microgels.[37-43]

Star polymers represent another polymer architecture explored in the realm of polymer mechanochemistry, where their mechanophore activation efficiencies compared to linear chains have been scrutinized.[44-46] These studies provide a mechanistic understanding that attributes the scission of star polymer chains more to their span rather than their total molar mass. However, existing research predominantly focuses on 3-armed star polymers with a single mechanophore located near the junction point. Nevertheless, star architectures offer substantial diversity. For instance, network core-structured star polymers (NCSPs) could feature a potential multi-mechanophore core and multiple long end chains. Despite this potential, the mechanochemical behavior of such NCSPs remains unexplored. Conducting a systematic investigation would not only enhance our comprehension of star polymer chain scission but also advance predictive models for mechanophore activation and facilitate the rational design of polymers tailored for specific biomedical applications.

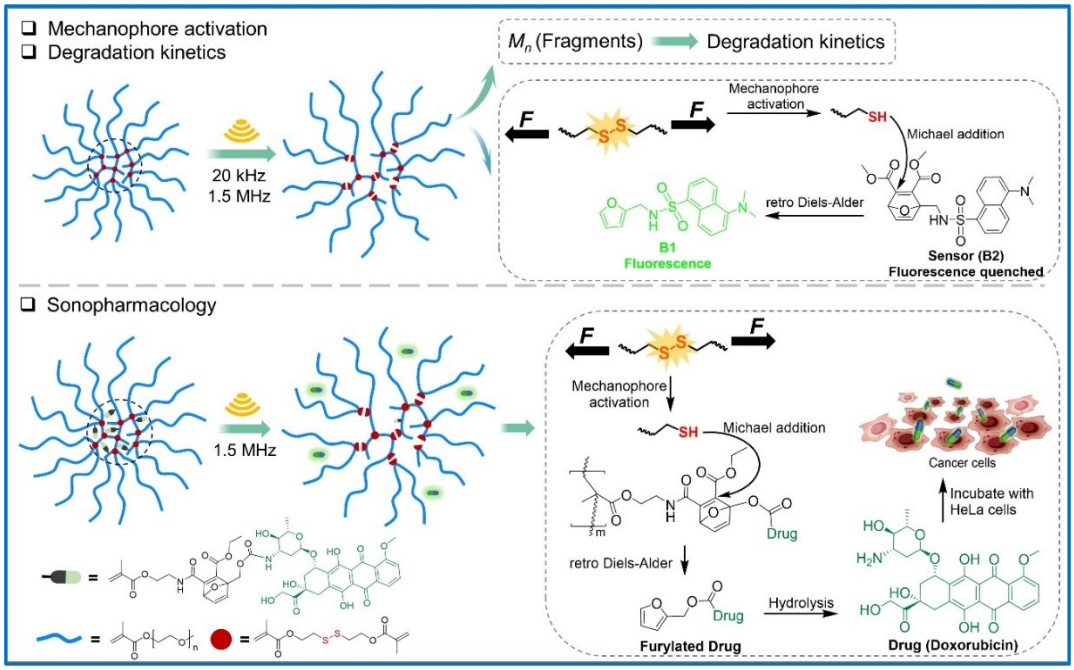

Figure 1. Schematic illustration of the mechanochemical NCSP fragmentation, activation of disulfide mechanophores, and drug release upon US irradiation.

In this study, we synthesized network core-structured star polymers (NCSPs) containing multiple disulfide mechanophores through reversible addition fragmentation chain-transfer (RAFT) polymerization (**Figure 1**). We investigated the mechanochemical responsiveness of NCSPs using both 20 kHz ultrasound (US) and 1.5 MHz high-intensity focused ultrasound (HIFU). Our study quantitatively evaluates the activation of disulfide mechanophores and the fragmentation of NCSP chains. To assess the impact of mechanophores on mechanochemical bond scission, mechanophore-free network core-structured star polymers (FNCSPs) were used as the control samples. Comparing the scission kinetics with linear polymers (LPs) highlights the superior mechanophore activation in NCSPs. Based on these findings, we demonstrate the feasibility of drug release from NCSPs using 1.5 MHz HIFU, despite with an MI of 2.4. *In vitro* experiments with HeLa cells exposed to the released drug illustrate the potential of mechanochemical drug delivery from NCSPs for applications in sonopharmacology.

3.3 Results and discussion

3.3.1 NCSP Preparation and Disulfide Mechanophore Activation

First, the disulfide crosslinker **A1** used in NCSP preparation was synthesized by methacryloylation of commercial 2, 2′-dithiodiethanol. From there, NCSPs were synthesized by RAFT copolymerization and chain extension from the endpoints of the NCSP core with the biocompatible PEG-analogue poly(ethylene glycol) methyl ether methacrylate (PEGMEMA). The synthesis involved two steps: (i) the fabrication of the polymeric core architecture and (ii) the growth of PEGMEMA chains on the surface of the polymeric core (**Figure 2a**, **Figure 2b**, and **Scheme S3**). The molar mass of the NCSPs was very roughly approximated to 109 kDa measured by GPC using a refractive index detector (**Figure S7**). The morphology and size distribution of the NCSPs were studied using transmission electron microscopy (TEM, **Figure 2c**) and dynamic light scattering (DLS), respectively. The diameter of NCSPs was in the range of 20 to 50 nm (**Figure 2d** and **Figure 2e**). Additionally, the structure of the NCSPs was analyzed using ^{1}H NMR and GPC, with the number of arms and degree of polymerization (X_n) estimated to be 7 and 37, respectively (see page 106).

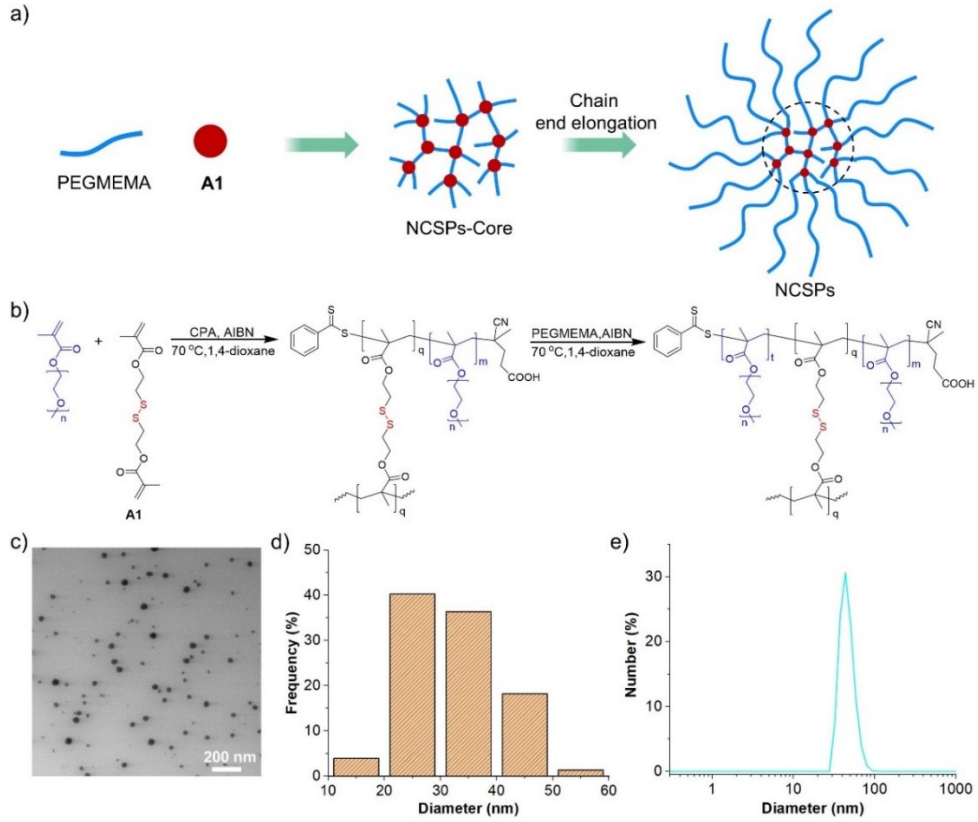

Figure 2. Synthesis and Characterization of NCSPs. **a**) Schematic diagram of the synthesis process of NCSPs. **b**) Chemical components of the synthesis: Red – disulfide mechanophore, Blue – PEGMEMA chains. **c**) TEM image of NCSPs. **d**) Size distribution histogram from panel c. **e**) DLS analysis of NCSPs.

To evaluate mechanophore activation in NCSPs, we synthesized non-fluorescent 7-oxanorbornadiene sensor **B2**, which incorporates a latent fluorophore **B1** (**Scheme S1**).[47] **B1** acted as a reporter, allowing the facile quantification of free thiols that reacted with **B2** in a Michael addition, whereupon fluorescent **B1** was released by retro Diels-Alder reaction.

As a kinetic control, linear polymers (LPs) containing chain-centered disulfide mechanophores were synthesized using Cu^0-mediated controlled radical polymerization (**Scheme S2**). The chain growth process was controlled *via* the reaction time at room temperature. LPs were obtained after 6 h with M_n = 47 kDa and $Đ_M$ = 1.4. These were subjected to sonication in H_2O/DMSO (v:v, 4:1) in the presence of sensor **B2**, and aliquots were analyzed by gel permeation chromatography (GPC) as well as fluorescence spectroscopy. Expectedly, significant fluorescence was recorded after using 20 kHz US at a sound intensity I of 12.4 W cm^{-2} (**Figure S3** and **Figure S4**). Thereafter, we identified the intensity threshold of mechanophore activation and polymer chain scission. We observed no polymers chain scission below I = 1.5 W/cm² with 20 KHz sonication (**Figure S5**) and under all tested conditions with 1.5 MHz HIFU (**Figure S6**).

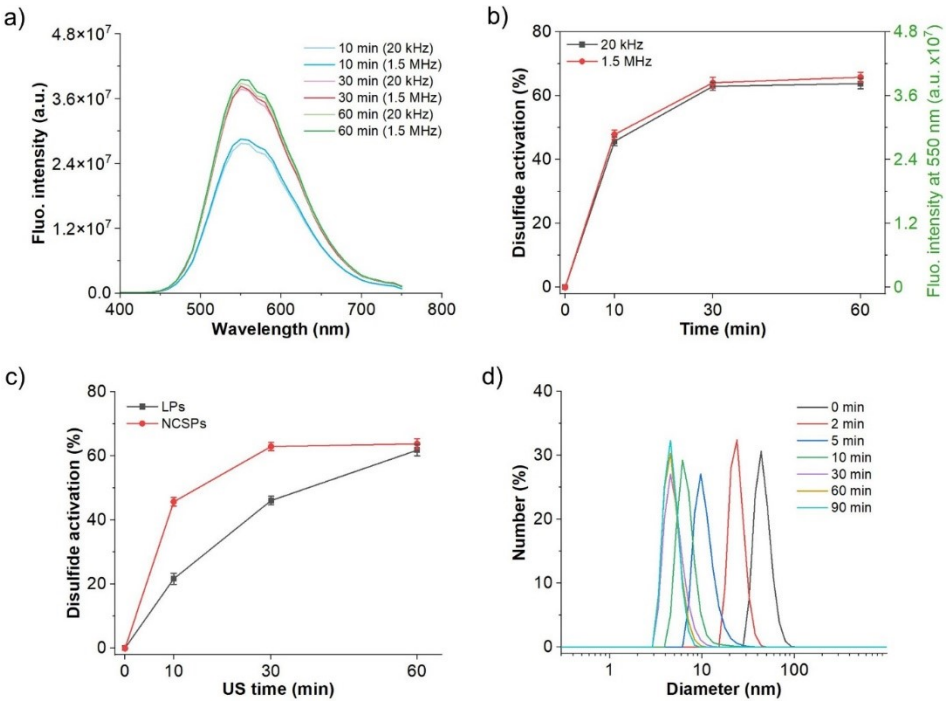

Figure 3. US-induced disulfide mechanophore activation in NCSPs. **a**) Fluorescence spectra of the mixture of **B2** and NCSPs after 20 kHz (I = 12.4 W cm^{-2}) and 1.5 MHz (I = 2300 W cm^{-2}) sonication (λ_{exc} = 330 nm). **b**) Disulfide mechanophore activation after 20 kHz and 1.5 MHz sonication. Mean ± SD from the mean. N = 3 independent sonications. The data correspond to both y-axes. **c**) Fraction of activated disulfide mechanophores in NCSPs compared to LPs using 20 kHz US at I = 12.4 W cm^{-2}. Mean ± SD from the mean. N = 3 independent sonications. **d**) DLS of NCSP solutions over the course of their sonication using 20 kHz US at I = 12.4 W cm^{-2}.

Next, we investigated the activation of disulfide mechanophores in NCSPs using ultrasound. Upon sonication (20 kHz with I = 12.4 W cm^{-2} or 1.5 MHz with I = 2300 W cm^{-2}, pulse sequence 2.0 s on, 1.0 s off) for 30 min, the green fluorescence of released **B1** was observed (**Figure S12**). The fluorescence intensity was measured to quantify mechanophore activation after the respective 20 kHz and 1.5 MHz sonications (**Figure 3a**). Samples treated by HIFU irradiation showed comparable fluorescence intensities to 20 kHz US in the same time regime

under the chosen conditions (**Figure 3b**). The activated mechanophore fraction was calculated by using the fluorescence of the mixture of **B2** and NCSPs treated with large excess of reducing agent tris(2-carboxyethyl)phosphine (TCEP) as an upper limiting value. More than 60% of **B2** were activated within 30 min at 20 kHz US using NCSPs, which was higher compared to LPs (**Figure 3c**). We attributed this difference to the higher molar mass and hence higher mechanochemical reactivity of the NCSPs.[48-49] Additionally, size distributions of NCSPs were also assessed by DLS. The hydrodynamic size showed a notable reduction within 10 minutes, dropping from approximately 50 nm to below 10 nm after 30 minutes of sonication, suggesting significant polymer chain fragmentation (**Figure 3d**).

3.3.2 Mechanochemical Reactivity of NCSPs

Subsequently, we systematically investigated the mechanochemical reactivity of the NCSPs depending on the ultrasound frequency and intensity (*I*) (**Figure 4**). The applied *I* for 20 kHz and 1.5 MHz US are listed in Table S1 and Table S2. In addition, we recorded the superposition of non-selective and selective chain scission as change in M_n (Table S4) as a function of time (**Figure 4b**). Comparing the M_n before and after sonication revealed that the NCSPs decomposed rapidly within 30 min, and the M_n decreased to less than 30% of its initial value (**Figure S16**). NCSP degradation began at a lower threshold intensity of 0.45 W/cm^2 at 20 KHz, compared to LPs, which required a threshold intensity of 1.5 W/cm^2. This highlights the enhanced mechanochemical reactivity of NCSPs toward inertial cavitation. At an *I* of 12.4 W cm^{-2}, the NCSPs degraded completely within 30 min reaching the limiting molar mass. This was underscored by DLS measurements, which revealed no further reduction in hydrodynamic size after this time. Conversely, the ultimate M_n of LPs was only reached after 60 min under identical conditions.

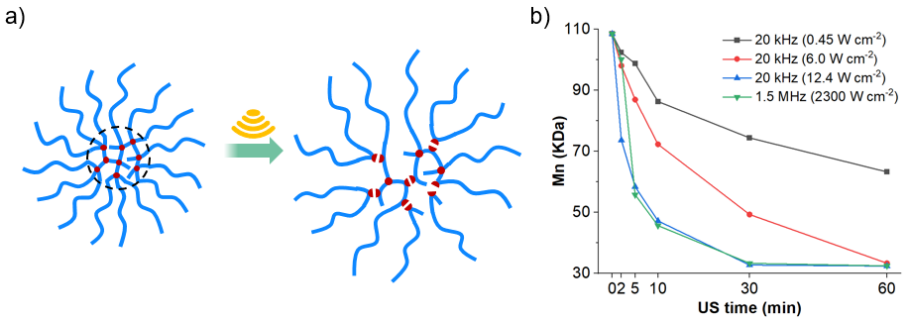

Figure 4. Mn analysis of NCSPs. **a**) Schematic representation of the degradation. **b**) M_n over the course of 20 kHz and HIFU sonication.

The mechanochemical reactivity of the NCSPs was quantitatively assessed under 20 kHz sonication using a previously reported method[50-51] by calculating the apparent scission rate constant k_{app}. Expectedly, increasing *I* led to higher k_{app} (**Figure 5a**). Comparable observations were made for HIFU sonication at 1.5 MHz. While the threshold *I* for chain scission was determined to 290 W cm^{-2} and a corresponding MI of 2.4 (**Figure 5b**, Table S5), k_{app} expectedly also increased with increasing *I* (**Figure 5c**).

The contribution of disulfide mechanophores was further examined by comparing NCSPs with mechanophore-free FNCSPs of similar size (M_n) (**Figure S17**). Over 10 minutes of HIFU sonication, the Mn of FNCSPs

showed a much slighter decrease than that of NCSPs (**Table S6, Figure 5d**), emphasizing the crucial role of disulfide mechanophores in enhancing the rate constant (K_{app}).

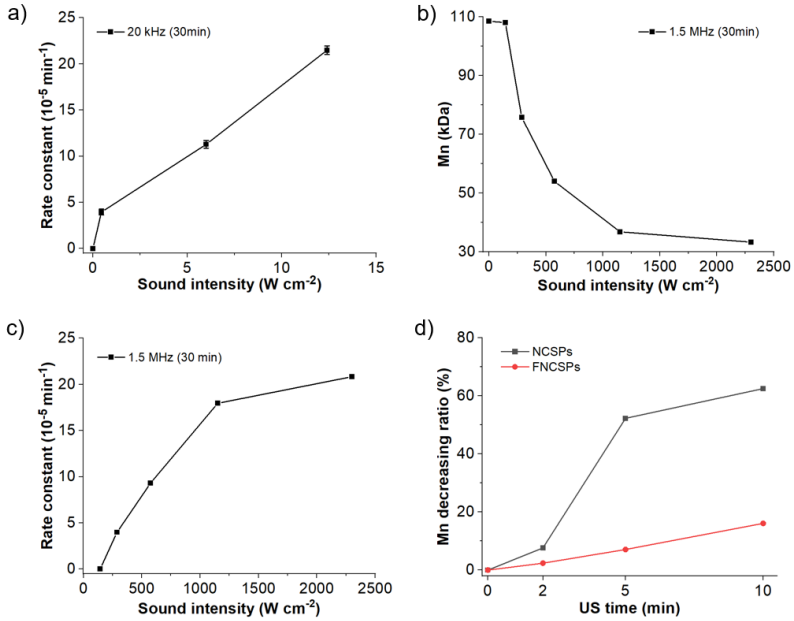

Figure 5. Mechanochemical reactivity analysis of NCSPs. **a**) Apparent scission rate constants under 20 kHz sonication as function of *I*. Mean ± SD from the mean. $N = 3$ independent sonications. **b**) Final M_n after 30 min sonication with HIFU at 1.5 MHz as a function of *I*. **c**) Apparent scission rate constants under HIFU at 1.5 MHz sonication as function of *I*. **d**) M_n decreasing ratio over the course of the sonication of NCSPs and FNCSPs with HIFU ($I = 2300$ W cm^{-2}).

From previous reports, the concept of the spanning molar mass (M_{span}) emerged.[34-36, 44-46] These studies confirmed a mechanistic interpretation of star polymer chain scission that is governed by the spanning rather than total molar mass. To verify whether the reported conclusions were applicable to NCSPs as well, M_{span} of NCSPs and LPs were calculated (details in page 106). NCSP star polymers with M_{span} = 54 kDa and k_{app} = 10.8 10^{-5} min^{-1} showed comparable performance to LPs with M_{span} = 47 kDa and k_{app} = 10.4 10^{-5} min^{-1} upon 60 min sonication at 20 kHz. The spanning molar mass concept thus holds true for LPs and NCSPs at 20 kHz sonication. However, under 1.5 MHz HIFU irradiation at $I = 2900$ W cm^{-2} for 60 min NCSPs and LPs showed k_{app} of 10.8 10^{-5} min^{-1} and 0.1 10^{-5} min^{-1} (Table S8) and thus an obvious rate difference in favor of the NCSPs. Therefore, we concluded that NCSPs demonstrated higher sensitivity to 1.5 MHz HIFU irradiation than LPs, both in terms of chain scission and disulfide mechanophore activation.

3.3.3 Ultrasound-Induced Drug Release from NCSPs

After successfully demonstrating superior disulfide mechanophore activation in NCSPs using HIFU, our goal was to illustrate a proof-of-concept application involving the release of a furylated drug molecule. For this purpose, we employed furylated Dox **D1**, which has previously shown promising anticancer activity in soft tissue, bone sarcomas, cancers of the breast, ovary, bladder, and thyroid.[52-53] However, it exhibits a short half-life as well as systemic and specific cardiac toxicity,[54] rendering it an ideal candidate for remote-controlled release.

In addition, we synthesized the acrylate-functionalized Diels-Alder adduct of furylated Dox **C3**, and this compound was incorporated into the core of NCSPs through copolymerization (**Figure 6b**). TEM analysis was then performed to examine the morphology of the resulting NCSPs (**Figure 6c**).

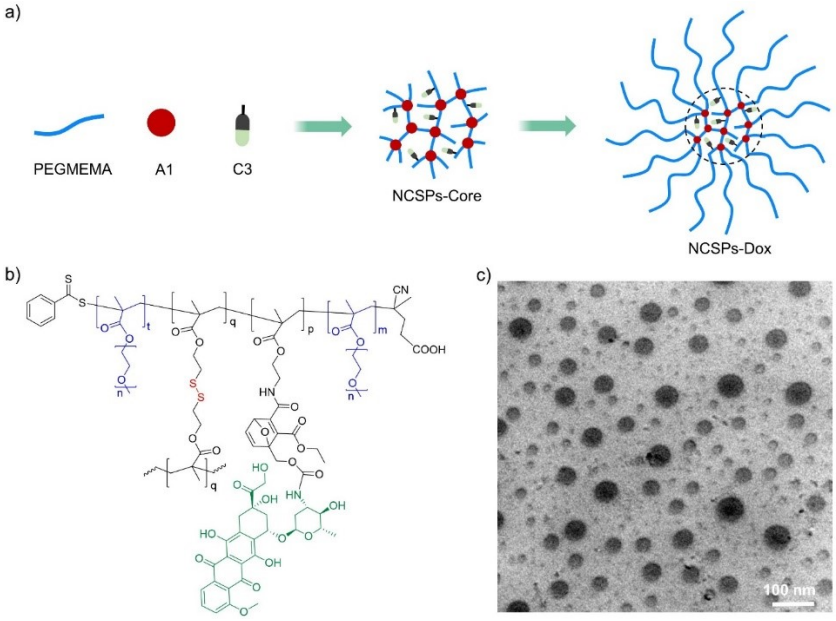

Figure 6. The synthesis of Dox-bearing NCSPs. **a**) Schematic representation of the synthesis process and **b**) final polymer. Disulfide mechanophore, Dox, and PEGMEMA chains are highlighted in red, green, and blue respectively. **c**) TEM micrograph.

HIFU at 1.5 MHz and an intensity of 2300 W/cm^2 was employed to trigger the release of **D1** (**Figure 7a**). The Dox-loaded NCSPs were carefully dispersed in a solvent blend of DMSO and PBS (v/v = 1:4) and subjected to sonication for up to 20 minutes. Fluorescence spectra were meticulously recorded at each interval to track the release of the fluorescent **D1** (**Figure 7b**). To further substantiate these findings, ultra-high-performance liquid chromatography-mass spectrometry (UPLC-MS) analysis was conducted throughout the sonication process, offering precise insights into the drug release dynamics. Additionally underpinning the successful release, ^{1}H NMR analysis demonstrated the emergence of characteristic peaks of **D1** in the aromatic region (**Figure 7c**). To quantify released **D1**, a correlation between its concentration and fluorescence intensity was established (**Figure S21**). To obtain a limiting upper value, 2-mercaptoethanol (MCE) was used to reduce all disulfide bonds within the NCSPs (**Figure S22a**). Thereby, a maximum release of **D1** by HIFU of around 40% was observed (**Figure 7d**). Additionally, we conducted experiments using 10% DMSO, 5% DMSO, and water to investigate the effect of solvents on molecular release. We found that with 5% DMSO solvent, approximately 20% of furan-Dox was released after 20 minutes of HIFU irradiation. Conversely, in experiments performed in water, over 5% of furan-Dox was released from NCSPs (**Figure S22c** and **S22e**).

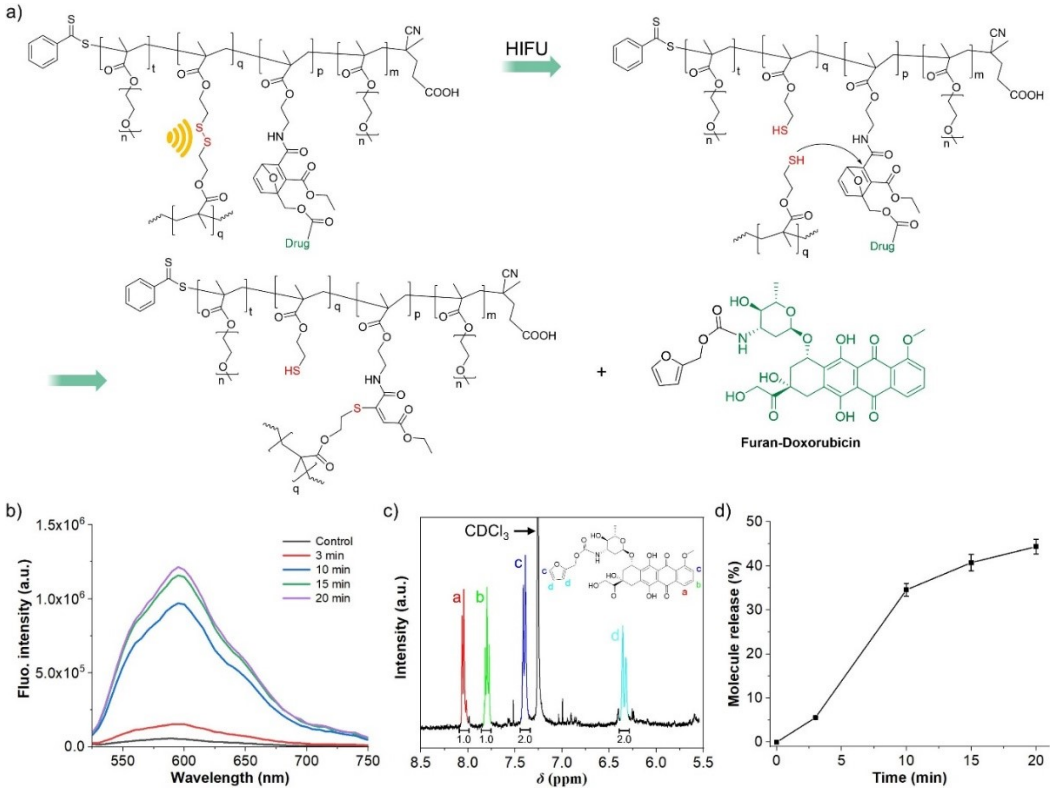

Figure 7. HIFU-induced disulfide mechanophore activation and D1 release from NCSPs. **a**) Schematic illustration. **b**) Fluorescence spectra (λ_{exc} = 485 nm) over the course of HIFU application (1.5 MHz, I = 2300 W cm^{-2}). **c**) Section of ^{1}H NMR (400 MHz, $CDCl_3$) spectrum showing characteristic **D1** peaks. **d**) The release profile of **D1** from NCSPs over sonication time (1.5 MHz, I = 2300 W cm^{-2}). Mean ± SD from the mean. N = 3 independent sonications.

3.3.4 *In Vitro* Cancer Therapy of Released Dox

Next, we explored the potential of Dox-loaded NCSPs for in vitro treatment using MTS proliferation assay and confocal laser scanning microscopy (CLSM) to evaluate the efficacy of the delivered drug in suppressing cancer cell growth (**Figure 8a**). We determined the half-maximal inhibitory concentrations (IC_{50}) of PBS, Dox-loaded NCSPs, pristine Dox, and Dox-loaded NCSPs after HIFU treatment and hydrolysis. The hydrolysis process to de-furylate released Dox was carried out in a solvent mixture of DMSO and PBS (v/v = 1:4) at a tumor-like pH of 5.5 for 48 h (**Figure 8b**) and confirmed by UPLC (**Figure S23**).[55]

Significantly, the IC_{50} of the sonicated and de-furylated Dox-loaded NCSPs was markedly lower compared to the control samples and comparable to that of pristine Dox (**Figure 8c**). As anticipated, PBS exhibited negligible cytotoxicity under the given conditions. At the same time, HeLa cells treated with varying concentrations of non-sonicated Dox-loaded NCSPs maintained remarkably high viability, highlighting the exceptional biocompatibility of the intact drug carrier. This effect was attributed to the protective hydrodynamic shielding of the solvated PEGMEMA chains around the Dox-loaded cores. Moreover, an in-depth investigation of sonicated Dox-loaded NCSPs before hydrolysis revealed that furylated Dox significantly inhibited HeLa cell proliferation. This outcome could stem from in situ de-furylation within cancer cells or the inherent cytotoxic nature of the furylated Dox itself, further underscoring the potential of this delivery system.

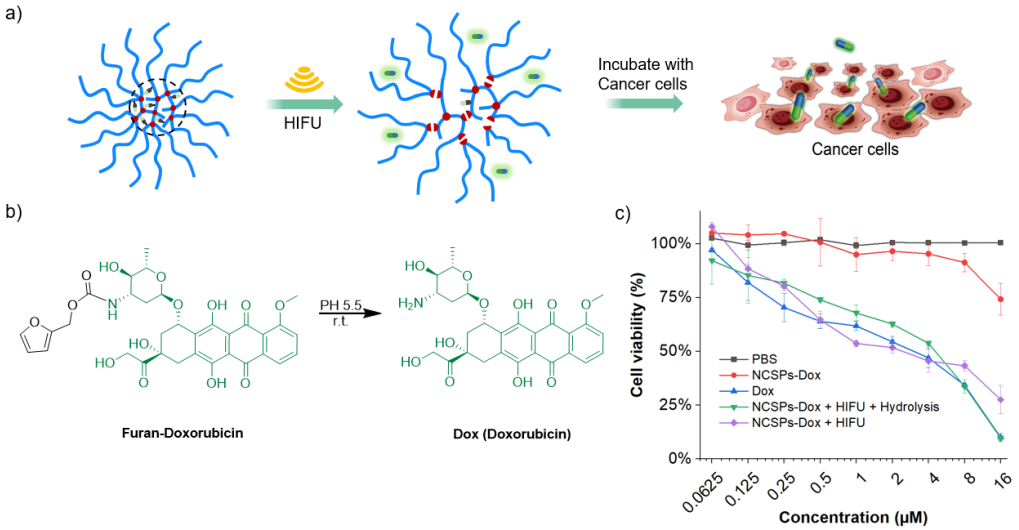

Figure 8. Dox-loaded NCSPs for *in vitro* sonopharmacology. **a**) Schematic illustration of the drug release. **b**) Hydrolysis of released furylated Dox. **c**) Cell viability using MTS proliferation assay. Samples: PBS, Dox-loaded NCSPs, Dox, Dox-loaded NCSPs after HIFU and hydrolysis, and Dox-loaded NCSPs after HIFU all *ex situ* mixed with HeLa cells. Mean values ± SD from the mean. $N = 3$ independent sonications.

Furthermore, CLSM was performed to underpin these results after live cell staining with calcein AM and dead cell staining with propidium iodide. Treatment with either pristine Dox or sonicated and hydrolyzed Dox-loaded NCSPs resulted in a significant decrease in the number of live HeLa cells (**Figure 9**), highlighting the effectiveness of HIFU-induced disulfide mechanophore activation and subsequent Dox release from NCSPs in sonopharmacology.

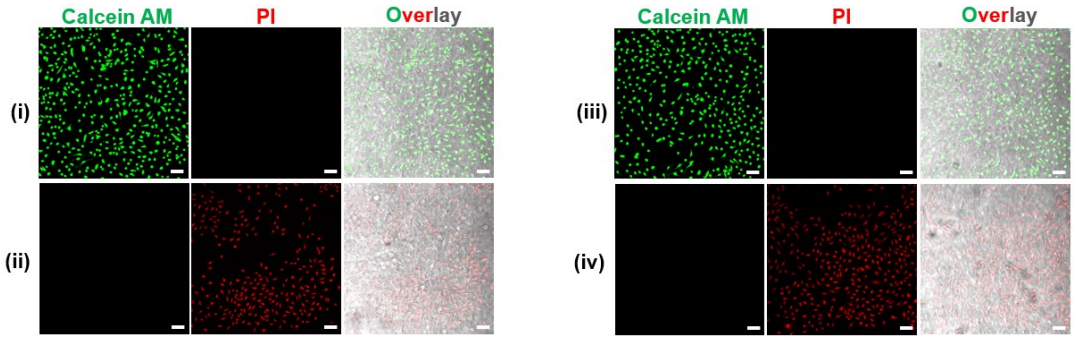

Figure 9. CLSM micrographs of HeLa cells treated with different samples (live cells: calcein AM, green; dead cells: propidium iodide, red). (i) PBS, (ii) pristine Dox, (iii) non-sonicated Dox-loaded NCSPs, (iv) sonicated and hydrolyzed Dox-loaded NCSPs (1.5 MHz, $I = 290$ W cm^{-2}, 30 min). HeLa cells were stained for 5 min. Scale bars: 50 μm.

3.4 Conclusions

Here, we demonstrate accelerated US-induced disulfide mechanophore activation in NCSPs, which exhibit higher sensitivity to US compared to LPs. Mechanophore activation was quantified by Michael addition of mechanochemically generated thiols to a 7-oxanorbornadiene scaffold carrying a latent fluorescent cargo, subsequently released via retro Diels-Alder reaction. NCSPs showed faster mechanophore activation and responded to lower sonication powers compared to linear chains with identical mechanophores centered within them. Moreover, we systematically investigated how mechanochemical NCSP fragmentation varied with sonication conditions, including frequency and intensity. While linear chains were responsive only to 20 kHz US, producing strong inertial cavitation, NCSPs also activated under biomedically relevant 1.5 MHz HIFU irradiations. These findings underscore the pivotal role of polymer architecture in efficient mechanophore activation. We applied this system in a proof-of-concept drug release experiment, releasing Dox using 1.5 MHz HIFU with an MI of 2.4 to inhibit cancer cell growth in vitro. These results represent a significant advancement of polymer mechanochemistry in sonopharmacology.

3.5 Experimental section

3.5.1 Materials

All chemical reagents and solvents were used without further purification unless otherwise stated. 2-hydroxyethyl disulfide (technical grade, Sigma-Aldrich), methacryloyl chloride (97%, Sigma-Aldrich), triethylamine (TEA, ⩾99%, Sigma-Aldrich), dichloromethane (CH_2Cl_2, anhydrous, ⩾99.8%, Sigma-Aldrich), 4-(dimethylamino)pyridine (DMAP, >99.0%, TCI Deutschland GmbH), toluene (⩾99.5%, Sigma-Aldrich), 1,4-dioxane (99.8%, Sigma-Aldrich), tris(2-carboxyethyl)phosphine hydrochloride (TCEP, ⩾98%, Sigma-Aldrich), 4-cyano-4-(phenylcarbonothioylthio)pentanoic acid (CPA, RAFT agent, Sigma-Aldrich), ethylenebis(2-bromoisobutyrate) (97%,SigmaAldrich), bis[2(2'bromoisobutyryloxy)ethyl]-disulfide (98%, Sigma-Aldrich), $CuBr_2$ (99%, Sigma-Aldrich), Me_6TREN (97%, Sigma-Aldrich), lithium bis(trimethylsilyl)amide solution (LHMDS, 1.0 M in THF), 4-(bromomethyl)benzoic acid (97%, Sigma-Aldrich), *N*,*N*'-disuccinimidyl carbonate (DSC, ⩾95%, Sigma-Aldrich), doxorubicin hydrochloride (Dox, Pharmaceutical Secondary Standard, Sigma-Aldrich) were used as received. 1, 6-hexanediol dimethacrylate (⩾90%, Sigma-Aldrich) and poly(ethylene glycol) methyl ether methacrylate (PEGMEMA, M_n ~ 300 Da, Sigma-Aldrich) were purified by a column of activated basic Al_2O_3 to remove the inhibitor. 2,2'-azobis(2-methylpropionitrile) (AIBN, 98%) was obtained from Sigma-Aldrich and recrystallized twice from MeOH. Dialysis membranes (3.5 kDa MWCO) were obtained from Spectrum Labs. Centrifugal filter (3000 MWCO) was obtained from Sartorius. HeLa cell line was obtained from ATCC: The Global Bioresource Center. Ultrapure Milli-Q water (18.2 MΩ·cm) was used for all experiments.

3.5.2 General Instrumentation

^{1}H and ^{13}C NMR spectra were recorded at room temperature in $CDCl_3$ on a 400 MHz Bruker Avance 400 spectrometer (^{13}C: 101 MHz). The chemical shifts are reported in δ units using residual protonated solvent signals as internal standard[56] (^{1}H: $CDCl_3$ ($^\delta$H = 7.26 ppm), ^{13}C: $CDCl_3$ ($^\delta$C = 77.16 ppm)). The following abbreviations were used: s = singlet, d = doublet, t = triplet, q = quartet, sept. = septet, dd = doublet of doublets etc., m = multiplet. Coupling constants (*J*) were given in Hz and refer to the respective H, H-couplings.

Thin-layer chromatography (TLC) was conducted on Merck TLC Silica Gel 60 F_{254} plates, which featured a fluorescence indicator for visualization under 254 nm or 365 nm UV light using a hand lamp. High-purity silica gel (40–63 μm) was utilized for flash column chromatography.

Gel permeation chromatography (GPC/SEC) with THF (HPLC grade) was performed using a Jasco PU-2080plus HPLC pump equipped with a Jasco RI-2031plus refractive index detector. As an internal standard, the sample solvent contained 250 mg/mL 3,5-di-*t*-4-butylhydroxytoluene (BHT, ⩾99%, Fluka). A pre-column (8×50 mm) and four SDplus gel columns (8×300 mm, SDplus, MZ Analysentechnik) were used at a controlled flow rate of 1.0 mL/min at 20 °C. The gel particles had a diameter of 5 μm, with nominal pore sizes of 50, 102, 103, and 104 Å. Calibration was performed using narrowly distributed poly(methyl methacrylate) (PMMA) standards from Polymer Standards Service. Molar masses (M_n and M_w) and molar mass distributions (M_w/M_n) were determined using PSS WinGPC UniChrom software (Version 8.1.1).

ESI MS: micrOTOF-Q II™ ESI-Qq-TOF mass spectrometer system (BRUKER).

Transmission electron microscopy (TEM) micrographs were captured on a LIBRA®120 transmission electron microscope (Carl Zeiss) with an accelerating voltage of 120 kV and images were recorded using a Gatan Ultra Scan 1000. Transmission electron microscopy (TEM) sample preparation: one drop (~ 10 μL) of sample was deposited onto carbon-coated copper grid, then air-dried.

Dynamic light scattering (DLS) was measured on a Zetasizer instrument (Zetasizer Ultra, Malvern). Samples were dispersed in H_2O/DMSO (4:1, v/v) and then the mixture was transferred to a disposable plastic cell.

Ultra-high performance liquid-chromatography (UHPLC) system: ACQUITY UPLC I-Class System (Waters) with the compatible ACQUITY UPLC PDA eλ Detector and ACQUITY QDa detector (Waters). Solvents: A= water (contained 0.1% TFA), B= acetonitrile (contained 0.1% TFA); Flow= 0.4 $mL \cdot min^{-1}$; Gradient (B): 0-1 min (10%), 1-5 min (10-90%), 5-7 min (90%), 7-10 min (90-10%).

3.5.3 Fluorescence Spectroscopy

Fluorescence spectra were collected by a SpectraMax iD3 multi-mode microplate reader (Molecular Devices) at room temperature. For fluorescence spectra measurements of the mixture of **B2** and polymers, samples were excited at 330 nm. The spectral bandwidth for emission was set to 10 nm (380-750 nm). To generate the standard curve for B1, fluorescence intensity was recorded at 550 nm. To obtain the fluorescence spectra of NCSP-Dox, excitation was performed at 485 nm, with an emission bandwidth of 5 nm (525-750 nm). The standard curve for Furan-Dox (D1) was obtained by collecting fluorescence intensity at 595 nm. Samples were incubated at room temperature for 72 hours to complete downstream reactions before the fluorescence intensity collection. The fluorescence intensity collection were conducted using a pureGrade™ 96-well plate from BRAND GmbH. In addition, before fluorescence measurements, the sonicated NCSP solution required a filtration step. This involved three times centrifugation (8000 ×g for 10 minutes), followed by filtration through a 3,000 MWCO centrifugal filter (5000 rpm).

3.5.4 Sonication Experiments

20 kHz sonicator and 1.5 MHz HIFU setup performed ultrasound sonication experiments (**Figure S1**).

20 kHz: Sonication experiments were carried out using a Qsonica Q125 ultrasonic system with a 3.2 mm probe, f = 20 kHz. Pulsed sonication (2 s on, 1 s off) was used. 10 mg polymers was dissolved in 1 mL H_2O/DMSO (4:1, v/v), then injected into a cooled Eppendorf tube (immersed in an ice-water bath). Then, the mixture was exposed to sonication for 2 min, 5 min, 10 min, 30 min, 60 min and 90 min.

1.5 MHz HIFU: Ultrasound sonication experiments were performed with a home-built HIFU setup. The core devices include waveform generator (33511B, Keysight Technologies), RF amplifier (AG1021, T&C Power Conversion, Inc.) and transducers (1.5 MHz, Precision Acoustics Ltd., UK). A 0.5 mm needle hydrophone (Precision Acoustics Ltd., UK) was used for locating the transducer focal point. Custom-made motorized 3D-manipulator/positioning system for controlling the well plate submerged in water was employed. Pulsed sonication (2 s on, 1 s off) was used. 10 mg polymers were dissolved in 1 mL H_2O/DMSO (4:1, v/v), then the solution was added into the 24 well plate that with an acoustically transparent base made of ultra-thin film

(lumox® multiwall 24, SARSTEDT). Samples exposed to constant sonication for 3 min, 10 min, 15 min and 20 min.

3.5.5 Cell Imaging

HeLa cells designated for imaging were meticulously cultured in Dulbecco's Modified Eagle's Medium (DMEM), enriched with 10% heat-inactivated fetal bovine serum (FBS) and supplemented with 100 U/mL penicillin and 100 μg/mL streptomycin. The incubation was maintained at 37 °C under a precisely controlled humidified atmosphere containing 5% CO_2 to ensure optimal cell viability and proliferation. For imaging studies, HeLa cells were carefully seeded into ibidi μ-Slide 8 Wells (glass-bottomed) at a density of 2.5×10^5 cells per well in 500 μL of culture medium, ensuring uniform distribution and adherence for high-resolution microscopy analysis. After 24 h, HeLa cells were incubated with different concentrated sonicated samples or non-sonicated samples in PBS for 2 h at 37 °C, then washed with phosphate-buffered saline (PBS) three times. Then, PBS was added into the wells (500 μL per well), 2 μL (1 mg/mL) calcein AM and 2 μL (1 mg/mL) propidium iodide were transferred to the wells mixed for 5min. PBS was used to wash out the free cell imaging agents. Then the fluorescence imaging of cells was performed on a confocal laser scanning microscope (STP8, Leica) (confocal excitation: calcein AM: 496 nm, propidium iodide: 561 nm) and analyzed by ImageJ.

3.5.6 MTS Proliferation Assays

HeLa cells were used to evaluate the cytotoxicity of different samples. HeLa cells were cultured in a basal medium containing DMEM (supplemented with 10% fetal bovine serum and 1% antibiotics/antimycotics) at 37 °C. Actual cell viability was monitored by using a tetrazolium compound 3-(4,5-dimethylthiazol-2-yl)-5-(3-carboxymethoxyphenyl)-2-(4-sulfophenyl)-2H-tetrazolium (inner salt, MTS reagent) and a chemical electron acceptor dye (phenazine ethosulfate; PES) (Promega, Germany) using an assay according to the manufacturer's instructions. Briefly, approximately 5,000 cells in 100 μL of medium were seeded into 96-well plates. Following overnight incubation, the existing medium was carefully aspirated and replaced with 100 μL of fresh medium containing varying concentrations of the test samples. Control wells received DMSO alone, ensuring that its final concentration did not exceed 0.5% to prevent cytotoxic interference. After 48 hours of incubation, the culture medium was gently removed, and the cells were rinsed with 100 μL of PBS buffer to eliminate residuals. Subsequently, 20 μL of MTS reagent was combined with 100 μL of fresh medium and added to each well. A mixture of MTS reagent with culture medium served as the negative control. To ensure homogeneity, the solution was thoroughly mixed, and absorbance was measured at 490 nm using a Synerg™ HT microplate reader (BioTek Instruments). The resulting MTS signals were analyzed to assess cell viability and proliferation. All experimental conditions were conducted in at least triplicate to ensure statistical reliability.

3.5.7 Quantification Method of Disulfide Activation Percentage

The disulfide activation percentage was calculated by a simple quantification method, as the following description:

For linear polymers: 10 mg linear polymers were dissolved in 1 mL H_2O/DMSO (4:1, v/v), then pipette 100 μl polymers solution into a tube, TCEP (0.3 mg) was added to the mixture to cleave all disulfide bonds within the polymers. Subsequently, DI water was used to wash the LPs two times (the mixture was filtered through a centrifugal filter (3,000 MWCO) by centrifugation at 5,000 rpm). Next, **B2** (0.1 mg) dissolved in the

H_2O/DMSO (1 mL) mixed with the filtered polymers residual. After 3 d reaction that make sure all the thiols reacted with B2, the fluorescence intensity at 550 nm of the solution was measured. We take the obtained fluorescence intensity at 550 nm as the maximum value (F_m). Then, **B2** (0.1 mg) dissolved in the H_2O/DMSO (1 mL) mixed with the sonicated polymers residual by the same method. We collected the fluorescence intensity at 550 nm (F_s) from the sonicated samples. When measuring the fluorescence intensity, the samples were diluted by the same factor to make sure the F_s and F_m were in the same range according to the standard curve of fluorescence molecule B1 (**Figure S13**). Finally, we take the value of F_s / F_m as the results of disulfide activation percentage.

For star polymers: 10 mg star polymers were dissolved in 1 mL H_2O/DMSO (4:1, v/v), then then pipette 100 μL polymers solution into a tube, TCEP (1.3 mg) was added to the mixture to cleave all disulfide bonds within the polymers. Subsequently, DI water was used to wash the star polymers two times (the mixture was filtered through a centrifugal filter (3,000 MWCO) by centrifugation at 5,000 rpm). Next, **B2** (0.5 mg) dissolved in the H_2O/DMSO (1 mL) mixed with the polymers residual. After 3 d reaction that make sure all the thiols reacted with B2, the fluorescence intensity at 550 nm of the solution was measured. We take this obtained fluorescence intensity at 550 nm as the maximum value (F_m). Then, **B2** (0.5 mg) dissolved in the H_2O/DMSO (1 mL) mixed with the sonicated polymers residual by the same method. We collected the fluorescence intensity at 550 nm (F_s) from the sonicated samples. When measuring the fluorescence intensity, the samples were diluted by the same factor to make sure the F_s and F_m were in the same range according to the standard curve of fluorescence molecule B1 (**Figure S13**). Finally, we take the value of F_s / F_m as the results of disulfide activation percentage.

In addition, for the quantification of the concentration of activated thiols or cleaved disulfide bonds, our established method can be used.[31]

3.5.8 Synthetic procedures and characterization data

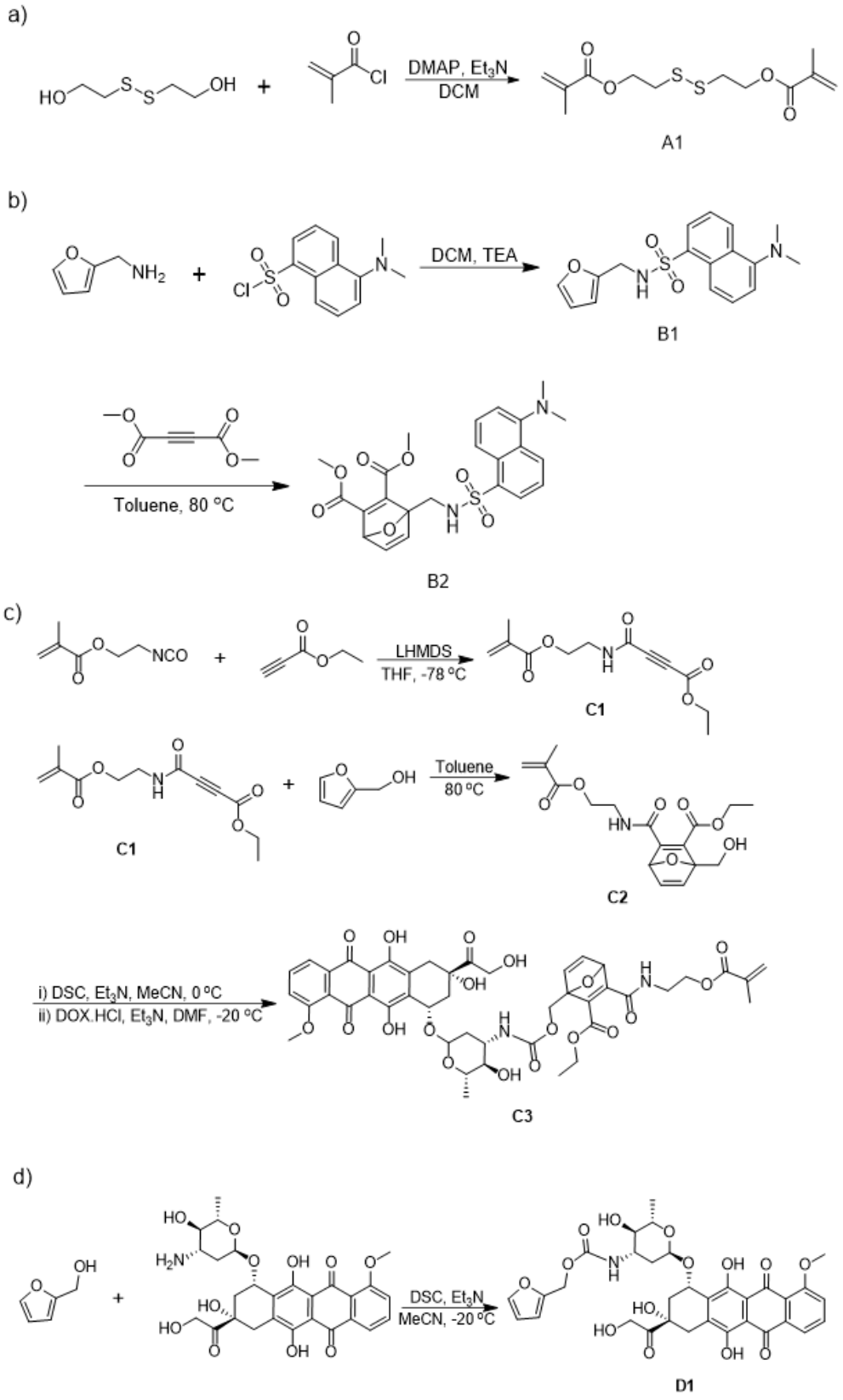

Scheme S1. Synthesis of **A1, B2, C3 and D1**.

Disulfanediylbis(ethane-2,1-diyl) bis(2-methylacrylate) (**A1**)

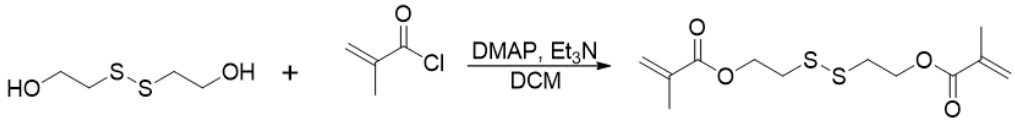

A1

2-hydroxyethyl disulfide (2.0 g, 13 mmol, 1 equiv.) and TEA (3.64 mL, 26 mmol, 2.0 equiv.) were added in THF (30 mL) with a constant flow of N_2. The mixture was subject into the ice-water bath to keep the temperature at 0 °C. Afterwards, a solution of methacryloyl chloride (2.54 mL, 26 mmol, 2.04 equiv.) and 15 mL CH_2Cl_2 was added dropwise (15 mL/h) to the reaction mixture via an injection pump. The reaction mixture was continuously stirred until the starting material was entirely consumed, as confirmed by TLC analysis. Then, it was washed with brine and deionized water three times, respectively. Afterwards, the crude product was purified by column chromatography on silica gel (hexane:EtOAc = 5:1) to give compound **A1** (3.2 g, 85% yield) as a colourless oil. **^{1}H NMR (400 MHz, $CDCl_3$):** δ (ppm): 6.12 (sept, *J*=1.6 Hz, 2H), 5.58 (sept, *J*=1.6 Hz, 2H), 4.4 (t, *J*=6.8 Hz, 4H), 2.97 (t, *J*=6.8 Hz, 4H), 1.94 (s, *J*=1.2 Hz, 6H). **^{13}C NMR (101 MHz, $CDCl_3$):** δ (ppm): 167.23, 136.12, 126.13, 62.6, 37.39, 18.4. **ESI-MS (*m/z*)** for $C_{12}H_{18}O_4S_2$ expected $[M+Na]^+$: 313.0539, Found for $[M+Na]^+$: 313.0590.

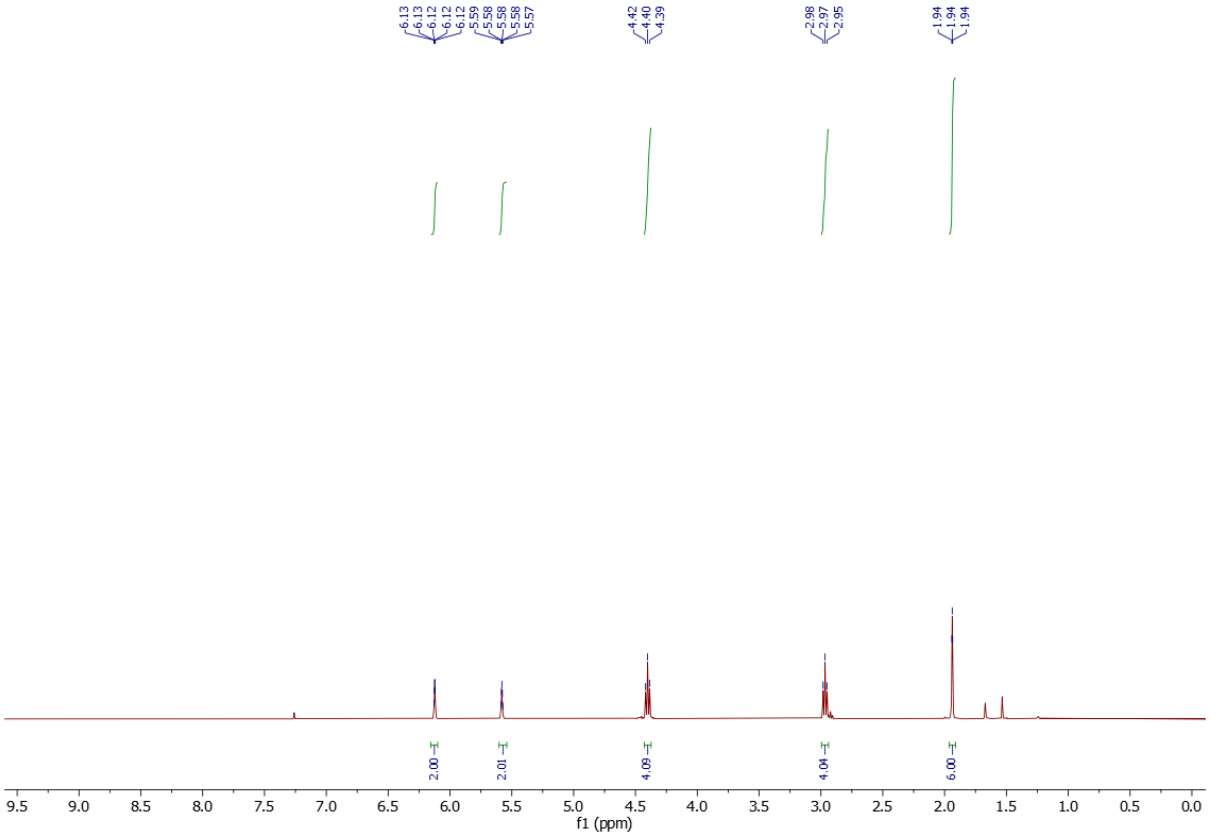

^{1}H NMR spectrum of **A1**.

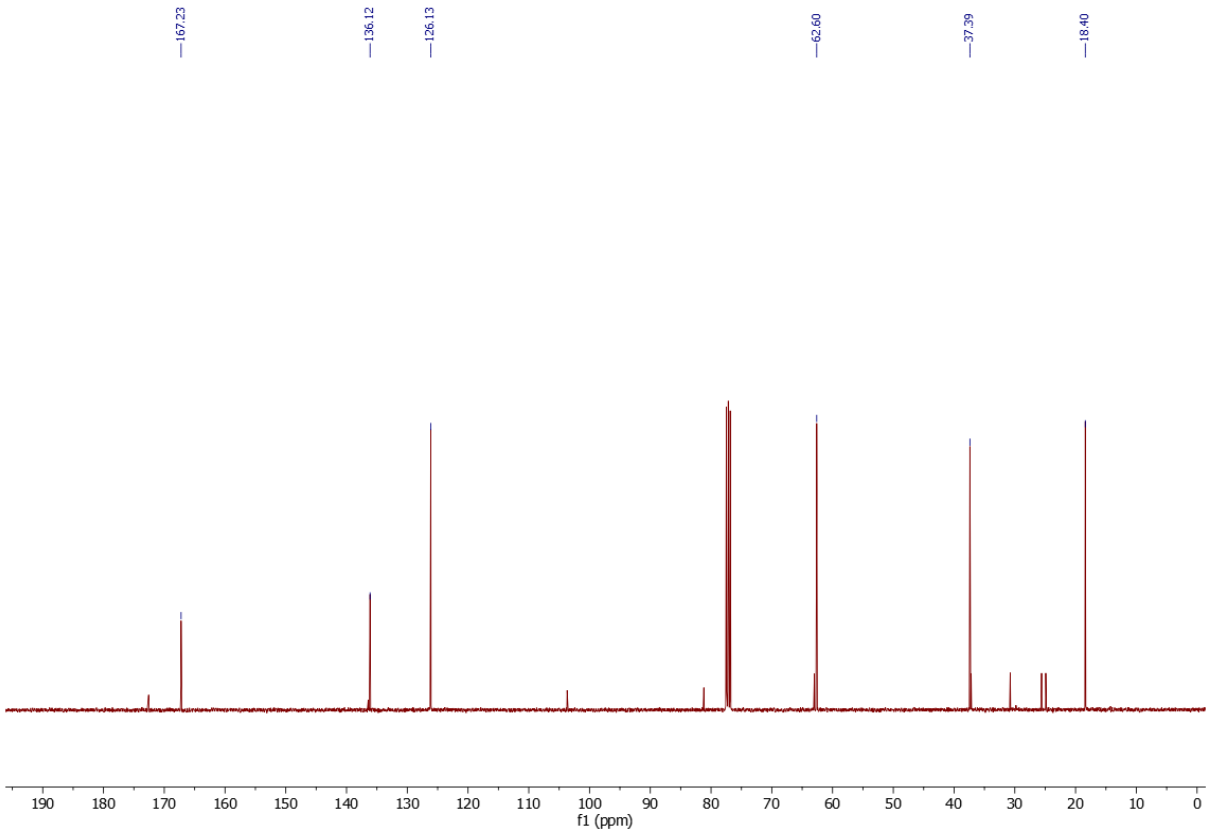

^{13}C NMR spectrum of **A1**.

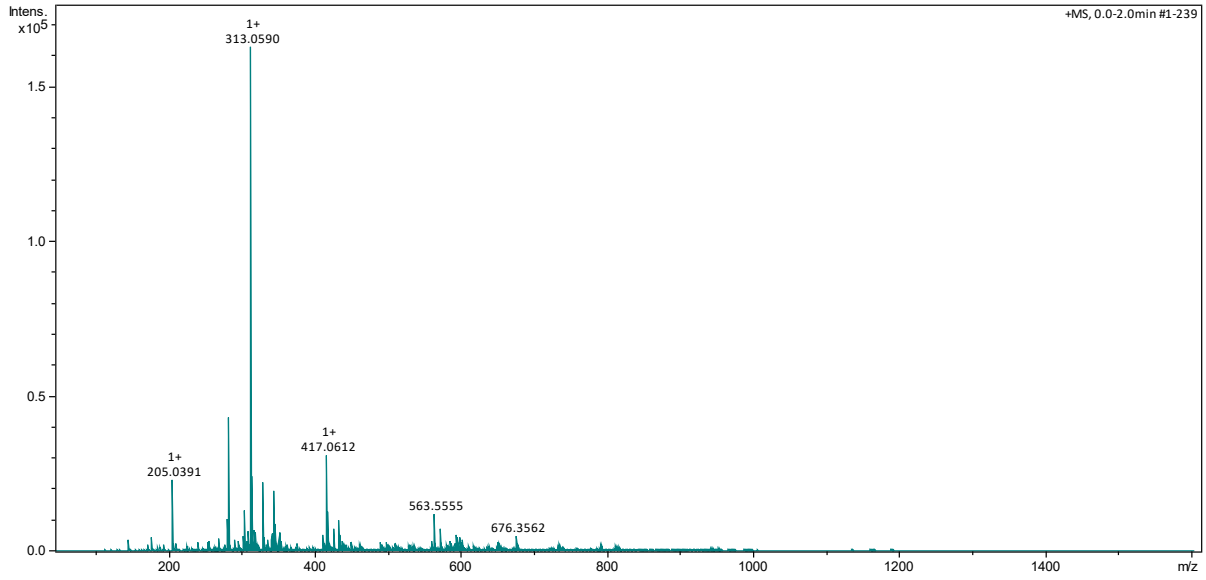

ESI-MS (*m/z*) of **A1**.

5-(dimethylamino)-N-(furan-2-ylmethyl)naphthalene-1-sulfonamide (**B1**)

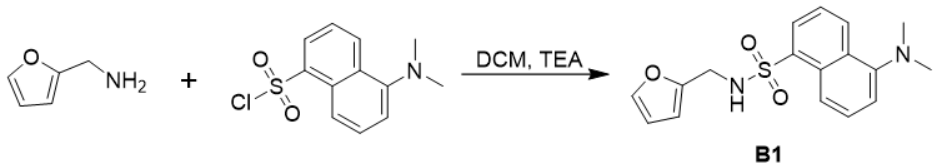

B1 is synthesized according to a modified literature reaction (Scheme S1).[47] A mixture of 5-(dimethylamino)naphthalene-1-sulfonyl chloride (1.00 g, 3.70 mmol, 1.0 equiv.) and Et_3N (1.0 mL, 7.2 mmol, 2.0 equiv.) in CH_2Cl_2 (20 mL) is added into a solution of furfurylamine (380 mg, 3.9 mmol, 1.05 equiv.) in CH_2Cl_2 (5 mL) via syringe under N_2 protection. The resulting solution is stirred for 5 h at room temperature and poured into 1.0 mM pH 7 phosphate buffer (30 mL). Afterwards, the crude product was purified by column chromatography on silica gel (hexane:EtOAc = 5:1) to give compound **B1** (1.16 g, 95% yield) as a yellow-green oil. **^{1}H NMR (400 MHz, $CDCl_3$):** δ (ppm): 8.50 (d, 1H, J = 8.0 Hz), 8.25-8.20 (m, 2H), 7.54-7.45 (m, 2H), 7.16 (d, 1H, J = 8.0 Hz), 7.01 (dd, 1H, J = 2.0 Hz, 0.8 Hz), 6.02 (dd, 1H, J = 3.2 Hz, 2.0 Hz), 5.87 (dd, 1H, J = 3.2 Hz, 0.6Hz), 5.19 (m, 1H), 4.12 (d, 2H, J = 6.0 Hz), 2.87 (s, 6H). **^{13}C NMR (101 MHz, $CDCl_3$):** δ (ppm): 151.95, 149.41, 142.20, 134.72, 130.50, 129.84, 129.60, 128.42, 123.13, 118.61, 115.14, 110.14, 107.98, 45.42, 40.20. **ESI-MS (*m/z*)** for $C_{17}H_{18}N_2O_3S$ expected $[M+H]^+$: 331.1111, Found for $[M+H]^+$: 331.1061.

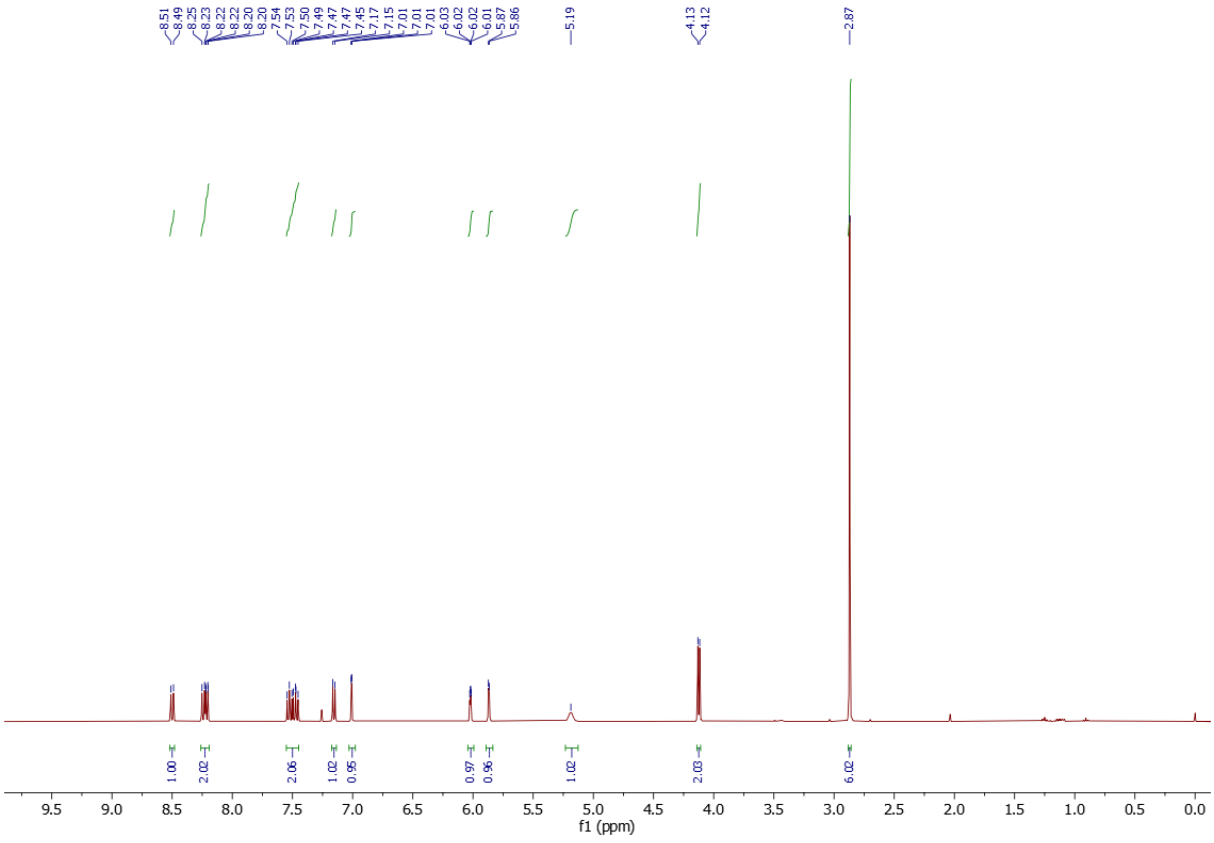

^{1}H NMR spectrum of **B1**.

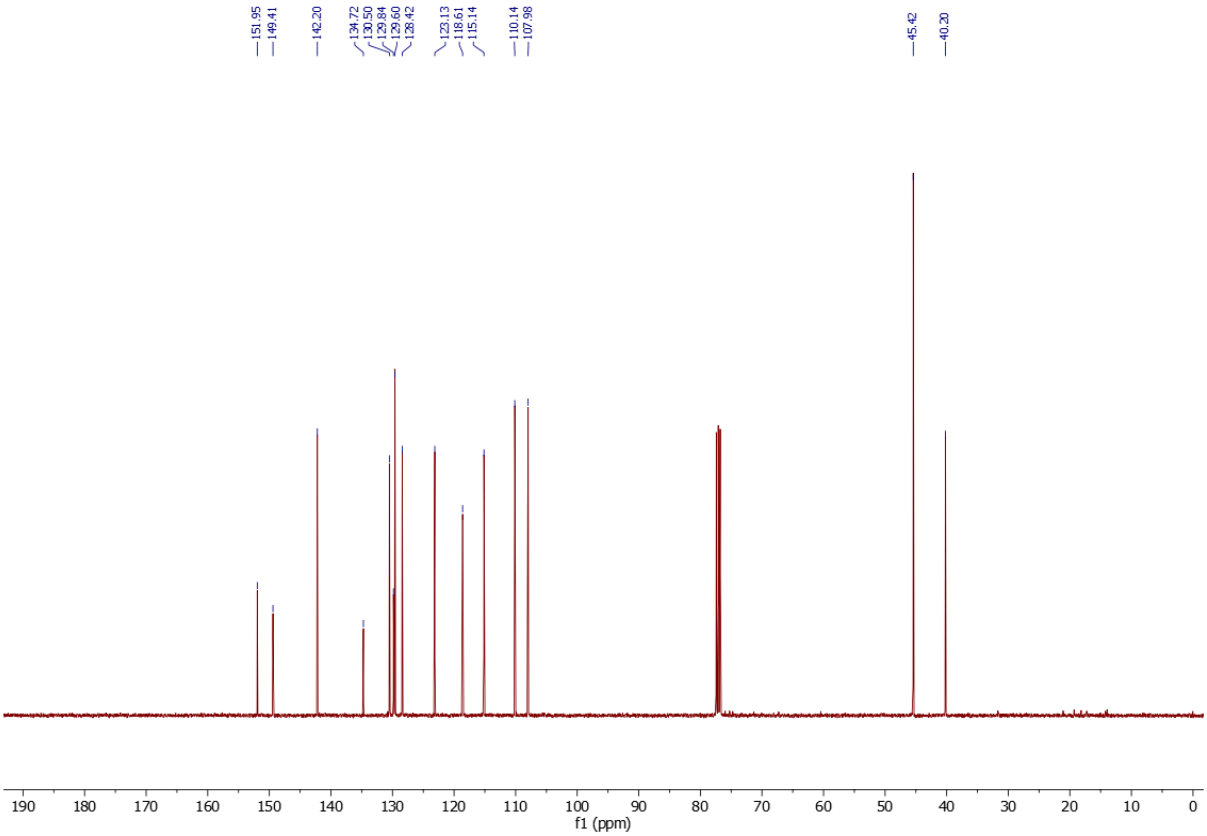

^{13}C NMR spectrum of **B1**.

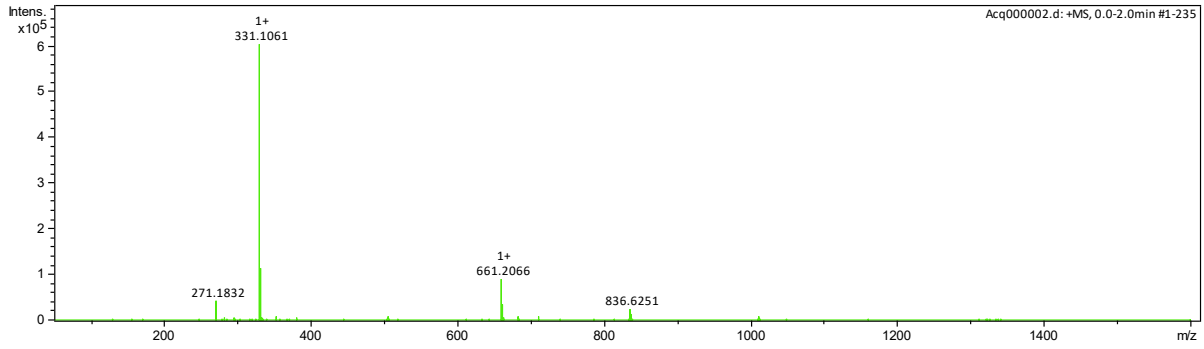

ESI-MS (*m/z*) of **B1**.

Dimethyl 1-(((5-(dimethylamino)naphthalene)-1-sulfonamido)methyl)-7-oxabicyclo[2.2.1]hepta-2,5-diene-2,3-dicarboxylate (**B2**)

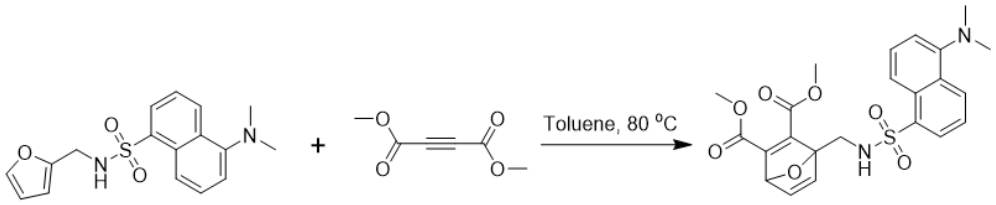

B1 **B2**

Dimethyl acetylenedicarboxylate (0.71 g, 5.0 mmol, 2.5 equiv.) and 5-(dimethylamino)-N-(furan-2-ylmethyl)naphthalene-1-sulfonamide (0.66 g, 2.0 mmol, 1.0 equiv.) are dissolved in 8 mL dry toluene. The solution was stirred at 70 °C for 48 h. After the solvent is removed *in vacuo*, the crude product was purified by column chromatography on silica gel (hexane:EtOAc = 2:1) to give compound **B2** (0.83 g, 88% yield) as a yellow oil. **^{1}H NMR (400 MHz, $CDCl_3$):** δ (ppm): 8.55 (d, 1H, J = 8.4 Hz), 8.28-8.23 (m, 2H), 7.59-7.51 (m, 2H), 7.19 (d, 1H, J = 7.6 Hz), 7.13 (dd, 1H, J = 5.2 Hz, 2.0 Hz), 6.89 (d, 1H, J = 5.2 Hz), 5.57 (d, 1H, J = 2.0 Hz), 5.25 (t, 1H, J = 6.0 Hz), 3.78 (s, 3H), 3.75-3.69 (m, 4H), 3.60 (dd, 1H, J = 14.0 Hz, 5.6 Hz), 2.89 (s, 6H). **^{13}C NMR (101 MHz, $CDCl_3$):** δ (ppm): 163.72, 162.72, 153.53, 152.02, 151.96, 144.88, 142.71, 134.32, 130.68, 129.92, 129.72, 129.60, 128.59, 123.19, 118.65, 115.31, 95.80, 83.96, 52.51, 52.42, 45.43, 41.93, 40.99. **ESI-MS (*m/z*)** for $C_{23}H_{24}N_2O_7S$ expected $[M+H]^+$: 473.1377, Found for $[M+H]^+$: 473.1349.

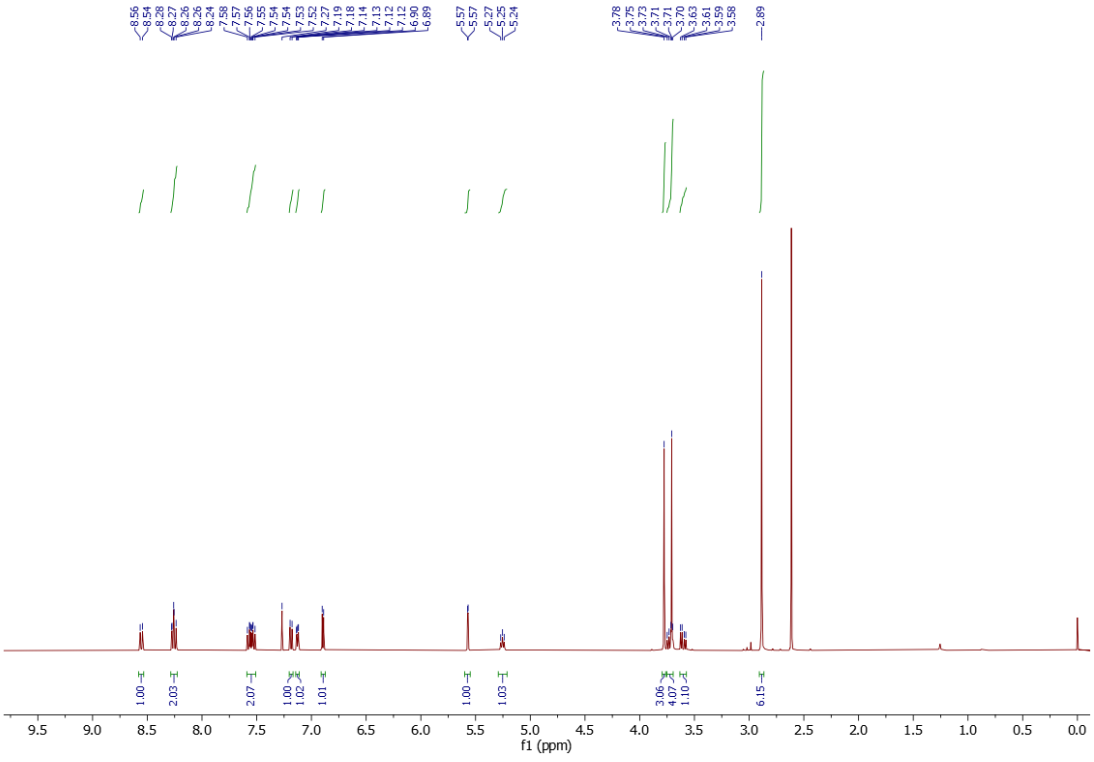

^{1}H NMR spectrum of **B2**.

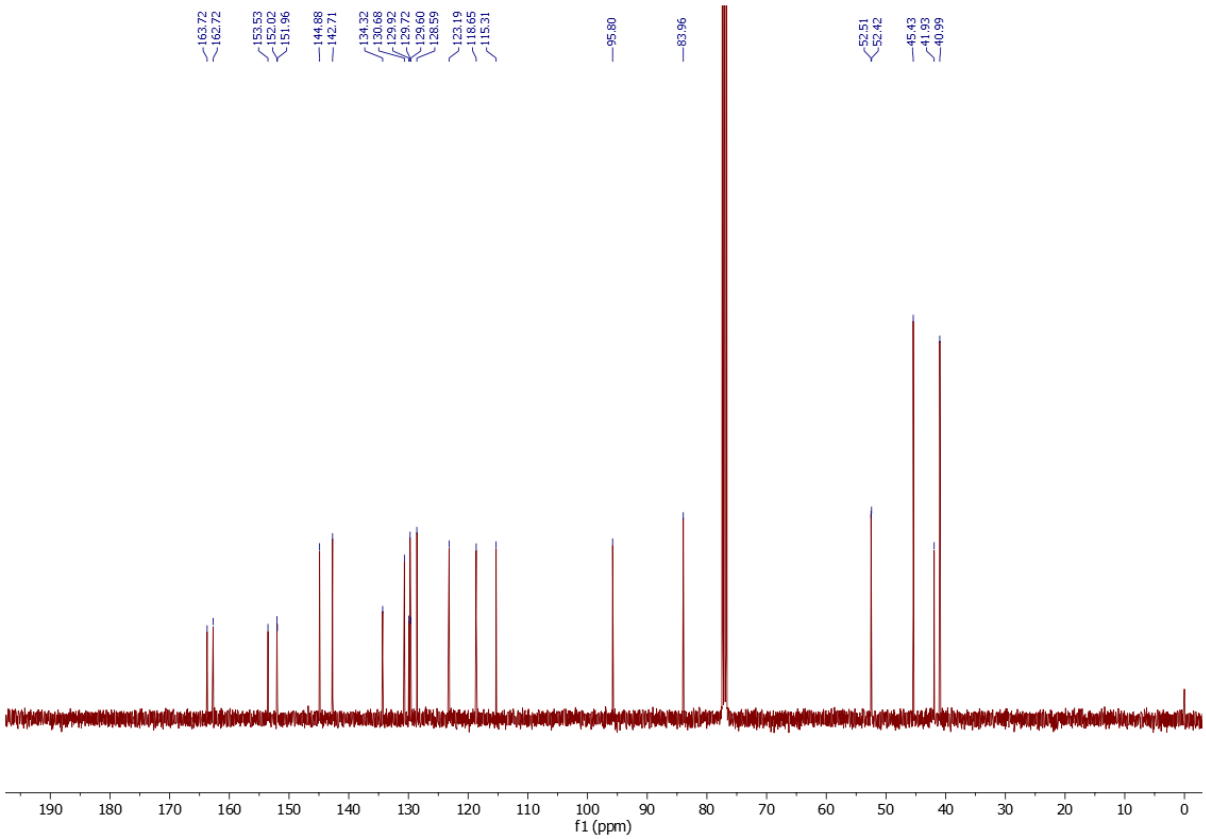

^{13}C NMR spectrum of **B2**.

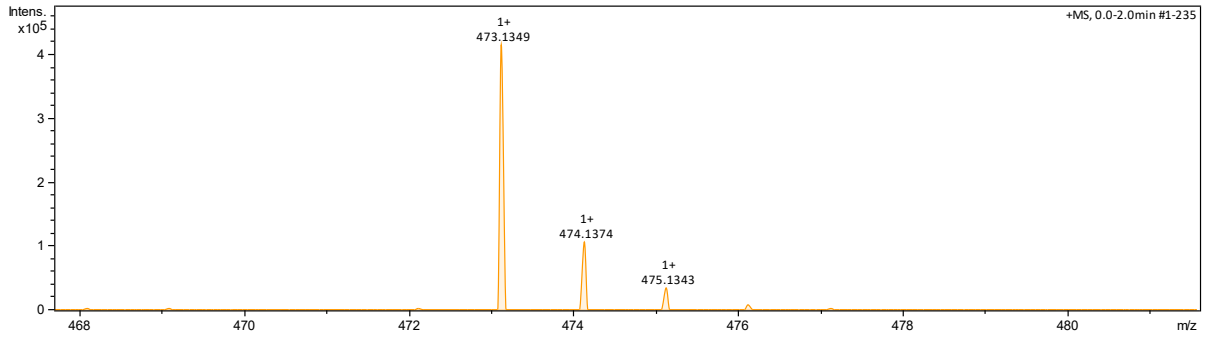

ESI-MS (*m/z*) of **B2**.

Ethyl 4-((2-(methacryloyloxy)ethyl)amino)-4-oxobut-2-ynoate (**C1**)

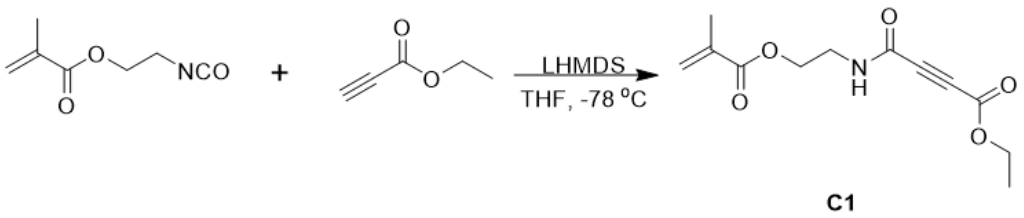

C1

C1 was synthesized following a reported procedure.[57] Ethyl propiolate (4.0 mL, 39.5 mmol, 1.0 equiv.) was dissolved in 60 mL of THF and cooled to -78 °C using a dry ice/acetone bath. LHMDS (1 M in THF, 40 mL, 40 mmol, 1.01 equiv.) was then added dropwise via a syringe pump over 30 minutes, and the reaction mixture was stirred for an additional 30 minutes at the same temperature. Subsequently, 2-isocyanatoethyl methacrylate (5.6 mL, 39.5 mmol, 1.0 equiv.) was introduced dropwise via a syringe pump. After stirring for another 30 minutes at -78 °C, the reaction was quenched with 80 mL of saturated aqueous NH_4Cl solution while maintaining the low temperature. Once the mixture gradually warmed to room temperature, 50 mL of water was added, and the organic and aqueous phases were separated. The aqueous layer was extracted with EtOAc (3 × 100 mL), and the combined organic extracts were sequentially washed with saturated aqueous $NaHCO_3$ and brine to remove impurities. Then, the organic layer was dried over $MgSO_4$, concentrated, and purified *via* a column chromatography (hexane:EtOAc = 10:1) to give compound **C1** (8.09 g, 81% yield) as a colourless oil. **^{1}H NMR (400 MHz, $CDCl_3$):** δ (ppm): 6.85 (t, J = 6.0 Hz, 1H), 6.10 (s, 1H), 5.61 – 5.56 (m, 1H), 4.28 – 4.20 (m, 4H), 3.61 (q, J = 5.6 Hz, 2H), 1.91 (s, 3H), 1.29 (t, J = 7.2 Hz, 3H). **^{13}C NMR (101 MHz, $CDCl_3$):** δ (ppm): 167.45, 152.34, 151.08, 135.77, 126.55, 76.93, 74.26, 63.03, 62.83, 39.28, 18.30, 13.94. **ESI-MS (*m/z*)** for $C_{12}H_{15}NO_5$ expected $[M+H]^+$: 254.1023, Found for $[M+H]^+$: 254.1030.

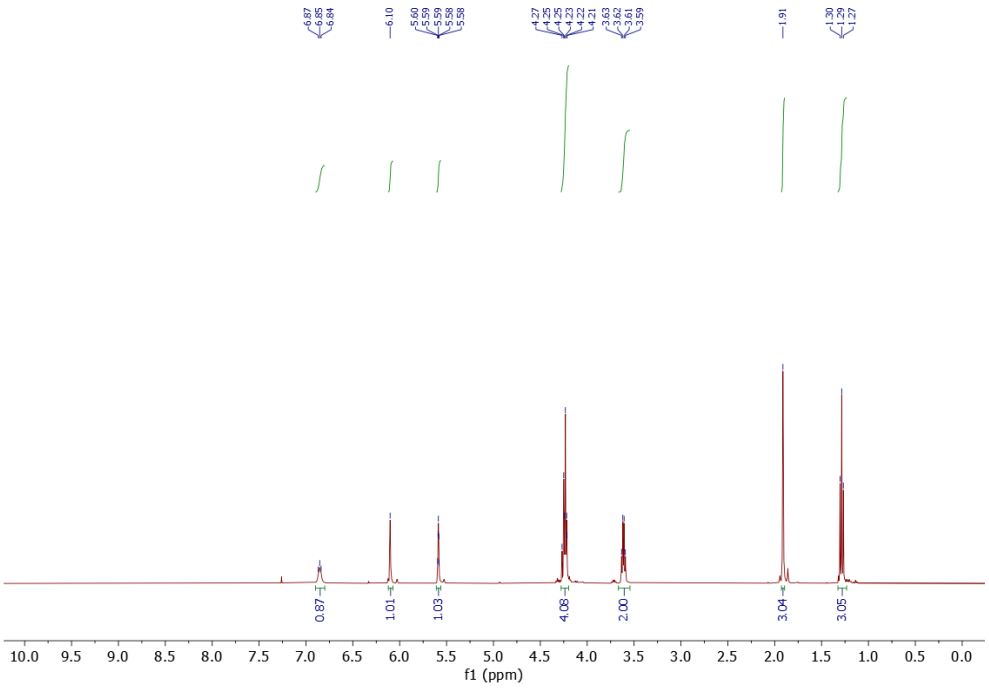

^{1}H NMR spectrum of **C1**.

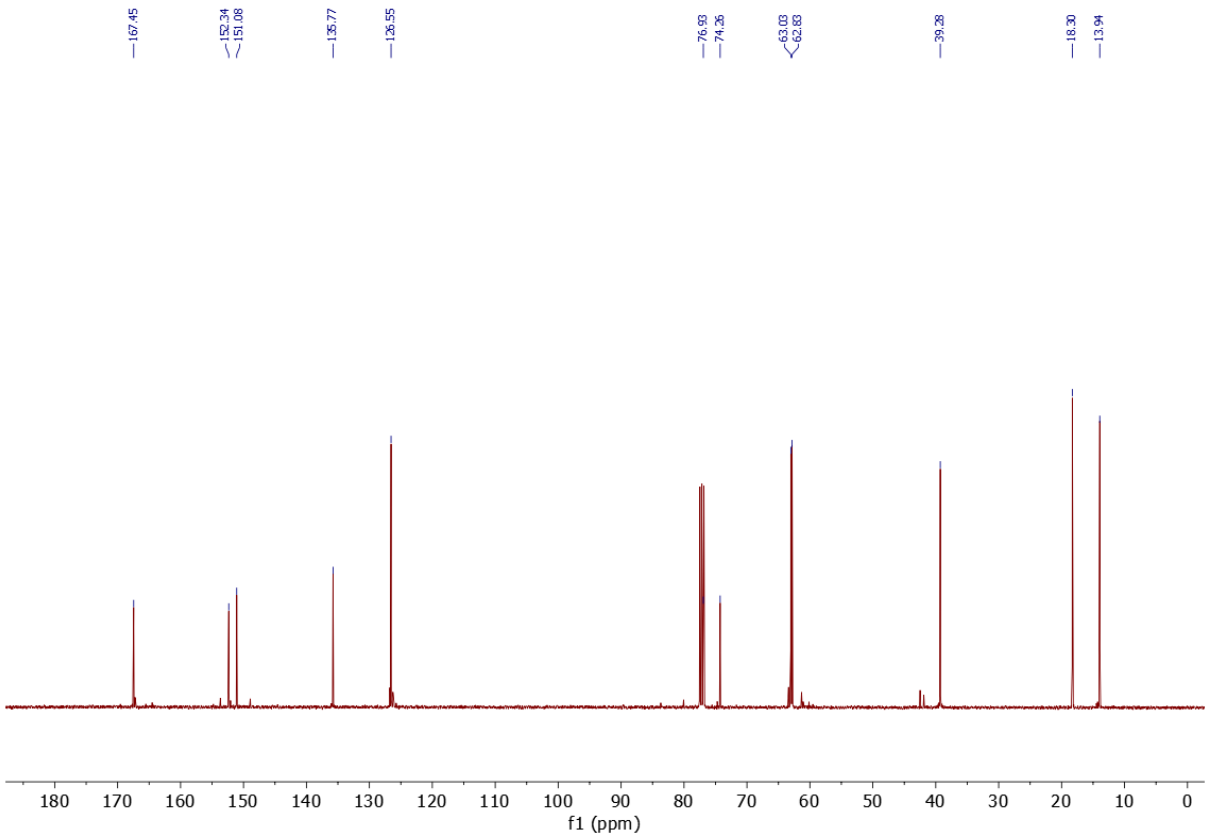

^{13}C NMR spectrum of **C1**.

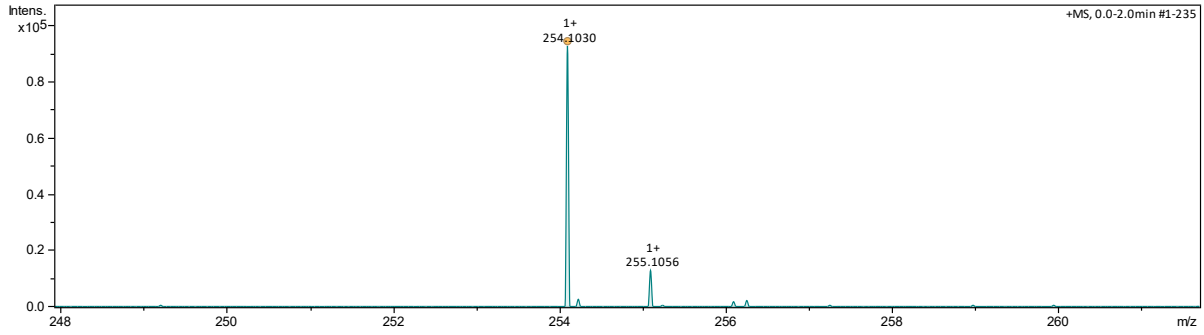

ESI-MS (*m/z*) of **C1**.

Ethyl 1-(hydroxymethyl)-3-((2-(methacryloyloxy)ethyl)carbamoyl)-7-oxabicyclo[2.2.1]hepta-2,5-diene-2-carboxylate (**C2**)

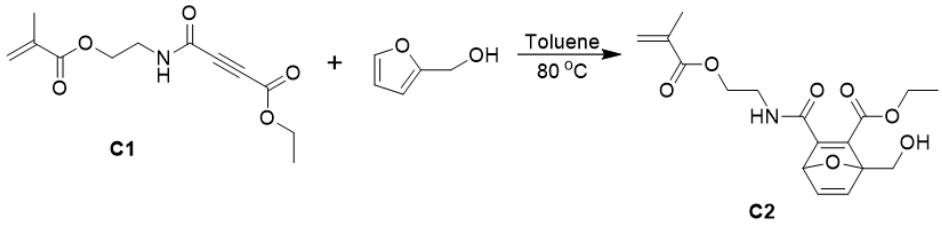

C1 (0.57 g, 2.26 mmol, 1.0 equiv.) and furan-2-ylmethanol (0.46 g, 4.7 mmol, 2.08 equiv.) are dissolved in 2.5 mL dry toluene. The solution was stirred at 80 ℃ for 48 h. After the solvent is removed *in vacuo*, the crude product was purified by column chromatography on silica gel (hexane:EtOAc = 2:1) to give compound **C2** (0.397 g, 50% yield) as a colorless oil. **^{1}H NMR (400 MHz, $CDCl_3$):** δ (ppm): 9.37 (t, J = 5.6 Hz, 1H), 7.23 (d, J = 5.2 Hz, 1H), 7.15 (dd, J = 5.2, 1.6 Hz, 1H), 6.17 (s, 1H), 5.64 (d, J = 1.6 Hz, 1H), 5.60 – 5.55 (m, 1H), 4.33 – 4.11 (m, 6H), 3.64 (q, J = 5.6 Hz, 2H), 1.94 (s, 3H), 1.33 (t, J = 7.2 Hz, 3H). **^{13}C NMR (101 MHz, $CDCl_3$):** δ (ppm): 167.25, 164.50, 163.15, 161.16, 150.32, 143.70, 143.39, 136.09, 126.12, 98.62, 83.75, 63.05, 62.36, 60.54, 38.82, 18.33, 14.14. **ESI-MS** (*m/z*) for $C_{17}H_{21}NO_7$ expected $[M+H]^+$: 352.1391, Found for $[M+H]^+$: 352.1363.

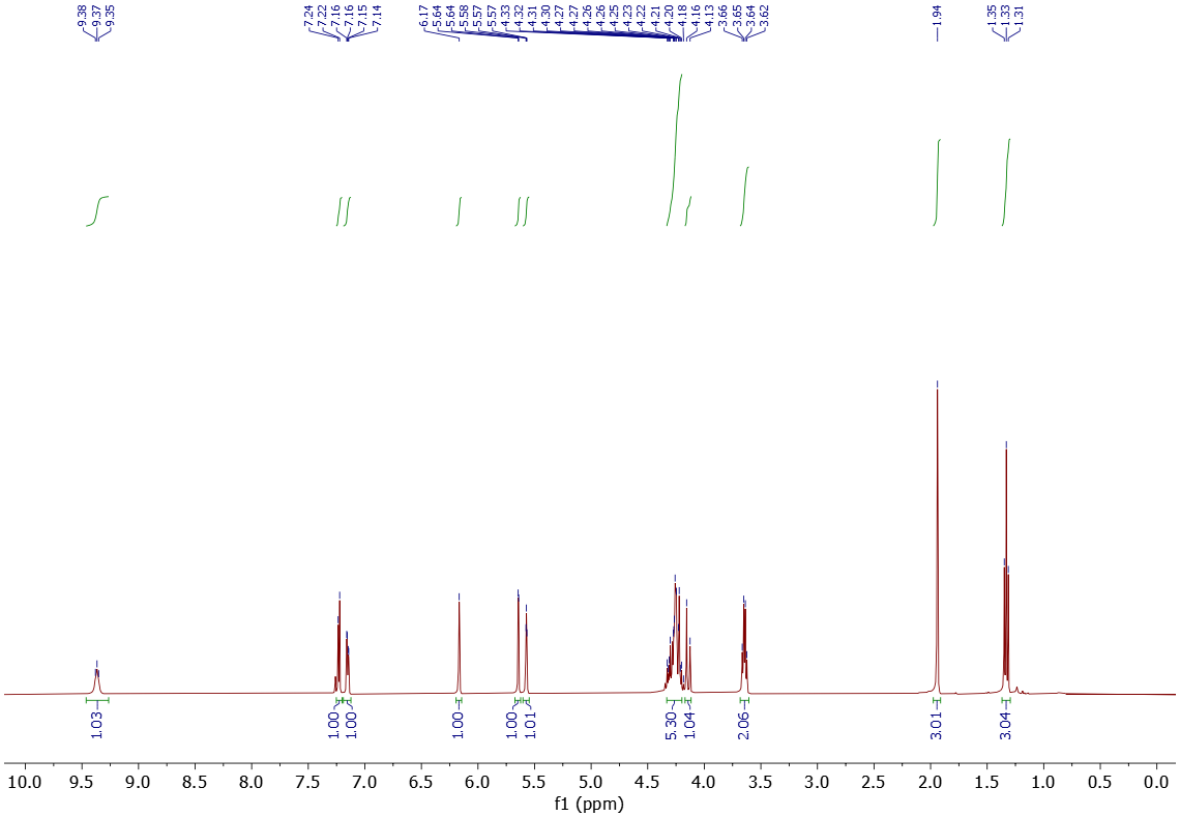

^{1}H NMR spectrum of **C2**.

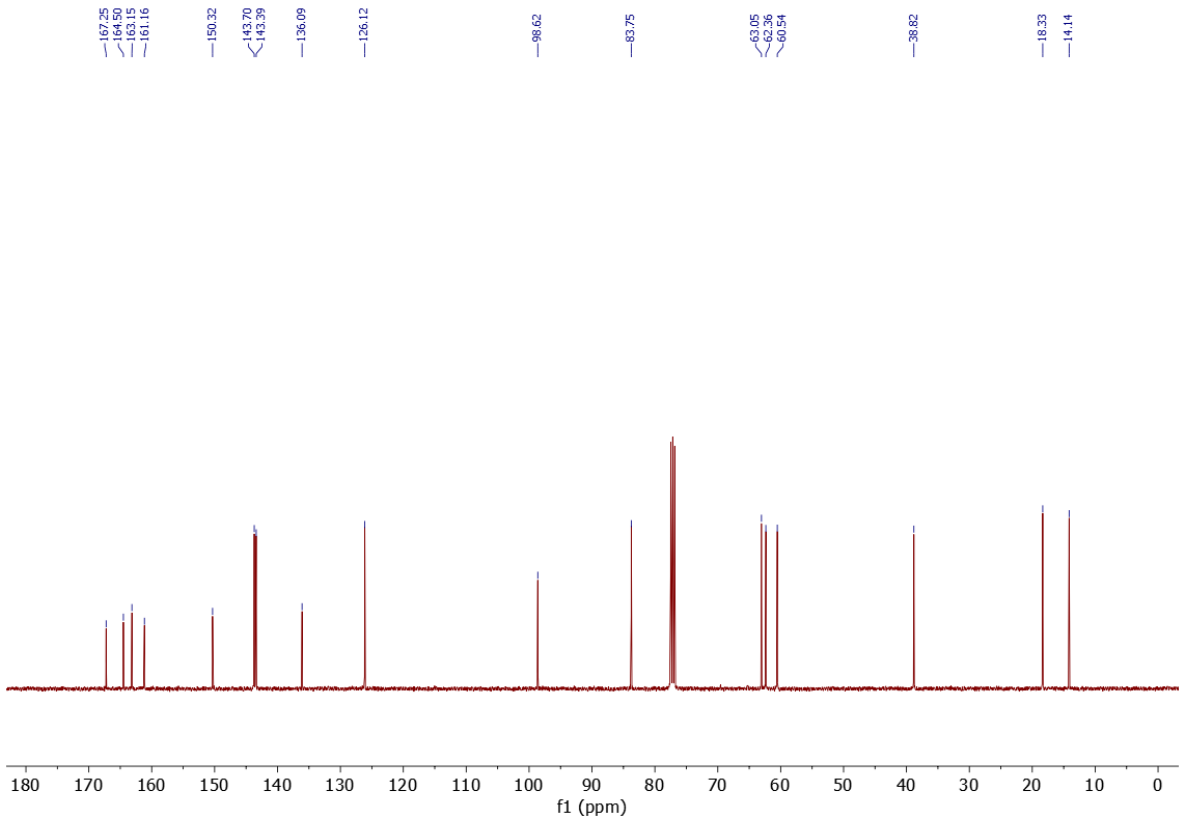

^{13}C NMR spectrum of **C2**.

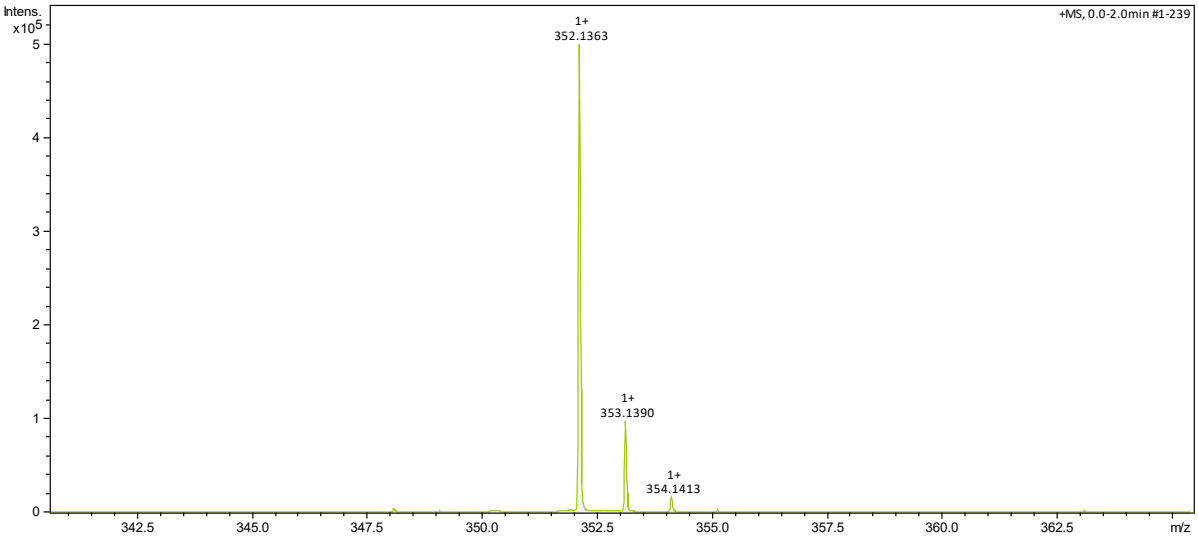

ESI-MS (*m/z*) of **C2**.

Ethyl 1-(((((2S,3R,4S)-3-hydroxy-2-methyl-6-(((1S,3S)-3,5,12-trihydroxy-3-(2-hydroxyacetyl)-10-methoxy-6,11-dioxo-1,2,3,4,6,11-hexahydrotetracen-1-yl)oxy)tetrahydro-2H-pyran-4-yl)carbamoyl)oxy)methyl)-3-((2(methacryloyloxy)ethyl)carbamoyl)-7-oxabicyclo[2.2.1]hepta-2,5-diene-2-carboxylate (**C3**)

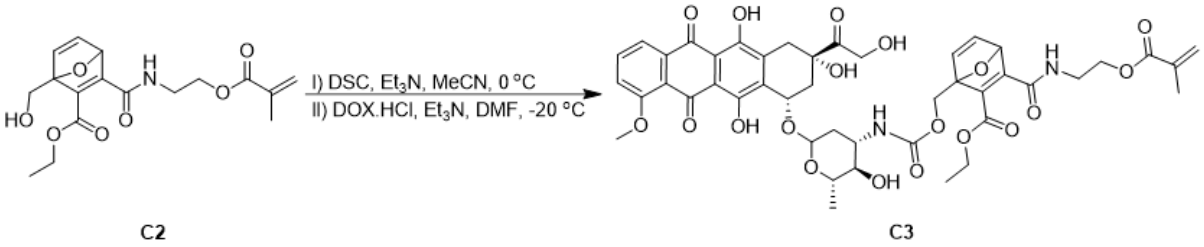

C2 C3

The synthesis followed a modified literature protocol.[55] *N,N′* -Disuccinimidyl carbonate (132 mg, 517 μmol, 1.0 equiv.) and Et_3N (90 μL, 690 μmol, 1.3 equiv.) were dissolved in 2 mL of MeCN in a round-bottom flask. The reaction mixture was cooled to 0 °C before adding a solution of **C2** (121 mg, 345 μmol, 0.67 equiv.) in 1 mL of MeCN. The reaction was stirred in an ice bath for 1 hour, after which the solvent was evaporated under reduced pressure, and the crude product was used without further purification. The obtained material was dissolved in CH_2Cl_2 and added dropwise into a precooled (-20 °C) solution of doxorubicin hydrochloride (70 mg, 120 μmol, 0.23 equiv.) and Et_3N (92.5 μL, 709 μmol, 1.0 equiv.) in 2 mL of DMF. The reaction was maintained at -20 °C for 1 hour, then gradually warmed to room temperature over 3 hours. The solvent was subsequently removed under reduced pressure, and the residue was redissolved in CH_2Cl_2 and washed three times with DI water. The organic phase was separated, dried, and concentrated to obtain the crude product. The mixture was then purified by silica column chromatography (MeOH : CH_2Cl_2 = 1:20) to give **C3** as a red powder (55 mg, 59.7 μmol, 50% yield). **^{1}H NMR (400 MHz, $CDCl_3$):** δ (ppm): 13.96 (s, 1H), 13.23 (s, 1H), 8.87-8.80 (m, 1H), 8.06-7.99 (m, 1H), 7.78 (td, *J* = 8.0, 2.8 Hz, 1H), 7.39 (d, *J* = 8.4 Hz, 1H), 7.28 (dd, *J* = 5.2, 2.0 Hz, 1H), 6.90 (dd, *J* = 14.0, 5.2 Hz, 1H), 6.18 (d, *J* = 4.0 Hz, 1H), 5.75-5.72 (m, 1H), 5.59-5.56 (m, 1H), 5.49 (d, *J* = 3.6 Hz, 1H), 5.30-5.22 (m, 2H), 4.92-4.82 (m, 1H), 4.75 (s, 2H), 4.72-4.65 (dd, *J* = 12.4, 2.4 Hz, 1H), 4.44-4.16 (m, 7H), 4.07 (d, *J* = 3.2 Hz, 3H), 3.87-3.78 (m, 1H), 3.68-3.57 (m, 4H), 3.26 (d, *J* = 18.8 Hz, 1H), 3.00 (d, *J* = 18.8 Hz, 1H), 2.33 (d, *J* = 14.8 Hz, 1H), 2.17 (dd, *J* = 14.8, 4.0 Hz, 1H), 1.98-1.90 (m, 5H), 1.37-1.28 (m, 6H). **^{13}C NMR (101 MHz, $CDCl_3$):** δ (ppm): 213.94, 187.21, 186.77, 167.28, 164.71, 162.14, 161.99, 161.16, 156.33, 155.76, 155.05, 146.30, 145.70, 141.27, 136.11, 135.96, 135.58, 133.79, 133.68, 126.19, 120.92, 119.99, 118.58, 111.67, 111.51, 100.69, 95.76, 84.92, 69.64, 69.40, 67.38, 65.67, 63.27, 62.50, 62.30, 56.81, 47.23, 38.66, 35.74, 34.13, 30.17, 18.39, 16.97, 14.07. **ESI-MS (*m/z*)** for $C_{45}H_{48}N_2O_{19}$ expected $[M+Na]^+$: 943.2743, Found for $[M+Na]^+$: 943.2670.

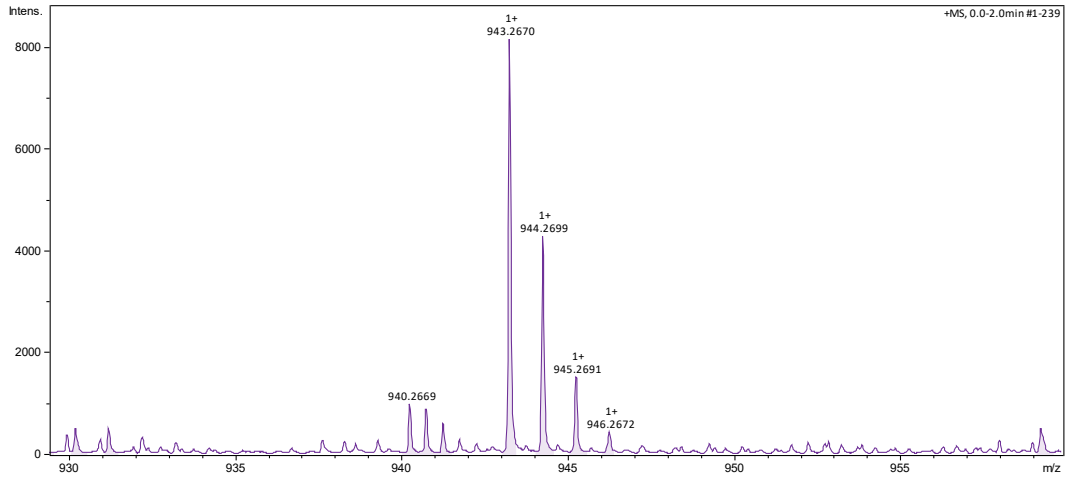

ESI-MS (*m/z*) of **C3**.

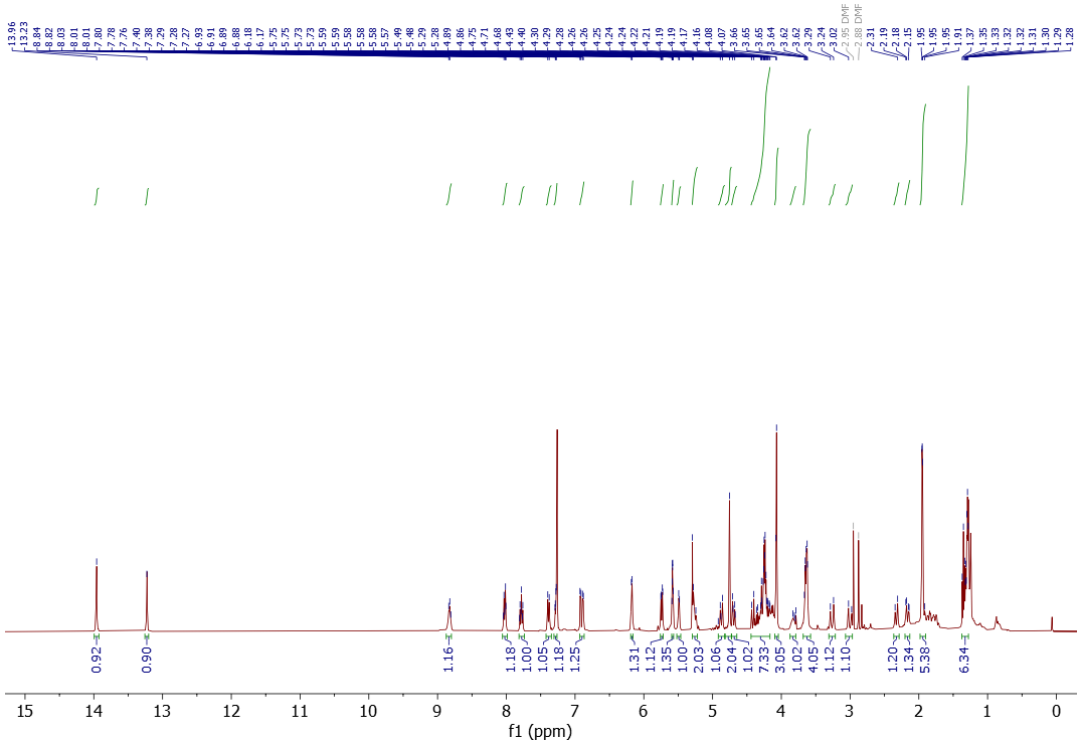

^{1}H NMR spectrum of **C3**.

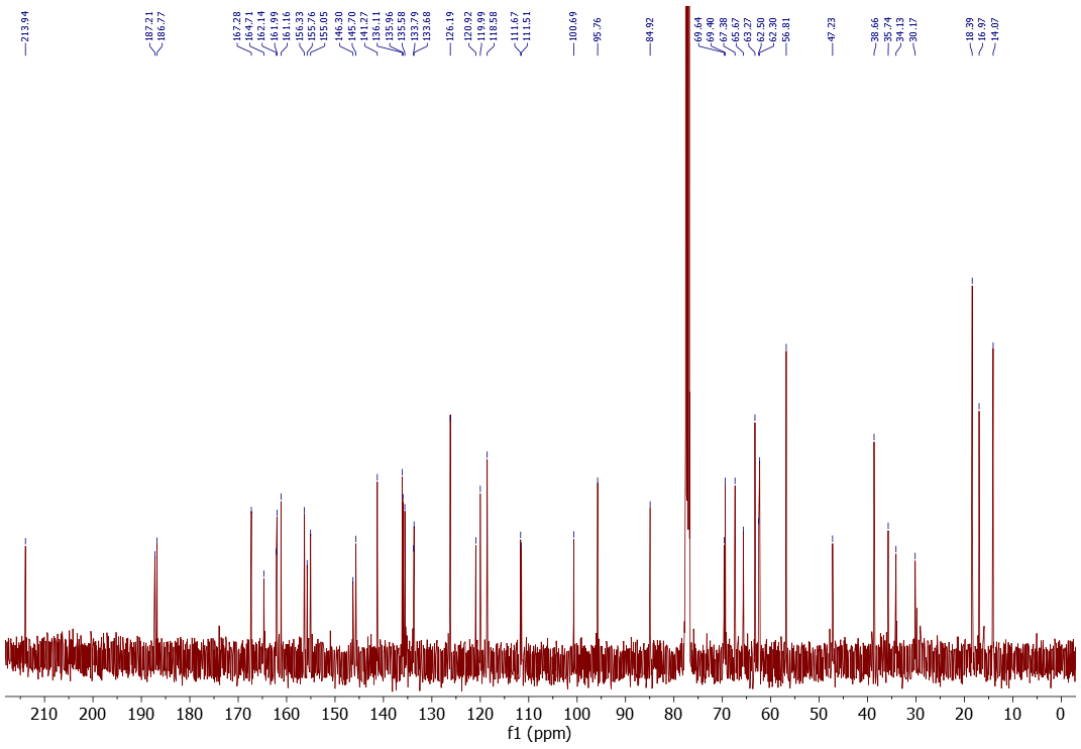

^{13}C NMR spectrum of **C3**.

Furan-2-ylmethyl ((2S,3R,4S,6R)-3-hydroxy-2-methyl-6-(((1S,3S)-3,5,12-trihydroxy-3-(2-hydroxyacetyl)-10-methoxy-6,11-dioxo-1,2,3,4,6,11-hexahydrotetracen-1-yl)oxy)tetrahydro-2H-pyran-4-yl)carbamate (**D1**)

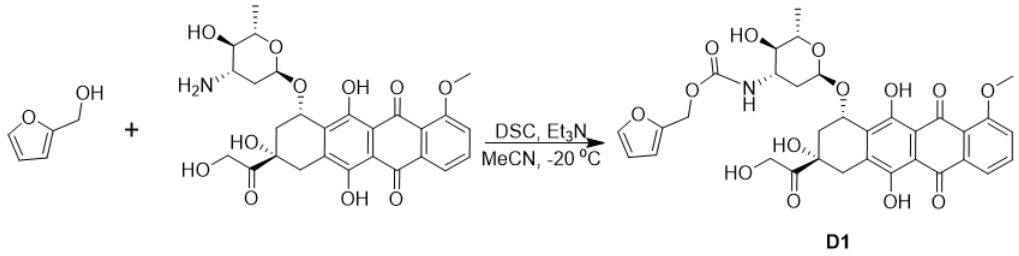

D1

The synthesis was carried out following a modified literature procedure.[55] *N,N′* -Disuccinimidyl carbonate (132 mg, 517 µmol, 3.0 equiv.) and Et_3N (90 µL, 690 µmol, 4.0 equiv.) were dissolved in 1 mL of MeCN in a round-bottom flask and cooled to 0 °C. A solution of 2-(hydroxymethyl)furan (51 mg, 520 µmol, 3.02 equiv.) in 1 mL of MeCN was then added dropwise. The reaction mixture was stirred in an ice bath for 1 hour, after which the solvent was evaporated under reduced pressure, and the crude product was used without further purification. The resulting material was dissolved in 1.5 mL of CH_2Cl_2 and added dropwise into a precooled (-20 °C) solution of doxorubicin hydrochloride (100 mg, 172 µmol, 1.0 equiv.) and Et_3N (96 µL, 689 µmol, 4.0 equiv.) in 2 mL of DMF. The reaction was maintained at -20 °C for 1 hour before being gradually warmed to room temperature over 3 hours. The solvent was then removed under reduced pressure, and the residue was redissolved in CH_2Cl_2 and washed three times with water. The organic phase was separated, dried, and concentrated to obtain the crude product. The mixture was then purified by silica column chromatography (MeOH : CH_2Cl_2 = 1:30) to give **D1** as

a red powder (75 mg, 65% yield). **^{1}H NMR (400 MHz, $CDCl_3$):** δ (ppm): 13.89 (s, 1H), 13.13 (s, 1H), 7.99 – 7.95 (m, 1H), 7.74 (t, J = 8.0 Hz, 1H), 7.4-7.3 (m, 2H), 6.36 – 6.23 (m, 2H), 5.47 (d, J = 3.2 Hz, 1H), 5.35 – 5.28 (m, 1H), 5.21 (s, 1H), 4.95 (s, 2H), 4.74 (s, 2H), 4.12 (q, J = 6.4 Hz, 1H), 4.04 (s, 3H), 3.84 (s, 1H), 3.64 (s, 1H), 3.20 (d, J = 18.8, 1H), 2.87 (d, J = 18.8, 1H), 2.30 (d, J = 14.8 Hz, 1H), 2.13 (dd, J = 14.8, 4.0 Hz, 1H), 1.86-1.72 (m, 2H), 1.27 (d, J = 6.4 Hz, 3H). **^{13}C NMR (101 MHz, $CDCl_3$):** δ (ppm): 214.00, 186.98, 186.59, 161.07, 156.27, 155.61, 155.38, 149.91, 143.26, 135.85, 135.44, 133.71, 133.68, 120.78, 119.89, 118.56, 111.56, 111.39, 110.61, 110.51, 100.83, 76.68, 69.69, 69.56, 67.45, 65.64, 58.60, 56.72, 47.15, 35.69, 33.98, 30.17, 16.93.

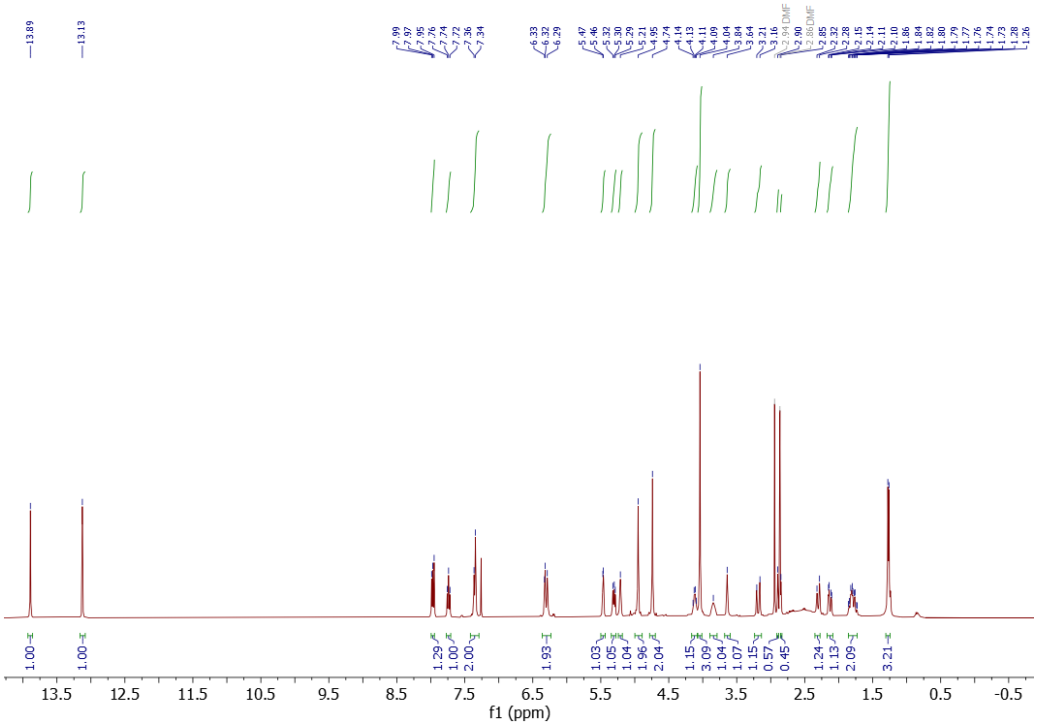

^{1}H NMR spectrum of **D1**.

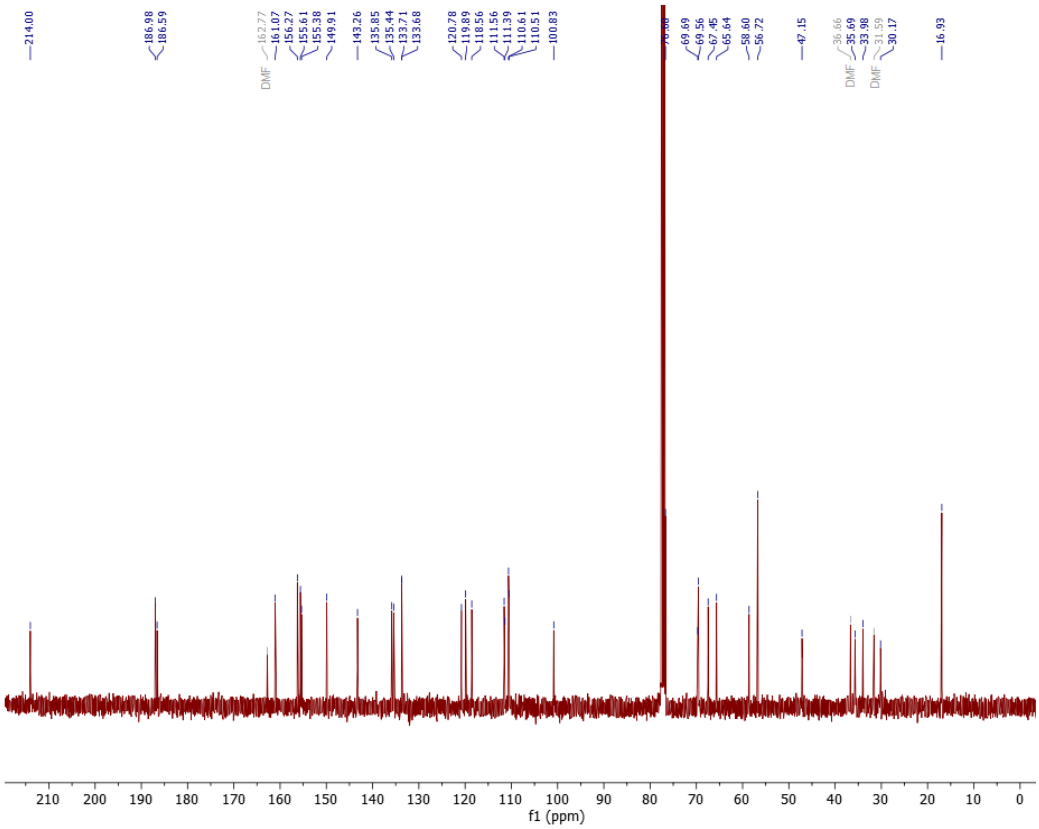

^{13}C NMR spectrum of **D1**.

Synthesis of Linear Polymers (LPs)

Disulfide mechanophore contained linear polymer (LPs) were prepared according reported literature.[1] LPs was synthesized as follows. PEGMEMA (4.0 g, 13.3 mmol, 121 equiv.), bis [2 (2' bromoisobutyryloxy)ethyl] disulfide (50 mg, 0.11 mmol, 1.0 equiv.), Me_6TREN (0.55 mg, 2.4 μmol) and $CuBr_2$ (0.29 mg, 1.3 μmol) were dissolved in DMSO (3 mL) in a Schlenk flask and sealed with a rubber septum reinforced with a cable tie. The solution underwent three consecutive freeze-pump-thaw cycles to remove dissolved gas. Simultaneously, a 6 cm copper wire was activated by immersion in 37% HCl for 30 minutes, followed by thorough washing with water and acetone before being dried. The activated copper wire was then introduced into the reaction mixture, initiating polymerization at room temperature for 6 hours, yielding a polymer with an approximate molecular weight of 47 kDa. To terminate the reaction, the viscous solution was diluted with THF and passed through a column of basic Al_2O_3. After solvent removal under reduced pressure, the polymer solution was slowly added dropwise into ice-cold Et_2O under continuous stirring, leading to precipitation. The supernatant was decanted, and the polymer was redissolved in THF before undergoing a second precipitation in fresh Et_2O to enhance purity. Disulfide centered linear polymers with molar masses of 47 kDa was obtained after repeating the precipitation process for three times.

Synthesis of Network Core-Structured Star Polymers (NCSPs).[58-59]

(1) Synthesis of NCSPs-core: The Network core-structured star polymers core was synthesized as follows. PEGMEMA (850 mg, 2.83 mmol, 14.1 equiv.), **A1** (58 mg, 0.2 mmol, 1.0 equiv.) were dissolved in 1,4-dioxane (3 mL) with CPA RAFT agent (29 mg, 0.1 mmol) and AIBN (4.3 mg, 0.026 mmol) in a reaction flask and sealed with a rubber septum reinforced with a cable tie. The solution was degassed by 3 consecutive freeze-pump-thaw cycles and then stirred at 70 °C for 24 h. After 24 h of the polymerization reaction, the solution was directly placed at -20 °C for approximately 20 min and then exposed to air for termination of the polymerization. Subsequently, 5 mL of THF was introduced into the mixture. Following solvent removal under reduced pressure, the concentrated mixture was slowly added dropwise to stirred, ice-cold Et_2O, inducing precipitation. The supernatant was decanted, and the resulting viscous polymer was redissolved in THF before undergoing a second precipitation in fresh Et_2O. This purification process was repeated three times to enhance polymer purity. Finally, any unreacted monomer and residual impurities were eliminated through dialysis for 48 hours.

(2) Synthesis of NCSPs: Network core-structured star polymers were synthesized by chain extension of a NCSPs -core with PEGMEMA. Briefly, NCSPs cores (50 mg) were dissolved in 1,4-dioxane (1 mL) with PEGMEMA (645 mg, 2.15 mmol, 10.7 equiv.) and AIBN (1.7 mg, 0.01 mmol) in a reaction flask and sealed with a rubber septum reinforced with a cable tie. The solution was degassed by 3 consecutive freeze-pump-thaw cycles and then stirred at 70 °C for 6 h, then 600 mg NCSPs was obtained.

(3) The structure of NCSPs: The structure of NCSPs was defined by GPC and ^{1}H NMR, the arms number and monomers number of an arm were calculated. First, the ratio of CPA and PEGMEMA in the core structure was calculated by ^{1}H-NMR with the following equation:[43]

$$\boldsymbol{R} = \frac{I^{4.0\ \mathrm{ppm}}}{2 \cdot I^{7.5\ \mathrm{ppm}}}$$

where $\mathbf{I}^{7.5\ ppm}$ corresponded to signal intensities at 7.5 ppm attributed to RAFT agent CPA (see **Figure S9a**) and where $\mathbf{I}^{4.0\ ppm}$ corresponded to signal intensities at 4.0 ppm attributed to **A1** (crosslinker) and PEGMEMA. Due to **A1** (290 Da) and PEGMEMA (M_n = 300 Da) having comparable molar mass, here we merge the two molecules and treat them as one molecule as PEGMEMA.

Then, we obtain the ratio (**R**) of PEGMEMA (300 Da) and CPA (279 Da) is 28:2 (14:1) (see **Figure S9b**). In addition, the GPC result show that the molar mass (M_n) of the core structure of star polymers is around 31000 Da (see **Figure 10**).

After our calculation:

M_{core} = 31000 Da $\approx$ (300·14+279·1)·**7**

Therefore, we extracted that the core structure contained ~7 CPA molecules, which means the core structure on average had 7 arms. In the next step of star polymers synthesis, PEGMEMA monomers are continuously inserted at the RAFT end to achieve chain elongation (see **Figure S11**).

Then, the average molar mass of an arm was calculated:

$M_{arm} = (M_{total} - M_{core})/7 = (108500–31000)/7 = 11071$ Da

Next, the average arm length (degree of polymerization) of an arm was calculated:

$X_n = M_{arm}/M_{monomer} = 11071/300 \approx 37$.

Then, we know that one arm contained 37 PEGMEMA monomers.

In addition, the "spanning molar mass" M_{span} of star polymers and linear polymers were calculated, defined as:[45]

For NCSPs: $M_{span} = 2M_{arm} + M_{core}$

where M_{core} is the molar mass of the core structure. We calculated the $M_{span} \approx 54$ kDa.

For linear polymers (LPs) with the molar mass of 47 kDa, $M_{span} = M = 47$ kDa.

Synthesis of Mechanophore-free Network Core-Structured Star Polymers (FNCSPs)

(1) Synthesis of FNCSPs-core: PEGMEMA (850 mg, 2.83 mmol, 14.1 equiv.), 1,6-hexanediol dimethacrylate (51 mg, 0.2 mmol, 1.0 equiv.) were dissolved in 1,4-dioxane (3 mL) with CPA RAFT agent (29 mg, 0.1 mmol) and AIBN (4.3 mg, 0.026 mmol) in a reaction flask and sealed with a rubber septum reinforced with a cable tie. The solution was degassed by 3 consecutive freeze-pump-thaw cycles and then stirred at 70 °C for 24 h. After 24 h of the polymerization reaction, the solution was directly placed at -20 °C for approximately 20 min and then exposed to air for termination of the polymerization. Subsequently, 5 mL of THF was introduced into the mixture. Following solvent removal under reduced pressure, the concentrated mixture was slowly added dropwise to stirred, ice-cold Et_2O, inducing precipitation. The supernatant was decanted, and the resulting viscous polymer was redissolved in THF before undergoing a second precipitation in fresh Et_2O. This purification process was repeated three times to enhance polymer purity. Finally, any unreacted monomer and residual impurities were eliminated through dialysis for 48 hours.

(2) Synthesis of FNCSPs: Non-mechanophore contained network core-structured star polymers were synthesized by chain extension of a FNCSP-core with PEGMEMA. Briefly, FNCSP-core (50 mg) was dissolved in 1,4-dioxane (1 mL) with PEGMEMA (645 mg, 2.15 mmol, 10.7 equiv.) and AIBN (1.7 mg, 0.01 mmol) in a reaction flask and sealed with a rubber septum reinforced with a cable tie. The solution was degassed by 3 consecutive freeze-pump-thaw cycles and then stirred at 70 °C for 6 h, then FNCSPs was obtained.

Synthesis of Drug-Containing Network Core-Structured Star Polymers (NCSPs)

(1) Synthesis of NCSP-core: The NCSP-core copolymer was synthesized as follows. PEGMEMA (850 mg, 2.83 mmol, 70.7 equiv.), **C3** (46 mg, 0.04 mmol, 1.0 equiv.) were dissolved in 1,4-dioxane (3 mL) with CPA RAFT agent (29 mg, 0.1 mmol), **A1** (58 mg, 0.2 mmol, 5.0 equiv.) and AIBN (4.3 mg, 0.026 mmol) in a reaction flask and sealed with a rubber septum reinforced with a cable tie. The solution was degassed by 3 consecutive freeze-pump-thaw cycles and then stirred at 70 °C for 24 h. After 24 h of the polymerization reaction, the solution was directly placed at -20 °C for approximately 20 min and then exposed to air for termination of the polymerization. Subsequently, 5 mL of THF was introduced into the mixture. Following solvent removal under reduced pressure, the concentrated mixture was slowly added dropwise to stirred, ice-cold Et_2O, inducing precipitation. The supernatant was decanted, and the resulting viscous polymer was redissolved in THF before undergoing a second precipitation in fresh Et_2O. This purification process was repeated three times to enhance polymer purity. Finally, any unreacted monomer and residual impurities were eliminated through dialysis for 48 hours.

(2) Synthesis of NCSP-Dox: Drug contained network core-structured star polymers were synthesized by chain extension of a core copolymer with PEGMEMA. Briefly, NCSP-core (50 mg) was dissolved in 1,4-dioxane (1 mL) with PEGMEMA (645 mg, 2.15 mmol, 53.7 equiv.) and AIBN (1.7 mg, 0.01 mmol) in a reaction flask and sealed with a rubber septum reinforced with a cable tie. The solution was degassed by 3 consecutive freeze-pump-thaw cycles and then stirred at 70 °C for 6 h.

3.6 Supporting figures and tables

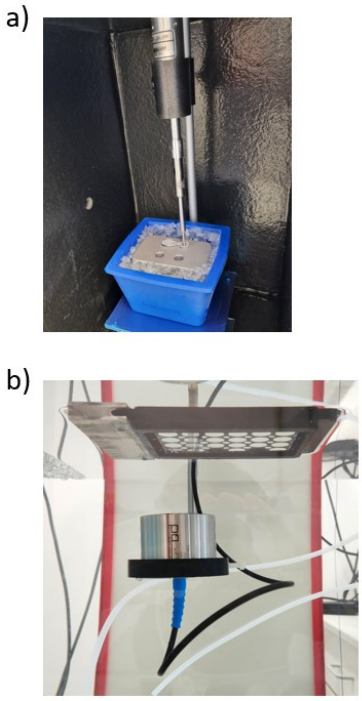

Figure S1. Sonication system. **a**) 20 kHz sonicator. **b**) 1.5 MHz HIFU transducer.

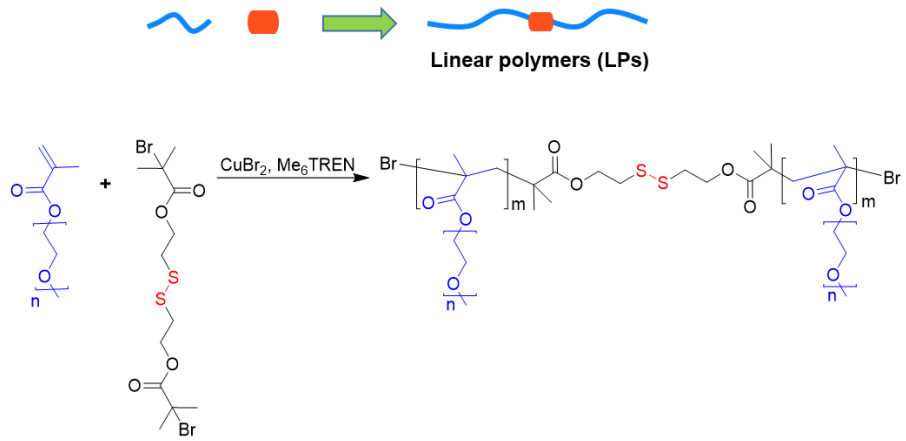

Scheme S2: Synthesis of LPs.

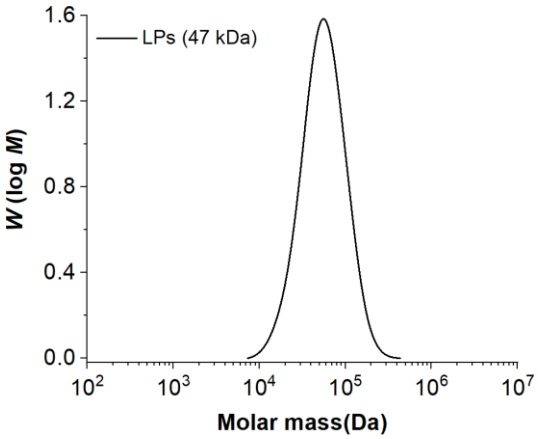

Figure S2. GPC RI molar mass distributions of LPs.

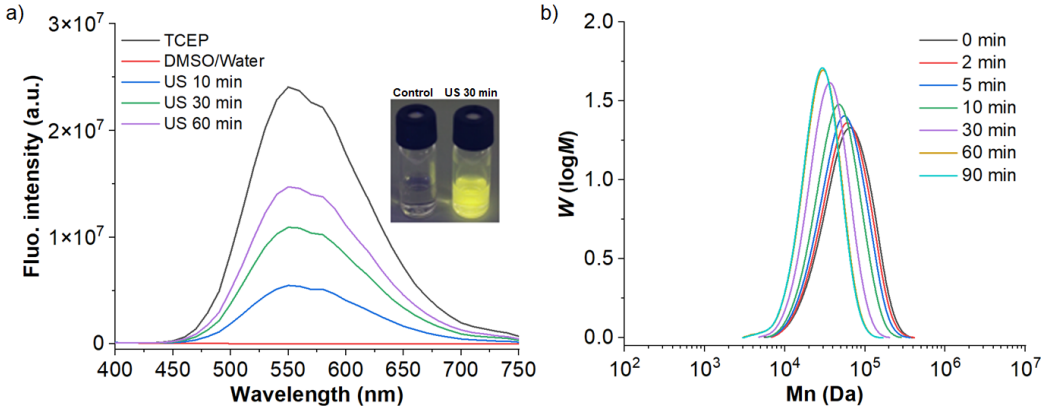

Figure S3. a) Fluorescence spectra of the mixture of LPs and OND sensor, before and after 20 kHz (I = 12.4 W cm^{-2}) sonication (solvent: DMSO/H_2O). Inset: photograph of the solutions under UV-light (λ_{exc} = 365 nm). **b**) M_n of LPs with different sonication time (20 kHz, I = 12.4 W cm^{-2}).

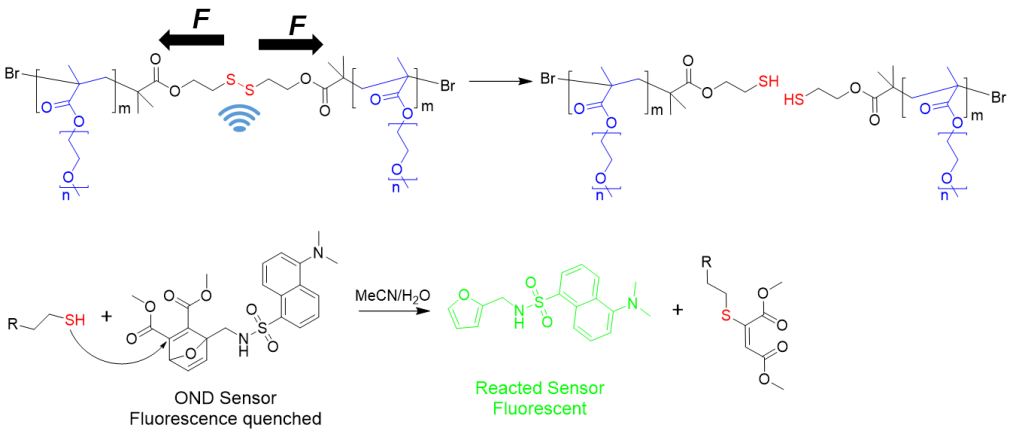

Figure S4. Disulfide mechanophore activation and the mechanism of thiols react with OND sensor.

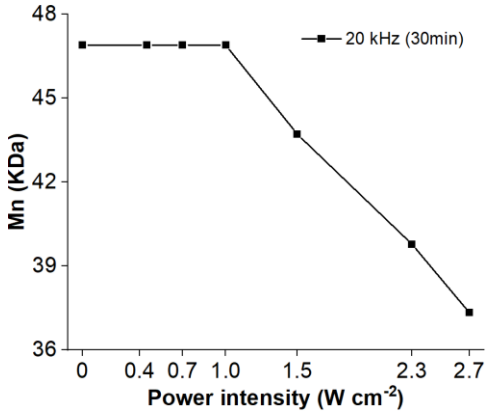

Figure S5. The M_n changes of LPs with the US I from 0 W cm^{-2} to 2.7 W cm^{-2}.

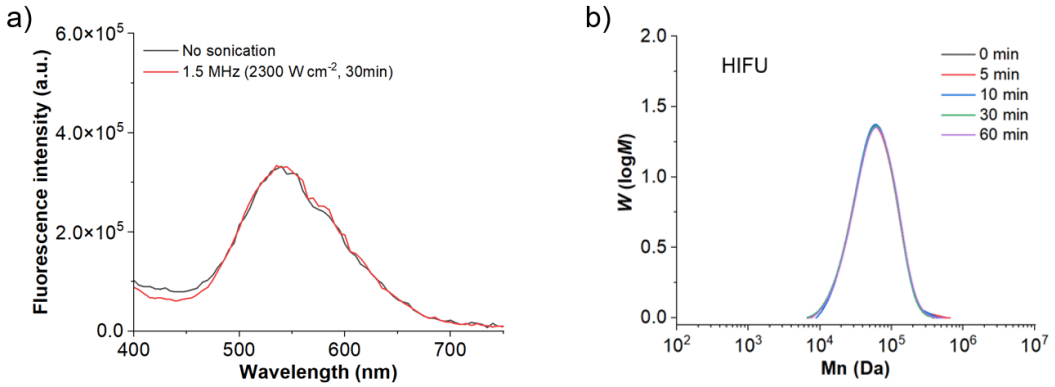

Figure S6. a) Fluorescence spectra of the mixture of **B2** and LPs, after 1.5 MHz (32 W, I = 2300 W cm^{-2}) HIFU sonication. **b**) GPC RI molar mass distributions of LPs after 1.5 MHz (32 W, I = 2300 W cm^{-2}) HIFU sonication.

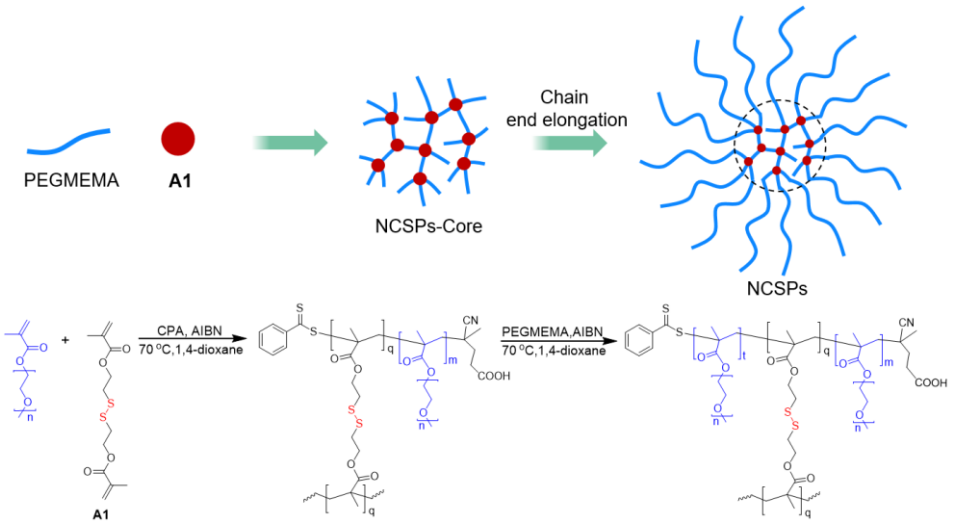

Scheme S3: Synthesis of NCSPs.

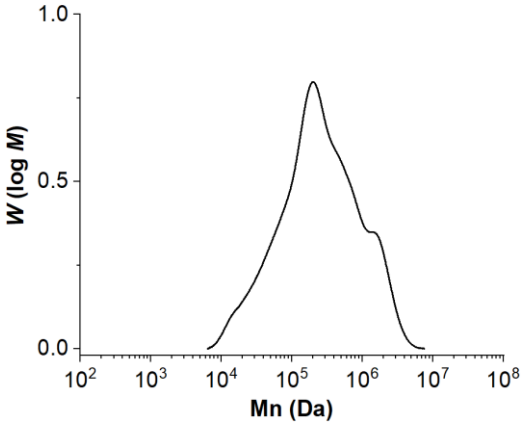

Figure S7. GPC RI molar mass distribution of NCSPs (M_n ~109 kDa)**.**

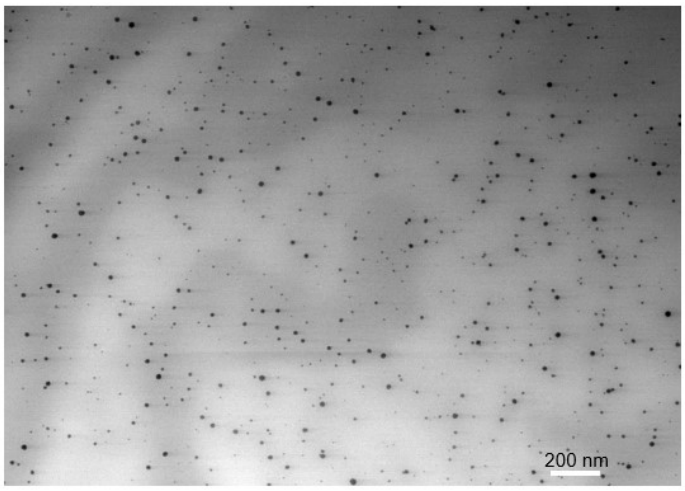

Figure S8. TEM image of NCSPs.

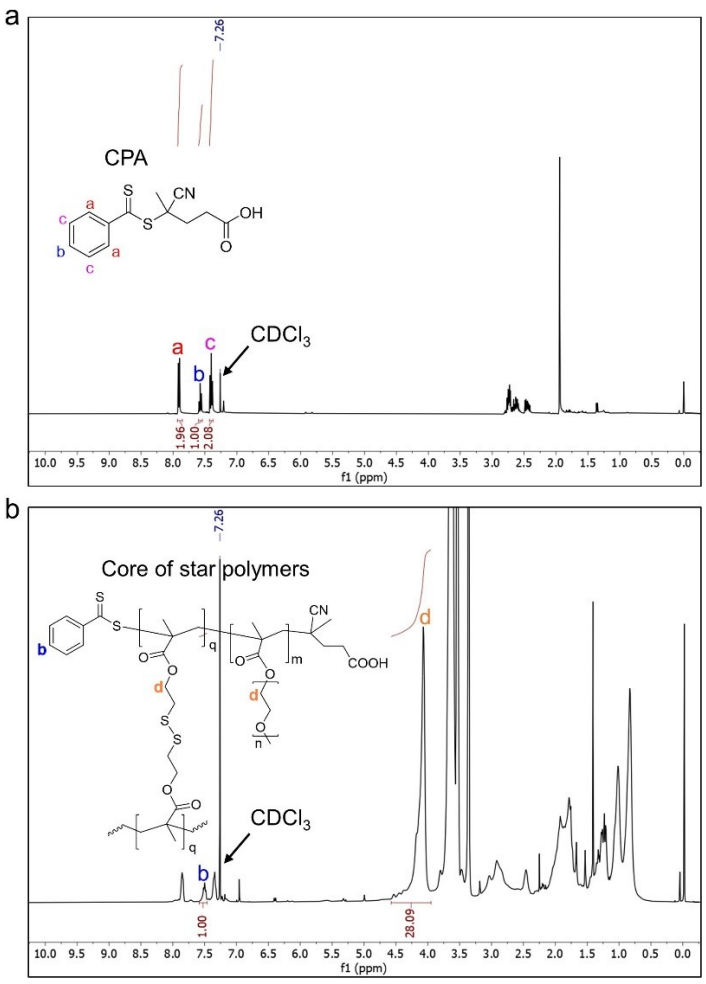

Figure S9. ^{1}H-NMR spectra of RAFT agent (CPA) and core of star polymers recorded in $CDCl_3$ at 20 °C.

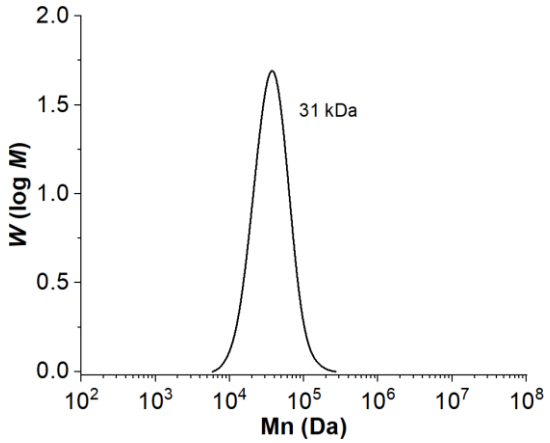

Figure S10. GPC result of core structure of star polymers.

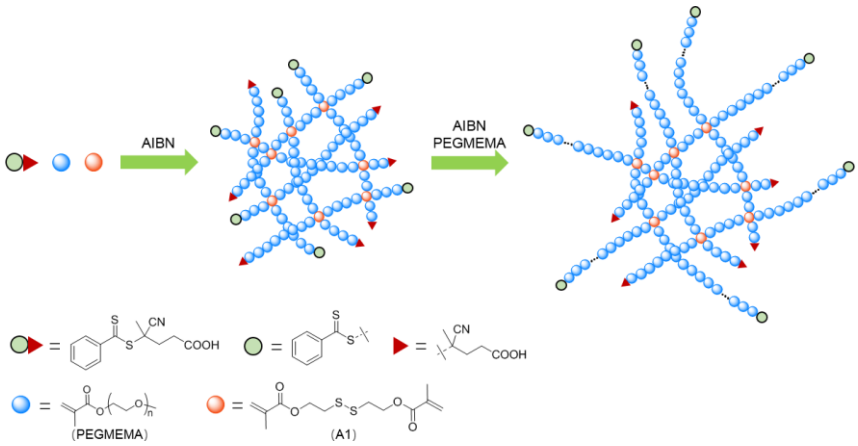

Figure S11. The synthesis process of NCSPs.

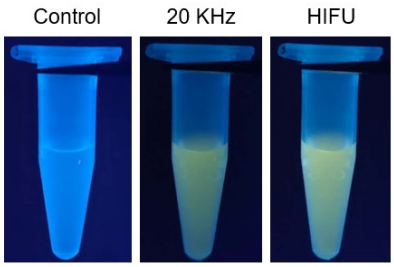

Figure S12. Fluorescence of the mixture of **B2** and NCSPs, after 30 min sonication. 20 kHz (I = 12.4 W cm^{-2}), 1.5 MHz (32 W, I = 2300 W cm^{-2}).

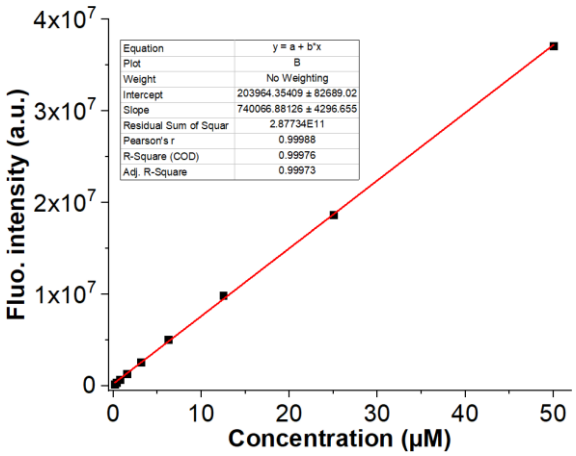

Figure S13. The standard curve plotted by **B1** concentration and fluorescence intensity.

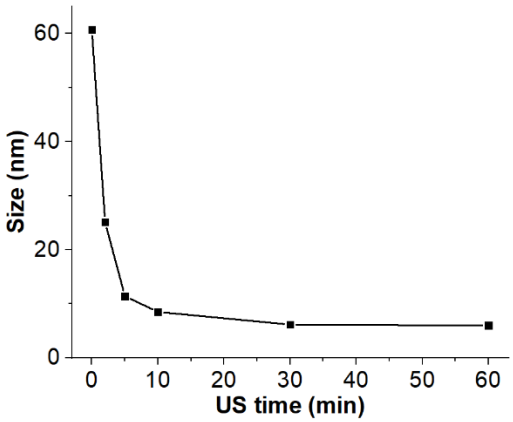

Figure S14. Size change of NCSPs after sonication (20 kHz, I = 12.4 W cm^{-2}).

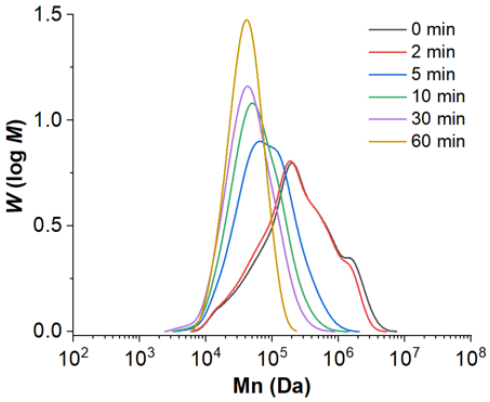

Figure S15. GPC RI molar mass distributions of NCSPs after different times of HIFU sonication (32 W, I = 2300 W cm^{-2}).

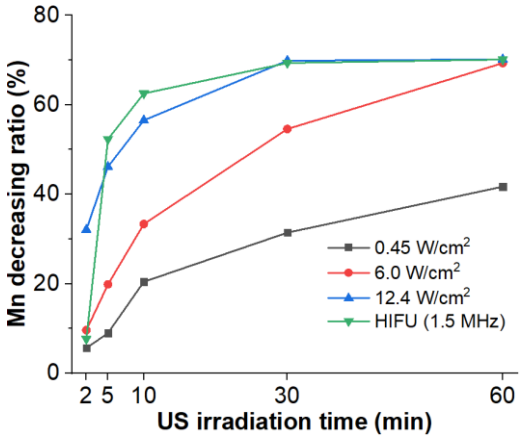

Figure S16. M_n decreasing ratio of NCSPs with different sonication intensity.

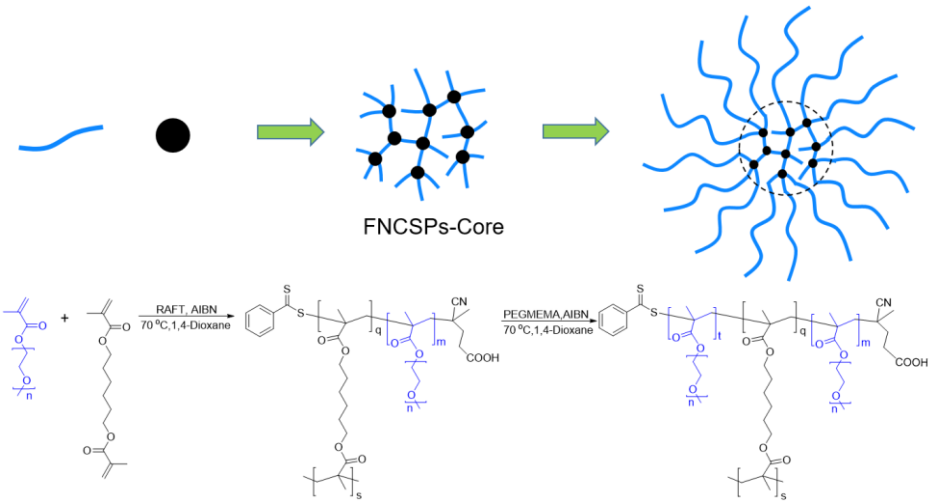

Scheme S4: Synthesis of FNCSPs.

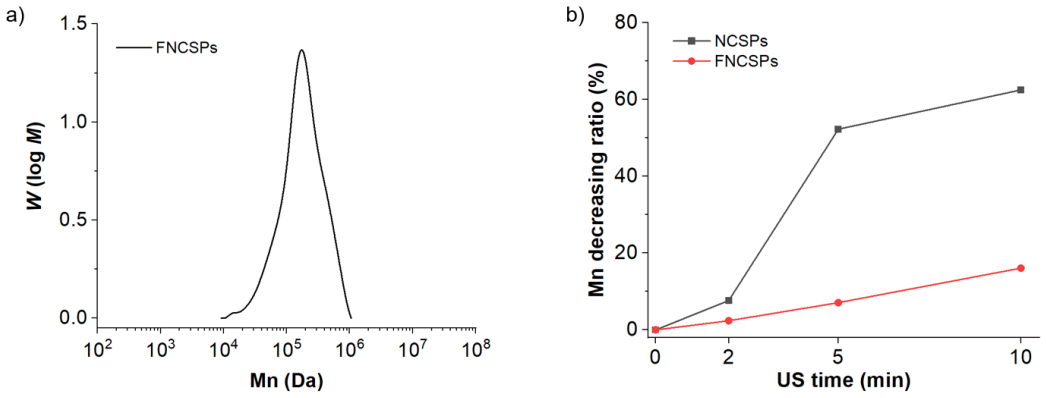

Figure S17. a) GPC RI molar mass distributions of FNCSPs (M_n ≈ 125 kDa). **b**) M_n decreasing ratio in 10 min with HIFU irradiation (32 W, I = 2300 W cm^{-2}).

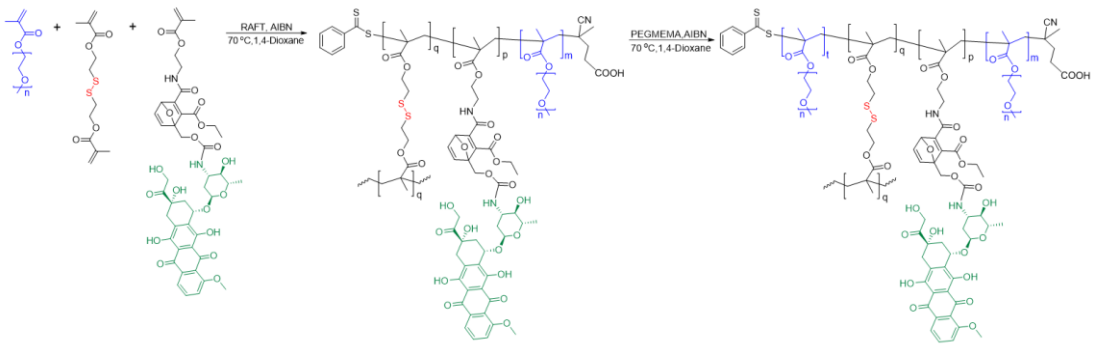

Scheme S5: Synthesis of NCSP-Dox.

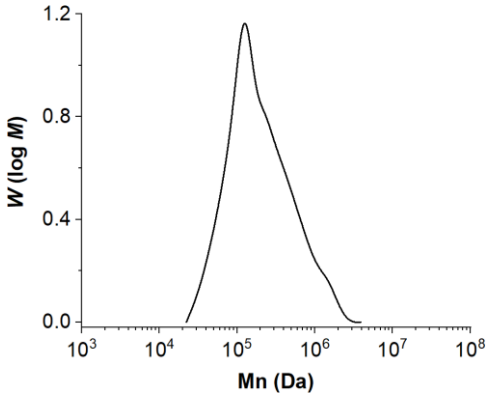

Figure S18. GPC RI molar mass distribution of NCSP-Dox (M_n ≈ 133 kDa).

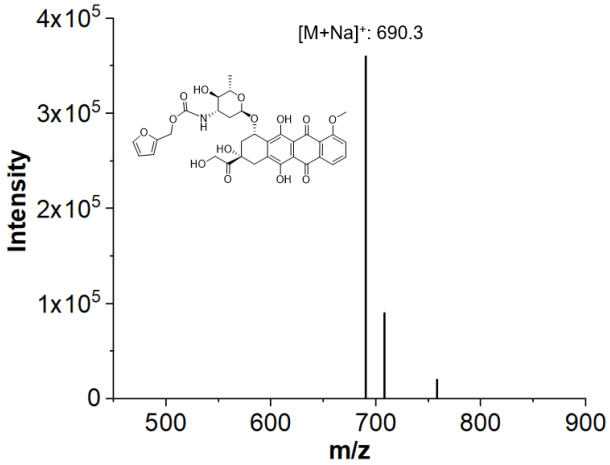

Figure S19. Molar mass of released molecule.

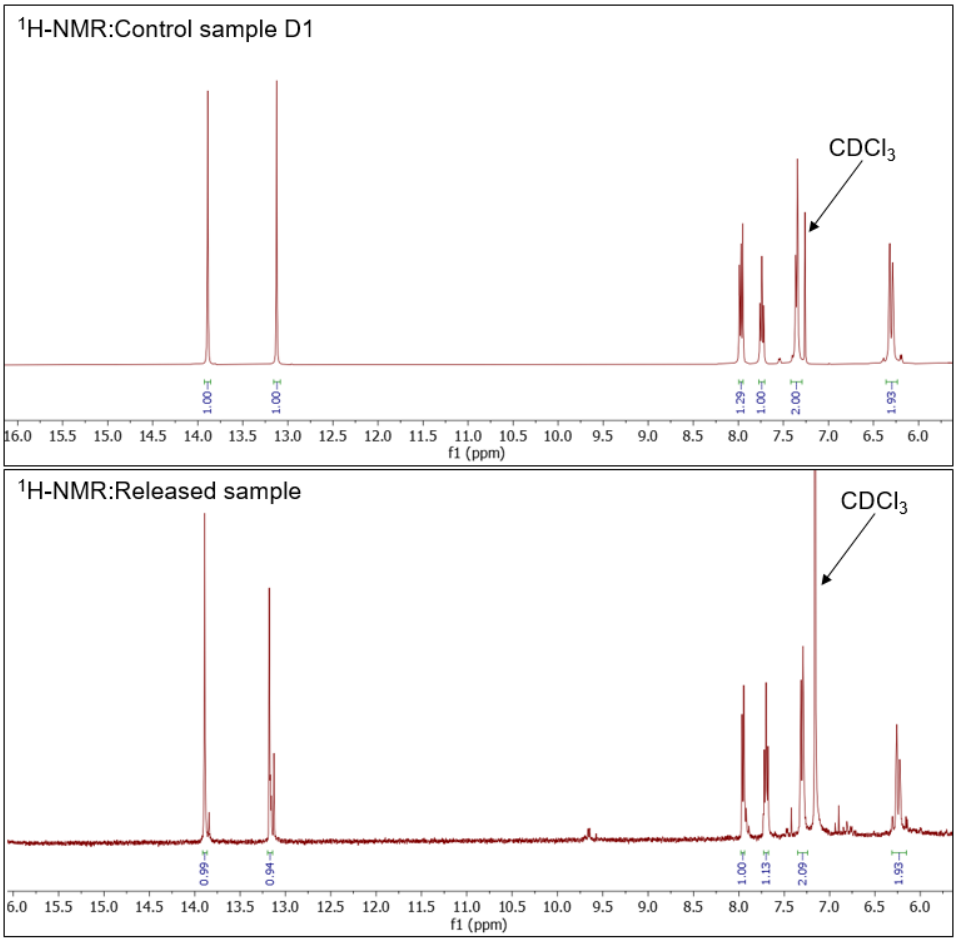

Figure S20. ^{1}H NMR of **D1** and released molecule.

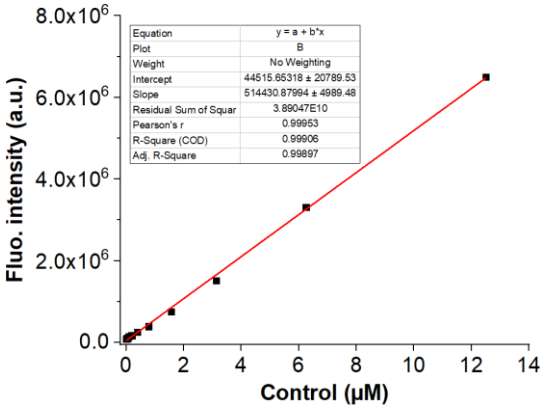

Figure S21. Furan-Dox standard curve (ex: 485 nm, em: 595 nm).

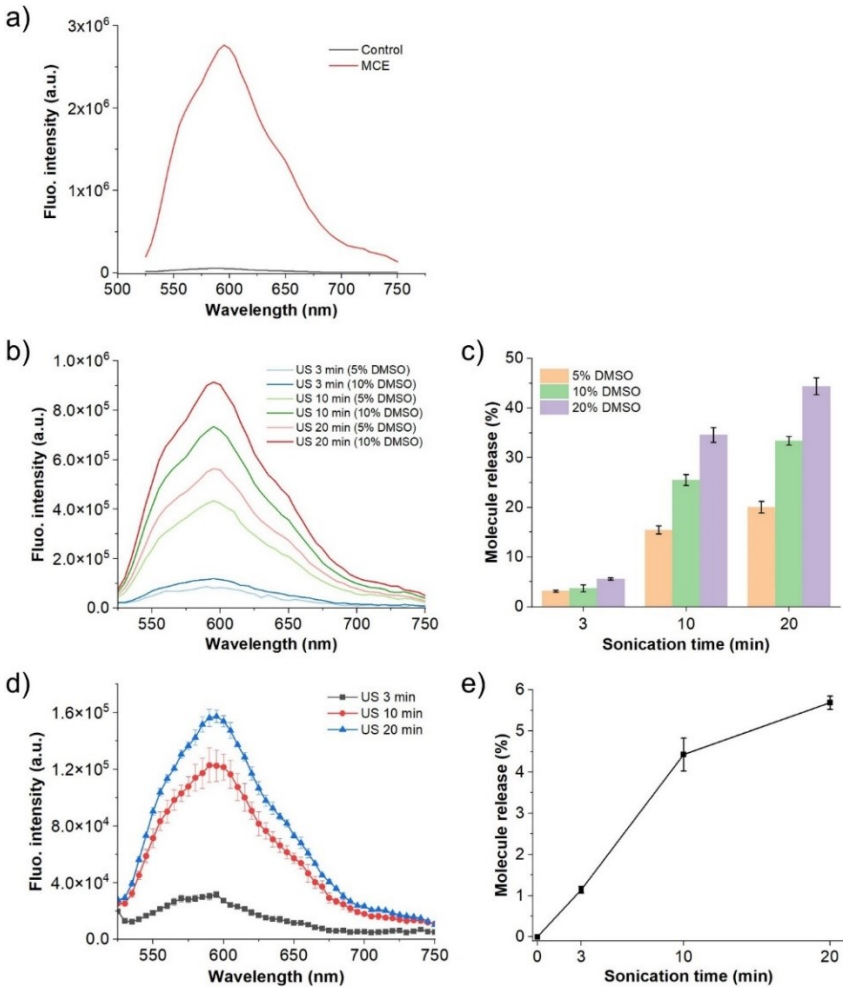

Figure S22. a) Fluorescence spectra of NCSP-Dox treated with excessive MCE (solvent: DMSO/H_2O). **b**) Fluorescence spectra (λ_{exc} = 485 nm) of NCSPs after HIFU irradiations (solvent: 5% and 10% DMSO, 1.5 MHz, I = 2300 W cm^{-2}). **c**) The release profile of **D1** (Furan-Dox) from NCSPs over sonication time (solvent: 5% and 10% DMSO, 1.5 MHz, I = 2300 W cm^{-2}). Mean ± SD from the mean. N = 3 independent sonications. **d**) Fluorescence spectra (λ_{exc} = 485 nm) of NCSPs after HIFU irradiations (solvent: water, 1.5 MHz, I = 2300 W cm^{-2}). **e**) The release profile of **D1** (Furan-Dox) from NCSPs over sonication time (solvent: water, 1.5 MHz, I = 2300 W cm^{-2}). Mean ± SD from the mean. N = 3 independent sonications.

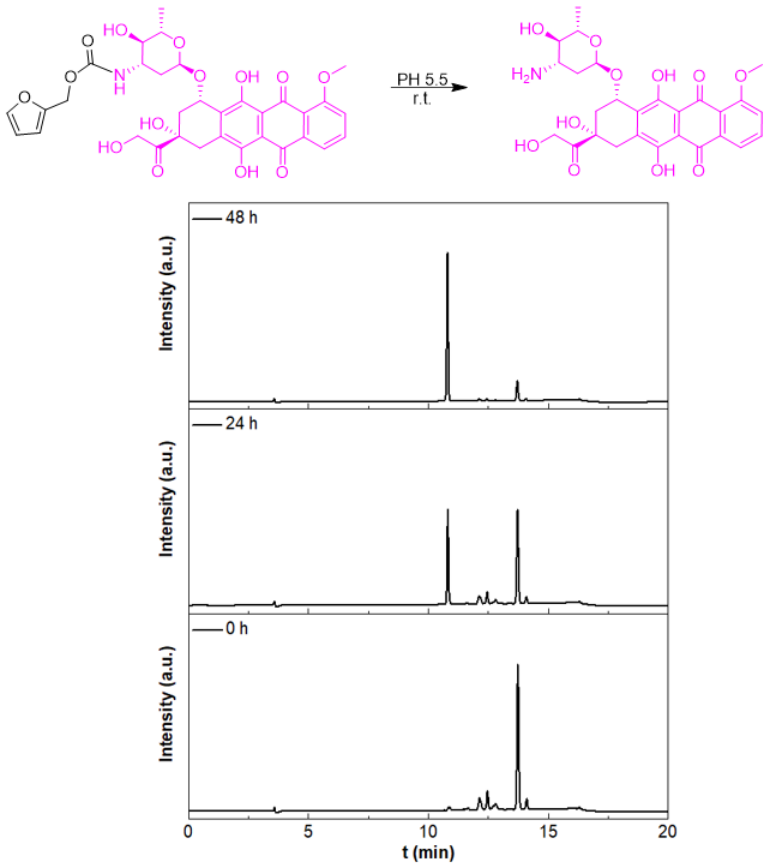

Figure S23. Release kinetics of Dox from released furan-Dox. Released sample was stirred in a mixture of DMSO and PBS buffer at pH = 5.5 for different times at rt, then subjected to UPLC analysis.

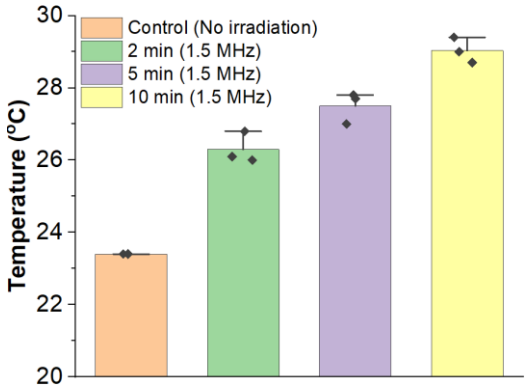

Figure S24. Temperature changes of samples under HIFU irradiation (1.5 MHz, 290 W cm^{-2}, 2, 5, and 10 min).

Table S1. The US intensities corresponding to the employed ultrasonic amplitudes for 20 kHz sonications.

Ultrasonic amplitude	25%	30%	35%	40%	45%	50%	75%	100%
Sound Intensity (*I*)	0.45 W/cm^2	0.7 W/cm^2	1.0 W/cm^2	1.5 W/cm^2	2.3 W/cm^2	2.7 W/cm^2	6.0 W/cm^2	12.4 W/cm^2

Table S2. HIFU intensities and mechanical indices (MI) of 1.5 MHz transducer.

Acoustic power	Focal sound intensity (*I*)	Focal pressure	Mechanical index (MI)
0 W	0 W/cm^2	0 kPa	0
2 W	140 W/cm^2	2100 kPa	1.7
3 W	220 W/cm^2	2500 kPa	2.0
4 W	290 W/cm^2	2900 kPa	2.4
8 W	580 W/cm^2	4100 kPa	3.3
16 W	1200 W/cm^2	5900 kPa	4.7
32 W	2300 W/cm^2	8300 kPa	6.7

Table S3. Equations to calculate the M_n decreasing ratio and degradation rate constant k.[51] M_i is the initial number average molar mass (M_n) of the polymer, M_t is the number average molar mass of the sonicated sample at time t. M_o is the molar mass of the monomer unit.

Equation 1	M_n decreasing ratio $= \frac{M_i - M_t}{M_i}$
Equation 2	$\frac{1}{M_t} = \frac{1}{M_i} + k' t$ $k' = \frac{k}{M_o}$

Table S4. M_n results of NCSPs with different conditions sonication.

Sonication		0 min	2 min	5 min	10 min	30 min	60 min
20 kHz	25% Amp (0.45 w cm^{-2})	108.5 (kDa)	102.4 (kDa)	98.7 (kDa)	86.3 (kDa)	74.4 (kDa)	63.3 (kDa)
	50% Amp (2.7 w cm^{-2})	108.5 (kDa)	98.1 (kDa)	86.9 (kDa)	72.3 (kDa)	49.3 (kDa)	33.3 (kDa)
	100% Amp (12.4 w cm^{-2})	108.5 (kDa)	73.7 (kDa)	58.4 (kDa)	47.2 (kDa)	32.7 (kDa)	32.4 (kDa)
1.5 MHz	32 W (2300 w cm^{-2})	108.5 (kDa)	100.2 (kDa)	51.7 (kDa)	40.6 (kDa)	33.3 (kDa)	32.4 (kDa)

Table S5. M_n results of FNCSPs with different acoustic power HIFU sonication.

1.5 MHz (30 min)	140 (w cm^{-2})	290 (w cm^{-2})	580 (w cm^{-2})	1200 (w cm^{-2})	2300 (w cm^{-2})
M_n	108.5 (kDa)	75.7 (kDa)	53.9 (kDa)	36.8 (kDa)	33.3 (kDa)

Table S6. M_n results of FNCSPs with HIFU sonication.

1.5 MHz (2300 w cm^{-2})	0 min	2 min	5 min	10 min
M_n	125.5 (kDa)	122.5 (kDa)	116.6 (kDa)	105.3 (kDa)

Table S7. Molar mass (M_n) changes and chain scission rate constant of star polymers and linear polymers with 20 kHz sonication.

Frequency	Polymers	Molecular weight (Mn)	Spanning molecular weight	Molecular weight Mn (60 min sonication)	Rate constant of chain scission (10^{-5} min^{-1})
20 kHz (12.4 W cm^{-2})	Star polymers (Mn 108.5 kDa)	108.5 kDa	53.5 kDa	32.4 kDa	10.8
	Linear polymers (Mn 47 kDa)	47 kDa	47 kDa	23.7 kDa	10.4

Table S8. Molar mass (M_n) changes and chain scission rate constant of star polymers and linear polymers with 1.5 MHz HIFU irradiation.

Frequency	Polymers	Molecular weight (Mn)	Spanning molecular weight	Molecular weight Mn (60 min sonication)	Rate constant of chain scission (10^{-5} min^{-1})
HIFU 1.5 MHz (2900 W cm^{-2})	Star polymers	108.5 kDa	53.5 kDa	32.4 kDa	10.8
	Linear polymers (Mn 47 kDa)	47 kDa	47 kDa	46.6 kDa	0.1

3.7 References

1. Shi, Z., Wu, J., Song, Q., Göstl, R., & Herrmann, A. (2020). Toward drug release using polymer mechanochemical disulfide scission. *Journal of the American Chemical Society*, *142*(34), 14725-14732.

2. Tong, Y., Li, M., Huang, H., Long, S., Sun, W., Du, J., Fan, J., Wang, L., Liu, B., & Peng, X. (2022). Urea-bond scission induced by therapeutic ultrasound for biofunctional molecule release. *Journal of the American Chemical Society*, *144*(37), 16799-16807.

3. Huo, S., Liao, Z., Zhao, P., Zhou, Y., Göstl, R., & Herrmann, A. (2022). Mechano-Nanoswitches for Ultrasound-Controlled Drug Activation. *Advanced Science*, *9*(12), 2104696.

4. Sun, Y., Neary, W. J., Burke, Z. P., Qian, H., Zhu, L., & Moore, J. S. (2022). Mechanically triggered carbon monoxide release with turn-on aggregation-induced emission. *Journal of the American Chemical Society*, *144*(3), 1125-1129.

5. Kim, G., Wu, Q., Chu, J. L., Smith, E. J., Oelze, M. L., Moore, J. S., & Li, K. C. (2022). Ultrasound controlled mechanophore activation in hydrogels for cancer therapy. *Proceedings of the National Academy of Sciences*, *119*(4), e2109791119.

6. Yao, Y., McFadden, M. E., Luo, S. M., Barber, R. W., Kang, E., Bar-Zion, A., Smith, C. A. B., Jin, Z., Legendre, M., Ling, B., Malounda, D., Torres, A., Hamza, T., Edwards, C. E. R., Shapiro, M. G., & Robb, M. J. (2023). Remote control of mechanochemical reactions under physiological conditions using biocompatible focused ultrasound. *Proceedings of the National Academy of Sciences*, *120*(39), e2309822120.

7. Zhao, P., Huo, S., Fan, J., Chen, J., Kiessling, F., Boersma, A. J., Göstl, R., & Herrmann, A. (2021). Activation of the catalytic activity of thrombin for fibrin formation by ultrasound. *Angewandte Chemie International Edition*, *60*(26), 14707-14714.

8. Zhou, Y., Huo, S., Loznik, M., Göstl, R., Boersma, A. J., & Herrmann, A. (2021). Controlling optical and catalytic activity of genetically engineered proteins by ultrasound. *Angewandte Chemie International Edition*, *60*(3), 1493-1497.

9. Küng, R., Pausch, T., Rasch, D., Göstl, R., & Schmidt, B. M. (2021). Mechanochemical Release of Non-Covalently Bound Guests from a Polymer‐Decorated Supramolecular Cage. *Angewandte Chemie International Edition*, *60*(24), 13626-13630.

10. Huo, S., Zhao, P., Shi, Z., Zou, M., Yang, X., Warszawik, E., Loznik, M., Göstl, R., & Herrmann, A. (2021). Mechanochemical bond scission for the activation of drugs. *Nature Chemistry*, *13*(2), 131-139.

11. Jochum, F. D., & Theato, P. (2013). Temperature-and light-responsive smart polymer materials. *Chemical Society Reviews*, *42*(17), 7468-7483.

12. Zhao, Y. (2012). Light-responsive block copolymer micelles. *Macromolecules*, *45*(9), 3647-3657.

13. Schmaljohann, D. (2006). Thermo-and pH-responsive polymers in drug delivery. *Advanced Drug Delivery Reviews*, *58*(15), 1655-1670.

14. Klaikherd, A., Nagamani, C., & Thayumanavan, S. (2009). Multi-stimuli sensitive amphiphilic block copolymer assemblies. *Journal of the American Chemical Society*, *131*(13), 4830-4838.

15. Du, J. Z., Du, X. J., Mao, C. Q., & Wang, J. (2011). Tailor-made dual pH-sensitive polymer-doxorubicin nanoparticles for efficient anticancer drug delivery. *Journal of the American Chemical Society*, *133*(44), 17560-17563.

16. Huh, K. M., Kang, H. C., Lee, Y. J., & Bae, Y. H. (2012). pH-sensitive polymers for drug delivery. *Macromolecular Research*, *20*, 224-233.

17. Wen, Y., Zhang, Z., & Li, J. (2014). Highly Efficient Multifunctional Supramolecular Gene Carrier System Self‐Assembled from Redox‐Sensitive and Zwitterionic Polymer Blocks. *Advanced Functional Materials*, *24*(25), 3874-3884.

18. Cho, H., Bae, J., Garripelli, V. K., Anderson, J. M., Jun, H. W., & Jo, S. (2012). Redox-sensitive polymeric nanoparticles for drug delivery. *Chemical Communications*, *48*(48), 6043-6045.

19. Cravotto, G., Gaudino, E. C., & Cintas, P. (2013). On the mechanochemical activation by ultrasound. *Chemical Society Reviews*, *42*(18), 7521-7534.

20. Mitragotri, S. (2005). Healing sound: the use of ultrasound in drug delivery and other therapeutic applications. *Nature Reviews Drug Discovery*, *4*(3), 255-260.

21. Levy, J., Barrett, D. L., Harris, N., Jeong, J. J., Yang, X., & Chen, S. C. (2021). High-frequency ultrasound in clinical dermatology: A review. *The Ultrasound Journal*, *13*, 1-12.

22. Wang, C., Sun, W., Xiang, Y., Wu, S., Zheng, Y., Zhang, Y., Shen, J., Yang, L., Liang, C., & Liu, X. (2023). Ultrasound‐Activated Piezoelectric MoS2 Enhances Sonodynamic for Bacterial Killing. *Small Science*, *3*(7), 2300022.

23. Kennedy, J. E. (2005). High-intensity focused ultrasound in the treatment of solid tumours. *Nature Reviews Cancer*, *5*(4), 321-327.

24. Brown, M. R. D., Farquhar-Smith, P., Williams, J. E., Ter Haar, G., & Desouza, N. M. (2015). The use of high-intensity focused ultrasound as a novel treatment for painful conditions-a description and narrative review of the literature. *BJA: British Journal of Anaesthesia*, *115*(4), 520-530.

25. Xiong, X., Sun, Y., Sattiraju, A., Jung, Y., Mintz, A., Hayasaka, S., & Li, K. C. (2015). Remote spatiotemporally controlled and biologically selective permeabilization of blood-brain barrier. *Journal of Controlled Release*, *217*, 113-120.

26. Leinenga, G., Langton, C., Nisbet, R., & Götz, J. (2016). Ultrasound treatment of neurological diseases-current and emerging applications. *Nature Reviews Neurology*, *12*(3), 161-174.

27. Sirsi, S. R., & Borden, M. A. (2014). State-of-the-art materials for ultrasound-triggered drug delivery. *Advanced Drug Delivery Reviews*, *72*, 3-14.

28. Liang, X., Gao, J., Jiang, L., Luo, J., Jing, L., Li, X., Jin, Y., & Dai, Z. (2015). Nanohybrid liposomal cerasomes with good physiological stability and rapid temperature responsiveness for high intensity focused ultrasound triggered local chemotherapy of cancer. *ACS Nano*, *9*(2), 1280-1293.

29. The United States Food and Drug Administration guidance documents, "Marketing Clearance of Diagnostic Ultrasound Systems and Transducers" February **2023**.
https://www.fda.gov/regulatory-information/search-fda-guidance-documents/marketing-clearance-diagnostic-ultrasound-systems-and-transducers

30. Escoffre, J. M., & Bouakaz, A. (2016). Therapeutic Ultrasound: From biophysics concepts to clinical applications. *Advances in Experimental Medicine and Biology; Springer International Publishing: Cham, Switzerland*, *880*, 35-78.

31. Xuan, M., Fan, J., Khiêm, V. N., Zou, M., Brenske, K. O., Mourran, A., Vinokur, R., Zheng, L., Itskov, M., Göstl, R., & Herrmann, A. (2023). Polymer mechanochemistry in microbubbles. *Advanced Materials*, *35*(47), 2305130.

32. Lammers, T., Koczera, P., Fokong, S., Gremse, F., Ehling, J., Vogt, M., Pich, A., Storm, G., Van Zandvoort, M., & Kiessling, F. (2015). Theranostic USPIO-loaded microbubbles for mediating and monitoring blood-brain barrier permeation. *Advanced Functional Materials*, *25*(1), 36-43.

33. Barmin, R. A., Dasgupta, A., Bastard, C., De Laporte, L., Rütten, S., Weiler, M., Kiessling, F., Lammers, T., & Pallares, R. M. (2022). Engineering the acoustic response and drug loading capacity of PBCA-based polymeric microbubbles with surfactants. *Molecular Pharmaceutics*, *19*(9), 3256-3266.

34. Peterson, G. I., & Choi, T. L. (2021). The influence of polymer architecture in polymer mechanochemistry. *Chemical Communications*, *57*(53), 6465-6474.

35. Schulte, M. F., Izak-Nau, E., Braun, S., Pich, A., Richtering, W., & Göstl, R. (2022). Microgels react to force: mechanical properties, syntheses, and force-activated functions. *Chemical Society Reviews*, *51*(8), 2939-2956.

36. Watabe, T., & Otsuka, H. (2024). Enhancing the Reactivity of Mechanically Responsive Units via Macromolecular Design. *Macromolecules*, *57*(2), 425-433.

37. Peterson, G. I., Bang, K. T., & Choi, T. L. (2018). Mechanochemical degradation of denpols: synthesis and ultrasound-induced chain scission of polyphenylene-based dendronized polymers. *Journal of the American Chemical Society*, *140*(27), 8599-8608.

38. Watabe, T., Aoki, D., & Otsuka, H. (2021). Enhancement of mechanophore activation in mechanochromic dendrimers by functionalization of their surface. *Macromolecules*, *54*(4), 1725-1731.

39. Peterson, G. I., Noh, J., Ha, M. Y., Yang, S., Lee, W. B., & Choi, T. L. (2021). Influence of Grafting Density on Ultrasound-Induced Backbone and Arm Scission of Graft Copolymers. *Macromolecules*, *54*(9), 4219-4226.

40. Zou, M., Zhao, P., Huo, S., Göstl, R., & Herrmann, A. (2021). Activation of antibiotic-grafted polymer brushes by ultrasound. *ACS Macro Letters*, *11*(1), 15-19.

41. Pan, Y., Zhang, H., Xu, P., Tian, Y., Wang, C., Xiang, S., Boulatov, R., & Weng, W. (2020). A mechanochemical reaction cascade for controlling load-strengthening of a mechanochromic polymer. *Angewandte Chemie*, *132*(49), 22164-22169.

42. Izak-Nau, E., Demco, D. E., Braun, S., Baumann, C., Pich, A., & Göstl, R. (2020). Shear-induced structural and functional transformations of poly (N-vinylcaprolactam) microgels. *ACS Applied Polymer Materials*, *2*(4), 1682-1691.

43. Zou, M., Zhao, P., Fan, J., Göstl, R., & Herrmann, A. (2022). Microgels as drug carriers for sonopharmacology. *Journal of Polymer Science*, *60*(12), 1864-1870.

44. Church, D. C., Peterson, G. I., & Boydston, A. J. (2014). Comparison of mechanochemical chain scission rates for linear versus three-arm star polymers in strong acoustic fields. *ACS Macro Letters*, *3*(7), 648-651.

45. Striegel, A. M. (2003). Influence of chain architecture on the mechanochemical degradation of macromolecules. *Journal of Biochemical and Biophysical Methods*, *56*(1-3), 117-139.

46. Göstl, R., & Sijbesma, R. P. (2016). π-extended anthracenes as sensitive probes for mechanical stress. *Chemical Science*, *7*(1), 370-375.

47. Hong, V., Kislukhin, A. A., & Finn, M. G. (2009). Thiol-selective fluorogenic probes for labeling and release. *Journal of the American Chemical Society*, *131*(29), 9986-9994.

48. May, P. A., Munaretto, N. F., Hamoy, M. B., Robb, M. J., & Moore, J. S. (2016). Is molecular weight or degree of polymerization a better descriptor of ultrasound-induced mechanochemical transduction? *ACS Macro Letters*, *5*(2), 177-180.

49. Schaefer, M., Icli, B., Weder, C., Lattuada, M., Kilbinger, A. F., & Simon, Y. C. (2016). The role of mass and length in the sonochemistry of polymers. *Macromolecules*, *49*(5), 1630-1636.

50. Malhotra, S. L. (1986). Ultrasonic solution degradations of poly (alkyl methacrylates). *Journal of Macromolecular Science-Chemistry*, *23*(6), 729-748.

51. Kryger, M. J., Munaretto, A. M., & Moore, J. S. (2011). Structure–mechanochemical activity relationships for cyclobutane mechanophores. *Journal of the American Chemical Society*, *133*(46), 18992-18998.

52. Sritharan, S., & Sivalingam, N. (2021). A comprehensive review on time-tested anticancer drug doxorubicin. *Life Sciences*, *278*, 119527.

53. Tacar, O., Sriamornsak, P., & Dass, C. R. (2013). Doxorubicin: an update on anticancer molecular action, toxicity and novel drug delivery systems. *Journal of Pharmacy and Pharmacology*, *65*(2), 157-170.

54. Injac, R., & Strukelj, B. (2008). Recent advances in protection against doxorubicin-induced toxicity. *Technology in Cancer Research & Treatment*, *7*(6), 497-516.

55. Tekkam, S., & Finn, M. G. (2017). Synthesis and Reactivity of 5-Substituted Furfuryl Carbamates via Oxanorbornadienes. *Organic Letters*, *19*(11), 2833-2836.

56. Fulmer, G. R., Miller, A. J., Sherden, N. H., Gottlieb, H. E., Nudelman, A., Stoltz, B. M., Bercaw, J. E., & Goldberg, K. I. (2010). NMR chemical shifts of trace impurities: common laboratory solvents, organics, and gases in deuterated solvents relevant to the organometallic chemist. *Organometallics*, *29*(9), 2176-2179.

57. Aioub, A. G., Higginson, C. J., & Finn, M. G. (2018). Traceless Release of Alcohols Using Thiol-Sensitive Oxanorbornadiene Linkers. *Organic Letters*, *20*(11), 3233-3236.

58. Pearce, A. K., Anane‐Adjei, A. B., Cavanagh, R. J., Monteiro, P. F., Bennett, T. M., Taresco, V., Clarke, P. A., Ritchie, A. A., Alexander, M. R., Grabowska, A. M., & Alexander, C. (2020). Effects of polymer 3D architecture, size, and chemistry on biological transport and drug delivery in vitro and in orthotopic triple negative breast cancer models. *Advanced Healthcare Materials*, *9*(22), 2000892.

59. Pal, S., Hill, M. R., & Sumerlin, B. S. (2015). Doubly-responsive hyperbranched polymers and core-crosslinked star polymers with tunable reversibility. *Polymer Chemistry*, *6*(45), 7871-7880.

4. High-intensity focused ultrasound-induced disulfide mechanophore activation in polymeric microgels for molecule release

The research contained within this chapter has been published in the journal of CCS Chemistry (**Jilin Fan**, Kuan Zhang, Mingjun Xuan*, Xiang Gao, Rostislav Vinokur, Robert Göstl, Lifei Zheng*, Andreas Herrmann*. High-Intensity Focused Ultrasound-Induced Disulfide Mechanophore Activation in Polymeric Nanostructures for Molecule Release. CCS Chem. 2024, 6, 1895-1907). The author (Jilin Fan) of this thesis contributed to experimental design; synthesized and characterized the materials; analyzed the data and co-wrote the manuscript. In addition, I (Jilin Fan) declare as follows:

1. I designed and performed the experiments (Polymer synthesis; Small molecules synthesis; Sonication Assay; Quantification of mechanophore activation; Quantification of drug release; MTS proliferation assay; Live/dead cell staining assay) contained in the publication.
2. I synthesized and characterized the materials (small molecules and polymers) contained in the publication.
3. I collected the data (TEM images; DLS analysis; NMR data; ESI-MS data; GPC data; Fluorescence intensity; MTS proliferation test; Live/dead cell staining test) contained in the publication.
4. I analyzed the data and drew all the figures and tables contained in the publication.
5. I wrote the first version of the manuscript and then co-revised the manuscript.
6. Other authors' contribution to this publication; Kuan Zhang gave suggestions on MTS proliferation assay; Xiang Gao gave suggestion on polymer synthesis. Rostislav Vinokur built the HIFU setup; Mingjun Xuan and Lifei Zheng gave suggestions on experimental design; Robert Göstl and Andreas Herrmann revised the first version of the manuscript.

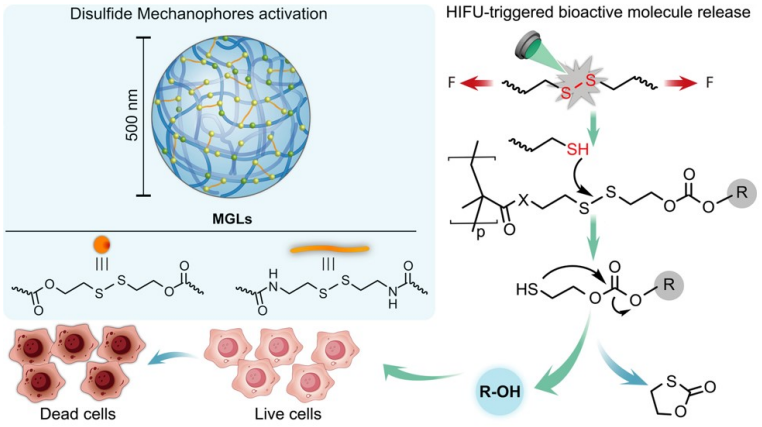

In **Chapter 4**, I present the design and synthesis of ultrasound-responsive polymeric microgels. The fluorescence probe (umbelliferone, UMB) and small molecule drug (camptothecin, CPT) were successively released from microgels via HIFU irradiation. This strategy relies on HIFU-induced selective scission of disulfide bonds to generate reducing agent sulfhydryl groups. Then, the generated thiols initiate thiol-disulfide exchange reaction and an intramolecular cyclization, to achieve small molecules release.

4.1 Abstract

The activation of mechanophores in polymers using ultrasound (US) to trigger cascade chemical reactions offers a promising approach for on-demand molecule release. However, the typical US frequency used for mechanochemistry is around 20 kHz, which produces inertial cavitation that exceeds biological tolerance limits. In this study, high-intensity focused US (HIFU) is employed as a mechanical stimulus to activate disulfide mechanophores in microgels (MGLs). The resulting molecular release mechanism involves a thiol-disulfide exchange reaction followed by the intramolecular cyclization. MGLs effectively convert HIFU-induced mechanical input into chemical output, as evidenced by the quantification of fluorescent umbelliferone (UMB) release. Additionally, an *in vitro* drug release study using camptothecin (CPT) as a model drug, covalently loaded in MGLs, highlights the potential of this system for controlled drug delivery to cancer cells.

4.2 Introduction

Polymer mechanochemistry aims to control chemical transformations by rearranging or cleaving specific bonds within polymer chains using mechanical forces such as tension, compression, or ultrasound.[1-4] The force-sensitive elements that facilitate this process are called mechanophores.[5-9] The development of various mechanophores has broadened the scope for creating polymer systems with tailored mechanochemical properties.[10-16] While polymer mechanochemistry has been widely applied in areas such as damage detection,[17-19] stress sensing,[20-22] nanolithography,[4] and self-regulating materials,[23] its application in biomedicine is still in the early stages.

Recently, our group[24-30] and others[31-33] have pioneered the field of sonopharmacology, which applies principles of polymer mechanochemistry for pharmacotherapy.[34] Ultrasound (US) offers deep tissue penetration and precise spatiotemporal control, making it ideal for achieving mechanochemical processes in biological systems and manipulating drug activation and release.[35-36] However, traditional polymer mechanochemistry using 20 kHz US poses risks of cellular and tissue damage due to strong cavitation effects and liquid micro-jet formation.[37] In contrast, high-intensity focused ultrasound (HIFU) at MHz frequencies is biocompatible and commonly used in biomedical applications.[38] Robb, Shapiro, and coworkers developed a platform combining selective activation of masked 2-furylcarbinol mechanophores in linear polymers with biocompatible focused US, using pressure-sensitive gas vesicles as acousto-mechanical transducers.[33] While this method allows precise control over drug release, it requires co-injection and co-localization of gas vesicles and polymers in tumor tissues, complicating practical implementation. Further research is needed to fully explore biocompatible US-based polymer mechanochemistry for developing advanced drug delivery systems.

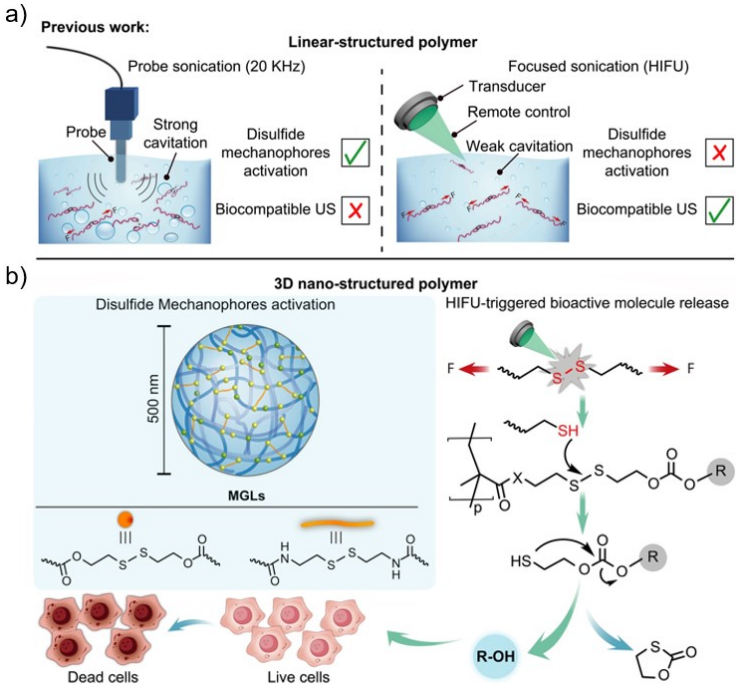

Figure 1. a) Summary of previous work on US-activated linear polymer structures containing disulfide mechanophores. **b**) Schematic illustration of the mechanism of the activation of disulfide mechanophores in crosslinked polymeric structures upon HIFU irradiation involving thiol-disulfide exchange reactions and the following intramolecular cyclization.

Disulfide mechanophore have garnered significant attention due to its low bond dissociation energy and thermal stability. Typically incorporated into linear polymers, disulfide can be activated by ultrasound (US) irradiations.[24-27, 39-44] However, the activation of disulfide mechanophore using high-intensity focused ultrasound (HIFU) in polymeric nanostructures remains unexplored. In this study, we design microgels (MGLs) containing disulfide mechanophores, inactive fluorescent probes (umbelliferone, UMB), or a small molecule drug (camptothecin, CPT). The disulfide mechanophores are covalently integrated into the polymer system. Upon HIFU irradiations, the mechanophores undergo bond scission, generating free thiols. These thiols activate a carbonate unit within the polymer scaffold through thiol-disulfide exchange and intramolecular cyclization, leading to the release of UMB or CPT (**Figure 1**). The cytotoxic effects of the released drug on HeLa cells are investigated to assess its potential for cancer treatment. This work highlights HIFU as a noninvasive method for triggering drug release from polymeric nanomaterials.

4.3 Results and discussion

4.3.1 Synthesis of MGLs-UMB and HIFU-Induced Disulfide Mechanophore Activation

Initially, we evaluated the release of cargo molecules from the disulfide-carbonate structure. To do this, we synthesized a monomer containing a disulfide, carbonate, and UMB unit (**A2-1**), as well as a model compound containing only a hexanol, carbonate, and UMB unit (**A3**) (**Scheme S1**). UMB was the designated fluorescent reporter, allowing facile quantification of molecule release. In compound **A2-1**, a carbonate linker was positioned in the β-position to the disulfide moiety. Upon thiol-initiated thiol-disulfide exchange and the following intramolecular cyclization, UMB was released and its fluorescence was turned on due to breakage of the carbonate linker. As shown in **Figure S1**, strong fluorescence of **A2-1** solution was observed under 365 nm UV light irradiation after the addition of 2-mercaptoethanol (MCE), indicating the occurrence of the thiol-disulfide exchange reaction, followed by the intramolecular cyclization. The formation of the released fluorescent UMB was further confirmed by ^{1}H NMR spectroscopy and Ultrahigh-Performance Liquid Chromatography (UPLC) (**Figure S3** and **S4**). As a control sample, **A3** without the disulfide group was also mixed with MCE. As anticipated, the reaction mixture containing **A3** and **MCE** exhibited no increase in fluorescence (**Figures S1** and **S2**).

Encouraged by these results, we proceeded to synthesize microgels incorporating the disulfide-carbonate structure. MGLs-umbelliferone (MGLs-UMB) were synthesized in two steps, as illustrated in **Figure 2a** and **Scheme S2**. The RAFT polymerization process involved the use of PEGMEMA, PFPMA, and acrylate-disulfide-UMB (**A2-1**) to produce copolymer P1 (**Figure S7**) with a molecular weight of 12.9 kDa. The molar ratio of PEGMEMA to PFPMA to **A2-1** was approximately 14:5:1 (**Figure S8**). Each P1 polymer contained approximately two acrylate-UMB molecules. Subsequently, P1 was cross-linked using cystamine to form MGLs-UMB. Notably, the leaving group pentafluorophenolate facilitated the crosslinking reaction, which was characterized by ^{19}F NMR spectroscopy (**Figure S9**). The morphology and size distribution of MGLs-UMB were examined using TEM imaging (**Figure 2b** and **Figure S10**). The observed size range of MGLs-UMB was between 150 and 450 nm (**Figure S11**). **Figure 2c** illustrates the mechanism of disulfide mechanophore activation and the release of UMB from MGLs-UMB under HIFU irradiation.

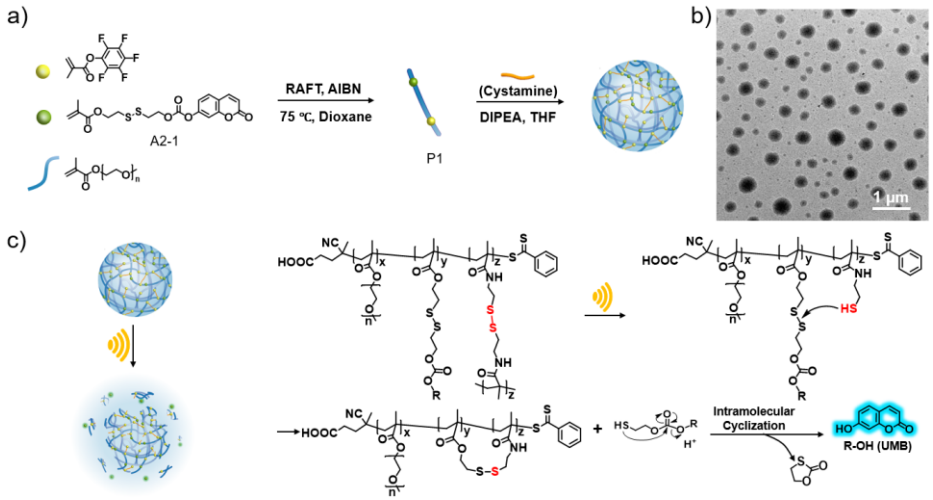

Figure 2. Synthesis and characterization of MGLs-UMB. **a**) The synthesis of copolymer (P1) using RAFT polymerization of PEGMEMA, PFPMA and **A2-1** and the following crosslinking by cystamine to form MGLs-UMB. **b**) TEM micrograph of MGLs-UMB. **c**) The mechanism of disulfide mechanophore activation in MGLs-UMB. Fluorescence spectra of MGLs-UMB samples after

Firstly, fluorescence measurements confirmed the activation of disulfide mechanophores using 0.66 MHz HIFU (**Figure 3a**). Subsequently, 1.5 MHz and 2.5 MHz HIFU were employed to test the response of MGLs. Both frequencies were able to trigger UMB release (**Figure 3b** and **3c**). However, with 0.66 MHz HIFU more disulfide mechanophores were activated, as indicated by higher fluorescence intensity compared to 1.5 MHz and 2.5 MHz. It was observed that UMB release reached its maximum (~ 27%) after 20 min of sonication under 0.66 MHz HIFU treatment (**Figure 3d**). Moreover, the MGLs-UMB responded to HIFU treatment more strongly compared to linear polymers, which typically have an ultrasonic response time of hours under 20 kHz sonication. TEM characterization of MGLs-UMB after 30 min of HIFU treatment revealed severe deformation and disintegration of the structure (**Figure S15**). From the bimodal size distribution histogram, we know that MGLs-UMB size increases with many small fragments occurring as well (**Figure S16**). However, not all MGLs-UMB were destroyed into smaller fragments. This phenomenon can possibly be attributed to two reasons. Firstly, the density of the crosslinked network is higher in the core part of the MGLs-UMB compared to the outer layer. During HIFU treatment, the mechanical forces caused by the US waves peeled off the corona layer from the surface of MGLs-UMB, leaving behind only the core parts.[45] Secondly, HIFU activation of the disulfide mechanophores in MGLs-UMB resulted in a reduction in crosslink density, causing the MGLs to lose their previous tight connections. This reduction in crosslink density led to structure swelling, which may have contributed to the retention of large-scale structures even after disintegration.

The correlation between HIFU power and UMB release from MGLs-UMB was examined at 0.66 MHz and 1.5 MHz frequencies, which showed higher disulfide mechanophore activation in MGLs-UMB. Fluorescence spectra of MGLs were measured after subjecting them to 30 min of HIFU sonication at different acoustic powers of 0, 4, 8, 16, and 32 W (**Figure 3e**). The results confirmed a positive relationship between fluorescence intensity and HIFU power. Notably, no fluorescence was observed at acoustic powers below 4 W, indicating that the disulfide mechanophore in MGLs-UMB remained inactive under lower HIFU power conditions (**Figure 3f**). Thus, the minimum acoustic power needed to activate disulfide mechanophores and release UMB from MGLs-UMB was approximately 8 W with the 0.66 MHz transducer.

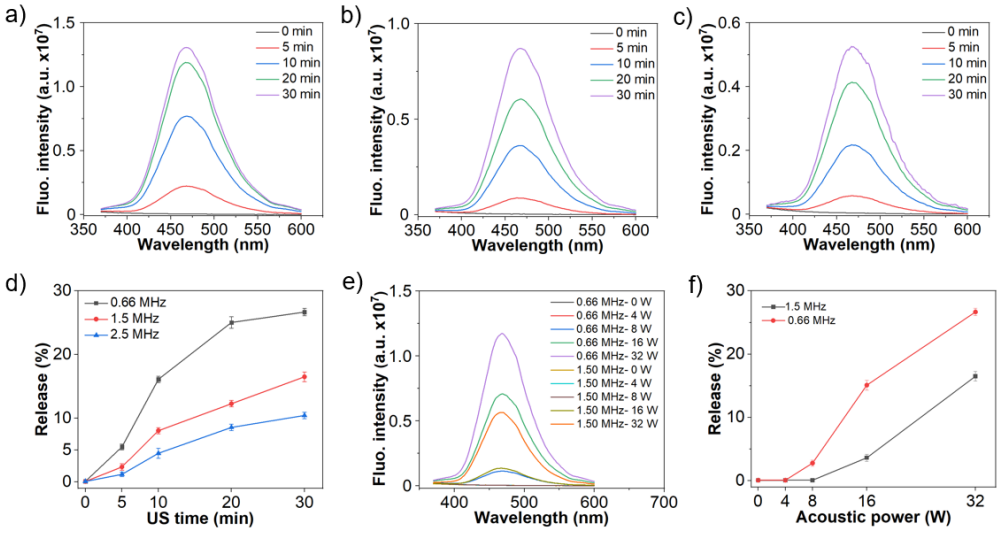

Figure 3. HIFU-induced activation of disulfide mechanophore in MGLs-UMB. **a**) 0.66 MHz, **b**) 1.5 MHz, and **c**) 2.5 MHz HIFU treatment with an acoustic power of 32 W. **d**) The release profile of UMB under HIFU treatment with different frequencies. **e**) Fluorescence spectra of MGLs after 30 min HIFU sonication at different acoustic power. **f**) UMB release from MGLs-UMB with different HIFU frequencies and acoustic power.

4.3.2 HIFU-Induced Disulfide Mechanophore Activation in MGLs for Drug Release

Having successfully demonstrated the release of UMB from polymeric MGLs, we expanded our investigation to include a drug molecule, specifically CPT. CPT has shown promising anticancer activity in preliminary clinical trials, particularly against breast, colon, and stomach cancers.[46] However, CPT has low solubility in aqueous medium and can exhibit systemic toxicity.[47] To address these challenges, we aimed to achieve the spatiotemporally controlled release of CPT using our system. Therefore, MGLs-camptothecin (MGLs-CPT) was synthesized by crosslinking copolymers (20.8 kDa) with cystamine, which contains a disulfide mechanophore (**Scheme S3** and **Figure S17**). In brief, CPT was covalently connected to the MGLs chains through the acrylate molecule **A2-2**. The molar ratio of PEGMEMA to PFPMA to **A2-2** was approximately 17:4:1, and each P2 copolymer contained approximately three acrylate-CPT (**A2-2**) molecules (**Figure S18**). Subsequently, P2 was then cross-linked with cystamine, achieving 70% crosslinking relative to the PFPMA moieties, to form MGLs-CPT. The size of MGLs-CPT was characterized using TEM (**Figure S19**).

To explore the release of CPT from MGLs-CPT upon HIFU irradiation (**Figure 4a**), MGLs-CPT were dispersed in a solvent mixture of DMSO and PBS (v/v = 1:4) and exposed to HIFU irradiation for durations of 0, 5, 10, 20, and 30 minutes. The solution was subsequently filtered, and fluorescence spectra were measured to qualitatively assess the release of CPT from MGLs. The fluorescence spectra of CPT, measured at an excitation wavelength of 335 nm, exhibited a steadily increasing intensity in direct correlation with prolonged HIFU irradiation (**Figure 4b**). Under UV illumination, a vivid and intense blue fluorescence was distinctly visible (Figure 4b inset). To further substantiate these findings, precise UPLC-MS analysis was conducted to track the emergence of CPT as a function of extended HIFU exposure (**Figure 4c** and **Figure S20**). Additionally, ^{1}H NMR spectroscopy revealed the distinct appearance of characteristic aromatic proton signals of CPT, providing compelling evidence of HIFU-triggered disulfide mechanophore activation and subsequent molecular release (**Figure 4d**). To accurately quantify the liberated CPT, a clear correlation between fluorescence intensity and CPT concentration was established (**Figure S21**). The maximum achievable release was determined by completely reducing all disulfide

linkages within MGLs-CPT using MCE and was assessed through fluorescence intensity measurements (**Figure S22**). Upon subjecting MGLs-CPT to HIFU irradiation, a maximum release of nearly 30% of CPT was achieved, with the release process plateauing after 20 minutes (**Figure 4e** and **Figure S23**).

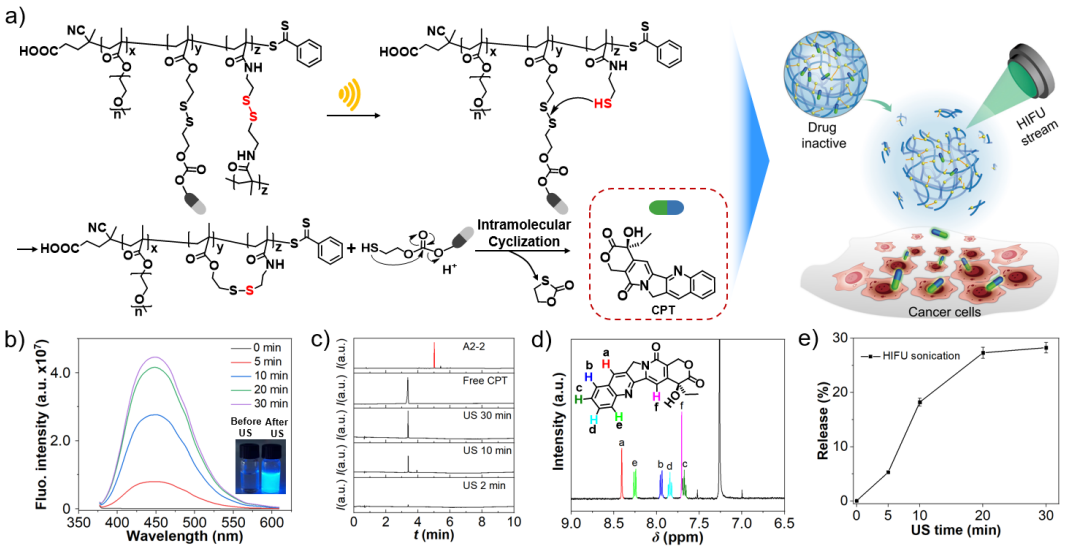

Figure 4. HIFU-induced disulfide mechanophore activation and model drug CPT release from MGLs. **a**) Schematic illustration of disulfide mechanophore activation in MGLs-CPT and the subsequent CPT release for *in vitro* cancer therapy. **b**) Fluorescence spectra of MGLs-CPT after HIFU treatment (0.66 MHz, 32W). Inset is the image of MGLs-CPT solution under 365 nm UV illumination before and after HIFU treatment. **c**) UPLC elugrams of A2-2, free CPT, and released CPT after HIFU treatment. **d**) Section from ^{1}H NMR spectrum of released CPT (400 MHz, $CDCl_3$). Color-coded signals indicate the characteristic peaks of CPT. **e**) The release profile of CPT from MGLs-CPT.

To evaluate MGLs-CPT for potential in vitro treatment, we conducted experiments to assess its ability to deliver the drug to cancer cells using CLSM and MTS proliferation assays. HeLa cells were treated with various conditions: PBS, free CPT, non-sonicated MGLs-CPT, and sonicated MGLs-CPT. Live cells were stained with calcein AM, and dead cells with propidium iodide (PI). Treatment with sonicated MGLs-CPT for 30 minutes resulted in nearly 100% cell death among HeLa cells (**Figure 5a**). Furthermore, the mixture of MGLs-CPT subjected to 20 minutes of sonication effectively inhibited HeLa cell growth (**Figure S24**). In contrast, PBS and non-sonicated MGLs-CPT showed no significant impact on HeLa cell survival.

Additionally, we investigated the half-maximal inhibitory concentration (IC_{50}) of PBS, CPT alone, CPT combined with HIFU (0.66 MHz, 30 min), non-sonicated MGLs-CPT, and sonicated MGLs-CPT (0.66 MHz, 20 min or 30 min). For MGLs-CPT, HIFU irradiation was applied *ex situ* before adding samples to the cell culture medium and incubating with HeLa cells. The IC_{50} values obtained after treating HeLa cells with these samples were analyzed (**Figure 5b**). Sonicated MGLs-CPT showed significantly lower IC_{50} compared to control samples. Control samples such as PBS exhibited no cytotoxic effects under the applied conditions. HeLa cells treated with different concentrations of non-sonicated MGLs samples showed high viability, suggesting minimal cell toxicity likely due to the good biocompatibility of the PEG chains. These results illustrate the successful HIFU-induced mechanochemical activation of disulfide bonds and drug release in MGLs-CPT for sonopharmacology.

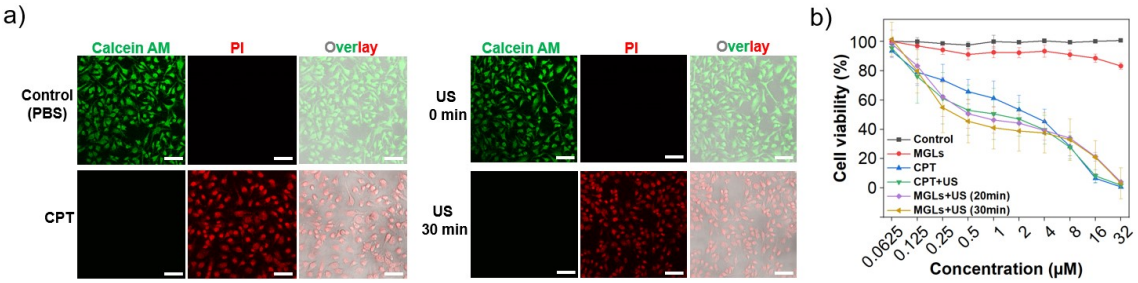

Figure 5. The potential of MGLs-CPT for in vitro treatment. **a**) CLSM images of HeLa cells treated with different conditions (Live cells: calcein-AM, green; Dead cells: Propidium Iodide (PI), red). (i) PBS. (ii) CPT. (iii) non-sonicated MGLs-CPT. (iv) Sonicated MGLs-CPT (0.66 MHz, 30 min). HeLa cells were stained for 5 min. Scale bars: 50 μm. **b**) Investigation of cell viability using MTS proliferation assay. Control (PBS), MGLs-CPT, CPT, CPT+US, and *ex situ* sonicated (0.66 MHz; 20 min or 30 min) MGLs-CPT mixed with HeLa cells. Mean values ± SD from the mean. $N = 3$ independent HIFU experiments (Table S2).

The activation efficiency of disulfide mechanophores in microgels depended on the crosslink density and size of the MGLs. For instance, 70% crosslinked MGLs-UMB (with respect to the PFPMA moieties) released 25% of UMB, whereas in 100% crosslinked MGLs-UMB, less than 5% was achieved (**Figure S25**). Higher crosslink density in MGLs enhances stability, potentially limiting chain solvation and facilitating interaction with flow fields in the surrounding medium. Conversely, minimal activation of disulfide mechanophores was observed in smaller (50 nm) MGLs-UMB (**Figure S25**), indicating that the size of polymer colloids also influences mechanophore activation. Previous studies have shown that 200 nm MGLs are highly responsive to low-frequency sonication, with 20 kHz treatment triggering releases exceeding 60%.[30] This suggests that larger MGLs require strong cavitation to activate mechanophores, explaining why 0.66 MHz sonication demonstrates superior activation efficiency compared to 1.5 or 2.5 MHz treatments at similar power intensities. The mechanical index (MI) serves as a crucial metric for evaluating cavitation bio-effects,[48-49] with diagnostic US scanners deemed safe by the FDA below an MI of 1.9. Here, for our polymeric nanomaterial system, we selected a 0.66 MHz transducer with 8 W acoustic power for the drug release assay due to its relatively low MI of 1.5.

4.4 Conclusions

In summary, our study demonstrates the activation of disulfide mechanophores in polymeric microgels (MGLs) via high-intensity focused ultrasound (HIFU), leading to the release of target molecules, including fluorophores and pharmaceuticals, through disulfide exchange and subsequent cleavage of a carbonate linker. MGL structures were characterized using TEM, the activation of mechanophores and molecular release were confirmed by ESI mass spectrometry and UPLC measurements. Fluorescence measurements quantified molecular release under various HIFU parameters, such as frequency, power, and duration. Additionally, an *in vitro* drug release study using the MGLs-CPT system evaluated the efficacy of released CPT with CLSM and MTS proliferation assays. A notable feature of this system is the use of HIFU, similar to that used in medical applications, marking a significant step in leveraging polymer mechanochemistry for biomedicine. This work also provides insights into designing new drug delivery systems based on polymer mechanochemistry with MHz HIFU, considering the diverse mechanophores and the versatile chemical reactions initiated by thiol groups.

4.5 Experimental section

4.5.1 Materials

All chemical reagents and solvents were used without further purification unless otherwise stated. 2-hydroxyethyl disulfide (technical grade, Sigma-Aldrich), methacryloyl chloride (97%, Sigma-Aldrich), triethylamine (TEA, ≥99%, Sigma-Aldrich), tetrahydrofuran (THF, anhydrous, Sigma-Aldrich), dichloromethane (DCM, anhydrous, ≥99.8%, Sigma-Aldrich), *N*,*N*′-disuccinimidyl carbonate (DSC, ≥95%, Sigma-Aldrich), toluene (≥99.5%, Sigma-Aldrich), 4-(dimethylamino)pyridine (DMAP, >99.0%, TCI Deutschland GmbH), 1,4-dioxane (99.8%, Sigma-Aldrich), triphosgene (TPS, 98%, Sigma-Aldrich) umbelliferon (UMB, 99%, ACROS ORGANICS), camptothecin (CPT, ≥95%, Abcr GmbH), 4-cyano-4-(phenylcarbonothioylthio)pentanoic acid (CPA, RAFT agent, Sigma-Aldrich), *N*,*N*-diisopropylethylamine (DIPEA, ≥99%, Sigma-Aldrich), $CuBr_2$ (99%, Sigma-Aldrich), Me_6TREN (97%, Sigma-Aldrich), cystamine dihydrochloride (≥97.0%, TCI Deutschland GmbH), 2-mercaptoethanol (MCE, >99.0%, TCI Deutschland GmbH), and bis[2-(2'-bromoisobutyryloxy)ethyl]disulfide (98%, Sigma-Aldrich) were used as received. Pentafluorophenyl methacrylate (PFPMA, 97%, Abcr GmbH) and poly(ethylene glycol) methyl ether methacrylate (PEGMEMA, M_n ~ 300 Da, Sigma-Aldrich) were purified by a column of activated basic Al_2O_3 to remove the inhibitor before utilization. 2,2'-azobis(2-methylpropionitrile) (AIBN, 98.0%) was obtained from Sigma-Aldrich and recrystallized twice from MeOH. Dialysis membranes (3.5 kDa MWCO) were obtained from Spectrum Labs. Centrifugal filter (3000 MWCO) was obtained from Sartorius. HeLa cell line was obtained from ATCC: The Global Bioresource Center. Ultrapure Milli-Q water (18.2 MΩ·cm) was used.

4.5.2 Analytical Instrumentation

^{1}H and ^{13}C NMR spectra were measured at room temperature in $CDCl_3$ with a 400 MHz Bruker Avance 400 spectrometer (^{13}C: 101 MHz). The chemical shifts are reported in δ units using residual protonated solvent signals as internal standard (^{1}H: $CDCl_3$ ($^{\delta}$H = 7.26 ppm), ^{13}C: $CDCl_3$ ($^{\delta}$C = 77.16 ppm)). Thin-layer chromatography (TLC) was conducted on Merck TLC Silica Gel 60 F_{254} plates, which featured a fluorescence indicator for visualization under 254 nm or 365 nm UV light using a hand lamp. High-purity silica gel (40-63 μm) was utilized for flash column chromatography. Gel permeation chromatography (GPC/SEC) with THF (HPLC grade) was performed using a Jasco PU-2080plus HPLC pump equipped with a Jasco RI-2031plus refractive index detector. As an internal standard, the sample solvent contained 250 mg/mL 3,5-di-*t*-4-butylhydroxytoluene (BHT, ≥99%, Fluka). A pre-column (8×50 mm) and four SDplus gel columns (8×300 mm, SDplus, MZ Analysentechnik) were used at a controlled flow rate of 1.0 mL/min at 20 °C. The gel particles had a diameter of 5 μm, with nominal pore sizes of 50, 102, 103, and 104 Å. Calibration was performed using narrowly distributed poly(methyl methacrylate) (PMMA) standards from Polymer Standards Service. Molar masses (M_n and M_w) and molar mass distributions (M_w/M_n) were determined using PSS WinGPC UniChrom software (Version 8.1.1). Ultra-high-performance liquid chromatography-mass spectrometry (UHPLC-MS) analysis was conducted using an ACQUITY UPLC I-Class System (Waters) equipped with an ACQUITY UPLC PDA eλ Detector and an ACQUITY QDa detector (Waters). Solvents: A= water (contained 0.1% TFA), B= acetonitrile (contained 0.1% TFA); Flow= 0.4 mL min^{-1}; Gradient (B): 0-1 min (10%), 1-5 min (10% - 90%), 5-7 min (90%), 7-10 min (90% - 10%). ESI MS: micrOTOF-Q II™ ESI-Qq-TOF mass spectrometer system

(BRUKER). Transmission electron microscopy (TEM) images were captured on a LIBRA®120 transmission electron microscope (Carl Zeiss) with an accelerating voltage of 120 kV and images were recorded using a Gatan Ultra Scan 1000. Transmission electron microscopy (TEM) sample preparation: a single drop (~10 μL) of the sample was carefully placed onto a carbon-coated copper grid and left to air-dry. Dynamic light scattering (DLS) measurements were performed using a Zetasizer Ultra instrument (Malvern). For analysis, samples were dispersed in H_2O/DMSO mixture (4:1, v/v) and subsequently transferred to a disposable plastic cuvette for measurement.

4.5.3 Fluorescence Spectroscopy

Fluorescence spectroscopy was performed on a SpectraMax iD3 spectrometer (Molecular Devices) at room temperature. For fluorescence spectra measurements of MGLs-UMB, samples were excited at 325 nm. The spectral bandwidths were set to 1 nm (370 ~ 600 nm) for emission. For obtaining the standard curve of UMB, the fluorescence value was collected at emission wavelength of 465 nm. For fluorescence spectra measurements of MGLs-CPT, samples were excited at 335 nm. The spectral bandwidths were set to 2 nm (375 ~ 610 nm) for emission. For obtaining the standard curve of CPT, the fluorescence value was collected at emission wavelength of 449 nm. The integration time was 0.1 s and all spectroscopic measurements were carried out with pureGrade™ 96-wells plate purchased from BRAND GmbH. Multiple essential filtration steps were necessary for the thoroughly sonicated solution of MGLs before proceeding with the crucial fluorescence measurements. The meticulous filtration process was carried out in the following detailed steps: First, rigorous centrifugation was performed thrice at a high speed of 10000 rpm for 10 minutes each. Following this intensive centrifugation process, the resulting suspensions were carefully filtered through a centrifugal filter with a molecular weight cutoff of 3000 MWCO (centrifugation at 5000 rpm).

4.5.4 Sonication Experiments

Sonication experiments were performed with a home-built HIFU setup. The core devices include waveform generator (33511B, Keysight Technologies), RF amplifier (AG1021, T&C Power Conversion, Inc.) and transducers (0.66 MHz, 1.5 MHz and 2.5 MHz, Precision Acoustics Ltd., UK). A 0.5 mm needle hydrophone (Precision Acoustics Ltd., UK) was used for locating the transducer focal point. Custom-made motorized 3D-manipulator/positioning system for controlling the well plate submerged in water was employed. Pulsed sonication (2 s on, 1 s off) was used. 10 mg of polymers was dissolved entirely in a prepared 1 mL mixture of H_2O/DMSO, maintaining a volume ratio of 4:1 (v/v). Next, 1 mL of this mixed solution was gently added into the wells of a specialized 24-well plate, designed with a highly transparent, ultra-thin film base (lumox® multiwall 24, SARSTEDT). The well plate was then securely positioned in the designated well plate holder, ensuring stability throughout the sonication process. Each sample underwent continuous sonication for a precisely controlled duration. Then, it will be kept for 72 hours, allowing sufficient time for the downstream release reactions at room temperature. Finally, the processed samples were prepared for detailed fluorescence measurements.

4.5.5 Cell Imaging

HeLa cells designated for imaging were meticulously cultured in Dulbecco's Modified Eagle's Medium (DMEM), enriched with 10% heat-inactivated fetal bovine serum (FBS) and supplemented with 100 U/mL

penicillin and 100 μg/mL streptomycin. The incubation was maintained at 37 °C under a precisely controlled humidified atmosphere containing 5% CO_2 to ensure optimal cell viability and proliferation. For imaging studies, HeLa cells were carefully seeded into ibidi μ-Slide 8 Wells (glass-bottomed) at a density of 2.5×10^5 cells per well in 500 μL of culture medium, ensuring uniform distribution and adherence for high-resolution microscopy analysis. After 24 h, HeLa cells were incubated with different concentrated sonicated samples or non-sonicated samples in PBS at 37 °C, then washed with phosphate-buffered saline (PBS) for three times. Then, PBS was added into the wells (500 μL per well), 2 μL (1 mg mL^{-1}) calcein AM and 2 μL (1 mg mL^{-1}) propidium iodide were transferred to the wells and mixed for 5 min. PBS was used to wash out the free cell imaging agents. Then the fluorescence imaging of cells was performed on a confocal laser scanning microscope (STP8, Leica) (confocal excitation: calcein AM: 496 nm, propidium iodide: 561 nm) and analyzed by ImageJ.

4.5.6 MTS Proliferation Assays

HeLa cells were used to evaluate the cytotoxicity of different samples. HeLa cells were cultured in a basal medium containing DMEM (supplemented with 10% fetal bovine serum and 1% antibiotics/antimycotics) at 37 °C. Actual cell viability was monitored by using a tetrazolium compound 3-(4,5-dimethylthiazol-2-yl)-5-(3-carboxymethoxyphenyl)-2-(4-sulfophenyl)-2H-tetrazolium (inner salt, MTS reagent) and a chemical electron acceptor dye (phenazine ethosulfate; PES) (Promega, Germany) using an assay according to the manufacturer's instructions. Briefly, approximately 5,000 cells in 100 μL of medium were seeded into 96-well plates. Following overnight incubation, the existing medium was carefully aspirated and replaced with 100 μL of fresh medium containing varying concentrations of the test samples. Control wells received DMSO alone, ensuring that its final concentration did not exceed 0.5% to prevent cytotoxic interference. After 48 hours of incubation, the culture medium was gently removed, and the cells were rinsed with 100 μL of PBS buffer to eliminate residuals. Subsequently, 20 μL of MTS reagent was combined with 100 μL of fresh medium and added to each well. A mixture of MTS reagent with culture medium served as the negative control. To ensure homogeneity, the solution was thoroughly mixed, and absorbance was measured at 490 nm using a Synerg^{TM} HT microplate reader (BioTek Instruments). The resulting MTS signals were analyzed to assess cell viability and proliferation. All experimental conditions were conducted in at least triplicate to ensure statistical reliability.

4.5.7 Synthetic procedures and characterization data

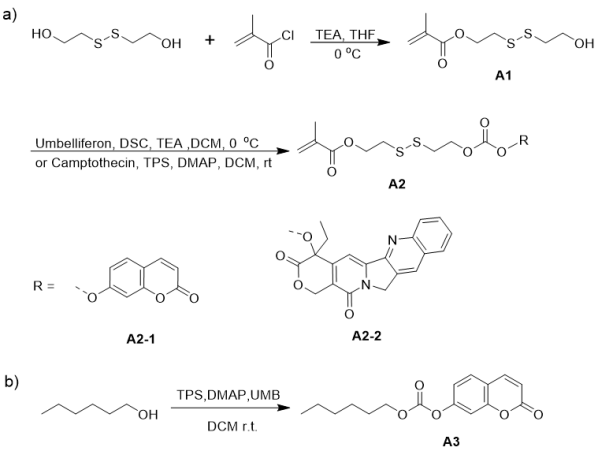

Scheme S1. Syntheses of **A2** and **A3**.

2-((2-hydroxyethyl)disulfaneyl)ethyl methacrylate (**A1**)

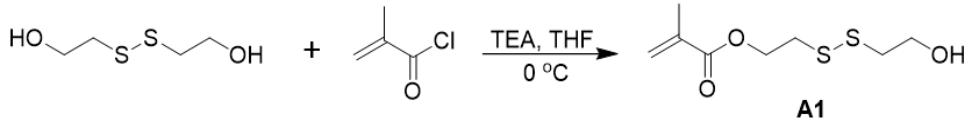

A1

The preparation of **A1** was carried out according to an adapted literature protocol.[50] 2-hydroxyethyl disulfide (2.0 g, 13 mmol, 1 equiv.) and TEA (3.0 mL, 21.5 mmol, 1.65 equiv.) were added in THF (30 mL) with a constant flow of N_2. The mixture was subjected into the ice-water bath to keep the temperature at 0 °C. Afterwards, a solution of methacryloyl chloride (1.3 mL, 13.3 mmol, 1.02 equiv.) and 15 mL CH_2Cl_2 was added dropwise (15 mL/h) to the reaction mixture via an injection pump. The reaction mixture was continuously stirred until the starting material was entirely consumed, as confirmed by TLC analysis. Then, it was washed with brine and deionized water three times, respectively. Afterwards, the crude product was purified by column chromatography on silica gel (hexane:EtOAc = 5:1) to give compound **A1** (2.2 g, 76% yield) as a colorless oil. **^{1}H NMR (400 MHz, $CDCl_3$):** δ (ppm): 6.12 (s, 1H), 5.55 (t, J=1.6 Hz, 1H), 4.41 (t, J=6.8 Hz, 2H), 3.87 (t, J=6.0 Hz, 2H), 2.96 (t, J=6.8 Hz, 2H), 2.87 (t, J=6.0 Hz, 2H), 2.21 (br, 1H), 1.93 (s, 3H). See Figure S1-1. **^{13}C NMR (101 MHz, $CDCl_3$):** δ (ppm): 167.37, 136.09, 126.24, 62.73, 60.30, 41.74, 37.08, 18.38. See Figure S1-2. **ESI-MS** (m/z) for $C_8H_{14}O_3S_2$ expected $[M+Na]^+$: 245.0277, Found for $[M+Na]^+$: 245.0242.

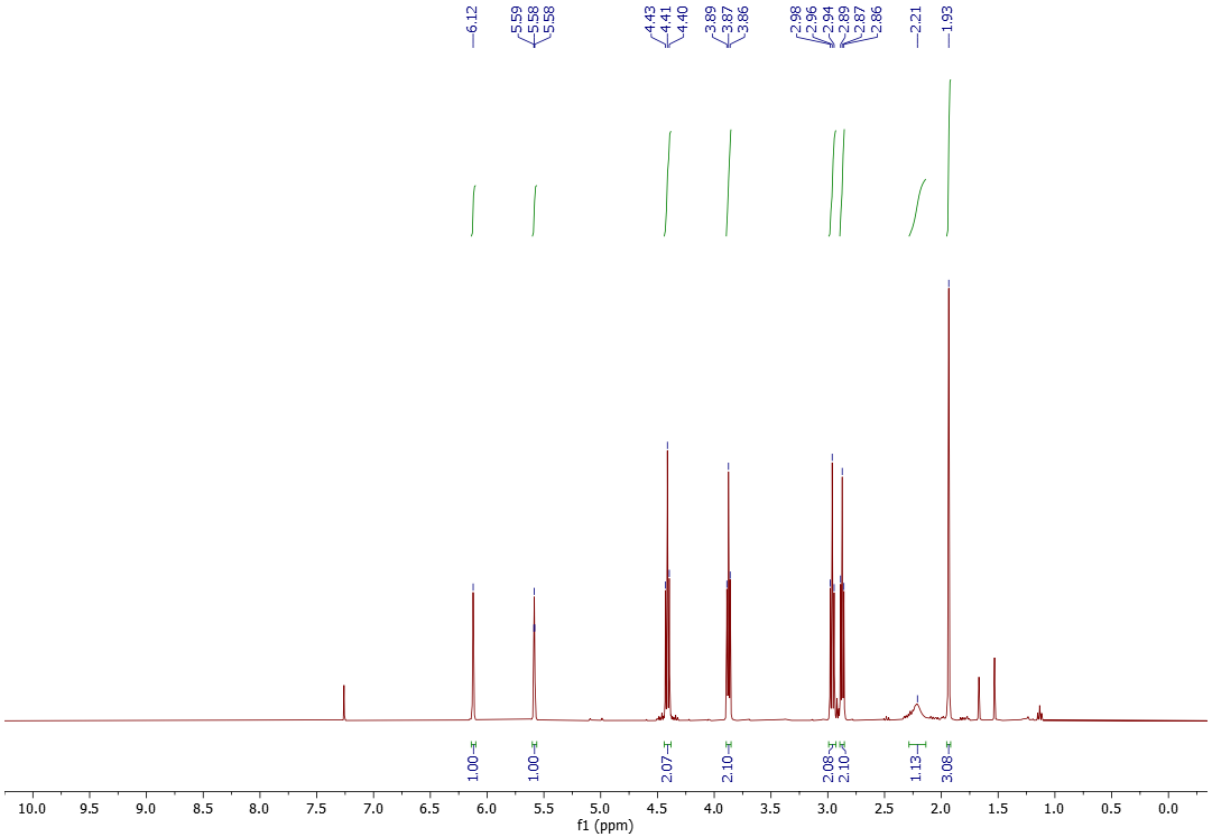

^{1}H NMR spectrum of **A1**.

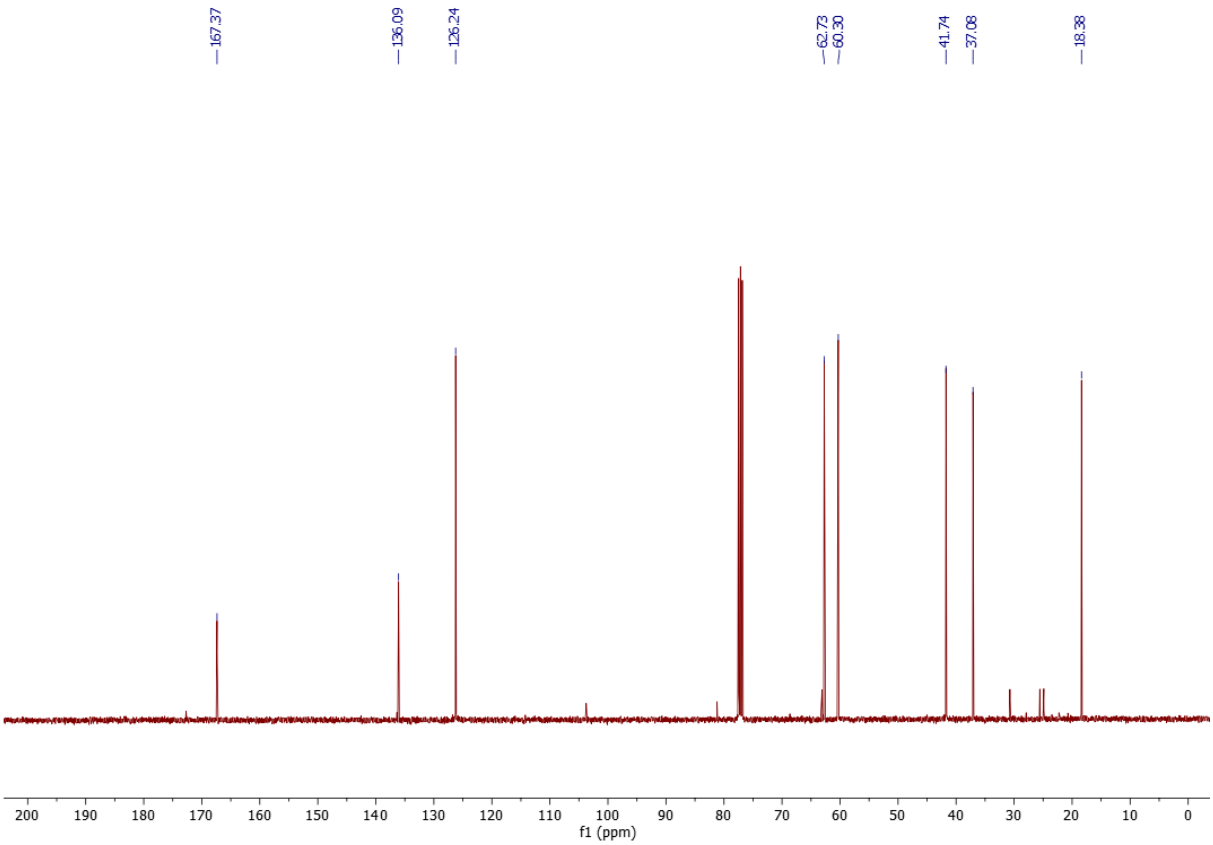

^{13}C NMR spectrum of **A1**.

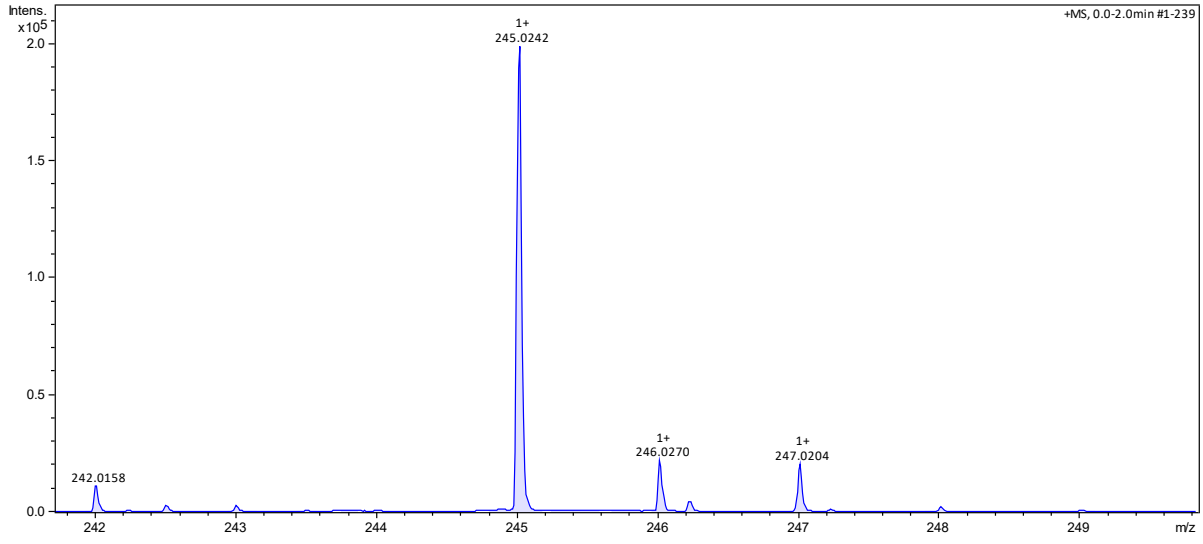

ESI-MS (*m*/*z*) of **A1**.

2-((2-((((2-oxo-2H-chromen-7-yl)oxy)carbonyl)oxy)ethyl)disulfaneyl)ethyl methacrylate (**A2-1**)

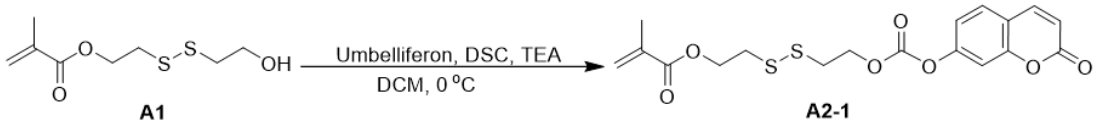

A2-1 was synthesized by following the reported literature.[24] *N,N'*-disuccinimidyl carbonate (133 mg, 0.52 mmol, 1.0 equiv.) and Et_3N (90 µL, 0.65 µmol, 1.25 equiv.) were dissolved in 1.5 mL CH_2Cl_2. The mixture was cooled to 0 °C with an ice-water bath. Then, a solution of **A1** (115 mg, 0.52 mmol, 1.0 equiv.) in 1 mL CH_2Cl_2 was added. The reaction mixture was allowed to stir in the ice-water bath for 1 h. Subsequently, a solution of umbelliferone (UMB, 84 mg, 0.52 mmol, 1 equiv.), Et_3N (90 µL, 0.65 mmol, 1.25 equiv.) and CH_2Cl_2/DMF (1.65 mL, v/v,10:1) was added into the reaction mixture. The reaction mixture was stirred for another 1 h at 0 °C. Then, the reaction mixture was allowed to warm up slowly to room temperature for further reaction. The reaction mixture was continuously stirred until the starting material was entirely consumed, as confirmed by TLC analysis. Then, the solvent was completely removed under reduced pressure. The remaining residue was then re-dissolved in CH_2Cl_2, and it was washed with deionized water three times. The mixture was then purified by silica column chromatography (hexane:EtOAc = 4:1) to give compound **A2-1** (128 mg, 60% yield) as a colorless oil. **^{1}H NMR (400 MHz, $CDCl_3$):** δ (ppm): 7.68 (d, *J*=9.6 Hz, 1H), 7.48 (d, *J*=8.4 Hz, 1H), 7.19 (d, *J*=2.4 Hz, 1H), 7.11-7.14 (dd, *J*=2.4, 8.4 Hz, 1H), 6.37 (d, *J*=9.6 Hz, 1H), 6.11 (s, 1H), 5.57 (t, *J*=1.6 Hz, 1H), 4.51 (t, *J*=6.8 Hz, 2H), 4.40 (t, *J*=6.8 Hz, 2H), 2.97-3.03 (m, 4H), 1.92 (s, 3H). See Figure S2-1. **^{13}C NMR (101 MHz, $CDCl_3$):** δ (ppm): 167.13, 160.20, 154.65, 153.25, 152.61, 142.80, 136.00, 128.79, 126.13, 117.69, 116.92, 116.31, 109.88, 66.73, 62.50, 37.25, 36.85, 18.32. See Figure S2-2. **ESI-MS (*m/z*)** for $C_{18}H_{18}O_7S_2$ expected $[M+H]^+$: 411.0567, Found for $[M+H]^+$: 411.0531.

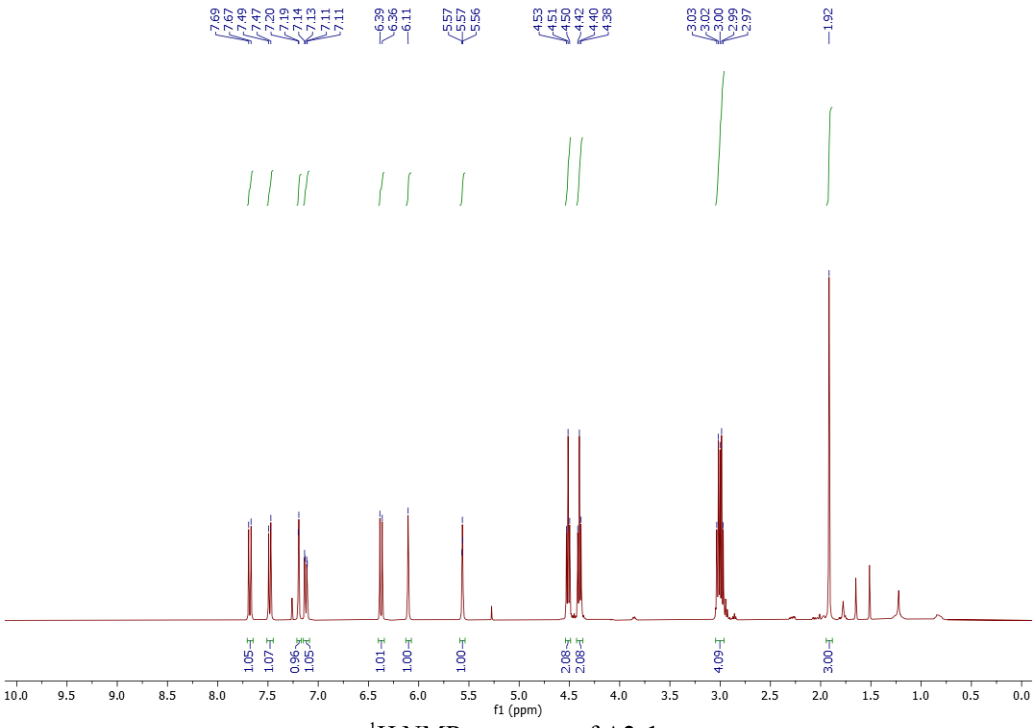

^{1}H NMR spectrum of **A2-1**.

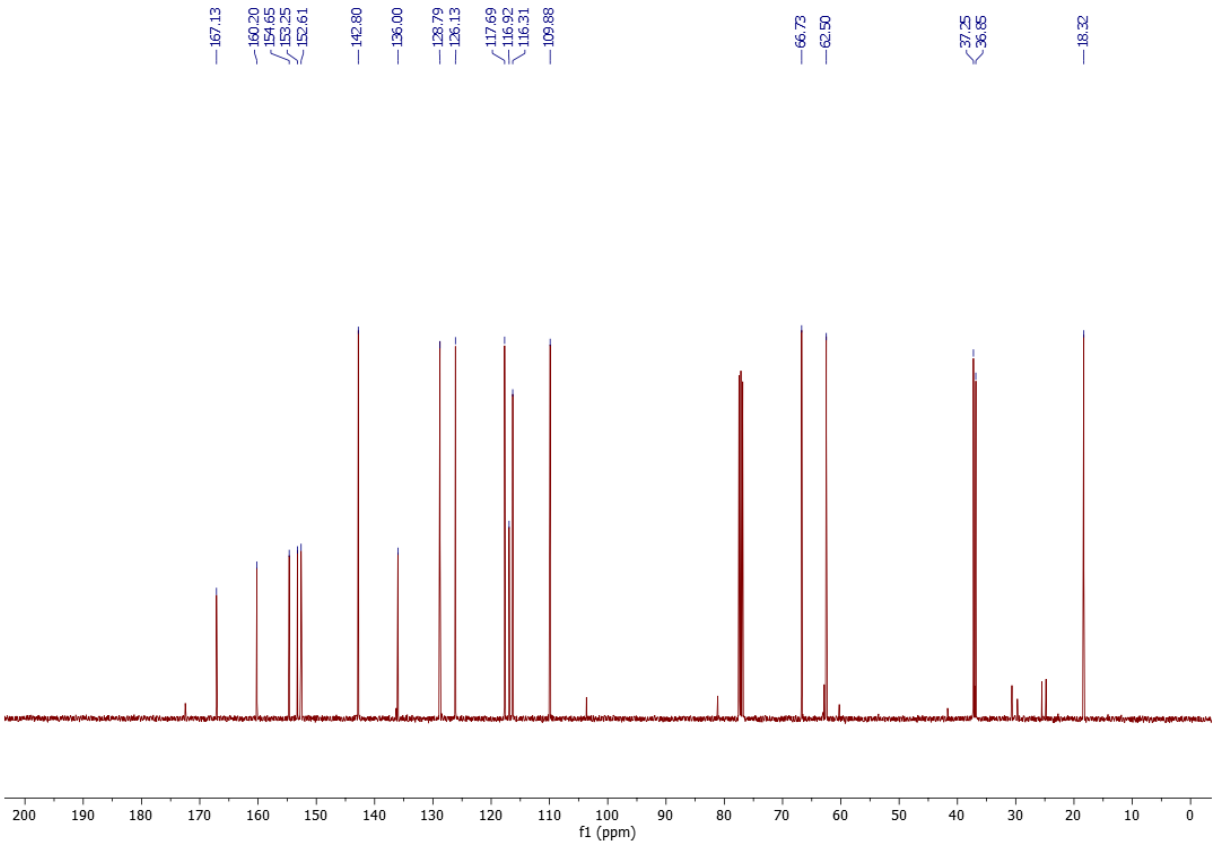

^{13}C NMR spectrum of **A2-1**.

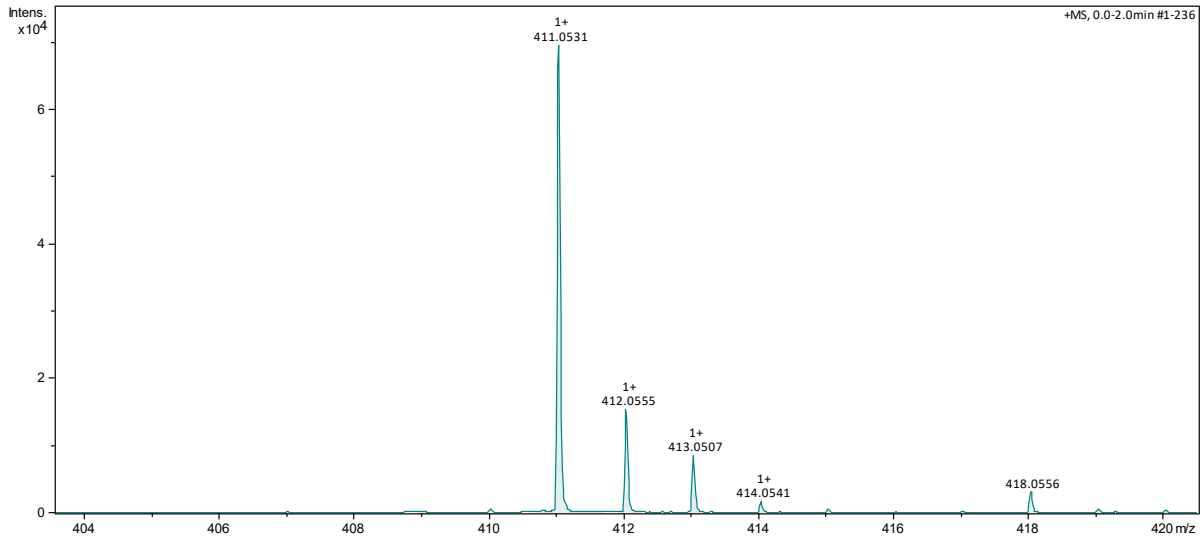

ESI-MS (*m/z*) of **A2-1**.

2-((2-((((4-ethyl-3,14-dioxo-3,4,12,14-tetrahydro-1H-pyrano[3',4':6,7]indolizino[1,2-b]quinolin-4-yl)oxy)carbonyl)oxy)ethyl)disulfaneyl)ethyl methacrylate (**A2-2**)

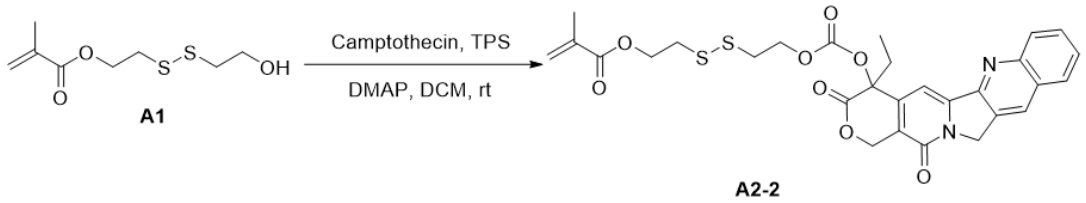

The synthesis of **A2-2** was performed using an adapted literature protocol.[51] Camptothecin (CPT, 200 mg, 0.57 mmol) was dissolved in 12 mL anhydrous CH_2Cl_2. Then, triphosgene (TPS, 70 mg, 0.23 mmol) was added under stirring. After 5 min stirring, DMAP (224 mg, 1.83 mmol) in 0.5 mL CH_2Cl_2 was added into the mixture and stirred for another 1 h at room temperature. Afterwards, a solution of **A1** (378mg, 1.7 mmol) and 1 mL CH_2Cl_2 was added to the reaction mixture for further reaction overnight. Subsequently, the excess phosgene (CAUTION: TOXIC) was removed by Ar purging and neutralized by bubbling the exhaust gas through a 2 M NaOH solution. Afterwards, the reaction mixture was washed three times with H_2O. Then, the crude product was purified by column chromatography on silica gel (hexane:EtOAc = 1:1) to give compound **A2-2** (180 mg, 53% yield) as a white solid. **^{1}H NMR (400 MHz, $CDCl_3$):** δ (ppm): 8.39 (s, 1H), 8.22 (d, *J*=8.4 Hz, 1H), 7.93 (d, *J*=8.0 Hz, 1H), 7.83 (m, 1H), 7.66 (m, 1H), 7.34 (s, 1H), 6.07 (s, 1H), 5.69 (d, *J*=17.2 Hz, 1H), 5.54 (t, *J*=1.6 Hz, 1H), 5.38 (d, *J*=17.2 Hz, 1H), 5.28 (s, 2H), 4.31-4.39 (m, 4H), 2.92 (q, *J*=6.0 Hz, 4H), 2.32-2.23 (m, 1H), 2.19-2.10 (m, 1H), 1.89 (s, 3H), 1.00 (t, *J*=7.6 Hz, 3H). See Figure S3-1. **^{13}C NMR (101 MHz, $CDCl_3$):** δ (ppm): 167.37, 167.15, 157.39, 153.57, 152.37, 148.94, 146.56, 145.71, 136.06, 131.35, 130.88, 129.74, 128.59, 128.32, 128.30, 128.23, 126.10, 120.40, 96.13, 78.14, 67.19, 66.65, 62.52, 50.12, 37.35, 36.67, 32.00, 18.36, 7.75. See Figure S3-2. **ESI-MS:** (*m/z*) for $C_{29}H_{28}N_2O_8S_2$ expected $[M+H]^+$: 597.1360, Found for $[M+H]^+$: 597.1328.

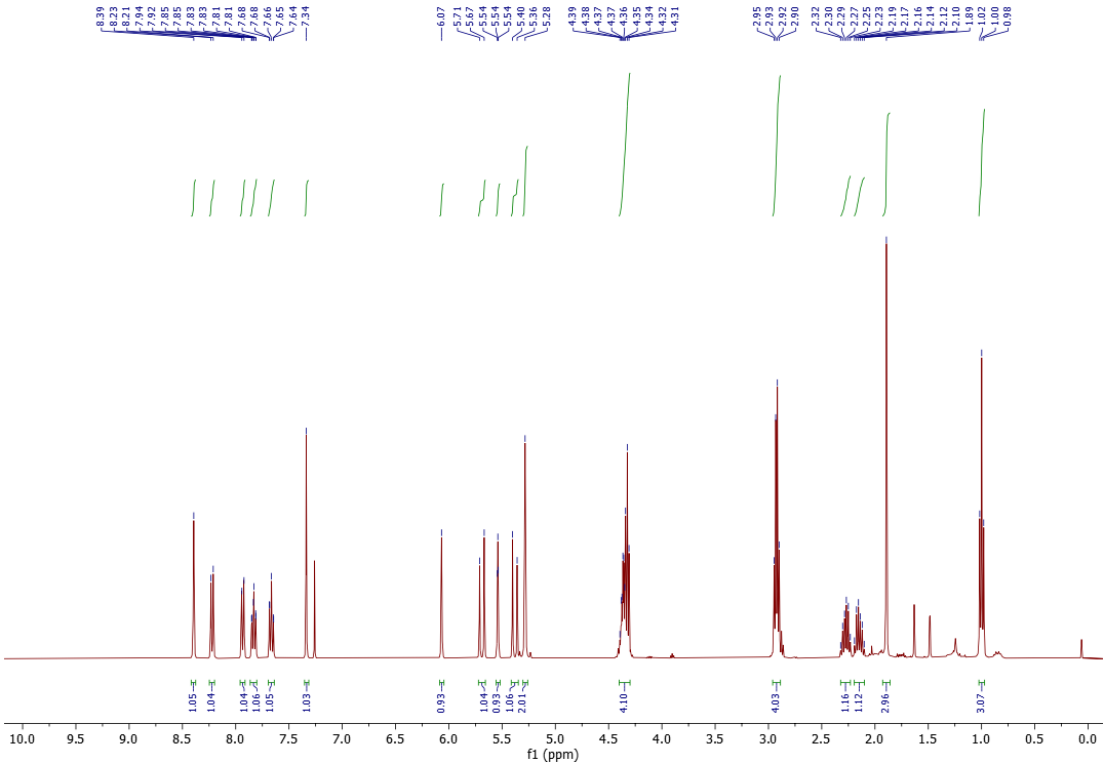

^{1}H NMR spectrum of **A2-2**.

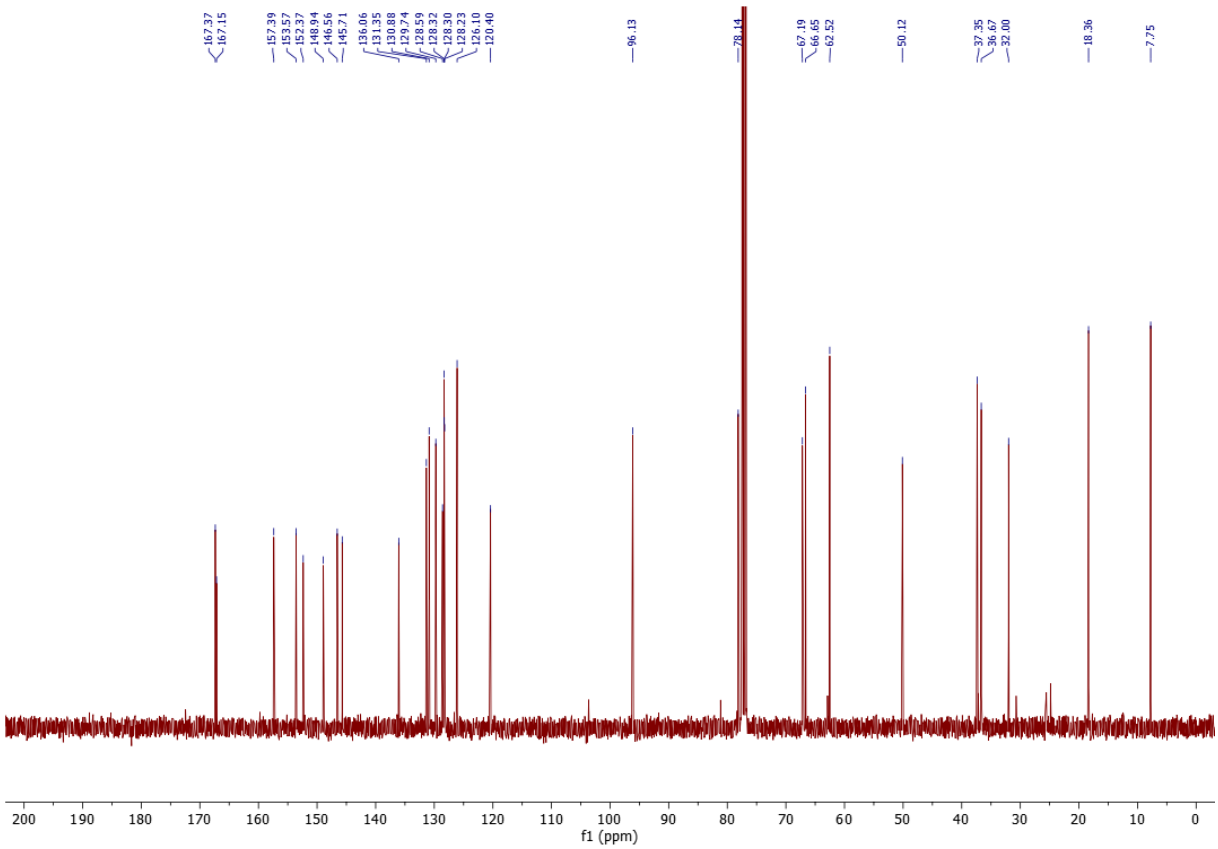

^{13}C NMR spectrum of **A2-2**.

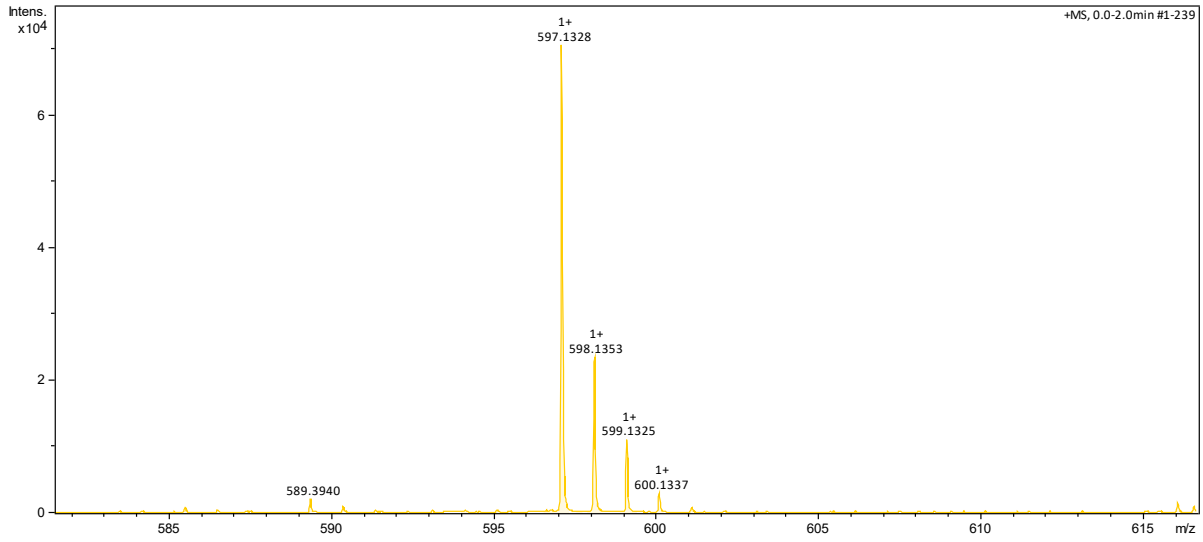

ESI-MS (*m/z*) of **A2-2**.

Hexyl (2-oxo-2H-chromen-7-yl) carbonate (**A3**)

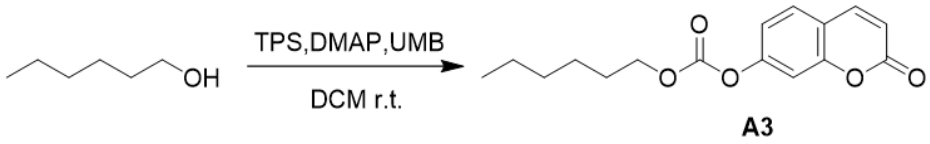

A3

Umbelliferone (UMB, 47 mg, 0.29 mmol) was dissolved in 6 mL anhydrous CH_2Cl_2. Then, triphosgene (TPS, 40 mg, 0.13 mmol) was added under stirring. After 5 min stirring, DMAP (112 mg, 0.91 mmol) was added into the mixture that was stirred for another 1 h at room temperature. Afterwards, a solution of hexanol (70 mg, 0.68 mmol) in 1 mL CH_2Cl_2 was added to the reaction mixture for further reaction overnight. Subsequently, the excess unreacted phosgene (CAUTION: TOXIC) was removed by Ar purging and neutralized by bubbling the exhaust gas through a 2 M NaOH solution. Afterwards, the reaction mixture was washed three times with H_2O and the crude product was purified by column chromatography on silica gel (CH_2Cl_2:MeOH = 50:1) to give compound **A3** (63 mg, 75% yield) as a white solid. **^{1}H NMR (400 MHz, $CDCl_3$):** δ (ppm): 7.68 (d, J=9.6 Hz, 1H), 7.48 (d, J=8.4 Hz, 1H), 7.20 (d, J=2.0 Hz, 1H), 7.13 (q, J=2.0 Hz, 1H), 6.38 (d, J=9.6 Hz, 1H), 4.27 (t, J=6.8 Hz, 2H), 1.78-1.70 (m, 2H), 1.45-1.30 (m, 6H), 0.89 (t, J=6.8 Hz, 3H). See Figure S3-1. **^{13}C NMR (101 MHz, $CDCl_3$):** δ (ppm): 160.36, 154.72, 153.51, 152.95, 142.88, 128.75, 117.85, 116.82, 116.24, 110.00, 69.64, 31.43, 28.56, 25.41, 22.58, 14.07. See Figure S3-2. **ESI-MS (*m/z*)** for $C_{16}H_{18}O_5$ expected $[M+H]^+$: 291.1227, Found for $[M+H]^+$: 291.1275.

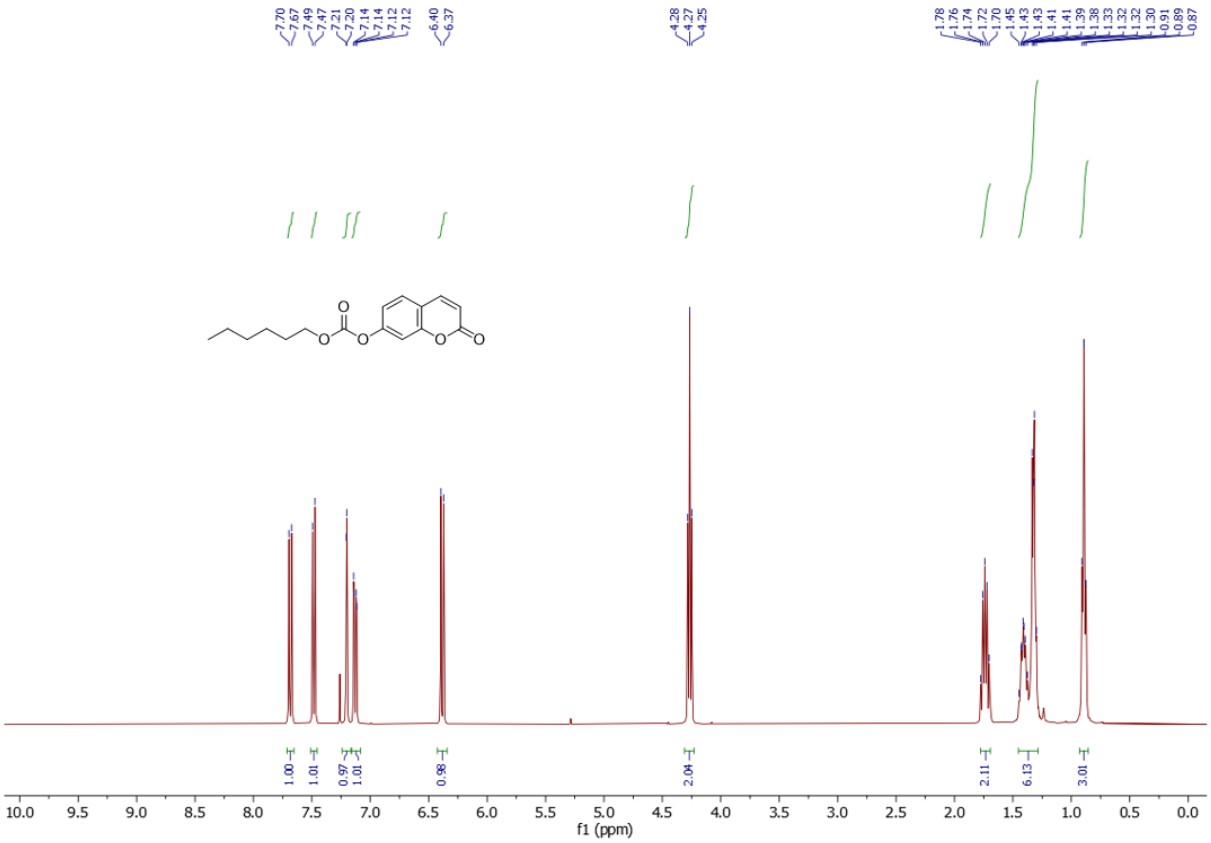

^{1}H NMR spectrum of **A3**.

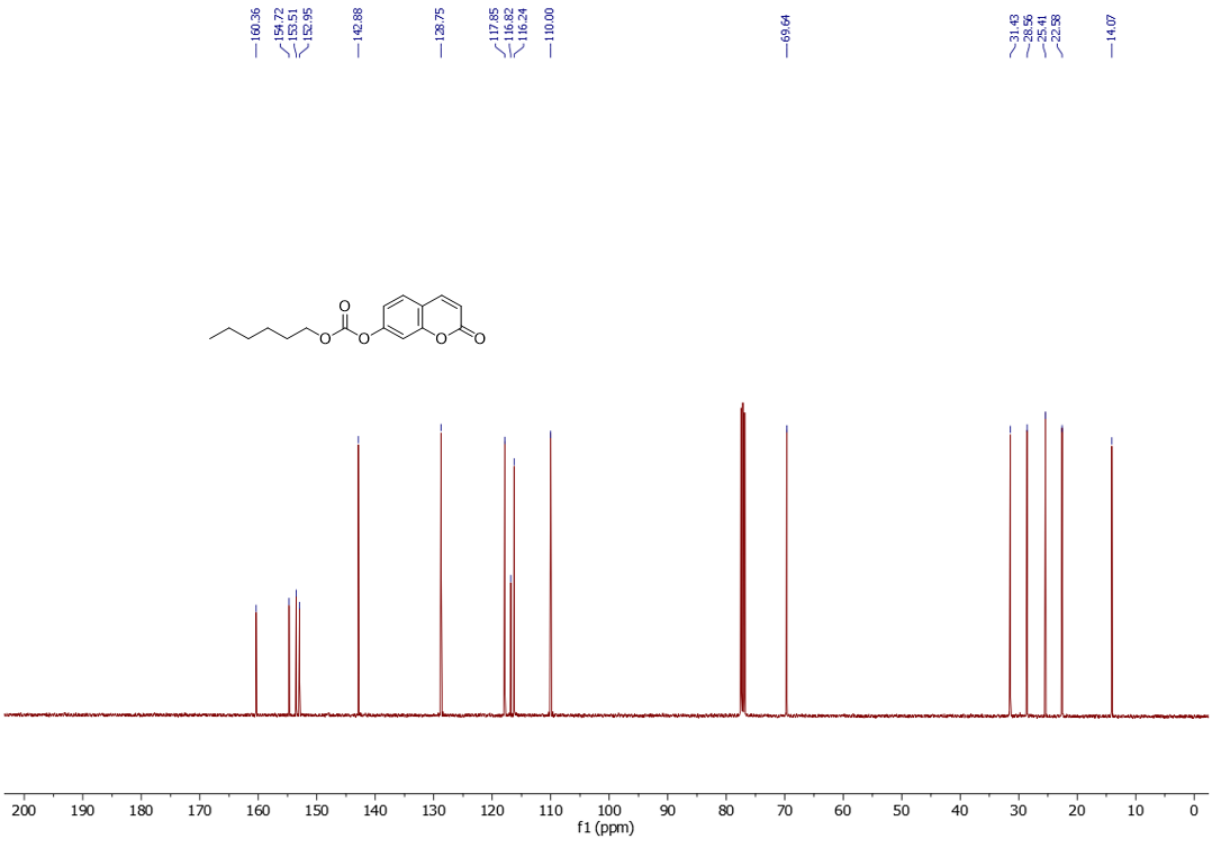

^{13}C NMR spectrum of **A3**.

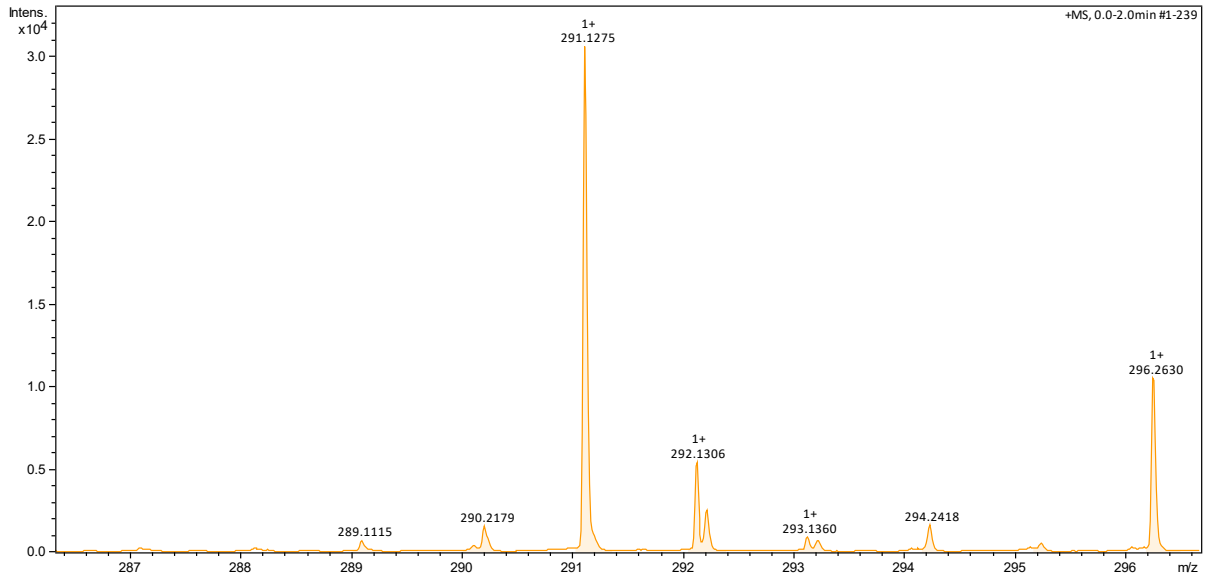

ESI-MS (*m/z*) of **A3**.

4.5.8 Synthesis of Microgels (MGLs)

4.5.8.1 Synthesis of MGLs-UMB

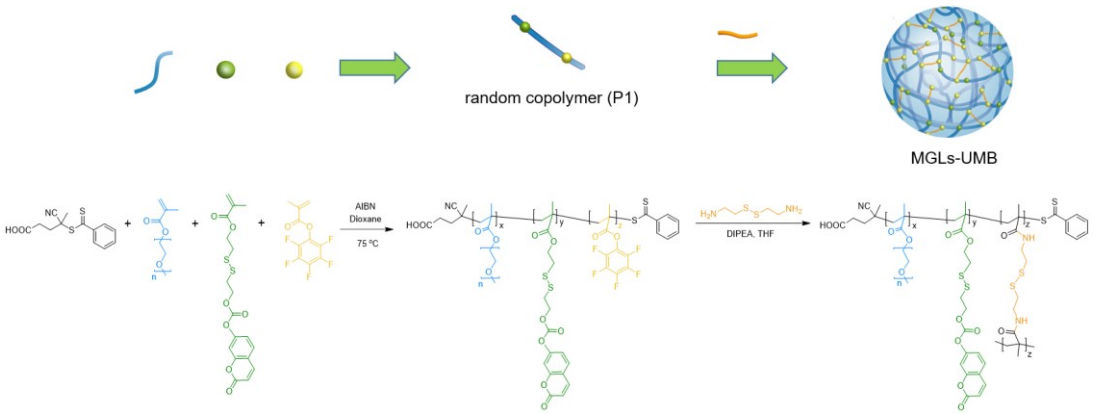

Scheme S2: Synthesis of MGLs-UMB.

Microgels-UMB (MGLs-UMB) were prepared by following reported literature rocedures.[30, 52-53]

(1) Synthesis of random copolymer P1: Copolymers P1 were obtained by a reversible addition-fragmentation chain-transfer (RAFT) polymerization reaction (Scheme S5). Pentafluorophenyl methacrylate (PFPMA, 215 mg, 0.9 mmol, 6.0 equiv.), poly(ethylene glycol) methyl ether methacrylate (PEGMEMA, 720 mg, 2.4 mmol, 16 equiv.), **A2-1** (62 mg, 0.15 mmol, 1.0 equiv.), 2,2'-Azobis(2-methylpropionitrile) (AIBN, 3 mg, 0.018 mmol), 4-cyano-4-(phenylcarbonothioylthio)pe-ntanoic acid (33.5 mg, 0.12 mmol) and 1,4-dioxane (2 mL) were added into a Schlenk-flask. The solution underwent three consecutive freeze-pump-thaw cycles to remove dissolved gas before the sealed Schlenk flask was placed in a 75 °C oil bath. Polymerization proceeded for 5 days and was then halted by immersing the flask in cold water (0 ºC) for 10 minutes. After solvent removal under reduced pressure, the polymer solution was slowly added dropwise into ice-cold hexane under continuous stirring, leading to precipitation. The supernatant was decanted, and the polymer was dissolved in THF before undergoing a second precipitation in hexane. This process was repeated three times to obtain the pure polymer. GPC (THF): P1 with the M_n = 12.9 kDa, $Đ_M$ = 1.43. By comparing the integral of the methylene protons adjacent to the ester in the polyethylene glycol unit and the polymer backbone proton in both the polyethylene glycol and the pentafluorophenyl units, the molar ratio was found to be 14:5:1 (PEGMEMA: PFPMA: **A2-1**).

(2) Synthesis of MGLs-UMB: The copolymers P1 showed amphiphilic character and formed stable assemblies in solution, which were then crosslinked to form MGLs-UMB (Scheme S5). MGLs-UMB synthesis was performed by base-catalyzed nucleophilic addition/elimination of cystamine to the PFPMA moieties in P1 polymers. First, P1 were dissolved in dry THF (10 mg/mL). Then, cystamine dihydrochloride (0.35 equiv. with respect to the PFPMA moieties) and DIPEA (1.0 equiv.) were added into the polymer solution. The solution was then heated at 55 °C for 6 h to afford 70% (relative to the PFPMA moieties) cross-linked MGLs-UMB. Pentafluorophenolate acted as a leaving group, allowing reaction monitoring via ^{19}F-NMR spectroscopy (Figure S23). H_2O was then added to the MGLs solution, and THF was removed by stirring in air for 24 h. Finally, the polymers solution was further purified by dialysis in Milli-Q water for 3 days. The MGLs-UMB were characterized by TEM (Figure 3b, Figure S24). In addition, smaller size (average size 50 nm) MGLs-UMB were synthesized by a slightly modified approach. P1 were dissolved in dry THF (2 mg/mL). Then, cystamine dihydrochloride (0.35 equiv. with respect to the PFPMA moieties) and DIPEA (1.0 equiv.) were added into the polymer solution. The solution was then heated at 55 °C for 6 h. Then, H_2O was added to the MGLs solution and

THF was evaporated by stirring the solution in air for 24 h. After that, the MGLs solution was further purified by dialysis in milliQ water for 3 d.

4.5.8.2 Synthesis of MGLs-CPT

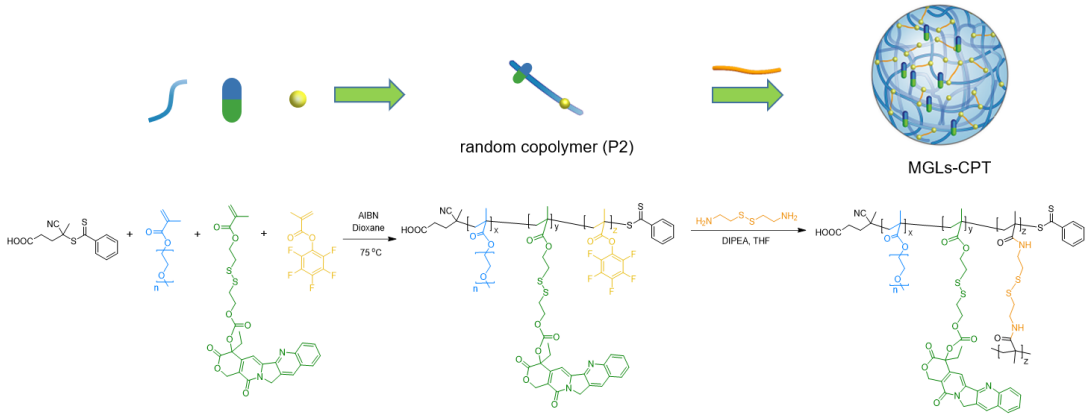

Scheme S3: Synthesis of MGLs-CPT.

(1) Synthesis of random copolymer P2: Pentafluorophenyl methacrylate (PFPMA, 200 mg, 0.84 mmol, 4.2 equiv.), poly(ethylene glycol) methyl ether methacrylate (PEGMEMA, 624 mg, 2.08 mmol, 10.4 equiv.), **A2-2** (120 mg, 0.2 mmol, 1.0 equiv.), 2,2'-azobis(2-methylpropionitrile) (AIBN, 4 mg, 0.024 mmol), 4-cyano-4-(phenylcarbonothioylthio)pentanoic acid (24 mg, 0.086 mmol) and 1, 4-dioxane (2.5 mL) were added into a Schlenk-flask. The solution underwent three consecutive freeze-pump-thaw cycles to remove dissolved gas before the sealed Schlenk flask was placed in a 75 °C oil bath. Polymerization proceeded for 5 days and was then halted by immersing the flask in cold water (0 °C) for 10 minutes. After solvent removal under reduced pressure, the polymer solution was slowly added dropwise into ice-cold hexane under continuous stirring, leading to precipitation. The supernatant was decanted, and the polymer was dissolved in THF before undergoing a second precipitation in hexane. This process was repeated three times to obtain the pure polymer. GPC (THF): **P2** with the M_n = 20.8 kDa, $Đ_M$ = 1.46. By comparing the integral of the methylene protons adjacent to the ester in the polyethylene glycol unit and the polymer backbone proton in both the polyethylene glycol and the pentafluorophenyl units, the molar ratio was found to be 17:4:1 (PEGMEMA: PFPMA: **A2-2**).

(2) Synthesis of MGLs-CPT: Microgels (MGLs) were prepared following literature procedures.[52-53] The copolymers P2 showed amphiphilic character and formed stable assemblies in solution, which were then cross linked to form MGLs-CPT (Scheme S6). MGLs-CPT synthesis was performed by the base-catalyzed nucleophilic addition/elimination of cystamine to the PFPMA moieties in polymers **P2**. First, **P2** were dissolved in dry THF (10 mg/mL). Then, cystamine dihydrochloride (0.35 equiv. with respect to the PFPMA moieties) and DIPEA (1 equiv.) were added into the polymer solution. The solution was then heated at 55 °C for 6 h to afford 70% cross-linked MGLs. Pentafluorophenolate acted as a leaving group, allowing reaction monitoring via ^{19}F-NMR spectroscopy. H_2O was then added to the MGLs solution, and THF was removed by stirring in air for 24 h. Finally, the polymers solution was further purified by dialysis in Milli-Q water for 3 days. The MGLs-CPT were characterized by TEM (Figure S30).

4.6 Supporting figures and tables

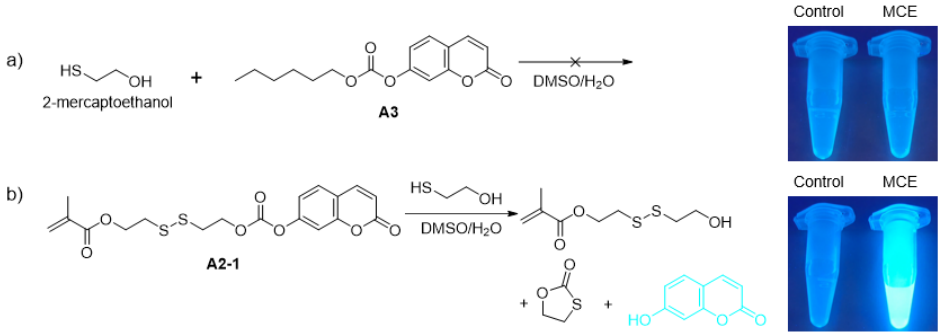

Figure S1. a) Reaction between 2-mercaptoethanol (MCE) and **A3**, and the photograph of the solution under UV light (ex: 365 nm). **b)** Reaction between MCE and **A2-1**, and photograph of the solution under UV-light (ex: 365 nm).

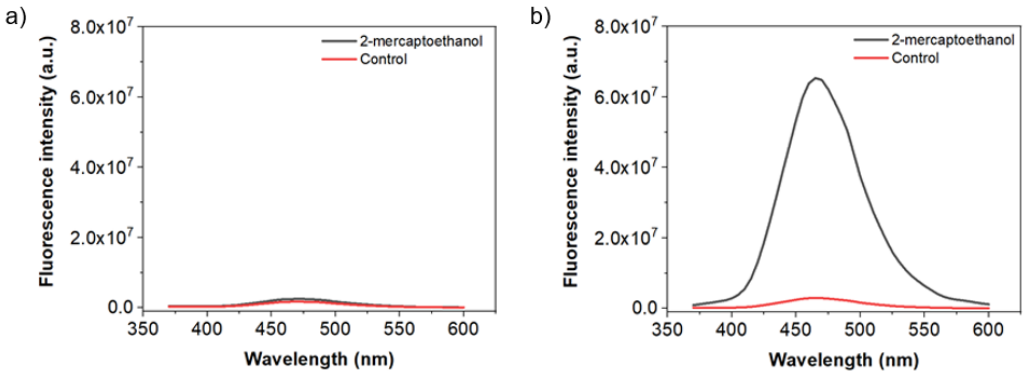

Figure S2. a) Fluorescence spectra of **A3** and **A3** mixed with MCE. **b)** Fluorescence spectra of **A2-1** and **A2-1** mixed with MCE.

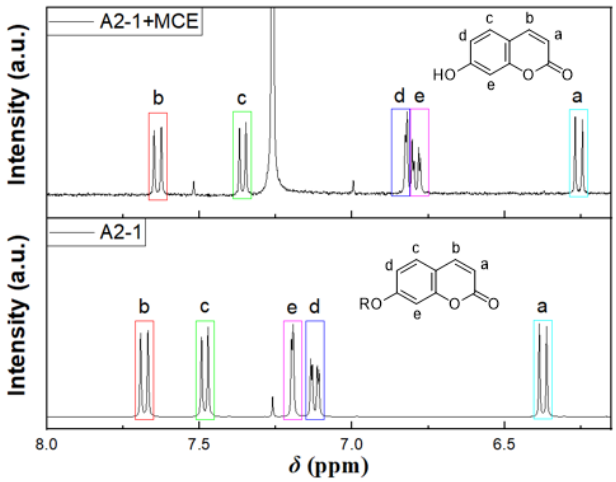

Figure S3. ^{1}H NMR spectroscopy of **A2-1** treated with excess MCE.

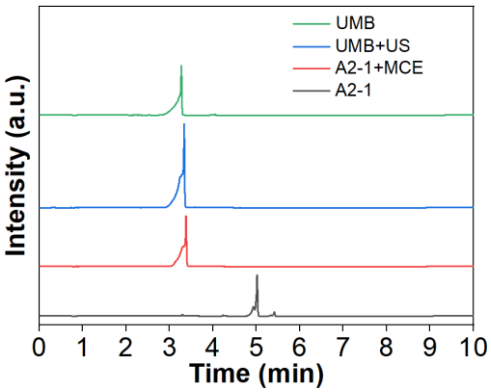

Figure S4. HPLC elugrams of UMB, UMB+US, **A2-1** and **A2-1** + MCE

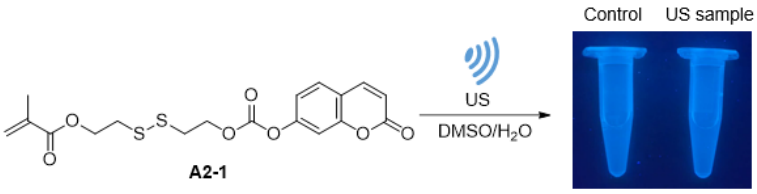

Figure S5. Photographs of the solution of **A2-1** with (1.5 MHz, 30 min) and without sonication under UV light (ex: 365 nm).

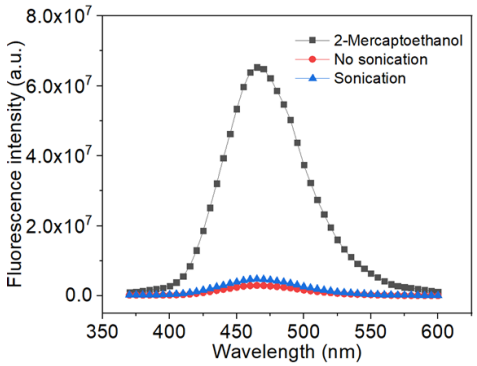

Figure S6. Fluorescence spectra of **A2-1** with sonication, without sonication and mixed with excess MCE.

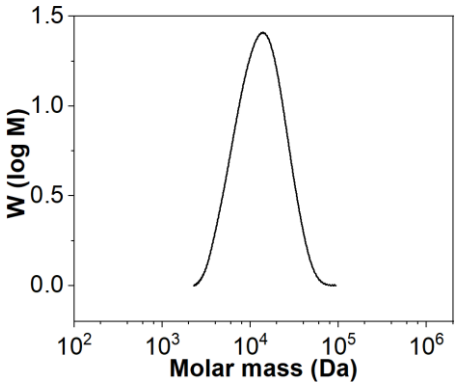

Figure S7. GPC RI molar mass distribution of copolymer **P1,** M_n = 12.9 kDa.

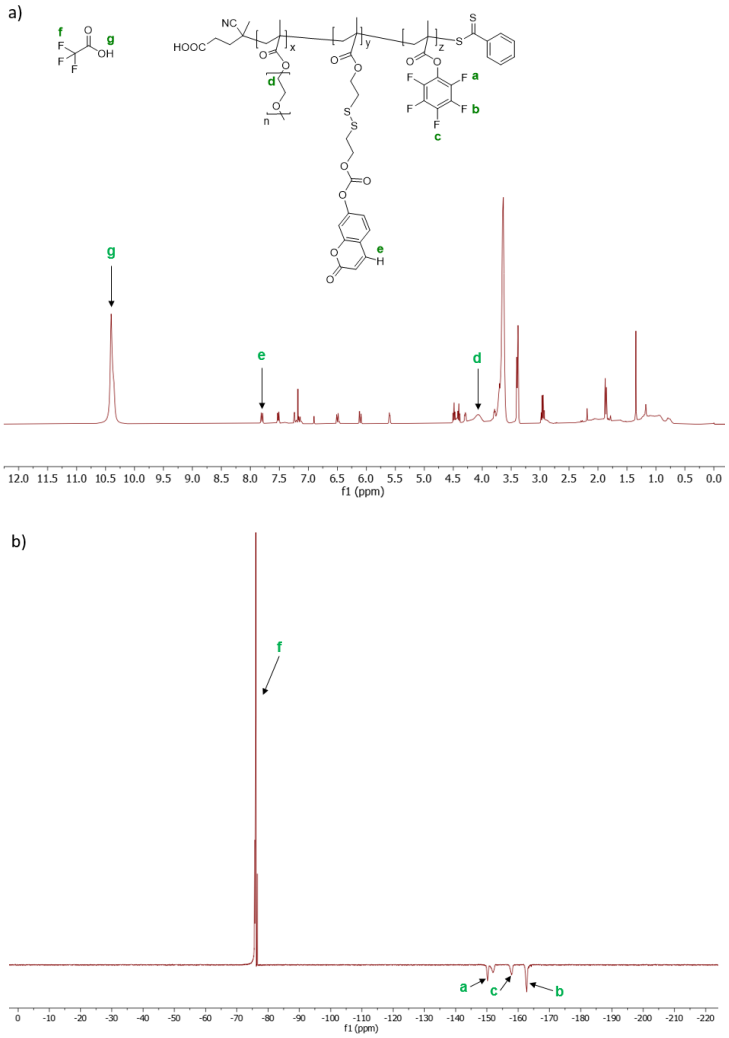

Figure S8. a) ^{1}H NMR and **b)** ^{19}F-NMR spectra of polymer **P1** recorded in $CDCl_3$ with trifluoroacetic acid (TFA, 5 v% in $CDCl_3$).

The composition ratio of polymer was determined using TFA as an internal reference in both ^{1}H NMR and ^{19}F NMR spectra according to the following formulas.[30]

$$A = \frac{I^{4.0\ \mathrm{ppm}}}{2 \cdot I^{10.4\ \mathrm{ppm}}}$$

In the ^{1}H NMR spectrum, $I^{4.0\ \mathrm{ppm}}$ and $I^{10.4\ \mathrm{ppm}}$ represent the signal intensities at 4.0 ppm and 10.4 ppm, corresponding to PEGMEMA and TFA, respectively;

$$B = \frac{I^{7.8\ \mathrm{ppm}}}{I^{10.4\ \mathrm{ppm}}}$$

In the ^{1}H NMR spectrum, $I^{7.8\ \mathrm{ppm}}$ and $I^{10.4\ \mathrm{ppm}}$ represent the signal intensities at 7.8 ppm and 10.4 ppm, corresponding to **A2-1** and TFA, respectively;

$$C = \frac{3 \cdot I^{-151\ \mathrm{ppm}}}{2 \cdot I^{-75\ \mathrm{ppm}}}$$

Lastly, in the ^{19}F NMR spectrum, $I^{-75\ \mathrm{ppm}}$ and $I^{-151\ \mathrm{ppm}}$ refer to the signal intensities at -75 ppm and -151 ppm, corresponding to TFA and PFPMA, respectively.

$$A : B : C = 14{:}1{:}5$$

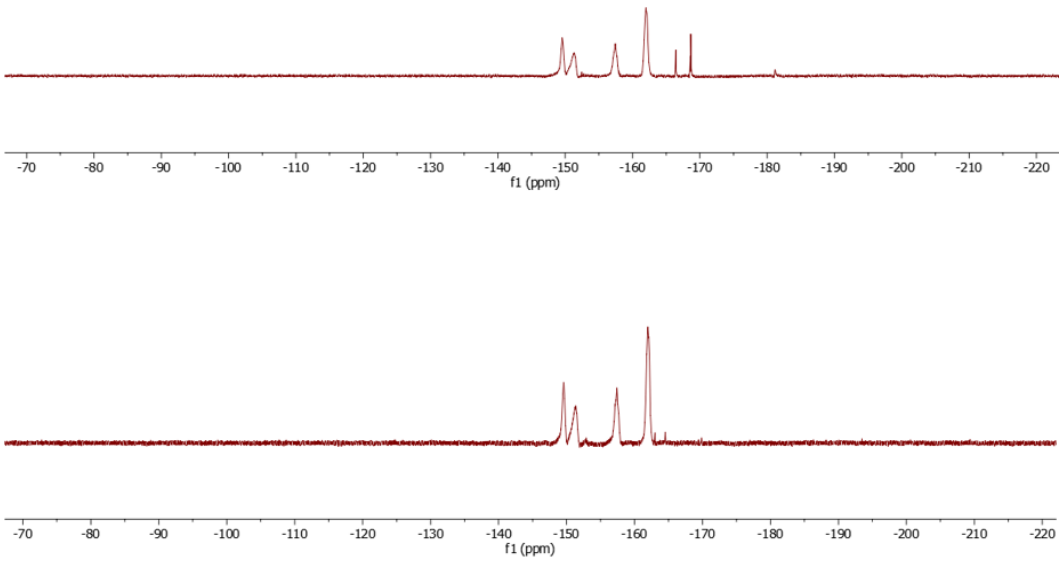

Figure S9. Characterization of crosslinking process from P1 to MGLs-UMB: release of pentafluorophenyl groups tracked by ^{19}F-NMR. Top: ^{19}F-NMR spectrum of reaction mixture after 4 h reaction time. Bottom: ^{19}F-NMR spectrum of polymer P1 before reaction.

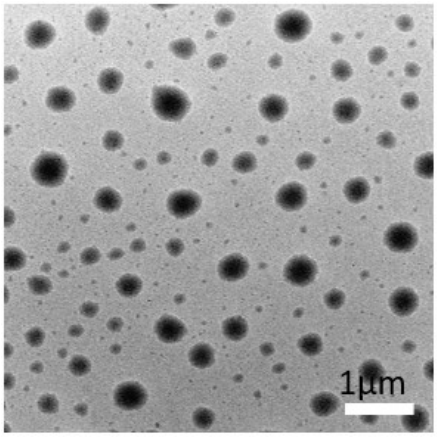

Figure S10. TEM micrograph of MGLs-UMB.

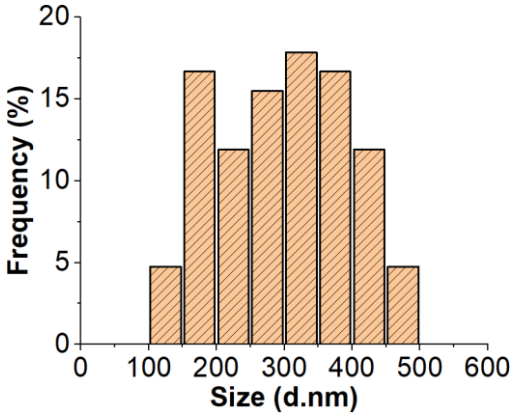

Figure S11. Size distribution of MGLs-UMB obtained from TEM micrograph.

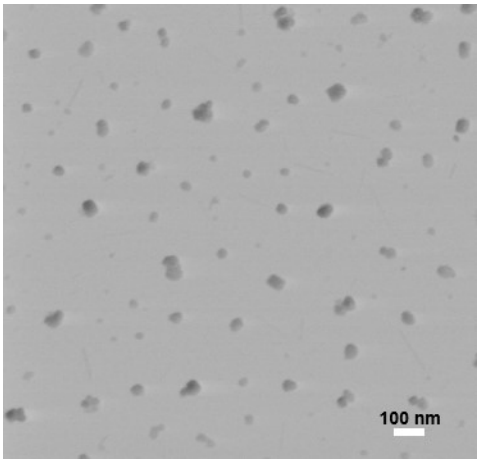

Figure S12. TEM micrograph of smaller size (50 nm) MGLs-UMB.

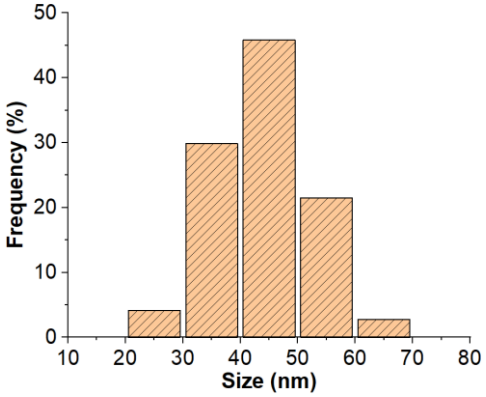

Figure S13. Size distribution of smaller size (average size 50 nm) MGLs-UMB obtained from TEM micrograph.

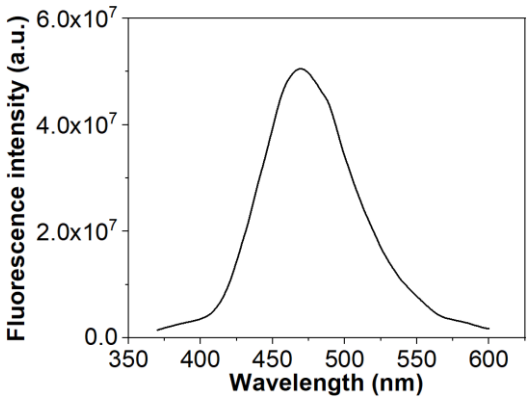

Figure S14. Fluorescence spectra of MGLs-UMB treated with excess MCE.

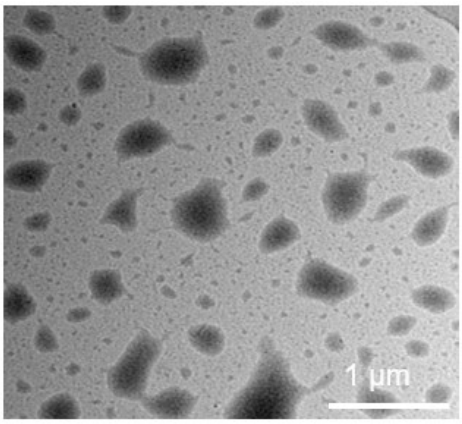

Figure S15. TEM micrograph of MGLs-UMB after 30 min HIFU sonication (0.66 MHz).

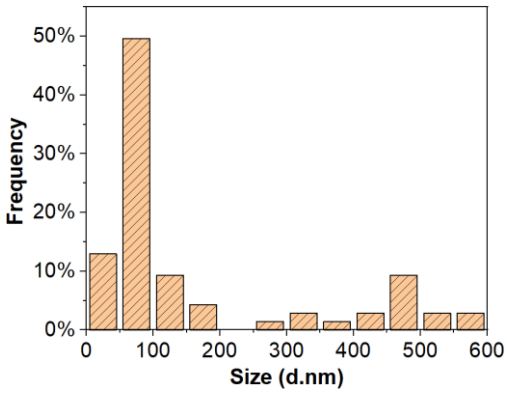

Figure S16. Size distribution of sonicated MGLs-UMB obtained from TEM micrograph.

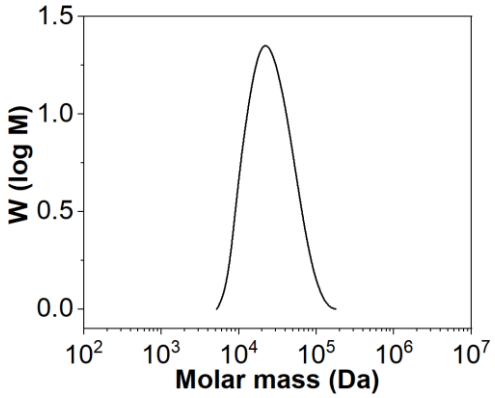

Figure S17. GPC RI molar mass distributions of copolymer **P2**, M_n = 20.8 kDa.

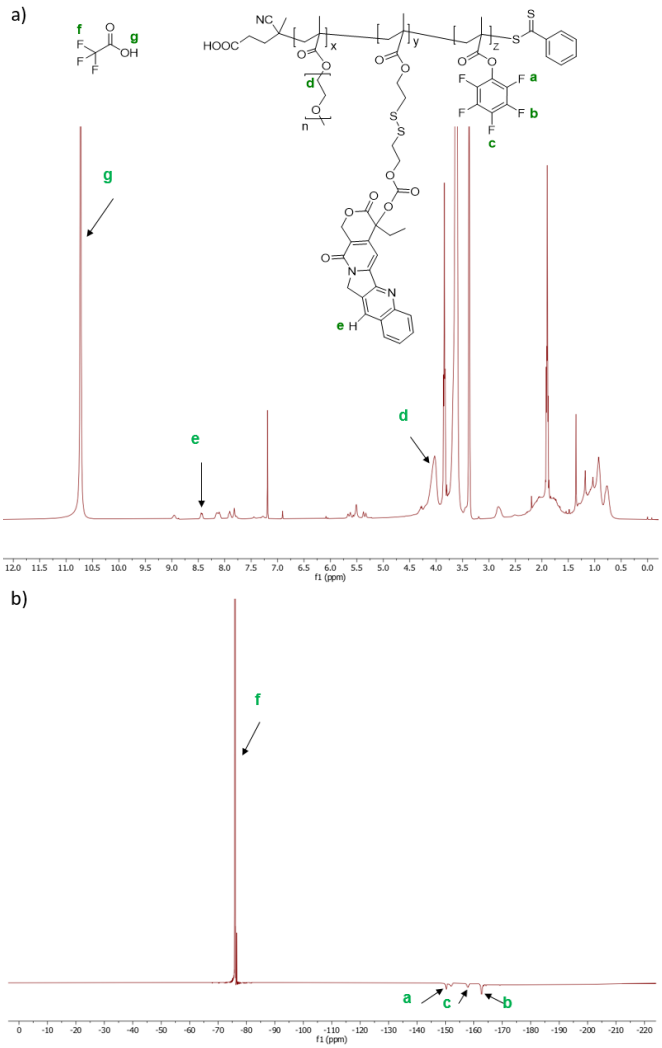

Figure S18. a) ^{1}H NMR and **b**) ^{19}F-NMR spectra of polymer **P2** recorded in $CDCl_3$ with trifluoroacetic acid (TFA, 5 v% in $CDCl_3$).

The composition ratio of polymer was determined using TFA as an internal reference in both ^{1}H NMR and ^{19}F NMR spectra according to the following formulas.[30]

$$A = \frac{I^{4.0\ \mathrm{ppm}}}{2 \cdot I^{10.4\ \mathrm{ppm}}}$$

In the ^{1}H NMR spectrum, $I^{4.0\ \mathrm{ppm}}$ and $I^{10.4\ \mathrm{ppm}}$ represent the signal intensities at 4.0 ppm and 10.4 ppm, corresponding to PEGMEMA and TFA, respectively;

$$B = \frac{I^{7.8\ \mathrm{ppm}}}{I^{10.4\ \mathrm{ppm}}}$$

In the ^{1}H NMR spectrum, $I^{7.8\ \mathrm{ppm}}$ and $I^{10.4\ \mathrm{ppm}}$ represent the signal intensities at 7.8 ppm and 10.4 ppm, corresponding to **A2-2** and TFA, respectively;

$$C = \frac{3 \cdot I^{-151\ \mathrm{ppm}}}{2 \cdot I^{-75\ \mathrm{ppm}}}$$

Lastly, in the ^{19}F NMR spectrum, $I^{-75\ \mathrm{ppm}}$ and $I^{-151\ \mathrm{ppm}}$ refer to the signal intensities at -75 ppm and -151 ppm, corresponding to TFA and PFPMA, respectively.

$$A : B : C = 17{:}1{:}4$$

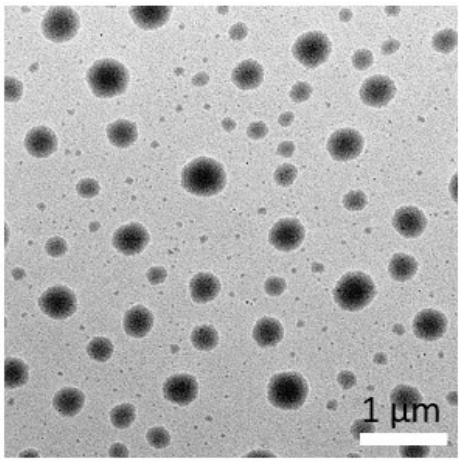

Figure S19. TEM micrograph of MGLs-CPT.

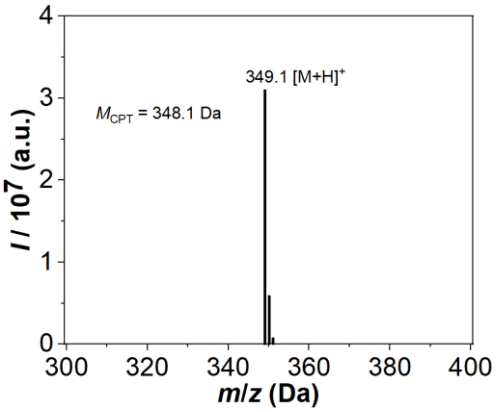

Figure S20. Mass spectrum of sonicated MGLs-CPT solution.

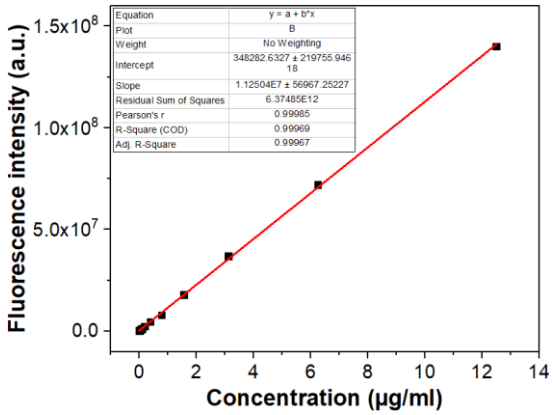

Figure S21. CPT standard curve obtained from fluorescence spectra of CPT; ex: 335 nm, em: 449 nm).

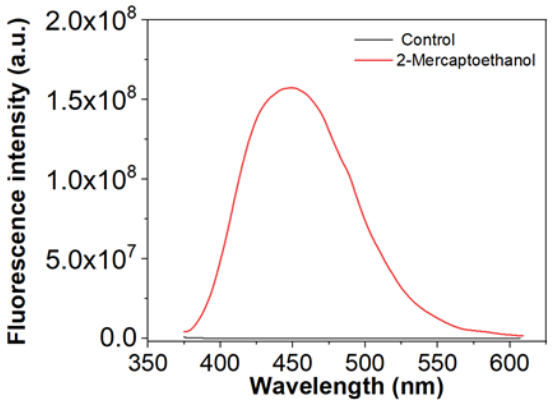

Figure S22. Fluorescence spectra of MGLs-CPT treated with excessive MCE.

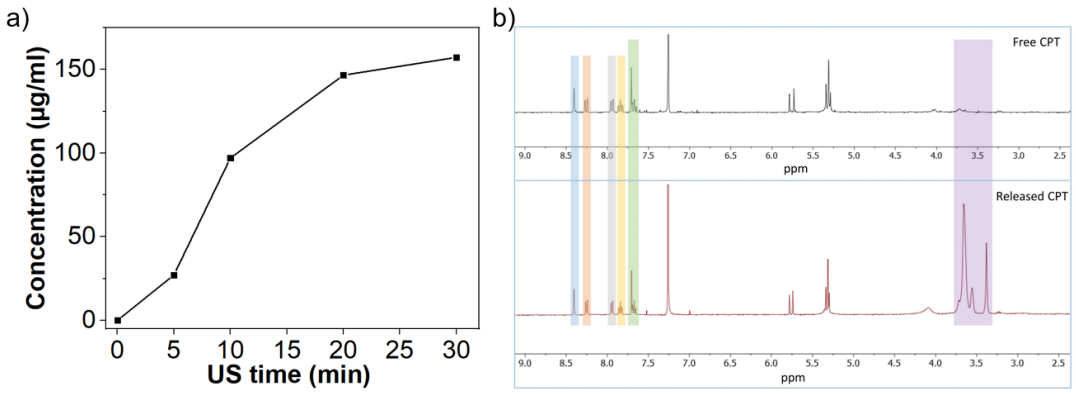

Figure S23. a) Concentrations of released CPT from the MGLs-CPT (Sonication: 0.66 MHz, 32 W). **b**) The ^{1}H NMR comparison of free CPT and released CPT in $CDCl_3$.

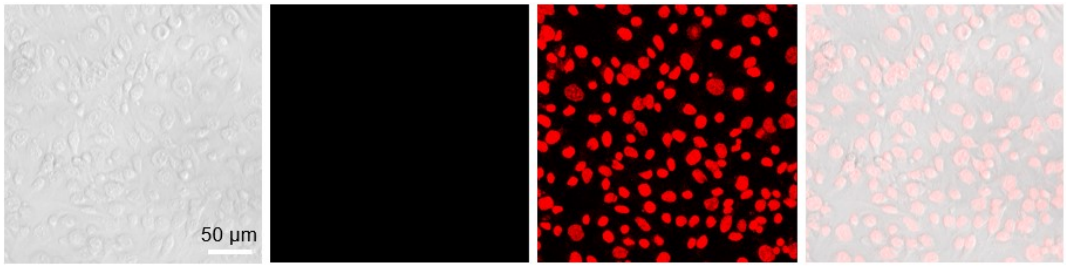

Figure S24. HeLa cells stained for 5 min with sonicated MGLs-CPT (HIFU 20 min). Bright field, CLSM-1(calcein-AM, excitation: 494 nm), CLSM-2 (PI, excitation: 535 nm), and merged micrographs (scale bar: 50 µm).

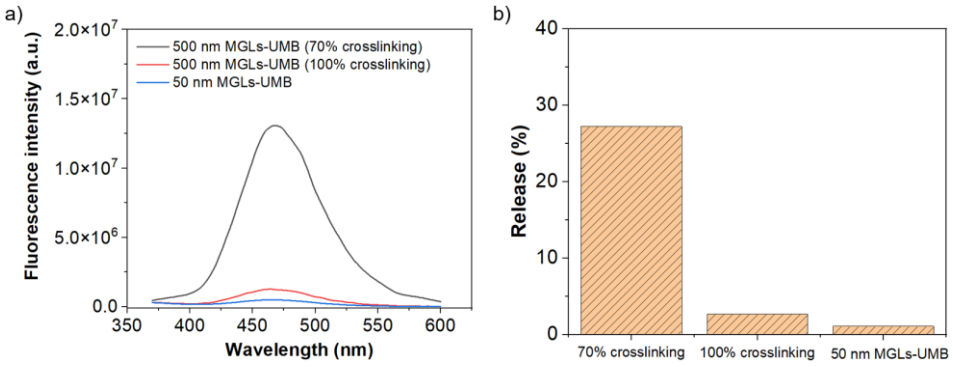

Figure S25. Disulfide mechanophores activation in different MGLs-UMB. **a**) Fluorescence spectra from the sonicated (0.66 MHz, 32W, 30 min) samples of 500 nm (70% cross-linked) MGLs-UMB, 500 nm (100% crosslinked) MGLs-UMB and 50 nm MGLs-UMB. **b**) UMB release from the 500 nm (70% cross-linked) MGLs-UMB, 500 nm (100% crosslinked) MGLs-UMB and 50 nm MGLs-UMB.

Table S1. HIFU parameters with 0.66 MHz, 1.5 MHz and 2.5 MHz transducers.

Transducer	Acoustic power (W)	Focal intensity (W/cm^2)	Focal pressure (Kpa)	Mechanical index[48-49]
0.66 MHz	4	25	850	1
	8	50	1240	1.5
	16	100	1720	2.1
	32	200	2470	3
1.50 MHz	4	290	2950	2.4
	8	580	4240	3.4
	16	1160	5830	4.7
	32	2320	8370	6.8
2.50 MHz	4	820	4900	3.1
	8	1640	7260	4.5
	16	3280	9630	6.1
	32	6530	14100	8.9

Table S2. Data points measured to plot Figure 5g of the manuscript. All values ± standard deviation.

Concentration (μM)	Control (PBS)	MGLs	CPT	CPT+US	MGLs+US (20 min)	MGLs+US (30 min)
32	1.007 ± 0.005	0.833 ± 0.023	0.007 ± 0.009	0.018 ± 0.012	0.041 ± 0.003	0.033 ± 0.105
16	1.001 ± 0.014	0.886 ± 0.029	0.066 ± 0.032	0.082 ± 0.043	0.214 ± 0.029	0.209 ± 0.114
8	0.994 ± 0.004	0.910 ± 0.031	0.282 ± 0.063	0.278 ± 0.079	0.340 ± 0.041	0.329 ± 0.142
4	1.004 ± 0.015	0.934 ± 0.041	0.453 ± 0.085	0.397 ± 0.098	0.393 ± 0.065	0.375 ± 0.138
2	0.994 ± 0.001	0.924 ± 0.034	0.535 ± 0.099	0.471 ± 0.115	0.443 ± 0.058	0.389 ± 0.137
1	0.999 ± 0.043	0.926 ± 0.038	0.613 ± 0.117	0.506 ± 0.174	0.464 ± 0.090	0.411 ± 0.144
0.5	0.976 ± 0.023	0.911 ± 0.036	0.657 ± 0.082	0.530 ± 0.170	0.507 ± 0.099	0.455 ± 0.146
0.25	0.986 ± 0.014	0.946 ± 0.031	0.737 ± 0.106	0.612 ± 0.175	0.622 ± 0.133	0.549 ± 0.171
0.125	0.999 ± 0.027	0.970 ± 0.013	0.790 ± 0.090	0.761 ± 0.182	0.833 ± 0.118	0.797 ± 0.148
0.0625	1.000 ± 0.020	1.000 ± 0.007	0.935 ± 0.040	0.956 ± 0.027	0.984 ± 0.096	1.015 ± 0.116

4.7 References

1. Davis, D. A., Hamilton, A., Yang, J., Cremar, L. D., Van Gough, D., Potisek, S. L., Ong, M. T., Braun, P. V., Martínez, T. J., White, S. R., Moore, J. S., & Sottos, N. R. (2009). Force-induced activation of covalent bonds in mechanoresponsive polymeric materials. *Nature*, *459*(7243), 68-72.

2. Lenhardt, J. M., Ong, M. T., Choe, R., Evenhuis, C. R., Martinez, T. J., & Craig, S. L. (2010). Trapping a diradical transition state by mechanochemical polymer extension. *Science*, *329*, 1057-1060.

3. Chen, Z., Mercer, J. A., Zhu, X., Romaniuk, J. A., Pfattner, R., Cegelski, L., Martinez, T. J., Burns, N. Z. & Xia, Y. (2017). Mechanochemical unzipping of insulating polyladderene to semiconducting polyacetylene. *Science*, *357*, 475-479.

4. Overholts, A. C., Granados Razo, W., & Robb, M. J. (2023). Mechanically gated formation of donor–acceptor Stenhouse adducts enabling mechanochemical multicolour soft lithography. *Nature Chemistry*, *15*(3), 332-338.

5. Shen, H., Larsen, M. B., Roessler, A. G., Zimmerman, P. M., & Boydston, A. J. (2021). Mechanochemical Release of N-Heterocyclic Carbenes from Flex-Activated Mechanophores. *Angewandte Chemie*, *133*(24), 13671-13675.

6. Lenhardt, J. M., Black, A. L., & Craig, S. L. (2009). gem-Dichlorocyclopropanes as abundant and efficient mechanophores in polybutadiene copolymers under mechanical stress. *Journal of the American Chemical Society*, *131*(31), 10818-10819.

7. Hu, X., Zeng, T., Husic, C. C., & Robb, M. J. (2019). Mechanically triggered small molecule release from a masked furfuryl carbonate. *Journal of the American Chemical Society*, *141*(38), 15018-15023.

8. Li, Y., Nese, A., Matyjaszewski, K., & Sheiko, S. S. (2013). Molecular tensile machines: anti-Arrhenius cleavage of disulfide bonds. *Macromolecules*, *46*(18), 7196-7201.

9. Hemmer, J. R., Rader, C., Wilts, B. D., Weder, C., & Berrocal, J. A. (2021). Heterolytic bond cleavage in a scissile triarylmethane mechanophore. *Journal of the American Chemical Society*, *143*(45), 18859-18863.

10. Sagara, Y., Karman, M., Verde-Sesto, E., Matsuo, K., Kim, Y., Tamaoki, N., & Weder, C. (2018). Rotaxanes as mechanochromic fluorescent force transducers in polymers. *Journal of the American Chemical Society*, *140*(5), 1584-1587.

11. Konda, S. S. M., Brantley, J. N., Varghese, B. T., Wiggins, K. M., Bielawski, C. W., & Makarov, D. E. (2013). Molecular catch bonds and the anti-Hammond effect in polymer mechanochemistry. *Journal of the American Chemical Society*, *135*(34), 12722-12729.

12. Chen, Y., Spiering, A. J. H., Karthikeyan, S., Peters, G. W., Meijer, E. W., & Sijbesma, R. P. (2012). Mechanically induced chemiluminescence from polymers incorporating a 1, 2-dioxetane unit in the main chain. *Nature Chemistry*, *4*(7), 559-562.

13. Larsen, M. B., & Boydston, A. J. (2013). "Flex-activated" mechanophores: using polymer mechanochemistry to direct bond bending activation. *Journal of the American Chemical Society*, *135*(22), 8189-8192.

14. Nixon, R., & De Bo, G. (2020). Isotope Effect in the Activation of a Mechanophore. *Journal of the American Chemical Society*, *143*(8), 3033-3036.

15. Li, J., Shiraki, T., Hu, B., Wright, R. A., Zhao, B., & Moore, J. S. (2014). Mechanophore activation at heterointerfaces. *Journal of the American Chemical Society*, *136*(45), 15925-15928.

16. Church, D. C., Peterson, G. I., & Boydston, A. J. (2014). Comparison of mechanochemical chain scission rates for linear versus three-arm star polymers in strong acoustic fields. *ACS Macro Letters*, *3*(7), 648-651.
17. Zhang, Y., Lund, E., Gossweiler, G. R., Lee, B., Niu, Z., Khripin, C., Munch, E., Couty, M., & Craig, S. L. (2021). Molecular damage detection in an elastomer nanocomposite with a coumarin dimer mechanophore. *Macromolecular Rapid Communications*, *42*(1), 2000359.
18. Clough, J. M., Van Der Gucht, J., & Sijbesma, R. P. (2017). Mechanoluminescent imaging of Osmotic stress-induced damage in a glassy polymer network. *Macromolecules*, *50*(5), 2043-2053.
19. Nofen, E. M., Zimmer, N., Dasgupta, A., Gunckel, R., Koo, B., Chattopadhyay, A., & Dai, L. L. (2016). Stress-sensing thermoset polymer networks via grafted cinnamoyl/cyclobutane mechanophore units in epoxy. *Polymer Chemistry*, *7*(47), 7249-7259.
20. Chen, Y., Yeh, C. J., Guo, Q., Qi, Y., Long, R., & Creton, C. (2021). Fast reversible isomerization of merocyanine as a tool to quantify stress history in elastomers. *Chemical Science*, *12*(5), 1693-1701.
21. Qian, H., Purwanto, N. S., Ivanoff, D. G., Halmes, A. J., Sottos, N. R., & Moore, J. S. (2021). Fast, reversible mechanochromism of regioisomeric oxazine mechanophores: Developing in situ responsive force probes for polymeric materials. *Chem*, *7*(4), 1080-1091.
22. Chen, Z., Ye, F., Shao, T., Wu, Y., Chen, M., Zhang, Y., Zhao, X., Zou, B., & Ma, Y. (2022). Stress-Dependent Multicolor Mechanochromism in Epoxy Thermosets Based on Rhodamine and Diaminodiphenylmethane Mechanophores. *Macromolecules*, *55*(6), 2310-2319.
23. Sulkanen, A. R., Sung, J., Robb, M. J., Moore, J. S., Sottos, N. R., & Liu, G. Y. (2019). Spatially selective and density-controlled activation of interfacial mechanophores. *Journal of the American Chemical Society*, *141*(9), 4080-4085.
24. Shi, Z., Wu, J., Song, Q., Göstl, R., & Herrmann, A. (2020). Toward drug release using polymer mechanochemical disulfide scission. *Journal of the American Chemical Society*, *142*(34), 14725-14732.
25. Huo, S., Zhao, P., Shi, Z., Zou, M., Yang, X., Warszawik, E., Loznik, M., Göstl, R., & Herrmann, A. (2021). Mechanochemical bond scission for the activation of drugs. *Nature Chemistry*, *13*(2), 131-139.
26. Shi, Z., Song, Q., Göstl, R., & Herrmann, A. (2021). Mechanochemical activation of disulfide-based multifunctional polymers for theranostic drug release. *Chemical Science*, *12*(5), 1668-1674.
27. Shi, Z., Song, Q., Göstl, R., & Herrmann, A. (2021). The Mechanochemical Release of Naphthalimide Fluorophores from β-Carbonate and β-Carbamate Disulfide-Centered Polymers. *CCS Chemistry*, *3*(11), 2333-2344.
28. Huo, S., Liao, Z., Zhao, P., Zhou, Y., Göstl, R., & Herrmann, A. (2022). Mechano-Nanoswitches for Ultrasound-Controlled Drug Activation. *Advanced Science*, *9*(12), 2104696.
29. Zou, M., Zhao, P., Huo, S., Göstl, R., & Herrmann, A. (2021). Activation of antibiotic-grafted polymer brushes by ultrasound. *ACS Macro Letters*, *11*(1), 15-19.
30. Zou, M., Zhao, P., Fan, J., Göstl, R., & Herrmann, A. (2022). Microgels as drug carriers for sonopharmacology. *Journal of Polymer Science*, *60*(12), 1864-1870.
31. Kim, G., Lau, V. M., Halmes, A. J., Oelze, M. L., Moore, J. S., & Li, K. C. (2019). High-intensity focused ultrasound-induced mechanochemical transduction in synthetic elastomers. *Proceedings of the National Academy of Sciences*, *116*(21), 10214-10222.

32. Kim, G., Wu, Q., Chu, J. L., Smith, E. J., Oelze, M. L., Moore, J. S., & Li, K. C. (2022). Ultrasound controlled mechanophore activation in hydrogels for cancer therapy. *Proceedings of the National Academy of Sciences*, *119*(4), e2109791119.

33. Yao, Y., McFadden, M. E., Luo, S. M., Barber, R. W., Kang, E., Bar-Zion, A., Smith, C. A. B., Jin, Z., Legendre, M., Ling, B., Malounda, D., Torres, A., Hamza, T., Edwards, C. E. R., Shapiro, M. G., & Robb, M. J. (2023). Remote control of mechanochemical reactions under physiological conditions using biocompatible focused ultrasound. *Proceedings of the National Academy of Sciences*, *120*(39), e2309822120.

34. Yildiz, D., Göstl, R., & Herrmann, A. (2022). Sonopharmacology: controlling pharmacotherapy and diagnosis by ultrasound-induced polymer mechanochemistry. *Chemical Science*, *13*(46), 13708-13719.

35. Küng, R., Göstl, R., & Schmidt, B. M. (2022). Release of molecular cargo from polymer systems by mechanochemistry. *Chemistry–A European Journal*, *28*(17), e202103860.

36. Versaw, B. A., Zeng, T., Hu, X., & Robb, M. J. (2021). Harnessing the power of force: development of mechanophores for molecular release. *Journal of the American Chemical Society*, *143*(51), 21461-21473.

37. Mitragotri, S. (2005). Healing sound: the use of ultrasound in drug delivery and other therapeutic applications. *Nature Reviews Drug Discovery*, *4*(3), 255-260.

38. Phenix, C. P., Togtema, M., Pichardo, S., Zehbe, I., & Curiel, L. (2014). High intensity focused ultrasound technology, its scope and applications in therapy and drug delivery. *Journal of Pharmacy & Pharmaceutical Sciences*, *17*(1), 136-153.

39. Park, I., Sheiko, S. S., Nese, A., & Matyjaszewski, K. (2009). Molecular tensile testing machines: breaking a specific covalent bond by adsorption-induced tension in brushlike macromolecules. *Macromolecules*, *42*(6), 1805-1807.

40. Kucharski, T. J., Huang, Z., Yang, Q. Z., Tian, Y., Rubin, N. C., Concepcion, C. D., & Boulatov, R. (2009). Kinetics of thiol/disulfide exchange correlate weakly with the restoring force in the disulfide moiety. *Angewandte Chemie International Edition*, *48*(38), 7040-7043.

41. Fritze, U. F., & von Delius, M. (2016). Dynamic disulfide metathesis induced by ultrasound. *Chemical Communications*, *52*(38), 6363-6366.

42. Wang, F., Burck, M., & Diesendruck, C. E. (2017). Following homolytic mechanochemical kinetics with a pyrenyl nitrone spin trap. *ACS Macro Letters*, *6*(1), 42-45.

43. Fritze, U. F., Craig, S. L., & von Delius, M. (2018). Disulfide‐centered poly (methyl acrylates): Four different stimuli to cleave a polymer. *Journal of Polymer Science Part A: Polymer Chemistry*, *56*(13), 1404-1411.

44. Kida, J., Aoki, D., & Otsuka, H. (2021). Self-strengthening of cross-linked elastomers via the use of dynamic covalent macrocyclic mechanophores. *ACS Macro Letters*, *10*(5), 558-563.

45. Izak-Nau, E., Demco, D. E., Braun, S., Baumann, C., Pich, A., & Göstl, R. (2020). Shear-induced structural and functional transformations of poly (N-vinylcaprolactam) microgels. *ACS Applied Polymer Materials*, *2*(4), 1682-1691.

46. Wang, X. H., Huang, M., Zhao, C. K., Li, C., & Xu, L. (2019). Design, synthesis, and biological activity evaluation of campthothecin-HAA-Norcantharidin conjugates as antitumor agents in vitro. *Chemical Biology & Drug Design*, *93*(6), 986-992.

47. Krishnan, P., Rajan, M., Kumari, S., Sakinah, S., Priya, S. P., Amira, F., & Kumar, S. S. (2017). Efficiency of newly formulated camptothecin with β-cyclodextrin-EDTA-Fe3O4 nanoparticle-conjugated nanocarriers as an anti-colon cancer (HT29) drug. *Scientific Reports*, *7*(1), 10962.

48. Apfel, R. E., & Holland, C. K. (1991). Gauging the likelihood of cavitation from short-pulse, low-duty cycle diagnostic ultrasound. *Ultrasound in Medicine & Biology*, *17*(2), 179-185.

49. Church, C. C., Labuda, C., & Nightingale, K. (2015). A theoretical study of inertial cavitation from acoustic radiation force impulse imaging and implications for the mechanical index. *Ultrasound in Medicine & Biology*, *41*(2), 472-485.

50. Dutta, K., Kanjilal, P., Das, R., & Thayumanavan, S. (2021). Synergistic Interplay of Covalent and Non-Covalent Interactions in Reactive Polymer Nanoassembly Facilitates Intracellular Delivery of Antibodies. *Angewandte Chemie*, *133*(4), 1849-1858.

51. Liu, B., Wu, R., Gong, S., Xiao, H., & Thayumanavan, S. (2020). In situ formation of polymeric nanoassemblies using an efficient reversible click reaction. *Angewandte Chemie International Edition*, *59*(35), 15135-15140.

52. Pal, S., Hill, M. R., & Sumerlin, B. S. (2015). Doubly-responsive hyperbranched polymers and core-crosslinked star polymers with tunable reversibility. *Polymer Chemistry*, *6*(45), 7871-7880.

53. Zhuang, J., Jiwpanich, S., Deepak, V. D., & Thayumanavan, S. (2012). Facile preparation of nanogels using activated ester containing polymers. *ACS Macro Letters*, *1*(1), 175-179.

5. Ultrasound-induced molecules release from polymeric microbubbles

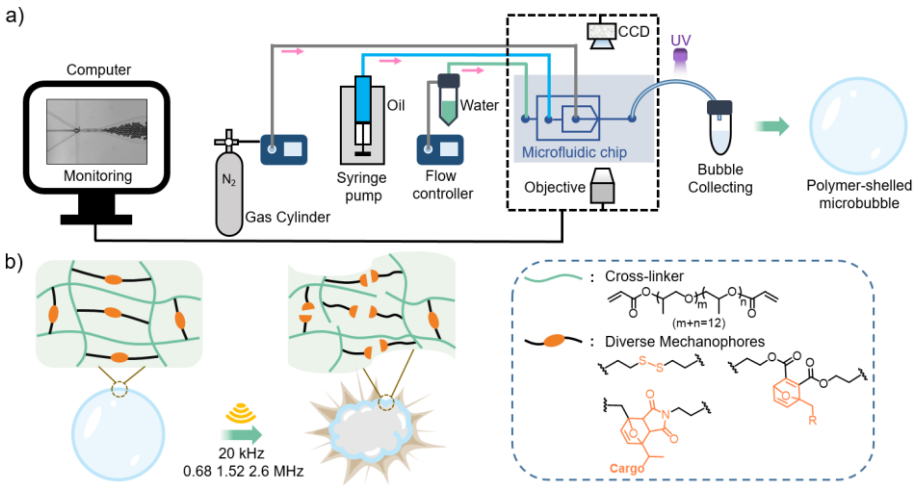

In **Chapter 5**, I present an ultrasound-responsive polymeric microbubbles (PMBs) system. Uniform-size N_2-filled PMBs were prepared by microfluidic engineering. We demonstrated US remote-controlled mechanochemical transformations in PMBs. In this chapter, the commonly used 20 kHz ultrasound and megahertz biocompatible HIFU were applied to investigate the mechanical response of microbubbles. This study explored the potential of ultrasound-induced mechanochemistry in polymeric microbubbles.

Thanks to Regina Lennarz and Jan Meisner for the computational simulations section in this chapter. Thanks to Ahmed Mourran for the stiffness measurements by Atomic Force Microscopy (AFM).

5.1 Abstract

The flow-induced activation of mechanophores embedded in linear polymers by ultrasound (US) suffers from slow mechanochemical conversions at the commonly used frequency of 20 kHz and in many cases remains ineffective with higher frequencies in the MHz regime. Here, we present polymeric microbubbles (PMBs) as a platform that accelerates the mechanochemical activation of several mechanophores under both 20 kHz and MHz irradiation, i.e., biocompatible high-intensity focused ultrasound (HIFU). By virtue of their pressure-sensitive gas core, PMBs act as an acousto-mechanical transducer for the transformation of energy, stretching and eventually fracturing the polymer shell by stable and inertial cavitation. Exemplarily, we investigate three different mechanophores among which one flex-activation derivative was unprecedentedly activated by US in solution. Through a combination of experiments and computation, we find that PMBs likely exert compressive force onto the copolymerized mechanophores rather than the typical elongational forces solvated chain fragments experience in flow. We thereby both underscore the fundamentally unprecedented mechanochemical properties of the PMB platform as well as its versatility for diverse accelerated mechanochemical transformations with a perspective on biomedical applications.

5.2 Introduction

Stimuli-responsive polymers that elicit a desired function when subjected to a specific chemical or physical stimulus are a subject of great interest.[1-5] Particularly, chemical transformations induced by mechanical force have received attention, since the force-activated alteration of polymer structures[6] or the generation of chemical functions for catalysis,[7-10] sensing,[11-13] cargo delivery,[14-17] or soft robotics[18] promise exciting future applications. In this light, US has become an accessible and widely used tool in polymer mechanochemistry due to its non-invasive nature, spatiotemporal control, and ease of use[19-21] for applications in mechanochemical synthesis[22] and activation of material function.[15,23-25] Because linear mechanophore-centered polymer chains conduct mechanical force along their backbone[26] and are straightforward to analyze by solution-borne methods, they are commonly employed to perform US-induced bond scission.[27-31] Recent research shows that the architecture of the mechanophore-bearing polymer is an important parameter that influences the mechanochemical efficiency. Therefore, helical polymers,[32] cyclic polymers,[33,34] star polymers,[35,36] polymer bottlebrushes,[37-39] dendronized polymers,[40-42] and polymer microgels[43-45] have been investigated.

Another architecture are polymer-shelled gas bubbles, which exhibit special topological characteristics, such as the absence of solvated end groups and restricted conformational freedom. PMBs are an established modality in theranostic biomedicine and have been used to enhance the US response for imaging, drug delivery, and sensing.[46-49] However, mechanochemical transformations in PMBs have remained unknown until we recently reported the US-induced cleavage of disulfide mechanophores.[50] There, PMBs have served as the acousto-mechanical transducers during the sonication, and subsequent disruption of the bubble shell was accompanied by mechanophore activation. However, the generality of this system remained unclear and we were unable to utilize biocompatible MHz US. Both aspects are crucial for the successful application of the PMB concept in a biomedical context.

Here, we show that the microfluidically engineered PMB system can accelerate the activation of several exemplarily chosen mechanochemical motifs for molecular release. Unprecedentedly, we find that even the flex activation, which was previously impossible to achieve by ultrasonication in solution, is enabled using PMBs. In addition, we investigate biocompatible MHz HIFU for the activation of PMBs.

Therefore, uniformly sized, N_2-filled PMBs are prepared by microfluidic engineering (**Figure 1a**). Mechanophores are copolymerized into the PMB shell and activated with 20 kHz US and MHz HIFU (**Figure 1b**). We demonstrate mechanochemical transformations in PMBs by four strategies (**Figure 1c**). Firstly, disulfide mechanophores and subsequent molecular release are achieved by thiol-initiated Michael addition and retro Diels-Alder (rDA) reaction consolidating our previous findings. Secondly, the fluorophore umbelliferone (UMB) and the active pharmaceutical ingredient camptothecin (CPT) are released by thiol/disulfide exchange and intramolecular cyclization, which also bases on the activation of disulfide mechanophores.[15,51,52] Third, we release a fluorogenic molecule from a masked furfuryl carbonate by mechanochemical rDA reaction and an autocatalytic effect, as principally conceived by Robb and coworkers.[53] Lastly, we achieve US-induced flex activation of a furan Diels-Alder adduct, which was pioneered by Boydston and coworkers.[54-58] These strategies underline the general applicability of the PMB system and even show that otherwise unobtainable mechanochemical reactions can be performed using US in solution.

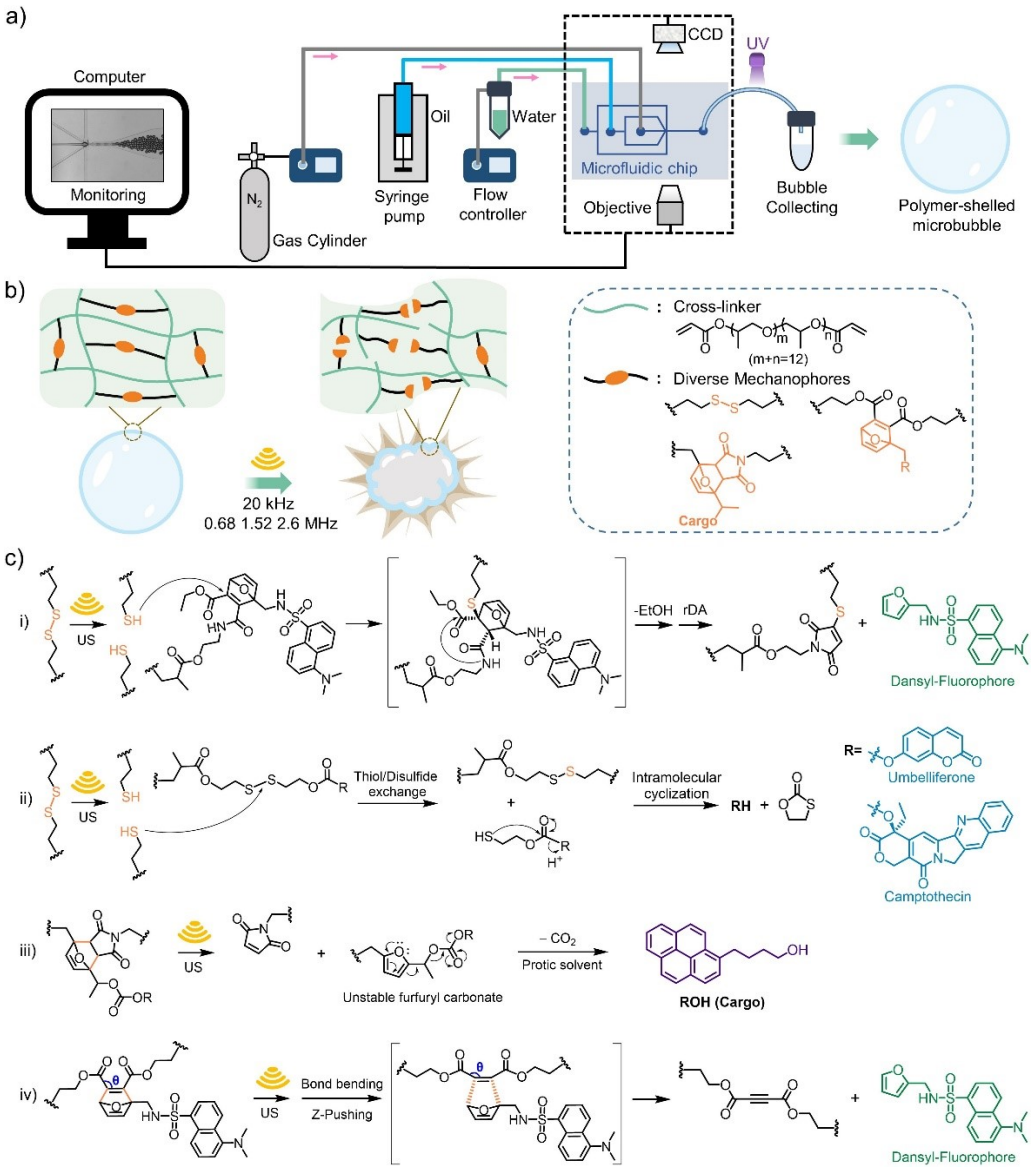

Figure 1. Schematic illustration of the various mechanophore activation processes possible in PMBs. **a,** The preparation of PMBs. **b,** Illustration of mechanophore activation in PMBs under US. **c,** The structural formula and reaction mechanisms of the employed mechanochemical released systems.

5.3 Results and discussion

5.3.1 Disulfide mechanophore activation for dansyl-fluorophore release

Previously we demonstrated the 20 kHz US-triggered disulfide mechanophore activation in microbubbles.[50] Hence, we first used this established system to understand the effect of HIFU in the MHz regime on the PMBs. A thiol-sensitive probe quantifying mechanochemical disulfide scission by fluorescence, a masked dansyl-fluorophore, was copolymerized into the polymer shell through photo-crosslinking. In addition, bis(2-methacryloyl)oxyethyl disulfide (**N1-CL**) was used as the mechanoresponsive crosslinker. US-induced deformation and explosion of the PMBs would expectedly lead to disulfide activation and the free thiols would react with neighboring masked dansyl-fluorophore molecules releasing the dansyl-fluorophore (**N1-A3**) *via* rDA reaction.

The gram-scale syntheses of the probe **N1-A3**, its complementary dienophile **N1-B3**, and the resulting Diels-Alder adduct monomer **N1-DA** are detailed in **Supplementary Scheme S1**.[59] Before copolymerization into the PMB shells, the reactivity of the constitutional isomers **N1-DA1** and **N1-DA2** toward thiols was verified by mixing with 2-mercaptoethanol for 4 d and subsequent fluorescence spectroscopy (**Supplementary Figure S3**). Due to a higher reactivity, **N1-DA2** was used as the masked dansyl-fluorophore (MDF) to prepare PMB-MDF.

Then, PMBs were prepared in a microfluidic device by gas-in-oil-in-water (G/O/W) double emulsion (**Figure 2a**). A UV lamp was set up surrounding the outlet tube for the PMB shell polymerization, which stabilized the gas (N_2) core. The shape of the PMBs was characterized by scanning electron microscopy (SEM) and optical microscopy (**Figure 2b**, **Supplementary Figure S4**) with an average PMB size of ~29 μm (**Figure 2c**). PMB samples were then treated with 20 kHz, 0.68 MHz, 1.52 MHz, and 2.6 MHz US (**Figure 2d**, **Supplementary Figure S6**). At 20 kHz and an intensity of I = 12 W cm^{-2}, sonication for 5 min led to bursting of the PMBs and the fragments sunk to the bottom of the solution. Under HIFU irradiation, PMB explosion commenced at a focal pressure of 1300 kPa for 0.68 MHz, 1800 kPa for 1.52 MHz irradiation, and 6000 kPa for 2.6 MHz irradiation (**Supplementary Figure S6**). Microscopy showed that the PMB fragment size gradually decreased with sonication time at 20 kHz while comparably larger fragments remained with HIFU (**Figure 2e**).

To quantify the mechanophore activation and fluorophore release (**Figure 2f**), the suspensions of PMB fragments after 15 min sonication runs were collected, filtered, and fluorescence was measured (**Figure 2g**). Approximately 23% of the copolymerized fluorophores were released at 20 kHz and 12 W cm^{-2}. When I was decreased to 1.0 W cm^{-2}, we found that the release accordingly decreased to around 10% (**Figure 2h**). Notably, more than 10% release was achieved when HIFU at 0.68 MHz and 2000 kPa was used while no significant release was found below a focal pressure of 1000 kPa (**Figure 2i**). Fluorophore release dropped to 5% when HIFU at 1.5 MHz and 2000 kPa was used (**Figure 2j**) and to < 1% release for HIFU at 2.6 MHz and the same focal pressure likely due the absence of PMB bursting and fragmentation (**Figure 2k**).

As negative control for non-specific activation, we prepared PMBs without disulfide crosslinker (**Supplementary Figure S14**) and expectedly did not observe fluorescence after sonication (**Figure 2l**). Furthermore, solid-core microgels were prepared by microfluidic single emulsion (**Figure 2m**), serving as negative control regarding the role of the gas core of the PMBs. **Figure 2n** shows the optical micrograph of these microgels with an average diameter of ~ 26 μm (**Supplementary Figure S15 and S16**). Upon sonication conditions identical to those of the PMBs, only a very weak increase of fluorescence was observed (**Supplementary Figure S17**) corresponding to < 0.1% release (**Figure 2o**). The absence of morphological

changes in the microgels after sonication indicated the important role of the gas core for mechanochemical activation (**Figure 2o**).

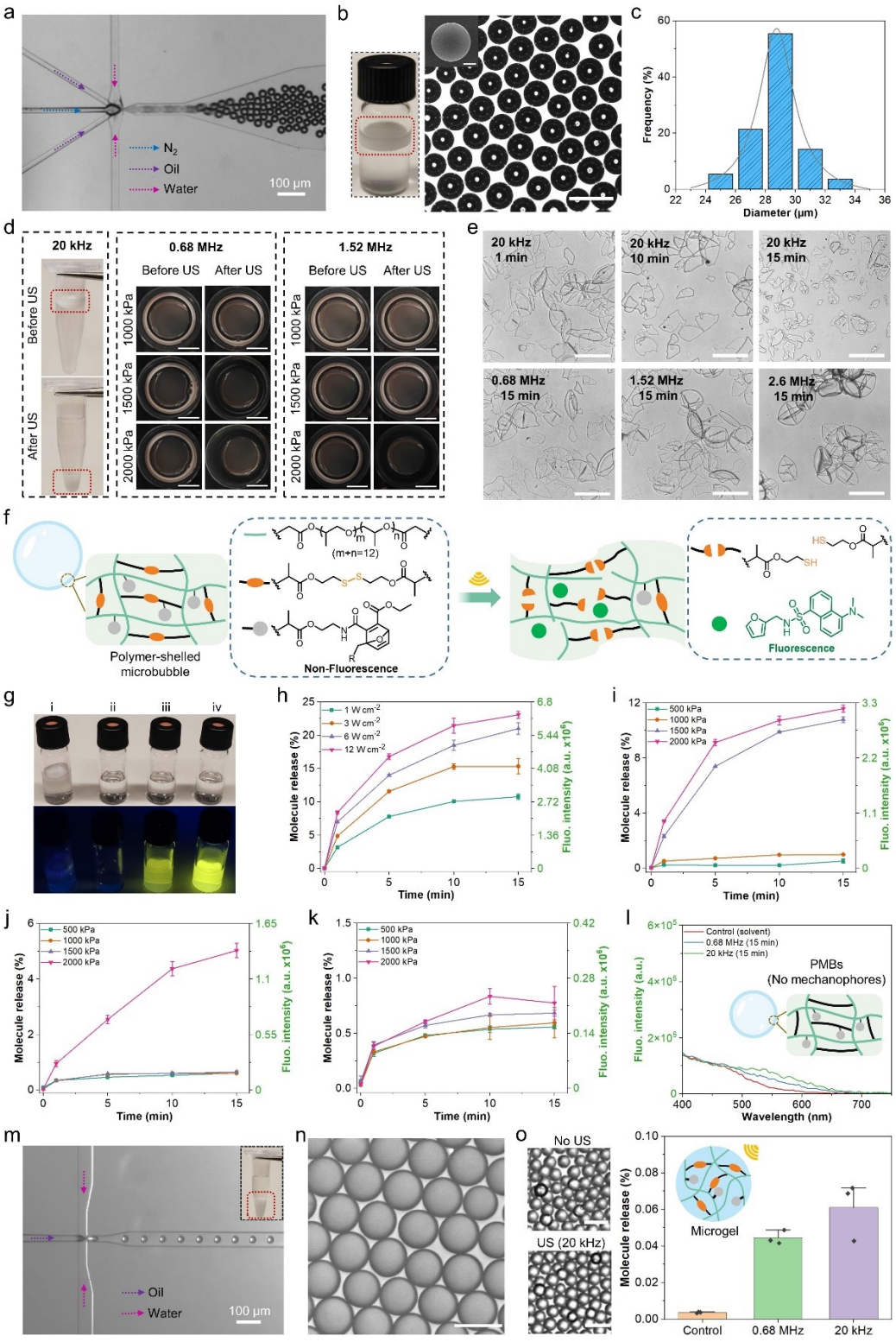

Figure 2. The activation of disulfide mechanophores and dansyl fluorophore release *via* rDA from PMB-MDF. **a,** The production of PMBs in microfluidic chip. **b**, The collection of PMBs in a glass vial and the associated optical micrograph (scale bar: 50 μm). Inset: SEM image, scale bar: 10 μm. **c**, Diameter distribution of the PMBs corresponding to Supplementary Figure S4. **d**, The response of PMBs to 20 kHz (12 W cm^{-2}), 0.68 MHz, or 1.52

MHz US for 5 min, scale bar: 5 mm. **e**, Fragments of PMBs, with 20 kHz US (12 W cm^{-2}) or HIFU (2000 kPa for 0.68 and 1.52 MHz, 6000 kPa for 2.6 MHz), scale bar: 50 µm. **f**, Scheme of mechanophore activation and fluorophore release. **g**, Photographs of samples under daylight and UV light (λ_{exc} = 365 nm), i) PMBs without sonication. ii) MeCN/H_2O blank. iii) The filtered solution of sonicated PMBs (0.68 MHz, 15 min). iv) The filtered solution of sonicated PMBs (20 kHz, 15 min). **h-k**, Fluorophore release from PMBs under 20 kHz, 0.68 MHz, 1.52 MHz, and 2.6 MHz irradiations. **l**, Fluorescence spectra of sonicated PMB control without disulfide. **m**, The production image of microgels in the microfluidic chip. **n**, Microscopy image of microgels, scale bar: 30 µm. **o**, The morphological of microgels and fluorophores release after 15 min US irradiations, scale bar: 50 µm.

5.3.2 Disulfide mechanophore activation for UMB and CPT release

In addition to the Michael addition of thiols with subsequent rDA release, thiol/disulfide exchange was activated mechanochemically in PMBs. Therefore, UMB (fluorophore) and CPT (drug) were selected as the functional target molecules.[51] The respectively carbonylated monomers **N2-A3** and **N2-B3** (**Supplementary Scheme S2**) would undergo intramolecular 5-*exo*-*trig* cyclization after mechanochemically initiated thiol/disulfide exchange releasing both UMB and CPT.

First, PMB-UMB was synthesized from **N2-A3** (**Figure 3a** and **b**) and US treatment qualitatively confirmed UMB release by fluorescence turn-on (**Figure 3c**). The maximum UMB loading was established by reduction of the disulfides with subsequent fluorescence spectroscopy (**Supplementary Figure S18**). 15 min sonication runs of PMB-UMB at 20 kHz and 12 W cm^{-2} released 19% UMB (**Figure 3d**) while 0.68 MHz and 2000 kPa led to 8% UMB release (**Figure 3e**). Proton nuclear magnetic resonance (^{1}H NMR) and mass spectrometry (MS) measurements of sonicated PMB-UMB cross-validated the successful release (**Figure 3f**, **Supplementary Figure S21**).

Having established the molecular proof-of-concept with UMB, pharmacologically active PMB-CPT was synthesized from **N2-B3** (**Figure 3g**) and its activity after sonication was investigated by MTS proliferation assays with HeLa cells (**Figure 3h**). Since CPT is also fluorescent, this mode of detection was used to qualitatively confirm CPT release in conjunction with ultra-high-performance liquid chromatography-mass spectrometry (UPLC-MS, **Figure 3i**). After 15 min sonication, 18% CPT were released at 20 kHz and 12 W cm^{-2} (**Figure 3j**) while 8% at 0.68 MHz could be achieved. Incubation of the sonicated PMB-CPT solutions with HeLa cells showed considerable lower IC_{50} of PMBs after sonication than before while highlighting the biocompatibility of the PMB system and of the mechanophore-free PMB fragments (**Figure 3k**).

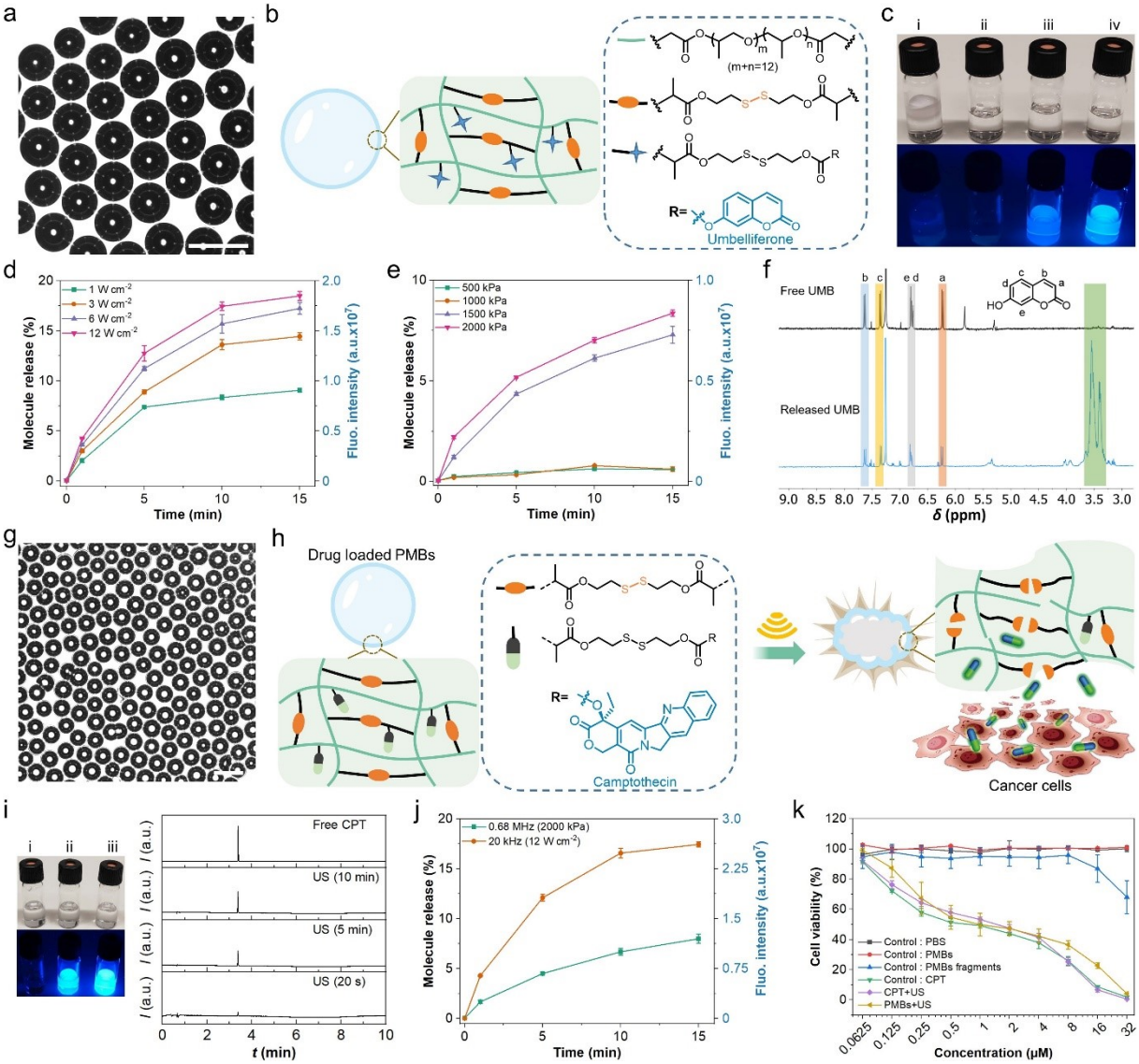

Figure 3. The activation of disulfide mechanophores and small molecule release *via* thiol/disulfide exchange from PMBs. **a**, Optical micrograph, scale bar: 50 μm. **b**, Structural composition of PMB-UMB shell. **c**, Photographs of samples under daylight and UV light (λ_{exc} = 365 nm), i) PMB-UMB without sonication. ii) DMSO/H_2O blank. iii) The filtered solution of sonicated PMB-UMB (0.68 MHz, 15 min). iv) The filtered solution of sonicated PMBs-UMB (20 kHz, 15 min). **d-e**, UMB release under 20 kHz and 0.68 MHz irradiations. **f**, ^{1}H NMR spectra of free UMB and released UMB. **g**, Morphological characterization by optical microscopy, scale bar: 50 μm. **h**, Structural composition of PMB-CPT and illustration of CPT release. **i**, Photographs of samples under daylight and UV light (λ_{exc} = 365 nm), i) DMSO/H_2O blank. ii) The filtered solution of sonicated PMB-CPT (0.68 MHz, 15 min). iii) The filtered solution of sonicated PMB-CPT (20 kHz, 15 min). UPLC elugrams of free CPT and released CPT (20 kHz). **j**, CPT release from PMBs under 20 kHz and 0.68 MHz irradiation. **k**, MTS proliferation assay of negative controls PBS, PMBs and mechanophore-free PMB fragments, positive controls CPT and CPT+US, and *ex situ* sonicated (0.68 MHz, 15 min) PMB-CPT mixed with HeLa cells. Mean values ± SD from the mean. N = 3 independent sonications (**Supplementary Table S3**).

5.3.3 2-Furylcarbinol Diels-Alder adduct mechanophore activation for pyrene fluorophore release

For the introduction of 2-furylcarbinol Diels-Alder adduct mechanophores, pioneered by Robb and coworkers,[53,60] into PMBs, we designed and synthesized the masked furfuryl carbonate (**N3-A5**) containing a fluorogenic pyrenebutanol (PBL) payload (**Figure 4a**, **Supplementary Scheme S3**). Subsequent to the mechanochemical scission of the furan-maleimide Diels-Alder adduct, PBL would be released based on the instability of furfuryl carbonate in polar protic solvents.

First, PMBs were prepared from **N3-A5** (PMBs-PBL) and analyzed by optical microscopy (**Figure 4b**). The latent instability of the small molecule **N3-A4**, and hence its capability for molecular release, (**Figure 4c**) were verified in a mixture of MeCN-d_3, MeOH, and H_2O (3:1:0.5, v/v/v) while monitored by ^{1}H NMR spectroscopy. The decomposition process of **N3-A4** was complete within in 4 d at 37 °C accompanied by the formation of **N3-A3** and PBL (**Figure 4d**) and negligibly slower at 23 °C (**Figure 4e** and **Supplementary Figure S24**).

The fluorogenic properties of PBL allowed the observation of the mechanochemical release process by fluorescence spectroscopy (**Figure 4f** and **g**). Around 24% PBL were released from PMBs-PBL using 20 kHz US at 12 W cm^{-2} for 15 min (**Figure 4h**). The PBL release expectedly correlated positively with both sonication time and US intensity. More than 10% released PBL were obtained using 20 kHz US at 1.0 W cm^{-2} while 9% could be measured using 0.68 MHz at 2000 kPa (**Figure 4i**).

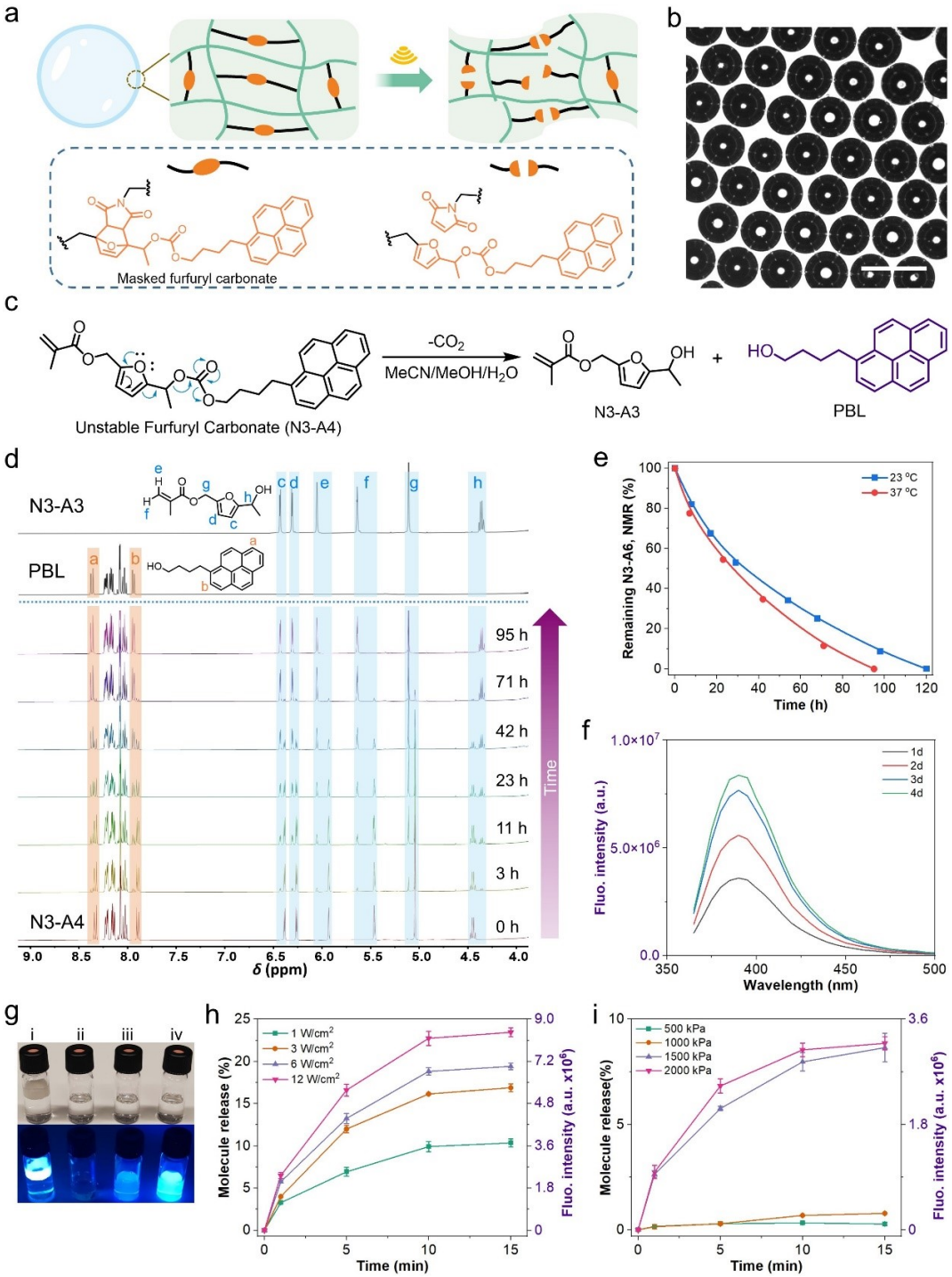

Figure 4. US-triggered activation of 2-furylcarbinol maleimide Diels-Alder adducts and fluorogenic cargo release**. a**, Scheme of mechanophore activation in the shell of PMB-PBL. **b**, Optical micrograph of PMB-PBL; scale bar: 50 μm. **c**, The decomposition mechanism of **N3-A4** in polar protic solvent. **d**, ^{1}H NMR characterization of the conversion of **N3-A4** to **N3-A3** and PBL (solvent: MeCN-d_3:MeOH:H_2O, 3:1:0.5; 5 mg **N3-A4** in 0.5 mL solvent). **e**, The time-dependent conversion of furfuryl carbonate **N3-A4** by ^{1}H NMR spectroscopy. **f**, Fluorescence spectra of sonicated PMB-PBL in MeCN:MeOH:H_2O (20 kHz, 12 W cm^{-2}). **g**, Photographs of samples under daylight and UV-light (λ_{exc} = 365 nm), i) PMB-PBL solutions without sonication. ii) MeCN/MeOH/H_2O blank. iii) The filtered solution of sonicated PMB-PBL (0.68 MHz). iv) The filtered solution of sonicated PMB-PBL (20 kHz). **h-i**, The release of fluorogenic cargo under 20 kHz and 0.68 MHz irradiation.

5.3.4 Flex-activation of mechanophores to release dansyl-fluorophore

The overwhelming majority of mechanophores are activated by the direct scission of bonds force-coupled along the pulling vector of the polymer chain. One notable exception are flex-activated mechanophores where the scission of bonds and the subsequent release of small molecules are induced by a distortion of adjacent bond angles.[55,57,58] However, up to today these could only be activated in bulk polymers by compression with single digit percentage released fractions[55,57,58] where double network hydrogels are a notable exception releasing ~ 20% of their payload.[61] Conversely, the ultrasound-induced flex-activation in solution has not been achieved.

To achieve flex-activation in PMBs, we synthesized the required oxanorbornadiene-based mechanophore **N4-A3** incorporating furylated dansyl as fluorogenic probe cargo (**Supplementary Scheme S4**). This was then either appended with initiator moieties for controlled radical polymerization yielding **N4-C4** toward linear control chains or with acrylates for use as crosslinker within the PMB system resulting in **N4-A4** and correspondingly PMB-Flex (**Supplementary Scheme S5**, **Figure 5a**). PMB-Flex showed a shell thickness of ~ 180 nm (**Supplementary Figure S28**) and were characterized by optical microscopy where no coalescence or rupture was observed for multiple days (**Figure 5b**).

Sonication of PMB-Flex with US at 20 kHz resulted in an immediate development of fluorescence (**Supplementary Figure S29a**), which led us to investigate the fluorescence intensities of sonicated samples in dependence of different applied sound intensities (**Supplementary Figure S30**). This yielded the activated mechanophore fractions (**Figure 5c**) with a positive correlation between US intensity released fraction. With 20 kHz US at 12 W cm^{-2} for 15 min, ~ 15% payload could be released comparing favorably to the original bulk polymer work of Boydston and coworkers.[54] Cross-validation by ^{1}H NMR underlined this result (**Figure 5d**). The application of 0.68 MHz US also successfully initiated the flex-activation release at focal pressures > 1000 kPa (**Supplementary Figure S31**, **Figure 5e**).

To scrutinize these results, we synthesized the monofunctional mechanophore **N4-B4** as a control sample that would not be able to undergo flex-activation, albeit being covalently copolymerized into the PMB shell (**Supplementary Figure S32**). No fluorescence was observed under sonication conditions identical to above excluding thermal or other interfering effects. Moreover, water-soluble, mechanophore-centered linear polymers (LPs) with M_n = 140 kDa were prepared to exclude the strong inertial cavitation of water as a source for the successful flex-activation. Also in this case sonication showed no fluorescence (**Figure 5f** and **g**) although the M_n decreased to ~ 100 kDa due to unproductive bond scission (**Figure 5h**). Likewise, no notable release could be discerned upon the sonication of solid microgel particles with diameters of ~ 25 µm containing **N4-A4** clarifying that dangling, solvated chain ends do not contribute to the observed PMB performance (**Supplementary Figure S33** and **S34**, **Figure 5i**).

We then measured force-distance curves by atomic force microscopy (AFM) equipped with an FMV-A tip. PMBs and control microgels revealed considerable differences in shape deformation when loading the same 5 nN force with average deformations of microgels and PMBs being 2.3 nm and 60.5 nm respectively (**Figure 5j**). PMBs showed an average stiffness of ~ 300 pN nm^{-1}, while the stiffness of microgels was one order of magnitude larger with ~ 4900 pN nm^{-1} (**Figure 5k** and **Supplementary Figure S35**). This relatively larger deformability of the PMB shells likely contributed significantly to stable as well as inertial cavitation induced by US.

An explanation of the flex-activation mechanism through combined experimental and computational studies was previously attempted by Boydston and coworkers and is the basis of the currently predominant interpretation of their observed results as caused by bond angle distortion.[54] To revisit the mechanistic interpretation of this activation mode, we first attempted to model the influence of the mechanical stress in PMBs by a pulling force, utilizing the approach of the "Force Modified Potential Energy Surface" (FMPES) according to Martínez and coworkers (**Figure 5l**).[62] In agreement with previously published literature, it became obvious that the simulation of a pulling force onto the system does not lead to a reduction of the activation energy of the flex-activation.[63-64] Even at high forces of 4.0 nN (**Figure 5m**), only a reduction in activation energy V_A of about 5.5 kcal mol^{-1} was observed, reflecting the mechanochemical inactivity of linear chains in elongational flow fields.[58] Since the US-induced deformation of PMBs arguably leads to the generation of a pressure load on the polymer shell,[50] a model based on the idea of the "Generalized Force Modified Potential Energy Surface"[65] (G-FMPES) was developed and applied to simulate uniaxial pressure onto the molecular system adding an external potential V_{ext} to the *ab initio* potential summing over all N atoms:

$$V_{ext} = \sum_{i=1}^{N} \frac{k}{2} \cdot z_i^2 \qquad (1)$$

In Eq. 1, z_i is the distance of the i-th atom to the plane created by the x- and the y-axes and k is an external parameter describing the strength of the uniaxial pressure acting on the system. Thus, every atom of the system was pushed towards the xy-plane by using a harmonic potential. The corresponding external force $\boldsymbol{F}_{ext}$ were then obtained by calculating the negative derivative of the external potential V_{ext} with respect to the spatial coordinates. When exposed to uniaxial pressure, an increase in activation energy V_A was observed at small values of k, which was caused by the rather unfavorable orientation of the transition state with respect to the xy-plane. With increasing force constants, a reduction of the activation energy V_A was obtained (**Figure 5n**). Using a force constant of 50 N m^{-1}, the activation energy V_A is reduced to 16 kcal mol^{-1}, which is a sufficiently small barrier for the reaction to occur.

In combination, our experimental and computational results on the one hand consolidate the findings of previous studies,[54,58] and on the other hand arguably suggest that the bursting of PMBs does not result in a stretching but rather in a compressive force. This would be in stark contrast to conventional US-based polymer mechanochemistry that relies on the overstretching of polymer segments in cavitation-induced flow fields.[66] Our findings on linear chains and microgels suggest that the uncoiling and overstretching of solvated chain segments is insufficient to drive the flex-activation mechanism. Contrarily, the elastic crosslinked network structure, expected stable and inertial cavitation of the PMB gas core, and the computationally demonstrated reduction of the activation barrier upon uniaxial compression indicate that compressive rather than extensional forces might act on the polymer system upon ultrasonication. The absence of activation of the monofunctional mechanophore is not in disagreement with this hypothesis since the accessible conformation space of a bifunctionally copolymerized mechanophore is considerably lower compared to its monofunctional counterpart inhibiting possible rotation of the molecule out of the direction of compression to avoid the energetically penalized bond angle distortion.

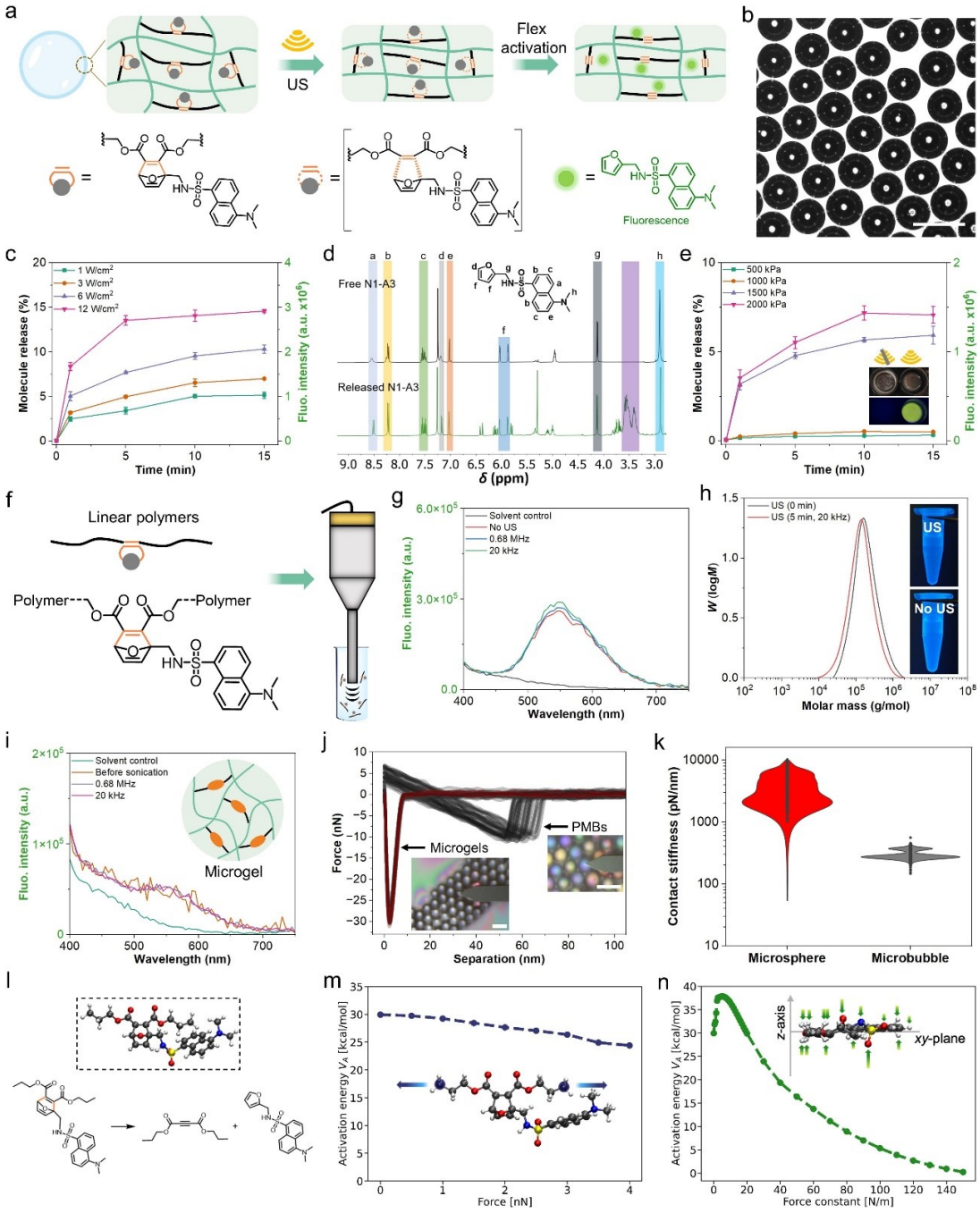

Figure 5. Ultrasound-triggered flex-activation of mechanophores in PMBs**. a**, Schematic illustration. **b**, Optical micrograph of PMB-Flex, scale bar: 50 µm. **c**, Fluorophore (**N1-A3**) release from PMB-Flex under 20 kHz US irradiation. **d**, ^{1}H NMR spectra of free **N1-A3** and released **N1-A3**. **e**, Fluorophore release from PMB-Flex under 0.68 MHz US irradiation. Inset: photographs of PMBs before (left) and after (right) HIFU treatment under daylight (top) and 365 nm UV (bottom) illumination in MeCN/H_2O. **f**, Representation of mechanophore-centered LPs upon sonication. **g**, Fluorescence spectra of LPs before and after US. **h**, GPC RI molar mass distributions of LPs before and after sonication. Insets: photographs of LP solutions under 365 nm UV in MeCN/H_2O. **i**, Fluorescence spectra of microgel suspension after 5 min US irradiation. **j**, Force-distance curves of PMB-Flex and microgels obtained by AFM. **k**, Stiffnesses of PMB-Flex and microgels obtained from panel **j**. **l**, Molecular structure that was used in computational modelling to investigate the flex activation. **m**, Activation energy V_A in dependence of the applied pulling force. **n**, Activation energy V_A in dependence of the force constant of the applied uniaxial pressure.

5.4 Conclusion

We here presented the versatile character and unique mechanochemical activation pathway of PMBs for polymer mechanochemistry. We showed that the PMB platform is suitable to activate several mechanophore classes, ranging from covalent disulfide scission over rDA reactions of furan-maleimide adducts to the flex activation of furan-acetylene adducts. Underscored by molecular computation, we found that the elastic polymer network shell in combination with stable and inertial cavitation of the PMBs' gas cores likely lead to the application of a compressive force onto the polymer structure rather than the elongational force usually observed for solvated polymer chains during ultrasonication. Thereby, the PMB system is able to drive mechanochemical reactions previously restricted to bulk polymer networks by US establishing a conceptual link between solution and network polymer mechanochemistry.[67]

With the employed mechanophores we moreover showed that several pathways to release small molecule cargo are accessible using the PMB platform. In addition, the PMB's unique cavitation response enabled the use of high frequency US up to the MHz range to achieve the desired release. In combination, these results underpin the high future potential of mechanoresponsive PMBs for targeted drug delivery applications, although several challenges, such as the PMB size, must be overcome in the future for diagnostic and therapeutic applications.

5.5 Experimental section

5.5.1 Materials

All chemical reagents and solvents were used without further purification unless otherwise stated. Dansyl chloride (98%), furfurylamine (99%), 2-isocyanatoethyl methacrylate (contains ≤ 0.1% BHT as inhibitor, 98%), ethyl propiolate (99%), lithium bis(trimethylsilyl)amide solution (LHDMS, 1.0 M in THF), toluene (≥99.5%), 2-hydroxyethyl disulfide (technical grade), methacryloyl chloride (97%), triethylamine (TEA, ≥ 99%), dichloromethane (CH_2Cl_2, anhydrous, ≥99.8%), MeCN (99.8%), N,N'-disuccinimidyl carbonate (DSC, ≥95%), methylmagnesium bromide (3.0 M in diethyl ether), diethyl ether (99.7%), 1-pyrenebutanol (PBL, 99%) 1-pyrenebutyric acid (97%), DMSO (99.9%), $CuBr_2$ (99%), Me6TREN (97%), acetylenedicarboxylic acid (95%), 1,6-hexanediol (97%), benzene (99.8%), α -bromoisobutyryl bromide (98%), 5-(hydroxymethyl)furfural (99%), triphosgen (TPS, 99%), 1,6-hexanediol dimethacrylate (≥90%), poly(propylene glycol) diacrylate (PPGDA, average Mn ~800), poly(propylene glycol) (PPG, average Mn ~2,000), poly(vinyl alcohol) (PVA, M_w 31,000-50,000), glycerol (99.5%), 2-mercaptoethanol (MCE, 99%), were obtained from Sigma-Aldrich.
Ethyl (2,4,6-trimethylbenzoyl)phenylphosphinate (TPO-L, 95%, Fluorochem), umbelliferon (UMB, 98%, Acros), camptothecin (CPT, 95%, abcr), 4-(dimethylamino)pyridine (DMAP, >99.0%, TCI Deutschland GmbH), p-toluenesulfonic acid monohydrate (PTSA, 98%, TCI Deutschland GmbH), N-(2-Hydroxyethyl)maleimide (98%, TCI Deutschland GmbH), were used as received. Poly(ethylene glycol) methyl ether methacrylate (PEGMEMA, M_n ~ 300 Da, Sigma-Aldrich) were purified by a column of activated basic Al_2O_3 to remove the inhibitor. Dialysis membranes (3.5 kDa MWCO) were obtained from Spectrum Labs. Centrifugal filter (3000 MWCO) was obtained from Sartorius. HeLa cell line was obtained from ATCC: The Global Bioresource Center. Ultrapure Milli-Q water (18.2 MΩ·cm) was used for all experiments.

5.5.2 Analytical instrumentation

(1) ^1H and ^{13}C NMR spectra were recorded at room temperature in $CDCl_3$ on a 400 MHz Bruker Avance 400 spectrometer (^{13}C: 101 MHz). The chemical shifts are reported in δ units using residual protonated solvent signals as internal standard[1] (^1H: $CDCl_3$ (δH = 7.26 ppm), ^{13}C: $CDCl_3$ (δC = 77.16 ppm); ^1H: $(CD_3)_2SO$ (δH = 2.50 ppm), ^{13}C: $(CD_3)_2SO$ (δC = 39.53 ppm)). The following abbreviations were used: s = singlet, d = doublet, t = triplet, q = quartet, sept. = septet, dd = doublet of doublets etc., m = multiplet. Coupling constants (*J*) were given in Hz and refer to the respective H, H-couplings.
(2) Electrospray ionization (ESI) MS: micrOTOF-Q II™ ESI-Qq-TOF mass spectrometer system (BRUKER).
(3) Thin-layer chromatography (TLC) was conducted on Merck TLC Silica Gel 60 F_{254} plates, which featured a fluorescence indicator for visualization under 254 nm or 365 nm UV light using a hand lamp. High-purity silica gel (40–63 μm) was utilized for flash column chromatography.
(4) Gel permeation chromatography (GPC/SEC) with THF (HPLC grade) was performed using a Jasco PU-2080plus HPLC pump equipped with a Jasco RI-2031plus refractive index detector. As an internal standard, the sample solvent contained 250 mg/mL 3,5-di-*t*-4-butylhydroxytoluene (BHT, ≥99%, Fluka). A pre-column (8×50 mm) and four SDplus gel columns (8×300 mm, SDplus, MZ Analysentechnik) were used at a controlled flow rate of 1.0 mL/min at 20 °C. The gel particles had a diameter of 5 μm, with nominal pore sizes of 50, 102, 103, and 104 Å. Calibration was performed using narrowly distributed poly(methyl methacrylate) (PMMA)

standards from Polymer Standards Service. Molar masses (M_n and M_w) and molar mass distributions (M_w/M_n) were determined using PSS WinGPC UniChrom software (Version 8.1.1).

(5) Transmission electron microscopy (TEM) images were captured on a LIBRA®120 transmission electron microscope (Carl Zeiss) with an accelerating voltage of 120 kV and images were recorded using a Gatan Ultra Scan 1000. Transmission electron microscopy (TEM) sample preparation: one drop (~ 10 μL) of sample was deposited onto carbon-coated copper grid, then air-dried.

(6) Ultra-high-performance liquid chromatography-mass spectrometry (UHPLC-MS) analysis was conducted using an ACQUITY UPLC I-Class System (Waters) equipped with an ACQUITY UPLC PDA eλ Detector and an ACQUITY QDa detector (Waters). Solvents: A= water (contained 0.1% TFA), B= acetonitrile (contained 0.1% TFA); Flow= 0.4 mL/min; Gradient (B): 0-1 min (10%), 1-5 min (10% - 90%), 5-7 min (90%), 7-10 min (90% - 10%).

(7) Optical microscopy: the imaging of PMBs was performed on a confocal laser scanning microscope (STP8, Leica).

5.5.3 Fluorescence spectroscopy

Fluorescence spectra were collected by SpectraMax iD3 Multi-Mode Microplate Reader (Molecular Devices) at room temperature. The fluorescence spectra measurements from PMBs-MDF, samples were excited at 340 nm. The spectral bandwidths were set to 5 nm (400 nm - 750 nm) for emission. To obtain the standard curve of dansyl-fluorophore (**N1-A3)**, the fluorescence intensity at the emission wavelength of 545 nm was collected. The fluorescence spectra measurements from PMBs-UMB, samples were excited at 325 nm. The spectral bandwidths were set to 5 nm (370 - 650 nm) for emission. To obtain the standard curve of UMB, the fluorescence intensity at the emission wavelength of 465 nm was collected. The fluorescence spectra measurements from PMBs-CPT, samples were excited at 335 nm. The spectral bandwidth for emission was set to 5 nm (375-600 nm). To generate the standard curve for CPT, fluorescence intensity was recorded at 450 nm. To obtain the fluorescence spectra of PMBs-PBL, excitation was performed at 320 nm, with an emission bandwidth of 5 nm (360-500 nm). The standard curve for PBL was obtained by collecting fluorescence intensity at 390 nm. To obtain the fluorescence spectra of PMBs-Flex, excitation was performed at 340 nm, with an emission bandwidth of 5 nm (400-750 nm). Samples were incubated at room temperature for 72 hours to complete downstream reactions before the fluorescence intensity collection. The fluorescence intensity collection were conducted using a pureGrade™ 96-well plate from BRAND GmbH. In addition, before fluorescence measurements, the sonicated PMBs solution required a filtration step. This involved a centrifugation (8000 ×g for 15 minutes), followed by filtration through a 3,000 MWCO centrifugal filter (5000 rpm).

5.5.4 Sonication experiments

20 kHz sonicator and 1.5 MHz HIFU setup were used to perform the ultrasound sonication experiments. The number concentration of PMBs (2.3×10^6 mL^{-1}), was calculated by an EVE Automatic cell counter (NanoEntek).

(1) 20 kHz sonicator: Sonication experiments were carried out using a Qsonica Q500 ultrasonic system with four 3.2 mm probes (No. A12628PRB20), f = 20 kHz. Pulsed sonication (2 s on, 1 s off) was used. The sound intensity I of applied ultrasound was calculated by $I = P{\cdot}A^{-1}$, where P is the output power obtained via the output energy over the sonication on-time t ($P = E{\cdot}t^{-1}$) and A is the surface area of the transducer probe ($A = \pi{\cdot}r^2$). The ultrasound properties (power intensity, amplification, and output energy) are shown in **Table S1**. Then, 100 μL

PMBs or 30 μL microgels was added to a 1.5 mL Eppendorf tube consisting of the corresponding solvent (immersed in an ice-water bath). Then, the samples were exposed to sonication for 1 min, 5 min, 10 min, and 15 min.

(2) HIFU: We used a home-made HIFU device for ultrasonic sonication experiments. The core components included a waveform generator (33511B, Keysight Technologies), an RF amplifier (AG1021, T&C Power Conversion, Inc.), and transducers operating at 0.66 MHz, 1.5 MHz, and 2.5 MHz (Precision Acoustics Ltd., UK). In addition, a 0.5 mm needle hydrophone (Precision Acoustics Ltd., UK) was used to position the transducer's focus. A custom-made motorized 3D manipulator/positioning system was used to control the position of the well plate submerged in water. The focal point of transducer was positioned in the center of the well, 3 mm above its bottom. Voltage applied to the transducer was measured by the oscilloscope and adjusted to obtain the desired acoustic power based on the transducer's factory calibration data extrapolated to low voltages. Pulsed sonication (2 s on, 1 s off) was used. 100 μL PMBs was mixed with 1 mL solvent, then transfer to the 24 well plate that with an acoustically transparent base made from ultra-thin film (lumox® multiwall 24, SARSTEDT). Then, the 24 well plate are placed on the well plate holder. Samples exposed to irradiation for 1 min, 5 min, 10 min and 15 min.

5.5.5 MTS proliferation assays

HeLa cells were used to evaluate the cytotoxicity of different samples. HeLa cells were cultured in a basal medium containing DMEM (supplemented with 10% fetal bovine serum and 1% antibiotics/antimycotics) at 37 °C. Actual cell viability was monitored by using the tetrazolium compound 3-(4,5-dimethylthiazol-2-yl)-5-(3-carboxymethoxyphenyl)-2-(4-sulfophenyl)-2H-tetrazolium (inner salt, MTS reagent) and a chemical electron acceptor dye (phenazine ethosulfate; PES) (Promega, Germany) using an assay according to the manufacturer's instructions. Briefly, approximately 5,000 cells in 100 μL of medium were seeded into 96-well plates. Following overnight incubation, the existing medium was carefully aspirated and replaced with 100 μL of fresh medium containing varying concentrations of the test samples. Control wells received DMSO alone, ensuring that its final concentration did not exceed 0.5% to prevent cytotoxic interference. After 48 hours of incubation, the culture medium was gently removed, and the cells were rinsed with 100 μL of PBS buffer to eliminate residuals. Subsequently, 20 μL of MTS reagent was combined with 100 μL of fresh medium and added to each well. A mixture of MTS reagent with culture medium served as the negative control. To ensure homogeneity, the solution was thoroughly mixed, and absorbance was measured at 490 nm using a Synerg^{TM} HT microplate reader (BioTek Instruments). The resulting MTS signals were analyzed to assess cell viability and growth. All experimental conditions were conducted in at least triplicate to ensure statistical reliability.

5.5.6 Computations

Computations were performed on the level of density functional theory (DFT) employing the B3LYP functional[68-70] using D3-dispersion correction[71] and the 6-31G* basis set.[72-74] TeraChem[75-76] was utilized for computing the electronic structure. Stationary points under the influence of external forces were obtained using DL-FIND,[77] which is interfaced to TeraChem *via* a python interface. This python interface allows to incorporate a module simulating the effects of a pulling force as well as the effects of a uniaxial acting force. The convergence criterium for the gradient was set to 1.0 10^{-4} atomic units. To confirm whether the geometry found is a minimum on the (force-modified) potential energy surface, the eigenvalues of the Hessian matrices were

considered, as for minima the Hessian matrix is positive definite. For the optimization of transition state structures, the dimer method was used.[78-79] The found structures were confirmed to be first order saddle points on the (force-modified) potential energy surface by the Hessian matrices as they show exactly one negative eigenvalue in case of a transition state. For calculations utilizing the FMPES approach, the external force was increased stepwise in increments of 0.5 nN up to 4.0 nN. For simulating a uniaxial pressure onto a system, the force constant k of the external harmonic potential was increased in general in increments of 10 N m^{-1}. At regions of low pressure smaller increments were chosen to achieve better resolution on the effects of lower uniaxial pressure onto a molecular system.

5.5.7 Microfluidic Engineering

(1) Microfluidic chip preparation

The template of chip channel is printed on glass slide using the high-resolution 3D printer (Photonic Professional GT2, Nanoscribe GmbH & Co. KG) with a 25× objective. Then, the glass slide is transferred into a PGMEA bath to remove uncured photoresist and develop the printed geometry patterns. Isopropanol is used to wash the glass slide once. SYLGARD™ 184 silicone elastomer kit (Dow Corning) is poured on the glass slide and cured for 4 h at 60 ℃. After cooling, PDMS replica is peeled off from the slide. Then, PDMS replica was punched to produce inlets and outlet. Subsequently, the PDMS replica is assembled with a clean glass slide by oxygen plasma treatment. Lastly, the assembly is heated in the oven for 3 d at 60 ℃ to obtain the microfluidic chip.

Dopamine is used for the surface hydrophilisation process of chip channel forward to prepare the polymeric microbubbles by microfluidic engineering. 2.0 mg·mL^{-1} dopamine solution (pH 8.0 Tris buffer) is filled to the microfluidic chip chanel and kept for 30 min. Then, DI water is injected to flush the microchannel twice. Finally, a hydrophilic-treated chip was obtained (as **Figure S1** shows), which was used to prepare polymeric microbubbles through microfluidic engineering.

(2) Microfluidics station

Self-made microfluidics station was used to prepare the microbubbles and microgels. The connection between the computer, microscopy, syringe pump, flow controller, and microfluidic chip is shown in **Figure S2**.

5.5.8 Preparation of polymeric microbubbles and microgels

(1) Preparation of PMBs that contain masked dansyl-fluorophore (PMBs-MDF)

High-purity N_2 was used as the gas phase to prepare the G/O/W double emulsion polymeric microbubbles. First, N_2 was blown into the microfluidic chip with a flow controller (digital pressure valve) to regulate the flow rate. Then, the oil phase solution that was loaded in a glass syringe (Hamilton-Gastight #1001) was introduced into the chip by a syringe pump (PHD ULTRA™, Harvard Apparatus). The H_2O phase solution was squeezed into the microfluidic chip through a flow controller (pressure pump, Millipore). Once the flow rate of each phase reaches the desired value, the double emulsion production in the microfluidic device proceeds automatically. The PMBs products were collected in a glass vial. Finally, PMBs were washed 3 times using DI H_2O before sonication. G/O/W emulsion: Gas: N_2; Oil phase (~ 1 ml): PPGDA (400 mg), PPG (50 mg), TPO-L (10 mg), toluene (440 mg), **N2-CL** (100 mg), **N1-DA2** (2 mg); H_2O phase: PVA (4.5%, w/w), glycerol (40%, v/v). Flow rate: gas (530 mbar), oil phase (90 nL min^{-1}), H_2O phase (2.3 bar). A high-power UV LED LZ1-10UV0R-0000 (set 200 mA, Osram) was fixated above the outlet tube to initiate the oil-phase shell polymerization. Next, 100

μL PMBs was mixed with 1 mL solvent (MeCN:H_2O, 1:1), then transferred to a 1.5 mL Eppendorf tube or 24 well plate (lumox® multiwall 24, SARSTEDT). The PMBs were exposed to US irradiation for constant time.

Quantification of molecules release: 100 μL PMBs-MDF were mixed with 1 mL solvent (MeCN:H_2O, 1:1), and were then transferred to a 1.5 mL Eppendorf tube. Next, the samples were sonicated for 30 minutes (20 kHz) to break the PMBs into fragments. Then, 3 mg MCE (1000 times excess in respect to the N1-DA2) was added to the mixture to react with the N1-DA2 in the fragments. This mixture was incubated for 3 days shaking (700 rpm) at 37 ºC to ensure that all the N1-DA2 reacted with MCE. After centrifugation at RCF 8000 ×g for 15 min, the the solutions were filtered through a centrifugal filter (3,000 MWCO) by centrifugation at 5,000 rpm. The filtration steps were carried out toremove the fragments, and then the collected solution was transferred to a cuvette for the fluorescence measurements. The fluorescence intensity at 545 nm of the solution was measured. The obtained fluorescence intensity at 545 nm was defined as the maximum value F_m. Subsequently, we measured the fluorescence intensity of sonicated PMBs by the same method and defined the intensity value as F_s. Finally, we calculated the ratio of F_s / F_m as the maximum molecular release percentage.

(2) Preparation of PMBs-UMB or PMBs-CPT

High-purity N_2 was used as the gas phase to prepare the G/O/W double emulsions polymeric microbubbles. First, N_2 was blown into the microfluidic chip with a flow controller (digital pressure valve) to regulate the flow rate. Then, the oil phase solution that was loaded in a glass syringe (Hamilton-Gastight #1001) was introduced into the chip by a syringe pump (PHD ULTRA™, Harvard Apparatus). The H_2O phase solution was squeezed into the microfluidic chip through a flow controller (pressure pump, Millipore). Once the flow rate of each phase reaches the desired value, the double emulsion production in the microfluidic device proceeds automatically. The PMBs products were collected in a glass vial. Finally, PMBs were washed 3 times using DI H_2O before sonication. G/O/W emulsion: Gas: N_2; Oil phase (~ 1 ml): PPGDA (400 mg), PPG (50 mg), TPO-L (10 mg), toluene (440 mg), **N2-CL** (100 mg), **N2-A3** or **N2-B3** (2 mg); H_2O phase: PVA (4.5%, w/w), glycerol (40%, v/v). Flow rate: gas (530 mbar), oil phase (90 nL min^{-1}), H_2O phase (2.3 bar). A high-power UV LED LZ1-10UV0R-0000 (set 200 mA, Osram) was fixated above the outlet tube to initiate the oil-phase shell polymerization. 100 μL PMBs was mixed with 1 mL solvent (DMSO:H_2O, 4:1), then transferred to a 1.5 mL Eppendorf tube or 24 well plate (lumox® multiwall 24, SARSTEDT). The PMBs were exposed to US irradiation for constant time.

Quantification of molecules release: 100 μL PMBs-UMB or PMBs-CPT were mixed with 1 mL solvent (DMSO:H_2O, 1:1), and were then transferred to a 1.5 mL Eppendorf tube. Next, the samples were subjected to 30 minutes of sonication (20 kHz) to break the PMBs into fragments. Then, 3 mg MCE was added to the mixture to react with the N2-A3 or N2-B3 in the fragments. This mixture was incubated for 3 days (700 rpm) at room temperature to ensure that all the N2-A3 or N2-B3 reacted with MCE. After centrifugation at RCF 8000 ×g for 15 min, the solutions were filtered through a centrifugal filter (3,000 MWCO) by centrifugation at 5,000 rpm. The filtration steps were carried out to remove the fragments, and then the collected solution was transferred to a cuvette for the fluorescence intensity measurements. The fluorescence intensity at 465 nm of the solution was measured for UMB release. The obtained fluorescence intensity at 465 nm was defined as the maximum value F_m. Subsequently, we measured the fluorescence intensity of sonicated PMBs by the same method and defined the intensity value as F_s. Finally, we calculated the ratio of F_s / F_m as the maximum molecular release percentage. The fluorescence intensity at 450 nm of sonicated PMBs-CPT were collected for CPT release quantification.

(3) Preparation of PMBs-PBL

High-purity N_2 was used as the gas phase to prepare the G/O/W double emulsion polymeric microbubbles. First, N_2 was blown into the microfluidic chip with a flow controller (digital pressure valve) to regulate the flow rate. Then, the oil phase solution that was loaded into a glass syringe (Hamilton-Gastight #1001) and was introduced into the chip by a syringe pump (PHD ULTRA™, Harvard Apparatus). The H_2O phase solution was squeezed into the microfluidic chip through a flow controller (pressure pump, Millipore). Once the flow rate of each phase reaches the desired value, the double emulsion production in the microfluidic device proceeds automatically. The PMBs products were collected in a glass vial. Finally, PMBs were washed 3 times using DI H_2O before sonication. G/O/W emulsion: Gas: N_2; Oil phase (~ 1 ml): PPGDA (500 mg), PPG (50 mg), TPO-L (10 mg), toluene (440 mg), **N3-A5** (2 mg); H_2O phase: PVA (4.5%, w/w), glycerol (40%, v/v). Flow rate: gas (530 mbar), oil phase (90 nL min^{-1}), H_2O phase (2.3 bar). A high-power UV LED LZ1-10UV0R-0000 (set 200 mA, Osram) was fixated above the outlet tube to initiate the oil-phase shell polymerization. 100 μL PMBs was mixed with 1 mL solvent (MeCN:MeOH:H_2O, 14:5:1), then transferred to a 1.5 mL Eppendorf tube or 24 well plate (lumox® multiwall 24, SARSTEDT). The PMBs were exposed to US irradiation for constant time.

Quantification of molecules release: We used N3-A4 (1.4 mg, 2.78 μmol) to prepare the control PMBs that contain equal molar mass N3-A4 compared to the N3-A5 in PMBs-PBL. The prepared control samples (100 μL PMBs) were mixed with 1 mL solvent (MeCN:MeOH:H_2O, 14:5:1), and were then transferred to a 1.5 mL Eppendorf tube. Next, the samples were subjected to 30 minutes of sonication (20 kHz, 12 W cm^{-2}) to break the PMBs into fragments. This mixture was incubated for 3 days (1000 rpm) at 37 °C to ensure that the intermediate was decomposed completely (decomposition of the free furfuryl carbonate in polar protic solvent). After centrifugation at RCF 8000 ×g for 15 min, the solutions were filtered through a centrifugal filter (3,000 MWCO) by centrifugation at 5,000 rpm. The filtration steps were carried out to remove the fragments, and then the collected solution was transferred to a cuvette for the fluorescence intensity measurements. The fluorescence intensity at 390 nm of the solution was measured. The obtained fluorescence intensity at 390 nm was defined as the maximum value (F_m). Subsequently, we measured the fluorescence intensity of sonicated PMBs-PBL by the same method and defined the intensity value as F_s. Finally, we calculated the ratio of F_s / F_m as the maximum molecular release percentage.

(4) Preparation of PMBs-Flex

High-purity N_2 was used as the gas phase to prepare the G/O/W double emulsion polymeric microbubbles. First, N_2 was blown into the microfluidic chip with a flow controller (digital pressure valve) to regulate the flow rate. Then, the oil phase solution that was loaded into a glass syringe (Hamilton-Gastight #1001) was introduced into the chip by a syringe pump (PHD ULTRA™, Harvard Apparatus). The H_2O phase was squeezed into the microfluidic chip through a flow controller (pressure pump, Millipore). Once the flow rate of each phase reaches the desired value, the double emulsion production in the microfluidic device proceeds automatically. The PMBs products were collected in a glass vial. Finally, PMBs were washed 3 times using DI H_2O before sonication. G/O/W emulsion: Gas: N_2; Oil phase (~ 1 ml): PPGDA (500 mg), PPG (50 mg), TPO-L (10 mg), toluene (440 mg), **N4-A4** (2 mg); H_2O phase: PVA (4.5%, w/w), glycerol (40%, v/v). For the control samples, **N4-A3** or **N4-B4** (2 mg) was used to prepare PMBs. Flow rate: gas (530 mbar), oil phase (90 nL min^{-1}), H_2O phase (2.3 bar). A high-power UV LED LZ1-10UV0R-0000 (set 200 mA, Osram) was fixated above the outlet tube to initiate the oil-phase shell polymerization. 100 μL PMBs was mixed with 1 mL solvent (MeCN:H_2O, 1:1), then

transferred to a 1.5 mL Eppendorf tube or 24 well plate (lumox® multiwall 24, SARSTEDT). The PMBs were exposed to US irradiation for constant time.

Quantification of molecules release: 100 µL PMBs-Flex were mixed with 1 mL solvent (MeCN:H_2O, 1:1), and were then transferred to a 1.5 mL Eppendorf tube. Next, the samples were subjected to 30 minutes of sonication (20 kHz) to break the PMBs into fragments. Then, 3 mg MCE was added to the mixture to react with the N4-A4 in the fragments. This mixture was incubated for 3 days incubation with shaking (700 rpm) at 37 ºC to ensure that all the N4-A4 reacted with MCE. After centrifugation at RCF 8000 ×g for 15 min, the solutions were filtered through a centrifugal filter (3,000 MWCO) by centrifugation at 5,000 rpm. The filtration steps were carried out to remove the fragments, and then the collected solution was transferred to a cuvette for the fluorescence intensity measurements. The fluorescence intensity at 545 nm of the solution was measured. The obtained fluorescence intensity at 545 nm was defined as the maximum value F_m. Subsequently, we measured the fluorescence intensity of sonicated PMBs by the same method and defined the intensity value as F_s. Finally, we calculated the ratio of F_s / F_m as the maximum molecular release percentage.

(5) Preparation of microgels

Preparation of microgels that contain masked dansyl-fluorophore

Microgels were prepared in an O/W single emulsion process. The oil phase solution was introduced into the microfluidic chip by a syringe pump (PHD ULTRA™, Harvard Apparatus). Then, the H_2O phase was squeezed into the chip by a flow controller. Once the flow rate of each phase reaches the desired value, the emulsion production in the microfluidic device proceeds automatically. The microgels were collected in a glass vial. Finally, microgels were washed 3 times using DI H_2O before sonication. O/W emulsion: Oil phase (~ 1 ml): PPGDA (840 mg), PPG (50 mg), TPO-L (10 mg), **N1-CL** (100 mg), **N1-DA2** (2 mg); H_2O phase: PVA (3%, w/w). Flow rate: Oil phase (150 nL min^{-1}), H_2O phase (0.27 bar). A high-power UV LED LZ1-10UV0R-0000 (set 400 mA, Osram) was fixated above the outlet tube to initiate the oil-phase polymerization. Then, the 30 µL microgels were mixed with 1 mL solvent (MeCN:H_2O, 1:1), transferred to a 1.5 mL Eppendorf tube or 24 well plate (lumox® multiwall 24, SARSTEDT). The microgels were exposed to US irradiation for constant time.

Quantification of molecules release: 30 µL microgel solution was mixed with 1 mL solvent (MeCN:H_2O, 1:1), and was then transferred to a 1.5 mL Eppendorf tube. Then, 3 µL MCE (excess in respect to the N1-DA2) was added to the mixture. This mixture was incubated for 3 days incubation with shaking (700 rpm) at 37 ºC to ensure that all the N1-DA2 reacted with MCE. After centrifugation at RCF 8000 ×g for 15 min, the collected solution was transferred to a cuvette for the fluorescence intensity measurements. The fluorescence intensity at 545 nm of the solution was measured. The obtained fluorescence intensity at 545 nm was defined as the maximum value F_m. Subsequently, we measured the fluorescence intensity of sonicated microgels by the same method and defined the intensity value as F_s. Finally, we calculated the ratio of F_s / F_m as the maximum molecular release percentage.

Preparation of microgels-Flex

Microgels that contain 'Flex-activated' mechanophores were prepared in an O/W single emulsion process. The oil phase solution was introduced into the microfluidic chip by a syringe pump (PHD ULTRA™, Harvard Apparatus). Then, the H_2O phase was squeezed into the chip by the flow controller. Once the flow rate of each phase reaches the desired value, the emulsion production in the microfluidic device proceeds automatically. The microgels were collected in a glass vial. Finally, microgels were washed 3 times using DI H_2O before sonication.

O/W emulsion: Oil phase (~ 1 ml): PPGDA (940 mg), PPG (50 mg), TPO-L (10 mg), **N4-A4** (2 mg); H_2O phase: PVA (3%, w/w). Flow rate: Oil phase (150 nL min^{-1}), H_2O phase (0.27 bar). A high-power UV LED LZ1-10UV0R-0000 (set 400 mA, Osram) was fixated above the outlet tube to initiate the oil-phase polymerization. Then, the 30 µL microgels were mixed with 1 mL solvent (MeCN:H_2O, 1:1), transferred to a 1.5 mL Eppendorf tube or 24 well plate (lumox® multiwall 24, SARSTEDT). The microgels were exposed to US irradiation for constant time.

Quantification of molecules release: 30 µL microgels-Flex were mixed with 1 mL solvent (MeCN:H_2O, 1:1), and were then transferred to a 1.5 mL Eppendorf tube. Then, 3 µL MCE (excess in respect to the N4-A4) was added to the mixture. This mixture was incubated for 3 days (700 rpm) at 37 ºC to ensure that all the N4-A4 reacted with MCE. After centrifugation at RCF 8000 ×g for 15 min, the collected solution was transferred to a cuvette for the fluorescence intensity measurements. The fluorescence intensity at 545 nm of the solution was measured. The obtained fluorescence intensity at 545 nm was defined as the maximum value F_m. Subsequently, we measured the fluorescence intensity of sonicated microgels by the same method and defined the intensity value as F_s. Finally, we calculated the ratio of F_s / F_m as the maximum molecular release percentage.

5.5.9 Preparation of linear polymers.

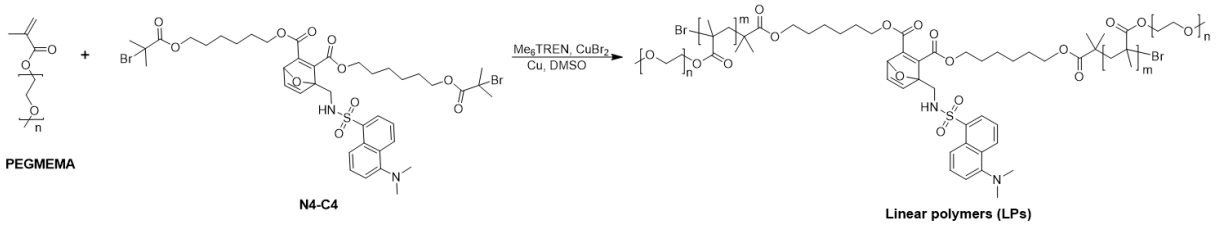

Linear polymers (LPs) were prepared according reported literature.[14] LPs were synthesized as follows. PEGMEMA (8 g, 26.6 mmol, 1330 equiv.), **N4-C4** (20 mg, 0.02 mmol, 1.0 equiv.), Me_6TREN (0.55 mg, 2.4 µmol) and $CuBr_2$ (0.29 mg, 1.3 µmol) were dissolved in DMSO (6 mL) in a Schlenk flask and sealed with a rubber septum reinforced with a cable tie. The solution underwent three consecutive freeze-pump-thaw cycles to remove dissolved gas. Simultaneously, a 6 cm copper wire was activated by immersion in 37% HCl for 30 minutes, followed by thorough washing with water and acetone before being dried. The activated copper wire was then introduced into the reaction mixture, initiating polymerization at room temperature for 11 hours. To terminate the reaction, the viscous solution was diluted with THF and passed through a column of basic Al_2O_3. After solvent removal under reduced pressure, the polymer solution was slowly added dropwise into ice-cold Et_2O under continuous stirring, leading to precipitation. The supernatant was decanted, and the polymer was re-dissolved in THF before undergoing a second precipitation in fresh Et_2O to enhance purity. Afterwards, it was again precipitated in fresh Et_2O. Linear polymers with molar masses of 140 kDa were obtained after repeating the precipitation process for three times.

5.5.9 Synthetic procedures and characterization data

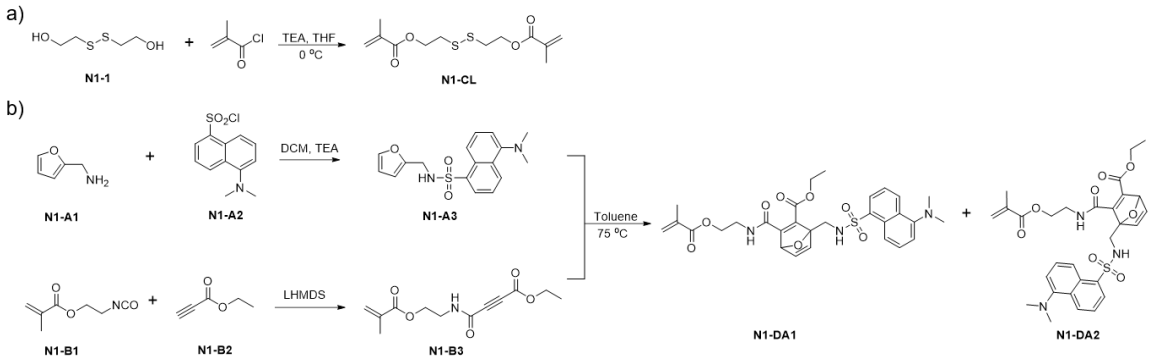

Scheme S1. Synthesis of bis(2-methacryloyl)oxyethyl disulfide (**N1-CL)** and probe molecule (**N1-DA2**).

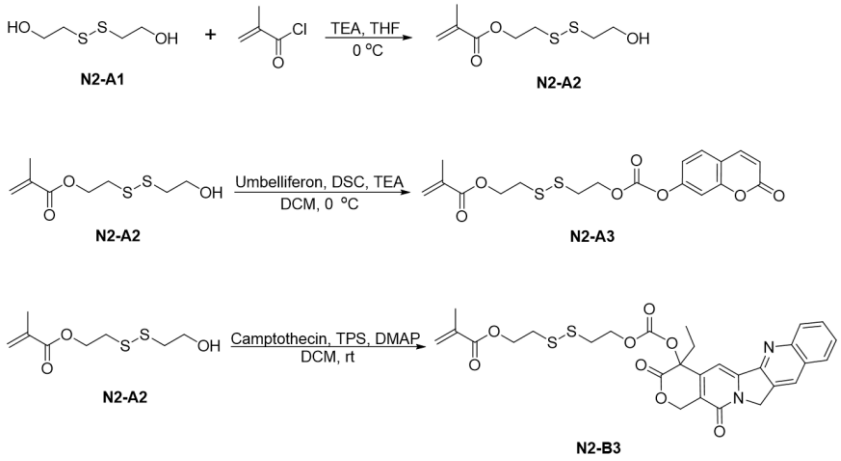

Scheme S2. Synthesis of probe molecule (**N2-A3**) and prodrug (**N2-B3**).

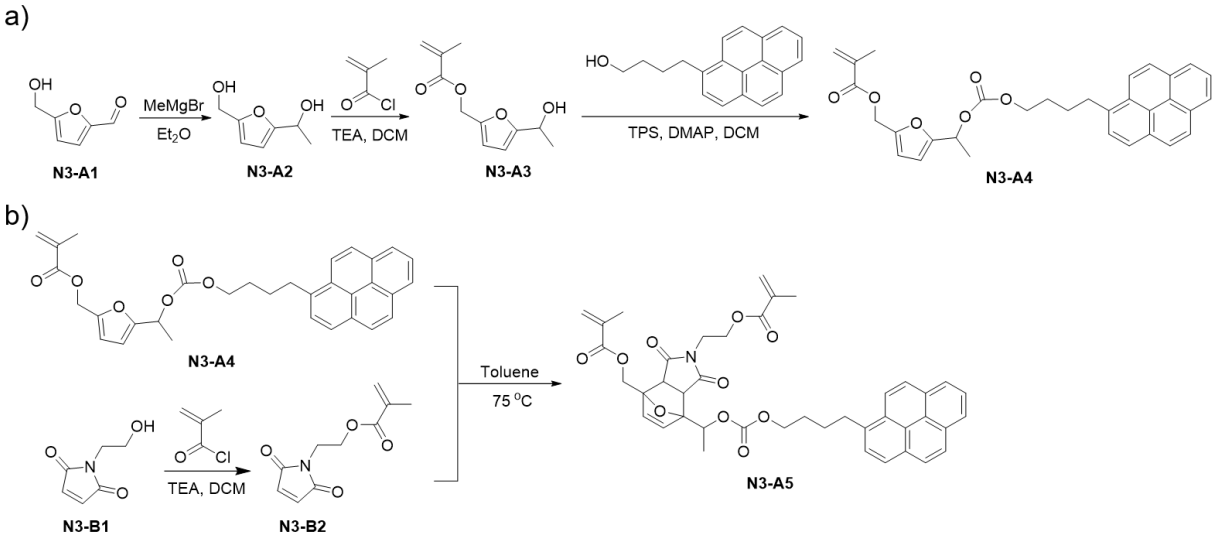

Scheme S3. Synthesis of probe molecule (**N3-A5**).

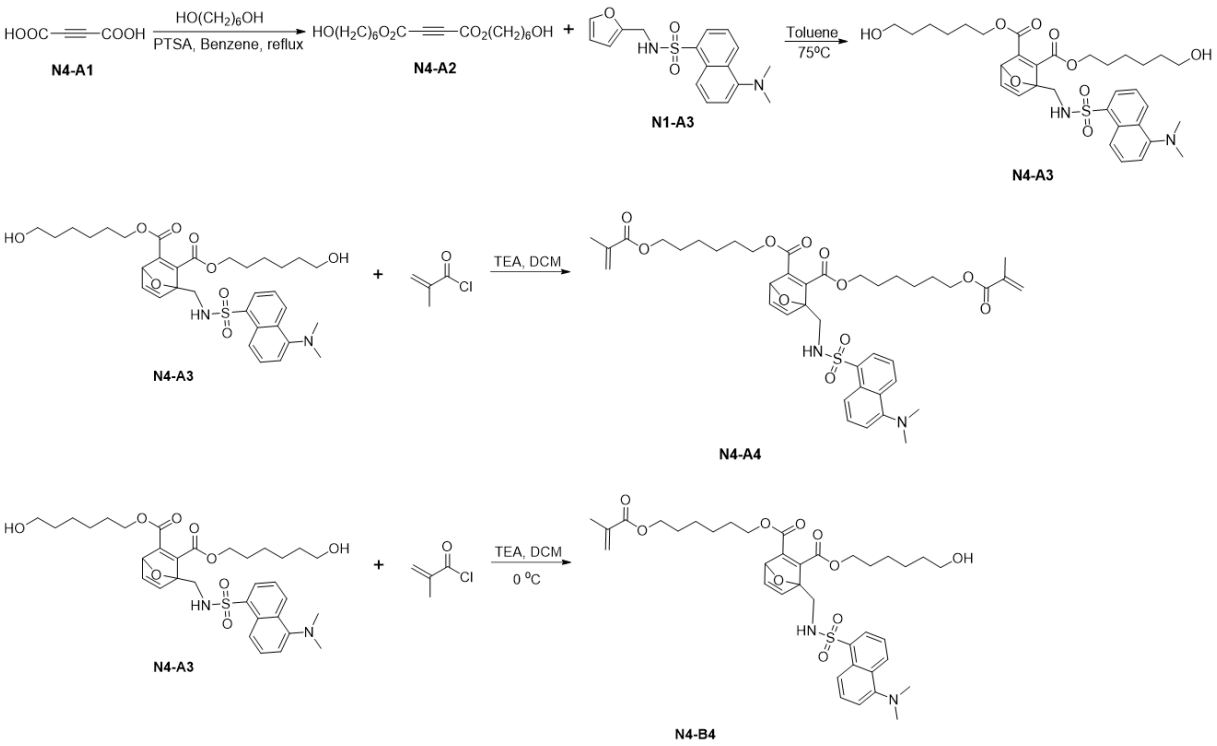

Scheme S4. Synthesis of probe molecule (**N4-A4**) and one side acrylate-probe (**N4-B4**).

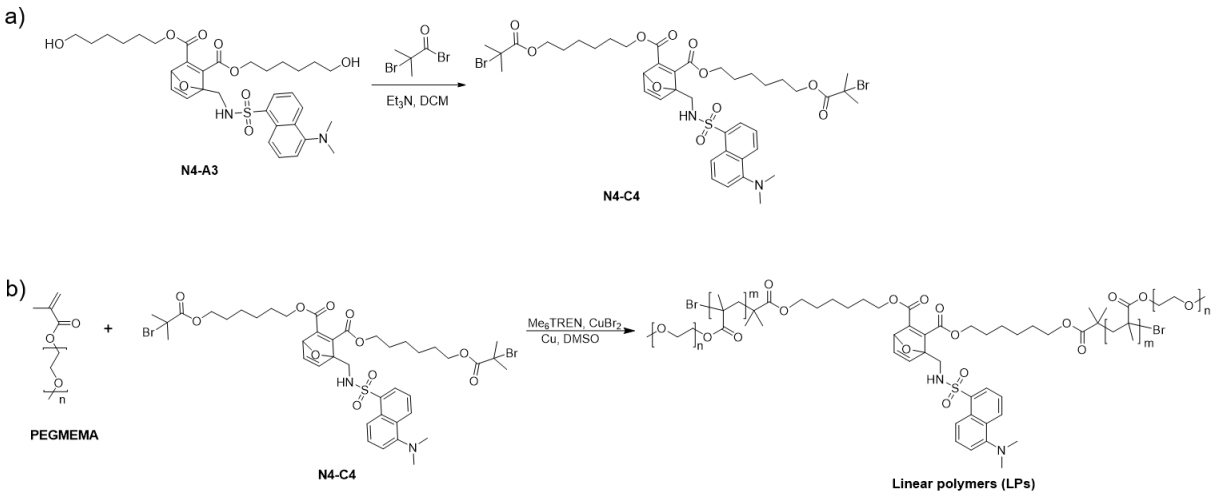

Scheme S5. Synthesis of alkyl bromide (**N4-C4**) and linear polymers (**LPs**).

Bis(2-methacryloyl)oxyethyl disulfide (**N1-CL**)

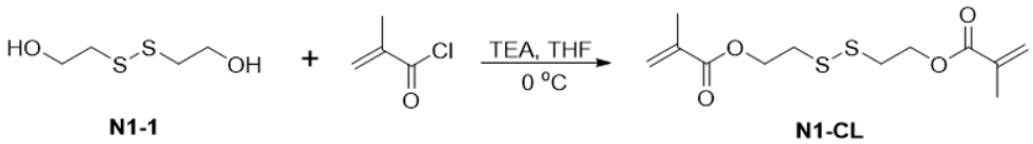

N1-1 **N1-CL**

2-hydroxyethyl disulfide (2.0 g, 13 mmol, 1 equiv.) and TEA (3.64 mL, 26 mmol, 2.0 equiv.) were added in THF (30 mL) with a constant flow of N_2. The mixture in a flask was placed into an ice-water bath to keep the temperature at 0 °C. Afterwards, a solution of methacryloyl chloride (2.54 mL, 26 mmol, 2.04 equiv.) and 15 mL CH_2Cl_2 were added dropwise (15 mL/h) to the reaction mixture via an injection pump. The reaction mixture was continuously stirred until the starting material was entirely consumed, as confirmed by TLC analysis. Then, it was washed with brine and deionized water three times, respectively. Afterwards, the crude product was purified by column chromatography on silica gel (hexane:EtOAc = 5:1) to give compound **N1-CL** (3.2 g, 85% yield) as a colourless oil. **^{1}H NMR (400 MHz, $CDCl_3$):** δ (ppm): 6.12 (sept, J=1.6 Hz, 2H), 5.58 (sept, J=1.6 Hz, 2H), 4.4 (t, J=6.8 Hz, 4H), 2.97 (t, J=6.8 Hz, 4H), 1.94 (s, J=1.2 Hz, 6H). **^{13}C NMR (101 MHz, $CDCl_3$):** δ (ppm): 167.23, 136.12, 126.13, 62.6, 37.39, 18.4. **ESI-MS** (*m/z*) for $C_{12}H_{18}O_4S_2$ expected $[M+Na]^+$: 313.0539, Found for $[M+Na]^+$: 313.0590.

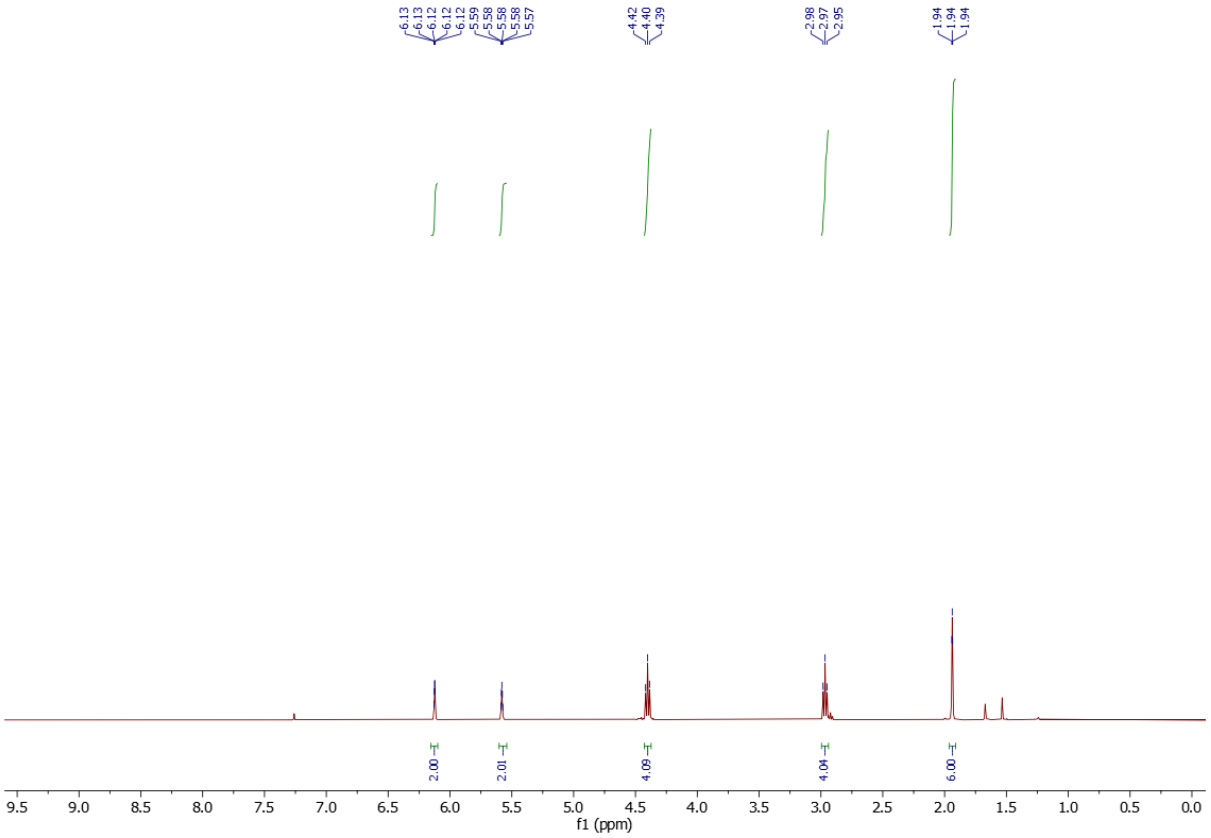

^{1}H NMR spectrum of **N1-CL**.

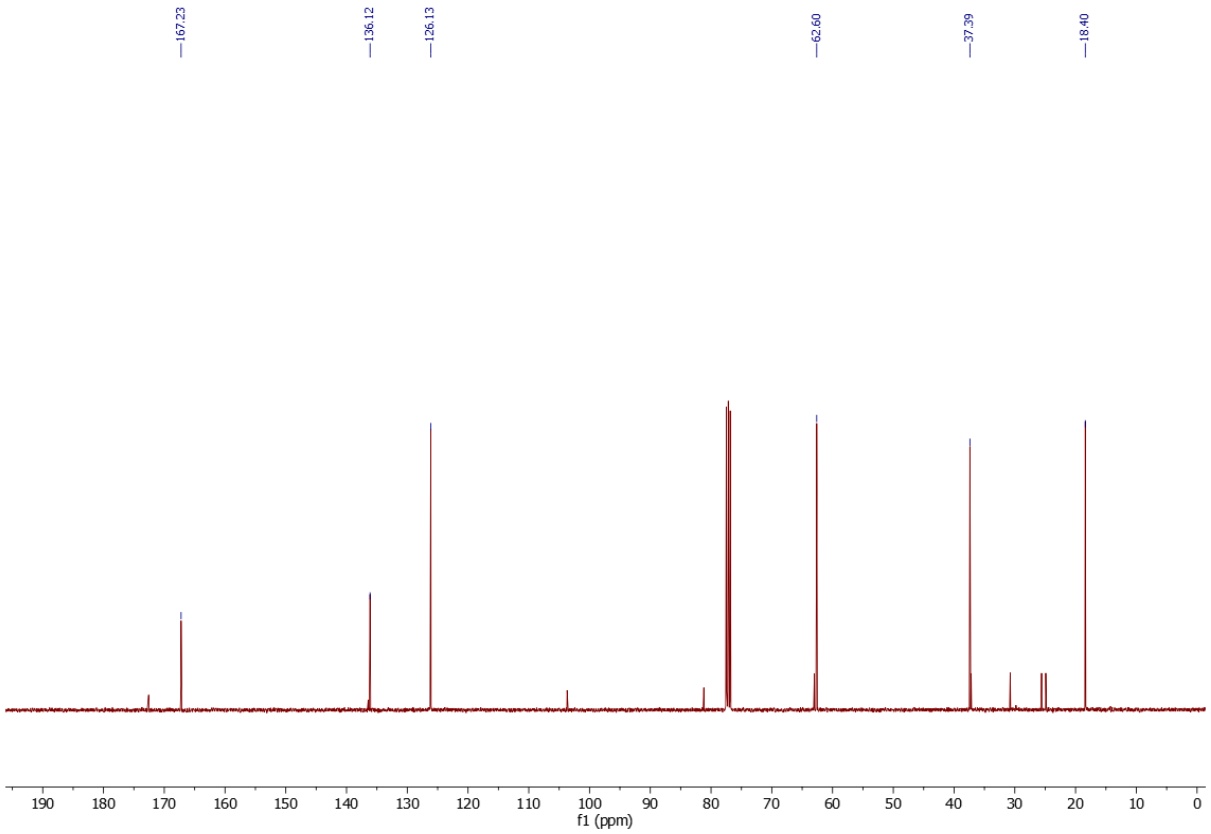

^{13}C NMR spectrum of **N1-CL**.

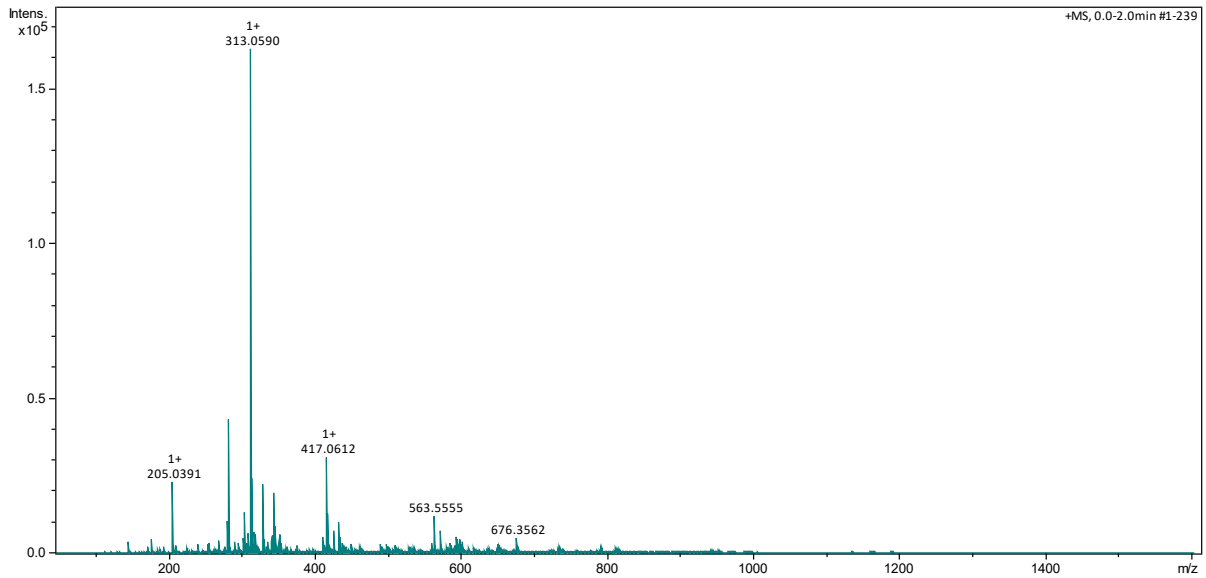

ESI-MS (*m/z*) of **N1-CL**.

5-(dimethylamino)-N-(furan-2-ylmethyl)naphthalene-1-sulfonamide (**N1-A3**)

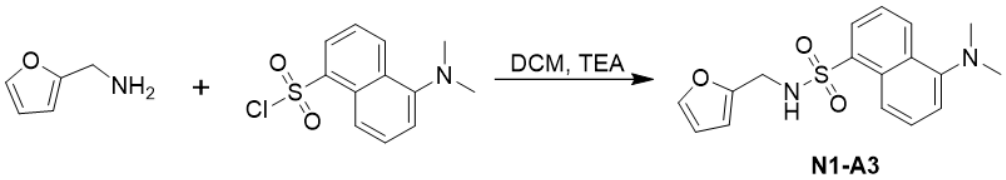

N1-A3 was synthesized according to a modified literature reaction.[59] A mixture of 5-(dimethylamino)naphthalene-1-sulfonyl chloride (1.00 g, 3.70 mmol, 1.0 equiv.) and Et_3N (1.0 mL, 7.2 mmol, 2.0 equiv.) in CH_2Cl_2 (20 mL) were added into a solution of furfurylamine (380 mg, 3.9 mmol, 1.05 equiv.) in CH_2Cl_2 (5 mL) via a syringe under N_2 protection. The resulting solution was stirred for 5 h at room temperature and poured into 1.0 mM pH 7 phosphate buffer (30 mL). Afterwards, the crude product was purified by column chromatography on silica gel (hexane:EtOAc = 5:1) to give compound **N1-A3** (1.16 g, 95% yield) as a yellow-green oil. **^{1}H NMR (400 MHz, $CDCl_3$):** δ (ppm): 8.50 (d, 1H, J = 8.0 Hz), 8.25-8.20 (m, 2H), 7.54-7.45 (m, 2H), 7.16 (d, 1H, J = 8.0 Hz), 7.01 (dd, 1H, J = 2.0 Hz, 0.8 Hz), 6.02 (dd, 1H, J = 3.2 Hz, 2.0 Hz), 5.87 (dd, 1H, J = 3.2 Hz, 0.6Hz), 5.19 (m, 1H), 4.12 (d, 2H, J = 6.0 Hz), 2.87 (s, 6H). **^{13}C NMR (101 MHz, $CDCl_3$):** δ (ppm): 151.95, 149.41, 142.20, 134.72, 130.50, 129.84, 129.60, 128.42, 123.13, 118.61, 115.14, 110.14, 107.98, 45.42, 40.20. **ESI-MS** (*m/z*) for $C_{17}H_{18}N_2O_3S$ expected $[M+H]^+$: 331.1111, Found for $[M+H]^+$: 331.1061.

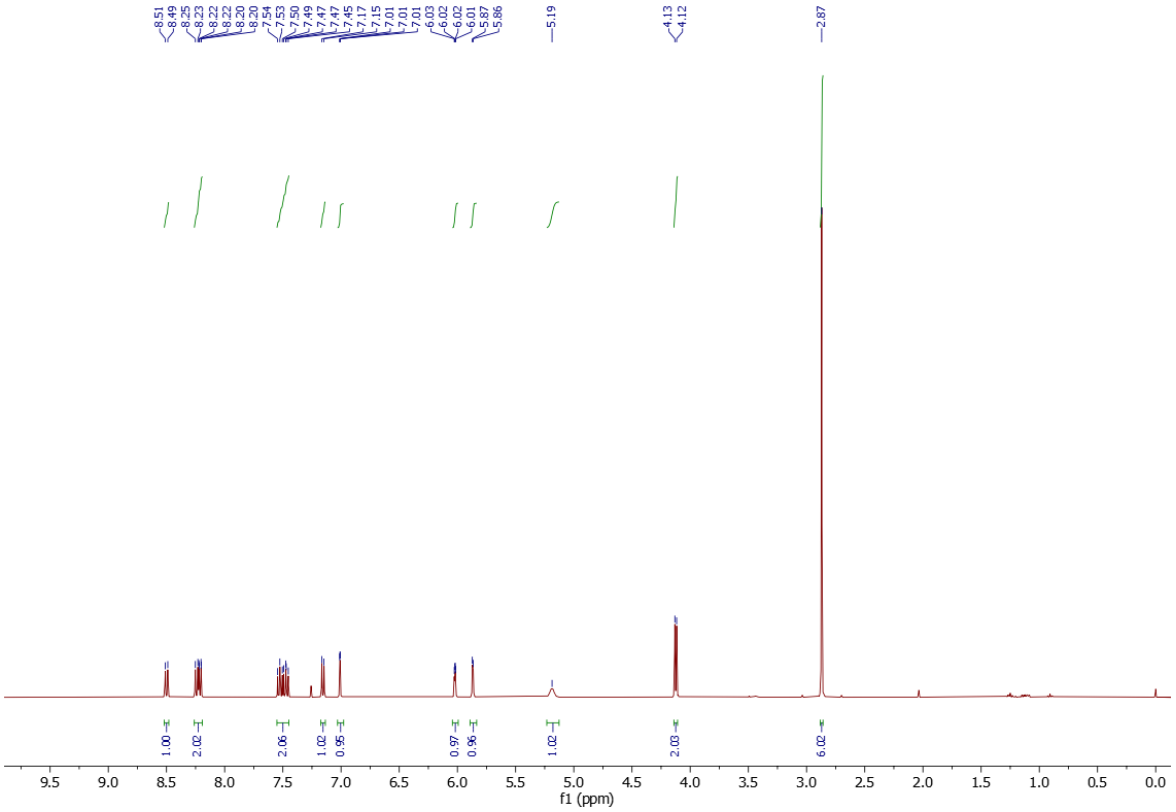

^{1}H NMR spectrum of **N1-A3**.

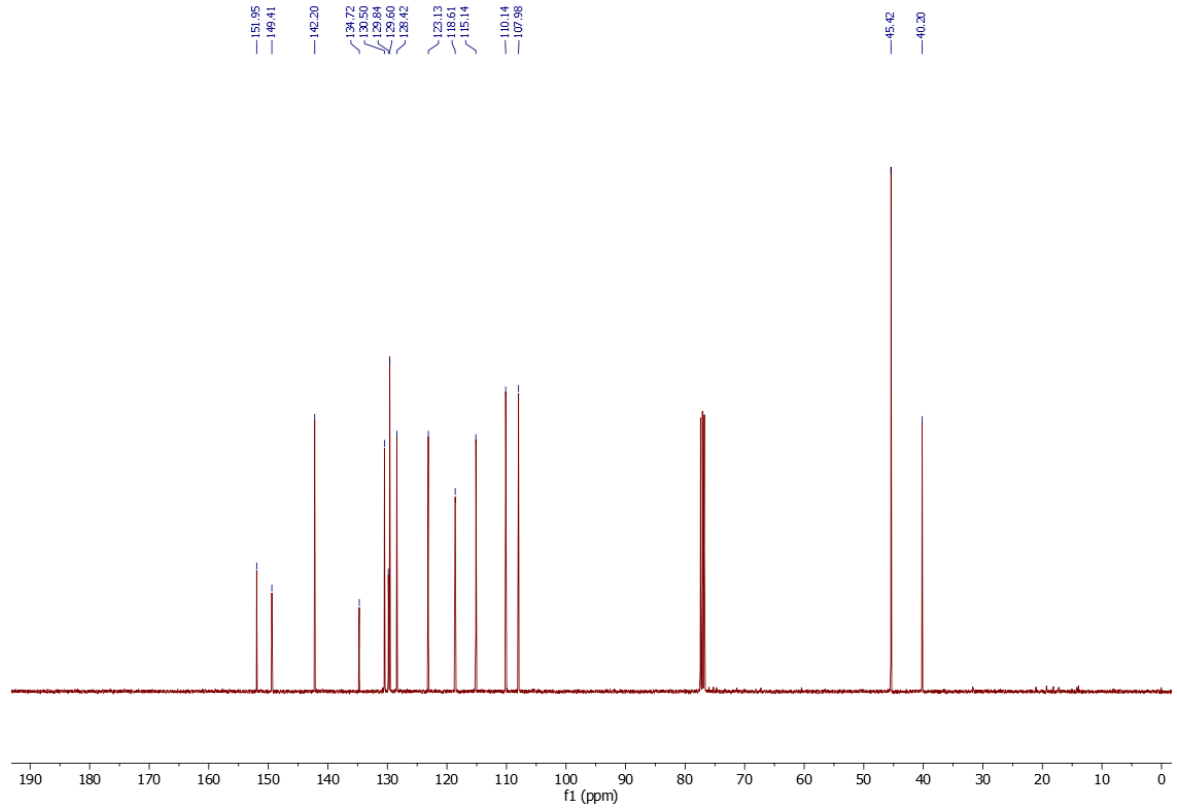

^{13}C NMR spectrum of **N1-A3**.

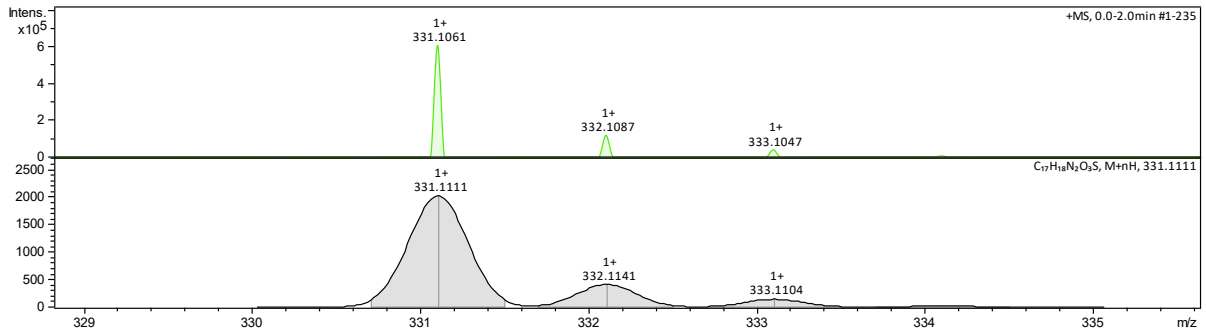

ESI-MS (*m/z*) of **N1-A3**.

Ethyl 4-((2-(methacryloyloxy)ethyl)amino)-4-oxobut-2-ynoate (**N1-B3**)

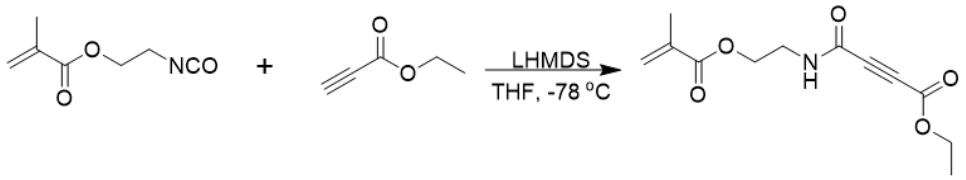

N1-B3

N1-B3 was synthesized following a reported procedure.[43] Ethyl propiolate (4.0 mL, 39.5 mmol, 1.0 equiv.) was dissolved in 60 mL of THF and cooled to -78 °C using a dry ice/acetone bath. LHMDS (1 M in THF, 40 mL, 40 mmol, 1.01 equiv.) was then added dropwise via a syringe pump over 30 minutes, and the reaction mixture was stirred for an additional 30 minutes at the same temperature. Subsequently, 2-isocyanatoethyl methacrylate (5.6 mL, 39.5 mmol, 1.0 equiv.) was introduced dropwise via a syringe pump. After stirring for another 30 minutes at -78 °C, the reaction was quenched with 80 mL of saturated aqueous NH_4Cl solution while maintaining the low temperature. Once the mixture gradually warmed to room temperature, 50 mL of water was added, and the organic and aqueous phases were separated. The aqueous layer was extracted with EtOAc (3 × 100 mL), and the combined organic extracts were sequentially washed with saturated aqueous $NaHCO_3$ and brine to remove impurities. Then, the organic layer was dried over $MgSO_4$, concentrated, and purified *via* column chromatography (hexane:EtOAc = 10:1) to give compound **N1-B3** (8.09 g, 81% yield) as a colourless oil. **^{1}H NMR (400 MHz, $CDCl_3$):** δ (ppm): 6.85 (t, J = 6.0 Hz, 1H), 6.10 (s, 1H), 5.61 – 5.56 (m, 1H), 4.28 – 4.20 (m, 4H), 3.61 (q, J = 5.6 Hz, 2H), 1.91 (s, 3H), 1.29 (t, J = 7.2 Hz, 3H). **^{13}C NMR (101 MHz, $CDCl_3$):** δ (ppm): 167.45, 152.34, 151.08, 135.77, 126.55, 76.93, 74.26, 63.03, 62.83, 39.28, 18.30, 13.94. **ESI-MS** (*m/z*) for $C_{12}H_{15}NO_5$ expected $[M+H]^+$: 254.1023, Found for $[M+H]^+$: 254.1030.

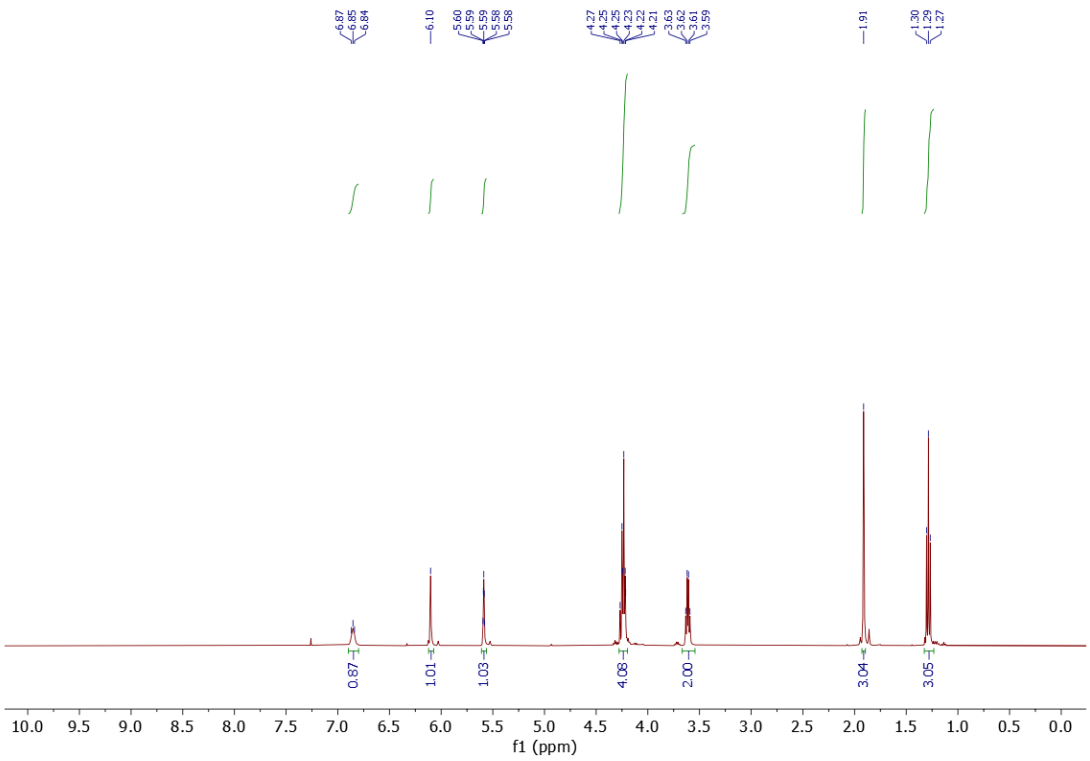

^{1}H NMR spectrum of **N1-B3**.

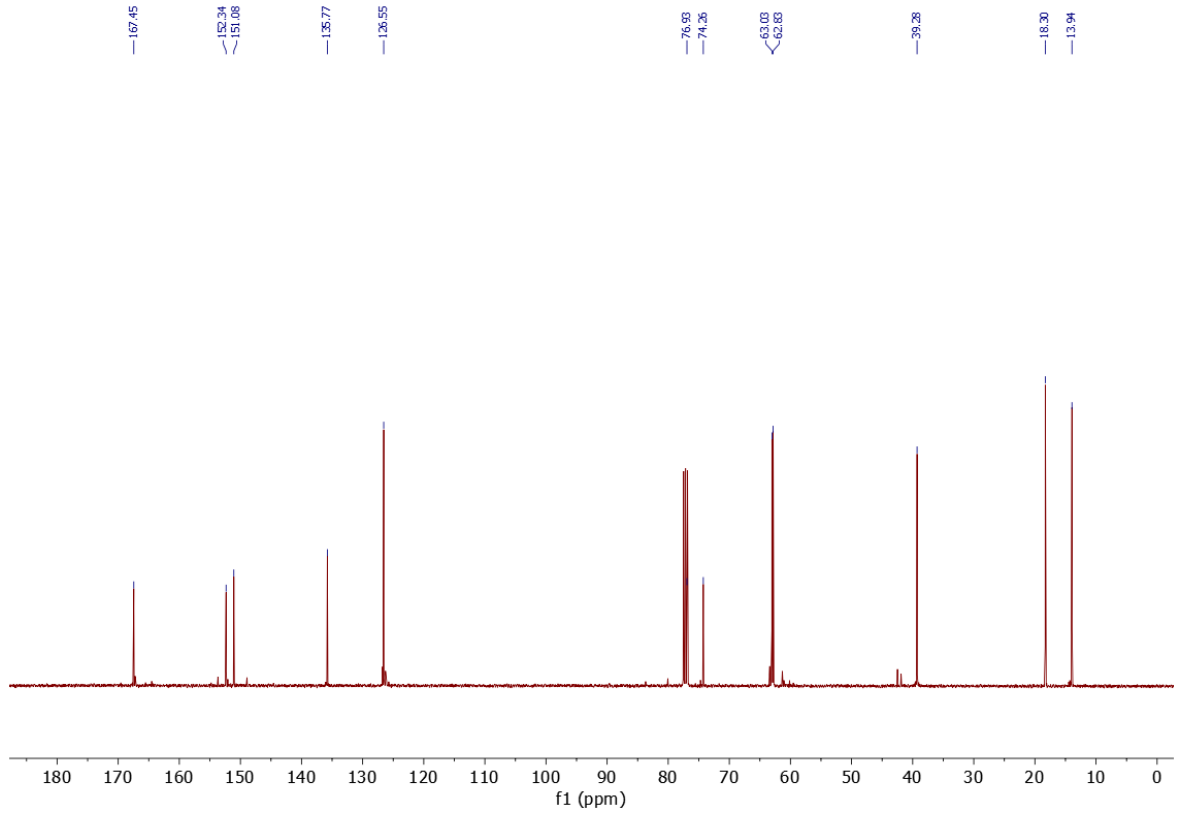

^{13}C NMR spectrum of **N1-B3**.

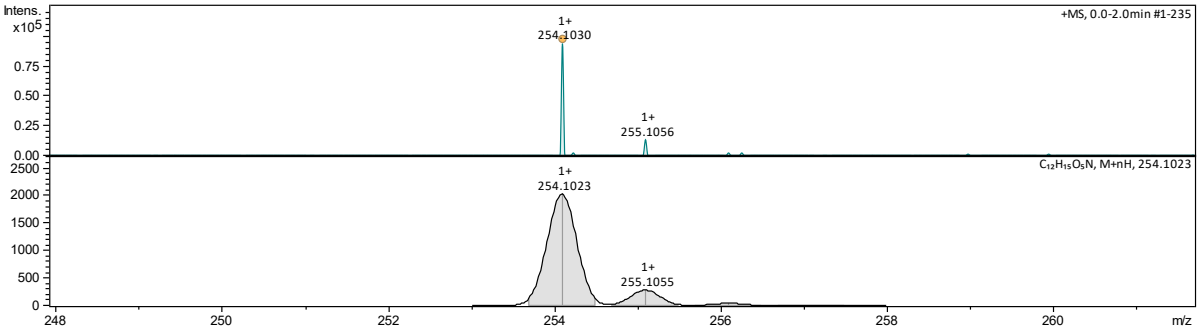

ESI-MS (*m/z*) of **N1-B3**.

Ethyl 1-(((5-(dimethylamino)naphthalene)-1-sulfonamido)methyl)-3-((2-(methacryloyloxy)ethyl)carbamoyl)-7-oxabicyclo[2.2.1]hepta-2,5-diene-2-carboxylate (**N1-DA1**) and Ethyl 4-(((5-(dimethylamino)naphthalene)-1-sulfonamido)methyl)-3-((2-(methacryloyloxy)ethyl)carbamoyl)-7-oxabicyclo[2.2.1]hepta-2,5-diene-2-carboxylate (**N1-DA2**)

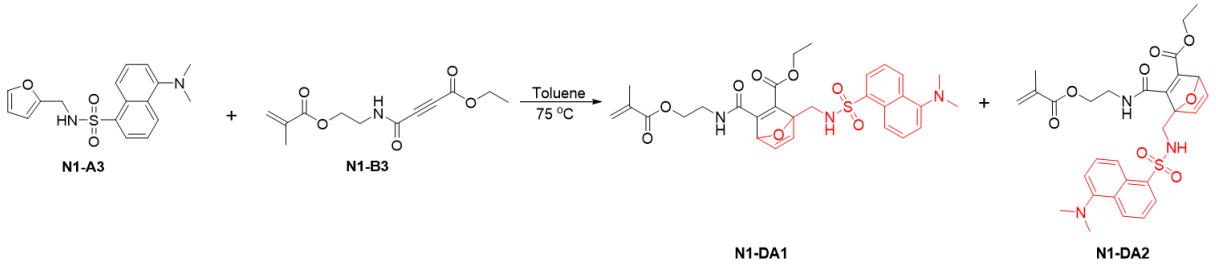

N1-A3 + N1-B3 → N1-DA1 + N1-DA2

N1-A3 (0.66 g, 2.0 mmol, 1.01 equiv.) and **N1-B3** (0.5 g, 1.97 mmol, 1.0 equiv.) were dissolved in 3.5 mL dry toluene. The solution was stirred at 75 ℃ for 48 h. After the solvent was removed *in vacuo*, the crude product was purified by column chromatography on silica gel (hexane:EtOAc = 3:1) to give compound **N1-DA1** (0.22 g, 19% yield, as a yellow oil) and **N1-DA2** (0.37 g, 32% yield, as a yellow solid).

N1-DA1, **^{1}H NMR (400 MHz, $CDCl_3$):** δ (ppm): 8.93 (t, J = 5.6 Hz, 1H), 8.53 (d, J = 8.4 Hz, 1H), 8.32 – 8.24 (m, 2H), 7.57 – 7.48 (m, 2H), 7.17 (d, J = 7.6 Hz, 1H), 7.05 – 7.01 (dd, J = 5.2 Hz, 1.6 Hz, 1H), 6.94 (d, J = 5.2 Hz, 1H), 6.15 (s, 1H), 6.02 (t, J = 6.4 Hz, 1H), 5.56 – 5.53 (m, 1H), 5.50 (d, J = 2.0 Hz, 1H), 4.28 – 4.14 (m, 4H), 4.78 – 4.68 (m, 2H), 3.54 – 3.43 (m, 2H), 2.88 (s, 6H), 1.92 (s, 3H), 1.29 (t, J = 7.2 Hz, 3H). **^{13}C NMR (101 MHz, $CDCl_3$):** δ (ppm): 167.22, 164.17, 162.23, 159.57, 149.52, 144.03, 143.11, 136.07, 134.95, 130.34, 129.92, 129.74, 128.27, 126.14, 123.44, 115.31, 96.78, 83.57, 63.04, 62.28, 45.57, 42.72, 38.63, 18.33, 14.11. **ESI-MS** (*m/z*) for $C_{29}H_{33}N_3O_8S$ expected $[M+H]^+$: 584.2061, Found for $[M+H]^+$: 584.2000.

N1-DA2, **^{1}H NMR (400 MHz, $CDCl_3$):** δ (ppm): 8.86 (t, J = 5.6 Hz, 1H), 8.59 (d, J = 8.0 Hz, 1H), 8.28 – 8.21 (m, 2H), 7.58 – 7.50 (m, 2H), 7.22 – 7.14 (m, 2H), 6.74 (d, J = 5.2 Hz, 1H), 6.18 (s, 1H), 5.63 (d, J = 2.0 Hz, 1H), 5.59 (m, 1H), 5.09 (m, 1H), 4.23 (t, J = 5.2 Hz, 2H), 4.16 – 4.09 (qd, J = 7.2 Hz, 2.4 Hz, 2H), 3.95 – 3.87 (m, 1H), 3.65 – 3.58 (m, 2H), 3.53 – 3.46 (m, 1H), 2.90 (s, 6H), 1.95 (s, 3H), 1.27 (t, J = 7.2 Hz, 3H). **^{13}C NMR (101 MHz, $CDCl_3$):** δ (ppm): 167.27, 164.38, 162.10, 161.84, 146.18, 145.65, 141.57, 136.08, 134.24, 130.81, 129.84, 129.74, 128.79, 126.21, 123.34, 115.65, 95.72, 84.53, 63.25, 62.49, 45.60, 42.90, 38.61, 18.39, 13.89. **ESI-MS** (*m/z*) for $C_{29}H_{33}N_3O_8S$ expected $[M+H]^+$: 584.2061, Found for $[M+H]^+$: 584.2016.

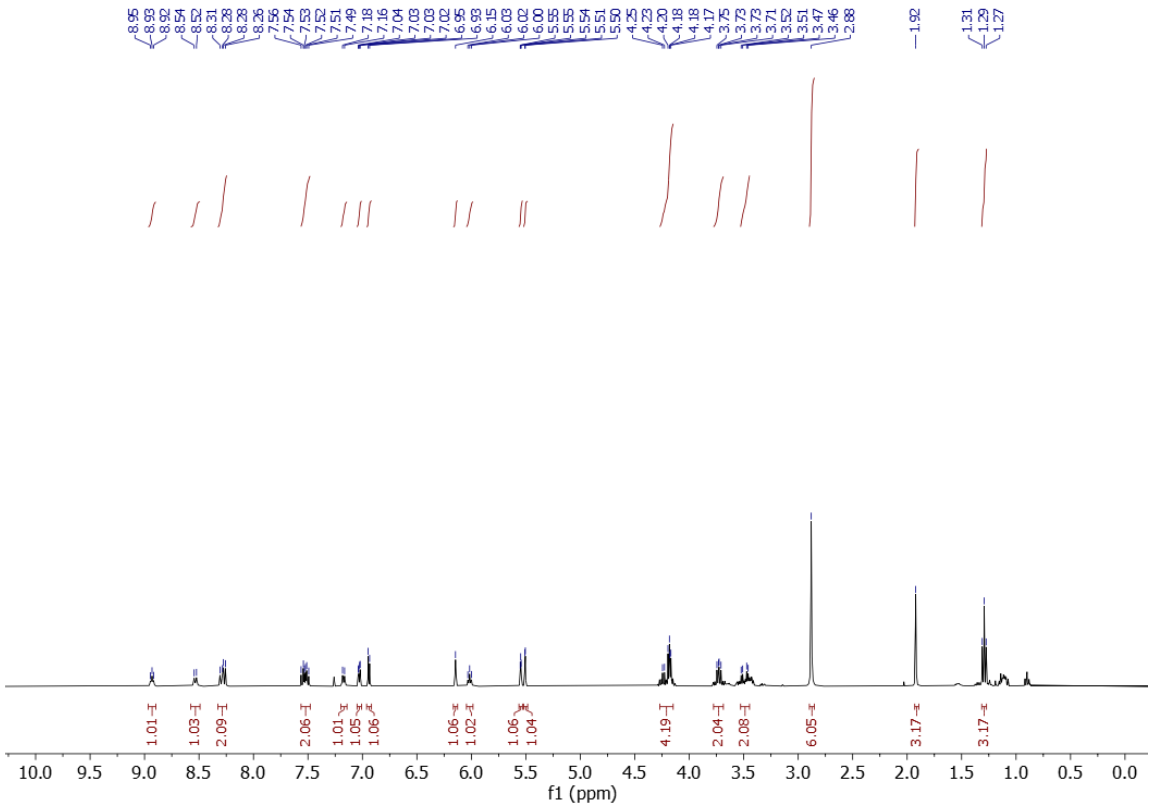

^{1}H NMR spectrum of **N1-DA1**.

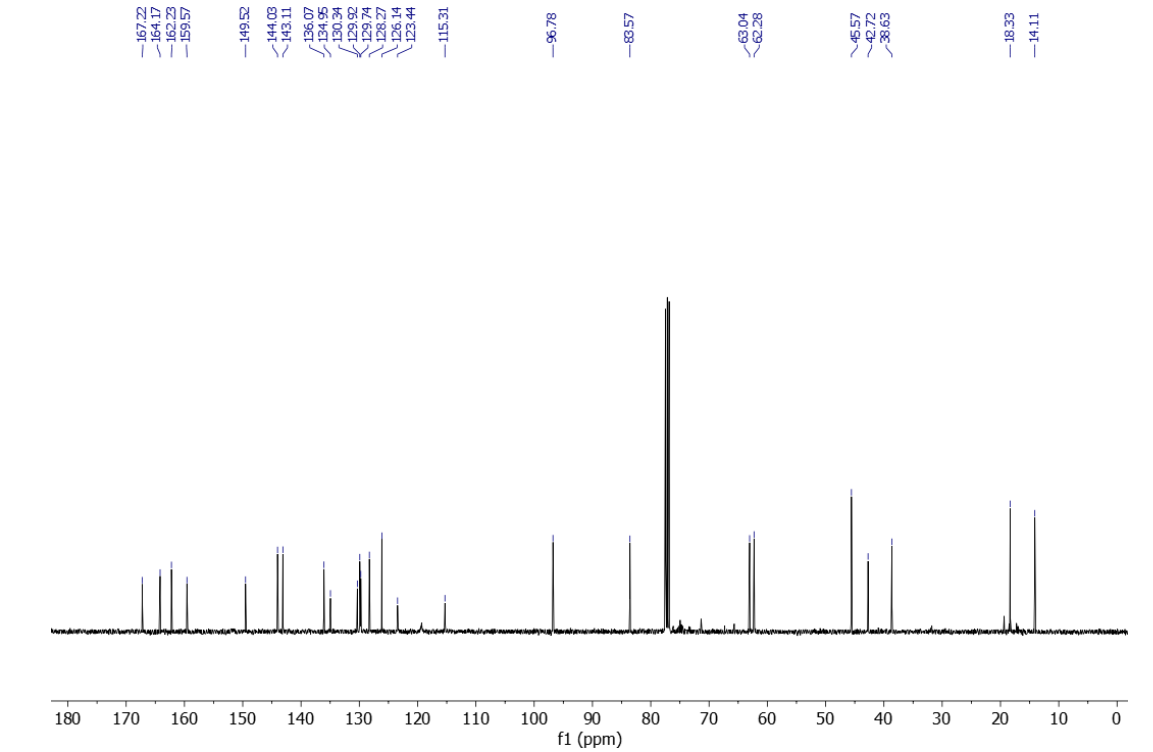

^{13}C NMR spectrum of **N1-DA1**.

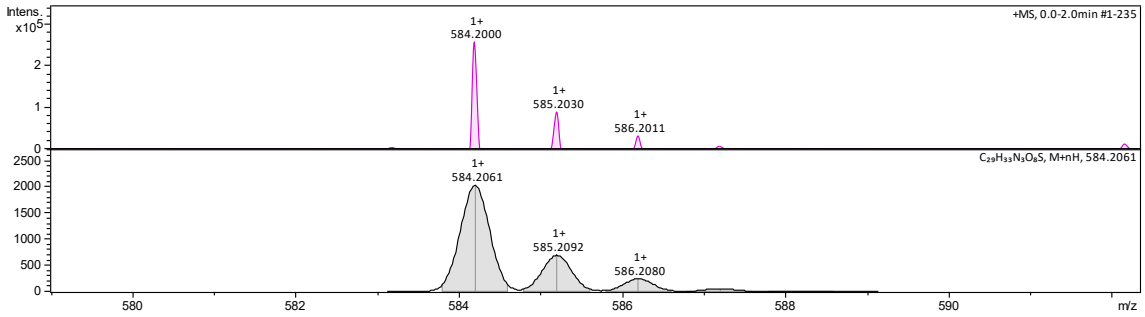

ESI-MS (*m/z*) of **N1-DA1**.

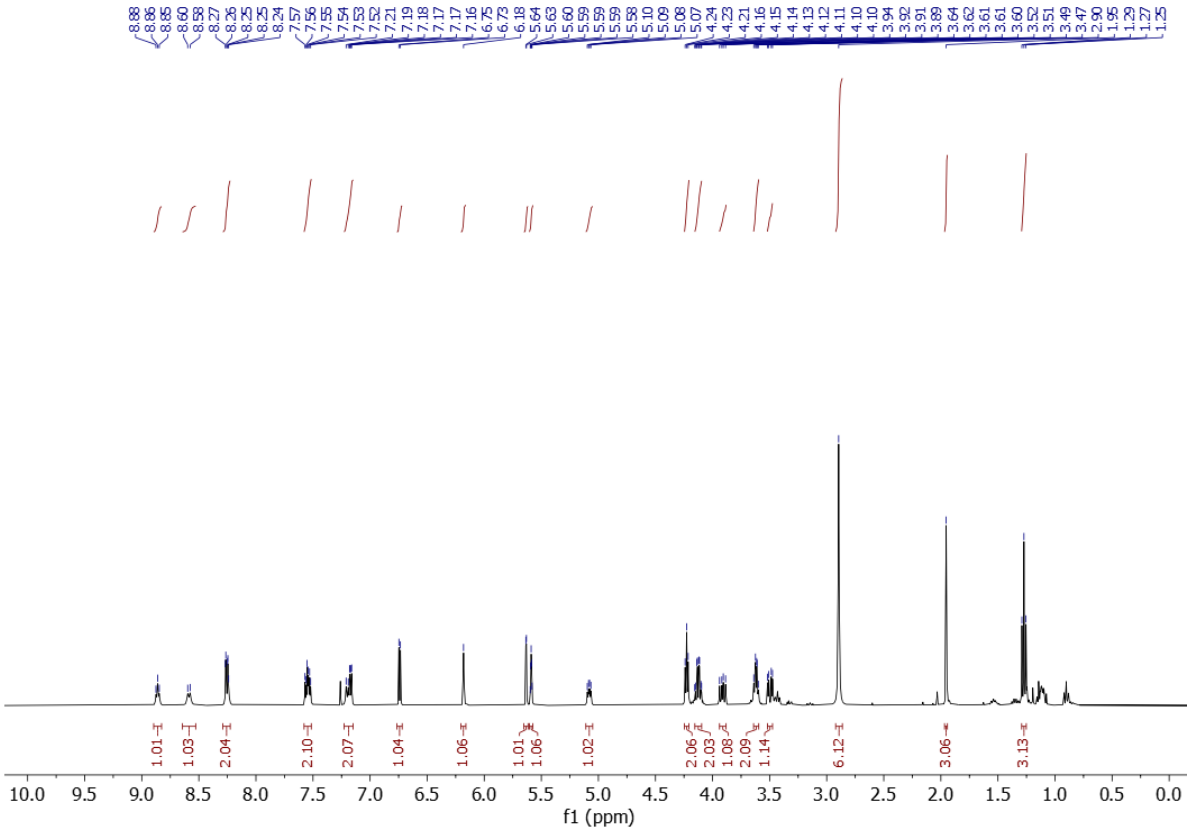

^{1}H NMR spectrum of **N1-DA2**.

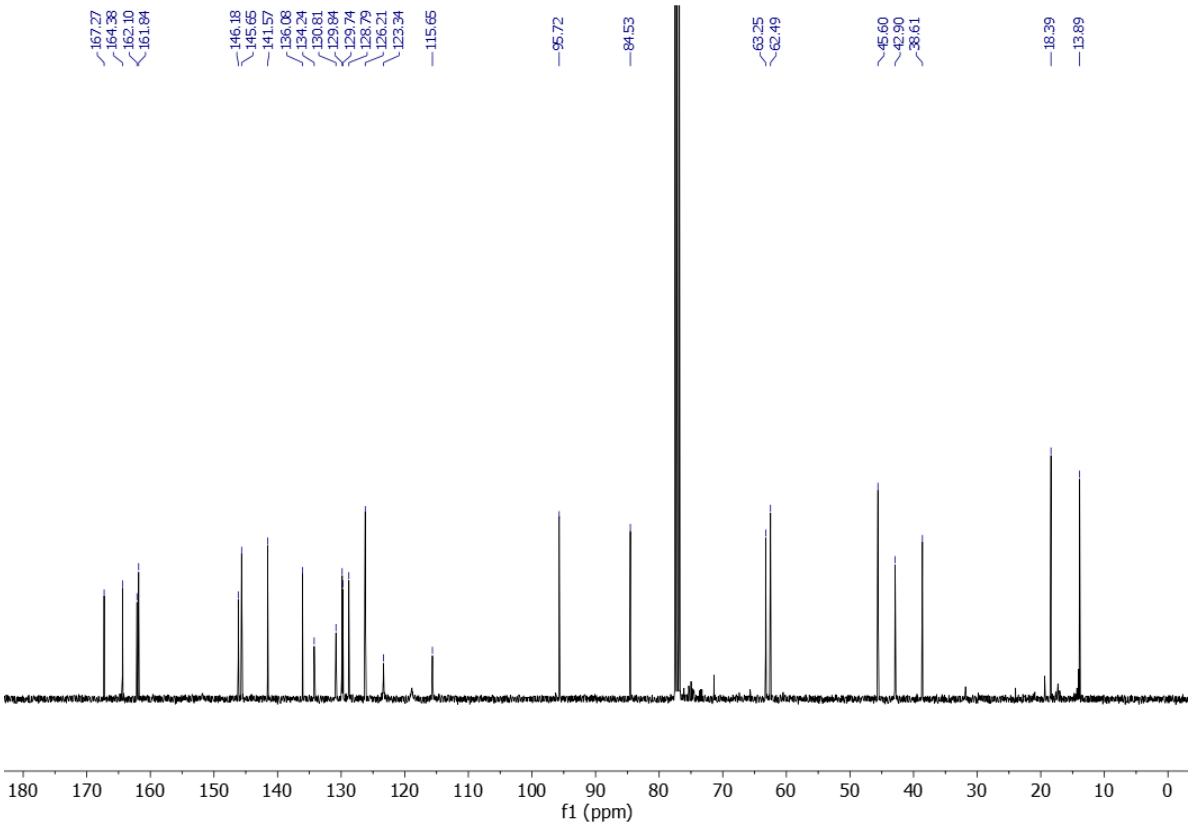

^{13}C NMR spectrum of **N1-DA2**.

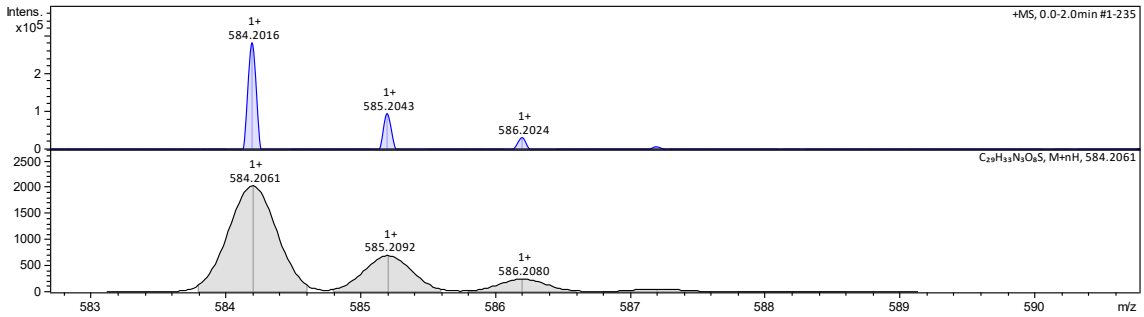

ESI-MS (*m/z*) of **N1-DA2**.

We distinguished **N1-DA1** and **N1-DA2** by ^{1}H NMR. The chemical shifts of proton peak of H-N (**b**) in the two compounds show a characteristic difference. One is around 5.1 ppm, the other one is around 6.0 ppm. This is due to the fact that H-N (**b**) in **N1-DA1** forms hydrogen bonds with the oxygen atom belonging to the oxanorbornadiene structure. The formation of hydrogen bonds increased the electron density around the proton, causing the chemical shift of the proton to a high field. In contrast, the H-N (**b**) in **N1-DA2** cannot form hydrogen bonds with any oxygen atom.

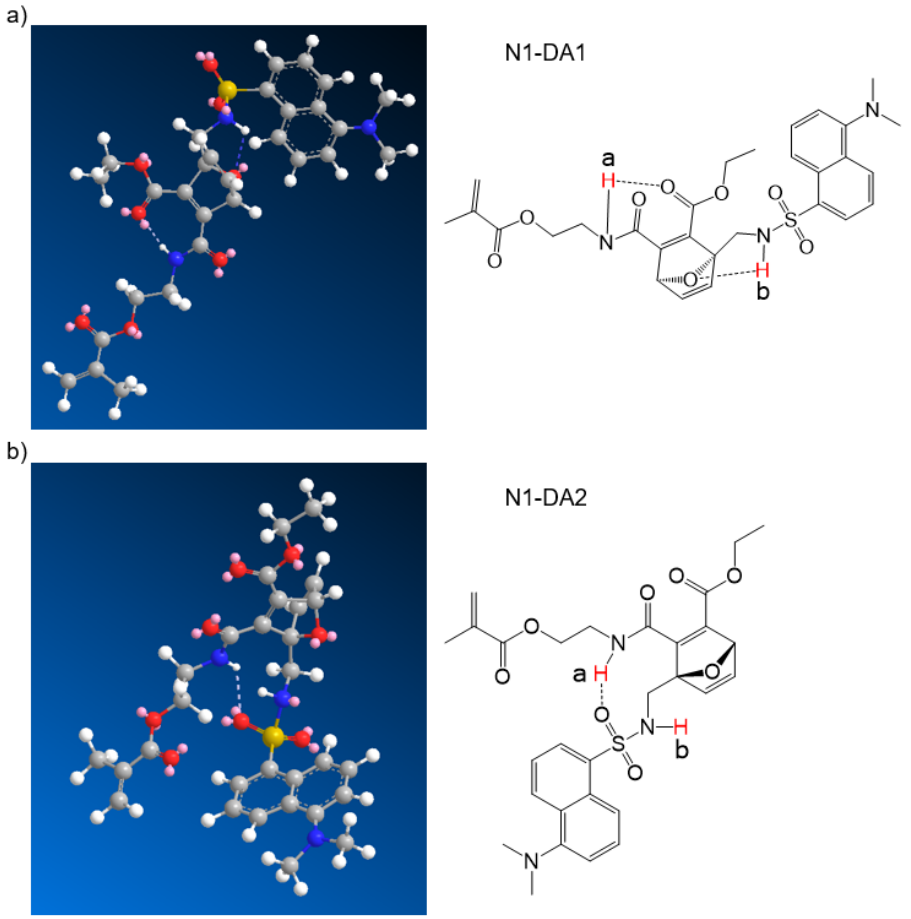

3D structure of **a**) **N1-DA1** and **b**) **N1-DA2** (The hydrogen bonds in **N1-DA1** and **N1-DA2** were calculated by Chem3D®, version: 19.0.1.28).

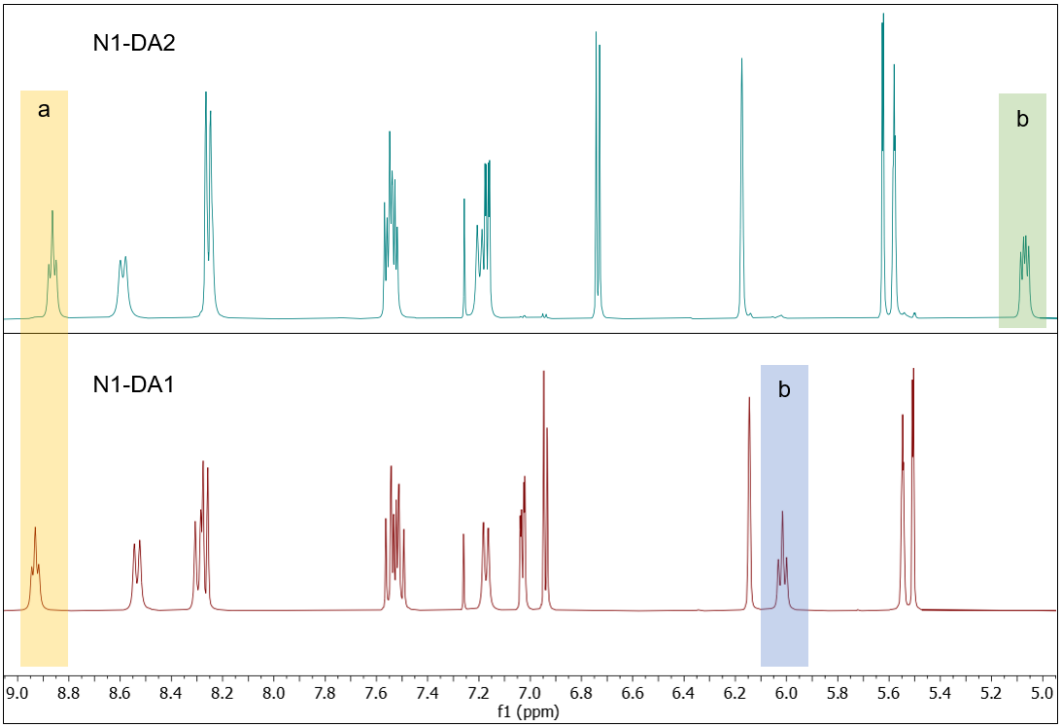

^{1}H NMR stack of **N1-DA1** and **N1-DA2**.

2-((2-hydroxyethyl)disulfaneyl)ethyl methacrylate (**N2-A2**)

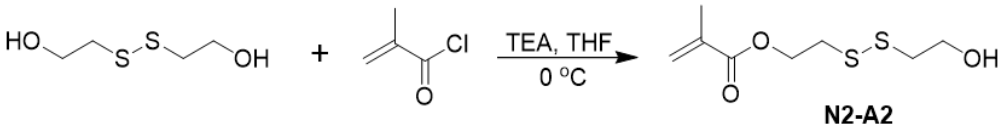

N2-A2

The preparation of **N2-A2** was carried out according to an adapted literature protocol.[80] 2-hydroxyethyl disulfide (2.0 g, 13 mmol, 1 equiv.) and TEA (3.0 mL, 21.5 mmol, 1.65 equiv.) were added in THF (30 mL) with a constant flow of N_2. The flask with the mixture was placed in an ice-water bath to keep the temperature at 0 °C. Afterwards, a solution of methacryloyl chloride (1.3 mL, 13.3 mmol, 1.02 equiv.) and 15 mL CH_2Cl_2 was added dropwise (15 mL/h) to the reaction mixture via an injection pump. The reaction mixture was continuously stirred until the starting material was entirely consumed, as confirmed by TLC analysis. Then, it was washed with brine and deionized water three times, respectively. Afterwards, the crude product was purified by column chromatography on silica gel (hexane:EtOAc = 5:1) to give compound **N2-A2** (2.2 g, 76% yield) as a colorless oil. **^{1}H NMR (400 MHz, $CDCl_3$):** δ (ppm): 6.12 (s, 1H), 5.55 (t, *J*=1.6 Hz, 1H), 4.41 (t, *J*=6.8 Hz, 2H), 3.87 (t, *J*=6.0 Hz, 2H), 2.96 (t, *J*=6.8 Hz, 2H), 2.87 (t, *J*=6.0 Hz, 2H), 2.21 (br, 1H), 1.93 (s, 3H). **^{13}C NMR (101 MHz, $CDCl_3$):** δ (ppm): 167.37, 136.09, 126.24, 62.73, 60.30, 41.74, 37.08, 18.38. **ESI-MS** (*m*/*z*) for $C_8H_{14}O_3S_2$ expected $[M+Na]^+$: 245.0277, Found for $[M+Na]^+$: 245.0242.

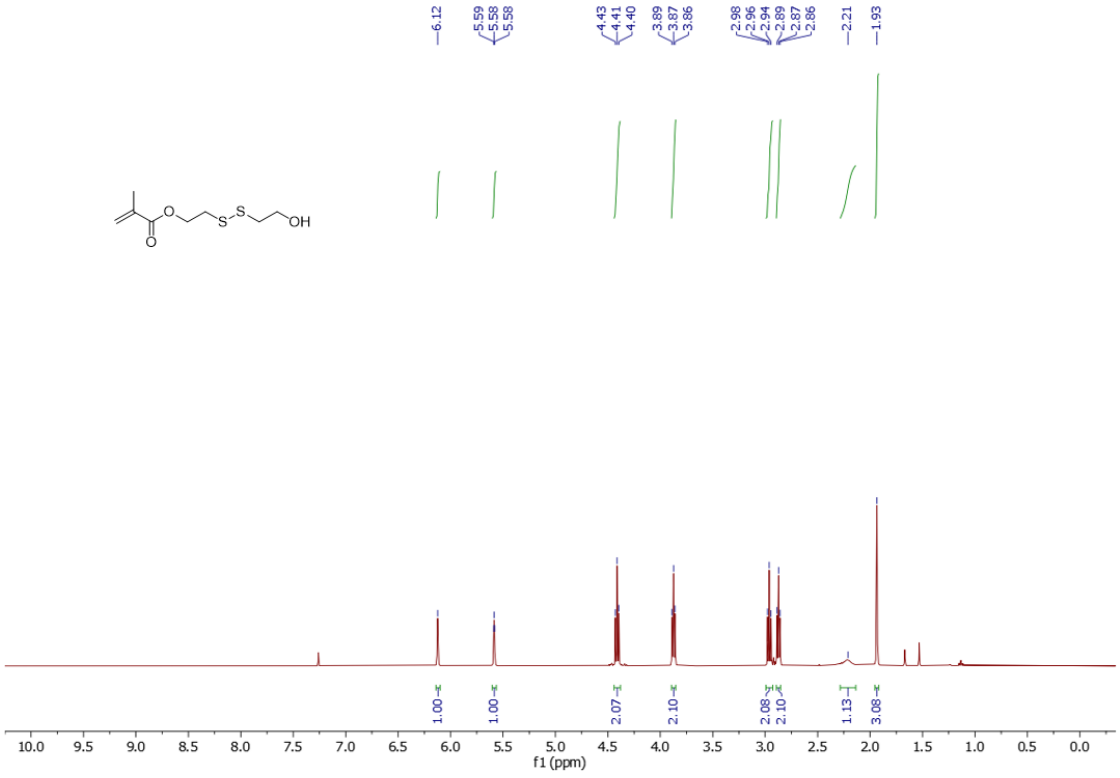

^{1}H NMR spectrum of **N2-A2**.

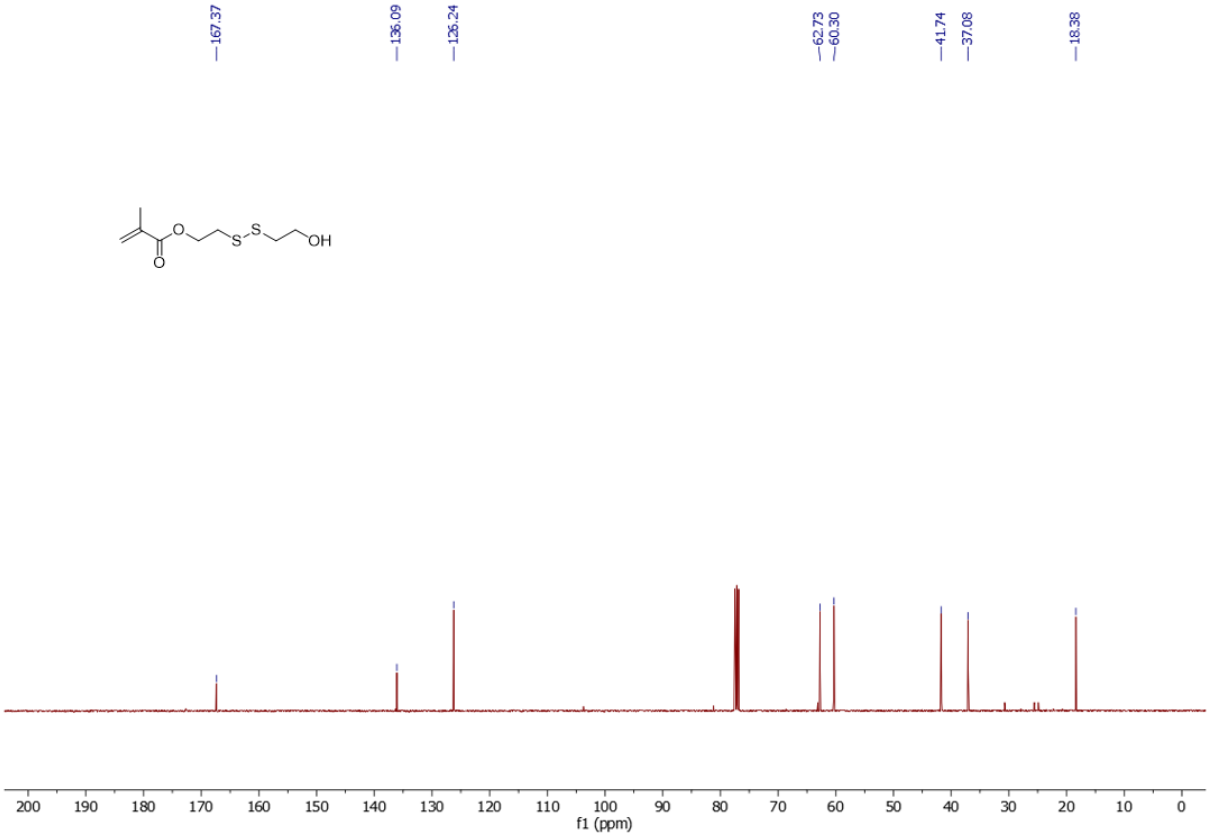

^{13}C NMR spectrum of **N2-A2**.

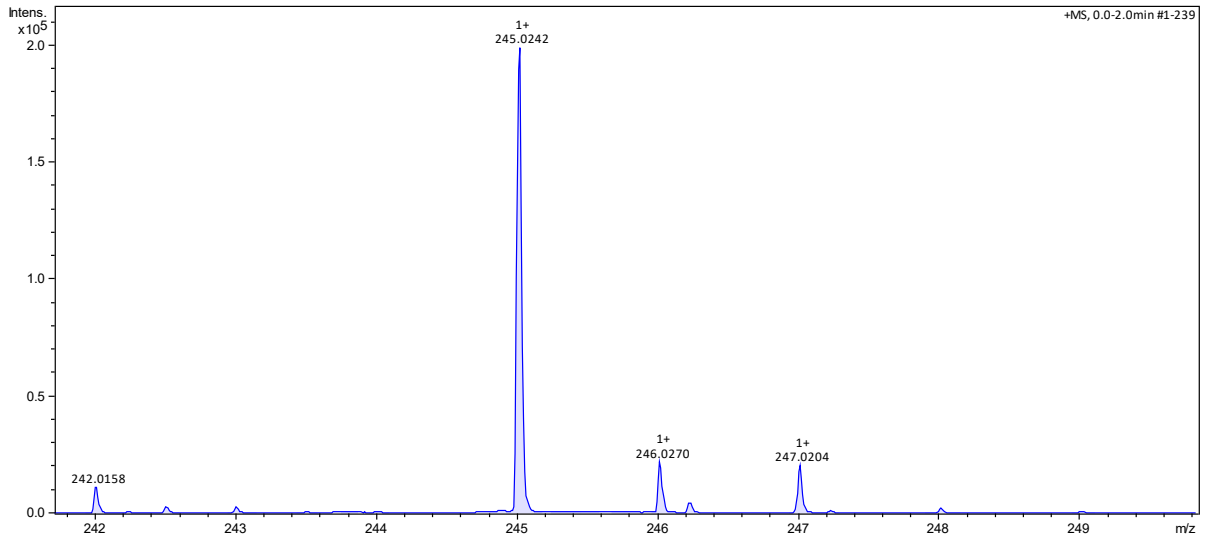

ESI-MS (*m*/*z*) of **N2-A2**.

2-((2-((((2-oxo-2H-chromen-7-yl)oxy)carbonyl)oxy)ethyl)disulfaneyl)ethyl methacrylate (**N2-A3**)

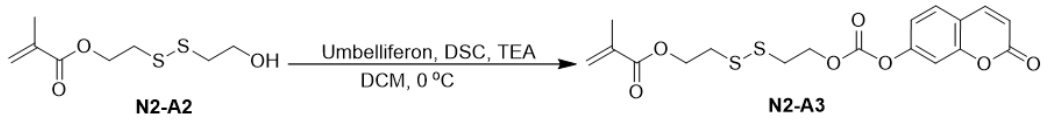

N2-A3 was synthesized by following the reported literature.[14] *N,N'*-disuccinimidyl carbonate (133 mg, 0.52 mmol, 1.0 equiv.) and Et_3N (90 µL, 0.65 µmol, 1.25 equiv.) were dissolved in 1.5 mL CH_2Cl_2. The mixture was cooled to 0 °C with an ice-water bath. Then, a solution of **N2-A2** (115 mg, 0.52 mmol, 1.0 equiv.) in 1 mL CH_2Cl_2 was added. The reaction mixture was allowed to stir in the ice-water bath for 1 h. Subsequently, a solution of umbelliferone (UMB, 84 mg, 0.52 mmol, 1 equiv.), Et_3N (90 µL, 0.65 mmol, 1.25 equiv.) and CH_2Cl_2/DMF (1.65 mL, v/v,10:1) was added into the reaction mixture. The reaction mixture was stirred for another 1 h at 0 °C. Then, the reaction mixture was allowed to warm up slowly to room temperature for further reaction. The reaction mixture was continuously stirred until the starting material was entirely consumed, as confirmed by TLC analysis. Then, the solvent was completely removed under reduced pressure. The remaining residue was then re-dissolved in CH_2Cl_2, and it was washed with deionized water three times. The mixture was then purified by silica column chromatography (hexane:EtOAc = 4:1) to give compound **N2-A3** (128 mg, 60% yield) as a colorless oil. **^{1}H NMR (400 MHz, $CDCl_3$):** δ (ppm): 7.68 (d, *J*=9.6 Hz, 1H), 7.48 (d, *J*=8.4 Hz, 1H), 7.19 (d, *J*=2.4 Hz, 1H), 7.11-7.14 (dd, *J*=2.4, 8.4 Hz, 1H), 6.37 (d, *J*=9.6 Hz, 1H), 6.11 (s, 1H), 5.57 (t, *J*=1.6 Hz, 1H), 4.51 (t, *J*=6.8 Hz, 2H), 4.40 (t, *J*=6.8 Hz, 2H), 2.97-3.03 (m, 4H), 1.92 (s, 3H). **^{13}C NMR (101 MHz, $CDCl_3$):** δ (ppm): 167.13, 160.20, 154.65, 153.25, 152.61, 142.80, 136.00, 128.79, 126.13, 117.69, 116.92, 116.31, 109.88, 66.73, 62.50, 37.25, 36.85, 18.32. **ESI-MS** (*m/z*) for $C_{18}H_{18}O_7S_2$ expected $[M+H]^+$: 411.0567, Found for $[M+H]^+$: 411.0531.

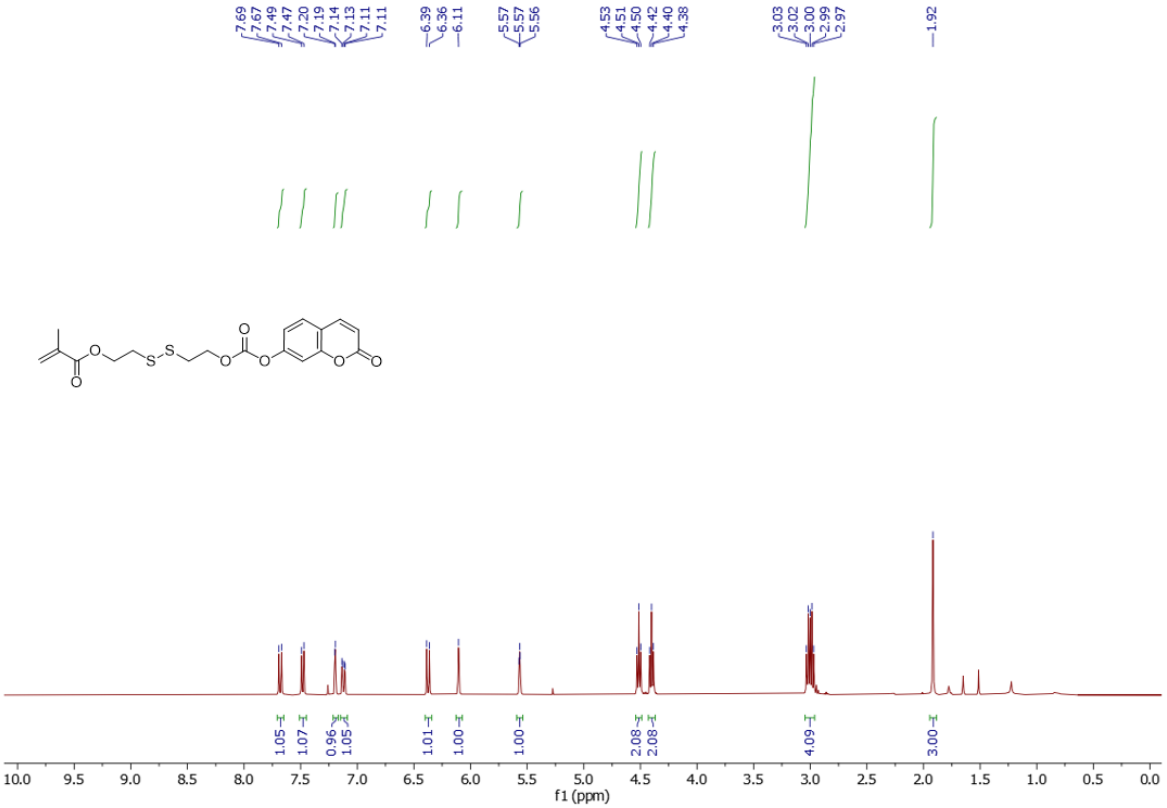

^{1}H NMR spectrum of **N2-A3**.

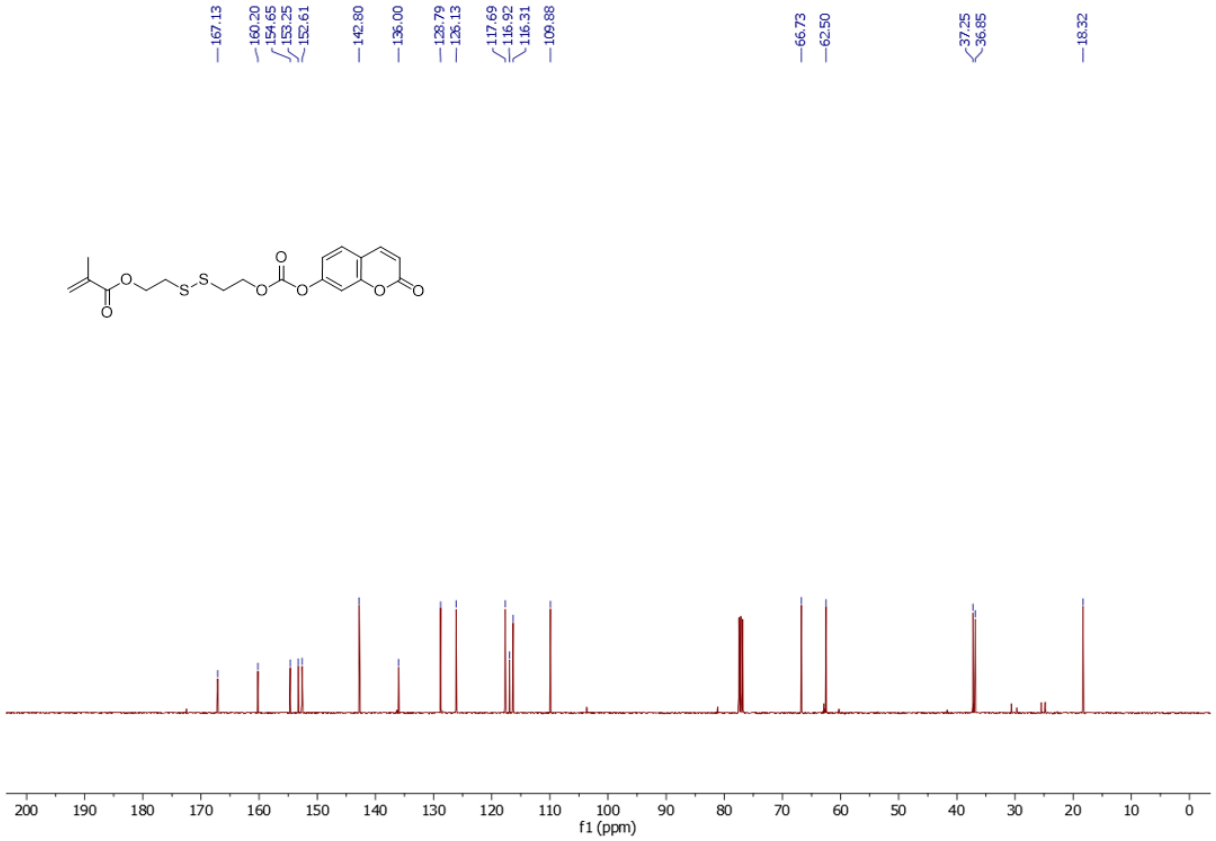

^{13}C NMR spectrum of **N2-A3**.

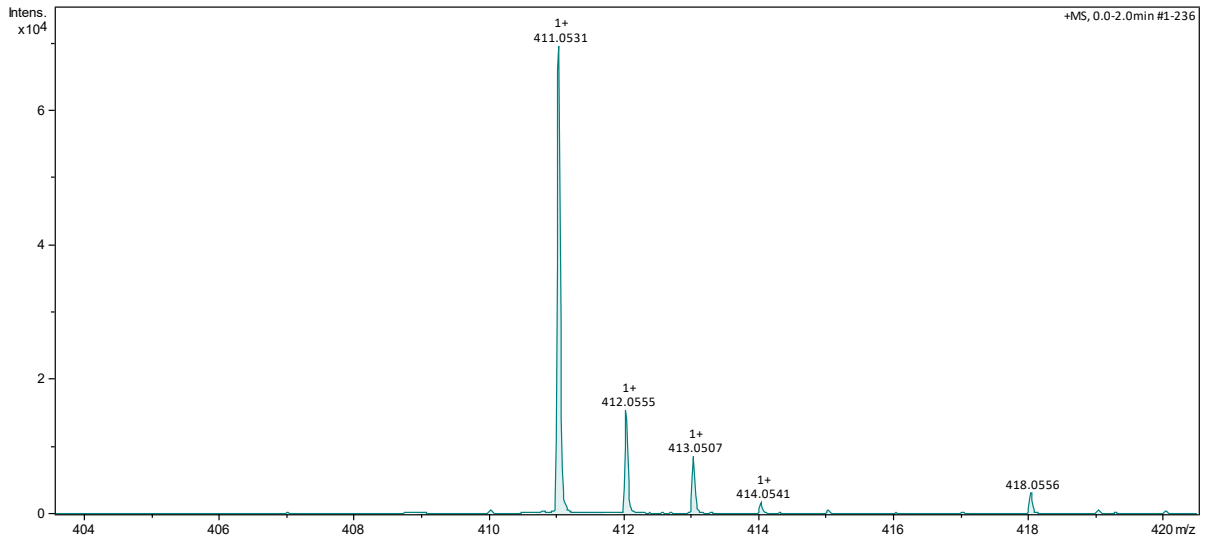

ESI-MS (*m/z*) of **N2-A3**.

2-((2-((((4-ethyl-3,14-dioxo-3,4,12,14-tetrahydro-1H-pyrano[3',4':6,7]indolizino[1,2-b]quinolin-4-yl)oxy)carbonyl)oxy)ethyl)disulfaneyl)ethyl methacrylate (**N2-B3**)

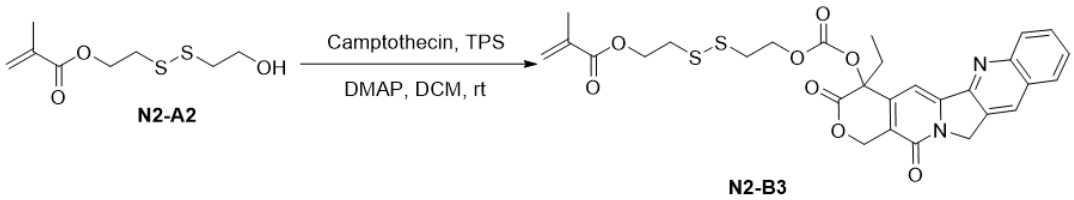

The synthesis of **N2-B3** was performed using an adapted literature protocol.[81] Camptothecin (CPT, 200 mg, 0.57 mmol) was dissolved in 12 mL anhydrous CH_2Cl_2. Then, triphosgene (TPS, 70 mg, 0.23 mmol) was added under stirring. After 5 min stirring, DMAP (224 mg, 1.83 mmol) in 0.5 mL CH_2Cl_2 was added into the mixture and stirred for another 1 h at room temperature. Afterwards, a solution of **N2-A2** (378mg, 1.7 mmol) in 1 mL CH_2Cl_2 was added to the reaction mixture for further reaction overnight. Subsequently, the excess phosgene (CAUTION: TOXIC) was removed by Ar purging and neutralized by bubbling the exhaust gas through a 2 M NaOH solution. Afterwards, the reaction mixture was washed three times with H_2O. Then, the crude product was purified by column chromatography on silica gel (hexane:EtOAc = 1:1) to give compound **N2-B3** (180 mg, 53% yield) as a white solid. **^{1}H NMR (400 MHz, $CDCl_3$):** δ (ppm): 8.39 (s, 1H), 8.22 (d, *J*=8.4 Hz, 1H), 7.93 (d, *J*=8.0 Hz, 1H), 7.83 (m, 1H), 7.66 (m, 1H), 7.34 (s, 1H), 6.07 (s, 1H), 5.69 (d, *J*=17.2 Hz, 1H), 5.54 (t, *J*=1.6 Hz, 1H), 5.38 (d, *J*=17.2 Hz, 1H), 5.28 (s, 2H), 4.31-4.39 (m, 4H), 2.92 (q, *J*=6.0 Hz, 4H), 2.32-2.23 (m, 1H), 2.19-2.10 (m, 1H), 1.89 (s, 3H), 1.00 (t, *J*=7.6 Hz, 3H). **^{13}C NMR (101 MHz, $CDCl_3$):** δ (ppm): 167.37, 167.15, 157.39, 153.57, 152.37, 148.94, 146.56, 145.71, 136.06, 131.35, 130.88, 129.74, 128.59, 128.32, 128.30, 128.23, 126.10, 120.40, 96.13, 78.14, 67.19, 66.65, 62.52, 50.12, 37.35, 36.67, 32.00, 18.36, 7.75. **ESI-MS:** (*m/z*) for $C_{29}H_{28}N_2O_8S_2$ expected $[M+H]^+$: 597.1360, Found for $[M+H]^+$: 597.1328.

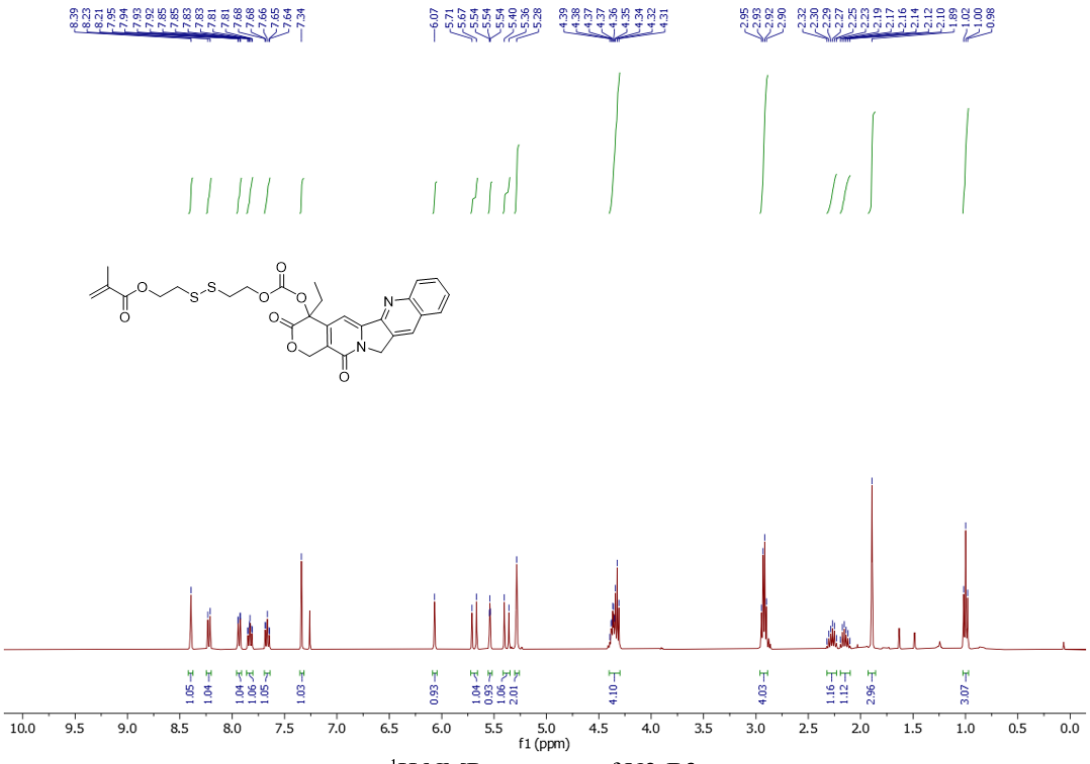

^{1}H NMR spectrum of **N2-B3**.

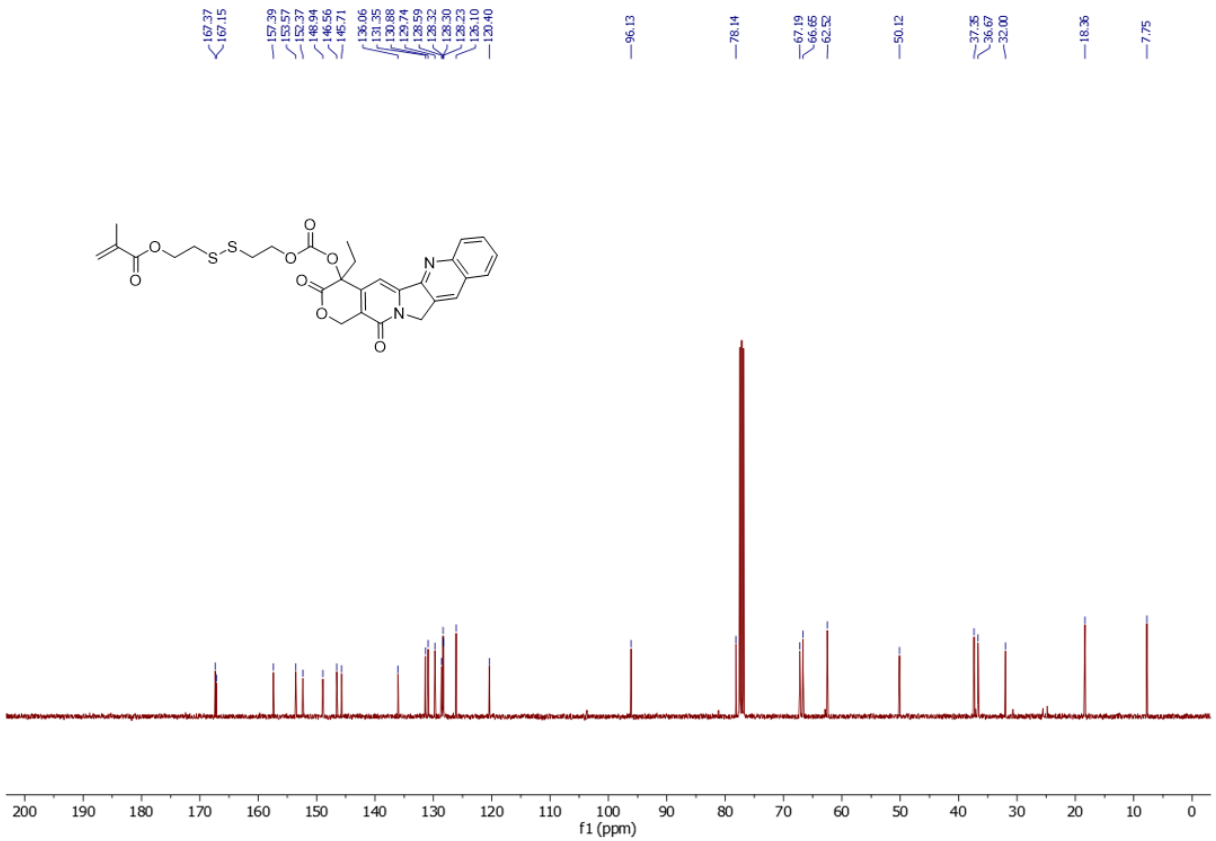

^{13}C NMR spectrum of **N2-B3**.

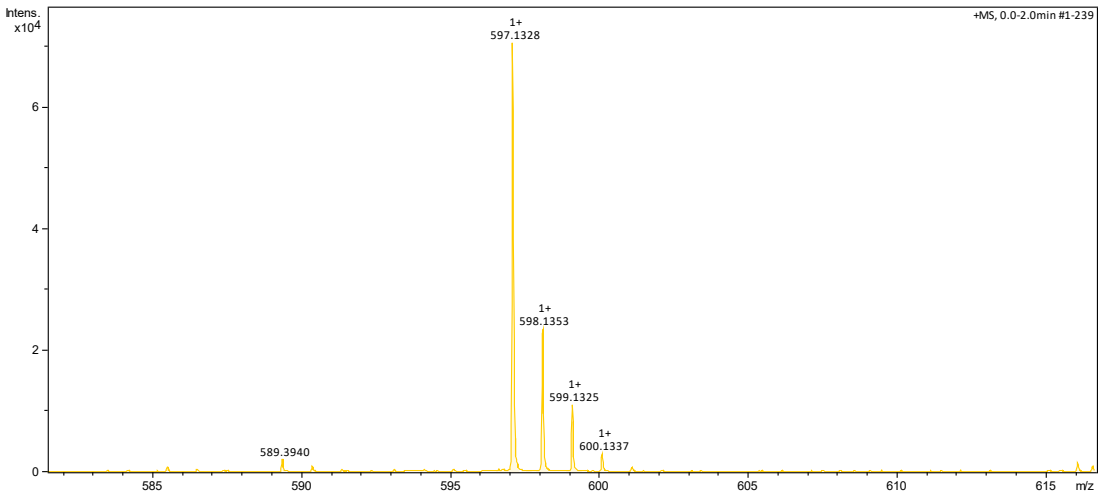

ESI-MS (*m/z*) of **N2-B3**.

1-(5-(hydroxymethyl)furan-2-yl)ethan-1-ol (**N3-A2**)

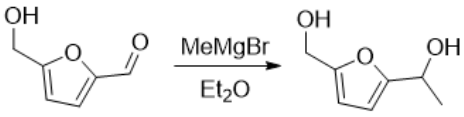

N3-A1 **N3-A2**

N3-A2 was synthesized by following the reported literature.[53, 60] **N3-A1** (1.14 g, 9.0 mmol) and diethyl ether (45 mL) were added into a round bottom flask. The solution was cooled to −30 °C, followed by the dropwise addition of methylmagnesium bromide (3 M in diethyl ether, 7.0 mL, 21.0 mmol). The mixture was allowed to warm to room temperature and stirred for another 12 h, after that the reaction was cooled to 0 °C and terminated with 10% NH_4Cl (30 mL). The reaction mixture was extracted with EtOAc (3 x 100 mL) and the combined organic phase was dried over $MgSO_4$, filtered, and concentrated under reduced pressure. Then, the crude product was purified by column chromatography on silica gel (CH_2Cl_2:MeOH = 100:5) to give compound **N3-A2** as a viscous yellow oil (1.18 g, 92%). **^{1}H NMR (400 MHz, $(CD_3)_2SO$):** δ (ppm): 6.16 (d, J=3.2 Hz, 1H), 6.12 (d, J=3.2 Hz, 1H), 5.21 (d, J=5.2 Hz, 1H), 5.16 (t, J=5.6 Hz, 1H), 4.68-4.60 (m, 1H), 4.34 (d, J=5.6 Hz, 2H), 1.34 (d, J=6.4 Hz, 3H). **^{13}C NMR (101 MHz, $(CD_3)_2SO$):** δ (ppm): 158.24, 154.06, 107.34, 105.10, 61.89, 55.77, 22.09.

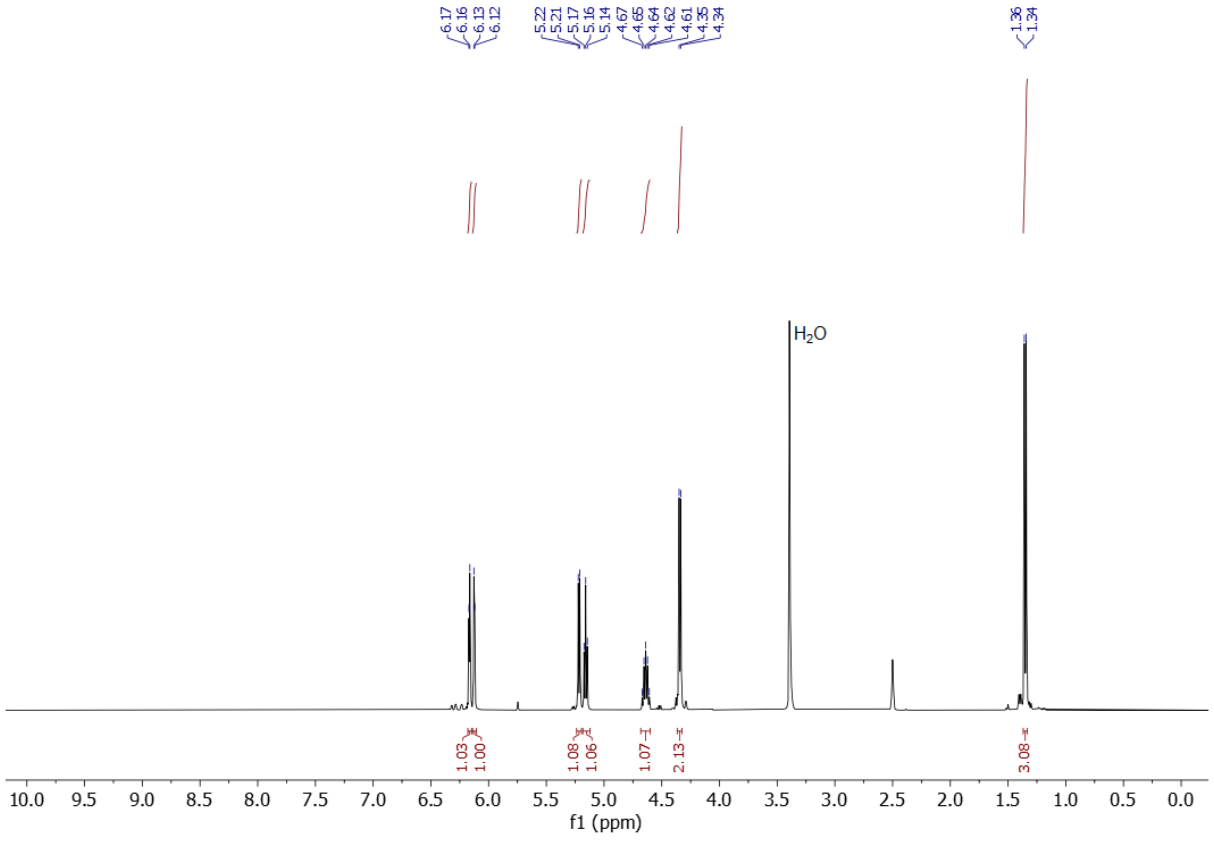

^{1}H NMR spectrum of **N3-A2**.

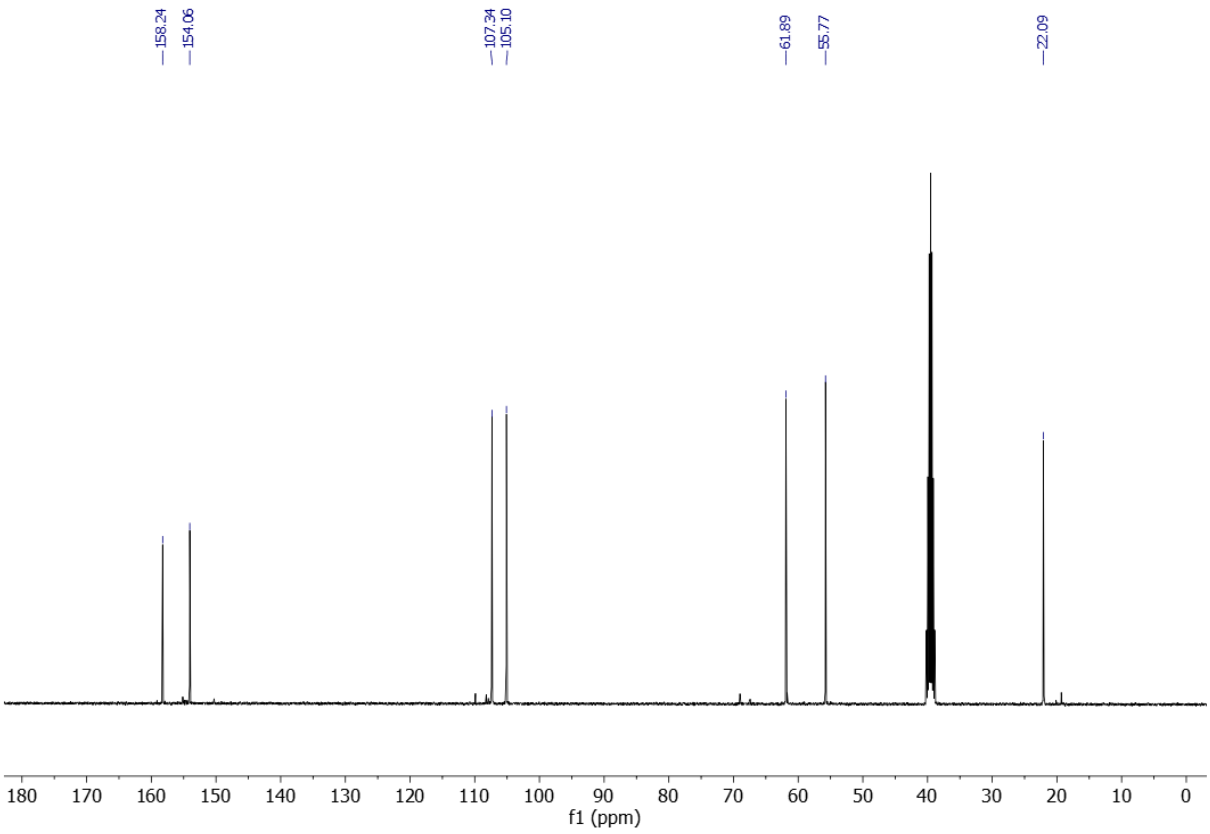

^{13}C NMR spectrum of **N3-A2**.

(5-(1-hydroxyethyl)furan-2-yl)methyl methacrylate (**N3-A3**)

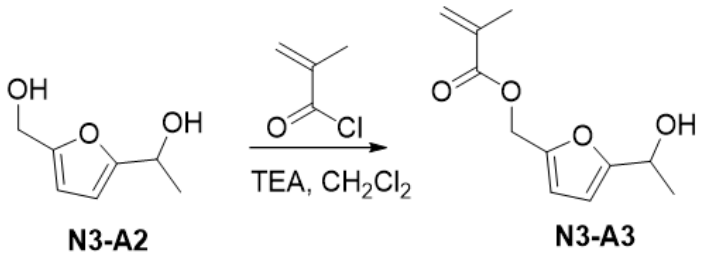

N3-A2 **N3-A3**

N3-A3 was synthesized by following the reported literature.[53, 60] **N3-A2** (0.45 g, 3.17 mmol), triethylamine (0.33 mL, 4.7 mmol), and CH_2Cl_2 (30 mL) were added into a three neck flask with a constant flow of N_2. The flask with the mixture was placed into an ice-water bath to keep the temperature at 0 °C. Afterwards, a solution of methacryloyl chloride (0.36 mL, 3.7 mmol, 1.17 equiv.) and 8 mL CH_2Cl_2 was added dropwise (10 mL/h) to the reaction mixture via an injection pump. The reaction mixture was stirred under nitrogen for another 30 min and was allowed to warm slowly to room temperature. After 15 h, the reaction mixture was extracted with EtOAc (3 x 20 mL) and the combined organic phase was dried over $MgSO_4$, filtered, and concentrated under reduced pressure. Then, the crude product was purified by column chromatography on silica gel (hexane:EtOAc = 6:1) to give compound **N3-A3** (0.64 g, 96% yield) as a colorless oil. **^{1}H NMR (400 MHz, $CDCl_3$):** δ (ppm): 6.34 (d, *J*=3.2 Hz, 1H), 6.18 (d, *J*=3.2 Hz, 1H), 6.11 (s, 1H), 5.58-5.54 (m, 1H), 5.08 (s, 2H), 4.85 (q, *J*=6.4 Hz, 1H), 2.26 (s, 1H), 1.92 (s, 3H), 1.52 (d, *J*=6.4 Hz, 3H). **^{13}C NMR (101 MHz, $CDCl_3$):** δ (ppm): 167.21, 158.51, 148.98, 136.08, 126.24, 111.41, 106.15, 63.67, 58.52, 21.27, 18.40. **ESI-MS:** (*m/z*) for $C_{11}H_{14}O_4$ expected $[M+Na]^+$: 233.0972, Found for $[M+H]^+$: 233.0784.

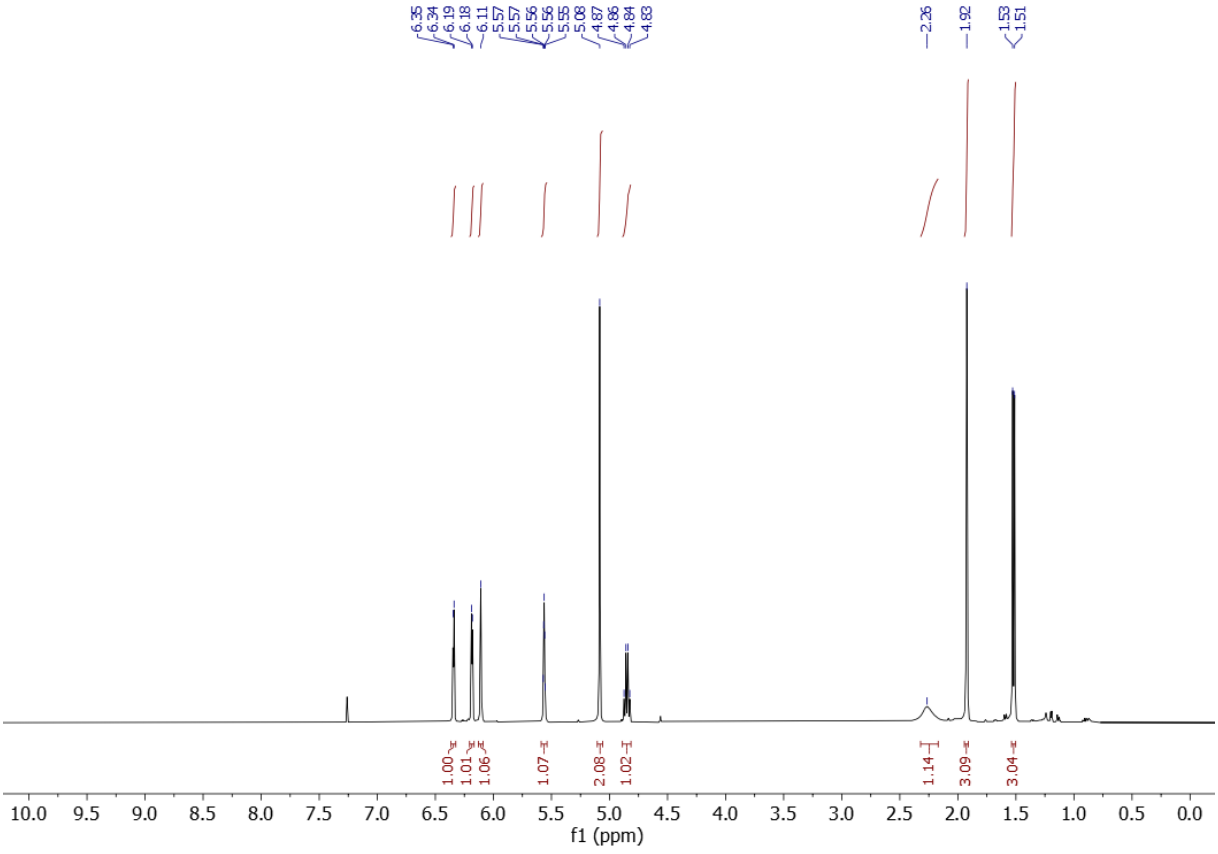

^{1}H NMR spectrum of **N3-A3**.

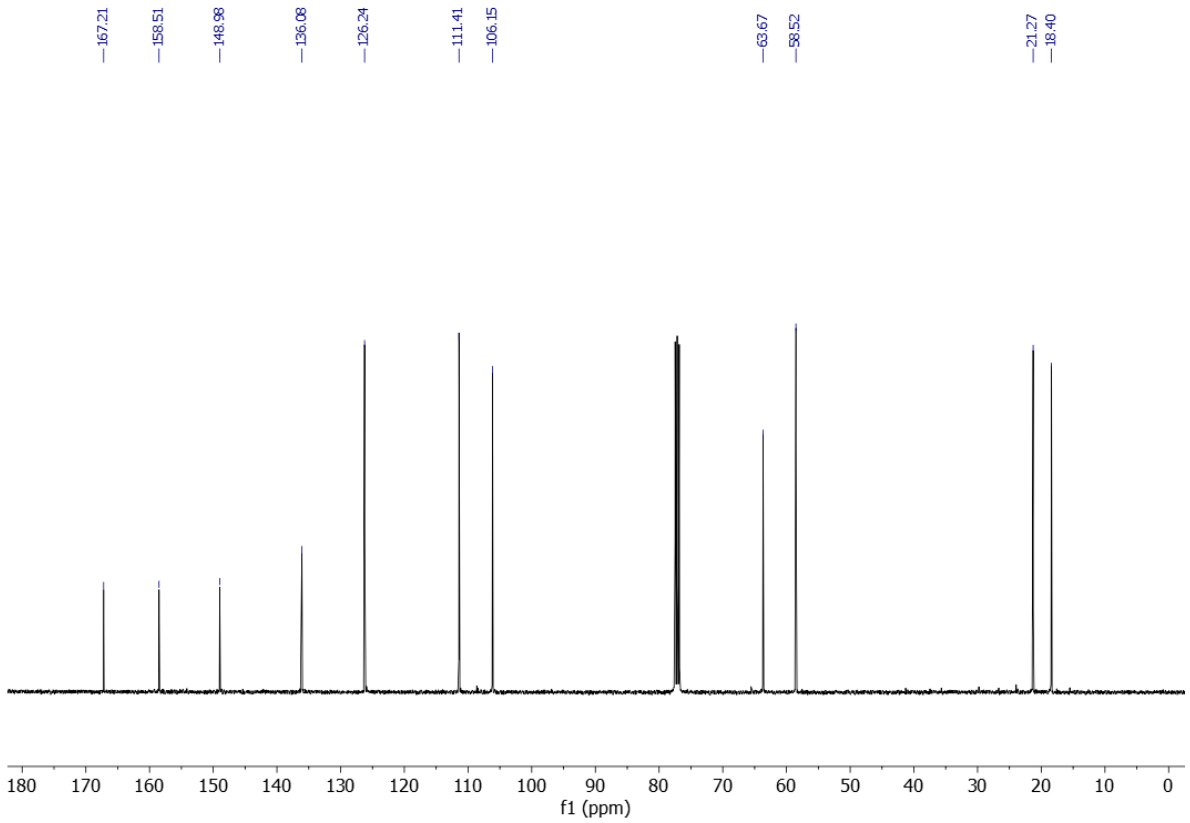

^{13}C NMR spectrum of **N3-A3**.

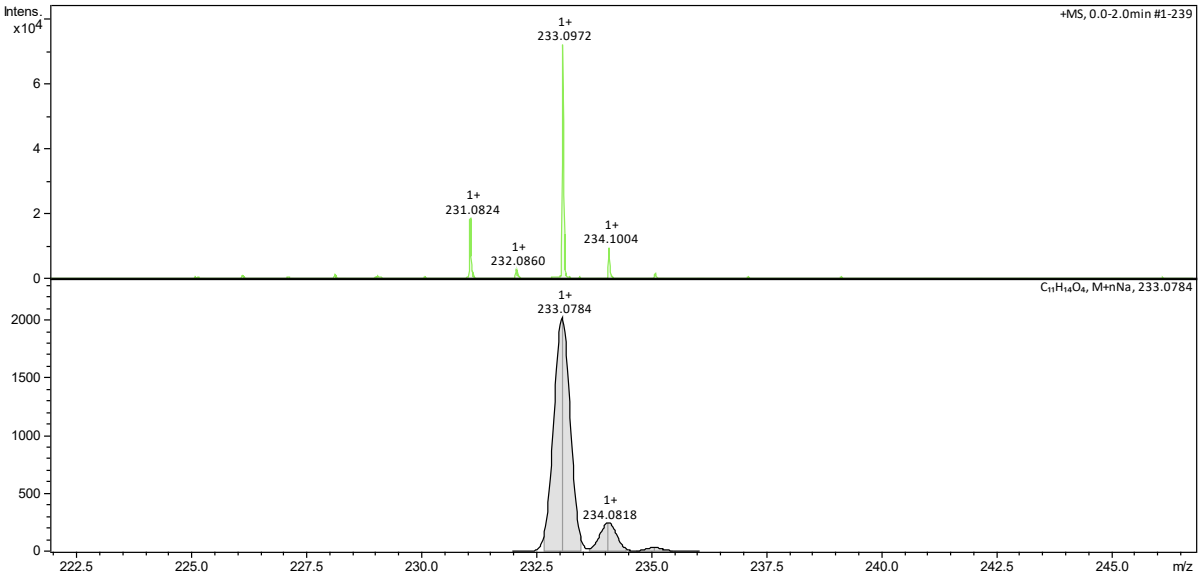

ESI-MS (*m/z*) of **N3-A3**.

2-(2,5-dioxo-2,5-dihydro-1H-pyrrol-1-yl)ethyl methacrylate (**N3-B2**)

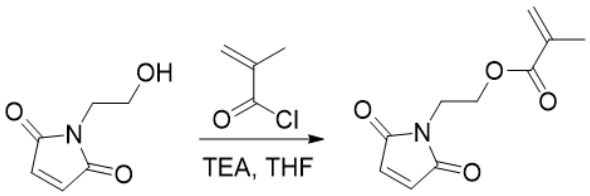

N3-B1 **N3-B2**

N3-B2 was synthesized by following the reported literature.[53, 60] **N3-B1** (1.0 g, 7.1 mmol, 1.0 equiv.) and Et_3N (1520 µL, 10.9 mmol, 1.5 equiv.) were dissolved in 50 mL THF. The mixture was cooled to 0 °C with an ice-water bath. Then, a solution of methacryloyl chloride (1.05 g, 10 mmol, 1.4 equiv.) in 1.5 mL THF was added slowly into the mixture. The reaction mixture was stirred further in the ice-water bath for 2 h. Then, the reaction mixture was allowed to warm up slowly to room temperature. The reaction mixture was continuously stirred until the starting material was entirely consumed, as confirmed by TLC analysis. Then, the solvent was completely removed under reduced pressure. The remaining residue was then dissolved in EtOAc, and it was washed with deionized water. After concentration under reduced pressure, the mixture was purified by silica column chromatography (hexane:EtOAc = 3:1) to give compound **N3-B2** (1.21 g, 82% yield) as a white solid. **^{1}H NMR (400 MHz, $CDCl_3$):** δ (ppm): 6.71 (s, 1H), 6.04 (s, 1H), 5.56-5.53 (m, 1H), 4.27 (t, *J*=5.2 Hz, 2H), 3.83 (t, *J*=5.2 Hz, 2H), 1.88 (s, 3H). **^{13}C NMR (101 MHz, $CDCl_3$):** δ (ppm): 170.48, 167.14, 135.85, 134.34, 126.35, 61.83, 36.90, 18.31. **ESI-MS:** (*m/z*) for $C_{10}H_{11}NO_4$ expected $[M+Na]^+$: 232.0581, Found for $[M+H]^+$: 232.0580.

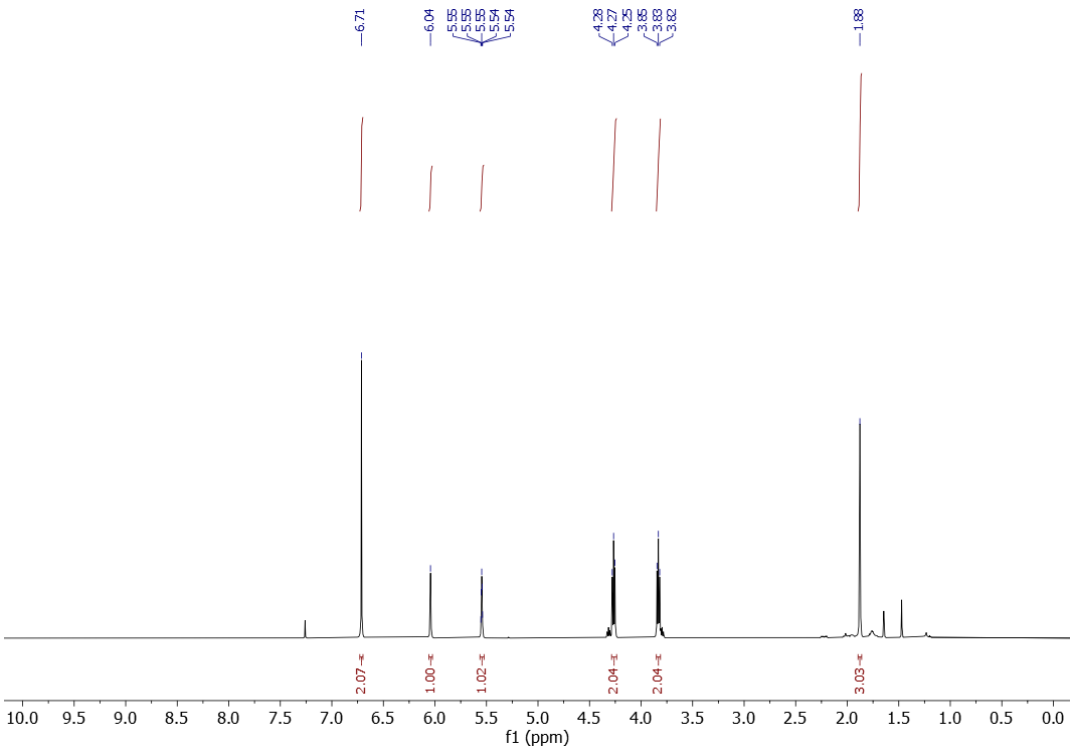

^{1}H NMR spectrum of **N3-B2**.

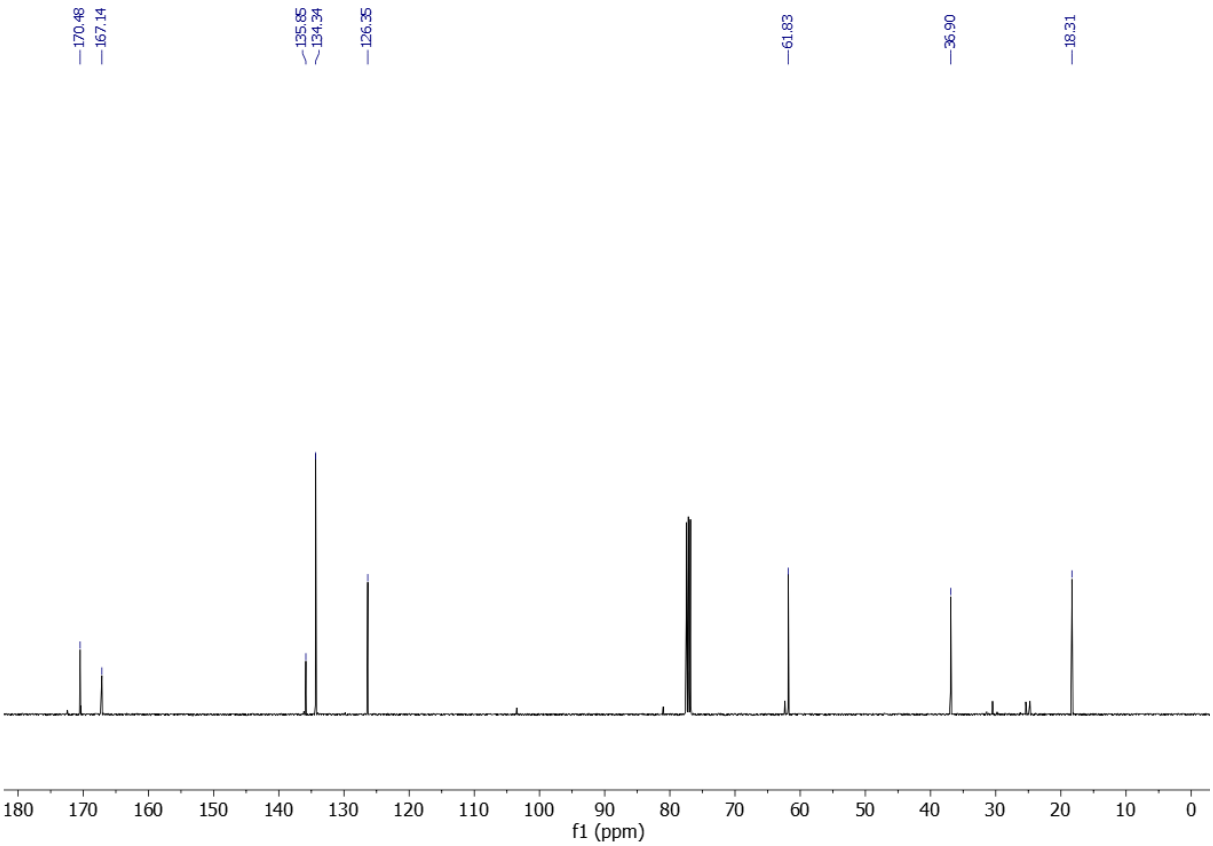

^{13}C NMR spectrum of **N3-B2**.

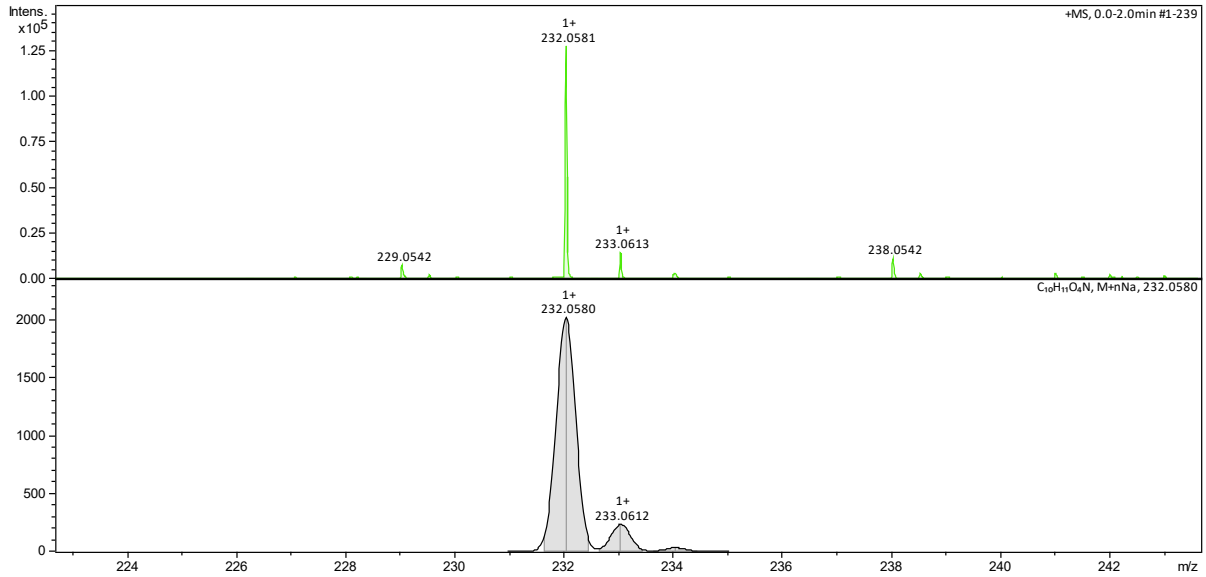

ESI-MS (*m/z*) of **N3-B2**.

(5-(1-(((4-(pyren-1-yl)butoxy)carbonyl)oxy)ethyl)furan-2-yl)methyl methacrylate (**N3-A4**)

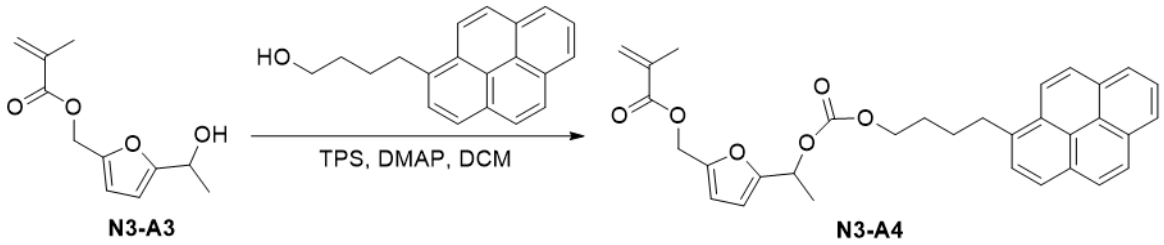

N3-A3 (140 mg, 0.66 mmol) was dissolved in 10 mL anhydrous CH_2Cl_2. Then, triphosgene (TPS, 94 mg, 0.31 mmol) was added under stirring. After 5 min stirring, DMAP (224 mg, 1.83 mmol) was added into the mixture and stirred for another 1 h at room temperature. Afterwards, a solution of 1-pyrenebutanol (300 mg, 1.09 mmol) in 2 mL CH_2Cl_2 was added to the reaction mixture and reacted overnight. Subsequently, the excess phosgene (CAUTION: TOXIC) was removed by Ar purging and neutralized by bubbling the exhaust gas through a 2 M NaOH solution. Afterwards, the reaction mixture was washed three times with H_2O. After evaporation of the solvent under reduced pressure, the crude product was purified by column chromatography on silica gel (hexane:EtOAc = 10:1) to give compound **N3-A4** (68 mg, 43% yield) as a white solid. **^{1}H NMR (400 MHz, $CDCl_3$):** δ (ppm): 8.27 (d, *J*=9.2 Hz, 1H), 8.18-7.96 (m, 7H), 7.85 (d, *J*=7.6 Hz, 1H), 6.34 (d, *J*=3.2 Hz, 1H), 6.20 (d, *J*=3.2 Hz, 1H), 6.08 (s, 1H), 5.50-5.47 (m, 1H), 5.09 (s, 2H), 4.44 (q, *J*=6.8 Hz, 1H), 3.54-3.42 (m, 2H), 3.34 (t, *J*=8.0 Hz, 2H), 1.96-1.87 (m, 5H), 1.79-1.70 (m, 2H), 1.51 (d, *J*=6.4 Hz, 3H). **^{13}C NMR (101 MHz, $CDCl_3$):** δ (ppm): 167.14, 156.94, 149.05, 137.01, 136.11, 131.56, 131.04, 129.88, 128.74, 127.64, 127.41, 127.25, 126.66, 126.09, 125.90, 125.20, 125.16, 124.93, 124.89, 124.76, 123.63, 111.19, 107.60, 70.85, 68.62, 58.60, 33.37, 29.95, 28.54, 19.90, 18.38.

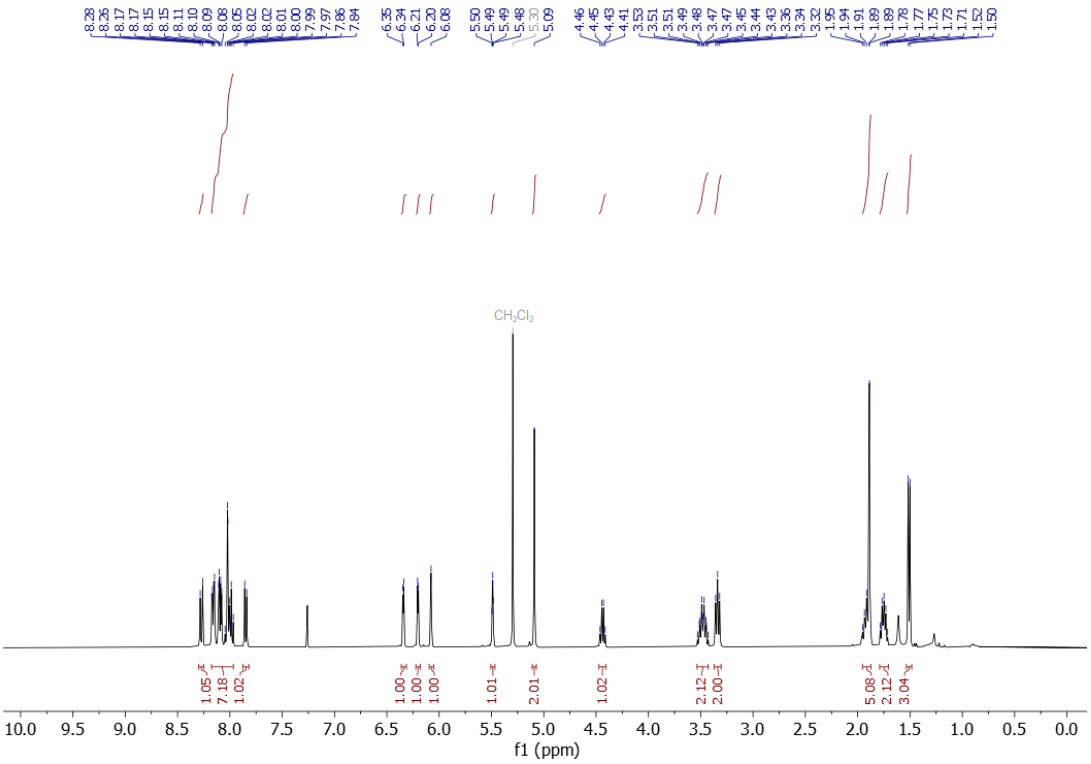

^{1}H NMR spectrum of **N3-A4**.

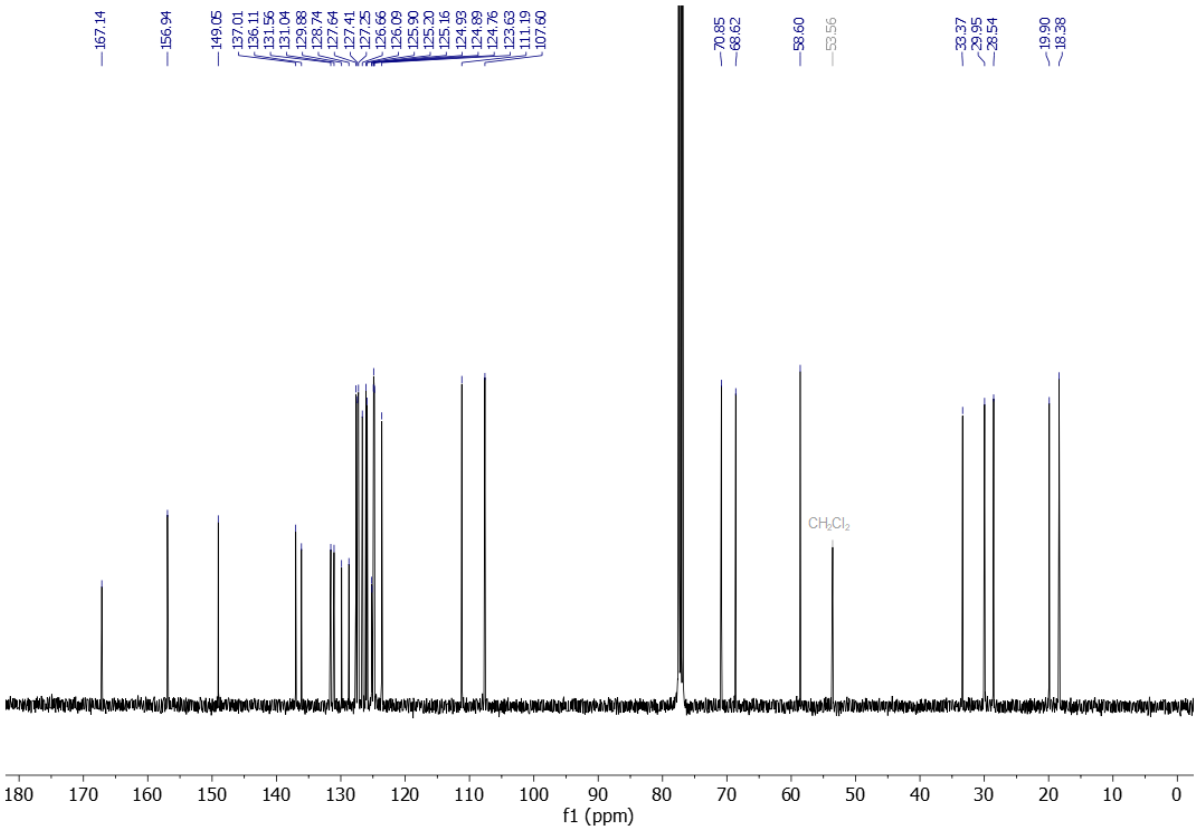

^{13}C NMR spectrum of **N3-A4**.

(2-(2-(methacryloyloxy)ethyl)-1,3-dioxo-7-(1-(((4-(pyren-1-yl)butoxy)carbonyl)oxy)ethyl)-1,2,3,3a,7,7a hexahydro-4H-4,7-epoxyisoindol-4-yl)methyl methacrylate (**N3-A5**)

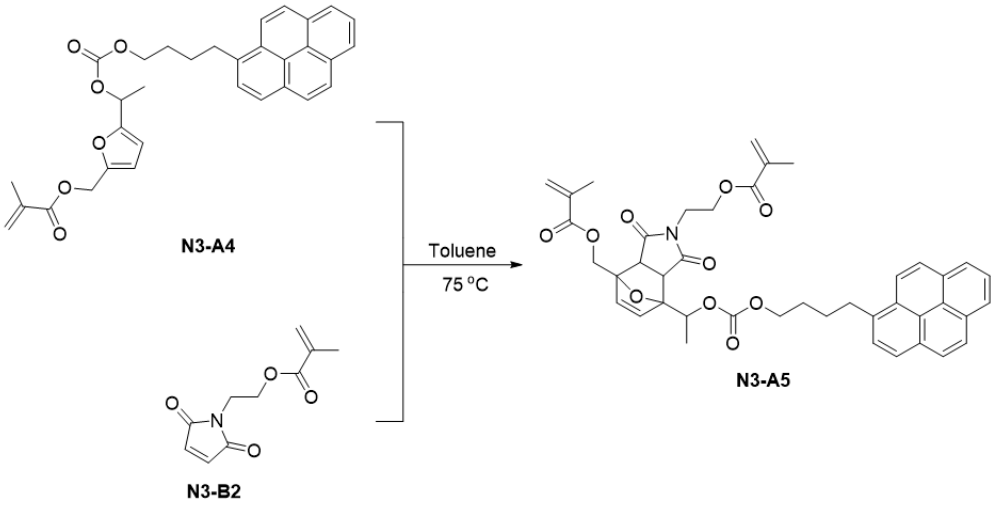

N3-A4 (60 mg, 0.11 mmol, 1.0 equiv.) and **N3-B2** (42 mg, 0.2 mmol, 1.8 equiv.) were dissolved in toluene (1.1 mL) and stirred for 48 h at 75 °C. Afterwards, the solvent was removed *in vacuo*. The residue was re-dissolved in EtOAc, and washed with H_2O. After removal of the solvent under reduced pressure, the crude reaction mixture was purified by column chromatography (hexane:EtOAc = 1:1) to give compound **N3-A5** (35 mg, 44% yield) as a yellow oil. **^{1}H NMR (400 MHz, $CDCl_3$):** δ (ppm): 8.31 (d, *J*=9.2 Hz, 1H), 8.15 (d, *J*=7.6 Hz, 2H), 8.12-8.06 (m, 2H), 8.04-7.95 (m, 3H), 7.88 (d, *J*=8.0 Hz, 1H), 6.46 (d, *J*=5.6 Hz, 1H), 6.29 (d, *J*=5.6 Hz, 1H), 6.10 (s, 1H), 6.03 (s, 1H), 5.58 (t, *J*=1.6 Hz, 1H), 5.48 (t, *J*=1.6 Hz, 1H), 4.88 (d, *J*=12.8 Hz, 1H), 4.41 (d, *J*=12.8 Hz, 1H), 4.33-4.20 (m, 2H), 3.89 (q, *J*=6.0 Hz, 1H), 3.78-3.67 (m, 4H), 3.40 (t, *J*=7.6 Hz, 2H), 2.92 (d, *J*=6.4 Hz, 1H), 2.82 (d, *J*=6.4 Hz, 1H), 2.04-1.95 (m, 2H), 1.94 (s, 3H), 1.85 (s, 3H), 1.83-1.76 (m, 2H), 1.13 (d, *J*=6.4 Hz, 3H). **^{13}C NMR (101 MHz, $CDCl_3$):** δ (ppm): 174.01, 173.97, 167.05, 166.87, 138.10, 137.25, 137.20, 136.00, 135.96, 131.55, 131.04, 129.87, 128.78, 127.66, 127.58, 127.20, 126.66, 126.25, 126.21, 125.95, 125.22, 125.16, 124.97, 124.91, 124.76, 123.73, 93.29, 89.44, 71.57, 68.94, 61.72, 60.82, 51.45, 50.25, 37.90, 33.55, 30.27, 28.58, 18.40, 18.31, 15.97.

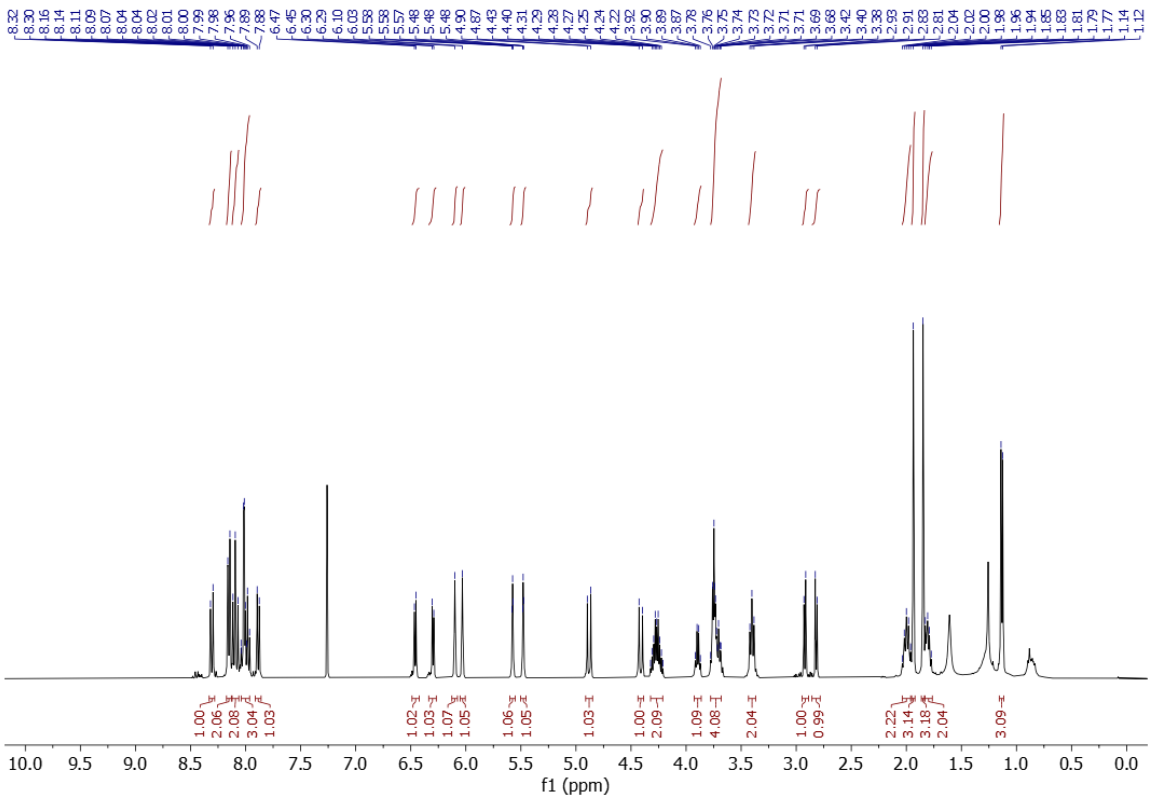

^{1}H NMR spectrum of **N3-A5**.

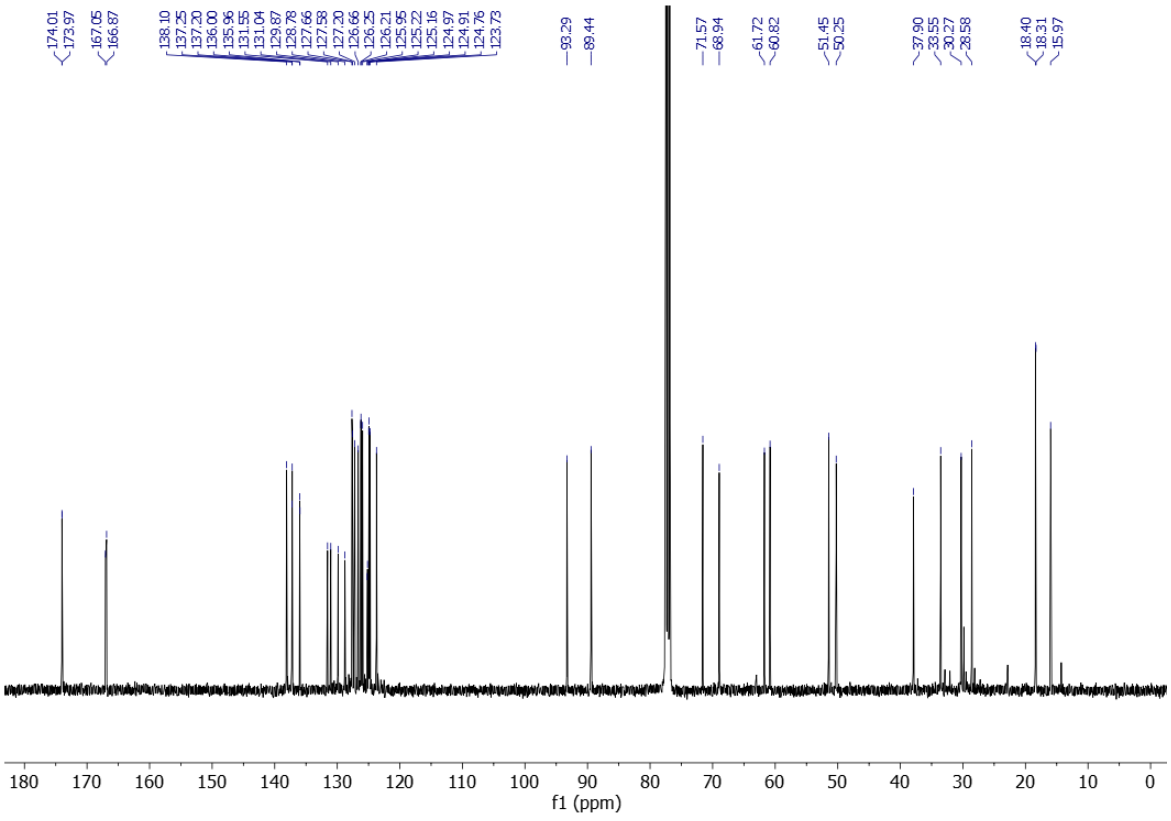

^{13}C NMR spectrum of **N3-A5**.

Bis(6-hydroxyhexyl) but-2-ynedioate (**N4-A2**)

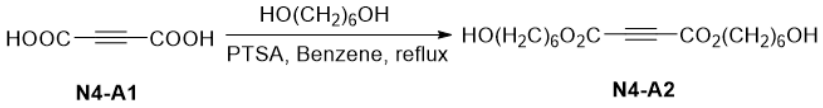

N4-A1 **N4-A2**

The synthesis of **N4-A2** was performed using an adapted literature protocol.[54, 55] Acetylenedicarboxylic acid (2.0 g, 17.5 mmol), 1,6-hexanediol (20.8 g, 176 mmol) and *p*-toluenesulfonic acid monohydrate (333.2 mg, 1.75 mmol) were dissolved in 28 mL benzene in a 100 mL round bottom flask. Then, the reaction flask was equipped with a reflux condenser fitted with a Dean-Stark trap. The reaction mixture was heated up to 100 °C. After 24 h, ca. 15 mL of solution had collected in the trap. The reaction mixture was allowed to cool down to room temperature. Then, the reaction solution was diluted with Et_2O (30 mL) and cooled to -10 °C for 1 h. The solution was decanted and the solids were rinsed with additional portions of Et_2O. The combined organic layer was washed with saturated $NaHCO_3$ (2 x 20 mL), water (3 x 20 mL) and brine (20 mL). Afterwards, the solvent was removed *in vacuo*. The crude product was purified by column chromatography (CH_2Cl_2:MeOH = 15:1) to give compound **N4-A2** (3.7 g, 67% yield) as a pale-yellow oil. **^{1}H NMR (400 MHz, $CDCl_3$):** δ (ppm): 4.24 (t, *J*=6.4 Hz, 4H), 3.63 (t, *J*=6.4 Hz, 4H), 2.08 (s, 2H), 1.75-1.67 (m, 4H), 1.62-1.54 (m, 4H), 1.45-1.36 (m, 8H). **^{13}C NMR (101 MHz, $CDCl_3$):** δ (ppm): 151.99, 74.75, 67.04, 62.62, 32.49, 28.27, 25.57, 25.34. **ESI-MS:** (*m/z*) for $C_{16}H_{26}O_6$ expected $[M+H]^+$: 315.1802, Found for $[M+H]^+$: 315.1951.

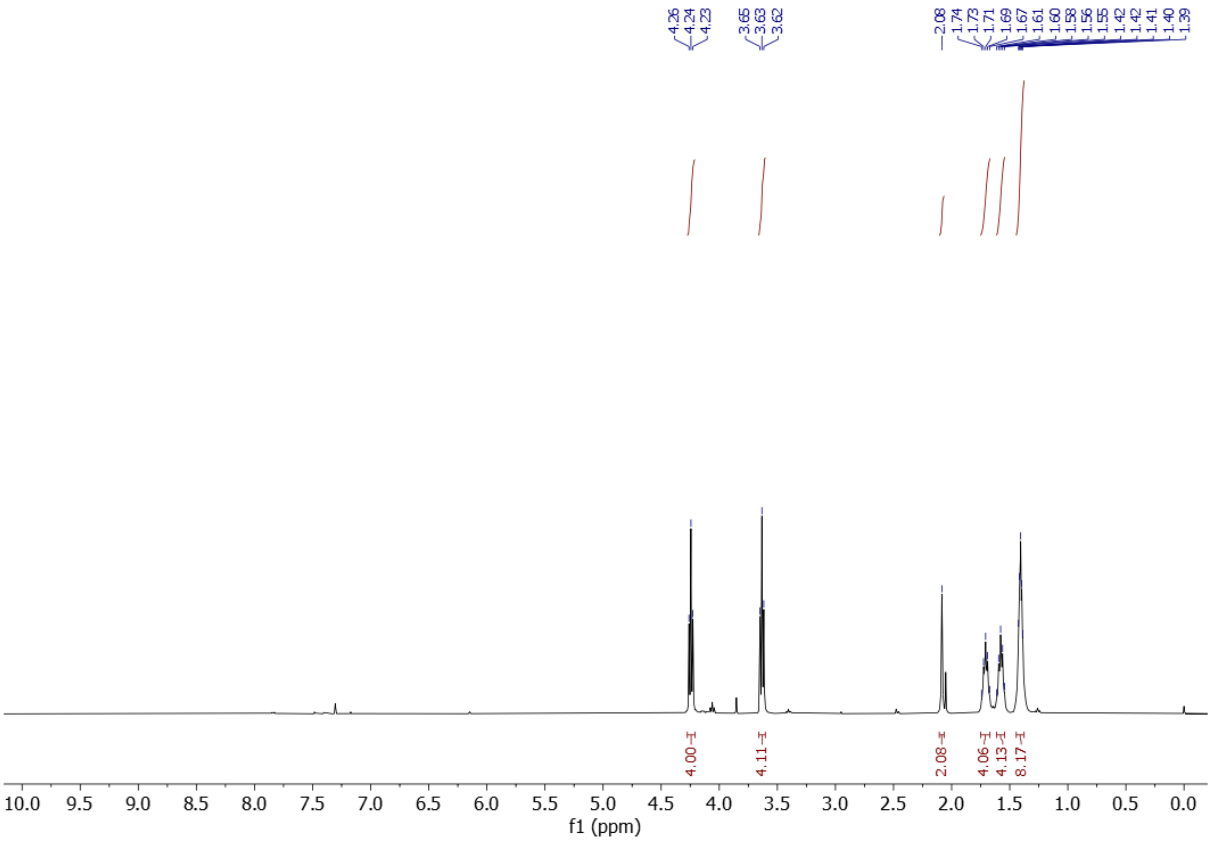

^{1}H NMR spectrum of **N4-A2**.

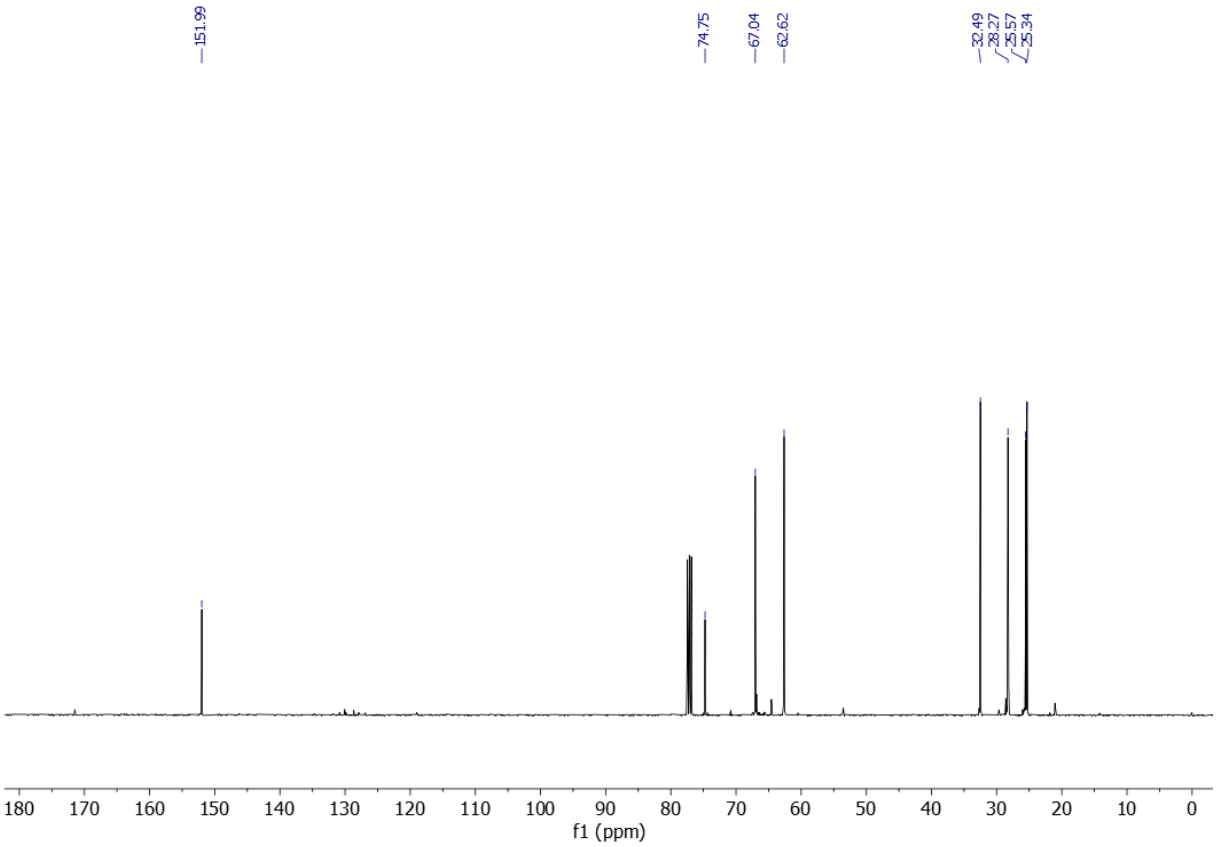

^{13}C NMR spectrum of **N4-A2**.

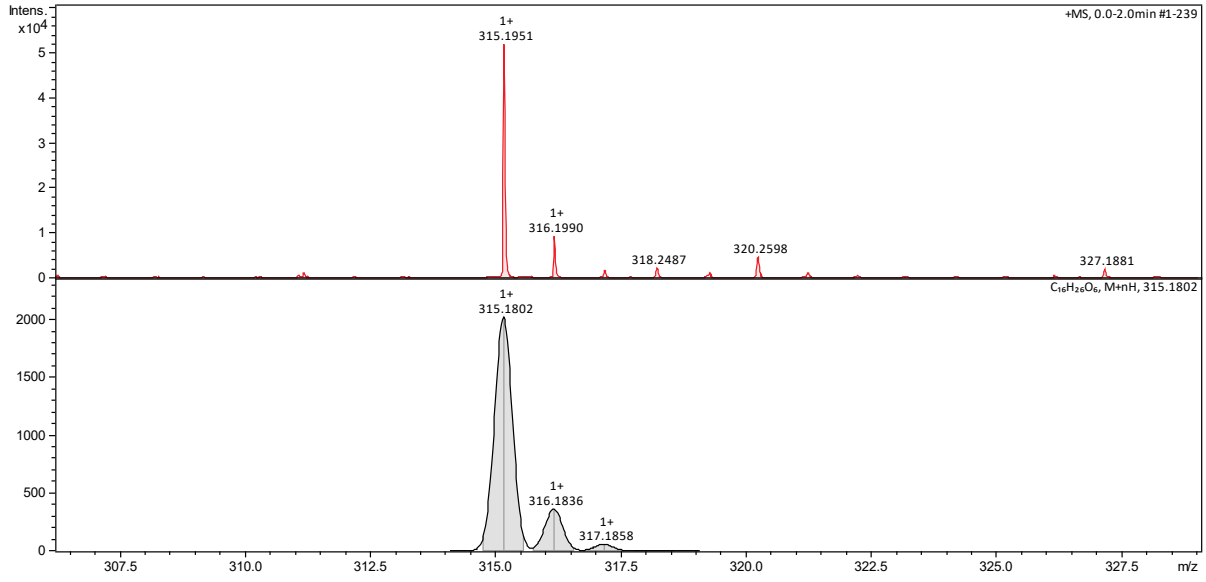

ESI-MS (*m/z*) of **N4-A2**.

Bis(6-hydroxyhexyl) 1-(((5-(dimethylamino)naphthalene)-1-sulfonamido)methyl)-7-oxabicyclo[2.2.1]hepta-2,5-diene-2,3-dicarboxylate (**N4-A3**)

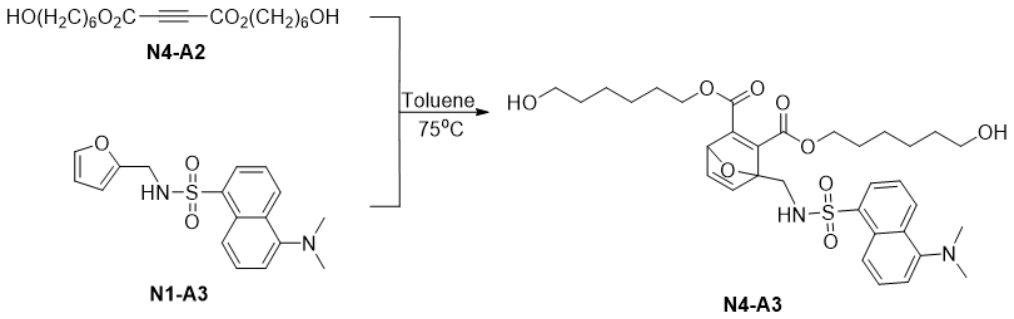

N4-A2 (2.0 g, 6.37 mmol, 1.0 equiv.) and compound **N1-A3** (3.16 g, 9.55 mmol, 1.5 equiv.) were dissolved in 10 mL toluene and stirred at 75 °C in a 50 mL round bottom flask. After 36 h, the reaction solution was cooled down to room temperature. Afterwards, the solvent was removed *in vacuo*. The residue was re-dissolved in EtOAc (50 mL), and washed with H_2O (30 mL). The organic layer was removed with a rotary evaporator. Then, the crude product mixture was purified by column chromatography (hexane:EtOAc = 1:5) to give compound **N4-A3** (2.3 g, 56% yield) as an orange oil. **^{1}H NMR (400 MHz, $CDCl_3$):** δ (ppm): 8.53 (d, *J*=8.4 Hz, 1H), 8.26-8.20 (m, 2H), 7.52 (q, *J*=8.8 Hz, 2H), 7.16 (d, *J*=7.6 Hz, 1H), 7.10 (dd, *J*=5.2 Hz 2.0 Hz, 1H), 6.86 (d, *J*=5.2 Hz, 1H), 5.54 (d, *J*=2.0 Hz, 1H), 5.46 (t, *J*=6.0 Hz, 1H), 4.19-4.05 (m, 4H), 3.70 (dd, *J*=13.6 Hz 7.2 Hz, 1H), 3.62-3.52 (m, 5H), 2.86 (s, 6H), 2.16 (s, 2H), 1.68-1.59 (m, 4H), 1.58-1.48 (m, 4H), 1.40-1.30 (m, 8H). **^{13}C NMR (101 MHz, $CDCl_3$):** δ (ppm): 163.69, 162.67, 153.19, 152.03, 151.73, 144.89, 142.73, 134.38, 130.70, 129.93, 129.69, 129.63, 128.62, 123.25, 118.68, 115.37, 95.91, 84.01, 65.91, 65.66, 62.58, 45.48, 41.98, 32.51, 28.48, 28.39, 25.66, 25.65, 25.44, 25.40. **ESI-MS:** (*m/z*) for $C_{33}H_{44}N_2O_9S$ expected $[M+H]^+$: 645.2840, Found for $[M+H]^+$: 645.3102.

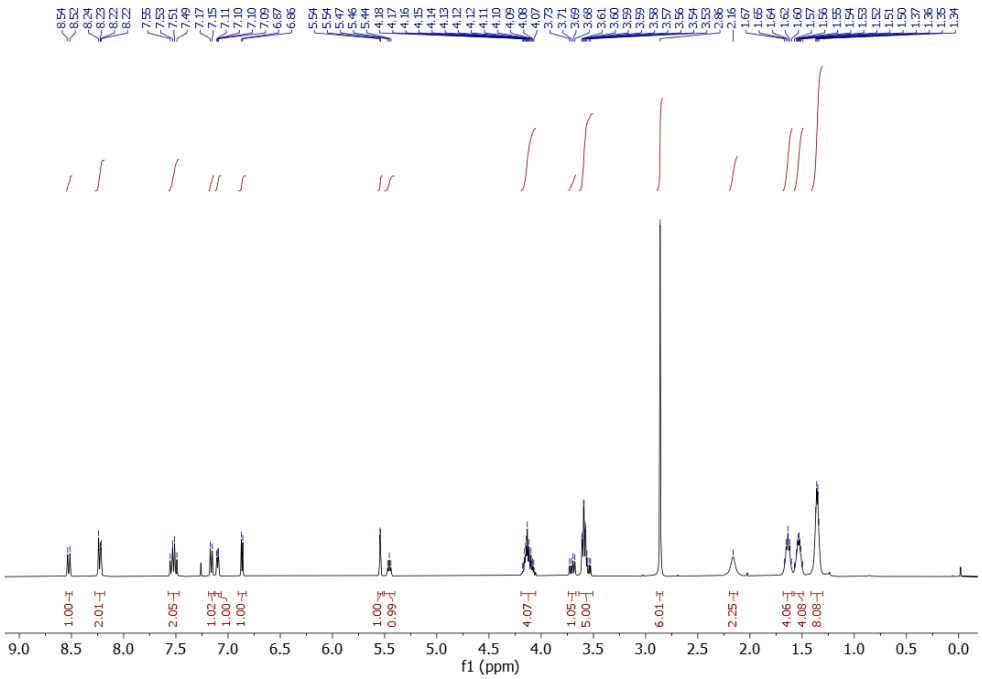

^{1}H NMR spectrum of **N4-A3**.

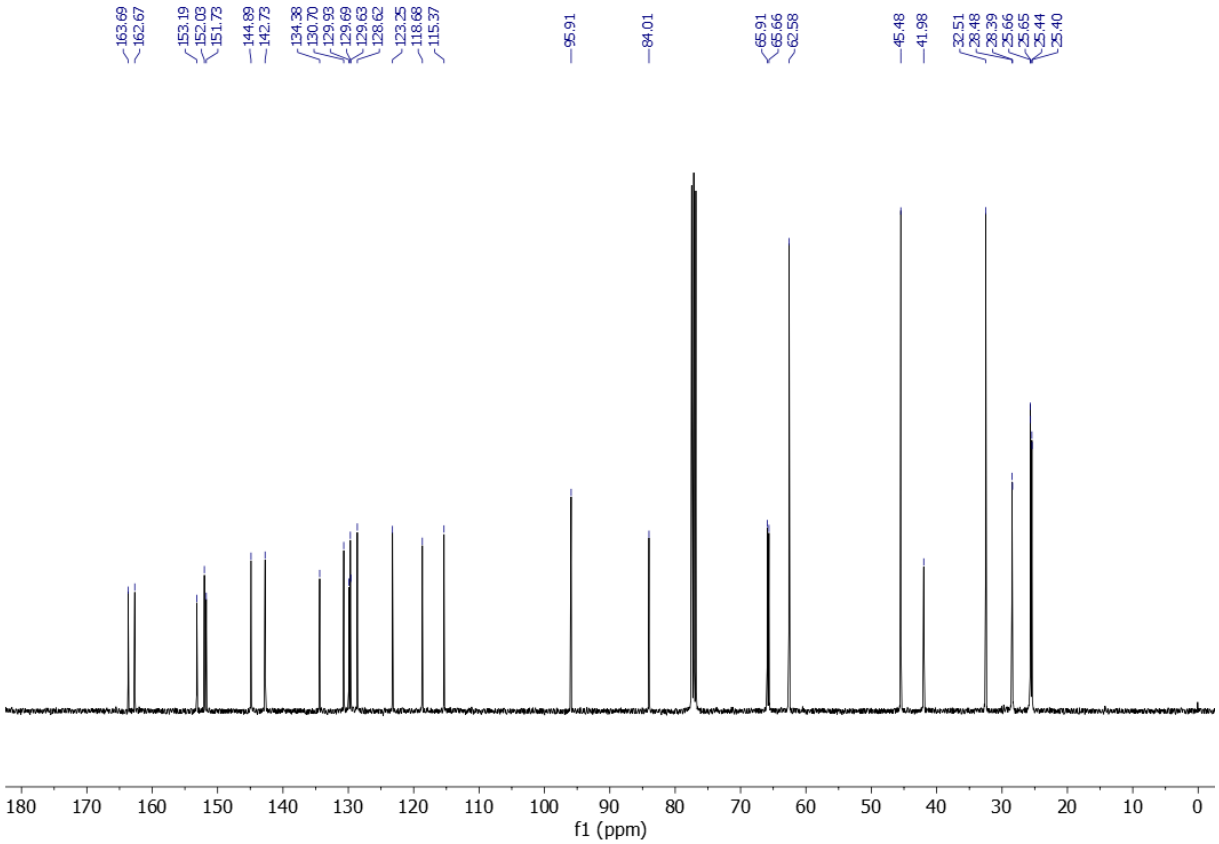

^{13}C NMR spectrum of **N4-A3**.

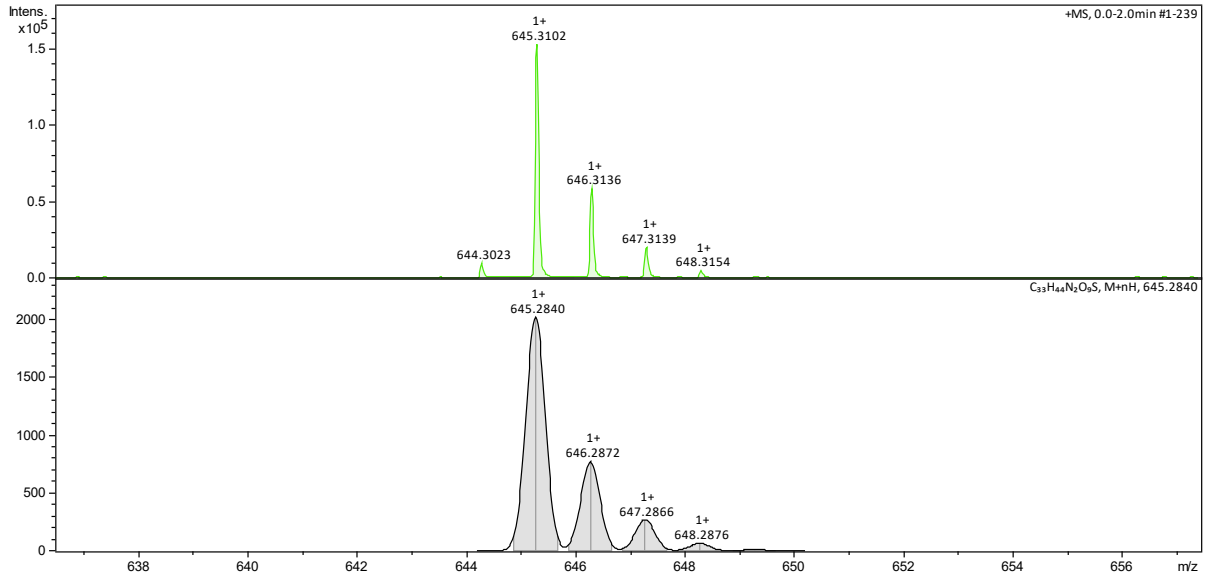

ESI-MS (*m/z*) of **N4-A3**.

Bis(6-(methacryloyloxy)hexyl) 1-(((5-(dimethylamino)naphthalene)-1-sulfonamido)methyl)-7-oxabicyclo[2.2.1]-hepta-2,5-diene-2,3-dicarboxylate (**N4-A4**)

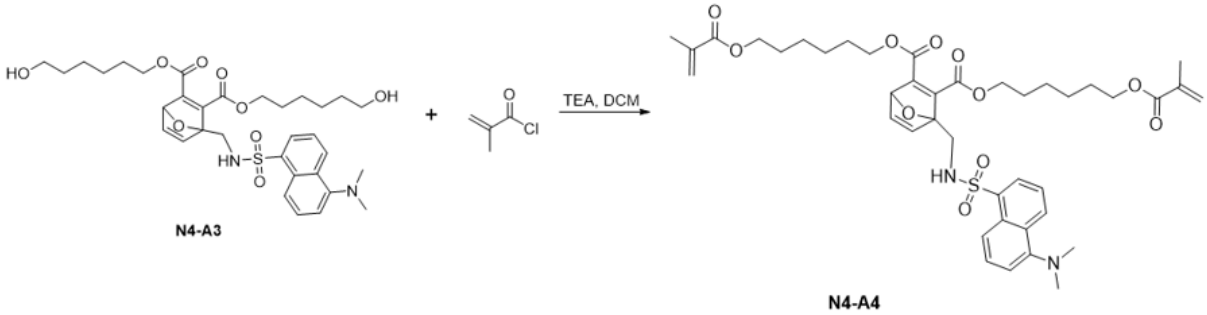

N4-A3 N4-A4

N4-A3 (1.74 g, 2.7 mmol, 1.0 equiv.) and Et_3N (964 uL, 6.9 mmol, 2.5 equiv.) were dissolved in 30 mL CH_2Cl_2. The mixture was cooled to 0 °C with an ice-water bath. Then, a solution of methacryloyl chloride (653 uL, 6.75 mmol, 2.5 equiv.) in 6 mL CH_2Cl_2 was added slowly into the mixture. The reaction mixture was stirred in the ice-water bath for 1 h. Then, the reaction mixture was allowed to warm up to room temperature to react further. The reaction mixture was stirred until complete consumption of the starting material, as indicated by TLC. Afterwards, 10 mL water was added into the reaction solution to hydrolyze the unreacted methacryloyl chloride. The organic solvent was collected and removed *in vacuo*. The crude product was then purified by silica column chromatography (hexane:EtOAc = 1:1) to give compound **N4-A4** (1.26 g, 60% yield) as a light yellow oil. **^{1}H NMR (400 MHz, $CDCl_3$):** δ (ppm): 8.53 (d, *J*=8.4 Hz, 1H), 8.26-8.20 (m, 2H), 7.57-7.48 (m, 2H), 7.17 (d, *J*=7.6 Hz, 1H), 7.10 (dd, *J*=5.2 Hz 2.0 Hz, 1H), 6.87 (d, *J*=5.2 Hz, 1H), 6.08 (s, 2H), 5.56-5.51 (m, 3H), 5.29-5.23 (m, 1H), 4.18-4.07 (m, 8H), 3.70 (dd, *J*=13.6 Hz 6.8 Hz, 1H), 3.57 (dd, *J*=13.6 Hz 5.6 Hz, 1H), 2.87 (s, 6H), 1.92 (s, 6H), 1.71-1.61 (m, 8H), 1.43-1.34 (m, 8H). **^{13}C NMR (101 MHz, $CDCl_3$):** δ (ppm): 167.58, 167.55, 163.54, 162.50, 153.47, 152.09, 151.82, 144.90, 142.79, 136.54, 136.51, 134.40, 130.73, 129.98, 129.74, 129.66, 128.66, 125.39, 125.37, 123.24, 118.67, 115.38, 95.84, 84.04, 65.81, 65.50, 64.65, 64.57, 45.50, 42.05, 28.56, 28.46, 28.36, 25.73, 25.70, 25.57, 18.42. **ESI-MS:** (*m/z*) for $C_{41}H_{52}N_2O_{11}S$ expected $[M+H]^+$: 781.3365, Found for $[M+H]^+$: 781.3690.

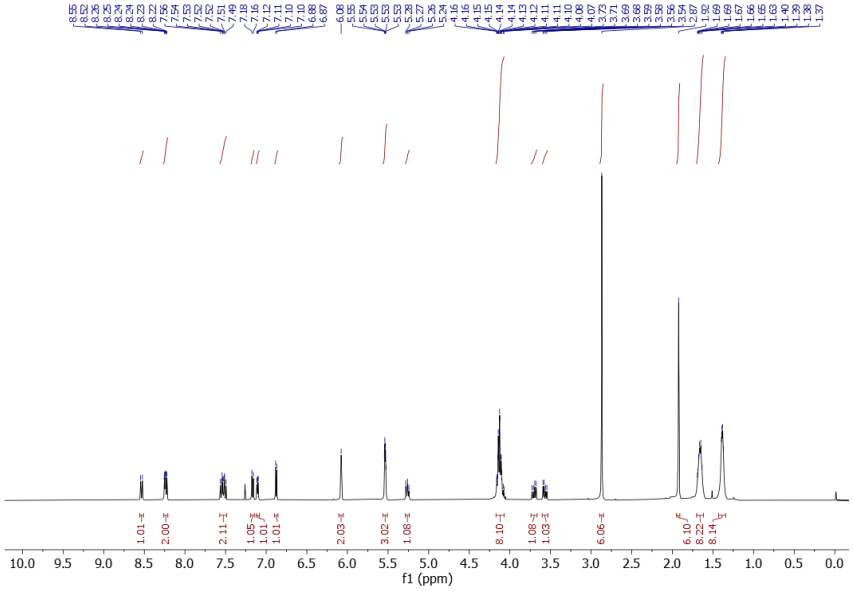

^{1}H NMR spectrum of **N4-A4**.

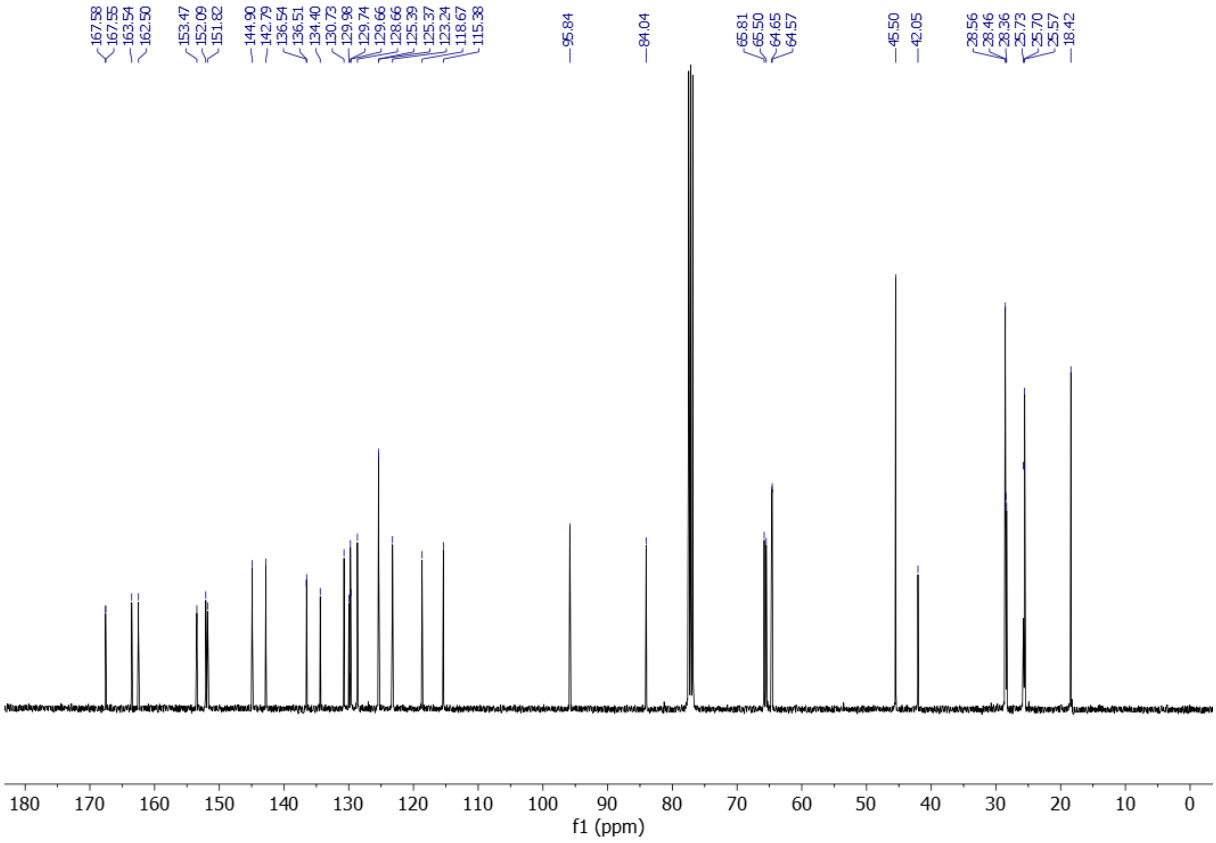

^{13}C NMR spectrum of **N4-A4**.

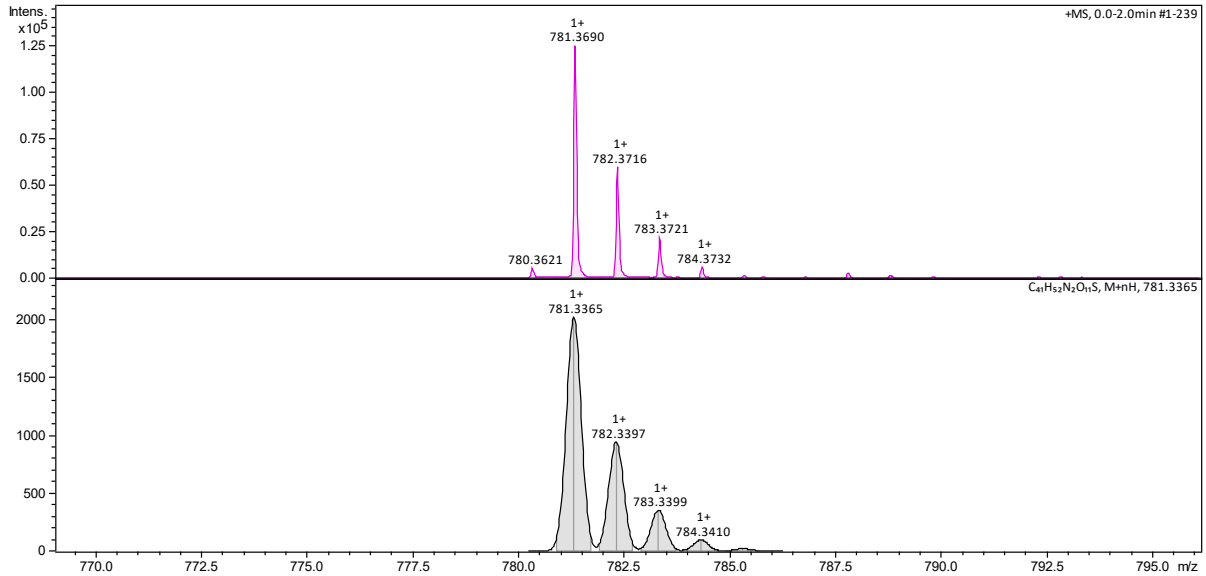

ESI-MS (*m/z*) of **N4-A4**.

2-(6-hydroxyhexyl) 3-(6-(methacryloyloxy)hexyl) 1-(((5-(dimethylamino)naphthalene)-1-sulfonamido)methyl)-7-oxabicyclo[2.2.1]hepta-2,5-diene-2,3-dicarboxylate (**N4-B4**)

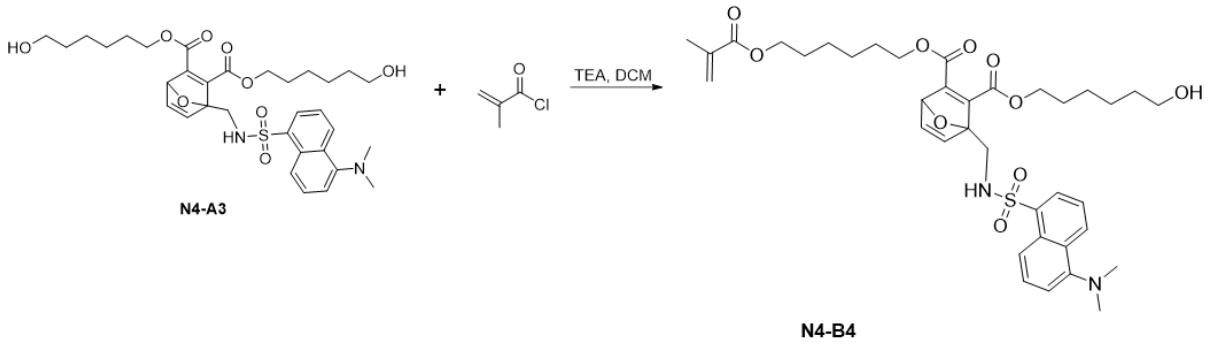

N4-A3 (0.64 g, 1.0 mmol, 1.0 equiv.) and Et_3N (154 uL, 1.1 mmol, 1.1 equiv.) were dissolved in 20 mL CH_2Cl_2. The mixture was cooled to 0 °C with an ice-water bath. Then, a solution of methacryloyl chloride (102 uL, 1.05 mmol, 1.05 equiv.) in 2 mL CH_2Cl_2 was added slowly into the mixture. The reaction mixture was stirred in the ice-water bath for 1 h. Then, the reaction mixture was allowed to warm up to room temperature to react further. The reaction mixture was stirred until complete consumption of the starting material, as indicated by TLC. Afterwards, 3 mL water was added into the reaction solution to hydrolyze the unreacted methacryloyl chloride. Then, the organic phase was collected and removed *in vacuo*. The crude product was then purified by silica column chromatography (hexane:EtOAc = 1:2) to give compound **N4-B4** (0.28 g, 39% yield) as a light yellow oil. **^{1}H NMR (400 MHz, $CDCl_3$):** δ (ppm): 8.54 (d, *J*=8.4 Hz, 1H), 8.27-8.20 (m, 2H), 7.57-7.49 (m, 2H), 7.17 (d, *J*=7.6 Hz, 1H), 7.11 (d, *J*=5.2 Hz 2.0 Hz, 1H), 6.87 (d, *J*=5.2 Hz, 1H), 6.08 (s, 1H), 5.56-5.51 (m, 2H), 5.27 (t, *J*=6.0 Hz, 1H), 4.19-4.08 (m, 6H), 3.70 (dd, *J*=13.6 Hz 6.8 Hz, 1H), 3.65-3.53 (m, 3H), 2.87 (d, *J*=4.4 Hz, 6H), 1.93 (s, 3H), 1.73-1.60 (m, 8H), 1.42-1.33 (m, 8H). **^{13}C NMR (101 MHz, $CDCl_3$):** δ (ppm): 167.66, 163.62, 162.59, 153.45, 152.10, 151.85, 144.93, 142.78, 136.53, 134.39, 130.76, 129.98, 129.79, 129.66, 128.69, 125.46, 123.25, 118.67, 115.39, 95.86, 84.05, 65.88, 65.62, 64.69, 62.72, 45.51, 42.05, 32.59, 28.57, 28.46, 28.37, 25.72, 25.57, 25.46, 25.41, 18.44.

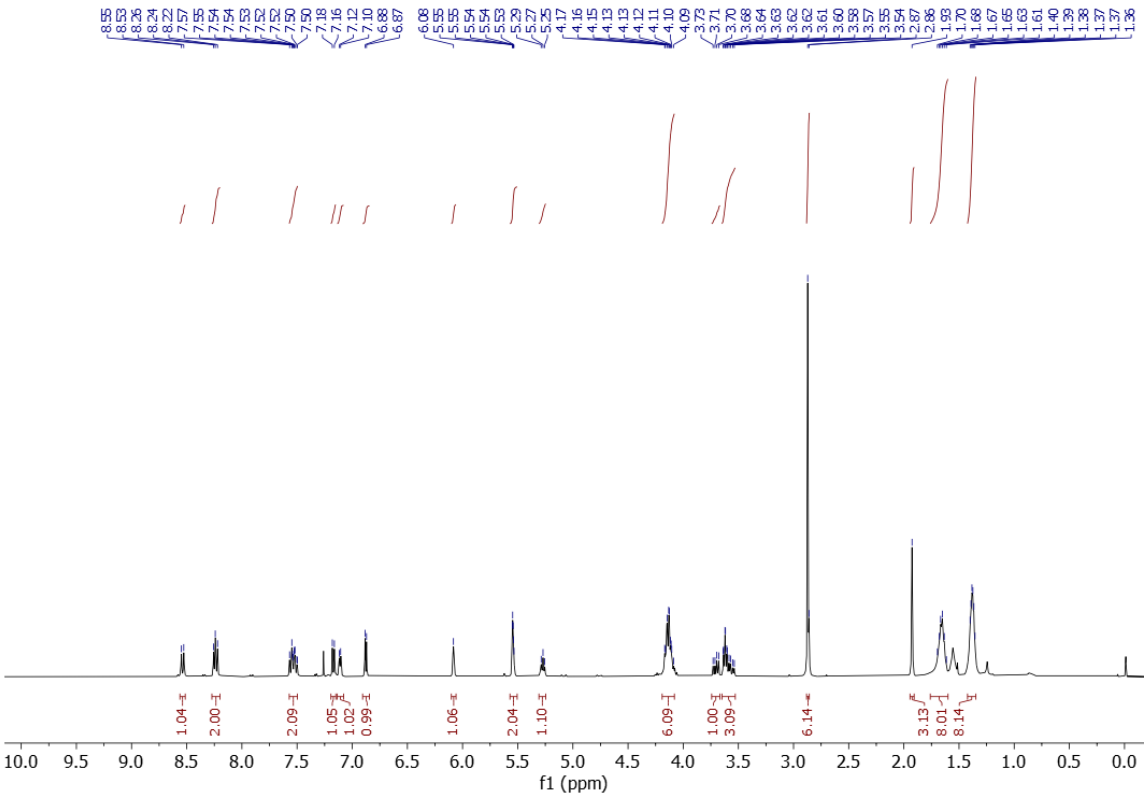

^{1}H NMR spectrum of **N4-B4**.

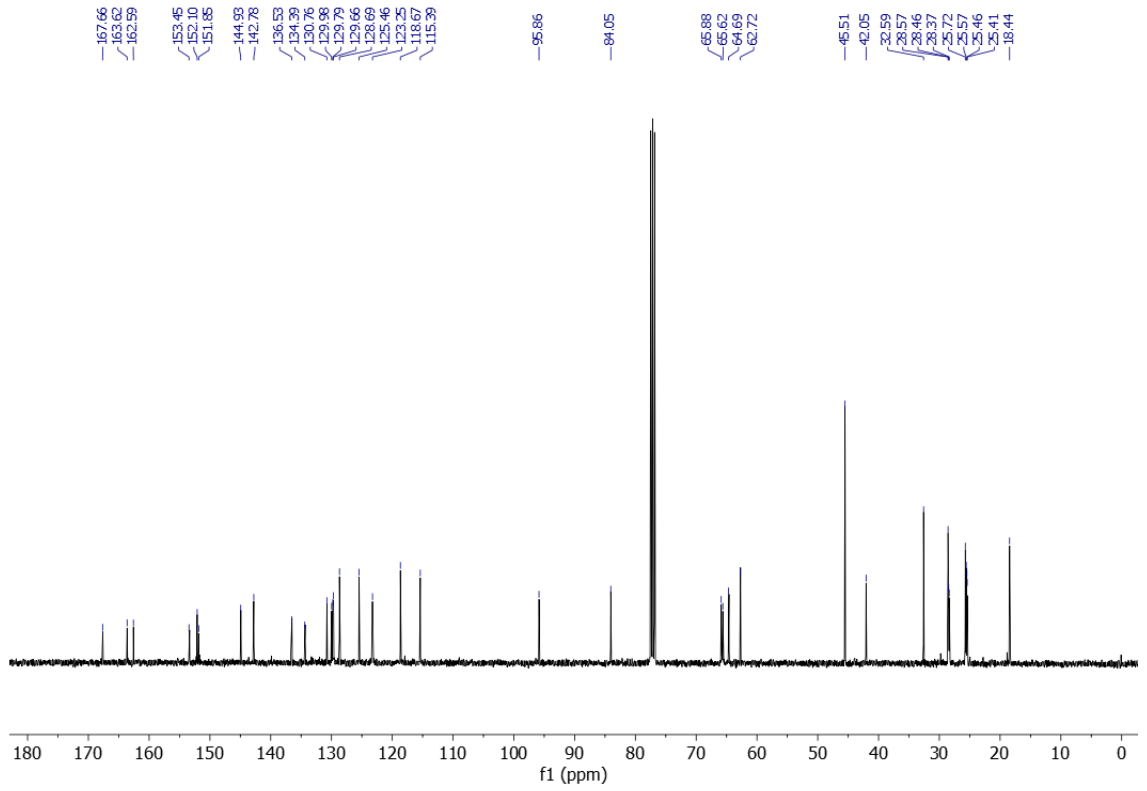

^{13}C NMR spectrum of **N4-B4**.

Bis(6-((2-bromo-2-methylpropanoyl)oxy)hexyl) 1-(((5-(dimethylamino)naphthalene)-1-sulfonamido)methyl)-7-oxabicyclo[2.2.1]hepta-2,5-diene-2,3-dicarboxylate (**N4-C4**)

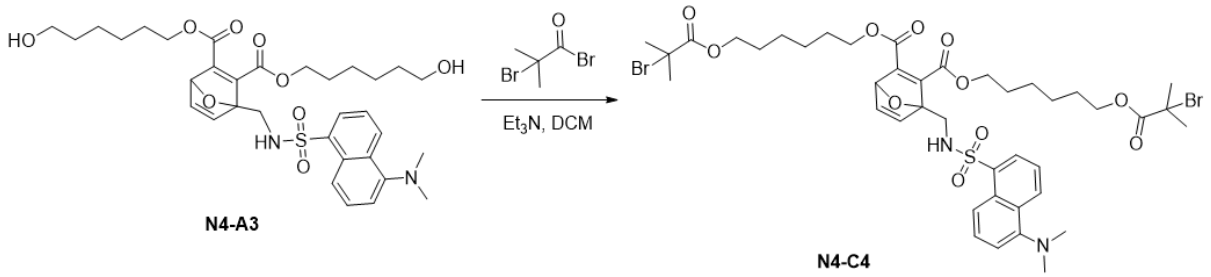

N4-A3 (0.13 g, 0.2 mmol, 1.0 equiv.) and Et_3N (69 uL, 0.5 mmol, 2.5 equiv.) were dissolved in 6 mL CH_2Cl_2. The mixture was cooled to 0 °C with an ice-water bath. Then, a solution of α-bromoisobutyryl bromide (102 mg, 0.44 mmol, 2.2 equiv.) was added dropwise into the mixture. The reaction mixture was stirred in the ice-water bath for 30 min. Then, the reaction mixture was allowed to warm up to room temperature to react further. The reaction mixture was continuously stirred until the starting material was entirely consumed, as confirmed by TLC analysis. Then, the solvent was completely removed under reduced pressure. The crude product was then purified by silica column chromatography (hexane:EtOAc = 2:1) to give compound **N4-C4** (0.16 g, 85% yield) as a yellow oil. **^{1}H NMR (400 MHz, $CDCl_3$):** δ (ppm): 8.57 (d, *J*=8.0 Hz, 1H), 8.25 (d, *J*=7.6 Hz, 2H), 7.54 (q, *J*=8.0 Hz, 2H), 7.19 (d, *J*=7.6 Hz, 1H), 7.11 (dd, *J*=5.2 Hz 2.0 Hz, 1H), 6.88 (d, *J*=5.2 Hz, 1H), 5.54 (d, *J*=1.6 Hz, 1H), 5.23 (t, *J*=6.0 Hz, 1H), 4.19-4.07 (m, 8H), 3.71 (dd, *J*=13.6 Hz 6.8 Hz, 1H), 3.56 (dd, *J*=13.6 Hz 5.6 Hz, 1H), 2.89 (s, 6H), 1.92 (s, 12H), 1.73-1.61 (m, 8H), 1.45-1.34 (m, 8H). **^{13}C NMR (101 MHz, $CDCl_3$):** δ (ppm): 171.78, 163.54, 162.49, 153.52, 151.81, 144.95, 142.79, 134.45, 130.69, 129.81, 129.67, 128.65, 123.40, 115.51, 95.83, 84.06, 65.97, 65.87, 65.80, 65.49, 56.13, 56.07, 45.59, 42.08, 30.87, 30.85, 28.45, 28.35, 28.30, 25.52. **ESI-MS:** (*m/z*) for $C_{41}H_{54}Br_2N_2O_{11}S$ expected $[M+H]^+$: 941.1888, Found for $[M+H]^+$: 941.2257.

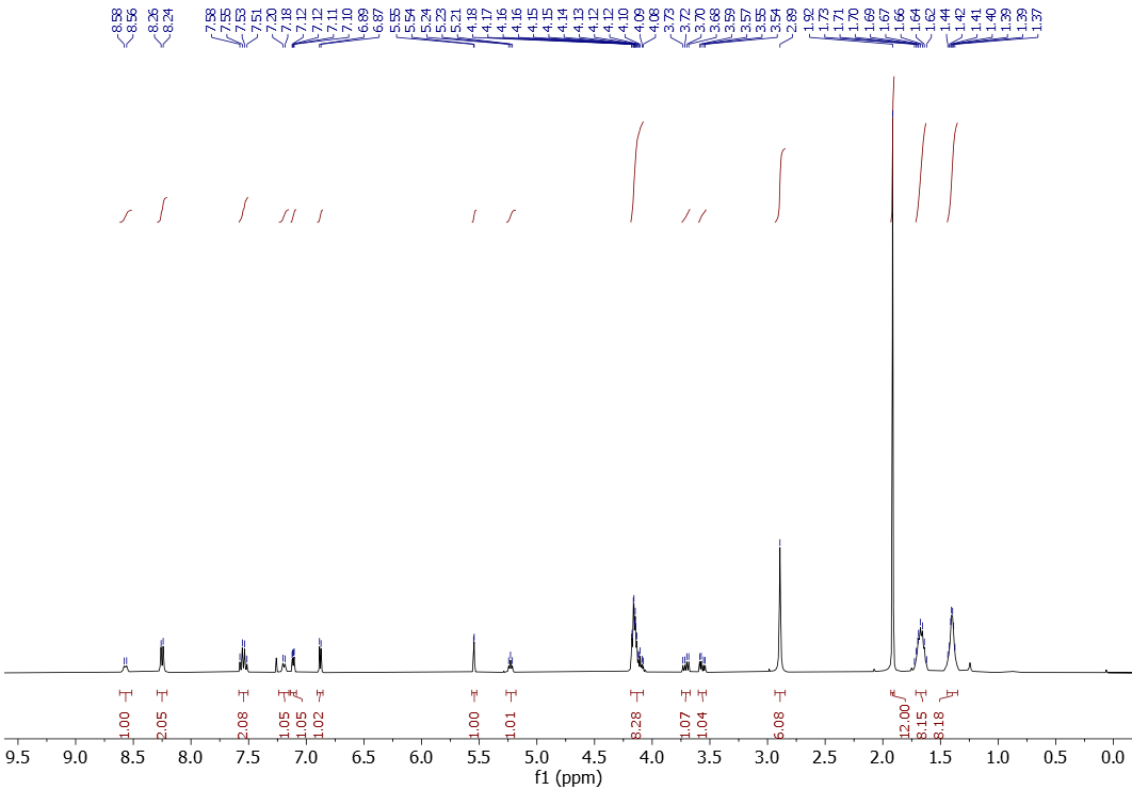

^{1}H NMR spectrum of **N4-C4**.

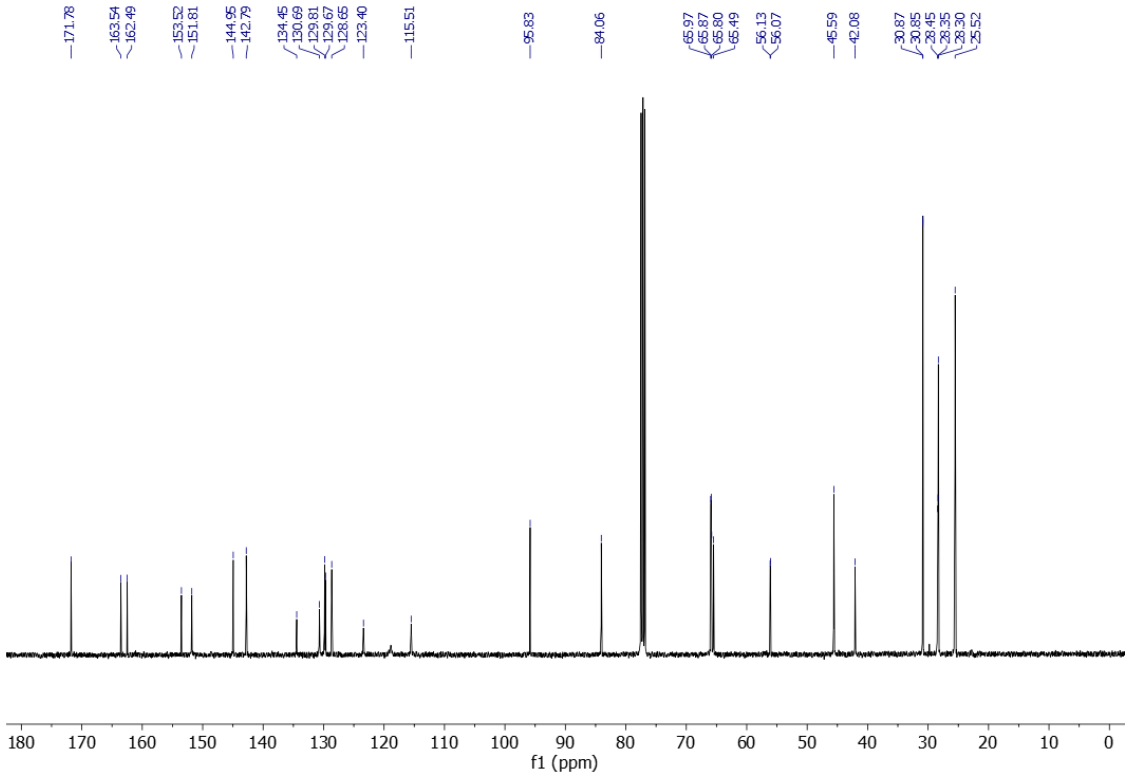

^{13}C NMR spectrum of **N4-C4**.

5.6 Supporting figures and tables

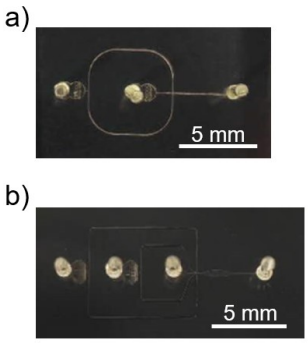

Figure S1. Microfluidic chips. The images of the microfluidic chips for the production of **a**) O/W emulsion, and **b**) G/O/W emulsions.

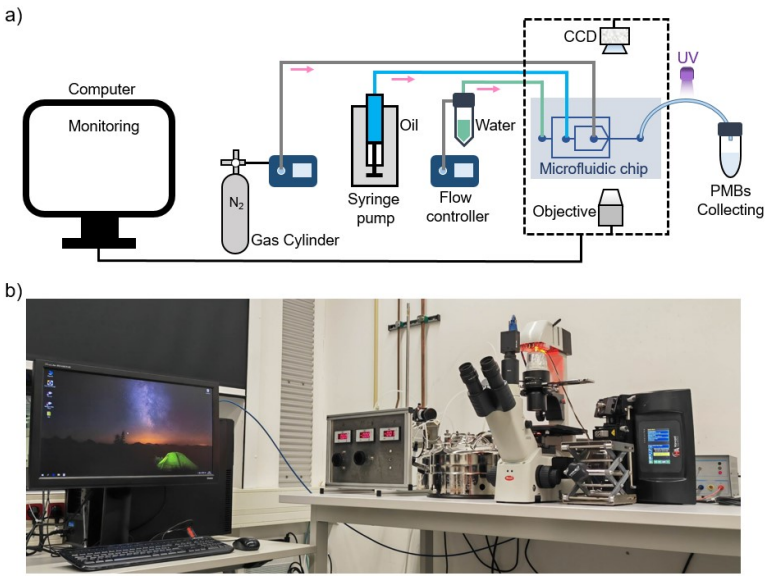

Figure S2. Microfluidic system. **a**) Schematic illustration of the process of the microfluidic system. **b**) Photograph of the setup of the microfluidic system.

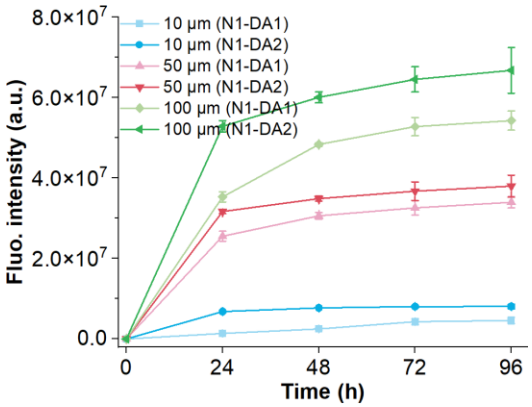

Figure S3. Kinetic analysis of 2-mercaptoethanol (MCE) reacting with **N1-DA1** and **N1-DA2**. **N1-DA1** and **N1-DA2 were** mixed with an excess of MCE (10 mM) in MeCN/H_2O.

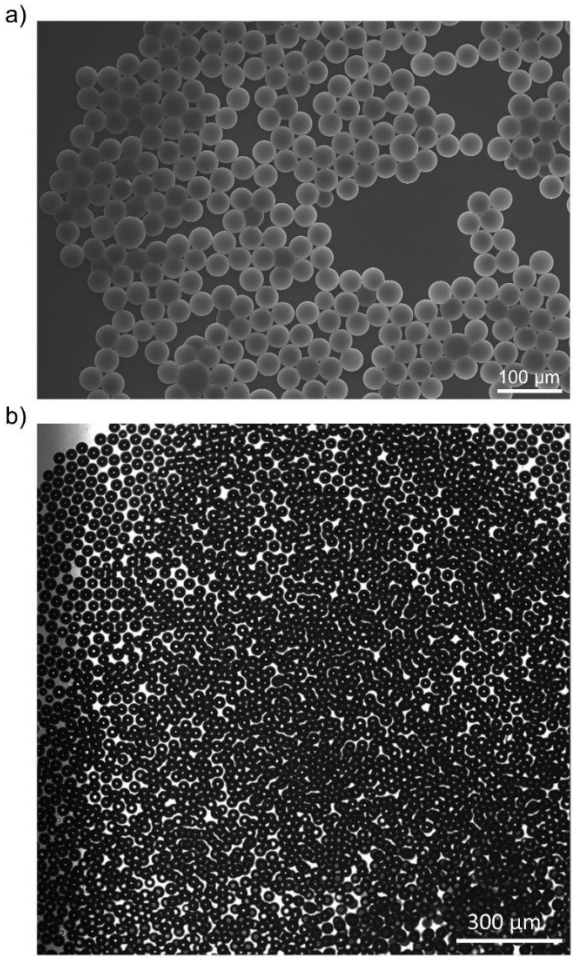

Figure S4. Morphological characterization of PMBs-MDF. **a**) Scanning electron microscope (SEM) image of microbubbles. **b**) Confocal microscope image of microbubbles.

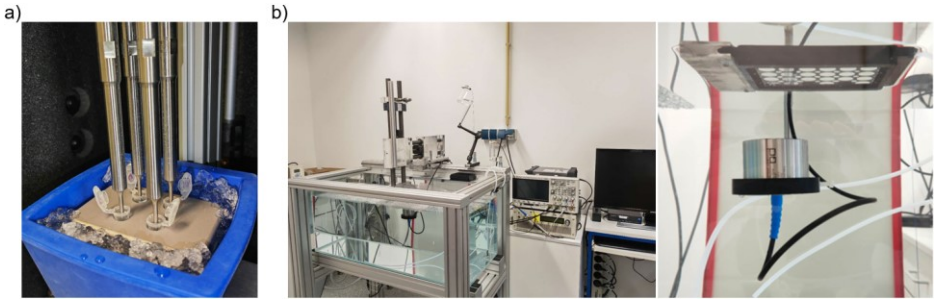

Figure S5. Sonication systems. **a**) 4-probes 20 kHz sonicator. **b**) HIFU sonication system (left), transducer and 24 wellplate (right).

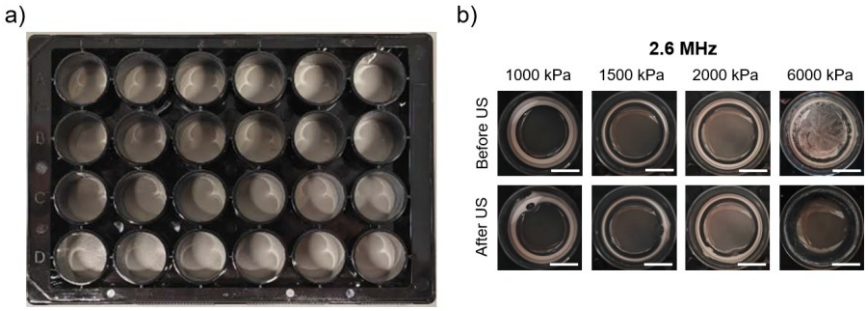

Figure S6. **a**) 24-well plate with an ultrasound-transparent bottom for HIFU experiments. **b**) The response of PMBs to different focal pressure irradiation (2.6 MHz, 5 min), scale bar: 5 mm.

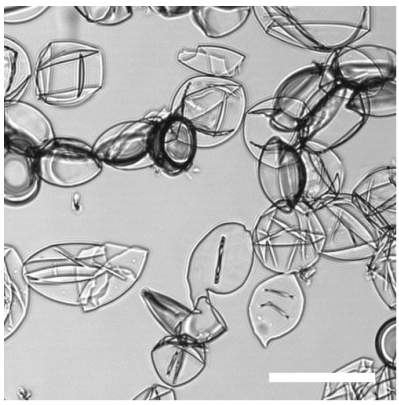

Figure S7. Confocal microscopy image of fragments of PMBs, after 2.6 MHz ultrasound irradiation (7000 kPa, 15 min), scale bar: 50 µm.

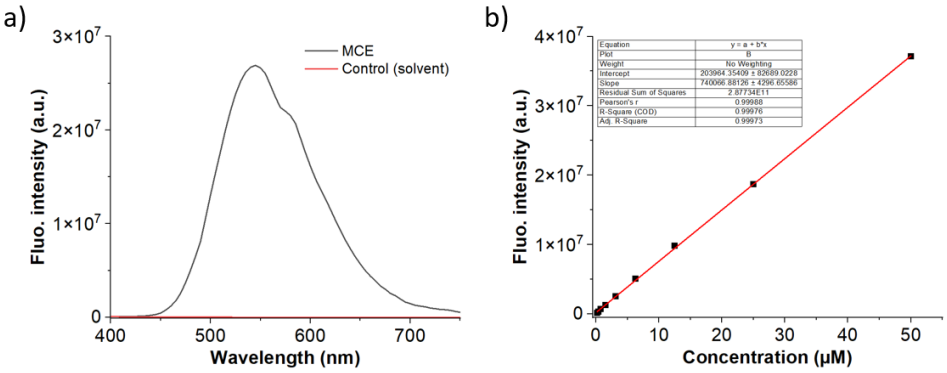

Figure S8. a) Fluorescence spectrum of PMBs-MDF mixed with an excess of MCE (solvent: MeCN/H_2O). **b**) Standard curve of dansyl-fluorophore (**N1-A3**, fluorescence intensity collected at 545 nm, Ex: 340 nm).

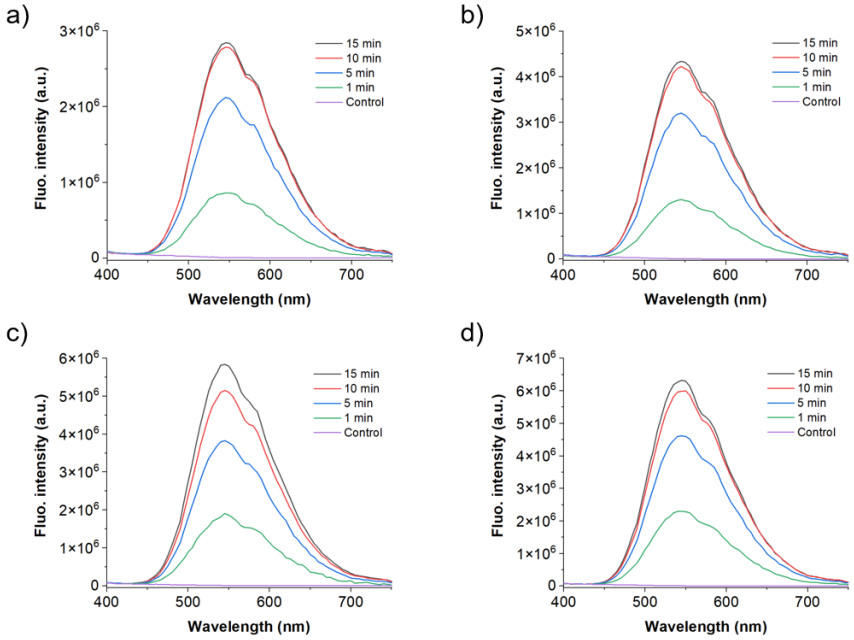

Figure S9. Fluorescence spectra collected from PMBs-MDF under 20 kHz irradiation (solvent: MeCN/H_2O). **a**) Sound intensity, 1 W cm^{-2}. **b**) Sound intensity, 3 W cm^{-2}. **c**) Sound intensity, 6 W cm^{-2}. **d**) Sound intensity, 12 W cm^{-2}.

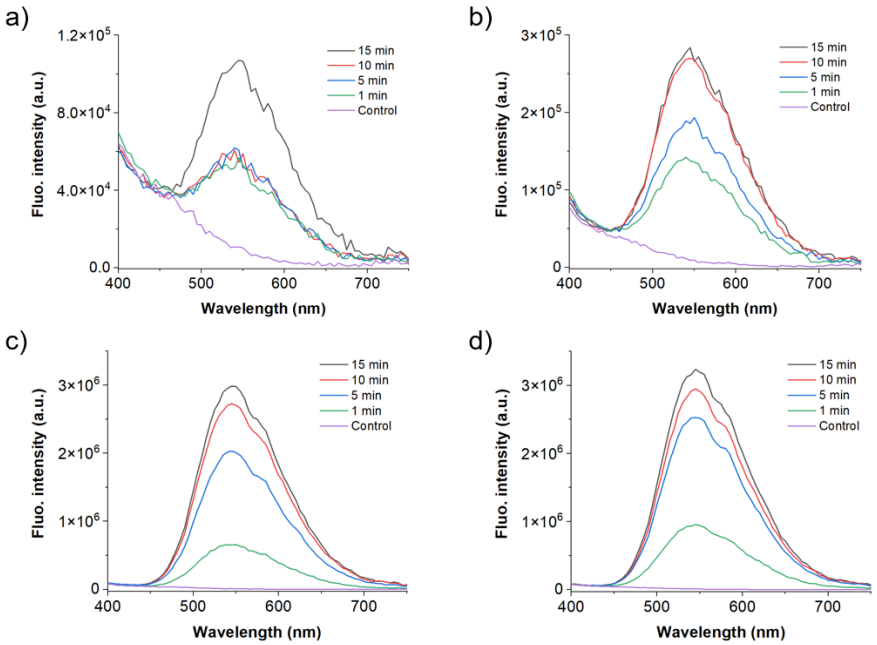

Figure S10. Fluorescence spectra collected from PMBs-MDF under 0.68 MHz irradiations (solvent: MeCN/H_2O). **a**) Focal pressure 500 kPa. **b**) Focal pressure 1000 kPa. **c**) Focal pressure 1500 kPa. **d**) Focal pressure 2000 kPa.

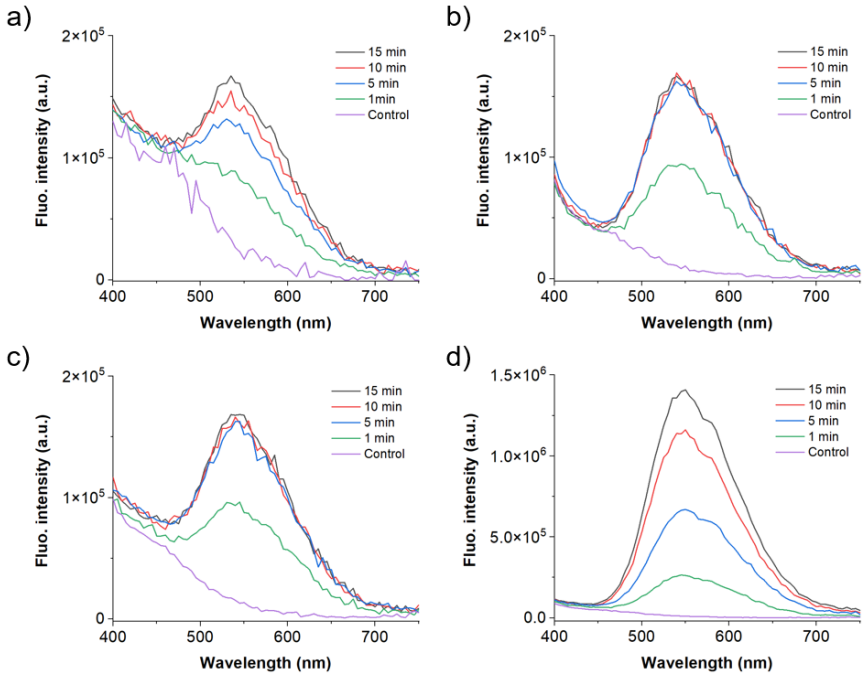

Figure S11. Fluorescence spectra collected from PMBs-MDF under 1.52 MHz irradiations (solvent: MeCN/H_2O). **a**) Focal pressure 500 kPa. **b**) Focal pressure 1000 kPa. **c**) Focal pressure 1500 kPa. **d**) Focal pressure 2000 kPa.

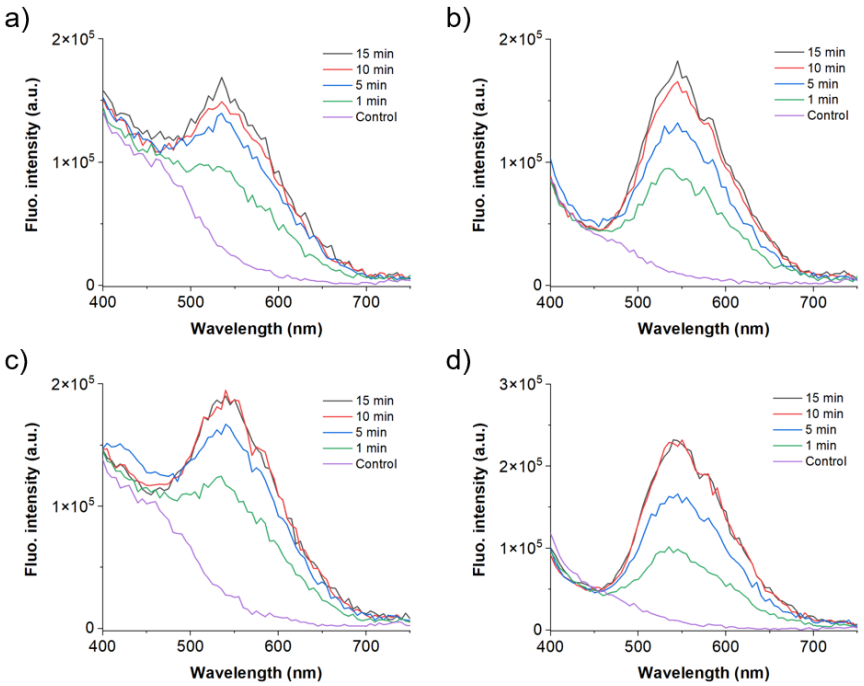

Figure S12. Fluorescence spectra collected from PMBs-MDF under 2.6 MHz irradiations (solvent: MeCN/H_2O). **a**) Focal pressure 500 kPa. **b**) Focal pressure 1000 kPa. **c**) Focal pressure 1500 kPa. **d**) Focal pressure 2000 kPa.

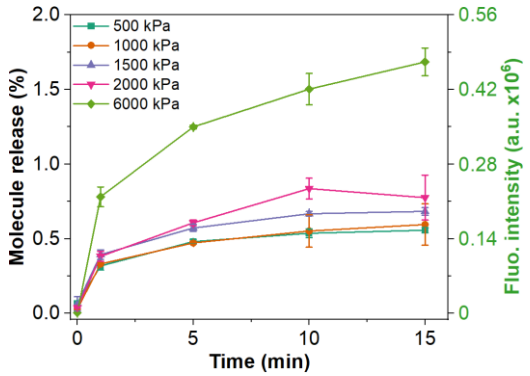

Figure S13. The percentage of fluorophores (**N1-A3**) release from PMBs-MDF with 2.6 MHz ultrasound irradiation.

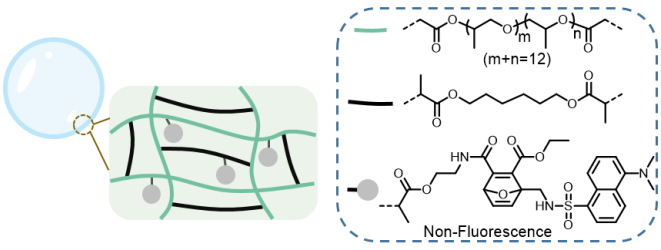

Figure S14. Schematic representation of the shell structure of PMBs without disulfide mechanophores.

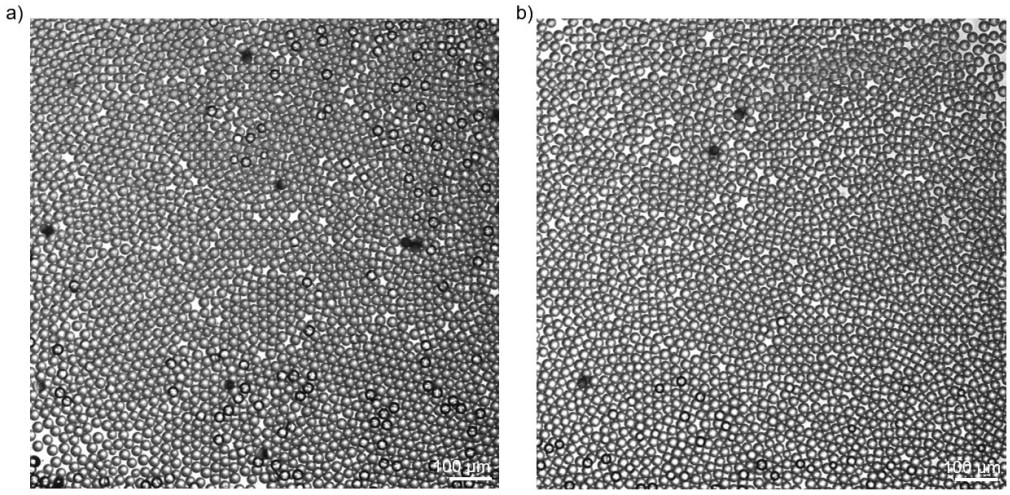

Figure S15. Optical micrograph of microgels, **a**) before sonication **b**) after sonication (20 kHz, 15 min).

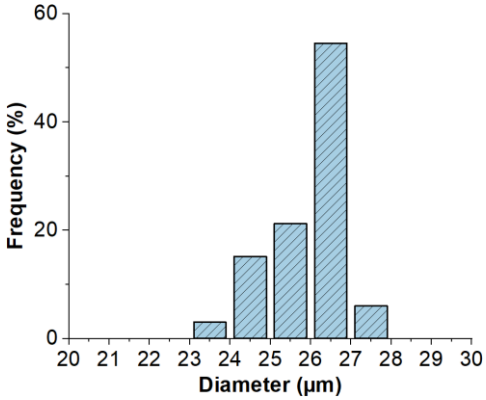

Figure S16. Size distribution of microgels. 200 microgels were analyzed.

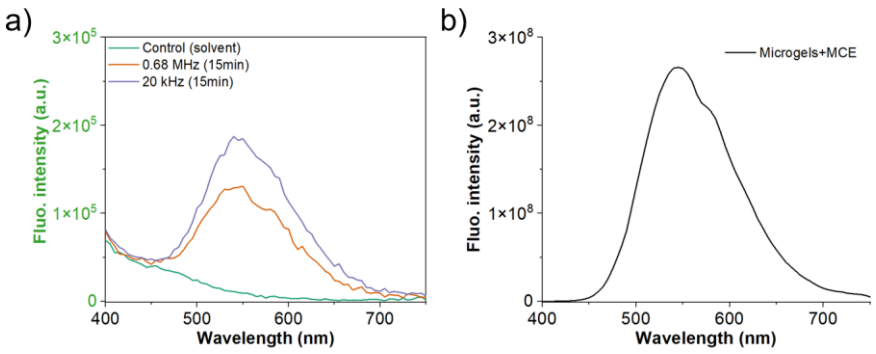

Figure S17. a) The fluorescence spectra of microgels treated with US irradiation (20 kHz, 12 W cm^{-2}; 0.68 MHz, 2000 kPa). **b**) The fluorescence spectra of microgels mixed with an excess of MCE (solvent: $MeCN/H_2O$).

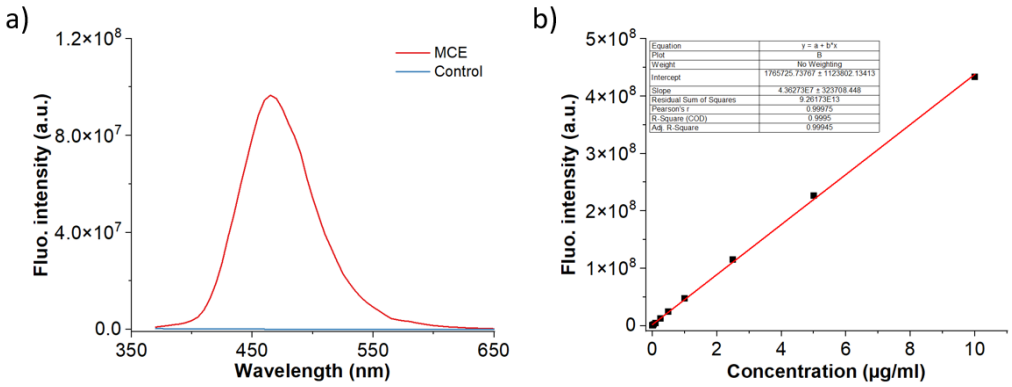

Figure S18. a) Fluorescence spectrum of PMBs-UMB mixed with an excess of MCE (solvent: DMSO/H_2O). **b**) UMB standard curve (fluorescence intensity collected at 465 nm, Ex: 325 nm).

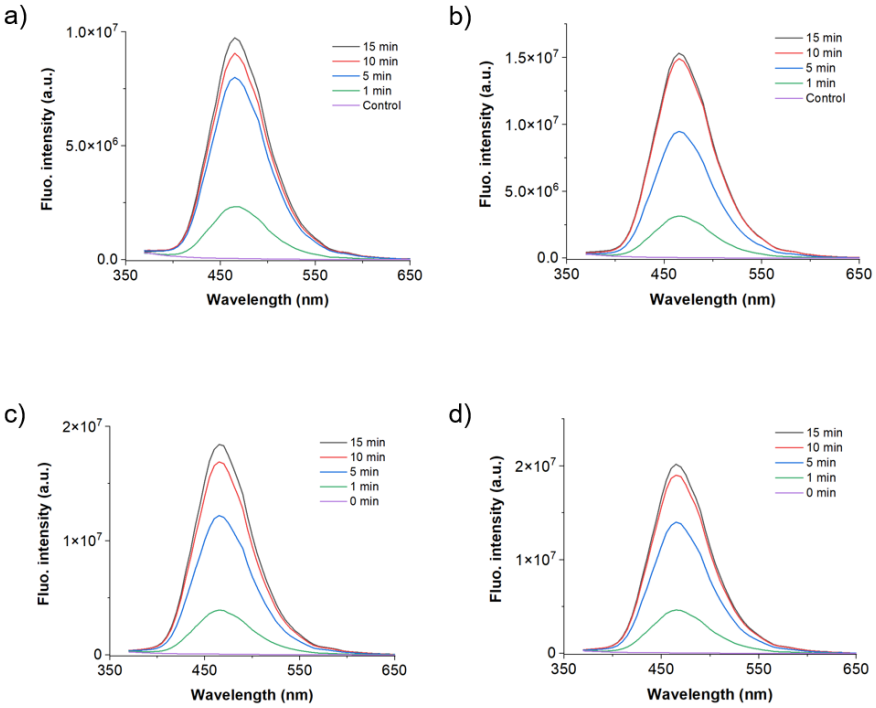

Figure S19. Fluorescence spectra collected from PMBs-UMB under 20 kHz ultrasound irradiations (solvent: DMSO/H_2O). **a**) Sound intensity, 1 W cm^{-2}. **b**) Sound intensity, 3 W cm^{-2}. **c**) Sound intensity, 6 W cm^{-2}. **d**) Sound intensity, 12 W cm^{-2}.

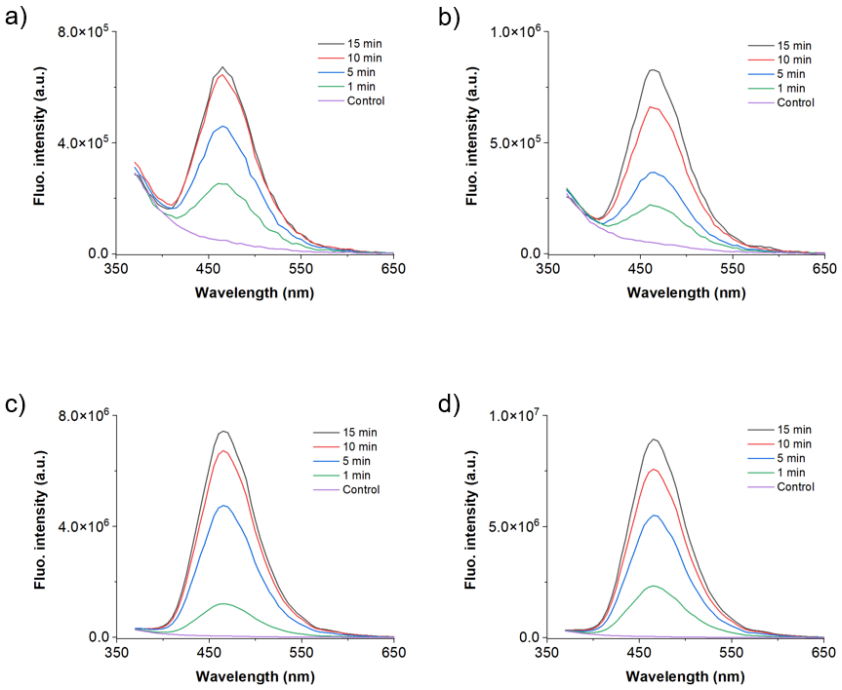

Figure S20. Fluorescence spectra collected from PMBs-UMB under 0.68 MHz ultrasound irradiation (solvent: DMSO/H_2O). **a**) Focal pressure 500 kPa. **b**) Focal pressure 1000 kPa. **c**) Focal pressure 1500 kPa. **d**) Focal pressure 2000 kPa.

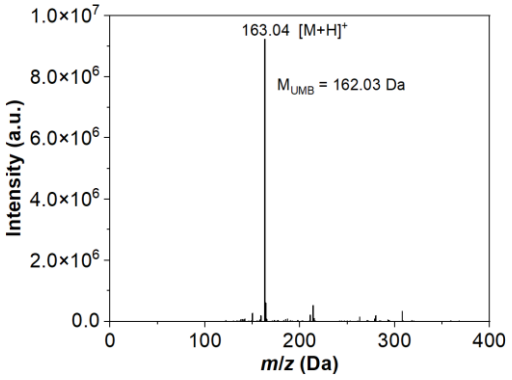

Figure S21. Molar mass of released UMB as determined by mass spectrometry.

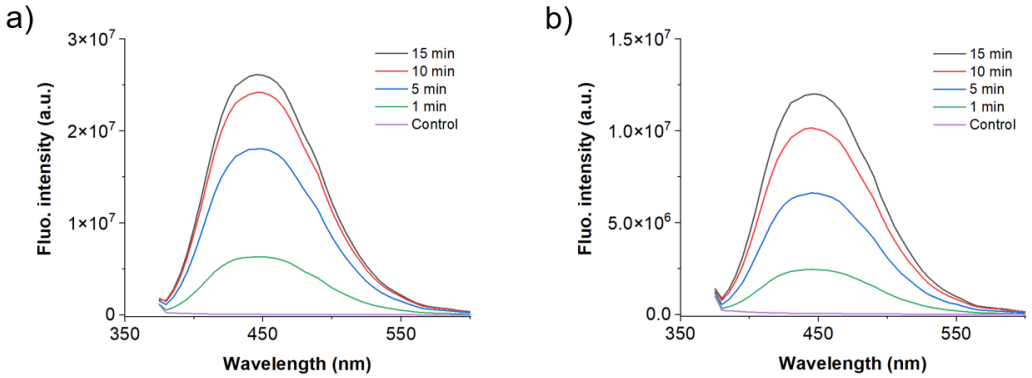

Figure S22. Fluorescence spectra collected from PMBs-CPT samples (solvent: DMSO/H_2O) under **a**) 20 kHz sonication (12 W cm^{-2}) and **b**) 0.68 MHz ultrasound irradiation (2000 kPa).

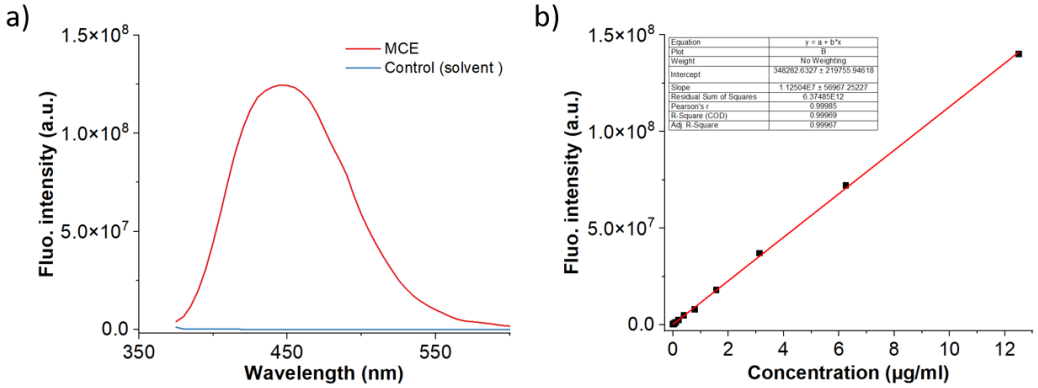

Figure S23. a) The fluorescence intensity of PMBs-CPT mixed with an excess of MCE (solvent: DMSO/H_2O). **b**) CPT standard curve (fluorescence intensity collected at 450 nm, Ex: 335 nm).

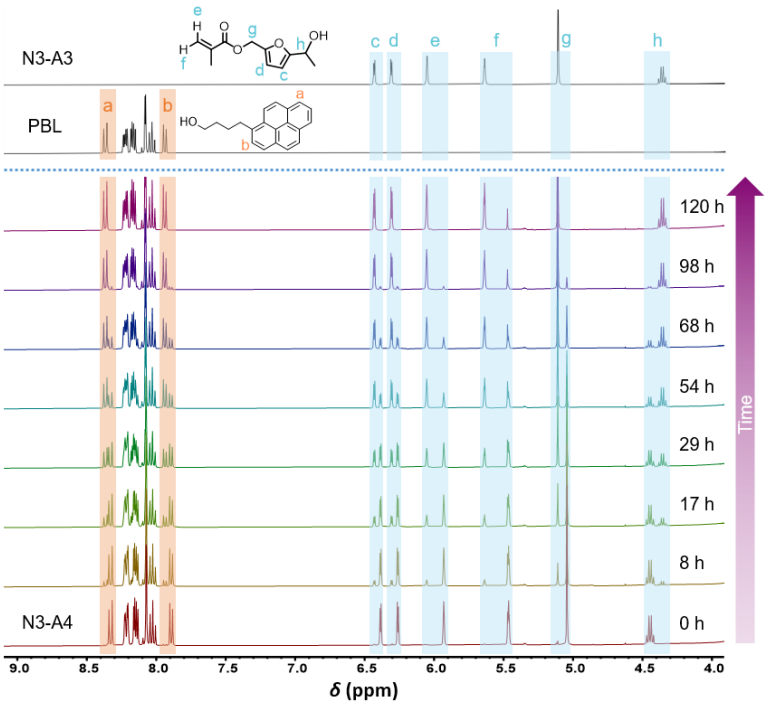

Figure S24. ^{1}H NMR spectra demonstrating the conversion of **N3-A4** into **N3-A3** and PBL at 23 °C (5 mg **N3-A4** in 0.5 mL solvent (MeCN-d_3:MeOH:H_2O, 3:1:0.5)).

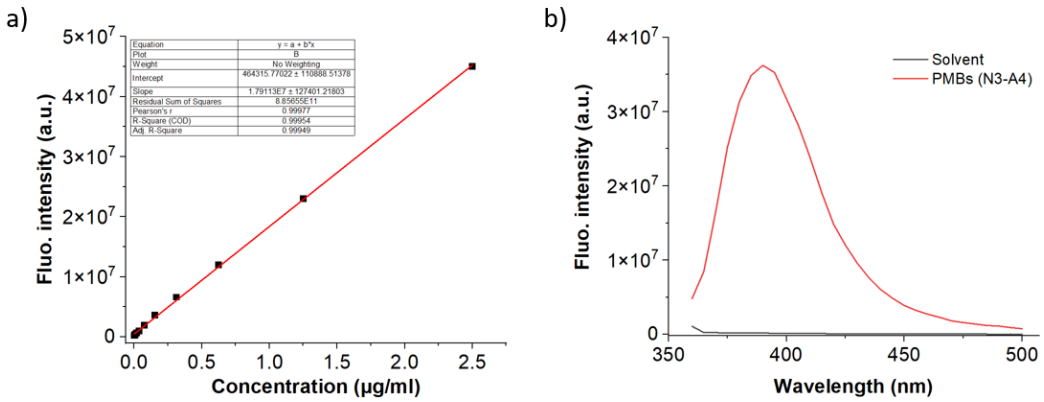

Figure S25. a) PBL standard curve in MeCN/MeOH/H_2O (fluorescence intensity collected at 390 nm, Ex: 320 nm). **b**) The fluorescence spectra from the PMBs that contain **N3-A4** for the quantification of PBL release.

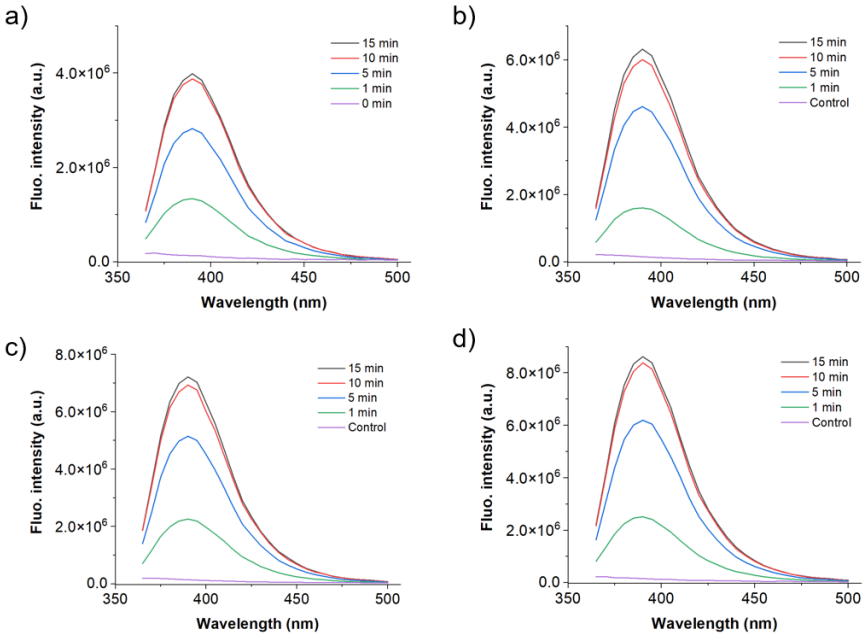

Figure S26. Fluorescence spectra collected from PMBs-PBL samples under 20 kHz ultrasound irradiations (solvent: MeCN/MeOH/H_2O). **a**) Sound intensity, 1 W cm^{-2}. **b**) Sound intensity, 3 W cm^{-2}. **c**) Sound intensity, 6 W cm^{-2}. **d**) Sound intensity, 12 W cm^{-2}.

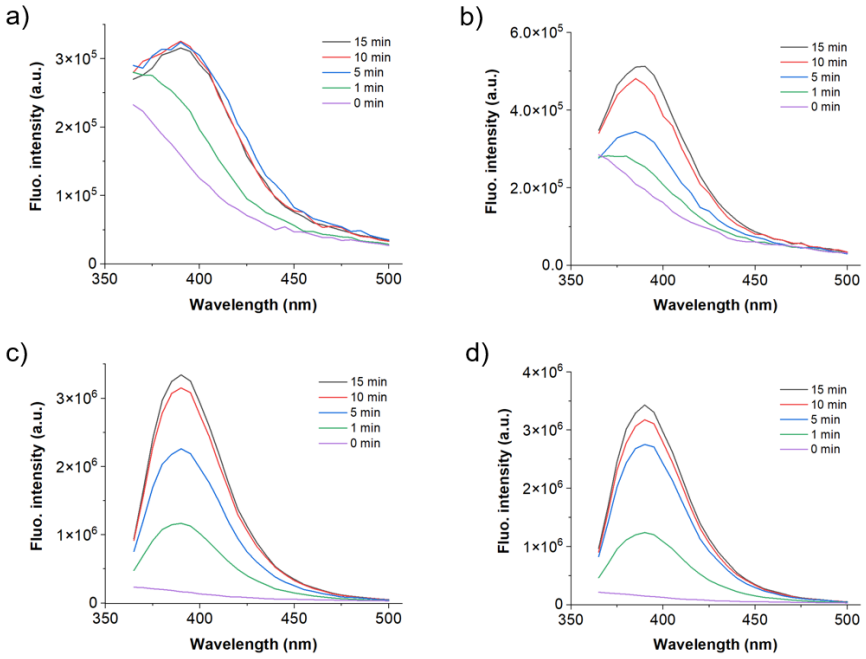

Figure S27. Fluorescence spectra collected from PMBs-PBL samples under 0.68 MHz ultrasound irradiation (solvent: MeCN/MeOH/H_2O). **a**) Focal pressure 500 kPa. **b**) Focal pressure 1000 kPa. **c**) Focal pressure 1500 kPa. **d**) Focal pressure 2000 kPa.

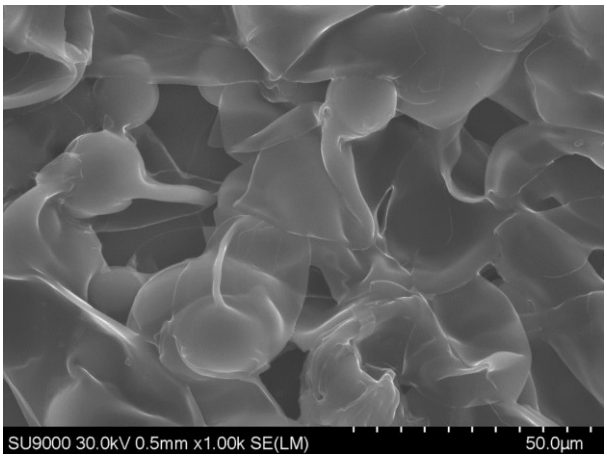

Figure S28. SEM image of fragments of PMBs-Flex. The shell thickness of PMBs was around 180 nm.

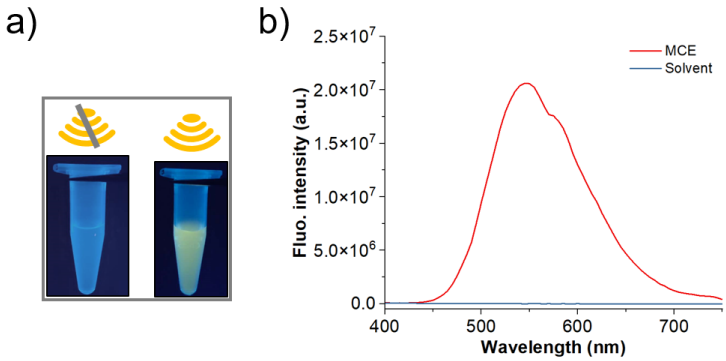

Figure S29. a) Photographs of the filtered PMBs solution, PMBs before and after ultrasound irradiation (20 kHz, 15 min; solvent: MeCN/H_2O, 365 nm UV illumination). **b**) Fluorescence spectra from PMBs-Flex mixed with an excess of MCE.

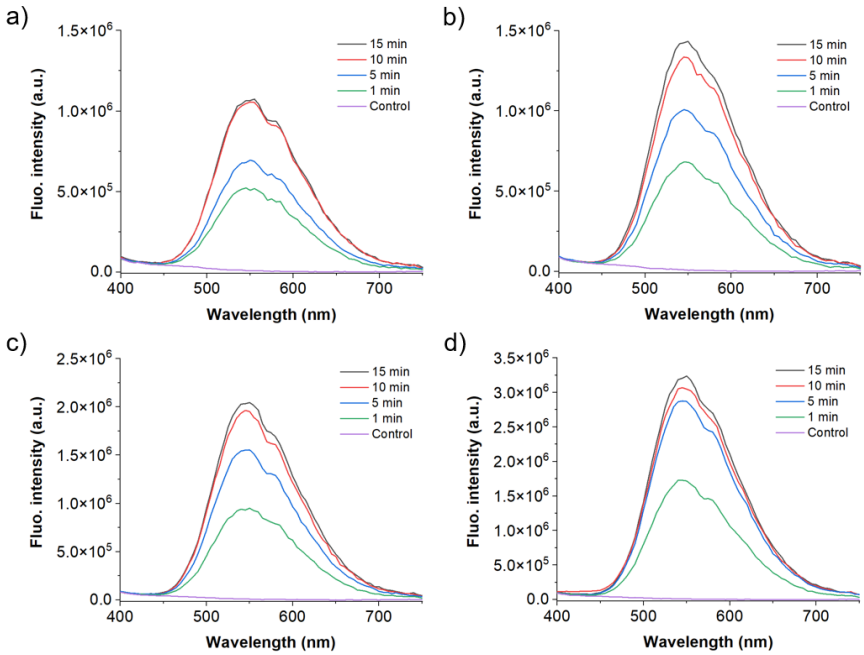

Figure S30. Fluorescence spectra collected from PMBs-Flex samples under 20 kHz ultrasound irradiation (solvent: MeCN/H_2O). **a**) Sound intensity, 1 W cm^{-2}. **b**) Sound intensity, 3 W cm^{-2}. **c**) Sound intensity, 6 W cm^{-2}. **d**) Sound intensity, 12 W cm^{-2}.

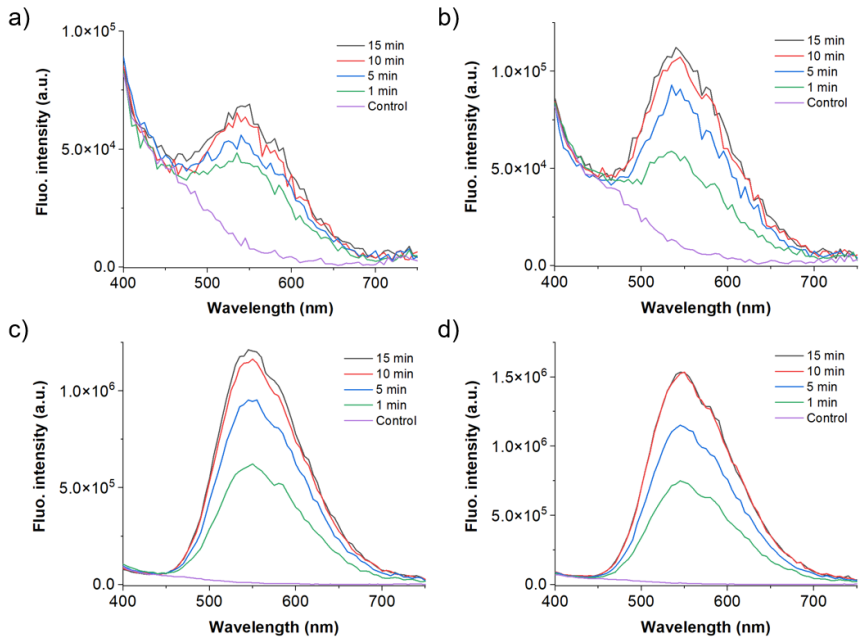

Figure S31. Fluorescence spectra collected from PMBs-Flex samples under 0.68 MHz ultrasound irradiation (solvent: MeCN/H_2O). **a**) Focal pressure 500 kPa. **b**) Focal pressure 1000 kPa. **c**) Focal pressure 1500 kPa. **d**) Focal pressure 2000 kPa.

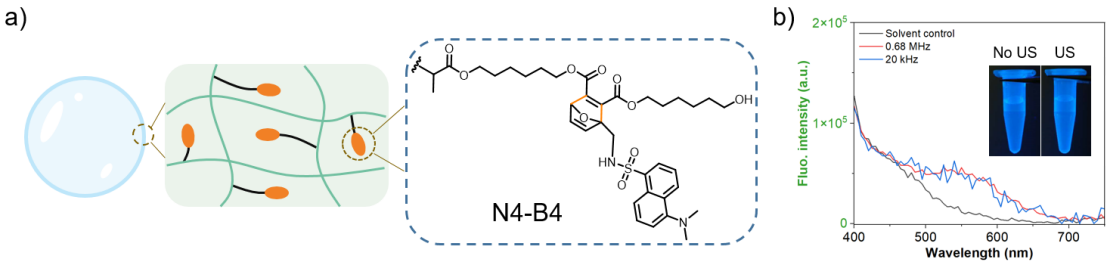

Figure S32. PMBs that contain acrylate-mechanophores (**N4-B4**) with only one polymerizable unit. **a**) Schematic structure of the polymeric shell. **b**) Fluorescence spectra of PMBs before and after US irradiation (20 kHz, 15min). Insets: photographs of the filtered solution of sonicated PMBs (20 kHz, solvent: MeCN/H_2O), under 365 nm UV illumination.

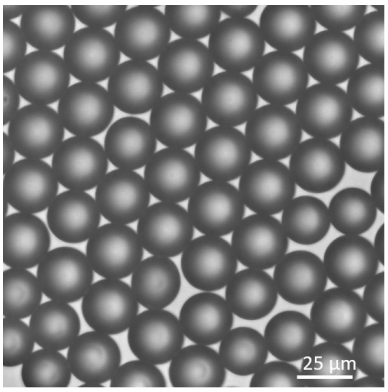

Figure S33. Optical micrograph of Microgels-Flex.

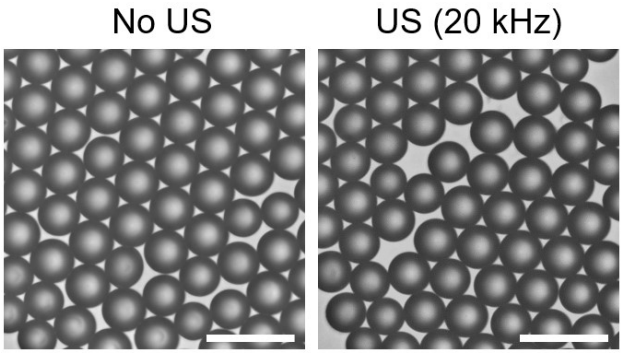

Figure S34. Optical brightfield micrograph of microgels before and after 5 min US irradiation (scale bar: 50 µm).

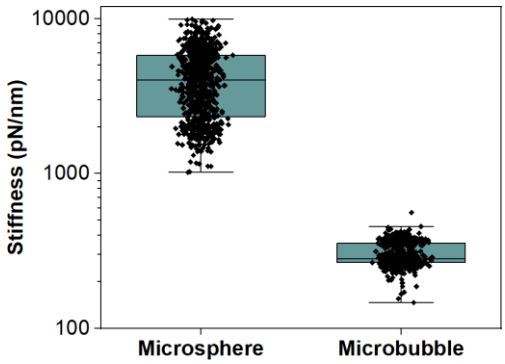

Figure S35. Stiffness of PMB-Flex and Microgels-Flex measured by AFM.

Table S1. The corresponding US intensity values of ultrasonic amplitudes.

Ultrasonic amplitude	35%	53%	75%	99%
Sound Intensity (*I*)	1.0 W/cm^2	3.0 W/cm^2	6.0 W/cm^2	12.0 W/cm^2

Table S2. HIFU intensity and mechanical index of 0.68 MHz, 1.52 MHz and 2.6 MHz transducer.

Frequency	Focal pressure	Focal sound intensity (*I*)	Acoustic power	Mechanical index (MI)
0.68 MHz	500 kPa	8.4 W/cm^2	1.34 W	0.6
	1000 kPa	33.6 W/cm^2	5.37 W	1.2
	1500 kPa	75.5 W/cm^2	12.08 W	1.8
	2000 kPa	134.2 W/cm^2	21.48 W	2.4
1.52 MHz	500 kPa	8.4 W/cm^2	0.12 W	0.4
	1000 kPa	33.6 W/cm^2	0.47 W	0.8
	1500 kPa	75.5W/cm^2	1.05 W	1.2
	2000 kPa	134.2 W/cm^2	1.87 W	1.6
2.6 MHz	500 kPa	8.4 W/cm^2	0.04 W	0.3
	1000 kPa	33.6 W/cm^2	0.16 W	0.6
	1500 kPa	75.5W/cm^2	0.37 W	0.9
	2000 kPa	134.2 W/cm^2	0.66 W	1.2

Table S3. Data points measured to plot Figure 3k of the manuscript. All values ± standard deviation.

Concentration (μM)	Control (PBS)	PMBs fragments	CPT	CPT+US	PMBs+US (15 min)
32	100.1 ± 2.0	68.0 ± 10.9	1.9 ± 0.7	0.6 ± 0.3	4.2 ± 0.3
16	99.3 ± 1.0	86.9 ± 9.1	8.7 ± 0.4	6.8 ± 1.5	22.8 ± 1.9
8	100.7± 1.5	95.8 ± 5.5	26.0 ± 2.7	25.3 ± 2.7	36.6 ± 2.9
4	99.8 ± 0.6	94.4 ± 7.4	37.9 ± 3.8	41.4 ± 2.9	42.3 ± 4.7
2	100.4 ± 5.0	94.7 ± 6.2	44.0 ± 1.0	47.5 ± 2.5	47.2 ± 4.6
1	97.8 ± 1.3	95.1 ± 5.8	49.2 ± 1.5	53.3 ± 1.6	49.8 ± 7.5
0.5	98.7 ± 1.5	93.7 ± 6.5	51.3 ± 2.5	57.9 ± 2.3	54.7 ± 7.9
0.25	100.0 ± 2.5	94.8 ± 6.8	58.0 ± 2.6	64.4 ± 2.4	67.3 ± 10.7
0.125	99.7 ± 2.3	97.8 ± 5.1	72.2 ± 1.0	76.3 ± 2.7	87.2 ± 6.1
0.0625	96.3 ± 0.8	94.8 ± 7.8	91.4 ± 0.5	92.2 ± 2.3	99.1 ± 1.2

5.7 References

1. Jochum, F. D., & Theato, P. (2013). Temperature-and light-responsive smart polymer materials. *Chemical Society Reviews*, *42*(17), 7468-7483.

2. Davis, D. A. et al. (2009). Force-induced activation of covalent bonds in mechanoresponsive polymeric materials. *Nature*, *459*, 68-72.

3. Klaikherd, A., Nagamani, C., & Thayumanavan, S. (2009). Multi-Stimuli Sensitive Amphiphilic Block Copolymer Assemblies. *Journal of the American Chemical Society*, *131*(13), 4830-4838.

4. Du, J. Z., Du, X. J., Mao, C. Q. & Wang, J. (2011). Tailor-made dual pH-sensitive polymer–doxorubicin nanoparticles for efficient anticancer drug delivery. *Journal of the American Chemical Society*, *133*(44), 17560-17563.

5. Li, J., Nagamani, C. & Moore, J. S. (2015). Polymer mechanochemistry: from destructive to productive. *Accounts of Chemical Research*, *48*(8), 2181-2190.

6. Shafranek, R. T., Millik, S. C., Smith, P. T., Lee, C. U., Boydston, A. J. & Nelson, A. (2019). Stimuli-responsive materials in additive manufacturing. *Progress in Polymer Science*, *93*, 36-67.

7. Piermattei, A., Karthikeyan, S. & Sijbesma, R. P. (2009). Activating catalysts with mechanical force. *Nature Chemistry*, *1*(2), 133-137.

8. Mohapatra, H., Kleiman, M. & Esser-Kahn, A. P. (2017). Mechanically controlled radical polymerization initiated by ultrasound. *Nature Chemistry*, *9*(2), 135-139.

9. McKenzie, T. G., Colombo, E., Fu, Q., Ashokkumar, M. & Qiao, G. G. (2017). Sono-RAFT polymerization in aqueous medium. *Angewandte Chemie International Edition*, *56*(40), 12302-12306.

10. Groote, R., Jakobs, R. T. & Sijbesma, R. P. (2013). Mechanocatalysis: forcing latent catalysts into action. *Polymer Chemistry*, *4*(18), 4846-4859.

11. Qian, H. et al. (2021). Fast, reversible mechanochromism of regioisomeric oxazine mechanophores: Developing in situ responsive force probes for polymeric materials. *Chem*, *7*(4), 1080-1091.

12. Chen, Z. et al. (2022). Stress-dependent multicolor mechanochromism in epoxy thermosets based on rhodamine and diaminodiphenylmethane mechanophores. *Macromolecules*, *55*(6), 2310-2319.

13. Brantley, J. N., Bailey, C. B., Wiggins, K. M., Keatinge-Clay, A. T. & Bielawski, C. W. (2013). Mechanobiochemistry: harnessing biomacromolecules for force-responsive materials. *Polymer Chemistry*, *4*(14), 3916-3928.

14. Shi, Z., Wu, J., Song, Q., Göstl, R. & Herrmann, A. (2020). Toward drug release using polymer mechanochemical disulfide scission. *Journal of the American Chemical Society*, *142*(34), 14725-14732.

15. Huo, S. et al. (2021). Mechanochemical bond scission for the activation of drugs. *Nature Chemistry*, *13*(2), 131-139.

16. Küng, R., Pausch, T., Rasch, D., Göstl, R. & Schmidt, B. M. (2021). Mechanochemical release of non-covalently bound guests from a polymer-decorated supramolecular cage. *Angewandte Chemie International Edition*, *60*(24), 13626-13630.

17. Yao, Y. et al. (2023). Remote control of mechanochemical reactions under physiological conditions using biocompatible focused ultrasound. *Proceedings of the National Academy of Sciences*, *120*(39), e2309822120.

18. Chen, G., Cui, Y. & Chen, X. (2019). Proactively modulating mechanical behaviors of materials at multiscale for mechano-adaptable devices. *Chemical Society Reviews*, *48*(6), 1434-1447.

19. Suslick, K. S. (1990). Sonochemistry. *Science*, *247*, 1439-1445.
20. O'Neill, R. T. & Boulatov, R. (2023). Experimental quantitation of molecular conditions responsible for flow-induced polymer mechanochemistry. *Nature Chemistry*, *15*(9), 1214-1223.
21. Chen, Z. et al. (2017). Mechanochemical unzipping of insulating polyladderene to semiconducting polyacetylene. *Science*, *357*, 475-479.
22. Boswell, B. R. et al. (2021). Mechanochemical synthesis of an elusive fluorinated polyacetylene. *Nature Chemistry*, *13*(1), 41-46.
23. Zhao, P. et al. (2021). Activation of the Catalytic Activity of Thrombin for Fibrin Formation by Ultrasound. *Angewandte Chemie International Edition*, *60*(26), 14707-14714.
24. Kim, G. et al. (2022). Ultrasound controlled mechanophore activation in hydrogels for cancer therapy. *Proceedings of the National Academy of Sciences*, *119*(4), e2109791119.
25. Li, J. et al. (2022). Precision cancer sono-immunotherapy using deep-tissue activatable semiconducting polymer immunomodulatory nanoparticles. *Nature Communications*, *13*(1), 4032.
26. May, P. A. & Moore, J. S. (2013). Polymer mechanochemistry: techniques to generate molecular force via elongational flows. *Chemical Society Reviews*, *42*(18), 7497-7506.
27. Klukovich, H. M., Kouznetsova, T. B., Kean, Z. S., Lenhardt, J. M. & Craig, S. L. (2013). A backbone lever-arm effect enhances polymer mechanochemistry. *Nature Chemistry*, *5*(2), 110-114.
28. Chen, Y., Spiering, A. J. H., Karthikeyan, S., Peters, G. W., Meijer, E. W. & Sijbesma, R. P. (2012). Mechanically induced chemiluminescence from polymers incorporating a 1, 2-dioxetane unit in the main chain. *Nature Chemistry*, *4*(7), 559-562.
29. Wu, M., Li, Y., Yuan, W., De Bo, G., Cao, Y. & Chen, Y. (2022). Cooperative and geometry-dependent mechanochromic reactivity through aromatic fusion of two rhodamines in polymers. *Journal of the American Chemical Society*, *144*(37), 17120-17128.
30. Zhang, M. & De Bo, G. (2018). Impact of a mechanical bond on the activation of a mechanophore. *Journal of the American Chemical Society*, *140*(40), 12724-12727.
31. Overholts, A. C., Granados Razo, W. & Robb, M. J. (2023). Mechanically gated formation of donor-acceptor Stenhouse adducts enabling mechanochemical multicolour soft lithography. *Nature Chemistry*, *15*(3), 332-338.
32. Noh, J., Peterson, G. I. & Choi, T. L. (2021). Mechanochemical reactivity of bottlebrush and dendronized polymers: solid vs. solution states. *Angewandte Chemie International Edition*, *60*(34), 18651-18659.
33. Noh, J., Koo, M. B., Jung, J., Peterson, G. I., Kim, K. T. & Choi, T. L. (2023). Monodisperse cyclic polymer mechanochemistry: Scission kinetics and the dynamic memory effect with ultrasonication and ball-mill grinding. *Journal of the American Chemical Society*, *145*(33), 18432-18438.
34. Lin, Y., Zhang, Y., Wang, Z. & Craig, S. L. (2019). Dynamic memory effects in the mechanochemistry of cyclic polymers. *Journal of the American Chemical Society*, *141*(28), 10943-10947.
35. Church, D. C., Peterson, G. I. & Boydston, A. J. (2014). Comparison of mechanochemical chain scission rates for linear versus three-arm star polymers in strong acoustic fields. *ACS Macro Letters*, *3*(7), 648-651.
36. Oka, H., Imato, K., Sato, T., Ohishi, T., Goseki, R. & Otsuka, H. (2016). Enhancing mechanochemical activation in the bulk state by designing polymer architectures. *ACS Macro Letters*, *5*(10), 1124-1127.
37. Peterson, G. I., Lee, J. & Choi, T. L. (2019). Multimechanophore graft polymers: mechanochemical reactions at backbone-arm junctions. *Macromolecules*, *52*(24), 9561-9568.

38. Li, Y. et al. (2016). Sonication-induced scission of molecular bottlebrushes: Implications of the “hairy” architecture. *Polymer*, *84*, 178-184.

39. Zou, M., Zhao, P., Huo, S., Göstl, R. & Herrmann, A. (2022). Activation of antibiotic-grafted polymer brushes by ultrasound. *ACS Macro Letters*, *11*(1), 15-19.

40. Peterson, G. I., Bang, K. T. & Choi, T. L. (2018). Mechanochemical degradation of denpols: synthesis and ultrasound-induced chain scission of polyphenylene-based dendronized polymers. *Journal of the American Chemical Society*, *140*(27), 8599-8608.

41. Watabe, T., Ishizuki, K., Aoki, D. & Otsuka, H. (2019). Mechanochromic dendrimers: the relationship between primary structure and mechanochromic properties in the bulk. *Chemical Communications*, *55*(48), 6831-6834.

42. Watabe, T., Aoki, D. & Otsuka, H. (2021). Enhancement of mechanophore activation in mechanochromic dendrimers by functionalization of their surface. *Macromolecules*, *54*(4), 1725-1731.

43. Zou, M., Zhao, P., Fan, J., Göstl, R. & Herrmann, A. (2022). Microgels as drug carriers for sonopharmacology. *Journal of Polymer Science*, *60*(12), 1864-1870.

44. Izak-Nau, E., Braun, S., Pich, A. & Göstl, R. (2022). Mechanically resistant poly (N-vinylcaprolactam) microgels with sacrificial supramolecular catechin hydrogen bonds. *Advanced Science*, *9*(12), 2104004.

45. Kharandiuk, T. et al. (2022). Mechanoresponsive diselenide-crosslinked microgels with programmed ultrasound-triggered degradation and radical scavenging ability for protein protection. *Chemical Science*, *13*(38), 11304-11311.

46. Kiessling, F., Fokong, S., Koczera, P., Lederle, W. & Lammers, T. (2012). Ultrasound microbubbles for molecular diagnosis, therapy, and theranostics. *Journal of Nuclear Medicine*, *53*(3), 345-348.

47. Lammers, T. et al. (2015). Theranostic USPIO-loaded microbubbles for mediating and monitoring blood-brain barrier permeation. *Advanced Functional Materials*, *25*(1), 36-43.

48. Athanassiadis, A. G. et al. (2022). Ultrasound-responsive systems as components for smart materials. *Chemical Reviews*, *122*(5), 5165-5208.

49. Li, X. et al. (2022). Cancer immunotherapy based on image-guided STING activation by nucleotide nanocomplex-decorated ultrasound microbubbles. *Nature Nanotechnology*, *17*(8), 891-899.

50. Xuan, M. et al. (2023). Polymer Mechanochemistry in Microbubbles. *Advanced Materials*, *35*(47), 2305130.

51. Shi, Z., Song, Q., Göstl, R., & Herrmann, A. (2021). Mechanochemical activation of disulfide-based multifunctional polymers for theranostic drug release. *Chemical Science*, *12*(5), 1668-1674.

52. Shi, Z., Song, Q., Göstl, R., & Herrmann, A. (2021). The Mechanochemical Release of Naphthalimide Fluorophores from β-Carbonate and β-Carbamate Disulfide-Centered Polymers. *CCS Chemistry*, *3*(11), 2333-2344.

53. Hu, X., Zeng, T., Husic, C. C. & Robb, M. J. (2019). Mechanically Triggered Small Molecule Release from a Masked Furfuryl Carbonate. *Journal of the American Chemical Society*, *141*(38), 15018-15023.

54. Larsen, M. B. & Boydston, A. J. (2013). “Flex-Activated” Mechanophores: Using Polymer Mechanochemistry To Direct Bond Bending Activation. *Journal of the American Chemical Society*, *135*(22), 8189-8192.

55. Larsen, M. B., & Boydston, A. J. (2014). Successive mechanochemical activation and small molecule release in an elastomeric material. *Journal of the American Chemical Society*, *136*(4), 1276-1279.

56. Cao, B., Boechler, N., & Boydston, A. J. (2018). Additive manufacturing with a flex activated mechanophore for nondestructive assessment of mechanochemical reactivity in complex object geometries. *Polymer*, *152*, 4-8.
57. Shen, H., Larsen, M. B., Roessler, A. G., Zimmerman, P. M. & Boydston, A. J. (2021). Mechanochemical Release of N-Heterocyclic Carbenes from Flex-Activated Mechanophores. *Angewandte Chemie International Edition*, *60*, 13559-13563.
58. Yang, F., Geng, T., Shen, H., Kou, Y., Xiao, G., Zou, B. & Chen, Y. (2023). Mechanochemical Release of Fluorophores from a "Flex-activated" Mechanophore. *Angewandte Chemie International Edition*, *62*(39), e202308662.
59. Hong, V., Kislukhin, A. A. & Finn, M. G. (2009). Thiol-selective fluorogenic probes for labeling and release. *Journal of the American Chemical Society*, *131*(29), 9986-9994.
60. Hu, X., Zeng, T., Husic, C. C., & Robb, M. J. (2021). Mechanically triggered release of functionally diverse molecular payloads from masked 2-furylcarbinol derivatives. *ACS Central Science*, *7*(7), 1216-1224.
61. Jayathilaka, P. B., Molley, T. G., Huang, Y., Islam, M. S., Buche, M. R., Silberstein, M. N., Kruzic, J. J. & Kilian, K. A. (2021). Force-mediated molecule release from double network hydrogels. *Chemical Communications*, *57*, 8484-8487.
62. Ong, M. T., Leiding, J., Tao, H., Virshup, A. M., & Martínez, T. J. (2009). First principles dynamics and minimum energy pathways for mechanochemical ring opening of cyclobutene. *Journal of the American Chemical Society*, *131*(18), 6377-6379.
63. Mier, L. J., Adam, G., Kumar, S., & Stauch, T. (2020). The Mechanism of Flex-Activation in Mechanophores Revealed By Quantum Chemistry. *ChemPhysChem*, *21*(21), 2402-2406.
64. Klein, I. M., Husic, C. C., Kovács, D. P., Choquette, N. J., & Robb, M. J. (2020). Validation of the CoGEF method as a predictive tool for polymer mechanochemistry. *Journal of the American Chemical Society*, *142*(38), 16364-16381.
65. Subramanian, G., Mathew, N., & Leiding, J. (2015). A generalized force-modified potential energy surface for mechanochemical simulations. *The Journal of Chemical Physics*, *143*(13), 134109.
66. O'Neill, R. T., & Boulatov, R. (2024). Mechanochemical Approaches to Fundamental Studies in Soft-Matter Physics. *Angewandte Chemie International Edition*, *63*(19), e202402442.
67. Lloyd, E. M., Vakil, J. R., Yao, Y., Sottos, N. R., & Craig, S. L. (2023). Covalent mechanochemistry and contemporary polymer network chemistry: a marriage in the making. *Journal of the American Chemical Society*, *145*(2), 751-768.
68. Becke, A. D. (1993). Density-functional thermochemistry. III. the role of exact exchange. *The Journal of Chemical Physics*, *96*(3), 2155-2160.
69. Vosko, S. H., Wilk, L., & Nusair, M. (1980). Accurate spin-dependent electron liquid correlation energies for local spin density calculations: a critical analysis. *Canadian Journal of Physics*, *58*(8), 1200-1211.
70. Stephens, P. J., Devlin, F. J., Chabalowski, C. F., & Frisch, M. J. (1994). Ab initio calculation of vibrational absorption and circular dichroism spectra using density functional force fields. *The Journal of Physical Chemistry*, *98*(45), 11623-11627.
71. Grimme, S., Antony, J., Ehrlich, S., & Krieg, H. (2010). A consistent and accurate ab initio parametrization of density functional dispersion correction (DFT-D) for the 94 elements H-Pu. *The Journal of Chemical Physics*, *132*(15), 154104.

72. Ditchfield, R., Hehre, W. J., & Pople, J. A. (1971). Self-consistent molecular-orbital methods. IX. An extended Gaussian-type basis for molecular-orbital studies of organic molecules. *The Journal of Chemical Physics*, *54*(2), 724-728.

73. Hariharan, P. C., & Pople, J. A. (1973). The influence of polarization functions on molecular orbital hydrogenation energies. *Theoretica Chimica Acta*, *28*, 213-222.

74. Hehre, W. J., Ditchfield, R., & Pople, J. A. (1972). Self-consistent molecular orbital methods. XII. Further extensions of Gaussian-type basis sets for use in molecular orbital studies of organic molecules. *The Journal of Chemical Physics*, *56*(5), 2257-2261.

75. Seritan, S. et al. (2020). TeraChem: Accelerating electronic structure and ab initio molecular dynamics with graphical processing units. *The Journal of Chemical Physics*, *152*(22), 224110.

76. Seritan, S. et al. (2021). TeraChem: A graphical processing unit-accelerated electronic structure package for large-scale ab initio molecular dynamics. *Wiley Interdisciplinary Reviews: Computational Molecular Science*, *11*(2), e1494.

77. Kästner, J., Carr, J. M., Keal, T. W., Thiel, W., Wander, A., & Sherwood, P. (2009). DL-FIND: an open-source geometry optimizer for atomistic simulations. *The Journal of Physical Chemistry A*, *113*(43), 11856-11865.

78. Henkelman, G., & Jónsson, H. (1999). A dimer method for finding saddle points on high dimensional potential surfaces using only first derivatives. *The Journal of Chemical Physics*, *111*(15), 7010-7022.

79. Kästner, J., & Sherwood, P. (2008). Superlinearly converging dimer method for transition state search. *The Journal of Chemical Physics*, *128*(1), 014106.

80. Dutta, K., Kanjilal, P., Das, R., & Thayumanavan, S. (2021). Synergistic Interplay of Covalent and Non-Covalent Interactions in Reactive Polymer Nanoassembly Facilitates Intracellular Delivery of Antibodies. *Angew. Chem. Int. Ed. 60*, 1821-1830.

81. Liu, B., Wu, R., Gong, S., Xiao, H., & Thayumanavan, S. (2020). In situ formation of polymeric nanoassemblies using an efficient reversible click reaction. *Angew. Chem. Int. Ed. 59*, 15135-15140.

PUBLICATIONS

1. **Jilin Fan**, Mingjun Xuan, Pengkun Zhao, Mark Loznik, Junlin Chen, Fabian Kiessling, Lifei Zheng*, Andreas Herrmann*. Ultrasound responsive microcapsules for antibacterial nanodrug delivery. *Nano Res.* **2023**, *16*, 2738-2748.

2. **Jilin Fan**, Kuan Zhang, Mingjun Xuan*, Xiang Gao, Rostislav Vinokur, Robert Göstl, Lifei Zheng*, Andreas Herrmann*. High-Intensity Focused Ultrasound-Induced Disulfide Mechanophore Activation in Polymeric Nanostructures for Molecule Release. *CCS Chem.* **2024**, *6*, 1895-1907.

3. **Jilin Fan**, Mingjun Xuan*, Kuan Zhang, Rostislav Vinokur, Lifei Zheng, Robert Göstl, and Andreas Herrmann*. Accelerated Mechanophore Activation and Drug Release in Network Core-structured Star Polymers Using High-Intensity Focused Ultrasound. *Small Science*. **2024**, *4*, 2400082.

4. **Jilin Fan**, Regina Lennarz, Kuan Zhang, Ahmed Mourran, Rostislav Vinokur, Jan Meisner, Mingjun Xuan*, Robert Göstl*, Andreas Herrmann*. Polymeric microbubble is an excellent platform for ultrasound-induced mechanochemical transformations. To be submitted.

5. Deepanshu Sharma, **Jilin Fan**, Metin Kayci*, and Andreas Herrmann*. Oligonucleotide-coated polyelectrolyte microcapsules for ODMR-based sensor platform for detection of nucleic acids. To be submitted.

6. Metin Kayci*, **Jilin Fan**, Onur Bakirman, and Andreas Herrmann*. Multiplexed sensing of biomolecules with optically detected magnetic resonance of nitrogen-vacancy centers in diamond. *PNAS*. **2021**, 118, e2112664118.

7. Mingjun Xuan, **Jilin Fan**, Vu Ngoc Khiêm, Miancheng Zou, Kai-Oliver Brenske, Ahmed Mourran, Rostislav Vinokur, Lifei Zheng, Mikhail Itskov, Robert Göstl*, Andreas Herrmann*. Polymer Mechanochemistry in Microbubbles. *Adv. Mater.* **2023**, *35*, 2305130.

8. Miancheng Zou, Pengkun Zhao, **Jilin Fan**, Robert Göstl, Andreas Herrmann*. Microgels as drug carriers for sonopharmacology. *J Polym Sci.* **2022**, *60*, 1864-1870.

9. Pengkun Zhao, Shuaidong Huo*, **Jilin Fan**, Junlin Chen, Fabian Kiessling, Arnold J. Boersma, Robert Göstl, Andreas Herrmann*. Activation of the Catalytic Activity of Thrombin for Fibrin Formation by Ultrasound. *Angew.Chem.Int.Ed.* **2021**, *60*, 14707-14714.

10. Ming Luo, Mingjun Xuan, Shuaidong Huo, **Jilin Fan**, Gurudas Chakraborty, Yixi Wang, Hui Zhao*, Andreas Herrmann*, Lifei Zheng*. Four-Dimensional Deoxyribonucleic Acid–Gold NanoparticleAssemblies. *Angew. Chem. Int. Ed.* **2020**, *59*, 17250-17255.

11. Hongyan Li, **Jilin Fan**, Eva Miriam Buhl, Shuaidong Huo, Mark Loznik, Robert Göstl*, Andreas Herrmann*. DNA hybridization as a general method to enhance the cellular uptake of nanostructures. *Nanoscale* **2020**, *12*, 21299-21305.